Datation et caractérisation de processus minéralisateurs à l'Archéen : Application à l'Antimony Line, Ceinture de Roches Vertes de Murchison, Afrique du Sud

Justine Jaguin

DATATION ET CARACTERISATION DE PROCESSUS MINERALISATEURS A L'ARCHEEN :

APPLICATION A L'ANTIMONY LINE,

CEINTURE DE ROCHES VERTES DE MURCHISON, AFRIQUE DU SUD

Justine Jaguin

Thèse pour le grade de docteur mention Sciences de la Terre – 2012

N° d'ordre : **ANNÉE 2012**

THÈSE / UNIVERSITÉ DE RENNES 1

sous le sceau de l'Université Européenne de Bretagne

pour le grade de

DOCTEUR DE L'UNIVERSITÉ DE RENNES 1

Mention : Sciences de la Terre

Ecole doctorale Sciences de la matière

présentée par

Justine Jaguin

préparée à l'unité de recherche Géosciences Rennes
OSUR (Observatoire des Sciences de l'Univers) – UMR 6118
U.F.R. Structure et Propriétés de la Matière

Datation et caractérisation de processus minéralisateurs à l'Archéen : Application à l'Antimony Line, Ceinture de Roches Vertes de Murchison, Afrique du Sud

Thèse soutenue à Rennes
le 7 décembre 2012

devant le jury composé de :

Jean-Jacques PEUCAT
Directeur de recherche, OSUR, Université de Rennes 1 / *examinateur*

Didier BEZIAT
Professeur, GET, Université Paul Sabatier, Toulouse / *rapporteur*

Etienne DELOULE
Directeur de recherche, CRPG, Nancy / *rapporteur*

Dominique CHARDON
Professeur, GET, Université Paul Sabatier, Toulouse / *examinateur*

Maarten DE WIT
Professeur, Nelson Mandela Metropolitan University / *examinateur*

Romain BOUSQUET
Professeur, OSUR, Université de Rennes 1 / *examinateur*

Marc POUJOL
Maitre de conférence, OSUR, Université de Rennes 1 / *directeur de thèse*

Philippe BOULVAIS
Maitre de conférence, OSUR, Université de Rennes 1 / *directeur de thèse*

Denis GAPAIS
Directeur de recherche, Université de Rennes 1 / invité

Jean-François MOYEN
Professeur, Université Jean Monnet / invité

REMERCIEMENTS

Mes remerciements vont avant tout à mes deux directeurs, Marc et Philippe. Ils m'ont pris sous leur aile dès la licence au fin-fond des mines d'Afrique du Sud, expérience radicale pour créer des liens. Puis ils m'ont préparé ce sujet de thèse. Ils ont partagé avec moi leur savoir-faire, leur rigueur, leur culture géologique et surtout leur enthousiasme. Merci à tous les deux !

Je suis reconnaissante aux membres du jury qui ont accepté de relire et juger ce travail : Jean-Jacques Peucat pour ses conseils patients ; Didier Béziat et Etienne Deloule pour leurs rapports encourageants ; Dominique Chardon, Maarten De Wit et Romain Bousquet pour les discussions stimulantes.

J'ai une pensée particulière pour les collaborateurs et co-auteurs lors des différentes phases de travail : Jean-François Moyen pour son accueil chaleureux et sa sympathie dès le master 1, Marie-Christine Boiron qui m'a appris les bases des « bulles », Denis Gapais en particulier pour ses anecdotes de terrain divertissantes, Valérie Bosse et son monde des « chipies de monazite », Gilles. Merci aussi à David, Dominique qui me laisse jouer avec le fer à souder, Yann et Xavier. J'ai aussi eu l'occasion de discuter géologie à de nombreuses reprises avec Pierre, Pavel, Erwan, Marc J., Michel, Christian et bien d'autres.

Le laboratoire de Géosciences Rennes est une joyeuse colonie dans laquelle je me suis fait beaucoup d'amis : mon colocataire de bureau et *mentor*, Romain (qui met la barre bien haut !) et son héritier Benoit ; Pipo ; les filles d'à coté (Gloria Sylvia et Laurie) ; Stéphane, le gang des taroteurs en série : Alain (avé l'accent, hein !), Lorraine, Claudine, Mélanie (stop au lactose !) et Céline ; le club des pleurnicheurs de co-rédaction de thèse (Fabou et Anne-Claire, heureusement que vous étiez là !) ; les gens de passage : Jacqueline, Ivar ; et j'en oublie. Un énorme merci à Mélody qui par son humour m'a mis du baume au cœur pendant ces trois ans. J'espère vous revoir tous bientôt au détour d'un p'tit verre dans un congrès. Je remercie chaleureusement les personnes extérieures au laboratoire qui m'ont donné des bouffées d'air pur : Marie D., Jeanne et évidement Isabelle.

Je voudrais conclure mes remerciements en me tournant vers ma famille. Parmi mes repères je peux toujours compter mes sœurs, mon sang, Marie et Chloé, mon presque frère Pierre ainsi que Anne et Jacky. Peu de mots rendront justice à tout ce que m'ont apporté mes parents Christian et Françoise, que ce soit le goût de l'application dans l'étude, la curiosité et la liberté de choix de parcours. Enfin je souhaite chanter les louanges de celui qui est entré dans ma vie l'exact jour de mon entrée dans ce projet et qui a été avec moi jusqu'au bout, Nicolas.

RESUME

Les circulations de fluides dans la croûte sont les vecteurs de mobilités élémentaires dont une des conséquences est la concentration de métaux et la genèse de gisements. Ces fluides circulent dans les zones de déformation où ils modifient la composition des roches encaissantes. Dans la ceinture archéenne de roches vertes de Murchison (Afrique du Sud), l'Antimony Line est une zone déformée qui a été le siège de circulations de fluides minéralisateurs en Sb-Au.

Pour caractériser les processus minéralisateurs, des données pétro-géochimiques, en particulier en isotopes stables et inclusions fluides, ont été associées à la datation multi-méthode (U-Th-Pb, Pb-Pb et Ar-Ar) des corps minéralisés et de leur encaissant au cœur et autour de l'Antimony Line. L'étude structurale de la région souligne le caractère distribué de la déformation. La ceinture a ainsi subi une phase majeure de collision d'arc, associée à un magmatisme important vers 2.97 Ga, contemporain d'une minéralisation en Au (±Sb) qui pourrait être responsable d'une phase de pré-enrichissement en Sb. La minéralisation principale en Sb est la conséquence de la circulation d'un fluide métamorphique à H_2O-CO_2, à 2-3 kbar et 350-450°C. L'albitisation de granitoïdes intrusifs dans l'Antimony Line, datée à 2.8 Ga, est génétiquement liée à cette circulation, laquelle s'inscrit donc dans l'histoire tectono-métamorphique tardive de la ceinture et est contemporaine de la mise en place de leucogranites sur la bordure sud. Ces résultats illustrent la pertinence du couplage pétro-géochimie/géochronologie pour la compréhension globale d'un système métallogénique.

ABSTRACT

Fluid flows through the crust result in the mobilization of elements that can, in turn, generate metal concentrations and the formation of ore bodies. The circulations of such fluids are mainly localized in zones affected by localized deformation, where they modify the chemical composition of the host lithologies. In the Archean Murchison Greenstone Belt (Kaapvaal Craton, South Africa), the Antimony Line is a brittle-ductile structure affected by the circulation of Sb-Au mineralizing fluids.

In order to characterize the ore-forming processes, we combined a petro-geochemical study, that focused on stable isotopes and fluid inclusions in particular, with a multi-method dating (U-Th-Pb, Pb-Pb and Ar-Ar) of the ore bodies and their host rocks in and around the Antimony Line. Furthermore, our structural study emphasizes the distributed character of the belt deformation. The Murchison Greenstone Belt experienced a major episode of arc collision and related magmatism at ca 2.97 Ga, contemporaneous with an Au(±Sb) mineralization that may be responsible for a pre-enrichment in Sb. The main Sb mineralization event must be related to the circulation of a metamorphic, H_2O-CO_2–dominated fluid at 2-3 kbar and 350-450°C. The

albitization of the granitoids intrusive into the Antimony Line is dated at 2.8 Ga and is genetically linked to this fluid flow, which took place during the late tectono-metamorphic history of the belt contemporaneously with the emplacement of leucogranites along the southern border of the belt. Therefore, this study further demonstrates that coupling petro-geochemistry and geochronology is a powerful tool in order to study and characterize a given metallogenic system.

TABLE DES MATIERES

LISTE DES FIGURES

PARTIE I

Article #1

Article #2

---

haematite grains from the Malati Pump mine and Weigel Formation displaying two populations with distinct isotopic Pb signature. (d) Isochron for the pyrite population (Type 1).

Fig. 4: *Sketch for the MGB metallogenic system as proposed in this study*

Table 1: *LA-ICP-MS U-Pb isotope data for zircon*

Table 2: *ID-TIMS Pb-Pb isotope data for pyrite and haematite.*

Figure 5—1 : *Photos au MEB des sulfures de la granodiorite de Malati Pump.*

Figure 5—2 : *Altération des sulfures par la paragénèse d'albitisation albite-rutile-monazite.*

Article #4

Fig. 1: *Geological map of the Murchison Greenstone Belt and foliation trajectories of the region.*

Fig. 2: *Map of the AL area and associated along-strike crosscut. Transversal crosscut across the AL in the Athens ore body. Picture from the Athens shaft showing a talc-carbonate-chlorite schist hosting a boudinaged quartz-carbonate-stibnite veins.*

Fig. 3: *Mine and hand sample pictures of veins.*

Fig. 4: *Thin section pictures of veins.*

Fig. 5: *Rare Earth Elements pattern for the studied veins.*

Fig. 6: *Oxygen isotopic compositions of quartz and carbonates in Sb-mine veins and regional veins.*

Fig. 7: *Carbon and oxygen isotopic compositions of carbonates from Sb-mine veins.*

Fig. 8: *Microphotographs of the different fluid inclusions observed in the studied samples.*

Fig. 9: *^{40}Ar-^{39}Ar age spectrum of fuchsite.*

Fig. 10: *Isochores calculated from fluid inclusions data.*

Fig. 11: *$\delta^{18}O$ of quartz from Archean lode gold deposits worldwide compare to our data from Antimony Line quartz veins.*

Table 1: *Chemical compositions of carbonate from selected veins along the Antimony Line.*

Table 2: *Isotopic compositions of veins in the Murchison Greenstone Belt with special emphasis on the Antimony Line.*

Table 3: *Summary of the microthermometric data from the different types of fluid inclusions and chemical compositions of the volatile phase obtained by Raman spectroscopy.*

Table 4: *Bulk chemical compositions obtained by Raman microprobe spectroscopy and corresponding microthermometric data of aqueous-carbonic (Lc-w) fluid inclusions from sample MUR 09-43.*

Article #5

Figure 1: *(a) location of the Murchison Greenstone Belt in the Kaapvaal Craton. (b) Simplified geological map of the Belt, its surrounding granitoids and the Antimony Line (c) cross-cuts from the geophysical study of de Beer et al. (1984), with available ages (Ga).*

Figure 2: *Pictures of the Baderoukwe pluton.*

Figure 3: *Pictures of the Albitites.*

Figure 4: *Feldspar composition ternary diagram from EMP measurements.*

Figure 5: *Muscovite ternary composition diagram after Miller et al (1981).*

Figure 6: *Geochemical diagrams of the albitites compared to the protolith (Baderoukwe) and its altered samples.*

Figure 7: *Diagram of oxygen and carbon isotopes composition of carbonate (symbols) and albitites (grey range).*

Figure 8: *Pictures of dated phases.*

Figure 9: *Concordia (U-Pb) diagrams of albitites (zircon, titanite, monazite)*

Figure 10: *Chemistry of monazite grains (structural formulae based on 4 oxygen atoms).*

Table 1: *Sampling and localization.*

Table 2: *Whole rocks geochemistry: major and trace element plus isotopic oxygen whole rock composition.*

Table 3: *Minerals composition.*

Table 4: *Radiogenic Sm-Nd and Rb-Sr isotopes.*

Table 5: *Isotope composition of the carbonate fraction from albitite rocks.*

Table 6: *Geochronological dating of zircon from albitites.*

Table 7: *Geochronological dating of monazite from albitites.*

Table 8: *Geochronological dating of titanite from albitites.*

Figure 8—1 : *Composition en Nd en fonction du La, en formule structurale pour 4 O.*

Figure 8—2 : *Taille caractéristique des grains de monazite en fonction de l'âge ^{235}U-^{207}Pb.*

Article #6

Figure 1*: (a) Map of the northeastern Kaapvaal craton (b) Map of the Murchison Granite Greenstone Belt Terrain.*

CONCLUSIONS GENERALES

Figure 9—10 : *Compilation des âges des roches plutoniques et des ceintures de roches vertes entre le gneiss de Makhutswi et la ceinture de Limpopo.*

AVANT-PROPOS

Ce manuscrit présente le travail effectué dans le cadre d'un doctorat de trois ans au sein du laboratoire Géosciences Rennes rattaché à l'Observatoire des Sciences de l'Univers de Rennes (OSUR) au sein de l'Université de Rennes 1 et de l'Université Européenne de Bretagne (UEB).

Il prolonge la thématique abordée lors de mes stages de Master sur des objets sud-africains archéens (ceinture de Barberton et bassin du Witwatersrand) étudiées grâce à la géochimie élémentaire et isotopique. De plus, ces stages ont permis d'amorcer l'encadrement par Philippe Boulvais et Marc Poujol et de collaborations externes (Jean-François Moyen, Université Jean Monnet, Saint-Étienne et Marie-Christine Boiron, G2R, Université de Lorraine). Au cours de la thèse, d'autres collaborations ont vu le jour dès le terrain avec Denis Gapais, puis avec Jean-Louis Paquette et Valérie Bosse du laboratoire Magma et Volcan (Clermont-Ferrand) et avec Laurence Robb (Université d'Oxford).

Le financement de ce travail provient du Ministère de la Recherche pour ce qui est de l'allocation de recherche, et de l'INSU-Action Incitative pour ce qui est des financements des missions et des analyses.

INTRODUCTION GENERALE

THEMATIQUE

Les terrains Archéens sont des objets géologiques spécialement porteurs de ressources minérales. La période archéenne présente quelques conditions géologiques originales, mais les minéralisations archéennes ont en commun avec beaucoup des minéralisations de l'histoire de la Terre d'être préférentiellement associées à des processus impliquant des fluides géologiques.

En effet, les fluides géologiques transportent les éléments chimiques à travers la croûte, en particulier ils transportent les métaux qui, s'ils sont déposés de façon suffisamment concentrée, forment des minéralisations. Ce rôle est essentiel tant les minéralisations associées aux fluides sont prépondérantes. Au sein d'un même objet géologique, les fluides peuvent provenir de différentes sources, comme des fluides dérivés de la surface, des fluides dérivés de magmas, ou encore de fluides dérivés de roches métamorphisées. Comprendre l'origine de fluides minéralisateurs est donc essentiel pour conceptualiser la métallogénie d'un système. La caractérisation du fluide dans un système minéralisé demande aussi de renseigner les conditions physiques de la circulation (température, pression) et l'interaction fluide-roche. Cette caractérisation s'accompagne par ailleurs de la compréhension des chemins des fluides à travers la croûte. Les fluides sont canalisés le long de discontinuités physiques, principalement dans les failles et zones de cisaillement où ils peuvent parcourir de grandes distances et avoir circulé pendant de longues périodes. Pour les intégrer à l'histoire géologique d'une zone il faut donc contraindre la géométrie des conduits de fluides et la chronologie des circulations.

In fine, la définition globale d'un modèle métallogénique contribue à construire l'histoire géologique d'une zone.

OBJET, DEMARCHE ET PROBLEMATIQUE

Le craton du Kaapvaal en Afrique du Sud est un des terrains les plus minéralisés; il est aussi l'un des plus étudiés. Il comprend par exemple la ceinture de Barberton ou le bassin aurifère du Witwatersrand qui ont fait l'objet d'études innombrables. Au nord du craton se trouve la ceinture de Murchison qui n'a pas fait l'objet de tant d'études mais dont un cadre global est disponible. La géologie de la ceinture a été posée lors de travaux précoces (van Eeden et al. 1939) et de travaux dans les années 1970-1980 notamment par le service géologique sud-africain puis entre 1988-1992 par le groupe de J. Vearncombe. Enfin la région et la ceinture ont vu des avancées géochronologiques majeures (par exemple les travaux de Kröner et Poujol).

Cette ceinture a attiré l'attention de par sa particularité d'abriter un gisement original à l'échelle du craton (et également mondialement), l'Antimony Line. De nombreux travaux ont postulé diverses origines pour cette minéralisation. Malgré la

synthèse de Pearton et Viljoen (1986) proposant une origine hydrothermale-métamorphique, peu de données sont disponible sur les fluides minéralisateurs et la question de l'origine de la minéralisation reste donc ouverte. Enfin le cadre géochronologique est encore insuffisant pour intégrer les circulations de fluides. Ainsi ce travail s'attache à résoudre la problématique générale suivante :

- **Quand et comment s'est formée la minéralisation en Antimoine de la ceinture de roches vertes de Murchison ?**

Cette problématique sera détaillée à la fin de la partie I après une réévaluation récente de la géodynamique de la région et de la ceinture.

L'objectif est d'obtenir une vision géologique synthétique des objets minéralisés à différentes échelles. La démarche scientifique de ce projet consiste à aborder les thématiques métallogéniques par une approche de géologie fondamentale. Il s'agit d'utiliser les outils de la géologie structurale, de la pétrologie, des géochimies élémentaire, stable et radiogénique, notamment la géochronologie, pour contraindre le système métallogénique dans son ensemble.

Les traces de paléofluides géologiques sont les veines et les roches affectées par ces fluides. Parmi les outils applicables aux fluides, la géochimie des isotopes stables permet l'accès aux fluides et aux interactions fluide-roche. Cet outil est associé à l'observation des roches en lames minces, à la mesure de la chimie des minéraux et des roches et à l'analyse des inclusions de fluides. Ils permettent ensemble de mieux comprendre et interpréter les âges mesurés.

ORGANISATION DU MANUSCRIT

La première partie est consacrée à un exposé des thèmes de la géologie dans lesquels ce travail évolue. Le chapitre 1 rappelle la définition de l'Archéen et illustre ensuite la problématique de la croissance crustale au travers d'un article en préparation. Le chapitre 2 décrit les ceintures de roches vertes et les terrains de granitoïdes associés, dont les problématiques tectoniques sont abordées dans la région de Murchison par un article. Le chapitre 3 présente un résumé rapide de l'histoire du craton du Kaapvaal, enfin le chapitre 4 synthétise les connaissances actuelles sur la formation des minéralisations.

La deuxième partie expose les résultats principaux de la thèse ainsi que les discussions et interprétations associées. Elle s'articule autour d'articles (publié, accepté, soumis ou en préparation) portant sur une minéralisation en or-antimoine datée à 2.97 Ga (chapitre 5), la caractérisation de la circulation de fluides crustaux dans l'Antimony Line (chapitre 6), la datation de cette circulation à 2.8 Ga par l'étude pétro-géochronologique d'albitite (chapitre 7) et enfin l'étude pétrologique, géochimique et modélisatrice du pluton de Lekkersmaak contemporain de cette circulation (chapitre 8).

Les conclusions générales synthétisent ces études en termes de géologie puis métallogéniques et proposent quelques perspectives méthodologiques, métallogéniques et géologiques.

PARTIE I

ÉTAT DES CONNAISSANCES ET QUESTIONS

L'Archéen, les ceintures de roches vertes, le craton du Kaapvaal, la ceinture de Murchison, les systèmes minéralisateurs

Chapitre 1 — L'Archéen et la croissance crustale

Ce chapitre rappelle tout d'abord les limites temporelles et spatiales de l'Archéen. Il présente ensuite une caractéristique essentielle de la géologie archéenne, la croissance crustale, et son étude géochimique. Cette croissance est illustrée et discutée par un article dans la région d'étude, le nord-est du craton du Kaapvaal.

A — Limites temporelles et répartition

L'Archéen est un éon, c'est-à-dire qu'il appartient au premier ordre de la division de l'échelle des temps géologiques (figure 1–1). Sa limite inférieure n'est pas clairement définie (voir par exemple Bleeker 2004). Elle varie donc selon que l'on prend en compte :

- l'âge des plus vielles roches différentiées en place ; les gneiss d'Amitsoq (et les formations associées d'Isua et d'Alilia), au Groenland occidental, sont reconnues sur des surfaces significatives (3.82-3.87 Ga, Nutman et al. 1993).
- l'âge des plus anciennes roches différentiées (granitoïdiques) connues, qui marquerait l'apparition de la croûte continentale. Dans ce cas, il s'agit des gneiss d'Acasta, au Canada, avec un âge U-Pb zircon de 4,1 Ga, mais ces roches sont en enclaves (Bowring et Williams 1999). Le plus souvent c'est cette occurrence qui est utilisée comme limite Hadéen/Archéen.
- l'âge des plus vielles roches crustales ; une croûte mafique serait datée de 4.28 Ga dans la ceinture de roches vertes de Nuvvuagittuq, au Canada ($^{142}Nd/^{146}Sm$ sur roches totales ; O'Neil et al. 2008)
- l'âge des plus vieux minéraux crustaux ; les célèbres zircons de Jack Hills (Australie) indiquent la présence d'une croûte évoluée dès 4.40 Ga (Wilde et al. 2001). En particulier Cavosie et al. 2005 proposent que l'apparition des hauts δ18O dans ces zircons à 4.20 Ga marque le refroidissement significatif de la surface de la Terre et le début de l'Archéen.

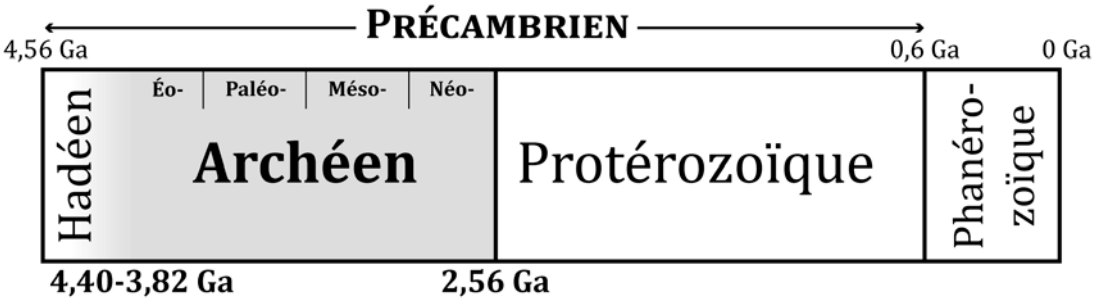

Figure 1—1 : *Echelle des temps géologiques. L'Archéen est limité à sa base par l'Hadéen à son sommet par le Protérozoïque.*

Sa limite supérieure est fixée conventionnellement à l'âge du Great Dyke au Zimbabwe (2.56 Ga ; Oberthür et al. 2002). Cette valeur n'est pas arbitraire. Elle correspond bien, vers 2.5 Ga, à une stabilisation de la lithosphère continentale (Kröner

1991) dont les causes sont en partie globale(s) mais aussi locale(s) (détails dans Moyen 2000). La très large majorité des âges obtenus dans la présente étude est confinée à l'Archéen.

La figure 1–1 détaille aussi les subdivisions de l'Archéen (Eoarchéen, Paléoarchéen, Mésoarchéen et Néoarchéen). Pourtant, l'évolution des terrains archéens est diachrone donc ces subdivisions s'appliquent mal à une étude locale comme celle présentée dans ce travail. Des échelles de temps régionales semblent plus adaptées : la figure 3–1 (chapitre 3) expose celle appliquée régionalement au craton du Kaapvaal. Pour faciliter les comparaisons, nous parlerons ici toujours en âges absolus.

Les objets géologiques archéens par excellence sont des blocs continentaux dits *cratons* (leur partie plus ancienne étant les *boucliers)*. Ils représentent 15 % des terrains précambriens (Goodwin 1981) et constituent les "noyaux" des continents actuels (figure 1–2) autour desquels se sont amalgamés les orogènes plus jeunes. Ils ont chacun une histoire propre bien que des études s'intéressent à leur coévolution (Condie 1998 ; Bleeker et Ernst 2006). Le terme de craton définit donc une croûte continentale qui, après des périodes actives longues, a atteint un état stable. La cratonisation est donc un stade tardif de l'évolution des terrains archéens, qui permet la préservation (partielle) des épisodes tectoniques, magmatiques et métamorphiques majeurs (Pollack 1986) ainsi que l'accumulation de grandes couvertures sédimentaires peu déformées.

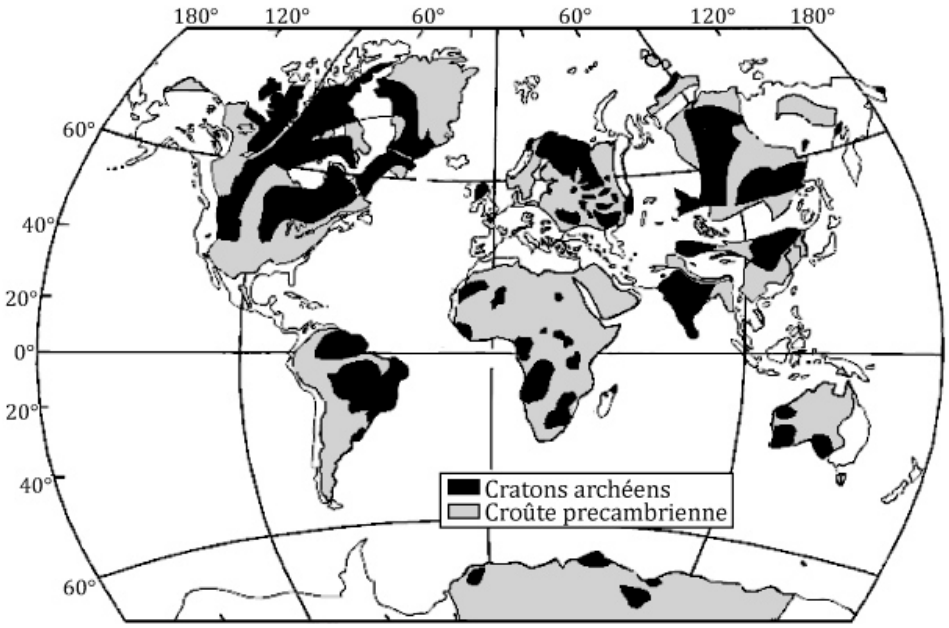

Figure 1–2 : *Carte mondiale de la répartition des terrains précambriens, dont ceux archéens (à l'affleurement ou recouverts par des roches plus jeunes). D'après la compilation de Kusky et Polat (1999, et références incluses). Le système de projection exagère les surfaces des hautes latitudes, par exemple le craton du Groenland et le bouclier canadien.*

B — Croissance crustale - l'exemple du craton du Kaapvaal

La préservation de la croûte archéenne n'a été que partielle au cours des temps géologiques. En effet, l'archéen n'affleure que sur 15% des terrains précambriens, et pourtant ce pourcentage est peu révélateur de la quantité de coûte juvénile produite alors (c'est-à-dire nouvellement extraite du manteau, par opposition à la croûte recyclée). Cette problématique de la croissance crustale demande de comprendre globalement à partir de quand, à quelle vitesse et avec quelle composition se forme la croûte. Le processus fondamental à l'origine d'un magma est la fusion partielle, qui produit un liquide en laissant un solide résiduel, tout deux avec des compositions différentes. Dans le cas de la Terre primitive, la chaleur interne produite était deux à trois fois supérieure à l'actuel (Lambert, 1976; Richter, 1988) et provoquait plus de fusion du manteau primitif, et *in fine* plus de croûte continentale. Étudier la croissance crustale revient donc à étudier le couplage croûte-manteau, et notamment son évolution à l'Archéen, c'est-à-dire la différentiation terrestre. D'autre part, étudier la croissance crustale permet de contraindre les modalités de la formation de croûte archéenne, c'est-à-dire sa géodynamique.

DEUX MODELES. Deux modèles géodynamiques "extrêmes" sont évoqués pour expliquer la formation de la croûte continentale primordiale (Albarède 1998 ; Windley 2003): le modèle de *subduction* et le modèle de *panaches mantelliques* (voir chapitre 2 et figure 2–3). Le premier modèle repose sur l'analogie avec l'actuel, où la croûte juvénile se forme principalement dans une tectonique horizontale (dans des arcs insulaires) à l'aplomb des zones de subduction. Un des arguments les plus convaincants est que la pétrogenèse des granitoïdes archéens (TTG) correspond bien à ce type de contexte. Le modèle des points chauds propose que des remontées de panaches mantelliques fondent et forment des plateaux océaniques puis des croûtes granitiques. Il s'appuierait principalement sur la nature épisodique de la production de croûte et sur une tectonique crustale marquant une rhéologie chaude (détails dans le chapitre 2).

LES DONNEES GEOCHIMIQUES. À la fin des années 70 et dans les années 80, de nombreux auteurs se sont intéressés à modéliser la croissance crustale. Ils s'appuient entre autres sur l'estimation de la composition de la croûte, des bilans volumiques de production et destruction, des bilans géochimiques élémentaires et isotopiques des réservoirs manteau-croûte (Fyfe 1978 ; Reymer et Schubert 1984 ; Taylor et McLennan 1985 ; Armstrong 1991 ; McCulloch et Bennett 1994). En 1994, Martin illustre ces différents modèles par leurs courbes de croissances (figure 1–3). Elle souligne ce qui apparait comme le consensus majeur de ces études : à la fin de l'Archéen, plus de 50% du volume crustal est produit (Taylor et McLennan confirment ce chiffre comme un minimum en 1995).

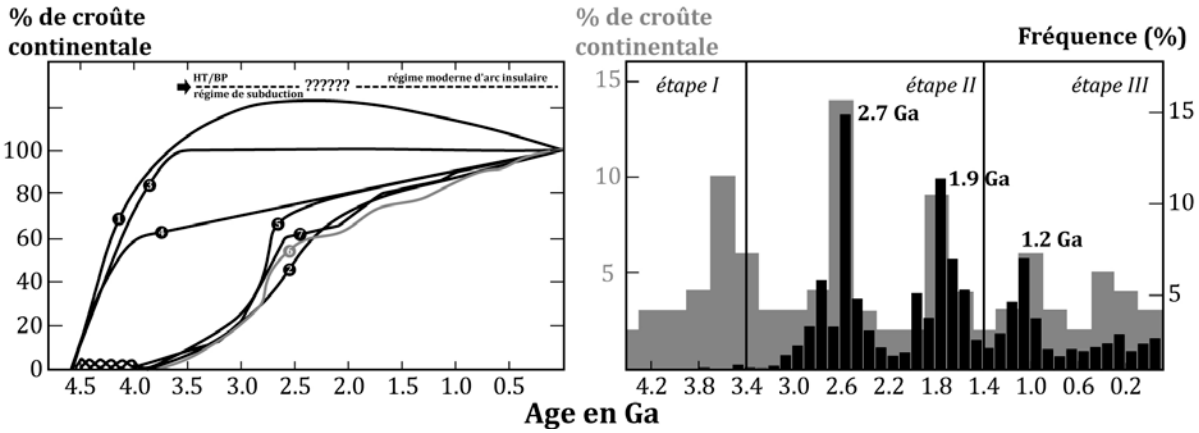

Figure 1—3 : *(a) Modèles de croissance crustale. De 1 à 5, compilation par Martin (1994) : 1 - Fyfe (1978) ; 2 - Veizer et Jansnen (1979) ; 3 - Amstrong (1981) ; 4 - Reymer et Shoubert (1984) ; 5 - Taylor et McLennan (1985). Modèles 6 – de McCulloch et Bennett (1994) et 7 - de Taylor et McLennan (1995, et ses annotations). Selon les auteurs, le protérozoïque et le phanérozoïque sont des périodes de recyclage (courbe plate), ou de destruction (baisse) ou encore de production faible, mais tous les auteurs indiquent une production crustale nette importante à l'Archéen. (b) épisodes majeurs de production crustale à partir d'une compilation d'âges zircons pondérés (noir, par pas de 100 Ma, Condie 1998) ou d'âges modèles Sm-Nd (gris, par pas de 200 Ma, McCulloch et Bennett 1994).*

Néanmoins, le modèle de croissance crustale à l'Archéen n'est pas pour autant totalement compris. Ces dernières années, les études se focalisent sur l'analyse des zircons, et tendent à préciser la nature épisodique ou non de ce phénomène. Des pics d'âges pourraient êtres interprétés comme aussi comme des pics de croissance et d'activité du manteau avec multiplication des plumes, supportant le modèle de panaches (figure 1–3). Mais des pics de croissance pourraient aussi s'intégrer dans le cadre du modèle en subduction par la fragmentation de supercontinents. Selon les données, les pics de production de matériel juvénile auraient lieu à 2.7, 1.9 et 1.2 Ga (U-Pb sur zircon, Condie 1998 ; figure 1–3) et, avec l'agrandissement des bases de données, aussi à 2.70, 2.55, 2.12, 1.90, 1.70, 1.65, 0.80, 0.57 et 0.45 Ga (U-Pb sur zircon et traçage Nd, respectivement Condie et al. 2009 et McCulloch et Bennett 1994). Cependant, le caractère épisodique est remis en question. Jahn et Condie (1995) interrogent la validité de l'utilisation des données Sm-Nd. Lancaster et al. (2011) soulignent le biais induit par la préservation des zircons lors des grandes collisions, et argumentent en faveur d'une production plus continue de croûte juvénile (Hf sur zircon). Ils distinguent toutefois trois pics (3.3, 2.2 et 1.7 Ga) mais dont l'importance mondiale n'est pas affirmée. De même, Campbell et al. (2012) indiquent que les pulses diffèreraient selon les continents (Hf sur zircon).

Les deux dernières études citées utilisent l'Hafnium sur zircons, dont l'utilisation a dynamisé la recherche sur la croissance crustale ancienne. En effet, cette technique, développée en 1981 par Patchett, permet de combiner datation et traçage primordial (i.e. manteau *versus* croûte). Les avancées techniques de l'analyse par ablation laser couplée à un ICP-MS permettent d'obtenir dans une même zone au sein d'un zircon l'âge U-Pb (cristallisation) et la signature en Hf (mantellique ou crustal). De plus, pour intégrer les données globales de croissance, il faut d'abord documenter et

discuter régionalement les données. L'article qui suit donne une application de ce couplage traçage-datation sur zircon (signature Hf et ages U-Pb), dans le nord-est du craton du Kaapvaal, où se situe la ceinture de Murchison, objet central de ce projet. Initié dans le cadre de ce travail de thèse, il a bénéficié de la collaboration d'A. Zeh qui lui a donné une ampleur régionale puis mondiale. En effet, A. Zeh a publié plusieurs travaux récents sur le craton du Kaapvaal, notamment sur la ceinture de Barberton (Zeh et al. 2009), l'Ancient Gneiss Complex (Zeh et al. 2011), la ceinture de Pietersburg (Zeh et Gerdes 2012) et la ceinture de Limpopo (Zeh et al. 2008, 2010). En particulier, cet article suggère une évolution linéaire du manteau à l'Archéen et donc, par extension, de la croute juvénile.

Article #1

"Juvenile crust formation in the northeastern Kaapvaal Craton at 2.97 Ga – Implications for Archean crust-mantle evolution, terrane accretion, and the source of the Witwatersrand gold"

En préparation pour *Precambrian Research*

Résumé en français

Une étude combinée U-Pb et Lu-Hf sur zircons magmatiques et détritiques fournit la preuve que la ceinture de roches vertes de Murchison (dans la zone nord-est du craton du Kaapvaal) comprend une zone de suture archéenne importante. Celle-ci s'est originellement formée par la collision à 2.97 Ga entre un système d'arc au nord et un terrain évolué au sud, le proto-Kaapvaal.

Ce modèle est étayé par le fait que les roches magmatiques du terrain septentrional (tonalites et porphyres à quartz du complexe du Rooiwater et de la Formations de Rubbervale) cristallisent à 2.97 Ga et montrent des signatures Hf supra-chondritiques (εHf_t de +4.4 à +5.1). A l'inverse, les données isotopiques U-Pb-Hf des zircons détritiques des unités méridionales (issus de schistes quartzeux de l'unité de Murchison et de la Formation de La France) indiquent une provenance depuis la zone plus au sud de la ceinture. En effet cette zone a été affectée par des intrusions granitoïdiques associées au recyclage crustal à 3.53-3.42 (εHf_t = +1.8 à -4.8), à 3.30-3.20 Ga (εHf_t = +1.8 à -6.3), et à 3.13-3.05 Ga (εHf_t = +1.3 à -5.6). Cela démontre une connexion avec les terrains de Barberton et du Swaziland.

De plus, la séparation physique des deux terrains avant 2.97 Ga est appuyée par le fait que les zircons les plus jeunes des unités méridionales ont 2.99 et 2.97 Ga alors qu'ils présentent des signatures εHf_t infra-chondritiques entre -6.5 et -1.5, contrastant ainsi avec les signatures supra-chondritiques des roches contemporaines du nord. L'origine juvenile des roches magmatiques Rooiwater et Rubbervale, où sont présents les gisements de type VMS, en font un candidat potentiel pour être la source des

sediments aurifères de la ceinture de roches vertes de Pietersburg voisine et du bassin du Witwatersrand.

Enfin, ces nouvelles données isotopiques U-Pb-Hf complètent la compilation mondiale et plaident en faveur d'une évolution linéaire du réservoir mantellique appauvri, en réponse à une formation continue de croûte durant l'Archéen, dès 4.0 Ga.

JUVENILE CRUST FORMATION IN THE NORTHEASTERN KAAPVAAL CRATON AT 2.97 GA – IMPLICATIONS FOR ARCHEAN CRUST-MANTLE EVOLUTION, TERRANE ACCRETION, AND THE SOURCE OF THE WITWATERSRAND GOLD

Armin Zeh[a,*], Justine Jaguin[b] Marc Poujol[b], Philippe Boulvais[b], Erwan Hallot[b], Sylvain Block[c], Jean-Louis Paquette[d]

[a] *Institut für Geowissenschaften, Facheinheit Mineralogie, Abt. Petrologie und Geochemie, Altenhöferallee 1, D-60438 Frankfurt, Germany*

[b] *UMR CNRS 6118, Géosciences Rennes, Université Rennes 1, 35042 Rennes Cedex, France*

[c] *Université Jean Monnet, 23 rue du Dr Paul Michelon, 42023 Saint-Étienne. France*

[d] *UMR CNRS 6524, Laboratoire Magmas et Volcans, Université Blaise Pascal, 63038 Clermont-Ferrand Cedex, France*

** Corresponding author. Email address:* a.zeh@em.uni-frankfurt.de*, Phone ++49 (0)69-798-40133, Fax: ++49 (0)69-798-40121*

ABSTRACT

Combined U-Pb and Lu-Hf isotope data of detrital and magmatic zircon grains provide evidence that the Murchison Greenstone Belt, NE Kaapvaal Craton, South Africa, hosts an important Archean suture zone, which primarily formed by a collision 2.7 Ga ago between a primitive island arc system to the north with an evolved terrane, the proto-Kaapvaal Craton, to the south. This model is supported by the observations that igneous rocks of the northern terrane, comprising tonalites and quartz-porphyries of the Rooiwater Complex and the felsic volcanics of the Rubbervale Formation, were both emplaced at about 2.97 Ga and show highly superchondritic εHf_t of +4.4 to +5.1. In contrast, U-Pb-Hf isotope data of detrital zircons from quartzitic schists of the Murchison Unit and the La France Formation, both part of the southern terrane, provide evidence for a southern provenance, which was affected by granitoid intrusions accompanied by crust re-working at 3.53-3.42 Ga (εHf_t = +1.8 to -4.8), 3.30-3.20 Ga (εHf_t = +1.8 to -6.3), and 3.13-3.05 Ga (εHf_t = +1.3 to -5.6); pointing to a connection with the Barberton greenstone belt and Swaziland. A spatial separation of the two terranes prior to 2.97 Ga, is furthermore supported by the facts that the youngest detrital zircon grains of the southern terrane, having ages between 2.99 and 2.97 Ga, show subchondritic εHf_t between -6.5 and -1.5, in contrast to the highly superchondritic εHf_t obtained from the contemporaneous magmatic rocks of the northern terrane. The juvenile character of the Rooiwater and Rubbervale magmatic rocks, along with the occurrence of VMS deposits, makes them a very likely candidate for the gold-bearing sediments exposed in the adjacent Pietersburg Greenstone Belt and in the Witwatersrand basin. The new U-Pb-Hf isotope datasets, along with data

from worldwide sources, furthermore support a model of a linearly evolving "normally" depleted mantle reservoir in response to continuous crust formation during the Archean, starting at 4.0 Ga.

Keywords: Archean terrane accretion, crust-mantle evolution, Murchison greenstone belt; U-Pb-Hf isotopes, Witwatersrand gold source

1. INTRODUCTION

Numerous studies have demonstrated that the application of combined U-Pb and Lu-Hf isotope data extracted from magmatic and detrital zircon grains provide a powerful tool to obtain detailed information about the secular evolution of the crust-mantle system during the Earth's early history, comprising the Hadean to Archean eons (e.g. Patchett et al.,1981; Stevenson & Patchett, 1990; Vervoort et al., 1996; Blichert-Toft & Albarède, 1997, 2008; Amelin et al., 1999, 2000; Vervoort & Blichert-Toft, 1999; Rino et al., 2004; Condie et al., 2005; Harrison et al., 2005, 2008; Hawkesworth & Kemp, 2006; 2010; Scherer et al., 2007; Zeh et al., 2007, 2008, 2009, 2011; Hiess et al., 2009; Kemp et al., 2009, 2010; Hawkesworth et al., 2010). Such data can help to constrain, whether the Earth's mantle was depleted "linearly" from 4.56 Ga until today (Griffin et al., 2000), or from 4.0 Ga until today (e.g. Pietrianik et al., 2009; Blichert-Toft & Puchtel, 2010; Kemp et al., 2010; Zeh et al., 2011; Guitreau et al., 2012), or if the mantle depletion (and complementary crust formation) occurred episodically (e.g., Nebel-Jacobsen et al., 2010). Answering these questions, in turn, has important consequences for global geotectonic interpretations, i.e., whether plate tectonics operated already during the Hadean (e.g., Harrison et al., 2005, 2008; Blichert-Toft & Albarède, 1997, 2008), or if the early Earth was covered by a long-lived stable protocrust (Kamber et al., 2003; Kemp et al., 2010) that became dismantled during the Archean, either by vertical tectonics (mantle plume activities and sagduction processes) and/or by horizontal tectonics (subduction-amalgamation processes) (e.g., Chardon et al., 1996; Kamber et al., 2003; Zeh et al., 2008, 2011; Jaguin et al., 2012a; Næraa et al., 2012).

On a more regional scale, combined U-Pb and Lu-Hf zircon datasets can provide detailed information about the timing of magmatic and metamorphic events, as well as about the magma sources, such as a juvenile depleted mantle, a reworked older crust or a combination of both (e.g. Vervoort & Blichert-Toft, 1999; Griffin et al., 2004; Condie et al., 2005; Davis et al., 2005; Harrison et al., 2005, 2008; Gerdes & Zeh, 2006, 2009; Hawkesworth & Kemp, 2006; Wu et al., 2006; Zeh et al., 2007, 2010a; Blichert-Toft & Albarède, 2008). Thus, these datasets help geoscientists to gain detailed insights into the complex formation mechanisms of Archean cratons, in particular, whether the craton or its hinterland formed by accretion of new depleted mantle-derived material or by re-working of an older crust. In addition, they can set tight constraints on the position of terrane boundaries in structurally highly affected gneiss terranes, for example, by the finding of significantly different U-Pb-Lu-Hf isotope signatures in zircon grains from metasedimentary and magmatic rocks present on each side of the

suture zone (for examples see Zeh & Gerdes, 2010, 2012; Zeh et al., 2009, 2012; and this study).

In this study, we present new U-Pb and Lu-Hf isotope data obtained on zircon grains from magmatic and metasedimentary rocks from different units of the Murchison Greenstone Belt (MGB) and the adjacent Rooiwater Complex (RC). These units are located at the north-eastern edge of the Witwatersrand Block of the Kaapvaal Craton in close vicinity to the WSW-trending Thabazimbi-Murchison-Lineament (Fig. 1). This lineament is interpreted on geophysical ground to represent an important crustal scale suture zone of the Kaapvaal Craton (e.g. du Plessis, 1990), even though its geotectonic significance, its position in the field, and the timing of its initial formation remain unknown. Some authors interpret the Thabazimbi-Murchison-Lineament as being the "leftover" of an Archean suture zone, along which rocks of the Pietersburg terrane to the north collided with rocks of the proto-Kaapvaal Craton to the south (e.g., Good and de Wit, 1997, Anhaeusser et al., 2006; Zeh et al., 2009, this study). If true, at least some rocks along the Murchison-Thabazimbi Lineament, comprising those of the MGB, should witness this important amalgamation process. This, however, is speculative at the moment, in particular since the provenance and the timing of sediment deposition in the MGB are mostly unknown, and since geochronological data obtained from magmatic rocks of the RC and the MGB are inconsistent. Furthermore, there are no reliable isotope data, which could provide information about the sources of the magmatic rocks, i.e., whether they stem from a depleted mantle or from a crustal source at the time of their formation.

Based on limited structural, geochemical and petrological datasets, Vearncombe (1991) suggested that the Murchison area hosts a primitive island arc (magmatic rocks of the RC and of the Rubbervale Formation of the MGB; also see Vearncombe *et al*., 1987), which collided with the proto-Kaapvaal Craton during a Himalayan-type orogeny at 2.7-2.65 Ga (=Limpopo Orogeny). Vearncombe (1991) compared the tectonic situation in the MGB area with that of the Kohistan island arc, situated above the Indus suture in the N-Pakistan Himalayas. However, he did not identify a suture zone within the MGB area nor he was able to detail a "subduction" configuration (for more discussion about this subject, and a potential suture zone within the MGB see Anhaeusser, 2006). Furthermore, the timing of the proposed accretion process was later refuted by U-Pb zircon dating, which yielded ages of 2975 to 2963 Ma for magmatic rocks of the Rubbervale formation of the MGB (Brandl et al., 1996; Poujol et al., 1996; Poujol, 2001; Schwarz-Shampera et al., 2010), and a much younger upper intercept age of 2740 ± 4 Ma for the magmatic rocks of the RC. This final age, even though highly precise, was interpreted to be a minimum age (Poujol et al., 1996) because of the high discordancy of the data points. The existing U-Pb ages hint that the Rubbervale magmatic rocks of the MGB emplaced much earlier that those of the RC. This interpretation, however, is inconsistent with the intrusive character of the RC within the Rubbervale Formation of the MGB (van Eeden et al., 1939; Viljoen et al., 1978) and the structural data (Jaguin et al. 2012a).

The U-Pb and Lu-Hf isotope data produced during this study will solve many of the outstanding problems mentioned above. They will constrain, for the first time, that magmatic rocks of the MGB and the RC formed contemporaneously from a depleted mantle source, and that the MGB area hosts an important Mesoarchean suture zone, which separates a terrane with a juvenile crust from a terrane with an evolved crust. They also set new constraints on the Archean crust-mantle formation in general, and on the source of the Witwatersrand and Pietersburg gold in particular.

2. GEOLOGICAL SETTING AND SAMPLES

The ENE-WSW trending Murchison greenstone belt (MGB) is one of the volcano-sedimentary belts of the Archean Kaapvaal Craton of Southern Africa (Poujol et al., 2006; Robb et al., 2006, Fig. 1). It is situated in the NW part of the Kaapvaal Craton about 200 km north of the ca. 3.5-3.2 Ga Barberton Greenstone Belt (e.g. Kröner et al., 1991, 1996; Kamo and Davis, 1994; Dziggel et al., 2002), and about 80 km to the south of the 3.2-2.8 Ga Giyani Greenstone Belt (Kröner et al, 2000, Zeh et al., 2009). It extents for ~140 km ENE-WSW, 10 – 15 km N-S, and is unconformably overlain by the Neoarchaean to Palaeoproterozoic sediments of the Transvaal Supergroup (Burger and Coertze, 1973; Altermann and Nelson, 1998) at its western extremity. Furthermore, it is located along the Murchison-Thabazimbi Lineament (du Plessis, 1990) – (Fig. 1).

2.1. Plutonic rocks

The MGB is bounded toward the north by the mostly mafic rocks of the RC, which has been considered so far to be unrelated to the MGB (South African Committee for Stratigraphy; SACS, 1980). Furthermore, it is limited by numerous granitoid rocks, collectively termed as Groot Letaba Gneiss (Brandl and Kröner, 1993) which is made of a series of locally migmatised tonalitic-trondhjemitic-granodioritic (TTG) gneisses that were emplaced mostly between 3180 and 3000 Ma, with the exception of some ca. 2885 Ma discordant leucogneisses (Brandl and Kröner, 1993). The basement to the south of the MGB is also dominated by granitoid rocks. It is made up by TTG's of the French Bob's Mine, emplaced at 3228 ± 12 Ma (Poujol et al., 1996), by a series of younger granitoids with ages between 3110 and 3060 Ma (Brandl and Kröner, 1993; Poujol and Robb, 1999), and by late-stage granite plutons and pegmatites, that emplaced at ca. 2970 Ma (Baderoukwe, Discovery, Malati Pump granites), 2900 Ma (minimum age for the Maranda granite), 2820 Ma (Willie granite), 2795 Ma (Lekkersmaak granite) and 2680 Ma (Mashishimale granite) - (Poujol et al. 1996; Poujol and Robb, 1999; Poujol, 2001; Zeh et al., 2009, Jaguin et al., 2012b).

The **Rooiwater Complex** (RC) is located along the northwestern margin of the MGB. It extents over a distance of 65 km, has a maximum thickness of around 7.5 km (Vearncombe et al., 1992), and thins out progressively to the east. Its contact with the MGB is mostly tectonically reworked (e.g., Vearncombe et al., 1992). According to SACS (1980) and Vearncombe et al. (1987, 1992) the RC is interpreted to represent the relic of a primitive island arc, which is made up by a differentiated mafic igneous complex. It

is divided into three main units, which are from north to south, the Novengilla Suite, the Quagga quartz amphibolite, and the Free State Suite.

Figure 1: *(a) Main tectonic units of the Kaapvaal Craton in southern Africa and exposed rock units older than 2.7 Ga (b) Simplified geological map of the Murchison greenstone belt and surroundings.*

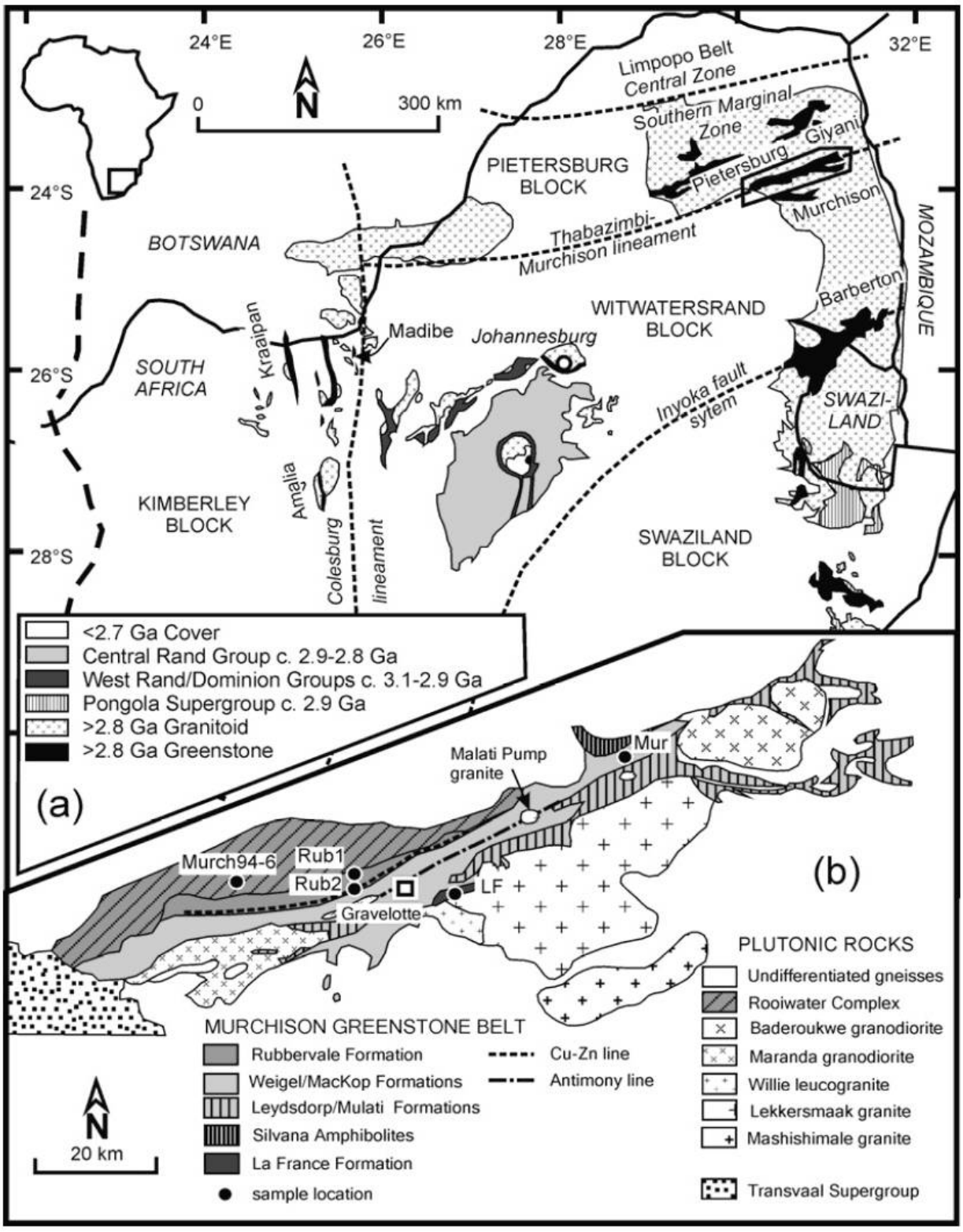

The Novengilla Suite comprises metamorphosed gabbro, anorthosite and minor pyroxenite, and contains sulphide-bearing horizons and titanium-vanadium-rich magnetite layers. The rocks of the Novengilla Suite have been pervasively hydrothermally altered, perhaps after an amphibolite-facies metamorphic overprint. The Quagga quartz amphibolite, which is located in the centre of the Complex, contains the metamorphic mineral assemblage hornblende-plagioclase-quartz-magnetite-garnet and shows a pronounced banding, which was interpreted by Vearncombe at al. (1992) to reflect the original igneous layering. The Free State Suite forms the southernmost, most differentiated unit of the RC, It appears to be intrusive into the Novengilla Suite in some places. It mainly consists of leucocratic "tonalites", which consists of albite, often bluish quartz and minor blue-green hornblende (Vearncombe et al., 1987). Geochronological data obtained by different methods for rocks of the RC scatter over a wide range of dates. Rb-Sr and Pb-Pb dating of rocks from the Novengilla Suite yielded ages of 2490±35 Ma and of ca. 2610 Ma, respectively (Vearncombe et al., 1987). Results of early Pb-Pb dating of the Free State tonalite gave imprecise dates of 2961 ± 150 Ma (Burger and Walraven, 1979) and 2544 +29/-31 Ma (Vearncombe et al., 1987). The most precise age constrain, so far, is provided by an upper intercept date of 2740 ± 4 Ma (Poujol et al., 1996: ID-TIMS U-Pb zircon), which is interpreted as a minimum age. LA-ICP-MS zircon dating of a mafic dike transecting the Novengilla Suite (i.e., Berlyn dike of Vearncombe et al., 1992), yielded an age of 2611 ± 10 Ma (Zeh et al., 2009).

2.2. Volcanites and sedimentary rocks of the MGB

The MGB was subdivided by Vearncombe et al. (1992) into four major, ENE-WSW-striking lithostratigraphic domains: Rubbervale formation, Murchison Unit, Silwana Amphibolites and the La France formation (Fig. 1b). The **Rubbervale formation** is exposed along the northwestern flank of the MGB, where it occurs in tectonic contact with the RC. It comprises basal quartz porphyroclastic schists (northern unit) overlain by felsic schists derived from tuffs and lavas (southern unit; Vearncombe, 1991). The quartz porphyroclastic schists mainly consist of blue quartz porphyroclasts (former phenocrysts) and less common feldspar in a schistose matrix of chlorite, white mica, and opaque minerals. Rarely, less deformed pods of quartz-feldspar porphyry are gradational into the schist, and hint that the schists were derived from a thick sequence of subvolcanic porphyries (Vearncombe, 1991; Schwarz-Schampera et al., 2010). The southern felsic schists also have blue quartz porphyroclasts, and include units of felsic lavas, well-bedded tuffs, lapilli and volcanic breccias. These schists are cut by bands of quartz porphyroclastic schist, which are interpreted to be deformed quartz porphyry dykes, and schistose mafic sills bearing the assemblages chlorite-plagioclase-actinolite. This southern unit also hosts the so-called 'Cu-Zn" line (Fig. 1b), a major VMS-type deposit (e.g., Schwarz-Schampera et al., 2010), with massive ore bodies consisting of pyrite, pyrrhotite, chalcopyrite, sphalerite, and minor magnetite. The emplacement of the Rubbervale volcanics is dated between 2.975- 2.963 Ga (Brandl et al. 1996; Poujol et al. 1996; Poujol 2001; Schwarz-Schampera et al., 2010). Based on field relationships, and limited petrological and geochemical evidence Vearncombe (1991) and Vearncombe et al. (1992) suggested

that the subvolcanic porphyries of the Rubbervale Formation might represent deformed equivalents of the Free State tonalite of the RC. In fact, rocks of both units follow the same calc-alkaline to tholeitic trend, are peraluminous, and characterized by high-Na/low-K, low La_N/Yb_N (0.5-2.0), and show pronounced Eu anomalies (Vearncombe 1991, Schwarz-Schampera et al., 2010). Furthermore, rocks of both units were obviously altered by fluids, and finally affected by a metamorphic overprint. Schwarz-Schampera et al. (2010) suggested that the felsic volcanics of the Rubbervale Formation, and the associated VMS deposits formed in a submarine environment, perhaps in a back-arc spreading centre.

The **Murchison Unit** forms the largest lithological domain in the MGB, and includes the MacKop, Weigel, Leydsdorp and Mulati formations of the SACS nomenclature (map 1 : 250 000 Geological Series, 2330 Tzaneen, 1985). It consists of mafic and ultramafic volcanic rocks, locally pillowed, along with volcano-sedimentary and sedimentary rocks. The volcano-sedimentary rocks are locally interbedded with BIFs and with quartzites and conglomerates. Massive hydrothermal carbonates and carbonate schists outcrop mostly along a high-strain shear zone in the center of the belt, the so-called Antimony Line (Fig. 1b). The Antimony Line is flanked by quartzite ridges to the north, and bears an economic Sb–Au mineralisation (Viljoen et al., 1978; Vearncombe et al., 1988, 1992). Jaguin et al. (2012b) demonstrated that granodiorite emplacement within the Antimony Line (i.e., the Malati Pump granodiorite), sulphide mineral deposition and gold mineralization all happened ca. 2.97 Ga ago. Serpentinite lenses occur in the southern part of the MGB. Stratigraphic relationships between the different formations within the Murchison Unit, as well as between the Murchison Unit and the Rubbervale Formation remain unclear, as deformation is intense (Vearncombe et al., 1988; Jaguin et al., 2012a; Block et al., 2012). U-Pb zircon ages provide evidence that the Weigel Formation volcanics were emplaced at ca. 3.09 Ga, while deposition for the MacKop conglomerate took place at <3.08 Ga (Poujol et al., 1996). The third unit, the **Silwana Amphibolites** (Vearncombe et al., 1992; part of the Rubbervale formation in the SACS terminology), is exposed in the north-eastern part of the MGB, and represent a 0.1-1.5 km wide sliver of amphibolites, rarely garnet-bearing, displaying a centimetric layering. It is of unknown origin. The **La France Formation** forms the southernmost unit of the MGB. It mostly consists of quartzite and kyanite-staurolite-garnet-bearing micaschists. Block et al. (2012) demonstrated that the Silwana Amphibolites, the Murchison Unit and the La France Formation underwent contrasting clockwise pressure-temperature-deformation (P-T-D) histories, and that the different units became juxtaposed during top-to-the-south directed, N-S compression between 2.97 and 2.92 Ga.

2.3. Samples

During this study, zircon grains from three igneous rocks and two sedimentary rocks were investigated. Zircon grains from the Free State tonalite of the Rooiwater Complex come from sample Murch 94-6 (coordinates: S 23°56’52.45’’, E 30°22’20.34’’ along the road R529), which was previously investigated by Poujol et al. (1996) by ID-

TIMS. Two samples are from quartz porphyry rocks of the Rubbervale Formation; one from a quartz porphyroclastic schist of the northern unit (sample Rub1: co-ordinates: S23°55'10.1'', E30°32'50.8'', near railway station Rubbervale), and the other from a felsic schist of the southern unit (sample Rub2: co-ordinates: S23°57'02.7'', E30°32'03.3'' along the dirt road from Rubbervale to Leydsdorp). In addition, detrital zircon grains were separated from a garnet-bearing quartzitic schist of the MacKop Formation of the Murchison Unit (sample Mur: co-ordinates: S23°48'53.49'', E30°57'09.69'', Sheiding stone quarry), and from an aluminous quartzitic schist, with large kyanite porphyroblasts from the La France Formation (sample LF: co-ordinates: S23°56'29.62'', E30°41'49.16''). For sample locations see figure 1b.

3. RESULTS OF U-PB AND LU-HF ISOTOPE ANALYSES

3.1. Generalities

U-Pb and Lu-Hf isotope analyses of zircons from all rocks were carried out by laser ablation - inductively coupled plasma - mass spectrometry (LA-ICP-MS) at the Goethe University of Frankfurt, Germany, using the methods and instruments described by Gerdes & Zeh (2006, 2009), with modifications explained in Zeh & Gerdes (2012). In addition, U-Pb isotope data of zircon grains from the Free State tonalite were obtained by LA-ICP-MS at the Laboratoire Magmas et Volcans in Clermont-Ferrand, France, using the method described in Hurai et al. (2010). Prior to LA-ICP-MS dating, all zircon grains were carefully characterised by cathodoluminescence (CL) and secondary electron microscopy (SEM) imaging (using a JEOL JSM-6490 instrument with Gatan MiniCL) to obtain information about their internal structure. Laser spots for Lu-Hf (mostly squared spots with an edge length of 40 μm) were placed mostly directly "on-top" of the U-Pb laser spots (mostly 19-26 μm in diameter), or within the same zone characterized by CL imaging (Fig. 2). A description of specific parameters used during the different analytical sessions and the results of standard measurements are presented in Appendix A. The results of U-Pb and Lu-Hf isotope analyses are shown in the Tables 1 and 2, and those of standard measurements in the supplementary material (Table S1 and S2).

3.2. Zircons from magmatic rocks

CL images of all zircon grains from samples Rub 1 and Rub 2 of the Rubbervale Formation reveal magmatic zoning, characterized by plain rectangular cores surrounded by rims with an oscillatory zoning (Fig. 2c, d). For sample Rub 1 eight domains (spots) on five zircon grains were analysed for U-Pb and Yb-Lu-Hf isotopes, and for sample Rub 2 nine spots on six zircon grains. U-Pb analyses of zircons from sample Rub1 and Rub2 yielded within error identical Concordia ages of 2966 ± 7 Ma and 2972 ± 7 Ma, respectively (Fig. 3 a, b), and identical initial $^{176}Hf/^{177}Hf$ of 0.280995 ± 0.000017 (2σ S.D.), which correspond to $\varepsilon Hf_{2.965\ Ga}$ = +4.4 ± 0.6 (2σ S.D) – (Table 2).

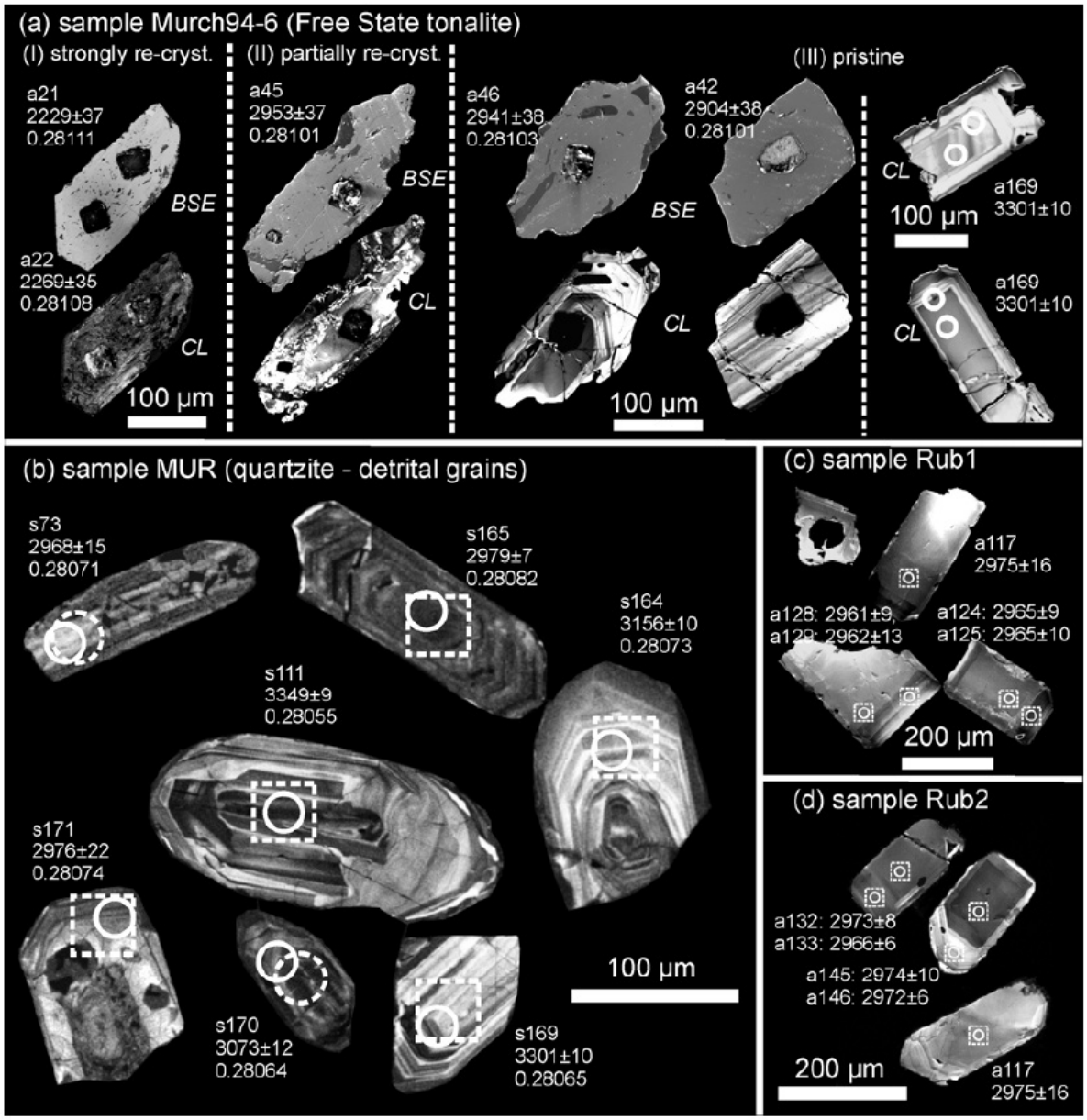

Figure 2: *Cathodoluminescence (CL) and back scattered electron (BSE) images of magmatic and detrital zircons from the (a) Free State tonalite – sample Murch94-6, (b) a quartzitic schist sample from the Murchison Unit (MacKop Formation) – sample Mur, (c-d) and quartz porphyroclastic schists (metavolcanitic rocks) of the Rubbervale Formation (sample Rub1: northern Rubbervale Formation; sample Rub2: southern Rubbervale Formation). For sample Murch94-6 (a) the zircons are shown with decreasing degree of alteration from left to the right: type I - strongly altered (with many pores and dark CL), type II - partially re-crystallized (with patchy domains), type III – pristine. Round circles with solid lines mark the position of laser spots for U-Pb analyses, and dotted spots (round or squared) those for Lu-Hf isotope analyses. Black squares in (a) represent Lu-Hf laser spots, drilled on top of the U-Pb laser spots. Attached to each zircon crystal is the analysis number, the* $^{207}Pb/^{206}Pb$ *age with 2σ error (in Ma), and the initial* $^{176}Hf/^{177}Hf$*, corresponding to the results presented in the Tables 1 and 2.*

Zircon extracted from sample MURCH 94-6 are either squat or elongated euhedral grains. They are usually highly fractured and often contain inclusions of quartz, calcite, albite, and apatite (Fig. 2a). SEM/CL images reveal a large diversity of internal structures (see Fig. 2a), which reflect different degrees of re-crystallisation and

fracturing. At least three zircon types can be distinguished: (type I) strongly re-crystallised zircon, showing numerous pores and a very weak cathodoluminescence; (type II) partially re-crystallized zircon, showing relic magmatic domains irregularly transformed into re-crystallized domains with a patchy luminescence, and (type III) pristine zircons, which either show a parallel banding, an oscillatory zoning, or plain cores surrounded by rims with an oscillatory zoning, very similar to the Rubbervale zircons (compare figures 2a and 2c). It is worth noting that many of the pristine zircon grains from the Free State tonalite are transected by microfractures, which could not be avoided during laser ablation.

Zircon of type I (strongly re-crystallised zircon) yielded always discordant analyses (level of concordance: 74-88%) and have the highest U contents (average 587 ppm, n=11) and highest $^{176}Lu/^{177}Hf$ and $^{176}Yb/^{177}Hf$ ratios of 0.0051 and 0.1478 (n=11), respectively, compared to zircon of type II (partially re-crystallized zircon; level of concordance: 93-100%; U = 171 ppm; $^{176}Lu/^{177}Hf$ = 0.0045; $^{176}Yb/^{177}Hf$ = 0.1387, n=9) , and type III (pristine zircons; level of concordance: 88-100%; U = 46 ppm (n=35); $^{176}Lu/^{177}Hf$ = 0.0023; $^{176}Yb/^{177}Hf$ = 0.0717: n=9) – (Table 1 and 2). All pristine zircon domains analysed at Clermont-Ferrand and Frankfurt yield a Concordia age of 2965 ± 6 (n=16). This is identical to a Concordia age of 2964 ± 7 (n=11) which just takes the Frankfurt data into account (see Fig. 3f). In contrast, analyses of the re-crystallized zircons (type I and II), and of strongly fractured zircons (type III), mostly yielded $^{207}Pb/^{207}Pb$ ages between 2992 and 2200 Ma, with a $^{207}Pb/^{207}Pb$ age cluster at about 2800 Ma (2795 ± 25, Fig. 3c-e; Table 1). The Lu-Hf isotope analyses of all pristine and partially re-crystallized zircon domains yield initial $^{176}Hf/^{177}Hf$ of 0.28102 ± 0.00003 (2σ S.D.), which correspond to $\varepsilon Hf_{2.965\ Ga}$ = +5.1 ± 1.2 (2 S.D., n=17) – (Table 2). If the Hf isotope data of the strongly re-crystallised zircons (type I) are taken into account, a similar average $\varepsilon Hf_{2.965Ga}$ of +5.3 is obtained, but with a much bigger error of ± 2.7 (2 S.D, n=29). The bigger error hints that the Lu-Hf system was significantly disturbed during the zircon re-crystallisation, an effect that has not been recognized, so far. In fact, all experimental and field based studies indicate that the initial $^{176}Hf/^{177}Hf$ of zircon will not change (measurably) during pseudomorphic zircon alteration, including the process of re-crystallisation (Gerdes & Zeh, 2009; Zeh et al., 2010a, b; Lenting et al., 2010).

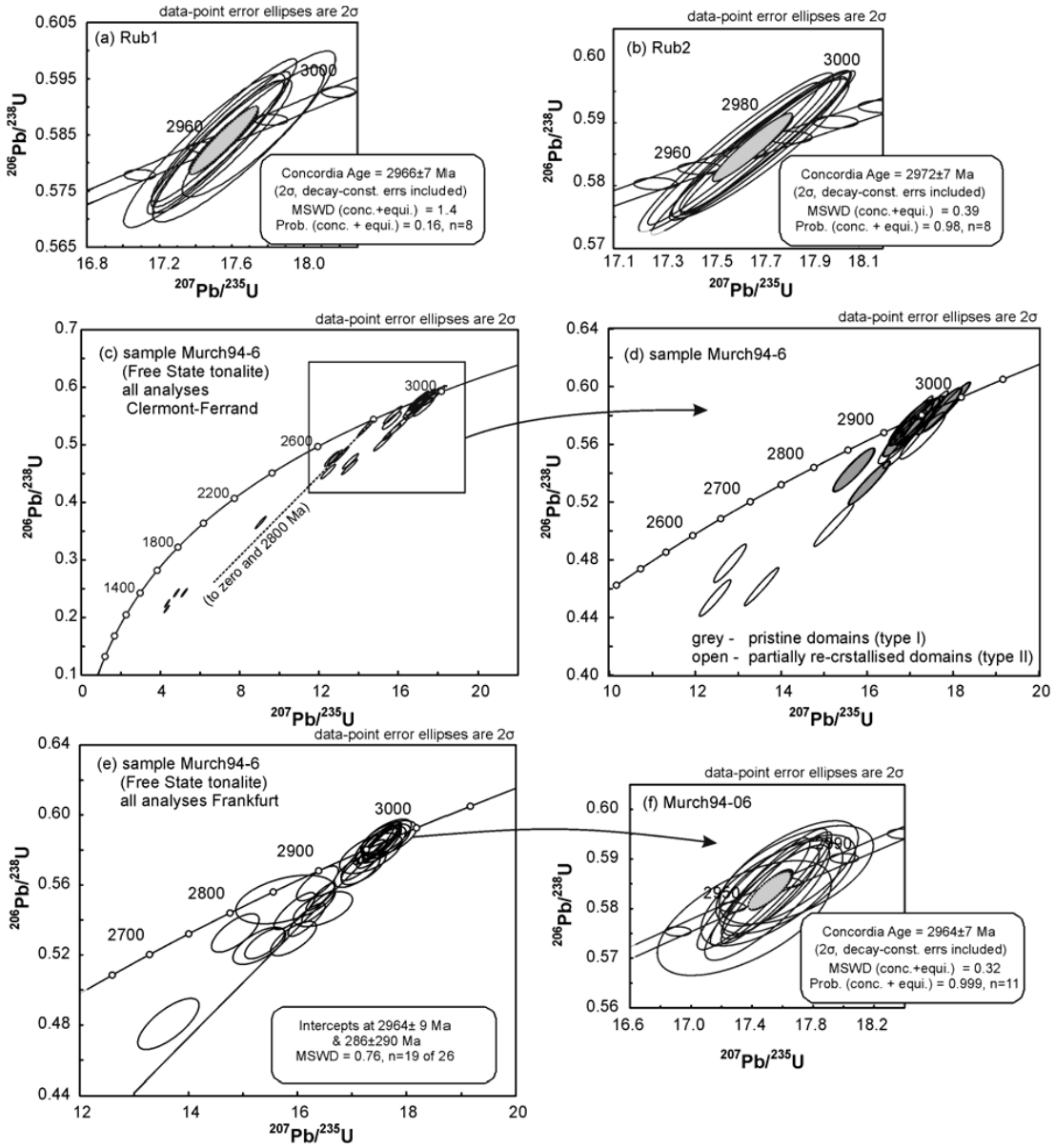

Figure 3: *Concordia diagrams showing the result of U-Pb dating of zircons from (a-b) two metavolcanic rocks of the Rubbervale Formation (sample Rub 1 and Rub 2), and from (c-d) the Free State tonalite of the Rooiwater Complex. (c-d) Results of zircon U-Pb analyses obtained by LA-ICP-MS at Clermont-Ferrand – (c) all data, (d) just zircons of type I (pristine zircon) and type II (partially re-crystallized zircon). (e-f) U-Pb data of pristine zircons (type I) analyzed by LA-ICP-MS at Goethe University Frankfurt, with upper intercept age (e) and concordia age (f).*

3.3. Detrital zircons from the Murchison and La France formations

During this study we carried out U-Pb analyses on 161 zircons of sample Mur (Murchison quartzite), and 29 on zircons of sample LF (La France quartzite). Subsequently, Lu-Hf isotope analyses were obtained from the same zircons by placing the laser spots directly on top or next to the U-Pb spots. The CL images show oscillatory zoning for most grains, typical for zircon growth in igneous rocks (Fig. 2b). Age spectra (Fig. 4) were plotted using the software AGEDISPLAY (Sircombe, 2004).

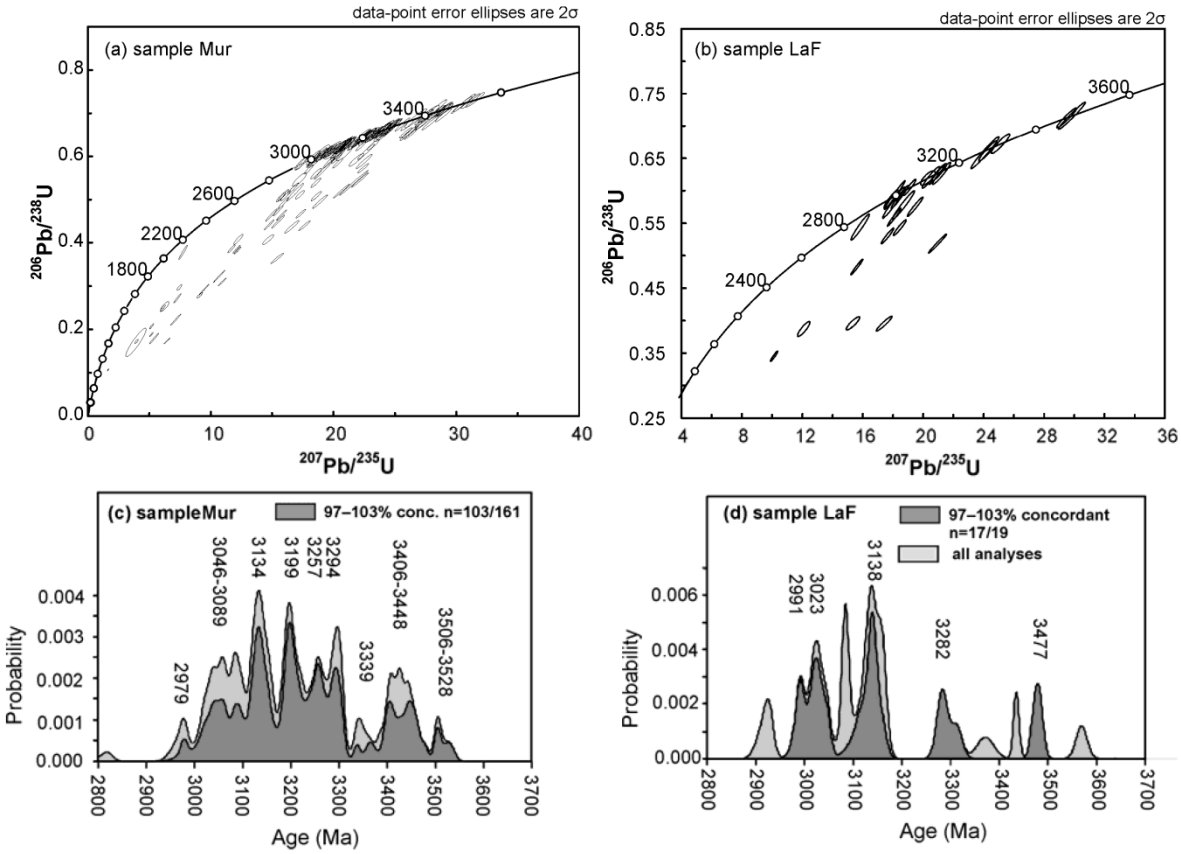

Figure 4: *(a-b) Concordia diagrams, and (c-d) populations density plots of zircon populations analyzed from a quartzitic schist from the Murchison Unit (sample Mur), and from a kyanite-rich metapelitic rock of the La France Formation (sample LF).*

The U-Pb isotope data obtained from zircon grains from sample Mur show a wide range of ages, with clusters at 3.53-3.51 Ga, 3.45-3.41 Ga, 3.37-3.30 Ga, 3.29-3.20 Ga, 3.13 Ga, and at 3.09-3.05 Ga, and a minor population at 2.98 Ga (Fig. 4a, c). Concordant analyses of the zircons of sample LF show a comparable age range with age peaks at 3.48 Ga, 3.28 Ga, 3.14 Ga, 3.02 Ga, and at 2.99 Ga (Fig. 4b,d), even though due to the limited number of analyses, the individual populations are not well constrained. The youngest zircon grain with magmatic zoning from sample Mur yielded an age of 2979 ± 7 Ma (grain s171), and of 2986 ± 12 Ma (grain s186) in sample LF (Table 1). Hafnium isotope data of the zircons from both samples show many similarities. Zircon grains with concordant ages plot mostly near to the chondritic uniform reservoir (CHUR; $\varepsilon Hf_t=0$) or subchondritic (down to εHf_t = -4.9), except a few grains showing superchondritic εHf_t up to +2.3 (Fig. 5, Table 2).

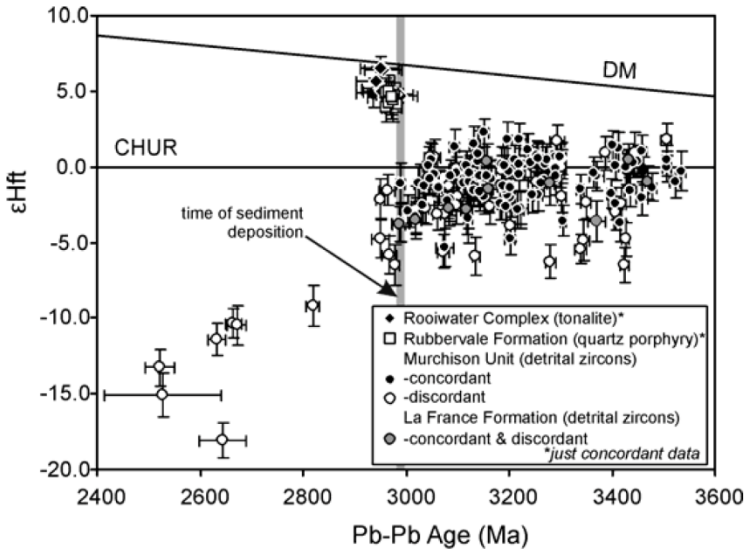

Figure 5: *εHf versus Pb-Pb age diagram showing the data obtained from magmatic zircons of the Free State tonalite (Rooiwater Complex) and of two (meta)quartz porphyry samples of the Rubbervale Formation, and from detrital zircons of a quartzitic schist of the Murchison Unit (MacKop Formation), and from the La France Formation. CHUR – chondritic uniform reservoire, DM- depleted mantle evolution (using MORB Lu-Hf data of Griffin et al., 2002).*

4. DISCUSSION

4.1. Intrusion and deposition ages

The results of U-Pb dating of pristine magmatic zircon grains yield, within error, ages that are comparable with the ages obtained on the quartz porphyries of the Rubbervale Formation (sample Rub 1: 2966 ± 7 Ma; sample Rub 2: 2972 ± 7 Ma) and for the Free State tonalite of the RC (sample MUR 09-06: 2965 ± 6 Ma) – (Fig. 3). As all units of the RC are genetically linked (Vearncombe et al. 1987), the entire RC must be 2.97 Ga old. Thus, the new data provide unambiguous evidence, for the first time, that igneous rocks of the RC and the MGB emplaced contemporaneously, as it has already been suggested on the basis of field relationships (e.g., van Eeden et al.,1939; Viljoen et al., 1978; Vearncombe et al., 1987), and on limited geochemical datasets (Vearncombe, 1991; Schwarz-Schampera, 2010). A genetic link is also supported by the similar zoning patterns of the pristine zircons, showing plain angular cores overgrown by oscillatory zoned rims (in all samples; Fig. 2a, c, d), and by the overlapping, highly superchondritic εHf_t of +4.4 ± 0.6 and +5.1 ± 1.2 (this study; see Table 2, Fig. 5).

The U-Pb ages obtained for the Rubbervale quartz-porphyries during this study, are identical within error to the ages obtained during previous studies, i.e., U-Pb zircon ages of 2966 ± 20 Ma and 2970 ± 10 Ma (Poujol et al., 1996, 2001), and Pb-Pb zircon evaporation ages of 2965.2 ± 1.4 Ma (Brandl et al., 1996), and between 2975± 4 Ma and 2963 ± 6 Ma (Schwarz-Shampera et al., 2010). In contrast, our U-Pb age for the Free State tonalite is much older than the ID-TIMS upper intercept age of 2740 ± 4 Ma, presented by Poujol et al. (1996). We assume that the final date results from the

analyses of partially re-crystallised or microfractured zircons. This is further demonstrated by the fact that mean $^{207}Pb/^{206}Pb$ age of 2795 ± 25 Ma was obtained for these grains.

Maximum deposition ages for the Murchison Unit (Mac Kop Formation) and La France Formation sediments are presented by the youngest detrital zircon grains with a typical magmatic zoning. These yielded concordant U-Pb ages of 2979 ± 7 Ma and 2986 ± 12 Ma, respectively (Fig. 2b, Table 1). The minimum deposition age is constrained by the crystallisation ages of the syn-compressional Baderoukwe (2970 ± 7 Ma) and Malati Pump (2964 ± 7 Ma) granitoids (Fig. 1b), which intruded the Murchison Unit along the Antimony Line (Minnitt & Anhausser, 1992; Jaguin et al., 2012a, b), and by the age of a syn-deformation granitoid dike (2964 ± 5 Ma), which intruded the sheared contact between the Silwana Amphibolites and the Murchison Unit (Block et al., 2012). This indicates that deposition of at least some of the **Murchison** Unit sediments took place immediately prior to their tectono-metamorphic overprint. It is worth noting that the maximum deposition ages for the Murchison Unit and the La France Formations estimated during this study are much younger than those previously derived for the Mac Kop conglomerate (ca. 3074 Ma; Poujol, 2001), and for the felsic volcanics of the Weigel Formation (3087 ± 21 Ma; Poujol et al., 1996). Taking the final data into account, deposition of the Murchison Unit sediments took place between 3090 and 2965 Ma, i.e. over a time span of more than 100 Ma, obviously in a composite basin.

4.2. Provenance of the metasediments

U-Pb ages of the detrital zircons indicate that deposition of the investigated sediments from the Murchison Unit and La France Formation finally took place between ca. 2985 and ca. 2965 Ma, i.e. immediately prior to their tectono-metamorphic overprint (Block et al., 2012). Overlapping age spectra and hafnium isotope data additionally point to a common source area for both sediments (Fig. 4, 5), located most likely to the south of the MGB, comprising regions potentially as far as the Barberton and Swaziland terranes, whereas a northern provenance can be ruled out. The final conclusion is supported by the fact that igneous rocks of the RC and the Rubbervale Formation, located to the north of the Murchison Unit and La France Formation (Fig. 1b), show highly superchondritic εHf_t of +4.4 to +5.1 at 2.97 Ga, whereas detrital zircons with similar ages always have subchondritic εHf_t of -3.7 to -4.1 (Fig. 5, Table 2). This excludes the RC and the Rubbervale Formation as a potential source for the detrital zircon grains, and suggests that both units became juxtaposed to the Murchison Unit and La France Formation immediately after sediment deposition.

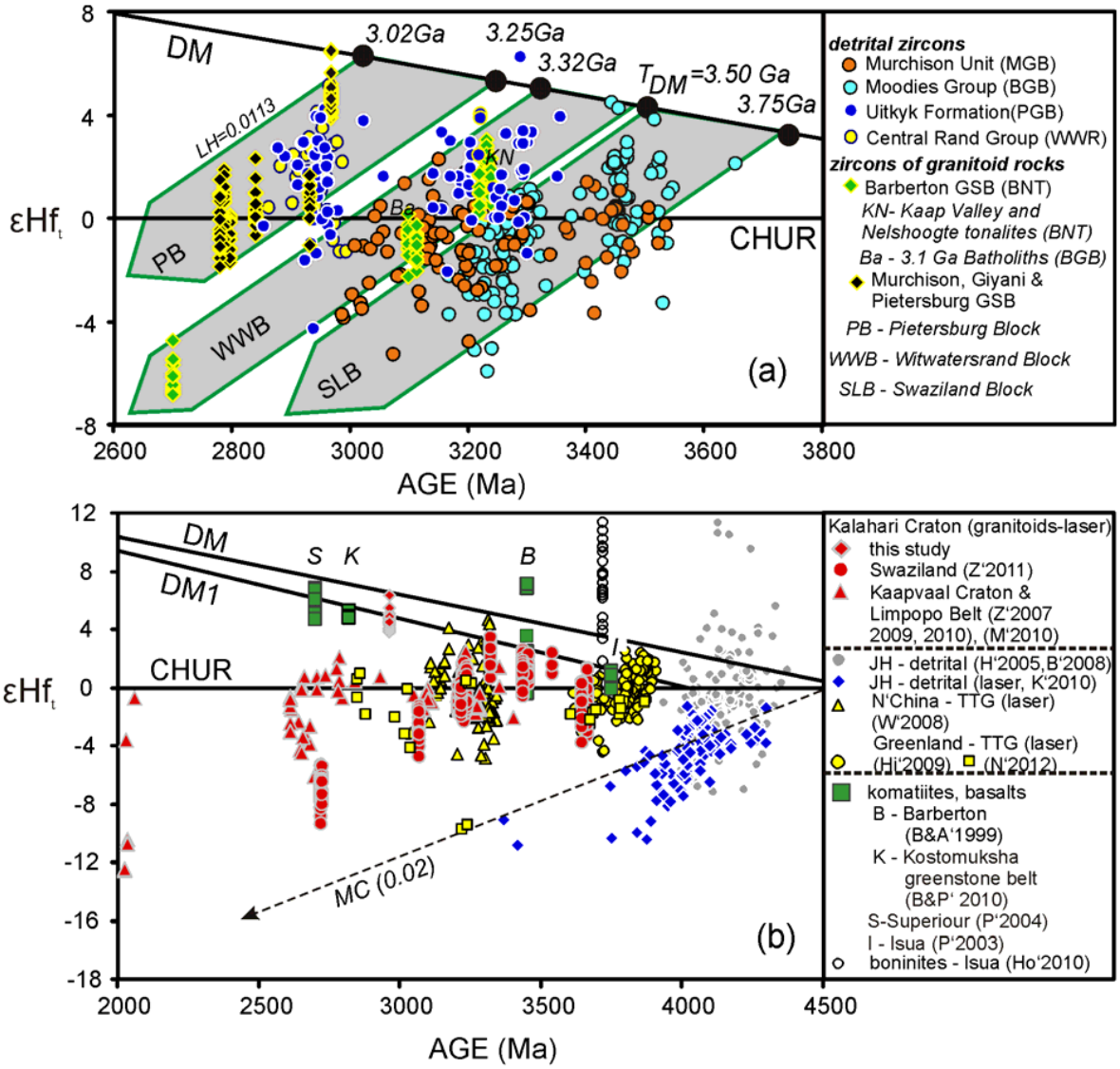

Figure 6: *(a) εHf versus age diagram showing data of detrital zircons analysed during this study (Murchison unit), in comparison to data obtained from (meta)sedimentary and magmatic rocks throughout the Kaapvaal Craton. Data sources (detrital zircons): MGB-Murchison greenstone belt (this study), BGB-Barberton greenstone belt - Moodies Group (Zeh et al., 2012), PBG-Pietersburg greenstone belt – Uitkyk formation (Zeh & Gerdes, 2012), WWR-Witwatersrand Basin – Central Rand Group (Koglin et al., 2010; just data <3.0 Ga). Data of magmatic zircons are from this study and from Zeh et al. (2009). TDM= hafnium model ages calculated with the constants explained in the caption of Table 2. LH=176Lu/176Hf. (b) Compilation of εHft from magmatic rocks of the Kalahari Craton (this study; M'2010, Millonig et al., 2010; Z'2007, '2009, '2010, '2011, Zeh et al., 2007, 2009, 2010a, 2011), from detrital zircons from the Jack Hills (JH) of West Australia (solution Hf data of H'2005, Harrison et al., 2005; B'2008, Blichert-Toft & Albaréde, 2008; and laser Hf data of K'2010, Kemp et al., 2010), the North Chine Craton (W'2008, Wu et al., 2008) and from W-Greenland (Hi'2009, Hiess et al., 2009). Data of Archean komatiites and basalts from the Barberton greenstone belt (B&A'1999, Blichert-Toft & Arndt, 1999), the Kostomuksha greenstone belt (B&P'2010, Blichert-Toft & Puchtel, 2010), from the Superior Province (P'2004, Polat and Münker, 2004) and from Isua (P'2003, Polat et al. , 2003). In addition data from strongly depleted Archean boninites from Isua are shown (Ho'2010: Hoffmann et al., 2010). CHUR – chondritic uniform reservoir, DM-depleted mantle, assuming a*

linear evolution from 4.56 Ga until today (Griffin et al., 2002); DM1- depleted mantle, assuming a linear evolution from 4.0 Ga (εHft=0) until today (εHft=16.4). Note that most of the data of the mafic rocks and those of the Murchison greenstone belt (this study) plot on the DM1 curve (for further explanation see text).

Sediment supply from a southern source is well supported by overlapping U-Pb ages and Hf isotope data obtained from detrital zircon grains of the MGB, and from zircon grains of (meta)igneous and (meta)sedimentary rocks exposed directly to the south of the MGB, as well as in the Barberton greenstone belt and in Swaziland (Fig. 1a, b, 6a). The age clusters at 3.53-3.51 Ga, 3.45-3.41 Ga, 3.37-3.30 Ga, and 3.29-3.20 Ga inferred for the Murchison detrital zircons overlap with crystallisation ages of granitoids and volcanic rocks of the Barberton and the Swaziland regions, comprising the Ancient Gneiss Complex and the Steynsdorp terrane (intrusion ages mostly at 3.56-3.51 Ga; e.g. Armstrong et al., 1990; Kamo & Davis, 1994; Amelin et al., 2000; Compston & Kröner, 1988; Kröner et al., 1989; Kröner & Tegtmeyer, 1994; Schoene et al., 2008; Zeh et al., 2009, 2011), granitoids of the Stolzburg terrane and the Tsawela gneisses (intrusion ages at 3.46-3.41 Ga: Armstrong et al., 1990; Byerly et al., 1996; Kamo & Davis, 1994; Amelin et al., 2000; Kröner et al., 1989; Dziggel et al., 2006; Schoene et al., 2008; Zeh et al., 2009, 2011), the Kromberg and Mendon Formation and Ngwane gneiss enclaves (intrusion ages at 3.33-3.30 Ga: Byerly et al., 1996; Zeh et al., 2011), as well as the Usutu Suite of Swaziland and the Kaap Valley and Nelshoogte tonalites of the BGB (intrusion ages at 3.25-3.22 Ga; Kamo & Davis, 2004; Schoene et al., 2008; Schoene & Bowring, 2010; Zeh et al., 2009, 2011). The younger ages at 3.13 Ga overlap with intrusion ages of the batholiths surrounding the Barberton greenstone belt (3.11 Ga: Nelspruit, Piggs Peak and Mpuluzi batholiths; e.g., Kamo & Davis, 1994; Zeh et al., 2009), and the 3.09-3.05 Ga ages with those of the voluminous granitoids exposed to the direct south of the Murchison GSB, comprising the Harmony and Makhustwi granitoids (intrusion ages at 3.09-3.06 Ga; Brandl & Kröner, 1993; Poujol & Robb, 1999). Furthermore, it should be noted that detrital zircon grains with ages of 3.53 ± 0.2, 3.46 ± 0.2, 3.37 ± 0.2, 3.29 ± 0.2, and 3.23 ± 0.2 Ga are also very common in sediments from the Barberton GSB, in particular in the ca. 3.20 Ga Moodies Group quartzite (Zeh et al., 2012), implying that the 2.97 Ga Murchison sediments might contain abundant reworked detritus of sediments, which were originally deposited further to the south. The suggested southern provenance for the Murchison sediments is also in agreement with the obtained Hf isotope data. In fact, εHf_t of all Murchison detrital zircon grains with ages ranging between 3.55 and 3.22 Ga overlap with εHf_t of detrital zircon grains from the Moodies Group sediments, which themselves follow a crust evolution trend defined by the granitoids of the Swaziland Block (comprising granitoids of the Stolzburg, Steynsdorp and Ancient Gneiss Complex terranes), having hafnium model ages between 3.75 and 3.50 Ga (Fig. 6a, also see Zeh et al., 2009, 2011). In contrast, detrital zircons of the MGB with ages between 3.19 and 2.99 Ga plot on a different crust evolution trend, which is typical for granitoids of the Witwatersrand Block, and characterised by younger hafnium model ages between 3.50 and 3.32 Ga (Fig. 6a, Zeh et al., 2009). The Hf isotope data of the detrital zircon population with ages at 3.13 ± 0.2 Ga (εHf_t between +0.2 and -1.9) overlap with those of zircons from the ca.

3.1 Ga old batholiths surrounding the Barberton GSB. Finally, it should be noted that the Murchison detrital zircon grains with Palaeoarchean ages between 3.35 and 3.18 Ga are less radiogenic (εHf_t mostly chondritic to subchondritic) than detrital zircon grains of similar age analysed from the Uitkyk quartzite of the Pietersburg Greenstone Belt (part of the Pietersburg Block, located ca. 100 km to the north-west of the MGB; Fig. 1), which mostly show superchondritic εHf_t up to +4 (Fig. 6a). This difference points to a different provenance for the Pietersburg sediments, perhaps a terrane which was located to the north of the RC prior to 2.965 Ga (for more discussion see Zeh & Gerdes, 2012).

4.3. Implications for the Mesoarchean accretion of the Kaapvaal Craton

The data obtained during this study provide clear evidence that the MGB and surroundings host two terranes of different origin which became accreted during the Mesoarchean at ca. 2.97 Ga; a northern terrane comprising igneous rocks of the RC and the Rubbervale Formation (=RR terrane), and a southern terrane, comprising rocks of the Murchison Unit and La France Formation (Fig. 7). The timing of the final accretion is constrained by the syn-tectonic intrusion of the Baderoukwe and Malati Pump granodiorite into the Murchison Unit at ca. 2.965 Ga (Jaguin et al., 2012b).

The geochronological, geochemical and isotope data from the magmatic rocks of the RR terrane, i.e., a common calc-alkaline to tholeitic trend, probable pristine high Na/K, trace element patterns with low La_N/Yb_N and negative Eu anomalies (Vearncombe, 1991; Schwarz-Shampera et al., 2010), and the highly superchondritic εHf_t of +4.4 to +5.1 at 2.965 Ga (this study) indicate that the RR terrane results from juvenile crust accretion, i.e. partial melting of mantle material, with further internal differentiation. Vearncombe (1991) suggested that rocks of the RR terrane formed in a primitive island arc. According to Schwarz-Shampera et al. (2010) interpretation, Rubbervale volcanics and associated VMS deposits are consistent with formation in an arc-back arc system in a rifted epicontinental volcanic arc setting.

However, the more detailed geochemical study of Schwarz-Shampera et al. (2010) do not show any LIL/HFSE fractionation compared to primitive mantle, which exclude slab-derived fluid influence. This conclusion is supported by the highly superchondritic εHf_t of the RR rocks, which require magma formation from a depleted mantle source and magma ascent without assimilation of (much) older crust; processes which are inconsistent with an evolved magmatic arc setting. Taking this into account, without influence of any slab-melt or slab-fluid component, it appears rather likely that the igneous rocks of the RR terrane formed within a foreland setting which occurred to the north of the proto-Kaapvaal Craton, prior to 2.965 Ga (Fig. 7a), rather than a supra-subduction setting.

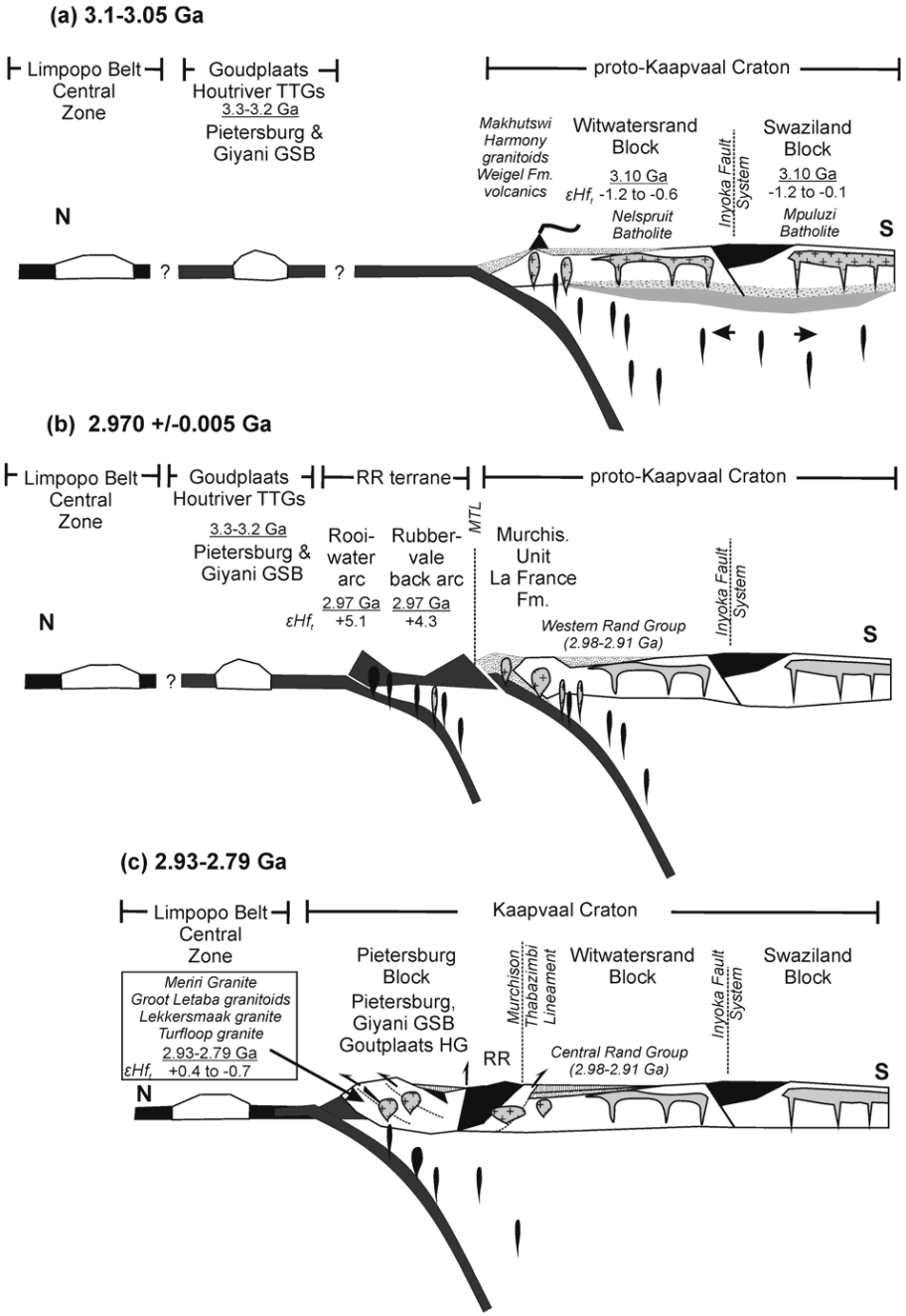

Figure 7: *Geotectonic model for the Mesoarchean amalgamation of the proto-Kaapvaal Craton with terranes now included in the "Pietersburg Block" between 3.1 and 2.79 Ga. (a) Start of southward directed subduction underneath the proto-Kaapvaal Craton at 3.1 Ga. Transformation of the northern edge of the craton from a passive margin into a continental magmatic arc. (b) Formation of the RR terrane immediately prior to the collision with the proto-Kaapvaal Craton, on which sediments of the Murchison- and La France formations (having a southern provenance) where deposited at nearly the same time (ca. 2.98 Ga). The collision event is accompanied by the intrusion of syntectonic granites (Malati pump and Baderoukwe), and by the differential subduction of Murchison GSB sediments (Murchison Unit and La France Formation), and followed by the deposition of sediments of the Western Rand Group. Initial formation of the Murchison-Thabazimbi lineament. (c) Formation of the Pietersburg Block (cordillera) by successive amalgamation of several older terranes, comprising the Goudplaats-Houtriver Gneisses, and mafic rocks of the Pietersburg and Giyany GSB's. Amalgamation was accompanied and followed by (perhaps subduction related) magmatic event at 2.93 Ga (Meriri granite), 2.84 Ga (Groot Letaba gneisses and at 2.79 Ga (Turfloop granite) - (for further explanation see text).*

In contrast to the northern terrane, zircon populations from the Murchison Unit sediments, as part of the southern terrane, reveal the existence of an evolved continental crust in the hinterland, i.e., the proto-Kaapvaal Craton. At 2.97 Ga, this proto-Kaapvaal Craton consisted of the amalgamated Witwatersrand and Swaziland blocks (Fig. 1), which became accreted along the Inyoka-Suture Zone at ca. 3.22 Ga (e.g., Kröner *et al.* 1991; de Wit *et al.* 1992; Kamo & Davis, 1994; Lowe 1994; de Ronde & de Wit 1994; Lowe & Byerly 1999; Schoene et al., 2008; Zeh *et al.* 2009, 2011, 2012; Schoene & Bowring 2010). Presently, nothing is known about the environment of sediment deposition in the MGB between 3.09 and 2.97 Ga (see section 4.1.: "Intrusion and deposition ages"). However, it is likely that deposition occurred at ca 3.09 along an active continental margin that limited the proto-Kaapvaal Craton to the north (Fig. 7). This setting is in agreement with the U-Pb-Hf isotope data for the youngest detrital zircon grains, having subchondritic εHf_t (-6.5 to +1.0) and ages between 3.09 and 2.97 Ga, with the age of the Weigel Formation volcanics (3.087 ± 0.021 Ma: Poujol et al., 1996) and with the numerous granitoids, which emplaced directly to the south of the MGB at 3.11 and then 2.97 Ga, comprising the Harmony, Makhutswi, Discovery and Baderoukwe plutons (see Fig. 8d) - (Brandl and Kröner, 1993; Poujol et al. 1996; Poujol and Robb, 1999; Poujol, 2001, Jaguin et al., 2012a). These granitoids formed perhaps in response to southward-directed subduction underneath the proto-Kaapvaal Craton (Fig. 7a), as it has been suggested by Poujol & Robb (2001), Poujol et al., (2003), Anhaeusser (2006) and Zeh et al. (2009). This geotectonic setting is consistent with out interpretation of a rifted zone, without island, preventing topographic highs to feed the southern MGB basin.

While a southward-directed subduction provides a reasonable explanation for the amalgamation of the proto-Kaapvaal Craton with the RR terrane at about 2.965 Ga, formation of the RR terrane itself within the very same subduction zone system seems to be unlikely. This final conclusion is in good agreement with pressure-temperature-deformation-time paths inferred for different units of the MGB, indicating quick burial of sediments and igneous rocks to depths reaching 30 km (along a relatively cold geotherm of ca. 25 to 35°C), followed by a quick exhumation along N-dipping thrust zones in a generally N-S directed compressional stress field between 2.965 and 2.92 Ga (for more details see Block et al., 2012).

The new age data obtained during this study clearly indicate that amalgamation of the RR terrane took place much earlier than the Limpopo Orogeny, which happened after 2.69-2.67 Ga, as demonstrated by age data from metamorphic and magmatic rocks of the Limpopo Belt's Southern Marginal Zone (Barton et al., 1992; Kreissig et al., 2001) - (Fig. 1). This hiatus in tectonic activity suggests that the northwestern edge of the proto-Kaapvaal Craton and the Limpopo Belt terrane were separated at 2.97-2.90 Ga. This also implies that the geotectonic model of Vearncombe (1991, 1992), suggesting the accretion of a primitive island arc during a Himalayan-type orogenesis (as was previously proposed for the Limpopo Belt by Coward, 1976 and Treloar et al., 1992) is incorrect. Instead of a Himalayan-type orogenesis, the northern margin of the proto-Kaapvaal Craton more likely hosted an Andean-type orogen at 2.97- <2.90 Ga,

similar to the modern day Cascade Mountains (USA), where terranes of different origin became accreted in a relatively short period of time (Fig. 7b), comprising the RR terrane (with magmatic rocks having ages between 2.975-2.963 Ga; this study), the Goudplaats-Houtriver gneiss terrane (with TTG gneisses having ages between 3.3-3.28 Ga, e.g., Brandl & Kröner, 1993; Kröner et al., 2000), and ancient greenstone terranes (comprising the mafic to ultramafic rocks of Pietersburg and Giyani greenstone belts, which formed prior to 3.4 Ga, e.g., Byron & Barton, 1990). Successive accretions of these terranes perhaps ended up in the formation of a cordillera, the relics of which being now assembled and exposed in the Pietersburg block, which was affected by several magmatic activities with crust re-working at 2.931 Ga (Meriri granite, εHf_t = +0.7 ± 1.5), at 2.839 Ga (Groot Letaba Gneiss, εHf_t = +0.4 ± 1.5), and at 2.782 Ma (Turfloop granite, εHf_t = -0.2 ± 2.1) – (Zeh et al., 2009).

4.4. Source of the Witwatersrand and Pietersburg gold

The new U-Pb-Hf isotope datasets also place new constraints on the provenance of the economically important Mesoarchean gold-bearing sediments in southern Africa, comprising those of the Central Rand Group of the Witwatersrand Basin, and the Uitkyk formation of the Pietersburg greenstone belt. The sediments in both areas were deposited in braided river and alluvial fan environments between 2.90 (2.88) and 2.78 (2.67) Ga (Robb et al., 1990; Poujol et al., 1999; de Wit et al., 1993; Zeh & Gerdes, 2012), i.e. after the subduction-amalgamation event suggested above, and affected by northward thrusting sometimes between 2.90 and 2.70 Ga (de Wit, 1991; de Wit et al., 1992). Furthermore, they contain abundant detrital zircon grains with ages between 2.97 and 2.92 Ga (e.g., Robb et al., 1990; Poujol et al., 1999; Kositcin and Krapez, 2004; Frimmel et al., 2005; de Wit et al., 1993; Zeh & Gerdes, 2012) – (see Fig. 8a, b), and with superchondritic εHf_t up to +5.2 (Koglin et al., 2010; Zeh & Gerdes, 2012 – (Fig. 6a). At least some of the detrital zircon grains overlap those from the RR terrane (ages: 2.973-2.963 Ga; εHf_t = +4.4 to +5.1), and most zircon grains (with ages <2.97 Ga) plot on the same crust evolution trend, as defined by magmatic rocks for the Pietersburg Block (Fig. 6a). In contrast, contemporaneous granitic and mafic rocks of the Witwatersrand Block with ages of about 3.06 Ga, show significantly lower εHf_t between +0.2 and -1.8 (Frimmel et al., 2009). Taking this into account, the magmatic rocks of the amalgamated RR terrane and the Pietersburg Block are a potential source not only for the zircon grains from the Witwatersrand and Pietersburg sedimentary basins, but also for the gold itself (only if gold has at least some detrital origin - for more discussion about this subject see Frimmel et al., 2005). The link between gold and zircon is provided by the facts that the RR terrane consists not only of juvenile magmatic rocks but also hosts several VMS deposits with gold contents up to 1.7 ppm in massive sulphide ores (Schwarz-Schampera, 2010). However, a discussion whether or not this gold content is high enough to account for the Witwatersrand deposit is beyond the scope of this paper. Instead, it should be considered that the RR terrane represents only a minor relic of the accreted arc-back arc system, and that the style of mineralisation

may have changed along strike, perhaps with domains similarly enriched in gold like the Taupo volcanic zone of New Zealand (e.g., Hedenquist, 1986; Simmons, 1995; Stoffers et al., 1999).

The proposed accretion of the RR terrane at 2.97 Ga and formation of a cordillera along the northern margin of the proto-Kaapvaal craton are in good agreement with the fact that the Witwatersrand Basin evolved from a passive continental margin (strata of the Western Rand Group with deposition ages between 2.98 and 2.91 Ga), toward a syn-collisional retroarc basin (strata of the Central Rand Group with deposition ages between 2.90 and 2.78Ga), even though the timing is not perfect. Furthermore the role of the proposed magmatic arc that existed at the north-eastern edge of the proto-Kaapvaal craton between 3.1 and 2.96 Ga remains unclear (see chapter 4.3.). It must be considered, however, that the transformation of the Witwatersrand Basin from a passive margin into a retro-arc basin, is not only controlled by the collision of the proto-Kaapvaal craton with the Pietersburg Block, but also by the accretion with the Kimberley Block along the Colesberg Lineament (Fig. 1), and that the amalgamation and collision of the different blocks was asynchronous. Based on the available age data it appears very likely that collision of the proto-Kaapvaal Craton with the Pietersburg Block started earlier (at 2.97 Ga, this study) than the collision with the Kimberley Block (between 2.93 and 2.88 Ga; Schmitz et al., 2004). Furthermore, it cannot be excluded that the Kimberley Block also hosted relics of a "primitive island arc" (similar to the RR terrane), which has been the source for detrital zircon grains and gold, as was proposed in a modified form by Koglin et al. (2010).

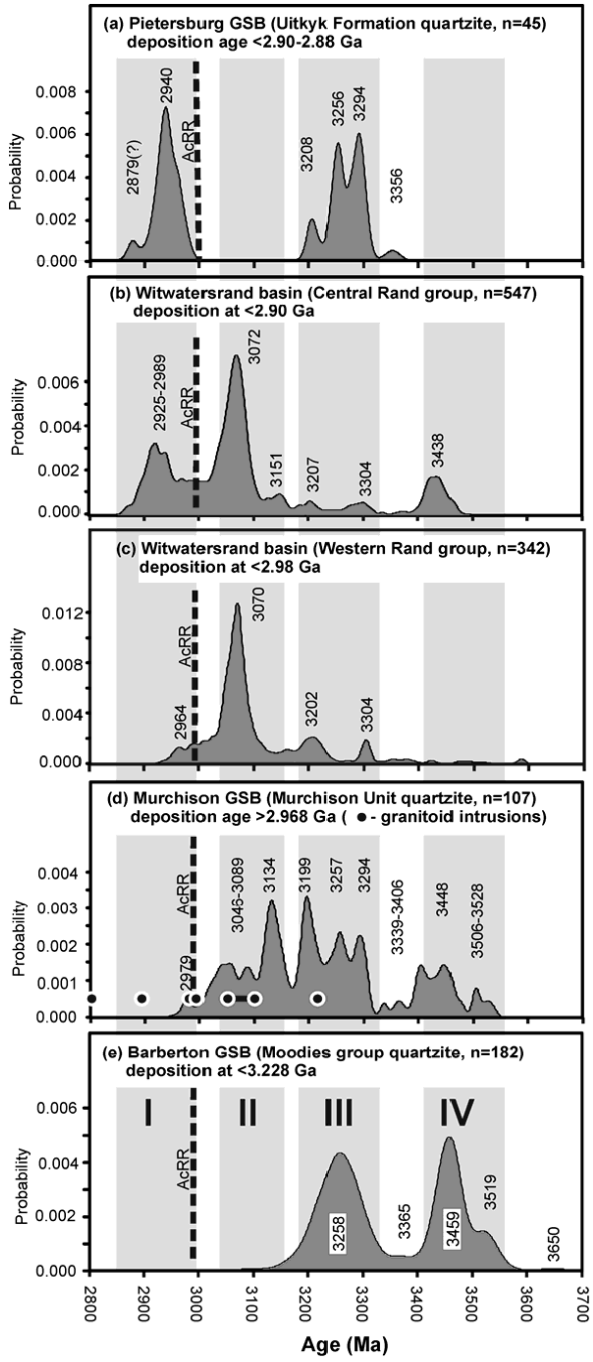

Figure 8: *Synopsis of probability density diagrams, showing age spectra of detrital zircons from (a) the Pietersburg greenstone belt (Uitkyk Formation; Zeh & Gerdes, 2012), (b) the Central Rand Group of the Witwatersrand basin (data of Kositcin & Krapez, 2004), (c) the Western Rand Group of the Witwatersrand basin (data of Kositcin & Krapez, 2004), (d) from a quartzitic schist of the Murchison greenstone belt (MacKop formation: this study), and (e) and from the Moodies Group of the Barberton Greenstone Belt (Zeh et al., 2012). The black cirles in (d) mark the intrusion ages of granitoids in the Murchison greenstone belt area. The grey fields I to IV mark predominant zircon age populations found in different sediments of the Kaapvaal Craton. I - in gold-bearing sediments of the Pietersburg GSB and in the Central Rand Group. II - Central Rand and Western Rand groups of the Witwatersrand basin and in the Murchison GSB. III – Murchison GSB, Barberton GSB and Pietersburg GSB (note, the zircons of the PGB show different Hf isotope patterns – see Fig. 6a). IV - Murchison GSB, Barberton GSB and Witwatersrand basin. The vertical dotted line marks the timing of the accretion of the proto-Kaapvaal Craton with the RR terrane (AcRR).*

4.5. Constraints for the secular Archean crust-mantle evolution

The highly superchondritic εHf_t obtained for the Free State tonalite (5.1 ± 1.2) and Rubbervale volcanics (4.4 ± 0.6) at 2.97 Ga provide robust evidence for the existence of a depleted mantle source during the Mesoarchean at 2.97 Ga. Such a source has not been recognised so far for basement rocks throughout the entire Kaapvaal Craton (Zeh et al., 2009, 2011). Existing U-Pb-Hf isotope datasets reveal superchondritic εHf_t only for granitoids with emplaced ages at 3.55, 3.45, 3.33 and 3.23 Ga (see Zeh et al. 2009, 2011), whereas granitoids with ages younger than 3.2 Ga are mostly chondritic to subchondritic (Fig. 6a, b). Thus, the εHf_t of the RR terrane rocks place new constraints on the secular evolution of the Earth's mantle during the Archean, in particular, since the RR rocks fulfil two important criteria: (1) their parental magmas were derived directly from a depleted mantle source at 2.97 Ga without contamination of much older crust, and (2) the depleted mantle source was representative of the Earth at the time of magma emplacement.

Point (1) is supported by the fact that all lithologies from the Rooiwater Complex, comprising the Novengilla Gabbro-Anorthosite Series, the Quagga-Quartz-Amphibolite, and the Free State Tonalite Series, show shallow MORB-like REE patterns with $La_N/Yb_N \sim 0.5\text{-}2.0$, and that the REE patterns of the Quagga-Quartz Amphibolite overlap with those of the Free State Tonalite Suite and Rubbervale volcanics (see Vearncombe, 1991; Schwarz-Schampera, 2010). This, and the overlapping U-Pb ages and Hf isotope data, point to a plausible fractionation of a mafic magma, which was directly derived from a depleted mantle source without any significant contamination, even though a detailed geochemical study has still to be done. If the Free State tonalite formed by re-melting of hydrated mafic crust (maybe a much older subducted oceanic crust), this would have likely taken place in an island arc setting, and the REE patterns would have been much steeper, due to garnet, clinopyroxen and/or hornblende fractionation (e.g., Smithies, 2000; Foley et al., 2002; Martin et al., 2005). Point (2) is supported by the fact that the Hf isotope data of the RR terrane rocks plot on the same depleted mantle evolution trend, like the Hf isotope data from many other Archean magmatic rocks worldwide (see Fig. 6b): comprising basalts and komatiites from W-Greenland (Polat et al. 2003), from the Kostomuksha greenstone belt in the Ukraine (Blichert-Toft & Puchtel, 2010), from the Superior province of Canada (Polat & Münker, 2004), and from the Barberton greenstone belt (Blichert-Toft & Arndt, 1999), as well as TTG gneisses from W-Greenland (Hiess et al., 2009), N-China Craton (Wu et al., 2008), and Swaziland (Zeh et al., 2011). In fact, most of these data plot on a linear mantle array between 4.0 Ga ($\varepsilon Hft=0$) and today ($\varepsilon Hf_t = +18$), designated as DM1-array on figure 6b. This array, which can be described by $^{176}Hf/^{177}Hf$ today =0.283294 and $^{176}Lu/^{177}Hf$ today =0.0402, plots clearly below the DM-array defined by the data of Griffin et al. (2002), but is almost identical to the array of Pietrianik et al. (2009), based on detrital zircon U-Pb-Hf data (see Hawkesworth et al., 2010).

Nevertheless, there are several Hf isotope data which clearly plot above the DM1-trend; e.g., some of the W-Greenland TTG's (Hiess et al., 2009), many of the Jack

Hills detrital zircon grains (Harrison et al., 2005), as well as the Isua boninites (Hofmann et al., 2010). These data might point to an earlier start of global mantle depletion during the Hadean. This is however controversial as, unfortunately, there are no data from exposed Hadean rocks to support this hypothesis. Zircons from the 4.03-3.94 Ga Acasta Gneisses, the oldest rocks exposed on Earth, only yield negative εHf_t, (Iizuka & Hirata, 2005; Iizuka et al., 2009; Amelin et al., 2000; all data are not shown in Fig. 6b). This is also true for all the Hadean detrital zircon grains from the Jack Hills analysed by LA-ICP-MS (Harrison et al., 2008; Kemp et al., 2010), as well as for the zircon Hf solution data of Amelin et al. (2000). In contrast, zircon solution Hf isotope data of Harrison et al. (2005), and Blichert-Toft & Albarede (2008) yield extremely superchondritic and subchondritic εHf_t (see grey dots in Fig. 6b). However, the usefulness of these data is questionable, since mixed analyses of zircon domains formed during different magmatic-metamorphic events cannot be ruled out (for more discussion about this subject see Kemp et al., 2010). Nonetheless, the data of the Jack Hills and Acasta zircon grains provide clear evidence for the existence of a non-radiogenic crust during the Hadean (e.g., Amelin et al., 2000; Kemp et al., 2010), which in turn requires the existence of a complementary depleted mantle reservoir. However, the zircon data provide no information about the quantity of the Hadean crust or about its composition (mafic proto crust *versus* TTG crust; for more discussion see Harrison et al., 2008; Hopkins et al., 2010; Kemp et al., 2010; Darling et al., 2010). Taking this into account, the evolution of the Earth's mantle is most robustly reflected by a linear mantle depletion trend between 4.0 and 2.5 Ga. Nevertheless, considering the errors and fluctuations of the data, a two-stage depleted mantle evolution model, e.g., Tolstikin et al. (2006) is also possible. This model requires little mantle depletion during the Hadean (4.56-4.0 Ga), explainable by the existence of a long-lived, volumetrically insignificant Hadean protocrust (e.g., Kamber et al., 2003, 2005; Kemp et al., 2010), followed by a period of more rapid mantle depletion, caused by important crustal growth and preservation during the Archean (also see Blichert-Toft & Puchtel., 2010; Hawkesworth et al., 2010; Kemp et al., 2010). Positive deviation of εHf_t from the DM1-array may be explained by differential depletion, meaning that restricted domains within the normally evolving mantle became "abnormally" depleted. Evidence for such restricted, highly depleted mantle reservoirs during the Hadean to Early Archean is provided by some of the Barberton komatiites (up to +7.1 at 3.45 Ga; Blichert-Toft & Arndt, 1999), and by the Isua boninites with εHf_t up to +13.5 at ca. 3.75 Ga (Hoffmann et al., 2010).

5. CONCLUSIONS

The MGB hosts an important Archean suture zone, perhaps the precursor of the present day Thabazimbi-Murchison Lineament, which separates rocks of a Mesoarchaean primitive island arc (RR terrane) to the north from evolved rocks of the proto-Kaapvaal Craton to the south.

Rocks of the primitive island arc were directly derived from a depleted mantle source at 2.975-2.963 Ga, as reflected by highly superchondritic εHf_t of 4.4 to 5.1, whereas sediments of the southern terrane were supplied from evolved granitoid rocks with intrusion ages between 3.55 and 2.98 Ga, such as the ones found in the Barberton Greenstone Belt, Swaziland, and in the basement immediately to the south of the MGB.

Amalgamation of the Murchison terranes occurred by subduction-collision at 2.97 Ga. This event may mark the end of a long lasting southward-directed subduction underneath the proto-Kaapvaal Craton starting at about 3.10 Ga. This accretion process ended up in the formation of the Pietersburg Block cordillera.

The Hf isotope composition together with the occurrence of VMS deposits within the RR terrane constitute a strong argument to propose that this terrane was a very likely source for the gold-bearing sediments deposited in the Witwatersrand Basin and the Pietersburg Greenstone Belt after 2.90 Ga.

Superchondritic εHf_t of the RR terrane rocks, along with data from worldwide sources provide evidence that mantle depletion started at 4.0 Ga, and continued linearly during the Archean between 4.0 and 2.5 Ga. This pattern can be explained by an enhanced but continuous crust formation and crust stabilisation during the Archean.

References

Altermann, W. & Nelson, D. R. (1998). Sedimentation rates, basin analysis and regional correlations of three Neoarchaean and Palaeoproterozoic sub-basins of the Kaapvaal Craton, Northern Cape Province, South Africa. *Journal of African Earth Sciences*, **13**, 415-435.

Amelin, Y., Lee, D., Halliday, A. N. & Pidgeon, R. T. (1999). Nature of the Earth's earliest crust from hafnium isotopes in single detrital zircons. *Nature*, **399**, 252-255.

Amelin, Y., Lee, D.-C. & Halliday, A. N. (2000). Early-middle Archean crustal evolution deduced from Lu-Hf and U-Pb isotopic studies of single zircon grains. *Geochimica et Cosmochimica Acta*, **64**, 4205-4225.

Anhaeusser, C. R. (2006). A reevaluation of Archean intracratonic terrane boundaries on the Kaapvaal Craton, South Africa: Collisional suture zones? In: W. U. Reimold & R. Gibbson (eds.) *Processes on the Early Earth.* Geological Society of America, Special Publications, **405**, 315-332.

Armstrong, R. A., Compston, W., De Wit, M. J. & Williams, I. S. (1990). The stratigraphy of the 3.5-3.2 Ga Barberton greenstone belt revisited: a single zircon ion microprobe study. *Earth and Planetary Science Letters*, **101**, 90-106.

Bard, J. P. (1983). Metamorphism of an obducted island arc: example of the Kohistan sequence (Pakistan) in the Himalayan collided range. *Earth and Planetary Science Letters,* **65**, 133-144.

Barton, J. M., Jr., Doig, R., Smith, C. B., Bohlender, F. & Van Reenen, D. D. (1992). Isotopic and REE characteristics of the intrusive charnoenderbite and enderbite geographically

associated with the Matok Pluton, Limpopo Belt, southern Africa. *Precambrian Research*, **55**, 451-467.

Blichert-Toft, J. & Albaréde, F. (1997). The Lu-Hf isotope geochemistry of chondrites and the evolution of the mantle-crust system. *Earth and Planetary Science Letters,* **148**, 243-258.

Blichert-Toft, J. & Albaréde, F. (2008). Hafnium isotopes in Jack Hills zircons and the formation of the Hadean crust. *Earth and Planetary Science Letters,* **265**, 686-702.

Blichert-Toft, J. & Arndt, N. T. (1999). Hf isotope compositions of komatiites. *Earth and Planetary Science Letters*, **171**, 439-451.

Blichert-Toft, J. & Puchtel, I. S. (2010). Depleted mantle sources through time: Evidence from Lu–Hf and Sm–Nd isotope systematics of Archean komatiites. *Earth and Planetary Science Letters*, **297**, 598–606.

Block, S., Moyen, J.-F., Zeh, A., Poujol, M., Jaguin, J., Paquette. J.-L. (2012). The Murchison Greenstone Belt, South Africa: accreted slivers with contrasting metamorphic conditions. *Precambrian Research, in press*

Bouvier A., Vervoort J. D. & Patchett P. J. (2008). The Lu-Hf and Sm-Nd isotopic composition of CHUR: constraints from unequilibrated chondrites and implications for the bulk composition of terrestrial planets, *Earth and Planetary Science Letters,* **273**, 48-57.

Brandl, G., Cloete, M. & Anhaeusser, C. R. (2006). Archaean greenstone belts. In: M. R. Johnson, C. R. Anhaeusser and R. J. Thomas (eds.) *The Geology of South Africa*. Geological Society of South Africa, Johannesburg/Council of Geosciences, Pretoria, pp. 9-57.

Brandl, G. & Kröner, A. (1993). Preliminary results of single zircon studies from various Archaean rocks of the north-eastern Transvaal. *Abstract. 16th Colloq. African Geology, Mbabane, Swaziland, Vol.* **2**, 54-56.

Brandl, G., Jaeckel, P. & Kröner, A. (1996). Single zircon age for the felsic Rubbervale Formation, Murchison greenstone belt, South Africa. *South African Journal of Geology*, **99**, 229-234.

Burger, A. J. & Coertze, F. J. (1973). Radiometric age measurements on rocks from southern Africa to the end of 1971. *Bulletin, Geological Survey of South Africa*, **58**, 46–46.

Burger, A. J. & Walraven, F. (1979). Summary of age determinations carried out during the period April 1978 to March 1978. *Annuals of the Geological Survey of South Africa*, **12**, 209-218.

Byerly, G. R., Kröner, A., Lowe, D. R., Todt, W. & Walsh, M. M. (1996). Prolonged magmatism and time constraints for sediment deposition in the early Archean Barberton greenstone belt: Evidence from the Upper Onverwacht and Fig Tree groups, *Precambrian Research*, **78**, 125 - 138.

Byron, C. L. & Barton, J. M., Jr. (1990). The setting of mineralization in a portion of the Eersteling goldfield, Pietersburg granite-greenstone terrane, South Africa. *South African Journal of Geology*, **93**, 463-472.

Chardon, D., Choukroune, P. & Jayananda, M. (1996). Strain patterns, décollement and incipient sagducted greenstone terrains in the Archaean Dharwar craton (south India). *Journal of Structural Geology*, **18**, 991–1004.

Cole, J. W. (1979). Structure, petrology, and genesis of Cenozoic volcanism, Taupo Volcanic Zone, New Zealand - a review. *Journal of Geology and Geophysics*, **22**, 631–657.

Compston, W. & Kröner, A. (1988). Multiple zircon growth within early Archean tonalitic gneiss from the Ancient Gneiss Complex, Swaziland. *Earth and Planetary Science Letters*, **87**, 13-28.

Condie, K. C., Beyer, E., Belousova, E., Griffin, W. L. & O'Reilly, S. Y. (2005). U-Pb isotopic ages and Hf isotopic composition of single zircons: The search for juvenile Precambrian continental crust. *Precambrian Research*, **139**, 42-100.

Coward, M. P., Windley, B. F., Broughton, R. D., Luff, I. W., Petterson, M. G., Pudsey, C. J., Rex, D. C. & Asif-Khan, M. (1986). Collision tectonics in the NW Himalayas. In: *Collision Tectonics* (Coward, M.P. and Ries, A. C. Eds.), Geological Society London, Special Publications, **19**, 203-219.

Darling, J., Storey, C. & Hawkesworth, C. (2009). Impact melt sheet zircons and their implications for the Hadean crust. *Geology*, **37**, 927–930.

Davis, D. W., Amelin, Y., Nowell, G. M. & Parrish, R. R. (2005). Hf isotopes in zircon from the western Superior province, Canada: Implications for Archean crustal development and evolution of the depleted mantle reservoir. *Precambrian Research*, **114**, 295-325.

De Ronde, C. E. J. & de Wit (1994). Tectonic history of the Barberton greenstone belt, Southern Africa: 490 million years of Archean crustal evolution. *Tectonics*, **13**, 983-1005.

De Wit, M. J., Roering, C., Hart, R. J., Armstrong, R. A., De Ronde, C. E. J., Green, R. W. E., Tredoux, M., Peberdy, E. & Hart, R. A. (1992). Formation of an Archaean continent. *Nature*, **357**, 553-562.

de Wit, M. J. (1991). Archaean greenstone belt tectonism and basin development: some insights from the Barberton and Pietersburg greenstone belts, Kaapvaal Craton, South Africa. *Journal of African Earth Sciences*, **13**, 45-63.

de Wit, M. J., Jones, M. G. & Buchanan, D. L. (1992). The geology and tectonic evolution of the Pietersburg Greenstone Belt, South Africa. *Precambrian Research*, 55, 111-122.

De Wit, M. J., Armstrong, R. A., Kamo, S. L. & Erlank, A. J. (1993). Gold-bearing sediments in the Pietersburg greenstone belt: age equivalents of the Witwatersrand Supergroup sediments, South Africa. *Economic Geology*, **88**, 1242-1252.

du Plessis, C. P. (1990). Tectonism along the Thabazimbi-Murchison lineament. Ph.D. Thesis (unpubl.), University of the Witwatersrand, Johannesburg, 243 pp.

Dziggel, A., Stevens, G., Poujol, M., Anhaeusser, C. R. & Armstrong, R. A. (2002). Metamorphism of the granite-greenstone terrane south of the Barberton greenstone belt, South Africa: An insight into the tectono-thermal evolution of the lower portions of the Onverwacht Group. *Precambrian Research*, **114**, 221-247.

Dziggel, A., Stevens, G., Poujol, M. & Armstrong, R. A. (2006). Contrasting source components of clastic metasedimentary rocks in the lowermost formations of the Barberton greenstone belt. In: W.U. Reimold and R. Gibson (eds.) *Processes of Early Earth*. Geological Society of America, pp. 157-172.

Frimmel, H. E., Groves, D. I., Kirk, J., Ruiz, J., Chesley, J. & Minter, W. E. L. (2005). The formation and preservation of the Witwatersrand goldfields, the largest gold province in the world. In: Hedenquist, J.W., Thompson, J.F.H., Goldfarb, R.J., Richards, J.P. (eds.), *Economic Geology One Hundredth Anniversary Volume. Society of Economic Geologists,* Littleton, pp. 769–797.

Frimmel, H..E., Zeh, A., Lehrmann, B., Hallbauer, D. & Frank, W. (2009). Geochemical and Geochronological Constraints on the Nature of the Immediate Basement next to the Mesoarchaean Auriferous Witwatersrand Basin, South Africa. *Journal of Petrology*, **50**, 2187 - 2220.

Foley, S. F., Tiepolo, M. & Vannucci, R. (2002). Growth of early continental crust controlled by melting of amphibolite in subduction zones. *Nature,* **417**, 637– 640.

Gerdes, A. & Zeh, A. (2006). Combined U-Pb and Hf isotope LA-(MC)ICP-MS analyses of detrital zircons: Comparison with SHRIMP and new constraints for the provenance and age of an Armorican metasediment in Central Germany. *Earth and Planetary Science Letters,* **249**, 47-61.

Gerdes, A. & Zeh, A. (2009). Zircon formation *versus* zircon alteration – new insights from combined U-Pb and Lu-Hf *in-situ* LA-ICP-MS analyses, and consequences for the interpretation of Archean zircon from the Central Zone of the Limpopo Belt. *Chemical Geology*, **261**, 230-243.

Good, N. & De Wit, M. J. (1997). The Thabazimbi-Murchison Lineament of the Kaapvaal craton, South Africa: 2700 Ma of episodic deformation. *Journal of the Geological Society* **154**, 93-97.

Griffin, W. L., Pearson, N. J., Belousova, E., Jackson, S. E., O'Reilly, S. Y., van Achterberg, E. & Shee, S. R. (2000). The Hf isotope composition of cratonic mantle: LAM-MCICPMS analysis of zircon megacrysts in kimberlites. *Geochimica et Cosmochimica Acta*, **64**, 133–147.

Griffin, W. L., Wang, X., Jackson, S. E., Pearson, N. J., O'Reilly, S. Y., Xu, X. & Zhou, X. (2002). Zircon chemistry and magma mixing, SE China: In-situ analysis of Hf isotopes, Tonglu and Pingtan igneous complexes. *Lithos*, **61**, 237–269.

Griffin, W. L., Belousova, E. A., Shee, S. R., Pearson, N. J. & O'Reilly, S. Y. (2004). Archean crustal evolution in the northern Yilgarn Craton: U-Pb and Hf-isotope evidence from detrital zircons. *Precambrian Research*, **131**, 231-282.

Guitreau, M., Blichert-Toft, J., Martin, H., Mojzsis, S. J. & Albaréde, F. (2012). Hafnium isotope evidence from Archean granitic rocks for deep-mantle origin of continental crust. *Earth and Planetary Science Letters*, **337–338**, 211–223.

Harrison, T. M., Blichert-Toft, J., Müller, W., Albaréde, F., Holden, P. & Mojzsis, S. J. (2005). Heterogeneous Hadean hafnium: Evidence of continental crust by 4.4–4.5 Ga. *Science*, **310**, 1947-1950.

Harrison, T. M., Schmitt, A. K., McCulloch, M. T. & Lovera, O. M. (2008). Early (≥ 4.5 Ga) formation of terrestrial crust: Lu-Hf, $\delta^{18}O$, and Ti thermometry results for Hadean zircons. *Earth and Planetary Science Letters,* **268**, 476-486.

Hawkesworth, C. J. & Kemp, A. I. S. (2006). Using hafnium and oxygen isotopes in zircons to unravel the record of crustal evolution. *Chemical Geology*, **226**, 144-162.

Hawkesworth, C. J., Dhuime, B., Pietranik, A. B., Cawood, P. A., Kemp, A. I. S. & Storey, C. D. (2010). The generation and evolution of the continental crust. *Journal of the Geological Society* London, **167**, 229-248.

Hedenquist, J. W. (1986). Geothermal systems in the Taupo Volcanic Zone: their characteristics and relation to volcanism and mineralisation. *Bulletin of the Royal Society of New Zealand*, **23**, 134–168.

Hiess, J., Bennett, V. C., Nutman, A.P., Williams, I. S. (2009). In situ U–Pb, O and Hf isotopic compositions of zircon and olivine from Eoarchaean rocks, West Greenland. *Geochimica et Cosmochimica Acta*, **73**, 4489–4516.

Hoffmann, J. E., Münker, C., Polat, A., König, S., Mezger, K. & Rosing, M. T. (2010). Highly depleted Hadean mantle reservoirs in the sources of early Archean arc-like rocks, Isua supracrustal belt, southern West Greenland. *Geochimica et Cosmochimica Acta*, **74**, 7236–7260.

Hopkins, M. D., Harrison, T.M & Manning, C. E. (2010). Constraints on Hadean geodynamics from mineral inclusions in >4 Ga zircons, *Earth and Planetary Science Letters*, **298**, 367–376.

Hurai, V., Paquette, J.-L., Huraiová, M. & Konečný, P. (2010). U-Th-Pb geochronology of zircon and monazite from syenite and pincinite xenoliths in Pliocene alkali basalts of the intra-Carpathian back-arc basin. *Journal of Volcanology and Geothermal Research*, **198**, 275-287.

Iizuka, T. & Hirata, T. (2005). Improvements of precision and accuracy in in-situ Hf isotope microanalysis of zircon using laser ablation-MC-ICPMS technique. *Chemical Geology*, **220**, 121-137.

Iizuka, T., Komiya, T., Johnson, S. P., Kon, Y., Maruyama, S. & Hirata, T. (2009). Reworking of Hadean crust in the Acasta gneisses, northwestern Canada: Evidence from in-situ Lu–Hf isotope analysis of zircon. *Chemical Geology*, **259**, 230–239.

Jackson, S. E., Pearson, N. J., Griffin, W. L. & Belousova, E. A. (2004). The application of laser ablation-inductively coupled plasma-mass spectrometry to in situ U–Pb zircon geochronology, *Chemical Geology*, **211**, 47–69

Jaguin, J., Gapais, D., Poujol, M., Boulvais, P. & Moyen, J.-F. (2012a). The Murchison Greenstone Belt (South Africa): a general tectonic framework. *South African Journal of Geology*, **115**, 65-76.

Jaguin, J., Poujol, M., Boulvais, P., Robb, L.J. and Paquette, J.L. (2012b). Metallogeny of precious and base metal mineralization in the Murchison Greenstone Belt, South Africa: Indications from U-Pb and Pb-Pb geochronology. *Mineralium Deposita, (in press).*

Kamber, B. S., Collerson, K. D., Moorbath, S. & Whitehouse M. J. (2003). Inheritance of early Archean Pb-isotope variability from long-lived Hadean protocrust. *Contributions to Mineralogy and Petrology,* **145,** 25-46.

Kamber, B. S., Whitehouse, M. J., Bolhar, R. & Moorbath S. (2005). Volcanic resurfacing and the early terrestrial crust: Zircon U-Pb and REE constraints from the Isua Greenstone Belt, southern Greenland. *Earth and Planetary Science Letters,* **240**, 276-290.

Kamo, S. L. & Davis, D. W. (1994). Reassesment of Archean crustal development in the Barberton Mountain Land, South Africa, based on U-Pb dating. *Tectonics*, **13**, 167-192.

Kemp, A. I. S., Foster, G. L., Schersten, A., Whitehouse, M. J., Darling, J. & Storey, C. (2009). Concurrent Pb–Hf isotope analysis of zircon by laser ablation multi-collector ICP-MS, with implications for the crustal evolution of Greenland and the Himalayas. *Chemical Geology*, **261**, 244–260.

Kemp, A. I. S., Wilde, S. A., Hawkesworth, C. J., Coath, C. D., Nemchin, A., Pidgeon, R. T., Vervoort, J. D. & DuFrane, S. A. (2010). Hadean crustal evolution revisited: New constraints from Pb–Hf isotope systematics of the Jack Hills zircons. *Earth and Planetary Science Letters*, **296**, 45–56.

Koglin, N., Zeh, A., Frimmel, H. E. & Gerdes, A. (2010). New constraints on the auriferous Witwatersrand sediment provenance from combined detrital zircon U-Pb and Lu-Hf isotope data for the Eldorado Reef (Central Rand Group, South Africa). *Precambrian Research,***183**, 817-824*.*

Kositcin, N. & Krapez, B. (2004). Relationship between detrital zircon age-spectra and the tectonic evolution of the Late Archaean Witwatersrand Basin, South Africa. *Precambrian Research*, **129**, 141–168.

Kramers J. D. (2007). Hierarchical Earth accretion and the Hadean Eon. *Journal of the Geological Society London*, **164**, 3-17.

Kreissig, K., Holzer, L., Frei, R., Villa, I. M., Kramers, J. D., Kröner, A., Smit, C. A. & Van Reenen, D. D. (2001). Chronology of the Hout River Shear Zone and the metamorphism in the Southern Marginal Zone of the Limpopo Belt, South Africa. *Precambrian Research*, **109**, 145-173.

Kröner, A., Compston, W. & Williams, I. S. (1989). Growth of early Archean crust in the Ancient Gneiss Complex of Swaziland as revealed by single zircon dating. *Tectonophysics*, **161**, 271-298.

Kröner, A., Byerly, G. R. & Lowe, D. R. (1991). Chronology of early Archean granite–greenstone evolution in the Barberton Moutain Land, South Africa, based on precise dating by single grain zircon evaporation. *Earth and Planetary Science Letters*, **103**, 41–54.

Kröner, A. & Tegtmeyer, A. (1994). Gneiss–greenstone relationships in the Ancient Gneiss Complex of southwestern Swaziland, southern Africa, and implications for early crustal evolution. *Precambrian Research*, **67**, 109–139.

Kröner, A., Hegner, E., Wendt, J. I. & Byerly, G. R. (1996). The oldest part of the Barberton granitoid–greenstone terrain, South Africa: evidence for crust formation at 3.5 and 3.7 Ga. *Precambrian Research*, **78**, 105–124.

Kröner, A., Jaeckel, P. & Brandl, G. (2000). Single zircon ages for felsic to intermediate rocks from the Pietersburg and Giyani greenstone belts and bordering granitoid orthogneisses, northern Kaapvaal Craton, South Africa. *Journal of African Earth Sciences*, **30**, 773-793.

Lenting, C., Geisler, T., Gerdes, A., Kooijman, E., Scherer, E., Zeh, A. (2010) The behaviour of the Hf isotope system of radiation-damaged zircon during experimental hydrothermal alteration. *American Mineralogist*, **95**, 1343-1348.

Lowe, D. R. (1994). Accretionary history of the Archean Barberton greenstone belt (3.55-3.22 Ga) southern Africa. *Geology*, **22**, 1099-1102.

Lowe, D.R. & Byerly, G.R. 1999. Stratigraphy of the west-central part of the Barberton Greenstone Belt, South Africa. In: Lowe, D. R. & Byerly, G. R. (eds.) *Geological Evolution of the Barberton Greenstone Belt, South Africa*. Special paper, Geological Society of America, **329**, 1-36.

Ludwig, K. (2001). Isoplot/Ex, rev. 2.49. A Geochronological Toolkit for Microsoft Excel. *Berkeley Geochronology Center, Special Publication* No. 1a.

Martin, H., Smithies, R. H., Rapp, R., Moyen, J.-F., & Champion, D. (2005). An overview of adakite, tonalite-trondhjemite-granodiorite (TTG) and sanukitoid relationships and some implications for crustal evolution. *Lithos*, **79**, 1-24.

Millonig, L., Zeh, A., Gerdes, A., Klemd, R. & Barton, J. M. Jr. (2010). Decompressional heating of the Mahalapye Complex (Limpopo Belt, Botswana): A Response to Paleoproterozoic Magmatic Underplating? *Journal of Petrology*, **51**, 703-729.

Minnitt, R. C. A. & Anhaeusser, C. R. (1992). Gravitational and diapiric structural history of the eastern portion of the Archean Murchison greenstone belt, South Africa. *Journal of African Earth Sciences*, **15**, 429–440.

Næraa, T., Scherstén, A, Rosing, M. T., Kemp, A. I. S., Hoffmann, J. E., Kokfelt, T. F. & M. J. Whitehouse, M. J. (2012). Hafnium isotope evidence for a transition in the dynamics of continental growth 3.2Gyr ago. Nature,

Nebel-Jacobsen, Y., Münker, C., Nebel, O., Gerdes, A., Mezger, K. & Nelson, D.R. (2010). Reworking of Earth's first crust: Constraints from Hf isotopes in Archean zircons from Mt. Narryer, Australia, *Precambrian Research*, **182,** 175–186.

Patchett, P. J., Kouvo, O., Hedge, C. E. & Tatsumoto, M. (1981). Evolution of continental crust and mantle heterogeneity: evidence from Hf isotopes. *Contributions to Mineralogy and Petrology*, **78**, 279-297.

Pietranik, A. B., Hawkesworth, C. J., Storey, C. & Kemp, T. (2009). Depleted mantle evolution and how it is recorded in zircon. Geochimica et Cosmochimica Acta, **73**, A1028.

Polat, A. & Münker, C. (2004). Hf-Nd isotope evidence for contemporaneous subduction processes in the source of late Archean arc lavas from the Superior Province, Canada. *Chemical Geology*, **213**, 403-429.

Polat, A., Hofmann, A. W., Münker, C., Regelous, M. & Appel, P. U. W. (2003). Contrasting geochemical patterns in the 3.7–3.8 Ga pillow basalt cores and rims, Isua greenstone belt, Southwest Greenland: Implications for postmagmatic alteration processes. *Geochimica et Cosmochimica Acta*, **67**, 441–457.

Poujol, M. (2001). U-Pb isotopic evidence for episodic granitoid emplacement in the Murchison greentone belt, South Africa. *Journal of African Earth Sciences*, **33**, 155-163.

Poujol, M. & Robb, L. J. (1999). New U-Pb zircon ages on gneisses and pegmatites from south of the Murchison greenstone belt, South Africa. *South African Journal of Geology*, **102**, 93-97.

Poujol, M., Robb, L. J., Respaut, J. P. & Anhaeusser, C. R. (1996). 3.07-2.97 Ga greenstone belt formation in the northeastern Kaapvaal Craton: implications for the origin of the Witwatersrand Basin. *Economic Geology*, **91**, 1455-1461.

Poujol, M., Robb, L. J. & Respaut, J.-P. (1999). U–Pb and Pb–Pb isotopic studies relating to the origin of gold mineralization in the Evander Goldfields, Witwatersrand Basin, South Africa. *Precambrian Research*, **95**, 167–185.

Poujol, M., Robb, L. J., Anhaeusser, C. R. & Gericke, B. (2003). A review of the geochronological constraints on the evolution of the Kaapvaal Craton, South Africa. *Precambrian Research*, **127**, 181-213.

Rino, S., Komiya, T., Windley, B. F., Katayama, I., Motoki, A. & Hirata, T. (2004). Major episodic increase of continental crustal growth determined from zircon ages of river sands; implications for mantle overturns in the Early Precambrian. *Physics of the Earth and Planetary Interiors*, **146**, 369-394.

Robb, L. J., Davis, D. W. & Kamo, S. L. (1990). U–Pb ages on single detrital zircon grains from the Witwatersrand Basin, South Africa: constraints on the age of sedimentation and the evolution of granites adjacent to the basin. *Journal of Geology*, **98**, 311–328.

Robb, L. J., Brandl, G., Anhaeusser, C. R. & Poujol, M. (2006). Archean granitoid intrusions.

In: Johnson, M. R., Anhaeusser, C. R. & Thomas R. J. (eds.). *The Geology of South Africa,* Geological Society of South Africa, Johannesburg/Council of Geosciences, Pretoria, 57-94.

Scherer, E., Münker, C. & Mezger, K. (2001). Calibration of the lutetium-hafnium clock, *Science*, **29**3, 683-687.

Scherer, E., Whitehouse, M. J. & Münker, C. (2007). Zircon as a monitor of crustal growth. *Elements*, **3**, 19-24.

Schmitz, M. D., Bowring, S. A., de Wit, M. J. & Gartz, V. (2004). Subduction and terrane collision stabilize the west Kaapvaal craton tectosphere 2.9 billion years ago. *Earth and Planetary Science Letters*, **222**, 363-376.

Schoene, B. & Bowring, S. A. (2010). Rates and mechanisms of Mesoarchean magmatic arc construction, eastern Kaapvaal craton, Swaziland. *Geological Society of America Bulletin*, **122**, 408–429.

Schoene, B., de Wit, M. J. & Bowring, S. A. (2008). Mesoarchean assembly and stabilization of the eastern Kaapvaal craton: A structural-thermochronological perspective. *Tectonics*, **27**, TC5010, doi:10.1029/2008TC002267.

Schwarz-Schampera, U., Terblanche, H. & Oberthür, T. (2010). Volcanic-hosted massive sulfid deposits in the Murchison greenstone belt, South Africa. *Mineralium Deposita*, **45**, 113-145.

Simmons S. F. (1995). Magmatic contributions to low-sulfidation epithermal deposits. In: Thompson JFH (*eds.*) *Magmas, Fluids, and Ore Deposits*, Mineralogical Association of Canada Short Course Series, **23**, 55-477.

Sircombe, K. N. (2004). AgeDisplay: an EXCEL workbook to evaluate and display univariate geochronological data using binned frequency histograms and probability density distributions. *Computers and Geosciences*, **30**, 21-31.

Smithies, R. H. (2000). The Archean tonalite-trondhjemite-granodiorite (TTG) series is not an analogue of Cenozoic adakite. *Earth and Planetary Science Letters*, **182**, 115-125.

Söderlund, U., Patchett, J. P., Vervoort, J. D. & Isachsen, C. E. (2004). The ^{176}Lu decay constant determined by Lu-Hf and U-Pb isotope systematics of Precambrian mafic intrusions. *Earth and Planetary Science Letters*, **219**, 311-324.

Stern, R. A., Bodorkos, S., Kamo, S. L., Hickman, A. H., Corfu, F. (2009). Measurement of SIMS instrumental mass fractionation of Pb isotopes during zircon dating. *Geostandards and Geoanalytical Research*, **33**, 145-168.

Stevenson, R. K. & Patchett, P. J. (1990). Implications for the evolution of continental crust from Hf isotope systematics of Archean detrital zircons. *Geochimica et Cosmochimica Acta*, **54**, 1683-1697.

Stoffers, P., Hannington, M. D., Wright, I., Herzig, P. M., de Ronde, C. & Party, S. S. (1999). Elemental mercury at submarine hydrothermal vents in the Bay of Plenty, Taupo Volcanic Zone, New Zealand. *Geology*, **27**, 931–934.

Taylor, S.R. & McLennan, S.M. 1985. The Continental Crust: its Composition and Evolution. Blackwell, Oxford.

Treloar, P.J., Coward, M.P. & Harris, N.B.W., 1992, Himalayan-Tibetan analogies for the evolution of the Zimbabwe Craton and Limpopo Belt: *Precambrian Research*, **55**, 571-587.

van Eeden O. R., Partridge, F. C., Kent, L. R. & Brandt, J. W. (1939). The mineral deposits of the Murchison Range east of Leydsdorp. *Memoirs of the Geological Survey of South Africa*, **8**, 172 p.

Vearncombe, J. R. (1991). A possible Archaean island arc in the Murchison Belt, Kaapvaal Craton, South Africa. *Journal of African Earth Sciences*, **13**, 299-304.

Vearncombe, J. R., Barton, J. M. & Walsh, K. L. (1987). The Rooiwater Complex and associated rocks, Murchison granitoid-greenstone terrane, Kaapvaal Craton. *South African Journal of Geology*, **90**, 361-377.

Vearncombe, J. R., Cheshire, P. E., De Beer, J. H., Killick, A. M., Mallinson, W. S. & McCourt, S., (1988). Structures related to the Antimony line, Murchison schist belt, Kaapvaal craton, South Africa. *Tectonophysics*, **154**, 285-308.

Vearncombe, J. R., Barton, J. M., Cheshire, P. E., De Beer, J. H., Stettler, E. H. & Brandl, G. (1992). Geology, geophysics and mineralisation of the Murchison schist belt, Rooiwater Complex and surrounding granitoids. *Memoirs of the Geological Survey of South Africa*, **81**, 139 pp.

Vervoort, J. D. & Blichert-Toft, J. (1999). Evolution of the depleted mantle: Hf isotope evidence from juvenile rocks through time. *Geochimica et Cosmochimica Acta*, **63**, 533-556.

Vervoort, J. D., Patchett, P. J., Gehrels, G. E. & Nutman A. P. (1996). Constraints on early Earth differentiation from hafnium and neodymium isotopes. *Nature,* **379**, 624-627.

Viljoen, M.J, Van Vuuren, C.J.J., Pearton, P.N., Minnitt, R.C.A., Muff, R. & Cillier, P. (1978). The regional geological setting of mineralization in the Murchison Range with particular reference to antimony. In : Verwoerd, W.J. (*Eds.*), *Mineralization in Metamorphic Terranes*. Special Publications, Geologica Society of South Africa, **1**, 661-668.

Wedepohl, K. H. (1995). The compositions of the continental crust. *Geochimica et Cosmochimica Acta*, **59**, 1217-1232.

Wiedenbeck M, Alle P, Corfu F, Griffin WL, Meier M, Oberli, F, Quadt A von, Roddick JC, Spiegel W (1995). Three natural zircon standards for U-Th-Pb, Lu-Hf, trace element and REE analysis. *Geostandards Newsletters*, **19**, 1-23.

Woodhead, J., Hergt, J., Shelley, M., Eggins, S. & Kemp, R. (2004). Zircon Hf-isotope analysis with an excimer laser, depth profiling, ablation of complex geometries, and concomitant age estimation*. Chemical Geology*, **209**, 121-135.

Wu, F. Y., Yang, Y. H., Xie, L. W., Yang, J. H. & Xu, P. (2006). Hf isotopic compositions of the standard zircons and baddeleyites in U–Pb geochronology. *Chemical Geology*, **234**, 105–126.

Wu, W.-Y, Zhang, Y.-B., Yang, J.-H., Xie, L.-W. & Yang, Y.-H. (2008) Zircon U–Pb and Hf isotopic constraints on the Early Archean crustal evolution in Anshan of the North China Craton. *Precambrian Research*, **167**, 339-362.

Zeh, A. & Gerdes, A. (2010). Baltica- and Gondwana-derived sediments in the Mid-German Crystalline Rise (Central Europe): implications for the closure of the Rheic ocean. *Gondwana Research,* **17***, 254-263.*

Zeh, A. & Gerdes, A. (2012). U-Pb and Hf isotope record of detrital zircons from gold-bearing sediments of the Pietersburg Greenstone Belt (South Africa) – Is there a common provenance with the Witwatersrand Basin? *Precambrian Research*, **204-205**, 46-56.

Zeh, A., Gerdes, A., Klemd, R. & Barton, J. M. Jr. (2007). Archean to Proterozoic crustal evolution in the Central Zone of the Limpopo Belt (South Africa/ Botswana): Constraints from combined U-Pb and Lu-Hf isotope analyses of zircon. *Journal of Petrology,* **48**, 1605-1639.

Zeh, A., Gerdes, A., Klemd, R. & Barton, J. M. Jr. (2008). U-Pb and Lu-Hf isotope record of detrital zircon grains from the Limpopo Belt – evidence for crustal recycling at the Hadean to early-Archean transition*. Geochimica et Cosmochimica Acta,* **72**, 5304–5329.

Zeh, A., Gerdes. A., Barton, J. M. Jr. (2009). Archean Accretion and Crustal Evolution of the Kalahari Craton – the Zircon Age and Hf Isotope Record of Granitic Rocks from Barberton/Swaziland to the Francistown Arc*. Journal of Petrology,* **50***, 933-966.*

Zeh, A., Gerdes. A., Barton, J. M. Jr., Klemd, R., (2010a). U-Th-Pb and Lu-Hf systematics of zircon from TTG's, leucosomes, anorthosites and quartzites of the Limpopo Belt (South Africa): constraints for the formation, recycling, and metamorphism of Paleoarchean crust. *Precambrian Research,* **179**, 50-68*.*

Zeh, A., Gerdes, A., Will, T. M. & Frimmel, H. (2010b). Hafnium isotope homogenization during metamorphic zircon growth in amphibolite-facies rocks, examples from the Shackleton Range (Antarctica). *Geochimica et Cosmochimica Acta*, **74**, *4740-4758*

Zeh, A., Gerdes, A. & Millonig, L. (2011). Hafnium isotope record of the Ancient Gneiss Complex, Swaziland, southern Africa: evidence for Archaean crust-mantle formation and crust reworking between 3.66 and 2.73 Ga. *Journal of the Geological Society of London*, **168**, 953-963.

Zeh, A., Gerdes, A. & Heubeck, C. (2012). U-Pb and Hf isotope data of detrital zircons from the Barberton Greenstone Belt: Constraints on provenance and Archaean crustal evolution. *Journal of the Geological Society of London*, in press.

Appendix A

U-Pb dating with LA-ICP-MS at Clermont-Ferrand

U-Pb geochronology of zircon was conducted by in-situ laser ablation inductively coupled plasma mass spectrometry (LA-ICPMS) at the Laboratoire Magmas et Volcans in Clermont-Ferrand, France, on a Agilent 7500 ICP-MS coupled with a Resonetics M-50E Excimer Laser system using spot diameters of 26 µm with repetition rates of 3 Hz. Data were corrected for U–Pb fractionation and for the mass bias by standard bracketing with repeated measurements of the 91500 zircon (Wiedenbeck et al., 1995). Data reduction was carried out with the GLITTER® software package developed by the Macquarie Research Ltd. (Jackson et al., 2004). Concordia diagram was generated using Isoplot/Ex (Ludwig, 2001). Further information on the instrumentation and the analytical technique is detailed in Hurai et al. (2010). The results are shown in Table 1 and of the standard measurements in Table S1 (supplementary material).

U-Pb dating with LA-ICP-MS at Goethe University Frankfurt

Uranium, thorium and lead isotopes were analyzed using a ThermoScientific Element 2 sector field ICP-MS coupled to a Resolution M-50 (Resonetics) 193 nm ArF excimer laser (ComPexPro 102F, Coherent) system at Goethe-University Frankfurt, using the procedures described by Gerdes & Zeh (2006, 2009) with modifications explained in Zeh & Gerdes (2012). Laser spot-size was 26 µm for unknowns and for the standard zircons GJ1 (Jackson et al. 2004), and 33 µm for the standard zircons 91500 (Wiedenbeck et al., 1995), and OG1 (Stern et al., 2009). Sample surface was cleaned directly before each analysis by three pulses pre-ablation. Ablation were performed in a 0.6 L min-1 He stream, which was mixed directly after the ablation cell with 0.07 L min-1 N2 and 0.69 L min-1 Ar prior introduction into the Ar plasma of the SF-ICP-MS. Signal was tuned for maximum sensitivity for Pb and U while keeping oxide production, monitored as 254UO/238U, below 0.3%. The sensitivity achieved was in the range of 11000-16000 cps/µg g-1 for 238U with a 26 µm spot size, at 5.5 Hz and 5-6 J cm-2 laser energy. The typical penetration depth was about 15-20 µm. Raw data were corrected offline for background signal, common Pb, laser induced elemental fractionation, instrumental mass discrimination, and time-dependent elemental fractionation of Pb/U using an in-house MS Excel© spreadsheet program (Gerdes & Zeh 2006, 2009). The accuracy of the method was verified by analyses of reference zircon 91500 (first session: 1067.4 ± 5.6 Ma, MSWD of concordance and equivalence = 0.27, n=8; second session: 1066.6 ± 6.3 Ma, MSWDC+E = 0.25, n=6), and OG1 (3458.3 ± 7.5 Ma, MSWDC+E = 0.74, n=5). The data were plotted using the software ISOPLOT (Ludwig 2001); and the data for the primary (GJ1) and secondary (91500 and OG1) zircon standards are represented in Table S1 (supplementary material).

Table 1: *Results of U-Pb dating of zircons from the Murchison area*

grain	^{207}Pb [a] (cps)	U [b] (ppm)	Pb [b] (ppm)	Th/U [b]	^{206}Pbc [c] (%)	$^{206}Pb/^{238}U$ [d]	±2σ (%)	$^{207}Pb/^{235}U$ [d]	±2σ (%)	$^{207}Pb/^{206}Pb$ [d]	±2σ (%)	rho [e]	$^{206}Pb/^{238}U$	±2σ (Ma)	$^{207}Pb/^{235}U$	±2σ (Ma)	$^{207}Pb/^{206}Pb$	±2σ (Ma)	conc. [f] (%)
sample Mur (Murchison quartzite) - analyses Frankfurt																			
s04	212691	80	68	0.60	0.00	0.6776	1.9	27.88	2.0	0.2985	0.4	0.98	3335	51	3415	20	3462	7	96
s05	61623	75	56	1.62	0.09	0.5112	1.6	17.27	1.7	0.2451	0.8	0.90	2662	34	2950	17	3153	12	84
s06	84048	70	61	0.82	0.02	0.6988	2.3	27.77	2.5	0.2882	0.9	0.93	3416	62	3411	25	3408	14	100
s07	19503	18	15	0.65	0.50	0.6511	1.8	22.93	2.0	0.2555	0.9	0.89	3233	45	3224	19	3219	14	100
s08	62751	60	29	0.64	0.00	0.3642	2.7	15.42	2.7	0.3070	0.6	0.97	2002	46	2841	27	3506	10	57
s09	123277	122	79	0.31	b.d.	0.5838	1.6	20.35	1.7	0.2528	0.5	0.95	2964	38	3108	16	3202	8	93
s10	37822	38	28	0.46	0.98	0.6199	1.9	20.08	2.1	0.2349	0.9	0.91	3110	47	3095	20	3086	14	101
s11	381713	1049	320	0.45	0.00	0.2719	3.3	7.286	3.4	0.1943	0.8	0.97	1550	46	2147	31	2779	13	56
s12	173328	166	140	0.98	0.00	0.6548	2.4	26.18	2.4	0.2900	0.6	0.97	3247	60	3353	24	3418	9	95
s13	221364	382	240	1.52	b.d.	0.5079	1.7	18.60	1.8	0.2656	0.6	0.94	2648	38	3021	18	3280	10	81
s14	98197	1172	120	0.01	0.03	0.1071	1.8	1.652	2.1	0.1119	1.0	0.88	656	12	990	13	1831	18	36
s15	225469	418	240	0.55	0.00	0.5058	1.8	15.71	2.0	0.2253	0.7	0.94	2639	40	2859	19	3019	11	87
s16	63173	66	50	0.60	0.06	0.6223	1.8	20.50	1.9	0.2389	0.6	0.94	3119	46	3115	19	3113	10	100
s17	79538	93	81	1.83	b.d.	0.6456	2.1	22.50	2.2	0.2527	0.6	0.96	3211	54	3205	22	3202	10	100
s18	156475	267	140	0.57	0.00	0.4418	2.1	14.76	2.2	0.2423	0.5	0.98	2359	43	2800	21	3135	8	75
s19	66363	72	53	0.64	0.32	0.6060	1.7	19.73	2.2	0.2361	1.4	0.78	3054	42	3078	21	3094	22	99
s20	132929	144	88	0.81	0.00	0.4672	1.8	17.33	1.9	0.2691	0.5	0.96	2471	37	2953	18	3301	8	75
s21	95907	87	79	1.43	0.08	0.6266	2.3	21.14	2.4	0.2447	0.5	0.98	3136	59	3145	24	3151	8	100
s22	64194	66	50	0.69	0.15	0.6156	1.9	20.09	2.0	0.2367	0.5	0.97	3092	47	3096	19	3098	8	100
s23	252815	579	260	0.87	0.00	0.3861	2.0	11.69	2.1	0.2196	0.6	0.95	2105	36	2580	20	2978	10	71
s26	257719	175	160	0.45	0.00	0.7314	1.9	31.53	2.0	0.3127	0.6	0.95	3538	52	3536	20	3534	9	100
s27	82818	78	63	0.49	0.11	0.6612	1.9	24.37	2.0	0.2673	0.5	0.96	3272	49	3283	19	3290	8	99
s28	287108	600	220	0.45	b.d.	0.3096	2.4	10.93	2.4	0.2561	0.4	0.99	1739	36	2517	23	3223	6	54
s29	114697	105	81	0.36	0.03	0.6567	2.0	23.71	2.0	0.2618	0.5	0.97	3254	51	3257	20	3258	8	100
s30	30353	27	25	1.16	0.06	0.6608	2.2	23.97	2.3	0.2631	0.9	0.93	3270	56	3267	23	3265	14	100
s31	121030	118	110	1.58	0.25	0.6447	2.1	22.60	2.2	0.2543	0.4	0.98	3208	54	3210	21	3212	7	100
s32	112636	101	86	0.88	0.12	0.6633	2.6	24.14	2.7	0.2640	0.5	0.98	3280	68	3274	26	3271	7	100
s33	276357	283	210	0.59	0.00	0.6267	1.6	20.75	1.7	0.2401	0.5	0.96	3137	40	3127	17	3121	8	100
s34	322359	654	340	0.75	b.d.	0.4082	2.3	12.25	2.5	0.2177	1.0	0.93	2207	44	2624	24	2963	15	74
s35	95273	108	81	0.86	1.63	0.5960	2.2	18.34	2.4	0.2232	1.0	0.91	3014	54	3008	24	3004	16	100
s36	64945	68	52	0.54	0.09	0.6284	1.8	20.98	1.9	0.2422	0.5	0.96	3143	46	3138	19	3134	8	100
s37	142338	126	100	0.48	0.17	0.6665	2.1	24.56	2.2	0.2672	0.5	0.98	3292	54	3291	21	3290	8	100
s38	84080	73	58	0.37	0.21	0.6692	2.0	24.87	2.1	0.2696	0.5	0.97	3303	53	3303	21	3304	7	100
s39	81870	83	68	0.74	0.07	0.6503	2.2	23.08	2.3	0.2574	0.6	0.97	3229	57	3230	23	3231	9	100
s40	319815	260	210	0.77	0.19	0.6865	2.7	27.69	2.8	0.2925	0.7	0.97	3369	72	3408	28	3431	10	98
s41	271519	301	200	0.65	0.00	0.5387	4.4	21.66	4.4	0.2916	0.4	1.00	2778	99	3169	43	3426	6	81
s42	49535	44	37	0.80	0.16	0.6592	2.3	24.06	2.4	0.2647	0.8	0.95	3264	58	3271	24	3275	12	100
s43	347411	1040	420	0.22	1.10	0.3782	3.6	7.75	3.7	0.1487	0.9	0.97	2068	63	2203	33	2331	15	89
s44	101770	105	76	0.25	0.00	0.6420	2.4	22.29	2.5	0.2518	0.5	0.98	3197	62	3197	24	3196	9	100
s45	48780	45	37	0.76	0.08	0.6560	1.8	23.63	1.9	0.2612	0.7	0.94	3252	46	3253	19	3254	10	100
s48	114480	88	81	0.77	0.07	0.7093	2.0	28.96	2.0	0.2961	0.6	0.96	3456	53	3452	20	3450	9	100
s49	37800	34	28	0.61	0.19	0.6626	1.8	24.08	2.0	0.2635	0.8	0.92	3277	47	3272	19	3268	12	100
s50	141385	295	170	1.57	0.00	0.5096	2.2	15.91	2.3	0.2264	0.6	0.97	2655	48	2871	22	3027	9	88
s51	77423	62	50	1.13	0.15	0.6513	2.5	23.31	2.5	0.2595	0.5	0.98	3233	63	3240	25	3244	8	100
s52	221785	221	170	0.58	0.11	0.6221	2.1	20.80	2.2	0.2425	0.5	0.97	3118	52	3130	21	3137	8	99
s53	86893	105	60	0.74	b.d.	0.4642	2.5	14.94	2.6	0.2334	0.5	0.98	2458	52	2811	25	3076	8	80
s54	106870	128	100	0.90	0.04	0.6555	2.5	23.65	2.5	0.2617	0.4	0.99	3250	64	3254	25	3257	6	100
s55	86934	93	72	0.68	0.37	0.6211	2.1	20.60	2.2	0.2406	0.6	0.97	3114	53	3120	22	3124	9	100
s56	284920	1384	280	0.28	0.59	0.1724	2.3	3.96	2.8	0.1665	1.7	0.80	1025	22	1626	23	2523	28	41
s57	55815	56	41	0.62	0.28	0.6064	2.3	20.88	2.6	0.2497	1.3	0.87	3056	55	3133	25	3183	20	96
s58	80072	65	55	0.95	0.00	0.6553	1.6	26.14	1.7	0.2893	0.5	0.96	3249	42	3352	17	3414	7	95
s59	283167	581	190	0.33	b.d.	0.2921	3.5	9.454	3.6	0.2347	0.4	0.99	1652	52	2383	33	3085	6	54
s60	117542	85	78	0.71	0.64	0.7022	1.9	28.40	2.0	0.2933	0.7	0.95	3429	52	3433	20	3435	10	100
s61	256040	218	150	0.74	0.00	0.5451	2.5	22.16	2.6	0.2949	0.4	0.99	2805	58	3191	25	3444	6	81
s62	172875	177	110	1.53	b.d.	0.4951	2.6	18.90	2.7	0.2769	0.6	0.98	2593	56	3037	26	3345	9	78
s63	177809	195	140	0.52	0.35	0.5927	2.2	18.46	2.2	0.2259	0.5	0.97	3000	52	3014	22	3023	9	99
s64	278698	333	260	1.10	0.88	0.5999	3.6	18.79	3.9	0.2272	1.5	0.93	3029	87	3031	38	3032	23	100
s65	112387	112	83	0.33	0.03	0.6404	1.7	22.19	1.7	0.2512	0.5	0.96	3191	42	3192	17	3193	8	100
s66	268022	1109	300	0.22	0.03	0.2490	2.6	6.100	2.8	0.1777	1.0	0.93	1433	34	1990	25	2631	17	54
s67	1450726	2281	870	0.23	14.30	0.1701	15.8	3.916	17.2	0.1670	6.8	0.92	1013	150	1617	150	2527	114	40
s70	87113	78	63	0.57	0.03	0.6558	2.2	23.67	2.3	0.2618	0.6	0.97	3251	57	3255	23	3258	9	100
s71	57103	62	48	0.94	0.50	0.6028	2.1	19.10	2.3	0.2298	0.7	0.95	3041	52	3047	22	3051	12	100
s72	105682	100	93	1.57	0.46	0.6457	1.6	23.13	1.9	0.2598	1.1	0.82	3211	41	3233	19	3246	17	99
s73	310445	1065	230	0.66	0.00	0.1792	5.5	5.392	5.6	0.2182	0.9	0.99	1063	54	1884	49	2968	15	36
s74	47251	51	39	0.77	0.00	0.6246	2.0	20.94	2.1	0.2431	0.6	0.95	3128	50	3136	21	3140	10	100
s75	68691	63	41	0.73	0.26	0.5252	2.0	16.70	2.1	0.2306	0.6	0.96	2721	45	2918	21	3056	9	89
s76	254664	340	190	0.97	0.00	0.4489	2.8	15.49	2.9	0.2502	0.5	0.98	2390	56	2846	28	3186	8	75
s77	177097	182	130	0.48	0.00	0.6426	2.2	22.71	2.4	0.2563	0.8	0.94	3199	57	3214	24	3224	13	99
s78	98759	100	81	0.95	0.21	0.6248	2.1	20.86	2.1	0.2422	0.5	0.98	3129	51	3132	21	3134	7	100
s79	157864	203	160	2.02	0.27	0.6201	3.4	20.68	3.4	0.2419	0.5	0.99	3110	84	3124	34	3132	8	99
s80	280100	251	220	0.86	0.13	0.6916	2.1	27.34	2.2	0.2867	0.5	0.97	3389	56	3396	22	3400	8	100
s81	339925	1137	360	0.35	2.51	0.2531	3.6	6.252	4.5	0.1791	2.7	0.80	1455	47	2012	40	2645	45	55
s82	53680	50	40	0.49	0.19	0.6686	2.4	24.79	2.4	0.2689	0.6	0.97	3301	61	3300	24	3300	10	100

s83	160574	234	160	0.91	0.19	0.5989	1.8	18.85	1.9	0.2283	0.6	0.95	3026	44	3034	18	3040	9	100
s84	91141	107	78	0.49	0.25	0.6152	2.1	20.02	2.1	0.2361	0.6	0.97	3091	51	3093	21	3094	9	100
s85	59011	65	50	0.76	0.26	0.6089	2.0	19.45	2.1	0.2317	0.7	0.95	3066	49	3065	21	3064	11	100
s86	121407	104	88	1.19	0.00	0.6546	1.5	25.89	1.6	0.2868	0.5	0.96	3246	40	3342	16	3401	7	95
s87	109921	163	80	0.73	0.00	0.4075	2.3	14.68	2.5	0.2613	1.1	0.90	2204	43	2795	24	3254	17	68
s88	108065	79	70	0.55	0.06	0.7094	1.7	28.96	1.8	0.2961	0.4	0.97	3456	46	3452	17	3450	7	100
s89	197208	218	170	0.65	0.00	0.6675	2.5	24.83	2.6	0.2698	0.4	0.99	3296	65	3302	25	3305	7	100
s92	226962	816	180	0.32	0.00	0.2077	2.4	5.191	2.6	0.1812	1.0	0.93	1217	27	1851	22	2664	16	46
s93	237967	601	350	1.35	0.00	0.4921	2.1	15.92	2.2	0.2347	0.6	0.96	2580	45	2872	21	3084	10	84
s94	89765	99	76	0.71	0.16	0.5915	2.1	21.86	2.3	0.2680	0.9	0.92	2996	50	3177	22	3294	14	91
s95	95494	52	45	3.80	0.23	0.6884	2.6	26.70	2.7	0.2813	0.9	0.95	3377	69	3373	27	3370	14	100
s96	46867	46	35	0.61	0.18	0.6207	1.8	20.50	2.0	0.2395	0.7	0.94	3113	46	3115	19	3117	11	100
s97	163450	143	98	0.39	0.00	0.5721	1.6	22.41	1.7	0.2842	0.4	0.97	2916	38	3202	16	3386	6	86
s98	186682	213	160	0.83	0.12	0.6108	2.0	19.72	2.1	0.2341	0.5	0.97	3073	50	3078	20	3081	9	100
s99	87052	88	70	1.02	0.04	0.6266	1.7	21.61	1.8	0.2501	0.6	0.94	3136	43	3166	18	3185	10	98
s100	173961	169	150	1.10	0.13	0.6436	1.7	22.40	1.8	0.2524	0.4	0.97	3203	44	3201	17	3200	6	100
s101	78136	64	59	0.98	0.28	0.6931	1.9	27.52	1.9	0.2879	0.5	0.97	3394	50	3402	19	3407	7	100
s102	63094	67	62	1.70	0.26	0.6263	1.9	21.00	2.0	0.2432	0.7	0.94	3135	46	3139	19	3141	11	100
s103	75460	74	55	0.24	0.12	0.6466	1.8	22.77	1.9	0.2554	0.6	0.95	3215	47	3217	19	3219	9	100
s104	459464	342	300	0.63	0.00	0.6957	1.8	28.94	1.9	0.3018	0.5	0.97	3404	47	3452	18	3479	7	98
s105	111829	137	89	0.97	0.01	0.5087	1.9	16.09	2.0	0.2294	0.7	0.94	2651	41	2882	19	3048	11	87
s106	92199	87	74	0.88	0.36	0.6608	2.5	23.93	2.5	0.2626	0.6	0.97	3270	64	3265	25	3263	10	100
s107	144304	153	92	0.66	0.00	0.4740	2.1	15.49	2.1	0.2370	0.5	0.97	2501	43	2846	20	3100	8	81
s108	137255	109	88	0.63	0.00	0.6512	1.5	26.27	1.6	0.2926	0.4	0.96	3233	38	3357	15	3431	7	94
s109	48151	49	44	1.43	0.37	0.6329	2.3	21.88	2.5	0.2507	0.8	0.95	3161	58	3178	24	3189	12	99
s110	172491	187	120	0.44	0.04	0.5386	1.7	18.56	1.8	0.2500	0.6	0.94	2778	38	3019	17	3185	9	87
s111	199552	264	190	0.84	0.00	0.5880	2.3	22.50	2.4	0.2775	0.6	0.97	2981	56	3206	24	3349	9	89
s114	107114	107	85	0.75	b.d.	0.6412	1.9	22.34	2.0	0.2527	0.5	0.97	3194	48	3199	19	3202	8	100
s115	35946	33	27	0.57	0.24	0.6672	1.7	24.62	1.9	0.2676	0.8	0.91	3295	45	3293	19	3292	13	100
s116	105738	104	81	0.60	0.14	0.6405	2.7	22.27	2.7	0.2522	0.6	0.97	3191	67	3196	27	3199	10	100
s117	146312	113	100	1.02	0.06	0.7034	1.8	28.58	1.8	0.2946	0.4	0.97	3434	47	3439	18	3442	7	100
s118	94008	58	60	1.56	0.10	0.7282	1.9	31.16	2.0	0.3104	0.6	0.95	3527	53	3524	20	3523	9	100
s119	59390	64	48	0.67	0.03	0.6101	1.7	19.77	1.8	0.2350	0.5	0.96	3070	42	3080	18	3087	8	99
s120	124261	124	96	0.59	0.27	0.6272	2.0	20.90	2.0	0.2417	0.5	0.97	3139	49	3134	20	3131	8	100
s121	138297	167	120	0.88	0.03	0.6068	2.1	19.39	2.1	0.2318	0.4	0.98	3057	52	3062	21	3064	6	100
s122	68946	66	52	0.64	0.05	0.6376	2.1	22.11	2.2	0.2515	0.5	0.97	3180	53	3188	21	3194	8	100
s123	59513	63	47	0.74	0.28	0.6129	2.1	19.71	2.4	0.2332	1.0	0.90	3081	53	3077	23	3074	17	100
s124	79515	89	64	0.53	0.27	0.6054	1.9	18.99	2.0	0.2275	0.6	0.96	3052	47	3041	20	3034	10	101
s125	154346	167	130	1.07	0.27	0.6049	1.9	20.33	2.4	0.2437	1.4	0.80	3050	46	3107	23	3145	22	97
s126	507950	666	390	0.86	0.00	0.4395	2.2	17.63	2.2	0.2910	0.5	0.97	2348	43	2970	22	3423	8	69
s127	162674	853	170	0.74	0.00	0.1882	2.3	5.165	2.4	0.1991	0.7	0.96	1112	23	1847	21	2819	12	39
s128	114674	81	80	1.01	0.41	0.7242	2.4	30.67	2.4	0.3071	0.5	0.98	3512	65	3508	24	3507	7	100
s129	153934	128	120	0.71	0.03	0.7194	2.2	30.44	2.3	0.3069	0.4	0.98	3494	61	3501	23	3505	6	100
s130	321631	395	270	0.47	0.00	0.5860	1.9	19.63	2.0	0.2430	0.6	0.95	2973	45	3073	19	3139	9	95
s131	146012	135	110	0.64	0.24	0.6500	2.1	22.90	2.2	0.2555	0.6	0.97	3228	54	3223	21	3219	9	100
s132	54721	62	51	0.49	0.18	0.6634	3.0	24.44	3.2	0.2672	0.8	0.97	3280	79	3286	31	3289	13	100
s133	103105	115	83	0.59	0.11	0.6030	2.0	19.01	2.1	0.2286	0.6	0.96	3042	49	3042	20	3043	9	100
s134	205692	726	320	0.74	b.d.	0.3851	2.0	12.11	2.0	0.2280	0.4	0.98	2100	36	2613	19	3038	7	69
s137	149380	171	130	0.73	0.03	0.6073	2.3	19.31	2.3	0.2306	0.4	0.98	3059	55	3058	22	3056	6	100
s138	195975	197	150	0.80	1.03	0.5952	1.7	20.26	1.8	0.2468	0.6	0.94	3010	40	3104	17	3165	10	95
s139	107403	92	84	1.17	0.07	0.6736	1.7	26.04	1.8	0.2804	0.6	0.94	3320	43	3348	17	3365	9	99
s140	130739	204	130	0.65	0.00	0.5710	3.5	19.28	3.6	0.2449	0.5	0.99	2912	83	3056	35	3152	8	92
s141	256298	1085	390	0.72	0.17	0.2970	1.8	7.453	2.2	0.1820	1.2	0.85	1676	27	2167	20	2671	19	63
s142	120518	119	120	1.82	0.56	0.6473	2.0	22.40	2.2	0.2510	0.9	0.91	3218	51	3201	22	3191	15	101
s143	299563	241	180	1.36	0.00	0.5192	2.6	20.63	2.6	0.2882	0.4	0.99	2696	57	3121	25	3408	6	79
s144	203978	207	160	1.07	0.01	0.5929	2.6	18.40	2.7	0.2251	0.6	0.97	3001	63	3011	26	3017	10	99
s145	244590	374	170	0.74	0.00	0.3825	1.8	12.19	1.8	0.2312	0.4	0.97	2088	32	2619	17	3060	7	68
s146	37783	39	29	0.58	0.00	0.6268	1.9	21.15	2.0	0.2448	0.7	0.93	3137	47	3146	20	3151	11	100
s147	69385	73	56	0.64	0.10	0.6321	2.0	21.32	2.0	0.2447	0.6	0.96	3158	49	3153	20	3151	9	100
s148	181514	427	120	2.13	b.d.	0.1735	3.1	6.443	3.2	0.2694	0.5	0.99	1031	30	2038	28	3302	8	31
s149	51029	72	49	0.71	b.d.	0.5697	1.5	17.99	1.6	0.2291	0.6	0.93	2907	35	2989	16	3046	9	95
s150	427552	498	260	0.13	b.d.	0.4640	2.1	15.76	2.1	0.2464	0.4	0.98	2457	43	2863	21	3162	6	78
s151	175827	177	150	1.68	0.00	0.6742	1.9	25.62	1.9	0.2757	0.4	0.97	3322	48	3332	19	3339	7	100
s152	262568	609	230	1.11	b.d.	0.3228	3.6	10.69	3.6	0.2402	0.4	0.99	1803	57	2497	34	3121	6	58
s153	183880	197	150	0.56	0.23	0.6247	2.2	20.71	2.2	0.2405	0.5	0.98	3129	55	3125	22	3123	7	100
s154	225872	330	260	1.80	0.00	0.6166	2.8	20.70	2.8	0.2435	0.5	0.98	3097	69	3125	28	3143	8	99
s155	93086	94	73	0.50	0.13	0.6464	1.8	22.53	1.9	0.2528	0.6	0.95	3214	47	3207	19	3202	10	100
s158	146469	170	110	0.60	0.69	0.5460	2.4	17.23	2.7	0.2289	1.3	0.87	2809	54	2948	26	3044	21	92
s159	233823	287	190	0.55	0.12	0.5599	1.8	18.58	1.9	0.2407	0.7	0.93	2866	42	3020	19	3125	11	92
s160	75165	54	52	0.96	0.18	0.7095	1.6	29.12	1.7	0.2977	0.6	0.93	3457	43	3458	17	3458	9	100
s161	26264	71	26	0.69	0.00	0.2788	1.9	9.101	2.1	0.2368	1.0	0.89	1585	27	2348	20	3098	16	51
s162	52835	47	36	0.48	0.05	0.6267	1.6	23.24	1.8	0.2689	0.7	0.93	3136	41	3237	17	3300	10	95
s163	503754	620	360	0.97	0.00	0.4368	2.8	16.60	2.9	0.2756	0.8	0.96	2337	55	2912	28	3338	12	70
s164	76121	81	65	0.87	0.31	0.6302	1.8	21.34	1.9	0.2455	0.6	0.95	3150	46	3154	19	3156	10	100
s165	182816	272	190	0.89	0.16	0.5850	1.9	17.73	2.0	0.2197	0.4	0.98	2969	46	2975	19	2979	7	100
s166	304170	316	250	0.71	b.d.	0.6266	1.9	22.34	1.9	0.2586	0.5	0.97	3136	46	3199	19	3238	7	97
s167	234293	382	240	0.87	0.00	0.5173	3.2	16.88	3.3	0.2367	0.7	0.97	2688	71	2928	32	3098	12	87
s168	76535	85	66	0.85	0.16	0.6231	2.5	20.79	2.5	0.2420	0.6	0.97	3122	61	3129	25	3133	9	100

s169	70454	63	47	0.59	0.03	0.6103	2.4	22.65	2.5	0.2692	0.6	0.97	3071	58	3212	24	3301	10	93
s170	247973	530	140	0.33	0.00	0.2228	4.7	7.158	4.8	0.2331	0.7	0.99	1296	56	2131	44	3073	12	42
s171	185733	336	220	0.54	b.d.	0.5878	2.2	17.78	2.5	0.2194	1.3	0.85	2981	52	2978	25	2976	22	100
s172	72550	56	53	0.94	0.03	0.7082	1.6	29.08	1.8	0.2978	0.7	0.92	3451	44	3456	18	3459	11	100
s173	27741	23	18	0.49	0.10	0.6462	1.6	23.83	1.8	0.2674	1.0	0.85	3213	40	3261	18	3291	15	98
s174	65861	70	57	0.94	0.00	0.6299	1.5	21.87	1.6	0.2518	0.5	0.94	3149	37	3178	15	3196	8	99
s175	60331	61	49	0.73	0.01	0.6650	2.6	24.53	2.7	0.2676	0.5	0.98	3286	67	3290	26	3292	8	100
s176	81282	81	63	0.44	0.23	0.6506	1.8	22.88	2.0	0.2550	0.7	0.94	3230	47	3222	19	3216	11	100
s179	80485	78	60	0.49	0.00	0.6517	1.6	23.36	1.7	0.2600	0.6	0.94	3235	40	3242	16	3247	9	100
s180	328239	331	300	1.09	0.25	0.7000	3.7	27.94	3.8	0.2895	0.7	0.98	3421	100	3417	38	3415	11	100
s181	265452	210	180	0.71	b.d.	0.6746	1.6	27.16	1.7	0.2920	0.5	0.96	3324	42	3389	17	3428	7	97
sample LF (La France quartzite)- analyses Frankfurt																			
s182	51931	57	44	0.73	0.08	0.6288	1.7	21.07	1.8	0.2430	0.7	0.93	3145	43	3142	18	3140	11	100
s183	335369	406	220	0.65	0.35	0.3958	2.1	15.35	2.4	0.2812	1.1	0.88	2150	38	2837	23	3370	17	64
s184	121246	143	110	0.63	0.10	0.6268	2.2	21.22	2.3	0.2455	0.6	0.96	3137	55	3149	23	3156	10	99
s185	165498	145	100	1.05	b.d.	0.5186	2.3	20.95	2.3	0.2929	0.4	0.99	2693	51	3136	23	3433	6	78
s186	112706	169	110	0.35	0.13	0.5869	2.0	17.87	2.1	0.2208	0.8	0.93	2977	48	2983	21	2986	12	100
s187	87153	76	60	0.28	0.18	0.6726	1.9	25.11	2.0	0.2708	0.7	0.93	3316	48	3313	20	3311	11	100
s188	155949	250	140	0.99	b.d.	0.4827	2.0	15.61	2.1	0.2345	0.4	0.98	2539	42	2853	20	3083	7	82
s189	83878	72	58	0.54	0.71	0.6587	3.1	24.09	3.1	0.2652	0.7	0.98	3262	79	3272	31	3278	11	100
s190	67800	77	57	0.54	0.19	0.6207	2.2	20.51	2.3	0.2397	0.7	0.95	3113	54	3116	22	3118	11	100
s191	112793	128	94	1.29	0.00	0.5431	1.8	18.45	1.9	0.2463	0.6	0.96	2796	41	3013	18	3161	9	88
s192	135540	104	92	0.50	0.07	0.7128	1.7	29.50	1.8	0.3001	0.5	0.96	3469	47	3470	18	3471	8	100
s193	203259	298	220	1.59	0.00	0.5776	2.8	17.95	2.9	0.2254	0.7	0.97	2939	67	2987	29	3020	11	97
s194	145011	223	130	1.28	1.09	0.3871	2.4	12.09	2.7	0.2265	1.3	0.88	2110	43	2611	26	3027	21	70
s195	173749	344	240	1.07	0.14	0.5780	3.1	18.70	3.2	0.2346	0.7	0.97	2941	74	3026	31	3084	12	95
s196	176073	486	200	1.07	0.00	0.3452	1.8	10.13	1.9	0.2127	0.6	0.96	1912	31	2446	18	2927	9	65
s197	161269	250	170	1.07	0.00	0.5902	2.5	18.44	2.5	0.2266	0.5	0.98	2990	59	3013	24	3028	9	99
s198	173344	178	150	2.73	0.34	0.5933	3.0	18.12	3.1	0.2215	0.5	0.99	3003	73	2996	30	2991	8	100
s199	158987	180	130	0.94	0.20	0.5754	2.1	19.46	2.2	0.2453	0.5	0.97	2930	50	3065	21	3155	8	93
s202	208081	395	270	1.23	0.11	0.5440	3.0	15.82	3.1	0.2109	0.8	0.97	2800	69	2866	30	2913	13	96
s203	57837	69	54	1.16	0.00	0.5950	1.5	18.46	1.6	0.2250	0.6	0.92	3010	36	3014	16	3016	10	100
s204	74892	82	62	0.61	0.08	0.6262	1.7	20.97	1.8	0.2429	0.5	0.96	3135	42	3137	17	3139	8	100
s205	98465	109	74	0.78	0.03	0.5304	1.9	17.63	1.9	0.2411	0.5	0.96	2743	41	2970	19	3127	8	88
s206	51484	54	47	1.31	0.64	0.6195	1.5	20.31	1.9	0.2378	1.2	0.76	3108	36	3106	19	3105	20	100
s207	70422	64	55	0.89	0.06	0.6613	1.9	24.28	2.0	0.2663	0.7	0.95	3272	49	3280	20	3284	10	100
s208	290489	363	200	0.79	0.00	0.3954	2.4	17.41	2.5	0.3194	0.7	0.95	2148	43	2958	24	3567	11	60
s209	152265	128	110	0.94	0.00	0.7159	2.4	29.84	2.4	0.3023	0.5	0.98	3481	64	3482	24	3482	8	100
s210	139557	159	110	0.52	0.06	0.6052	1.7	19.10	1.7	0.2289	0.5	0.95	3051	40	3047	17	3044	8	100
s211	162966	197	130	0.56	0.01	0.5592	2.0	18.08	2.0	0.2345	0.4	0.98	2863	47	2994	20	3083	6	93
s212	69834	77	61	0.88	0.11	0.6234	1.8	20.85	1.9	0.2426	0.5	0.96	3123	44	3132	18	3137	8	100
sample Rub1 (quartz-porphyroclastic schist) - analyses Frankfurt																			
a117	43591	149	100	0.72	0.09	0.5847	2.1	17.67	2.3	0.2192	1.0	0.91	2968	51	2972	23	2975	16	100
a119	27499	83	58	0.72	0.06	0.5855	1.6	17.72	1.8	0.2194	0.8	0.89	2971	39	2974	18	2977	13	100
a121	94718	265	180	0.90	0.01	0.5706	1.6	17.28	1.7	0.2196	0.6	0.94	2910	38	2950	17	2978	10	98
a124	60743	168	120	0.85	0.07	0.5828	1.7	17.51	1.8	0.2179	0.6	0.95	2960	40	2963	17	2965	9	100
a125	51486	141	100	0.85	0.05	0.5842	1.7	17.54	1.8	0.2178	0.6	0.94	2966	40	2965	17	2965	10	100
a127	74437	216	150	0.95	0.01	0.583	1.7	17.55	1.8	0.2184	0.7	0.93	2961	40	2966	17	2969	11	100
a128	128549	364	270	1.11	0.02	0.5858	1.8	17.56	1.9	0.2174	0.6	0.95	2972	42	2966	18	2961	9	100
a129	70563	209	150	0.85	0.08	0.5822	1.9	17.45	2.1	0.2174	0.8	0.92	2958	46	2960	20	2962	13	100
sample Rub 2 (felsic schist-quartz porhyroclastic) - analyses Frankfurt																			
a132	72191	196	140	0.79	0.00	0.5859	1.6	17.69	1.7	0.2190	0.5	0.95	2973	38	2973	16	2974	8	100
a133	146876	403	290	1.04	b.d.	0.5851	1.6	17.59	1.6	0.2181	0.4	0.97	2970	38	2968	16	2966	6	100
a138	79573	226	160	0.80	0.00	0.5867	1.6	17.70	1.7	0.2188	0.5	0.96	2976	39	2973	16	2972	8	100
a139	91437	258	180	0.82	0.01	0.587	1.6	17.72	1.6	0.2190	0.5	0.96	2977	37	2975	16	2973	7	100
a140	128575	363	270	1.10	0.00	0.5868	1.6	17.73	1.6	0.2192	0.4	0.97	2977	38	2975	16	2974	6	100
a143	77814	217	150	0.87	0.02	0.5861	2.0	17.82	2.1	0.2205	0.4	0.98	2974	49	2980	20	2985	6	100
a144	59924	175	120	0.71	0.00	0.5853	1.8	17.60	1.8	0.2181	0.5	0.96	2971	42	2968	18	2966	9	100
a145	64106	182	130	0.88	0.00	0.5859	1.5	17.70	1.7	0.2191	0.6	0.93	2973	37	2974	16	2974	10	100
a146	141107	394	280	0.92	0.00	0.5847	1.7	17.64	1.8	0.2188	0.4	0.98	2968	42	2970	17	2972	6	100
sample Murch94-6 (Free State tonalite) - analyses Clermont-Ferrand																			
Roi5-pr		139	84	0.62	b.d.	0.57674	2.4	17.02	2.4	0.2140	2.1	0.98	2935	56	2936	24	2936	34	100
Roi6-pr		179	93	0.55	b.d.	0.50413	2.4	15.22	2.5	0.2190	2.1	0.97	2632	52	2829	24	2974	35	95
Roi8-pris		81	50	0.76	b.d.	0.58597	2.4	17.86	2.4	0.2210	2.1	0.97	2973	57	2982	24	2988	34	100
Roi9-pr		45	26	0.58	b.d.	0.58023	2.4	17.37	2.5	0.2171	2.1	0.97	2950	57	2955	24	2959	34	100
Roi10-r		455	146	0.14	b.d.	0.36508	2.4	9.06	2.4	0.1800	2.1	0.97	2006	41	2344	22	2653	35	88
Roi11-pris		23	13	0.53	b.d.	0.57665	2.4	17.26	2.5	0.2171	2.2	0.96	2935	56	2949	24	2959	35	100
Roi12-pris		27	15	0.54	b.d.	0.57614	2.4	17.21	2.6	0.2167	2.3	0.94	2933	57	2947	25	2956	37	100
Roi15-r		333	178	0.91	b.d.	0.53043	2.3	14.40	2.4	0.1969	2.1	0.98	2743	53	2776	23	2800	34	99
Roi16-r		386	177	0.36	b.d.	0.48332	2.3	13.13	2.4	0.1970	2.1	0.98	2542	49	2689	23	2801	34	96
Roi17-pr		167	81	0.38	b.d.	0.46144	2.3	13.55	2.4	0.2129	2.1	0.97	2446	48	2718	23	2928	34	93
Roi18-r		862	196	0.65	b.d.	0.24321	2.3	5.20	2.4	0.1549	2.1	0.97	1403	29	1852	21	2401	36	77
Roi20-r		1087	245	2.67	b.d.	0.21488	2.3	4.31	2.4	0.1454	2.1	0.97	1255	27	1695	20	2293	36	74
Roi21-r		1058	220	0.57	b.d.	0.22431	2.3	4.34	2.4	0.1402	2.1	0.97	1305	27	1700	20	2229	37	76
Roi22-r		1032	228	0.42	b.d.	0.24261	2.3	4.80	2.4	0.1435	2.1	0.97	1400	29	1785	20	2269	36	79
Roi25-pris		43	24	0.61	b.d.	0.5331	2.3	16.04	2.4	0.2182	2.2	0.95	2755	52	2879	24	2967	35	97
Roi26-r		331	178	0.61	b.d.	0.5218	2.3	15.67	2.4	0.2178	2.1	0.96	2707	51	2857	23	2965	34	96
Roi27-pr		190	111	0.67	b.d.	0.55911	2.3	16.87	2.4	0.2188	2.2	0.96	2863	53	2927	23	2972	35	99
Roi28-pr		51	29	0.59	b.d.	0.566	2.3	17.29	2.5	0.2216	2.3	0.93	2891	55	2951	24	2992	37	99
Roi29-r		452	214	0.73	b.d.	0.47147	2.3	13.59	2.4	0.2091	2.2	0.95	2490	48	2722	23	2899	35	94
Roi31-r		164	90	0.56	b.d.	0.55153	2.3	15.73	2.4	0.2068	2.2	0.95	2832	53	2861	23	2881	35	99

Roi35-pr		472	207	1.01	b.d.	0.45351	2.3	12.46	2.4	0.1993	2.2	0.95	2411	46	2640	23	2820	36	94
Roi36-pris		20	11	0.31	b.d.	0.56742	2.3	16.88	2.5	0.2158	2.3	0.92	2897	54	2928	24	2949	37	99
Roi37-pr		156	74	0.49	b.d.	0.47757	2.3	12.81	2.4	0.1945	2.2	0.94	2517	47	2666	23	2781	36	96
Roi38-pris		64	39	0.70	b.d.	0.58302	2.3	17.66	2.4	0.2197	2.2	0.94	2961	54	2971	24	2978	36	100
Roi39-pris		37	21	0.52	b.d.	0.57609	2.3	17.15	2.5	0.2160	2.3	0.92	2933	54	2944	24	2951	37	100
Roi41-r		293	132	0.48	b.d.	0.47557	2.3	12.66	2.4	0.1930	2.2	0.93	2508	47	2655	23	2768	37	96
Roi42-pris		30	16	0.42	b.d.	0.54218	2.3	15.68	2.5	0.2098	2.3	0.92	2793	52	2858	24	2904	38	98
Roi45-pr		140	82	0.70	b.d.	0.56204	2.3	16.76	2.4	0.2163	2.3	0.92	2875	52	2921	24	2953	37	99
Roi46-pris		36	20	0.51	b.d.	0.57499	2.3	17.02	2.5	0.2146	2.3	0.91	2928	53	2936	24	2941	38	100
sample Murch94-6 (Free State tonalite) - analyses Frankfurt																			
a10pris	23634	28	20	0.33	3.43	0.5868	1.4	17.69	2.3	0.2186	1.9	0.59	2977	33	2973	23	2970	30	100
a11pris	20207	26	18	0.48	0.53	0.5742	1.7	17.22	2.0	0.2175	1.1	0.84	2925	39	2947	19	2962	17	99
a12pris	47837	69	45	0.48	1.44	0.5252	1.6	15.30	2.6	0.2113	2.0	0.64	2721	37	2834	25	2915	32	93
a13pris	21494	26	18	0.57	b.d.	0.5831	1.5	17.53	2.2	0.2181	1.6	0.69	2962	35	2965	21	2967	25	100
a14pris	22549	30	22	0.46	b.d.	0.5871	1.5	17.63	2.2	0.2178	1.6	0.68	2978	35	2970	21	2965	26	100
a15pris	25307	34	24	0.53	0.33	0.5844	1.4	17.56	1.6	0.2179	0.9	0.84	2967	33	2966	16	2965	14	100
a16pris	10408	14	9	0.35	0.08	0.5462	1.5	16.47	2.7	0.2187	2.3	0.55	2810	34	2905	26	2971	36	95
a17pris	23872	27	18	0.34	2.80	0.5326	1.7	14.86	2.4	0.2024	1.7	0.70	2752	38	2806	23	2846	28	97
a18pris	77678	105	80	0.73	0.70	0.5842	1.6	17.56	1.7	0.2180	0.6	0.93	2966	37	2966	16	2966	10	100
a19pris	66348	87	66	0.72	0.15	0.5843	1.7	17.51	1.8	0.2174	0.7	0.92	2966	39	2963	17	2961	11	100
a20pris	46788	60	44	0.59	0.02	0.5831	1.3	17.52	1.5	0.2179	0.8	0.86	2961	31	2964	14	2965	12	100
a21pris	47955	62	44	0.51	2.56	0.5609	1.4	16.37	1.9	0.2117	1.3	0.76	2870	34	2899	19	2919	20	98
a22pris	62888	88	60	0.52	0.22	0.5533	1.2	16.43	1.3	0.2154	0.6	0.88	2839	27	2902	13	2947	10	96
a24pris	50524	65	44	0.56	0.12	0.5476	1.3	16.39	1.5	0.2170	0.7	0.87	2815	31	2900	15	2959	12	95
a33pris	51232	67	47	0.52	2.07	0.5451	1.6	15.95	1.9	0.2122	1.1	0.82	2805	36	2874	19	2922	18	96
a34pris	32354	43	29	0.54	1.16	0.5401	1.4	16.17	1.7	0.2171	1.0	0.83	2784	33	2887	17	2960	15	94
a35pris	37870	64	42	0.30	3.28	0.5294	1.5	15.93	2.1	0.2183	1.5	0.71	2739	34	2873	21	2968	25	92
a36pris	15500	22	15	0.44	b.d.	0.57	1.4	17.22	2.0	0.2191	1.4	0.72	2908	33	2947	19	2974	22	98
a37pris	30740	29	22	0.29	2.44	0.4806	2.5	13.63	3.4	0.2057	2.3	0.73	2530	52	2724	32	2872	37	88
a38pris	31886	43	31	0.48	1.42	0.5812	1.6	17.50	1.9	0.2184	1.0	0.85	2954	39	2963	19	2969	16	99
a39pris	51939	68	51	0.72	2.61	0.5682	1.4	17.10	2.0	0.2182	1.5	0.69	2900	32	2940	19	2968	24	98
a40pris	45115	63	45	0.51	b.d.	0.583	1.6	17.41	1.7	0.2166	0.7	0.91	2961	38	2958	17	2955	12	100
a41pris	14019	17	12	0.38	2.36	0.5781	1.6	17.35	2.7	0.2176	2.1	0.61	2941	39	2954	26	2963	34	99
a42pris	61228	52	47	0.60	14.54	0.5517	2.1	15.78	4.7	0.2074	4.2	0.44	2832	47	2864	46	2886	69	98
a43pris	15412	22	15	0.49	b.d.	0.5849	1.4	17.63	2.1	0.2186	1.5	0.67	2969	33	2970	20	2970	25	100
a44pris	16835	25	16	0.27	0.38	0.5266	1.4	15.40	1.9	0.2122	1.4	0.70	2727	30	2841	19	2922	22	93

Spot size = 20 and 30µm, repectively; depth of crater ~20µm. $^{206}Pb/^{238}U$ error is the quadratic additions of the within run precision (2 SE) and the external reproducibility (2 SD) of the reference zircon. $^{207}Pb/^{206}Pb$ error propagation (^{207}Pb signal dependent) following Gerdes & Zeh (2009). $^{207}Pb/^{235}U$ error is the quadratic addition of the $^{207}Pb/^{206}Pb$ and $^{206}Pb/^{238}U$ uncertainty.

[a]Within run background-corrected mean ^{207}Pb signal in cps (counts per second).

[b] U and Pb content and Th/U ratio were calculated relative to GJ-1 reference zircon.

[c] percentage of the common Pb on the ^{206}Pb. b.d. = below dectection limit.

[d] corrected for background, within-run Pb/U fractionation (in case of $^{206}Pb/^{238}U$) and common Pb using Stacy and Kramers (1975) model Pb composition and subsequently normalised to GJ-1 (ID-TIMS value/measured value); $^{207}Pb/^{235}U$ calculated using $^{207}Pb/^{206}Pb/(^{238}U/^{206}Pb*1/137.88)$

[e] rho is the $^{206}Pb/^{238}U/^{207}Pb/^{235}U$ error correlation coefficient.

[f] degree of concordance = $^{206}Pb/^{238}U$ age / $^{207}Pb/^{206}Pb$ age x 100

for sample Murch94-6: r-recystallized zircon, pr - partially recrystallised zircon, pris - pristine zircon

Lu-Hf isotope analyses with LA-ICP-MS at Goethe University Frankfurt

Hafnium isotope measurements were performed with a Thermo-Finnigan NEPTUNE multi collector ICP-MS coupled to the same laser as described in the U-Pb method, during three sessions. Rectangular laser spots with edge lengths of 43 µm were drilled with repetition rate of 5.5 Hz and an energy density of 6 J/cm2 during 55 s of data acquisition. All data were adjusted relative to the JMC475 of 176Hf/177Hf ratio = 0.282160 and quoted uncertainties are quadratic additions of the within run precision of each analysis and the reproducibility of the JMC475 (2SD = 0.0033%, n = 8). Accuracy and external reproducibility of the method was verified by repeated analyses of reference zircon GJ-1, MudTank and 91500, which yielded 176Hf/177Hf well within the range of solution mode data (Woodhead & Hergt 2005; Gerdes & Zeh 2006). For results of standard measurements during the three sessions see Table S2 (supplementary material).

For calculation of the epsilon Hf [εHft] the chondritic uniform reservoir (CHUR) was used as recommend by Bouvier et al. (2008; 176Lu/177Hf and 176Hf/177Hf of 0.0336 and 0.282785, respectively), and a decay constant of 1.867 x10-11 (average of Scherer et al. 2001; Söderlund et al. 2004). Initial 176Hf/177Hft and εHft for all analysed zircon domains were calculated using the apparent Pb-Pb ages obtained for the respective domains (supplementary material). Depleted mantle hafnium model ages (TDM) were calculated using values for the depleted mantle as suggested by Blichert-Toft & Puchtel (2010), with 176Hf/177Hf = 0.283294 and a 176Lu/177Hf of 0.03933, corresponding to a straight DM-evolution line with εHftoday=+18 and εHf4.558Ga=0.0. TDM ages for all data were calculated by using the measured 176Lu/177Hf of each spot for the time since zircon crystallization, and a mean 176Lu/177Hf of 0.0113 for the Palaeoproterozoic-Archaean crust [mean of average continental crust as suggested by Taylor & McLennan (1985) and Wedepohl (1995); see supplementary material].

Supplementary material:

Table S1: Results of U-Pb zircon standard measurements

Table S2: Lu-Hf isotope data of standard zircons

Table 2: *Lu-Hf isotope data of zircons from the Murchison Greenstone Belt and Rooiwater Complex*

	$^{176}Yb/^{177}Hf$ [a]	±2σ	$^{176}Lu/^{177}Hf$ [a]	±2σ	$^{178}Hf/^{177}Hf$	$^{180}Hf/^{177}Hf$	Sig_{Hf} [b] (V)	$^{176}Hf/^{177}Hf$	±2σ	$^{176}Hf/^{177}Hf_{(t)}$ [d]	$\varepsilon Hf_{(t)}$ [d]	±2σ [c]	T_{DM2} [e] (Ga)	age [f] (Ma)	±2σ	conc %
Rooiwater sample (02.01.2012)																
Roi5	0.0808	136	0.00268	41	1.4671	1.8861	26	0.281163	27	0.281012	4.3	1.0	3.07	2936	34	100
Roi6	0.1297	47	0.00415	18	1.4672	1.8867	26	0.281244	25	0.281007	5.0	0.9	3.06	2974	34	88
Roi7	0.0950	101	0.00279	25	1.4672	1.8867	24	0.281160	23	0.280997	6.3	0.8	3.04	3042	33	99
Roi8	0.0891	69	0.00285	20	1.4672	1.8867	21	0.281166	27	0.281002	5.2	1.0	3.06	2988	34	99
Roi9	0.0851	73	0.00264	22	1.4672	1.8868	23	0.281150	23	0.281000	4.4	0.8	3.08	2959	34	100
Roi10	0.1686	56	0.00674	22	1.4672	1.8866	26	0.281453	26	0.281111	1.1	0.9	3.02	2653	35	76
Roi11	0.0528	12	0.00179	8	1.4671	1.8863	18	0.281110	27	0.281009	4.7	1.0	3.06	2959	35	99
Roi12	0.0643	21	0.00206	3	1.4671	1.8864	21	0.281170	24	0.281053	6.2	0.8	2.97	2956	37	99
Roi15	0.1424	43	0.00557	23	1.4672	1.8865	27	0.281376	26	0.281077	3.4	0.9	3.01	2800	34	98
Roi16	0.1601	210	0.00492	61	1.4672	1.8866	27	0.281307	33	0.281043	2.2	1.2	3.08	2801	34	91
Roi17	0.1194	42	0.00384	14	1.4672	1.8868	26	0.281233	21	0.281017	4.3	0.7	3.06	2928	34	84
Roi18	0.1384	49	0.00540	12	1.4671	1.8865	37	0.281316	23	0.281069	-6.3	0.8	3.23	2401	36	58
Roi19	0.0703	14	0.00211	3	1.4671	1.8866	25	0.281135	22	0.281003	11.5	0.8	2.91	3255	35	99
Roi20	0.2341	104	0.00677	37	1.4670	1.8862	37	0.281340	23	0.281044	-9.6	0.8	3.33	2293	36	55
Roi21	0.1936	76	0.00668	14	1.4672	1.8865	26	0.281391	26	0.281107	-8.9	0.9	3.24	2229	36	59
Roi22	0.1780	137	0.00575	28	1.4671	1.8863	27	0.281325	23	0.281076	-9.1	0.8	3.28	2269	36	62
Roi25	0.0938	41	0.00287	16	1.4671	1.8866	23	0.281167	25	0.281003	4.7	0.9	3.07	2967	35	93
Roi26	0.0989	71	0.00325	20	1.4672	1.8865	25	0.281191	24	0.281006	4.7	0.8	3.06	2965	34	91
Roi27	0.1551	75	0.00469	16	1.4670	1.8861	23	0.281284	33	0.281017	5.3	1.2	3.04	2972	35	96
Roi28	0.0785	35	0.00251	7	1.4672	1.8866	18	0.281228	23	0.281083	8.1	0.8	2.90	2992	37	97
Roi29	0.1523	91	0.00483	25	1.4672	1.8870	23	0.281290	28	0.281021	3.7	1.0	3.07	2899	35	86
Roi30	0.1806	64	0.00557	30	1.4670	1.8860	17	0.281234	23	0.280915	1.9	0.8	3.23	2980	35	100
Roi31	0.1331	61	0.00487	17	1.4673	1.8873	26	0.281402	22	0.281133	7.3	0.8	2.86	2881	35	98
Roi32	failed															0
Roi35	0.2119	108	0.00664	35	1.4672	1.8867	24	0.281382	26	0.281023	1.9	0.9	3.11	2821	35	85
Roi36	0.0274	5	0.00094	3	1.4672	1.8870	18	0.281108	28	0.281055	6.1	1.0	2.97	2949	37	98
Roi37	0.1821	64	0.00639	24	1.4670	1.8861	21	0.281374	27	0.281033	1.4	1.0	3.11	2781	36	90
Roi38	0.0958	46	0.00302	15	1.4671	1.8866	18	0.281177	27	0.281005	5.0	1.0	3.06	2978	36	99
Roi39	0.0686	31	0.00205	9	1.4672	1.8870	26	0.281134	24	0.281018	4.8	0.9	3.05	2951	37	99
Roi40	failed															
Roi41	0.0962	50	0.00333	15	1.4672	1.8869	23	0.281214	22	0.281038	1.2	0.8	3.10	2768	36	91
Roi42	0.0793	50	0.00262	17	1.4672	1.8870	21	0.281155	23	0.281009	3.4	0.8	3.09	2904	37	96
Roi45	0.0922	125	0.00308	35	1.4671	1.8866	26	0.281187	25	0.281013	4.7	0.9	3.06	2953	37	97
Roi46	0.0608	20	0.00207	6	1.4672	1.8869	20	0.281147	22	0.281031	5.1	0.8	3.03	2941	37	100
sample Rub 1 (17.12.2011)																
a117	0.0856	54	0.0030	18	1.4672	1.8864	11	0.281156	30	0.280982	4.1	1.1	3.17	2975	16	100
a119	0.1077	41	0.0037	13	1.4672	1.8862	12	0.281214	29	0.281001	4.8	1.0	3.11	2977	13	100
a121	0.0727	33	0.0025	10	1.4672	1.8867	23	0.281147	25	0.281003	5.0	0.9	3.10	2978	10	98
a124	0.1090	19	0.0036	9	1.4672	1.8865	15	0.281188	25	0.280986	4.0	0.9	3.17	2965	9	100
a125	0.0447	49	0.0013	11	1.4672	1.8866	16	0.281074	26	0.281000	4.5	0.9	3.13	2965	10	100
a127	0.1025	8	0.0034	5	1.4672	1.8866	14	0.281183	29	0.280987	4.2	1.0	3.16	2969	11	100
a128	0.0514	20	0.0018	6	1.4672	1.8865	13	0.281087	28	0.280983	3.8	1.0	3.18	2961	9	100
a129	0.1225	28	0.0043	9	1.4672	1.8867	14	0.281252	28	0.281009	4.8	1.0	3.11	2962	13	100
sample Rub 2 (17.12.2011)																
a132	0.0633	31	0.0021	9	1.4672	1.8867	15	0.281120	28	0.280999	4.7	1.0	3.12	2974	8	100
a133	0.1893	79	0.0058	21	1.4672	1.8866	15	0.281342	28	0.281013	5.0	1.0	3.09	2966	6	100
a138	0.0748	13	0.0023	3	1.4673	1.8868	16	0.281121	28	0.280989	4.3	1.0	3.15	2972	8	100
a139	0.0978	28	0.0031	6	1.4671	1.8865	16	0.281172	27	0.280998	4.7	0.9	3.12	2973	7	100
a140	0.0913	33	0.0029	7	1.4672	1.8865	15	0.281163	26	0.280996	4.6	0.9	3.13	2974	6	100
a143	0.0832	47	0.0028	15	1.4672	1.8866	15	0.281146	30	0.280987	4.5	1.1	3.14	2985	6	100
a144	0.0506	14	0.0017	4	1.4672	1.8868	15	0.281085	30	0.280991	4.2	1.1	3.15	2966	9	100
a145	0.0948	24	0.0031	5	1.4672	1.8867	21	0.281173	29	0.280995	4.6	1.0	3.13	2974	10	100
a146	0.0637	38	0.0020	12	1.4672	1.8867	16	0.281117	29	0.281001	4.7	1.0	3.11	2972	6	100

(a) $^{176}Yb/^{177}Hf = (^{176}Yb/^{173}Yb)_{true} \times (^{173}Yb/^{177}Hf)_{meas} \times (M_{173(Yb)}/M_{177(Hf)})^{\beta(Hf)}$, $\beta(Hf) = \ln(^{179}Hf/^{177}Hf_{true} / {}^{179}Hf/^{177}Hf_{measured}) / \ln(M_{179(Hf)}/M_{177(Hf)})$, M=mass of respective isotope. The $^{176}Lu/^{177}Hf$ were calculated in a similar way by using the $^{175}Lu/^{177}Hf$ and β(Yb).
Quoted uncertainties (absolute) relate to the last quoted figure. The effect of the inter-element fractionation on the Lu/Hf was estimated to be about 6 % or less based on analyses of the GJ-1 and Plesovice zircons.
(b) Mean Hf signal in volt.
(c) Uncertainties are quadratic additions of the within-run precision and the daily reproducibility of the zircon GJ-1. Uncertainties for GJ-1 is 2SD (2 standard deviation).
(d) Initial $^{176}Hf/^{177}Hf$ and εHf calculated using the apparent Pb-Pb age determined by LA-ICP-MS dating (see column f), and the CHUR parameters: $^{176}Lu/^{177}Hf = 0.0336$, and $^{176}Hf/^{177}Hf = 0.282785$ (Bouvier et al., 2008).
(e) two stage model age in billion years using the measured $^{176}Lu/^{177}Lu$ and Pb-Pb age of each spot (first stage = age of zircon), a value of 0.0113 for the average continental crust (second stage), and a depleted mantle $^{176}Lu/^{177}Hf$ and $^{176}Hf/^{177}Hf$ of 0.03933 and 0.283294, see Blichert-Toft & Puchtel (2010).
(f) Pb-Pb age determined by LA-SF-ICP-MS

Commentaires

Les complexes mafiques lités ne sont pas rares dans le craton du Kaapvaal. Ils se trouvent couramment associés avec les ceintures de roches vertes sud-africaines mais sous forme de petites lentilles dont les tailles ne sont pas comparables avec celle du complexe du Rooiwater (revue dans Anhaeusser 2006). Indépendamment des ceintures de roches vertes, les intrusions mafiques litées peuvent atteindre des tailles considérables, comme le complexe du Bushveld (environ 60 000 km^2). La particularité du complexe du Rooiwater est d'avoir subi une différenciation magmatique qui permet la cristallisation de zircons et les mesures U-Pb-Hf.

J'apporte maintenant une précision pétrographique nécessaire quant à la nature de l'échantillon de la suite de Free State du complexe de Rooiwater pour l'interprétation des données géochronologiques, car le format d'article où nous présentons ces résultats ne laisse que peu de place à une telle description. L'échantillon est une roche constituée majoritairement de grains sub-automorphes de plagioclase albitique et de quartz (75-85 % vol., faible relief, macles polysynthétiques et à deux éléments, angle d'extinction faible, figure 1–4f). La lame mince est parcourue par une paragénèse sans orientation comprenant, parfois isolés, souvent en amas : une amphibole bleue-verte (probable hornblende sodique, figure 1–4a, b), un minéral

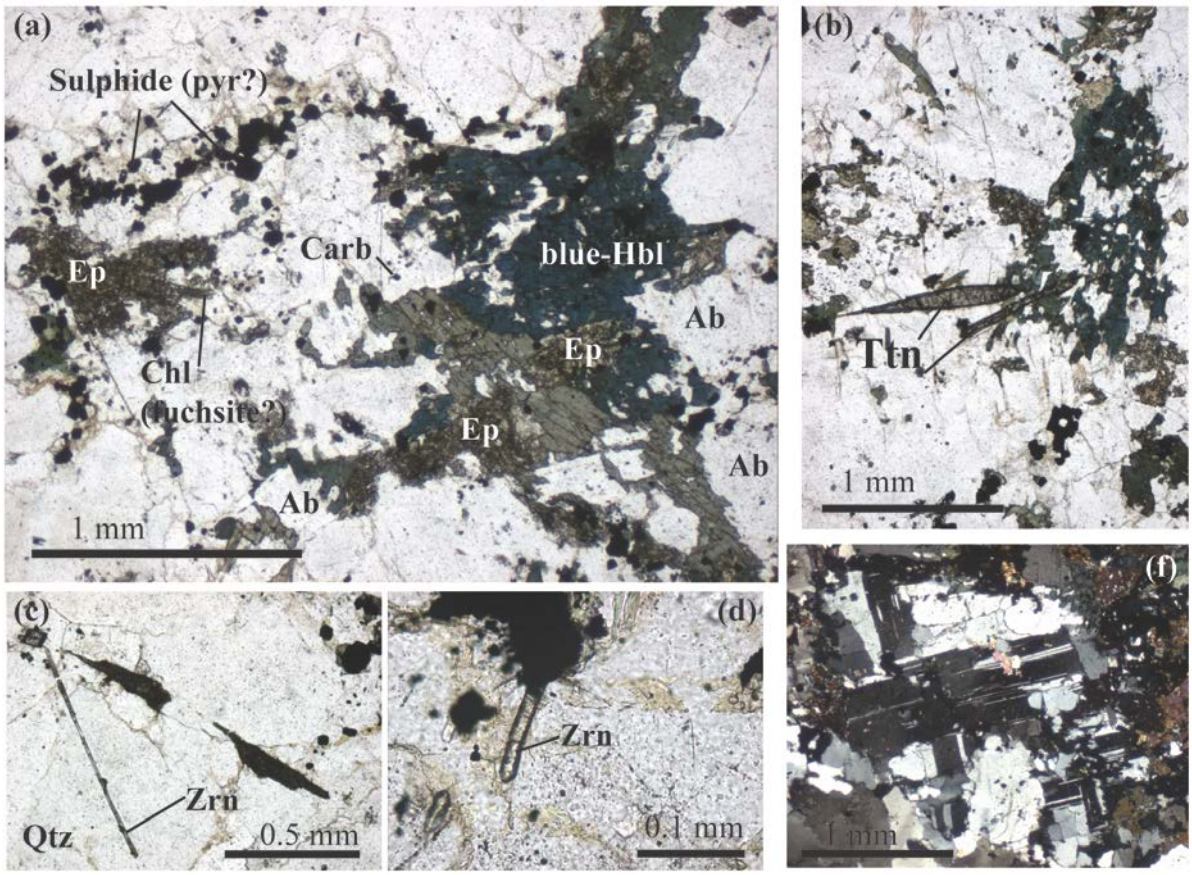

Figure 1—4 : *Photos en lumière polarisée de la "tonalite" de Free State (échantillon MURCH 96-4). (a) Ep : épidote ; Carb : carbonate ; Ab : albite ; Chl : chlorite ; Zrn : zircon ; Hbl : hornblende ; Ttn : titanite (sphène) ; Qtz : quartz. Voir texte pour commentaires.*

opaque (figure 1–4a), de l'épidote (figure 1–4a), du sphène (figure 1–4b) et rarement des phyllosilicates vert-bleu (chlorite ou fuchsite ? Figure 1–4a). L'amphibole a une texture en dentelle qui indique une altération par l'assemblage quartzo-albitique (figure 1–4 a, b). De plus, l'épidote et la chlorite se développent préférentiellement au détriment de l'amphibole (figure 1–4a). Le minéral opaque sub-automorphe est dispersé dans les zones à albites ou amphiboles, où parfois ses grains s'alignent en chapelets le long des joints de grains de quartz et de feldspath ce qui montre son association avec l'albitisation (figure 1–4a). Des pseudo-veines de carbonate (possiblement ankerite) ± mica vert (fuchsite) sont également présents et recoupent parfois les grains de quartz ou d'albite. Enfin, apatite et zircon complètent la minéralogie de l'échantillon. Il n'est pas possible de reconnaitre deux habitus ou deux contextes différents pour les zircons : les seuls observés avec certitude sont aciculaires (figure 1–4c et d).

A la fois la quantité d'albite dans la roche et la texture de celle-ci (macles et remplissage des figures de dissolution des amphiboles) démontrent que cette roche a été altérée en conditions hydrothermales, pour former une albitite. Cette nature hydrothermale peut être la cause de la confusion sur la nomenclature de cette suite, tantôt granite, tantôt tonalite, tantôt diorite selon les auteurs (Vearncombe et al. 1987 ; Poujol et al. 1996 ; Reynolds 1986 respectivement). Cette albitisation a affecté une paragenèse antérieure à amphibole tandis qu'elle pourrait être contemporaine de la paragenèse à chlorite-épidote et suivie de la phase à carbonate-opaque. Ainsi, comme interprétée dans les résultats et en cohérence avec les relations intrusives, l'âge vieux de 2964 ± 7 Ma correspond à la cristallisation du protolithe. Les dates plus jeunes (2795 ± 25 Ma) peuvent correspondre à un âge : dans ce cas il s'agit soit du métamorphisme amphibolitique, soit de l'albitisation. Ces événements et en particulier leur chronologie (cristallisation à 2.97 Ga, métamorphisme-albitisation à ca 2.8 Ga) rappellent beaucoup ceux affectant les albitites du centre de la ceinture décrites au chapitre 7 (article #5). L'âge du métamorphisme au nord et l'âge de l'albitisation dans le centre sont discutés en détail à la suite de l'article #2 (chapitre 3) et dans l'article #5 (chapitre 7) respectivement. Plus généralement les implications, à l'échelle de la ceinture, de la délimitation de deux types de terrains et de la chronologie seront discutées en lien avec les considérations structurales et métamorphiques à la fin du chapitre 2.

Chapitre 2 — Les terrains à granitoïdes et ceintures de roches vertes

Le chapitre 1 évoque la géodynamique archéenne en termes d'évolution géochimique du système croûte-manteau à l'échelle globale ou régionale (article #1). Ce chapitre 2 aborde plus concrètement les objets géologiques qui constituent les cratons archéens, les ceintures de roches vertes et leurs terrains granitoïdiques associés. Il rappelle rapidement leurs particularités pétrologiques et pétrogénétiques. Ces particularités, en combinaison avec les caractéristiques métamorphiques et tectoniques, délimitent les grands modèles géodynamiques archéens.

Enfin, pour illuster ces propos, la tectonique dans la région de la ceinture de roches vertes de Murchison est réexaminée dans l'article #2. Le modèle que nous proposons est confronté, à la fin du chapitre, aux données métamorphiques (article en annexe) et à la chronologie de l'amalgamation des deux terrains (article #1). Cela permet une réévaluation de la géodynamique globale de la zone.

NOTE SUR LES *"HIGH-GRADE TERRANE"* ET LES *"GRANITE-GREENSTONE-BELT TERRANE".* Pour décrire les objets archéens, la division choisie ci-après est ceintures de roches vertes *versus* granitoïdes. À celle-ci se superpose une division classique opposant terrains de hauts degrés (*high-grade*) et terrains de plus bas degrés dits « terrains à granite et ceinture de roches vertes » (*granite greenstone belt terrane*). Les premiers sont recristallisés en faciès amphibolite supérieur à granulite et sont composés de gneiss mais aussi, parfois, de roches supra-crustales équivalentes aux séquences des ceintures de roches vertes (e.g. roches d'Isua). Les terrains à granites et ceinture de roches vertes sont métamorphisés en faciès schiste vert à amphibolite. Cette distinction est métamorphique et non-géochimique (e.g. Kreissig *et al.* 2000 pour le craton du Kaapvaal). La(les) relation(s) entre les deux *terranes* est ambiguë : ils représenteraient des terrains équivalents à différentes profondeurs et/ou des terrains aux histoires tectoniques distinctes (par exemple la zone sud de la ceinture du Limpopo : voir chapitre 3-D; brève revue dans Chardon 1997).

A — Les granitoïdes

Les granitoïdes archéens sont les roches matérialisant la formation de la croûte sialique, d'autant plus qu'ils représentent le volume fondamental de la croûte archéenne (70-80% des roches archéennes). Leur pétrogenèse peut donc renseigner sur les modalités de la géodynamique archéenne. Les études de ces dernières décennies ont montré leur uniformité dans un groupe dit "TTG" ; la grande avancée des dernières années est la reconnaissance de la diversité intrinsèque aux TTG et la caractérisation de types mineurs en volumes mais important en termes d'évolution.

LES TTG (revue et références exhaustives par exemple dans Moyen et Martin 2012, Smithies et al. 2003, Condie 2005). La majeure partie des gneiss gris formant les socles archéens présente une pétrologie type : les TTG (pour Tonalite, Trondhjemite, Granodiorite), roches quartzo-plagioclasiques à biotite et ± hornblende.

La définition géochimique des TTG est précise (e.g. Martin et al. 2005 ; figure 2–1). Elles sont acides (SiO_2 > 64%, communément > 70% pds) et riches en Na, surtout par rapport au K (Na_2O 3-7% pds, corrélativement K_2O/Na_2O < 0.5), ce dernier rapport n'évoluant que peu au cours de la différentiation. L'Al est moyen (A/CNK ≈ 1). Elles sont pauvres en éléments incompatibles LIL (*Large Ion Lithophile*) et ferromagnesiens majeurs (Fe_2O_3 + MgO + MnO + TiO_2 ≤ 5% pds, Mg# ≈ 0.43) et en éléments traces (Ni ≈ 14 ppm, Cr ≈ 29 ppm). Les spectres de Terres Rares sont fortement fractionnés (La_N/Yb_N ≥ 30).

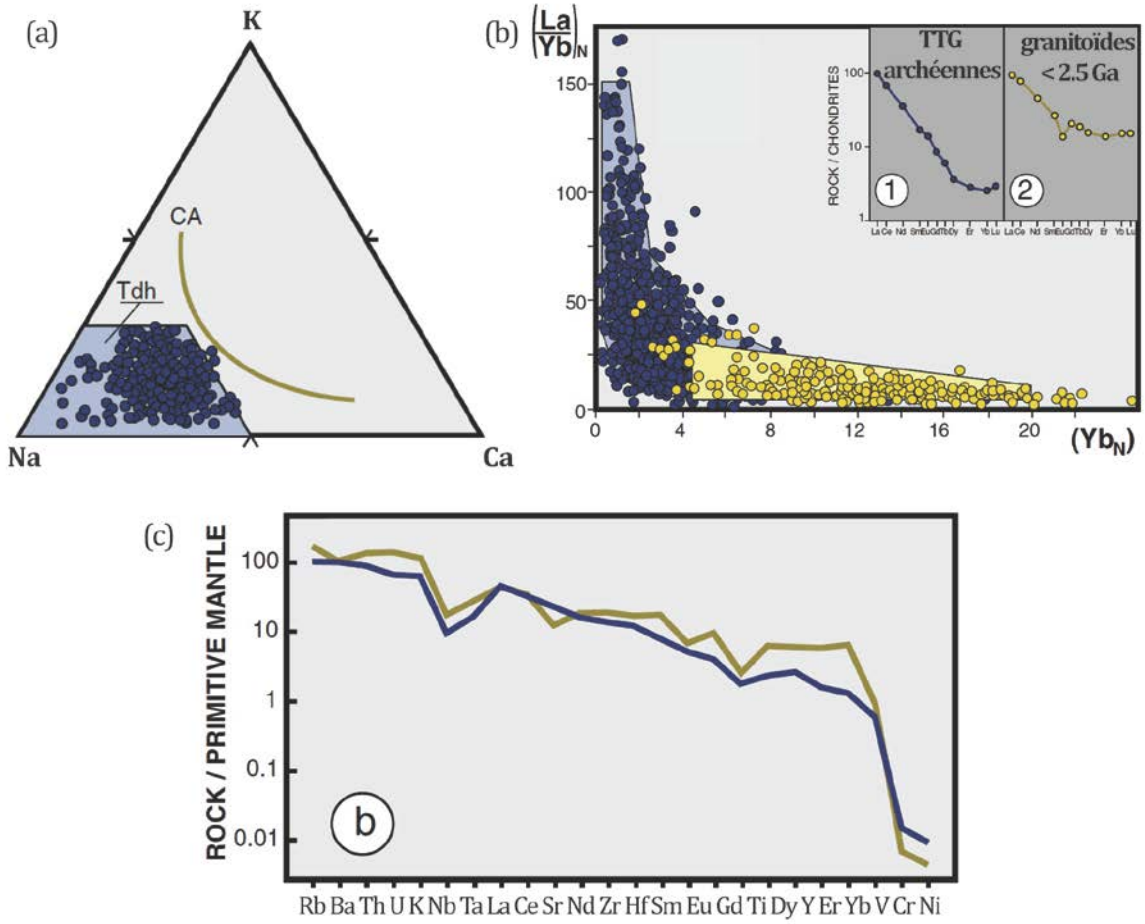

Figure 2—1: *Chimie des TTG. (a) Pour les alcalins, le triangle K-Ca-Na différencie la série TTG archéenne (points bleus, sans enrichissement en K) de la série calc-alcaline moderne (ligne jaune CA, avec enrichissement en K). (b) Pour les Terres Rares, le graphique La/Yb en fonction de Yb reflète la forme du spectre (encart) : les TTG ont des spectres significativement plus fractionnés que les granitoïdes phanérozoïques, et sans anomalie négative en Eu (normalisé aux chondrites). (c) Le spider diagram (normalisé au manteau primitif) indique aussi une anomalie négative en Nb-Ta et Ti. D'après Moyen et Martin (2012) et références incluses.*

Les modélisations géochimiques, l'analogie avec les adakites actuelles et la pétrologie expérimentale ont contraint la pétrogenèse de ces roches comme étant issues de la fusion partielle, sous un taux de fusion faible à moyen, de basaltes hydratés à haute pression (dans le champ de stabilité du grenat ± amphibolite), parfois avec un peu de cristallisation fractionnée intra-crustale (figure 2–2).

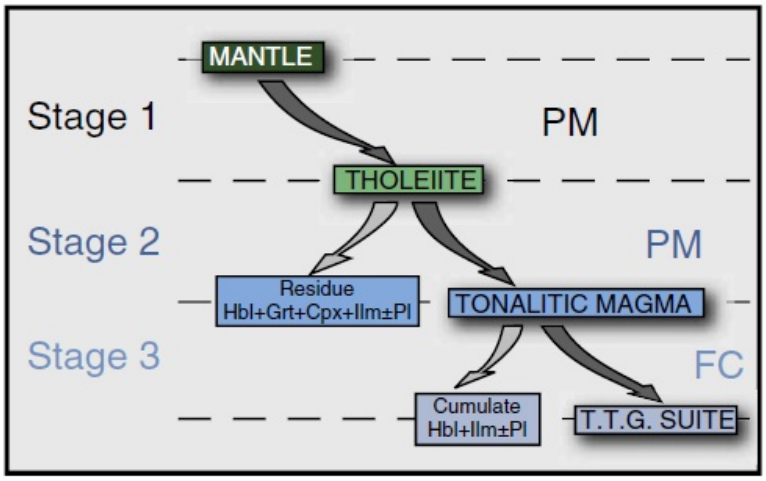

***Figure 2–2** : Organigramme pétrogénétique résumant la formation des TTG (Martin 1993).*

Dans le détail, les TTG au sens strict se sub-divisent en fonction des teneurs précises en Al, Na, Sr (indicateurs du plagioclase), Terres Rares lourdes (HREE, indicatrices de grenat), et éléments incompatibles HFS (*High-field Strengh*, e.g. Nb/Ta, indicateurs de rutile). Ces compositions reflètent alors la profondeur de fusion de façon plus fine (10-12, 15, 18 kbar). Enfin, il existe des roches référencées par erreur comme TTG, qui sont issues de contextes potentiellement très différents (Moyen 2011).

CONTEXTES DE FORMATION. Beaucoup de contextes géodynamiques ont été proposés pour expliquer la fusion de matériel basique à partir des conditions pétrogénétiques définies ci-dessus. Ils s'articulent autour de deux grands axes (figure 2–3):

- Dans un contexte de subduction chaude, où la croûte océanique basaltique du panneau plongeant atteindrait la fusion avant déshydratation, produisant des liquides TTG.
- Dans des contextes sans subduction, où un plume provoquerait la fusion du manteau et la production de matériel basique sous forme de plateau basaltique, qui subirait alors une fusion produisant les liquides TTG. Alternativement la formation de TTG dans une association rift-point chaud est évoquée.

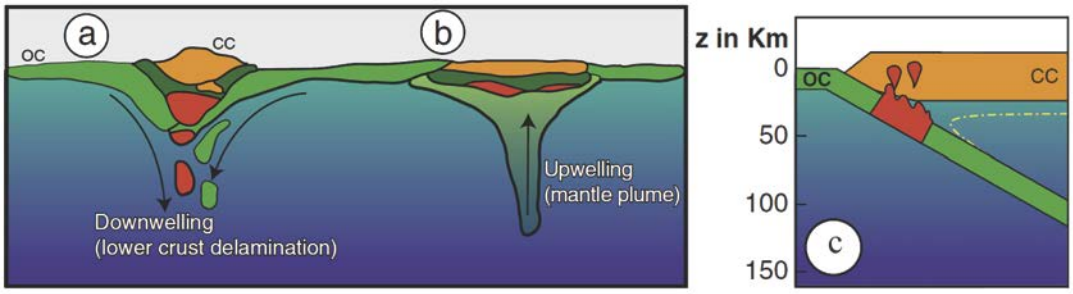

Figure 2–3 : *Modèles géodynamiques de formation des TTG (a) et (b) par un plume (c) par fusion du panneau plongeant (Moyen et Martin 2012).*

AUTRES GRANITOÏDES. Ils ne représentent que 10-15% de la croûte archénne mais sont plus diversifiés que les TTG (e.g. Laurent *et al.*, 2011).

Des granites potassiques, riches en plagioclase, forment typiquement des plutons de granodiorites à phénocristaux d'orthose, bien délimités, elliptiques, tardifs (syn- à post-tectoniques), qui sont responsables de la virgation des CRV. Ils forment une série calco-alcaline c'est-à-dire qu'ils sont relativement riches en K_2O (et LILE) et corrélativement pauvres en ferromagnésiens (surtout en Fe) par rapport aux TTG et aux tholéites. Leur pétrogenèse reste sujette à interprétation mais ils correspondraient au remaniement de matériel plus enrichi que les TTG, plus crustal (Sylvester 1994 ; TTG, métasédiments, andésites). Toutefois, les gneiss gris contiennent aussi une part non négligeable de ces phases, acquise précocément (e.g. Sanchez-Garrido *et al.* 2011). Les sanukitoïdes et le type "Closepet" sont des roches similaires aux TTG, mais avec de fortes valeurs Mg# et de hautes teneurs en Cr et Ni (figure 2–4). Elles sont interprétées comme résultant de la fusion de péridotite mantellique métasomatisée par les liquides dérivés de slabs et sont transitoires entre l'Archéen et le protérozoïque (e.g. Moyen 2011).

Il faut aussi souligner que ces roches peuvent former des séries continues avec les TTG et que des roches intermédiaires, aux pétrogénèses complexes, sont aussi observées (par exemple mélange sanukitoids-TTG, de Almeida *et al.* 2011). Enfin, dans le chapitre 8, nous aborderons la question des granites alumineux, rares à cette période en raison des difficultés de production de sédiments alumineux, de préservation, d'enfouissement, voire de fusion de la croûte.

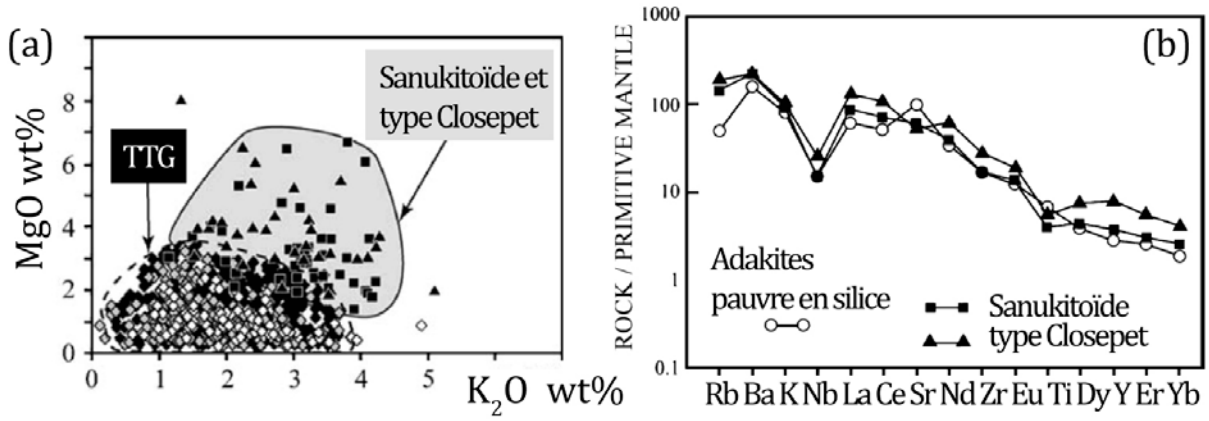

Figure 2–4 : *(a) Diagramme MgO vs. K_2O illustrant l'enrichissement en K et Mg des granitoïdes tardifs Sanukitoïdes et type Closepet (b) Spider diagram (normalisé au manteau primitif, McDonough et al. 1992) soulignant la similarité entre ces granitoïdes et les adakites pauvres en silice, pointant une source péridotitique (d'après Martin et al. 2005 et références incluses).*

L'augmentation de la fréquence de ces granitoïdes et à l'inverse la raréfaction des suites TTG constitue donc un changement fondamental de processus de formation crustale vers la fin de l'Archéen. Ce changement matérialise la transition depuis des contributions de plaques plongeantes et/ou de croûte basaltique vers des contributions du manteau hydraté et de la croûte continentale, donc vers des processus comparables à l'actuel (Condie 2008).

B — Les ceintures de roches vertes (CRV)

Les CRV sont des bassins volcano-sédimentaires préservés aux lithologies variées. Elles constituent 10 à 20% en volume des roches archéennes (Goodwin 1991), part mineure des volumes archéens, alors qu'elles sont l'objet d'un nombre élevé d'études car leur interêt est majeur sur plusieurs aspects. (i) Leurs roches témoignent d'interactions avec les enveloppes externes (atmosphère, océan) et la vie. (ii) Les séquences volcaniques enregistrent des processus magmatiques primordiaux et, conjointement, les séquences sédimentaires enregistrent indirectement des processus crustaux (reliefs, préservation des socles ; e.g. article #1). (iii) Les roches formées en surface, en particulier les roches basiques, sont les indicateurs métamorphiques privilégiés pour tracer les chemins Pression-Température, et les intégrer aux reconstitutions géodynamiques (voir article en annexe Block *et al.* 2012). (iv) Enfin la richesse des roches archéennes en certains métaux (chapitre 4-A) est en grande partie portée par les CRV (e.g. Au, Cu-Zn-Pb, Ni ; Groves et Barley 1994).

PETROLOGIE ET STRATIGRAPHIE. (D'après les synthèses de de Wit et Ashwal 1997, de Chardon 1997 et de Moyen 2000). Les CRV comprennent des niveaux de sédiments détritiques terrigènes (argilites, quartzites, conglomérats), des roches carbonatées et des sédiments chimiques typiques de cette époque (cherts et BIF - *Banded Iron Formation*). Ces sédiments traduisent un environnement de dépôt marin peu profond, parfois alluvial ou lacustre. Les laves et les sédiments volcano-dérivés sont bimodaux

entre des compositions ultramafiques-mafiques et intermédiaires-felsiques. Les komatiites représentent le pôle ultramafique (SiO_2 = 30-40% pds). Elles sont restreintes aux CRV mais ne sont pas présentes dans toutes. Ce sont des roches très riches en Mg (MgO = 20-40% pds). Elles sont le produit de la fusion partielle à taux de fusion élevé (20-50%) de protolithe peridotitique et déposées à des températures très importantes (1600°C). Ces komatiites sont intercalées avec des basaltes tholéitiques similaires aux tholéites actuelles. Les laves (et dérivés) intermédiaires à acides constituent des séries andésite-dacite-rhyolite, donc des séries calco-alcalines. Des intrusions basiques litées sont observées communément en lien étroit avec les successions des CRV (voir l'exemple du Rooiwater au chapitre 1).

En carte, les ceintures de roches vertes montrent des formes alongées et digitées (e.g. de Wit et Ashwal 1997). Ces bassins ont un rapport laves/sediments et laves mafiques/ laves felsiques plus importants que les bassins actuels (0.5-0.8 pour le premier ; figure 2–5). En effet, bien que le contact entre les unités soit souvent tectonisé, la succession caractéristique comprend une base mafique-ultramafique, puis des sédiments chimiques, suivis d'une association à volcanisme acide et sédiments terrigènes, et enfin d'une séquence terrigène immature typiquement discordante. L'ensemble a des épaisseurs variables selon les ceintures (5 à 15km ; de Wit et Ashwal 1997).

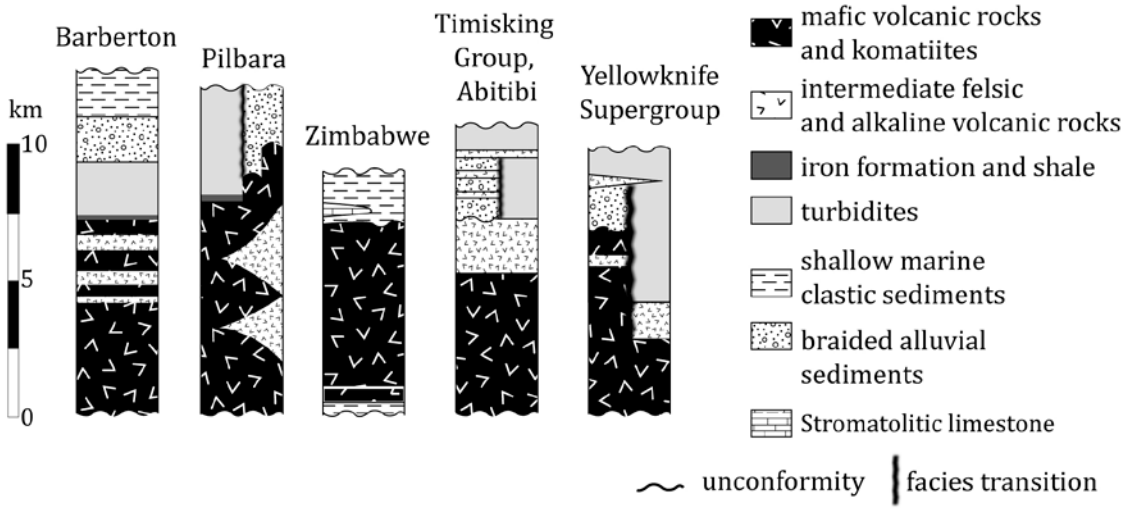

Figure 2—5 : *stratigraphie de quelques ceintures de roches vertes (modifié d'après Bickle et al. 1982)*

CONTEXTES DE FORMATION. Le modèle ophiolitique historique est apparemment aujourd'hui quasiment abandonné. Cependant, l'hypothèse de marge active s'est reportée sur un modèle d'arc insulaire qui explique la forme allongée, le parallélisme et l'espacement régulier des séries de ceintures, ansi que les successions terrigènes. A l'opposé, un rift continental est parfois invoqué pour expliquer la formation des CRV (et les grandes acccumulations de laves). Enfin, pour certains, le volcanisme des CRV serait analogue à celui des trapps, c'est-à-dire qu'il résulterait de la mise en place de provinces magmatiques (type plateau océanique ou continentaux actuel) lors de l'arrivée de plumes mantelliques. Aucun modèle ne satisfait tous les critères

observables dans les CRV et les auteurs se tournent vers des modèles composites dans le temps (par exemple succession rift-arc) ou dans l'espace (cratons à ceintures d'arc et cratons à ceintures de trappes ; figure 2–6).

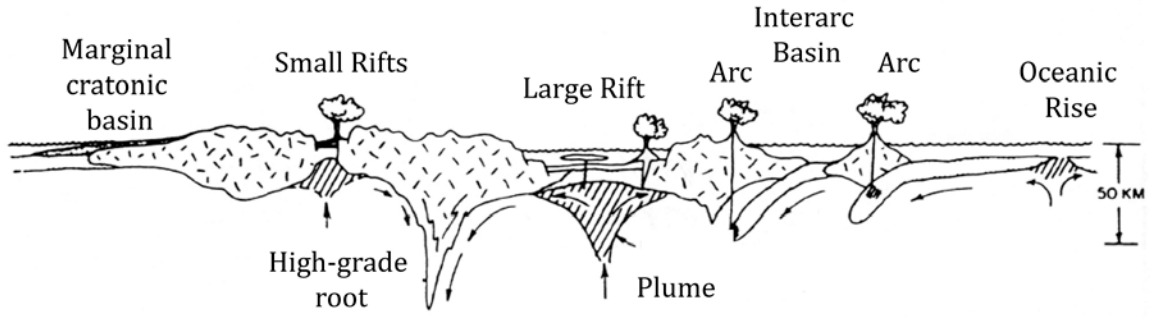

Figures 2—6 : *Formation des ceintures de roches vertes dans plusieurs contextes en même temps (Kröner 1985 et références incluses).*

Les ceintures de roches vertes et les granitoïdes du craton du Kaapvaal sont décrits dans le chapitre 3.

C — Géodynamiques archéennes – l'exemple de la Murchison Greenstone Belt

GRADIENT THERMIQUE ET PARADOXE THERMIQUE ARCHEEN. Les modélisations des désintégrations radiogéniques indiquent que 2 à 3 fois plus de chaleur était produite à l'Archéen par rapport à l'actuel. Ajoutée à la chaleur d'accrétion primordiale, le flux de chaleur mantellique archéen était donc plus fort qu'aujourd'hui. L'occurrence des komatiites en serait l'une des expressions (e.g. Nisbet et al. 1993). Or un flux de chaleur mantellique supérieur influence énormément la dynamique du manteau et la rhéologie de la lithosphère. Cependant les modalités d'évacuation de cette chaleur restent débattues, autrement dit les modalités géodynamiques (par exemple la possibilté d'une croûte advective, la taille des plaques ; pour des discussions détaillées voir par exemple de Wit et Hart 1993, Hamilton 1998). De plus, l'enregistrement métamorphique dans les roches archéennes ne montre pas particulièrement d'exces de chaleur, c'est-à-dire ne montre pas un régime thermique élevé comparé aux mesures à l'actuel (figure 2–7). C'est ce qui constitue le paradoxe thermique archéen.

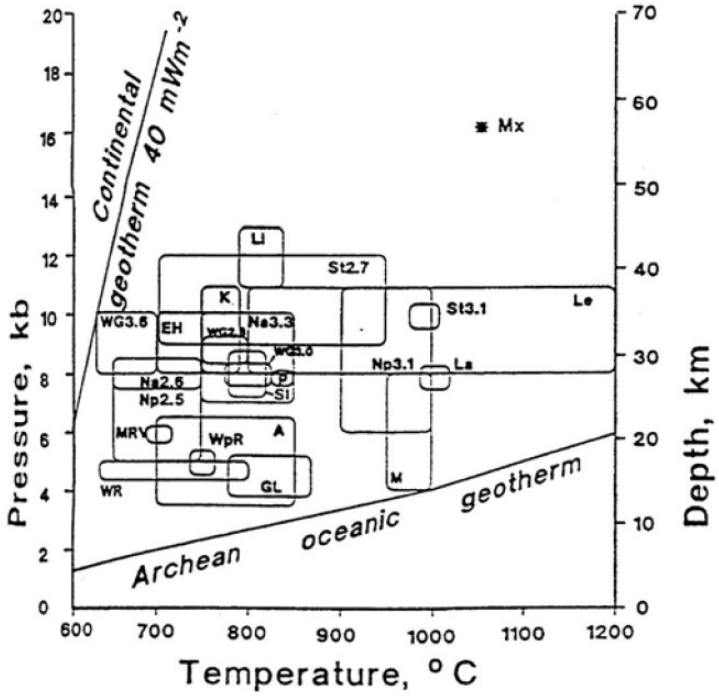

Figures 2–7 : *Diagramme P–T illustrant le domaine de stabilité de granulites archéennes (Percival 1994)*

Les parties A et B exposent les données relatives à la pétrologie des roches intrusives et effusives et les modalités pétrogénétiques associées. La transition vers les modèles géodynamiques interprétatifs impose la compréhension de la tectonique ayant affectée ces roches.

RELATIONS PLUTONS-CRV (synthèse d'après Kusky et Vearncombe 1997, Chardon 1997, Choukroune *et al.* 1997). Dès lors que les roches supracrustales et plutoniques sont spatialement associées, les modèles géodynamiques doivent intégrer les contraintes apportées par ces deux types d'objets. Dans ces zones, les roches magmatiques sont dominantes (> 60% ; Shakelton 1995). Les CRV se répartissent différemment d'un craton à l'autre (figure 2–8a) mais sont souvent linéaires et parallèles. La géométrie des CRV en profondeur dans les cratons est obtenue grâce aux données géophysiques. Elles montrent des objets généralement peu profonds par rapport à leur largeur (figure 2–8c). À l'échelle plus petite de la CRV, les relations sont diverses avec les plutons :

- Un contact normal, sédimentaire (discordance basale) peut être observé entre la CRV et son socle sous-jacent. C'est commun dans les CRV du craton du Dharwar occidental, mais plus rare ailleurs (reporté dans le craton du Kaapvaal pour la CRV de Pietersburg, de Wit et al. 1992b).
- Plus souvent, c'est un contact tectonique qui sépare les séquences crustales des plutons : le contact peut être un chevauchement plat de décollement basal (*sole thrust* ; figure 2–8b, rares exemples dans la CRV de Giyani, de Barberton, de Selukwe, par exemple Chardon et al. 1996) ou un cisaillement vertical (figure 2–8b3 ; c'est la règle dans le craton de Ylgarn ou dans la Province Supérieure).

- Mais la relation caractéristique, illustrée sur la figure 2–8a, consiste en des CRV aux contours courbés autour de granitoïdes elliptiques intrusifs typiquement tardifs et potassiques. Ce « motif » est nommé le *dome-and-basin pattern* (par exemple dans le craton du Pilbara et du Zimbabwe)**.**

Caractéristiques structurales. Au premier ordre, les CRV sont caractérisées par des structures pervasives très pentées à verticales (foliations et plis *upright*), souvent à cinématique inverse. Ces structures très pentées restent ambiguës, elles sont interprétées :

- comme des plis d'interférence complexes
- comme des dômes diapiriques (*balloning*) quand les plutons montrent peu de déformations et des foliations parallèles en bordures à celles de la CRV (figure 2–8b cas 1)
- comme des phénomènes de sagduction des CRV (enfouissement des séquences supra-crustales dans les granitoides peu résitants, sans contrastes de densité ; figure 2–9b, droite)
- comme des nappes chevauchant les plutons ou internes à la CRV
- comme des champs de déformation coaxiale homogène à grande échelle quand les foliations sont retrouvées dans les terrains plutoniques (y compris dans les granites tardifs).

Les trois dernières interprétations traduisent essentiellement un raccourcissement crustal horizontal, alors que les dômes diapiriques font d'avantage appel à un processus gravitaire vertical. Concrètement, les CRV sont fortement tectonisées. Les études structurales proposent souvent plusieurs phases tectoniques et invoquent parfois la combinaison ou la succession de ces processus (figure 2–9b).

En dehors de ces structures, la synthèse de Kusky et Vearncombe (1997) et Chardon (1997) insistent sur la nature précoce des phases chevauchantes à faible angle (parfois même synsédimentaires). De même, des cisaillements-décrochements verticaux à cinématique horizontale sont attribués à des déformations tardi-orogéniques localisantes et peuvent former des réseaux anastomosés. Un caractère structural essentiel des terrains archéens est la quasi-absence de structures extensives avérées : les déformations observées sont toujours convergentes (Kusky et Vearncombe 1997).

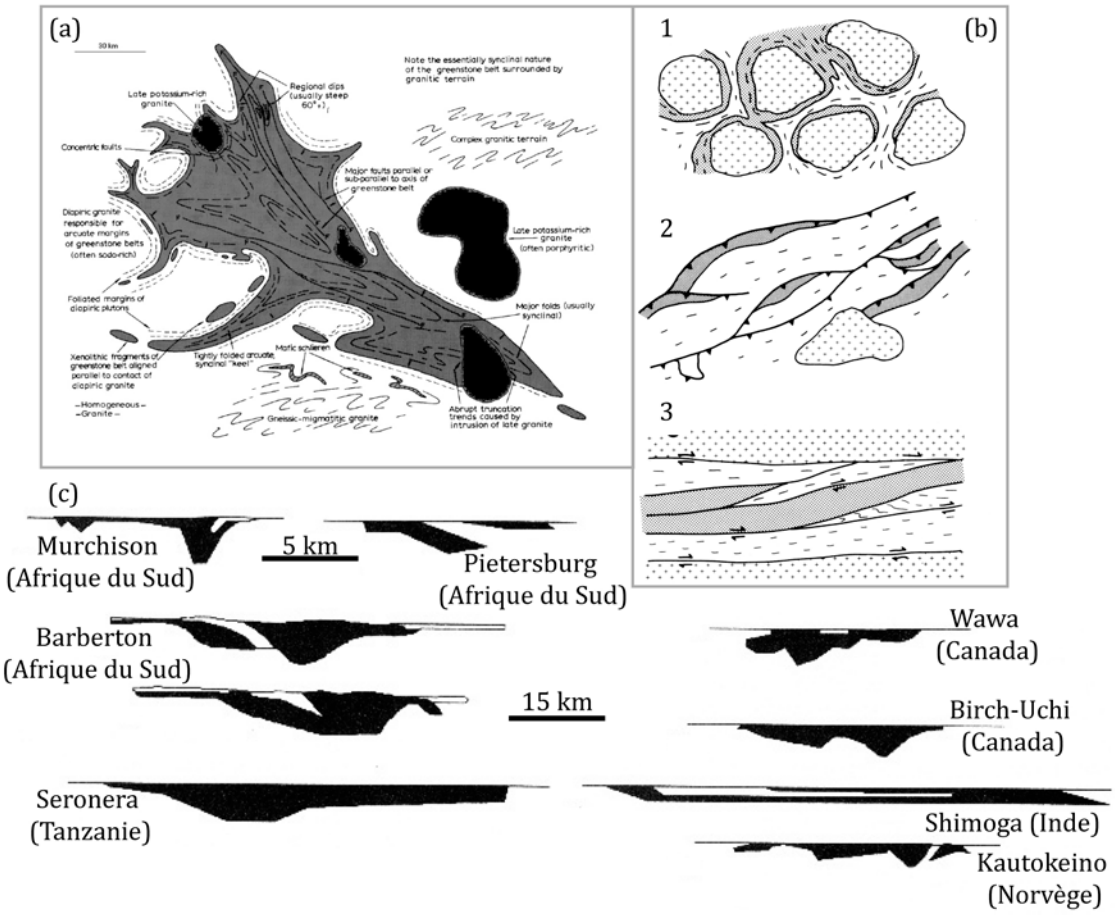

Figure 2-8: *(a) Ceinture idéalisée de Anheusser et al. (1969) montrant une ceinture moulée par des plutons ou des recoupements (noir). (b) Géométries en coupe de ceintures de roches vertes compilées à partir des données géophysiques (lithologies des ceintures en noir, granitoïdes en blanc ; de Wit et Ahwal 1997). (c) Trois types de relation plutons–ceintures de roches vertes (ceintures de roches vertes en gris, pluton avec croissillons ; Kusky et Vearncombe 1997) (1) en dôme (2) bifurquante (3) linéaire.*

LE METAMORPHISME. Les CRV sont quasi-exclusivement les objets sur lesquels le métamorphisme des terrains archéens est estimé. Le métamorphisme varie de faciès prehnite-pumpellyite à granulitique, mais il est communément dans le faciès schiste vert entre 2.5 et 4.5 kbar (e.g. Shakelton 1995). Il semble que le métamorphisme régional soit homogène à l'intérieur d'un *grade*, i.e. identique au "socle". Il est donc logiquement syn-tectonique. Plusieurs événements métamorphiques sont parfois reconnus mais montrent essentiellement des gradients thermiques de basse pression-haute température (50-70°C/km) ou moyenne pression-moyenne température (30-40°C/km ; figure 2–7).

Les avancées récentes principales dans l'étude des CRV révèlent une certaine diversité avec l'association de degrés métamorphiques différents dans une même CRV et dans les CRV d'une même zone (*terrane*, références dans Block et *al.* 2012). De plus, l'absence de roches signant des processus de subduction (eclogites, schistes bleus) est remise en cause par les études de Dziggel et al. 2006 et Moyen et al. 2006. Cette dernière documente des enclaves de haute pression-basse température à un gradient similaire à l'actuel (15°C/km).

Il existe un large panel de modèles de formation des terrains archéens. Un pôle actualiste argumente en faveur d'une tectonique horizontale d'accrétion de blocs dans des conditions similaires à l'actuel tandis qu'un pôle "archéen" favorise une géodynamique spéciale de points chauds et de diapirs, provoquant une tectonique gravitaire verticale (figure 2–9b). Les déformations archéennes ne sont pas uniformément interprétées et plusieurs contextes tectoniques sont possibles.

Aujourd'hui, la pétrologie des roches intrusives et le métamorphisme des CRV soulignent de plus en plus la diversité des terrains. Ceci argumente en faveur non pas d'une seule mais de plusieurs contextes archéens comme cela était déjà proposé dans les années 1990 (e.g. de Wit et Ashwal 1997). Ainsi, les modèles géodynamiques intermédiaires, ou bien évolutifs ou encore variables spatialement, réconcilient ces différences, en proposant par exemple la co-existence de sudductions chaudes, de collisions de blocs continentaux et de panaches.

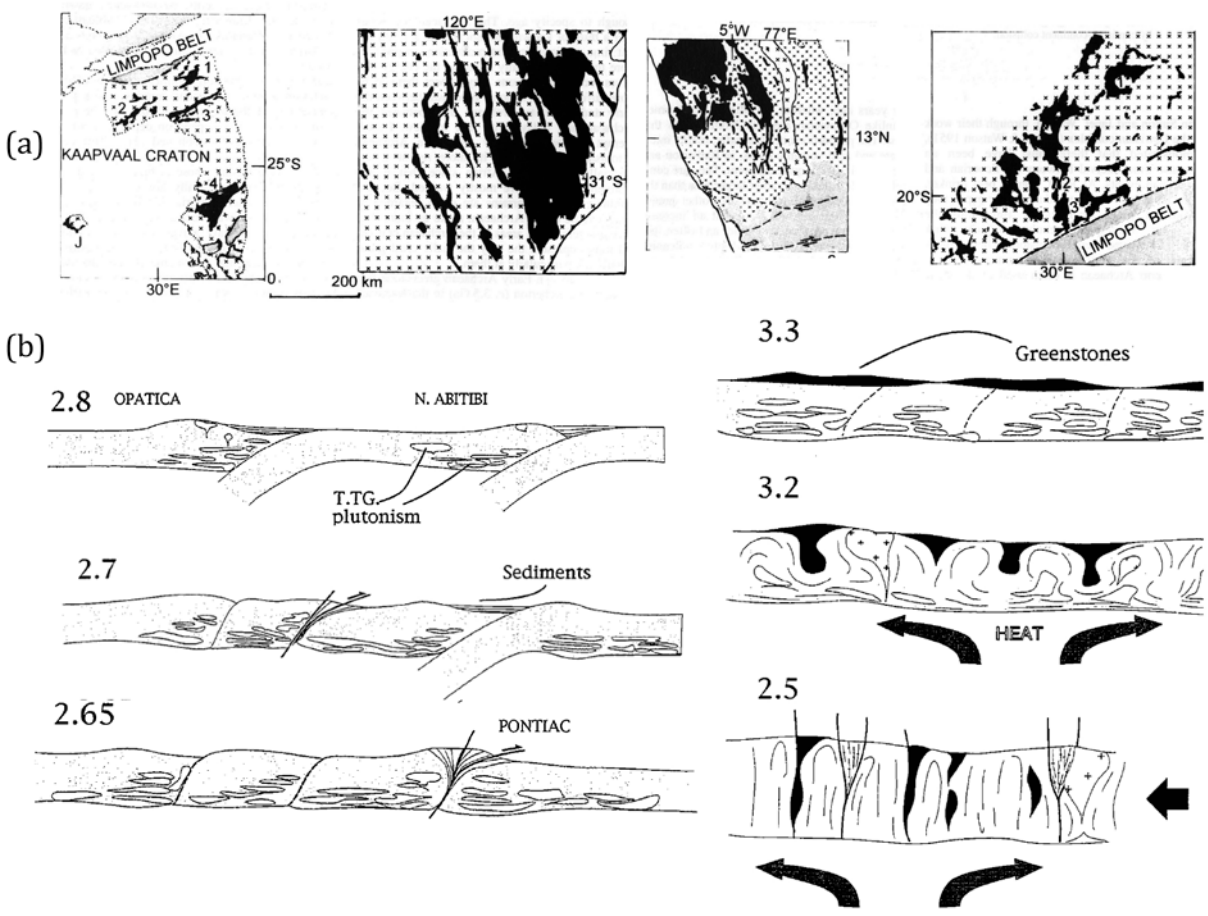

Figure 2–9 : *(a) Variabilité cartographique des cratons archéens : de gauche à droite Kaapvaal, Yilgarn ; Dawhar ; Zimbabwe (noir : volcanites et sédiments ; croix : granitoïdes ; gris ou blanc : couverture ; Shackleton 1995). (b) Coupes schématiques de Choukroune et al. (1997) comparant l'évolution tectonique de l'Abitibi (gauche) et du Dawhar (droite).*

LA CEINTURE DE ROCHES VERTES DE MURCHISON

Peu de modèles géodynamiques ont été proposés pour la ceinture de Murchison. Pourtant, les terrains de bas grades comme celui-ci permettent d'observer les relations entre les roches des CRV et les plutons intrusifs, ainsi que les conditions métamorphiques. L'étude qui suit propose un nouveau modèle tectonique.

Article #2

"The Murchison Greenstone Belt (South Africa): A general tectonic framework"

Publié à *South African Journal of Geology, vol. 115 (1) 65-76*

Résumé en français

Cet article traite du style de déformation de la ceinture de roches vertes de Murchison, située dans le nord-est du craton de Kaapvaal (Afrique du Sud). La ceinture de direction nord-est/sud-ouest est entourée de gneiss et granitoïdes, et elle est constituée de roches métavolcaniques et métasédimentaires meso-archéennes. Elle est étroite, très déformée, et enracinée profondement en son centre avec une géométrie globalement "en quille".

Les fabriques régionales consistent en une foliation sub-verticale à faible angle par rapport à la direction de la ceinture, qui porte une linéation d'étirement fortement plongeante. D'après les données disponibles et nos propres observations, nous avons construit une carte des trajectoires de foliations. Cette carte révèle les points suivants : les déformations sont distribuées ; à la fois la ceinture et le gneiss adjacent au nord sont déformés ensemble de façon ductile ; les plutons se sont mis en place durant la déformation régionale.

La structure générale, combinée à l'existence de roches intrusives et extrusives contemporaines à la surface aujourd'hui, soutient un modèle tectonique vertical avec enfouissement des roches supra-crustales dans le matériel sous-jacent mou pendant le raccourcissement crustal horizontal.

L'observation de leucogranites est cohérente avec la fusion des sédiments de la ceinture enfouis en profondeur. Enfin, les âges disponibles sur les granitoides syn-cinématiques (2.97 à 2.77 Ga) suggèrent un processus tectonique long.

THE MURCHISON GREENSTONE BELT (SOUTH AFRICA): A GENERAL TECTONIC FRAMEWORK

J. JAGUIN, D. GAPAIS, M. POUJOL AND P. BOULVAIS
Géosciences Rennes, UMR CNRS 6118, Université de Rennes 1, Campus de Beaulieu, 35042 Rennes CEDEX, France.
e-mails: justine.jaguin@univ-rennes1.fr, denis.gapais@ univ-rennes1.fr, marc.poujol@ univ-rennes1.fr, philippe.boulvais@ univ-rennes1.fr

J.-F. MOYEN
Laboratoire Magmas et Volcans, Université Jean Monnet, 42000 Saint-Étienne.
e-mail: jean.francois.moyen@univ-st-etienne.fr

ABSTRACT

This paper discusses the deformation pattern of the Murchison Greenstone Belt, which is located in the northeastern Kaapvaal Craton, South Africa. The belt strikes northeast to southwest, is surrounded by gneisses and granitoids, and contains Meso-Archaean metavolcanics and metasediments. It is narrow, strongly deformed, and deeply rooted in the centre with a bulk keel geometry. Regional fabrics consist of a sub-vertical foliation at a low angle to the belt strike and bears steeply plunging lineations. From available data and our observations, we constructed a map of the foliation trajectories. The map reveals the following: the deformations are distributed, both the belt and the northern bounding gneisses are deformed together in a ductile way, and the plutons were emplaced during regional deformation. The overall structural pattern, together with the existence of contemporaneous intrusive and extrusive rocks outcropping at the surface, supports a vertical tectonic model, with burial of the upper crustal rocks within the underlying weak material during horizontal crustal shortening. The occurrence of leucogranite intrusions is consistent with the melting of buried sediments belonging to the belt at depth. Finally, ages available on syn-kinematic granitoids (2.97 to 2.77 Ga) suggest a long-lasting tectonic process.

Introduction

Deformation modes of Archaean and Palaeoproterozoic orogenic belts are still strongly debated (see reviews in Windley, 1992; Hamilton, 1998; Marshak, 1999; Chardon et al., 2009). Most models invoke either modern-type tectonics involving stiff lithospheres or accretionary-type orogens involving hot lithospheres and juvenile materials. In the first type of orogens involving a strong lithospheric mantle, strain localization occurs along crustal-scale shear zones, whereas in hot and weak lithospheres, deformation tends to be distributed and marked by vertical burial (sagduction) of upper crustal material within an underlying weak crust (see Chardon et al., 2009 and references therein). Several papers have discussed deformation modes in Archaean greenstone belts where upper crustal rocks are juxtaposed with basement gneisses within dome and basin patterns (see discussions in Choukroune et al., 1997; Chardon et al., 2009).

Our study focuses on the 3.09 to 2.97 Ga Murchison Greenstone Belt (MGB), one of the Archaean greenstone belts situated on the Kaapvaal craton of Southern Africa (Figure 1). It is located to the northeast of the Kaapvaal craton, about 200 km north of the Barberton Greenstone Belt (BGB), and 40 km to the south of the southern boundary of the Limpopo Belt. It extends a distance of approximately 140 km from the Transvaal Drakensberg Escarpment in the western part of South Africa toward the east.

Contrary to areas such as the Barberton or Limpopo Belts, only few structural studies have been published for the MGB (Graham, 1974; Vearncombe, 1988; Minnitt and Anhaeusser, 1992). In this paper, we reappraise existing structural, geophysical and geochronological data. These data, combined with our field observations, allow us to illustrate the overall geometry of the belt and discuss a possible tectonic model associated with its development.

Geological setting

Figure 1 shows the northeastern part of the Kaapvaal craton where three major events have been recognized (see Poujol, 2007):

1. formation of the gneissic basement and of the greenstone belts (~3.7 to ~3.0 Ga, the northern domain of Poujol et al., 2003);
2. the Limpopo orogen resulting from the collision between the Kaapvaal and Zimbabwe cratons (the area is marked by a complex metamorphosed belt exhibiting at least two clusters of ages at ~2.6 and ~2.0 Ga, respectively (review in Kramer et al., 2006 and refs. therein),
3. emplacement of the Bushveld complex, the largest layered mafic complex in the world, which intruded the Kaapvaal craton at ~2.06 Ga.

The gneissic and greenstone belt domain comprises four northeasterly to east-northeasterly trending volcanic and sedimentary units. To the north, a group of three

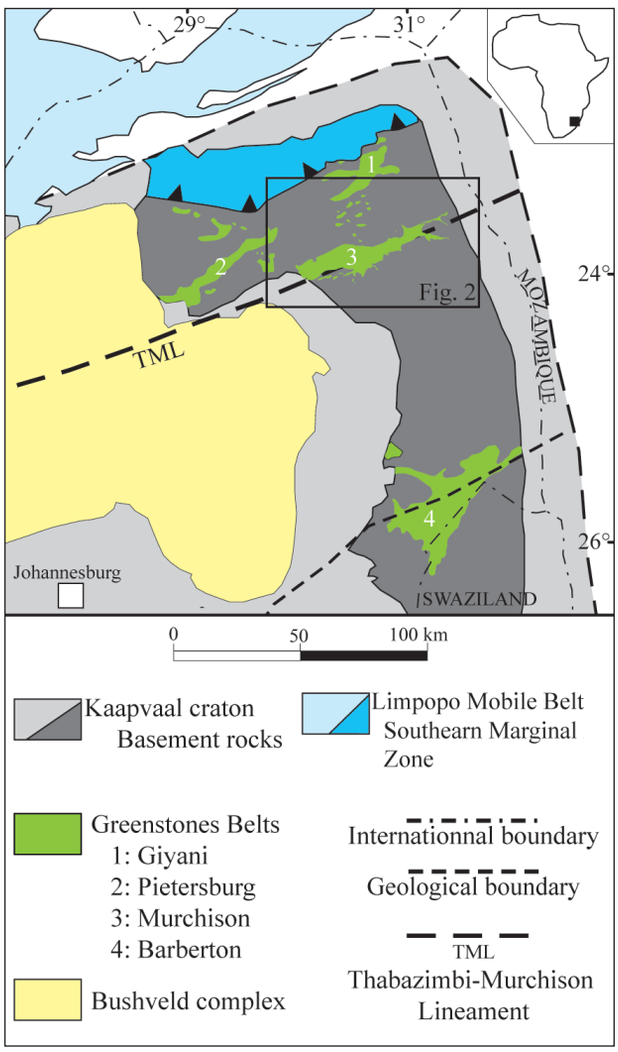

Figure 1. *Map of the northeastern part of the Kaapvaal Craton, with the Murchison Greenstone Belt area framed (after Poujol, 2007).*

greenstone belts is observed (the Murchison, Giyani and Pietersburg Belts), whereas the world-famous BGB lies further to the southeast. De Wit et al. (1992a) argued that various crustal blocks made up the Kaapvaal craton, one of the sutures being the Thabazimbi-Murchison Lineament (TML). The location of the MGB with respect to the different Archaean blocks is still ambiguous. Fripp et al. (1980) locate the TML along the northern border of the MGB (Letaba Shear Zone). However, Anhaeusser (2006) extends what he calls a "collision zone" from the MGB itself up to ultramafic rocks occurring south of the MGB. The TML has a long-lived tectonic history (Good and de Wit, 1997), with age clusters at ~2.7 to 2.6 Ga and ~2.0 Ga that may be linked to the Limpopo orogeny (McCourt, 1995).

Lithologies within the MGB

The MGB consists of metavolcanic and metasedimentary rocks surrounded or intruded by granitoid rocks (Figures 2 and 3). Lithologies are described here from roughly south to north using the combined terminologies used by Vearncombe (1988, in italics) and SACS (1980). Geochronological data are reported in Table 1.

The *La France Formation* is a small area in the south-centre part of the belt. It comprises quartzites as well as kyanite- and staurolite-bearing micaschists, indicating recrystallisation under amphibolite facies conditions (Block and Moyen, 2011). Decametric quartz veins occur and locally contain large euhedral kyanite crystals.

The *Murchison ultramafic, mafic, carbonated and metasedimentary schists* (following Vearncombe et al., 1988) represent the largest domain of the MGB. The age of the mafic-to-ultramafic successions (Leydsorp and Mulati Formations), which occupy the southern flank of the unit, remains unknown. Metamorphic conditions are mainly of lower greenschist grade (Block and Moyen, 2011). The local occurrence of kyanite (van Eeden et al., 1939; Vearncombe, 1988) indicates pressure conditions above 3.5 kbar. Mafic to felsic volcanics and volcanoclastic sediments (Weigel Formation), and meta-arenites of the MacKop Formation occupy the central portion of the MGB. The maximum age of deposition for the MacKop Formation is defined at 3076 ± 4 Ma by U-Pb dating on detrital zircons (Poujol et al., 1996). Some volcanics from the Weigel Formation have been consistently dated at 3087 ± 21 Ma (Poujol et al., 1996). In the centre of the MGB, a world-class antimony (± gold) mineral deposit occurs along a narrow (hundreds of metres in width), east-northeast trending zone known as the "Antimony Line" (Figure 3). Besides the Sb (±Au) mineralisation, the Antimony Line is marked by an intense transformation of granodioritic intrusives into albitic rocks found in the vicinity of the Sb-Au mines (Malati Pump quarry, Athens Shaft, Gravelotte, e.g. Pearton and Viljoen, 1986).

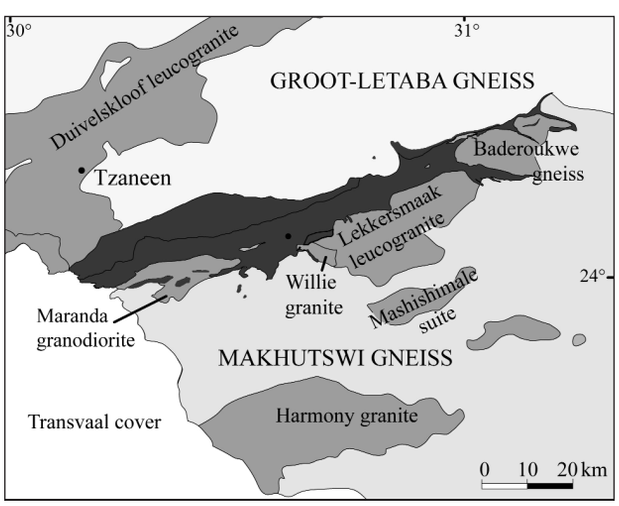

Figure 2. *General map of the region with the surrounding granitoids (after Robb et al., 2006).*

Table 1. Summary of ages for the Murchison Greenstone Belt area.

Unit name		Sample nature	Age (Ma)	Method	Ref	Interpretation
Northern basement of the MGB	Groot Letaba	migmatitic tonalitic gneiss	3333 ± 5	A	1	Crystallisation
			2839 ± 8	B	2	Crystallisation
			2784 ± 8	B		Crystallisation
	Turfloop	porphyritic granodiorite	2777 ± 10	C	3	Crystallisation
	Rooiwater complex	Hornblende tonalite	2671 ± 10	B	2	Crystallisation
			2740 ± 4	C	4	Crystallisation
The Murchison Belt (MGB)	Rubbervale Formation	dacite	2969 ± 20	C	5	deposition
		rhyolite	2965.2 ± 1.4	C	6	deposition
			2971 ± 10	C	4	deposition
			2974.8 ± 3.6 to 2963.2 ± 6.4	A	7	deposition
	MacKop Formation	meta-conglomerates	> 3076 ± 4	C	5	max. age of deposition
	Weigel Formation	felsic volcanic	3087 ± 21	C	4	deposition
	Baderoukwe	trondhjemitic gneiss	2966.2 ± 2.9	B	submitted	Crystallisation
			3018 ± 15	C	5	min. age of crystallisation
	Malati Pump mine	granodiorite	2964 ± 6	B	submitted	Crystallisation
	Maranda	granodiorite	2901 ± 20	C	4	min. age of crystallisation
	Lekkersmaak	peraluminous granite	2795 ± 8	B	2	Crystallisation
	Willie	peraluminous granite	2820 ± 38	C	5	Crystallisation
Southern basement of the MGB	Discovery	granite	2969 ± 17	C	5	Crystallisation
	Mashishimale	peraluminous granite	2671 ± 8	B	2	Crystallisation
			2698 ± 21	C	5	Crystallisation
	Harmony	trondhjemitic gneiss	3091 ± 5	C	8	Crystallisation
	Makhustwi	tonalitic gneiss	3063 ± 12	C	8	Crystallisation
		tonalitic gneiss	3078 ± 6	A	1	Crystallisation
	Makhustwi (French Bob)	trondhjemitic and tonalitic gneiss	3228 ± 12	C	4	Crystallisation

Method: (**A**) Pb-Pb zircon evaporation; (**B**) U-Pb zircon LA-ICPMS; (**C**) U-Pb zircon ID-TIMS.

References: (**1**) Brandl and Kröner, 1993 (**2**) Zeh el al., 2009 (**3**) Henderson, 2000 (**4**) Poujol et al., 1996 (**5**) Poujol, 2001 (**6**) Brandl et al., 1996 (**7**) Schwarz-Shampera et al, 2010 (**8**) Poujol and Robb, 1999. All errors at 2σ.

The northern margin of the belt is occupied by the *Rubbervale Formation* that comprises intermediate to felsic lavas and tuffs deposited at ~2.97 Ga (Brandl et al., 1996; Poujol et al., 1996; Poujol, 2001; Schwartz-Schampera et al., 2010) and metamorphosed into the greenschist facies. The Rubbervale Formation hosts the "Cu-Zn Line" described as the largest volcanic-hosted massive sulfide (VHMS) district in Southern Africa (see Schwartz-Schampera et al., 2010).

The *Silwana Amphibolite* unit located to the northeast of the MGB is a thin slice (around 300 m wide) made up of hornblende and biotite schists and deformed amphibolite gneisses whose protolith may have been mafic layered rocks (Block and Moyen, 2011).

Finally, the Rooiwater Complex in the northwestern part of the MGB is a layered igneous complex of gabbros-anorthosites, amphibolites and tonalite that is up to 7.5 km wide. Two ages have been reported so far for rocks from the Rooiwater Complex: 2740 ± 4 Ma for the emplacement of a hornblende tonalite (Poujol et al., 1996), and 2611 ± 10 Ma for gabbros (Zeh et al., 2009). These two ages are more than 100 m.y. apart and therefore their significance is still a matter of debate, but they suggest that the Rooiwater Complex is much younger than the MGB itself. Its exact origin remains uncertain, but it has been proposed that the Rooiwater Complex is allochtonous and was potentially tectonically juxtaposed to the MGB (Poujol et al., 1996).

Granitoids and orthogneisses in and around the MGB (Figure 2, Table 1)

The oldest granitic rock found so far is known as the French Bob Mine Granite, a tonalitic to trondhjemitic gneiss that crops out to the south of the MGB. Its crystallisation has been dated at 3228 ± 12 Ma, suggesting the existence of an older granitoid basement in the vicinity of the MGB (Poujol et al., 1996). Further south, the intrusion of the Harmony Granite, a trondhjemitic gneiss, has been dated at 3091 ± 5 Ma. A date of 3063 ± 12 Ma has been obtained in a migmatitic gneiss belonging to the Makhutswi gneiss, which has been interpreted as a magmatic age (Poujol and Robb, 1999). These ages overlap with the age of ca. 3.09 obtained for the volcano-sedimentary Weigel Formation (Poujol et al., 1996), which suggests that the MGB may represent a volcanic arc (as previously proposed by Vearncombe, 1991), possibly linked to a subduction zone (Poujol et al., 1996).

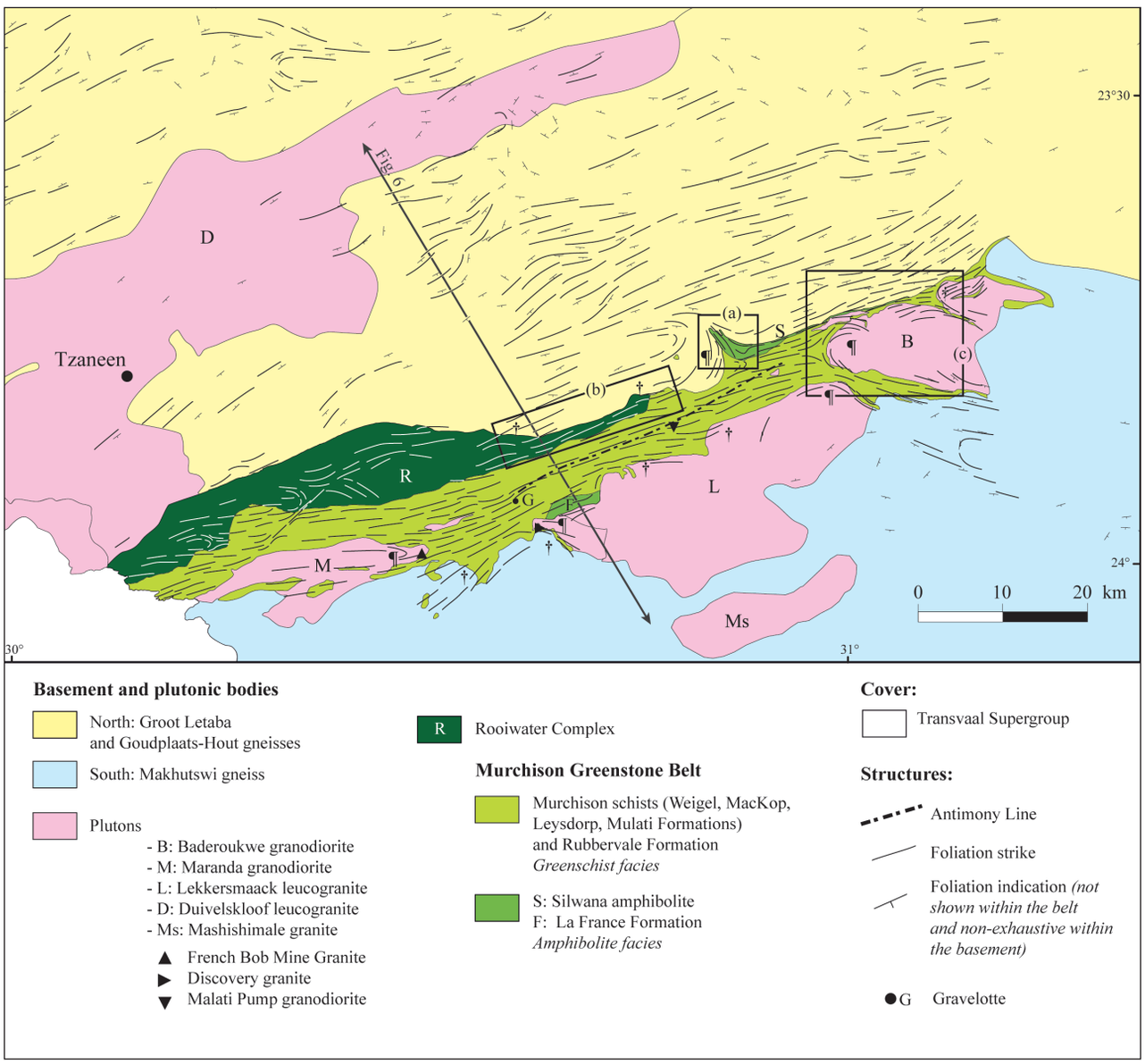

Figure 3. *Geological map of the Murchison Greenstone Belt with foliation strike. Data are compiled from maps of the MGB (Vearncombe et al., 1992), the 1:250 000 map of Tzaneen (Sheet 2330, 1985) and our own measurements.* †, *and inset (**a**), (**b**) and (**c**): see Figure 6.*

A second period of contemporaneous volcanic and plutonic activity has also been demonstrated with the intrusion of several plutonic bodies around 2.97 Ga: the Discovery Granite (2969 ± 14 Ma; Poujol, 2001), the Malati Pump granodiorite (2970 ± 15 Ma, Poujol et al., 1997), the Baderoukwe orthogneiss (concordia zircon age of 2969 ± 12 Ma, Jaguin et al., to be published). All these ages are indistinguishable from the deposition of the volcanic Rubbervale Formation ca. 2.97 Ga ago (see above). The minimum crystallisation age of the Maranda granodiorite is 2901 ± 20 Ma (Poujol et al., 1996).

A third period of important magmatic activity around 2.8 Ga is demonstrated by the emplacement of the Groot Letaba orthogneiss to the north of the belt (2839 ± 8 Ma, Zeh et al., 2009), and to the south of the belt with the crystallisation of:

1. pegmatitic dykes intrusive into the Makhutswi gneiss (2848 ± 58 Ma, Poujol and Robb, 1999),
2. the Willie Granite (2820 ± 38 Ma, Poujol, 2001), and
3. the Lekkersmaak leucogranite (2795 ± 8 Ma, Zeh et al., 2009).

A last episode of magmatic activity occurred around 2.7 Ga with the emplacement of the undeformed Mashishimale granite (2698 ± 21 Ma, Poujol, 2001; 2671 + 8 Ma, Zeh et al., 2009). The Duivelskloof leucogranite is thought to be Neoarchaean in age but to date no geochronology is available (Robb et al., 2006).

Structures

The MGB area is a narrow belt trending east-northeast, that is 10 to 15 km wide and 140 km long. Combined electrical sounding and gravity surveys suggest that the

depth of the greenstone-basement interface varies between 4.5 km or less, with a maximum of about 9 to 12 km in the middle of the belt (De Beer et al., 1984). Some authors invoked a northward younging for the sequences (Viljoen et al., 1978; Anhaeusser and Wilson, 1981). Northward younging is supported by geochronological arguments (Poujol, 2001). On the other hand, several authors have proposed that the overall structures define a syncline (van Eeden et al., 1939; Graham, 1974; Viljoen et al., 1978; Anhaeusser and Wilson, 1981). This hypothesis is supported by polarity indicators such as the chemical evolution of igneous rocks and deposits, cross-beddings, graded beddings, and erosion surfaces in sediments, that are mostly consistent with the series getting younger toward the centre of the belt (Vearncombe, 1988). However, the lithologies are not symmetrically distributed between the northern and southern sides (Pearton and Viljoen, 1986; Vearncombe, 1988).

Several authors have emphasized the pervasive and intense deformation of the MGB (Graham, 1974; Viljoen et al., 1978; Vearncombe, 1988). The main belt (Rubbervale Formation and Murchison schists) shows superposed fold structures (Graham, 1974; Maiden, 1984; Maiden and Boocock, 1987; Vearncombe, 1988; Vearncombe et al., 1988). The east-northeast trending folds are the best expressed, and are characterized by steep axial planes and shallowly plunging axes. They are reworked by folds with east-west trending axial planes and steeply plunging axes. In the horizontal plane, fold interferences lead to S geometries (Graham, 1974; Vearncombe et al., 1992). Conjugate late N30° and N160° kink-bands are locally reported in the Antimony Line (Vearncombe et al., 1988). Despite the heterogeneities in

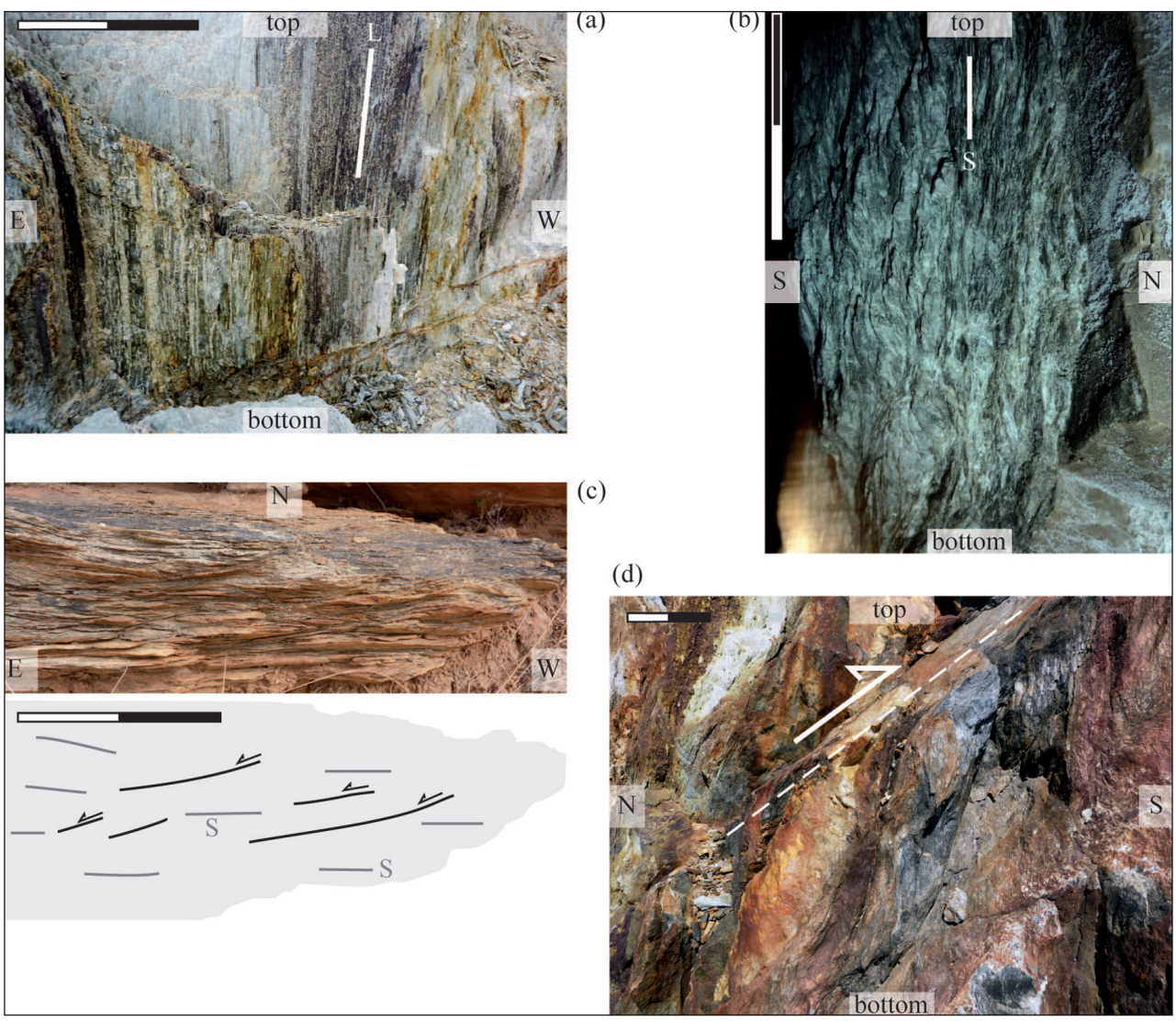

Figure 4. *Pictures of the main structures within the MGB. Scale bar is 10 cm. (**a**) greenschist showing a marked stretching lineation (noted "L", Malati Pump) (**b**) talc-chlorite schist with well-expressed foliation (noted "S", β-shaft, Antimony Line) (**c**) shear bands in a horizontal plan and associated sketch, showing an apparent sinistral shear (Murchison schist, Athens) (**d**) top-to-the-south-east reverse thrust (Cobra mine).*

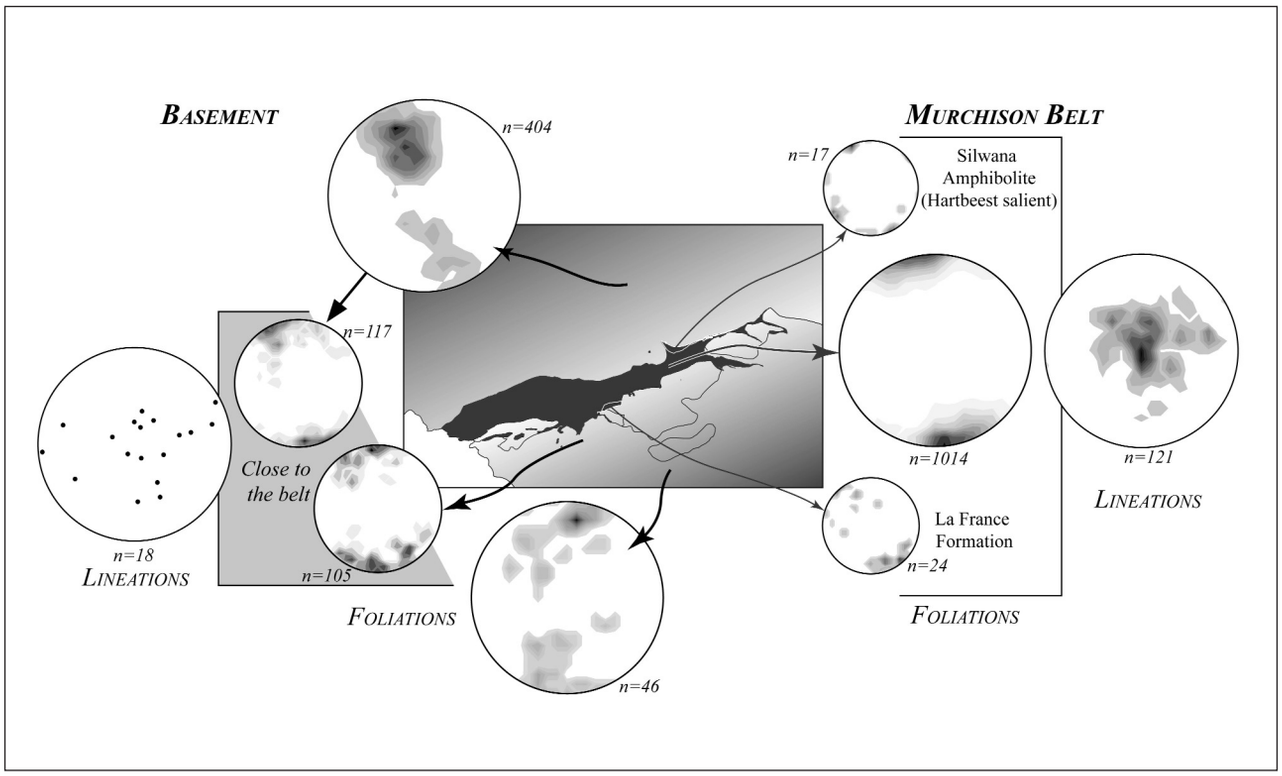

Figure 5. *Stereograms (equal area, lower hemisphere) showing density contours for the foliations poles and lineations. Data compiled from 1:50 000 maps of the Belt (Vearncombe et al., 1992), the 1:250 000 map of Tzaneen (Sheet 2330, 1985) and our own measurements. 1% σ error, except for the Silwana amphibolites and La France formation: 2% σ.*

the folded structures, Graham (1974) summarises the dominant regional fabrics of the belt as a strong sub-vertical foliation bearing a steeply plunging stretching lineation.

The Sb mineralisation is hosted in quartz-carbonate veins in the centre of the Murchison schists along the Antimony Line, and is clearly structurally controlled (Pearton and Viljoen, 1986; Maiden and Boocock, 1987; Vearncombe et al., 1988). Some authors have favoured left-lateral shear motion along the Antimony Line (Pearton and Viljoen, 1986), while others (Vearncombe et al., 1988) have favoured a reverse motion, with the northern units overriding the southern ones. Horizontal movement is also described for the Letaba Shear Zone (northeastern limit of the MGB), where gently plunging lineations are observed (Vearncombe, 1988).

Regional-scale structures

Figure 3 presents the foliation strikes in and outside the belt. The extent of this map emphasizes that the strains are distributed throughout the entire studied area. The map was drawn using fabric data available in Vearncombe et al. (1992) and in the 1:250 000 geological map of Tzaneen (Sheet 2330, 1985). Our own observations in different areas confirmed the relevance of the data used. Foliation trajectories are drawn where data were sufficiently numerous and consistent at the scale of the map. In other places, available data are reported only.

The Belt

The belt is marked by a strong sub-vertical foliation. There are few stretching lineations measured in the belt, but our own observations together with those from Vearncombe et al. (1992) highlight the fact that they are steeply plunging in most places (Figures 3, 4a, b and c, and 5). The east-northeasterly strike of the foliation planes is parallel to the trend of the belt (Figures 3 and 5). Generally, the trend of the foliation appears consistent throughout the different units, even within the Rooiwater Complex, although it is a less deformed (Vearncombe et al., 1987) and younger unit (Poujol et al., 1996). The contacts between the Rooiwater and surrounding units are deformed (Barton, 1984) and cross-cut by the regional fabric (Vearncombe et al., 1987).

Kinematic indicators are often poorly expressed, but the clearest and most frequent ones indicate top-to-the-south motions (Figure 4d). Along the Antimony Line, kinematic indicators point to a sinistral strike-slip component (Figure 4c). A component of sinistral strike-slip is supported by the foliation map, which suggests the occurrence of a discrete northeast-southwest trending sinistral shear band north of the Maranda granodiorite (Figure 3). This is also consistent with De Beer et al.'s interpretations (1984; also see the review in Vearncombe, 1988 and references therein), who suggested a potential sinistral relative motion within the belt.

Country-rocks around the MGB

To the south, available structural data (foliation and lineation) for the basement are scarce (Figure 3) but indicate an average foliation strike in an east to west direction (Figure 5). Stretching lineations are also scattered between steep to shallow plunges (Figure 5).

To the north, away from the belt, foliation patterns are complex. Foliations show variable dips and may even be shallowly dipping (Figure 5). Locally, these patterns suggest folded foliations. However, an unequivocal interpolation between the data cannot be made in several places. In contrast, toward the northern margin of the belt, the southern exposures of the northern gneisses unit show more regular patterns, where the trajectories are defined by sub-vertical foliations that are sub-parallel to the belt margin (Figure 5). For the poorly-outcropping Duivelskloof leucogranite, available fabric data are scarce (Robb et al., 2006).

Belt margins

On average, foliation trajectories trend east-northeast-west-southwest, sub-parallel to the belt boundaries, with consistent steep dips (Figures 3, 5 and 6a). Where the belt margin deviates from its regional east-northeast-west-southwest trend, foliation trajectories either cut across it or follow it. This is particularly the case in the Hartebeest Salient area (Figure 6b). Here, both the interface and foliation are sub-parallel along the contact and change progressively from northeast-southwest to north-northwest-south-southeast (Figures 3, 5 and 6b). In this area, lineation pitches are between 50° and 80° (Figure 6b). This particular area is discussed in more detail below.

Granitic intrusions

Several leucogranitic and granodioritic plutons occur both within the belt and in the surrounding Makhutswi gneisses. Pluton shapes are elongate at a low angle to the belt (Figures 2 and 3). In most places, fabrics are poorly expressed in the cores of the granites (Vearncombe et al., 1992).

The Baderoukwe and associated Sugam granitoids located in the northeastern part of the belt (Figure 3) have been studied in detail by Minnitt and Anhaeusser (1992). On the basis of the geometrical relationships

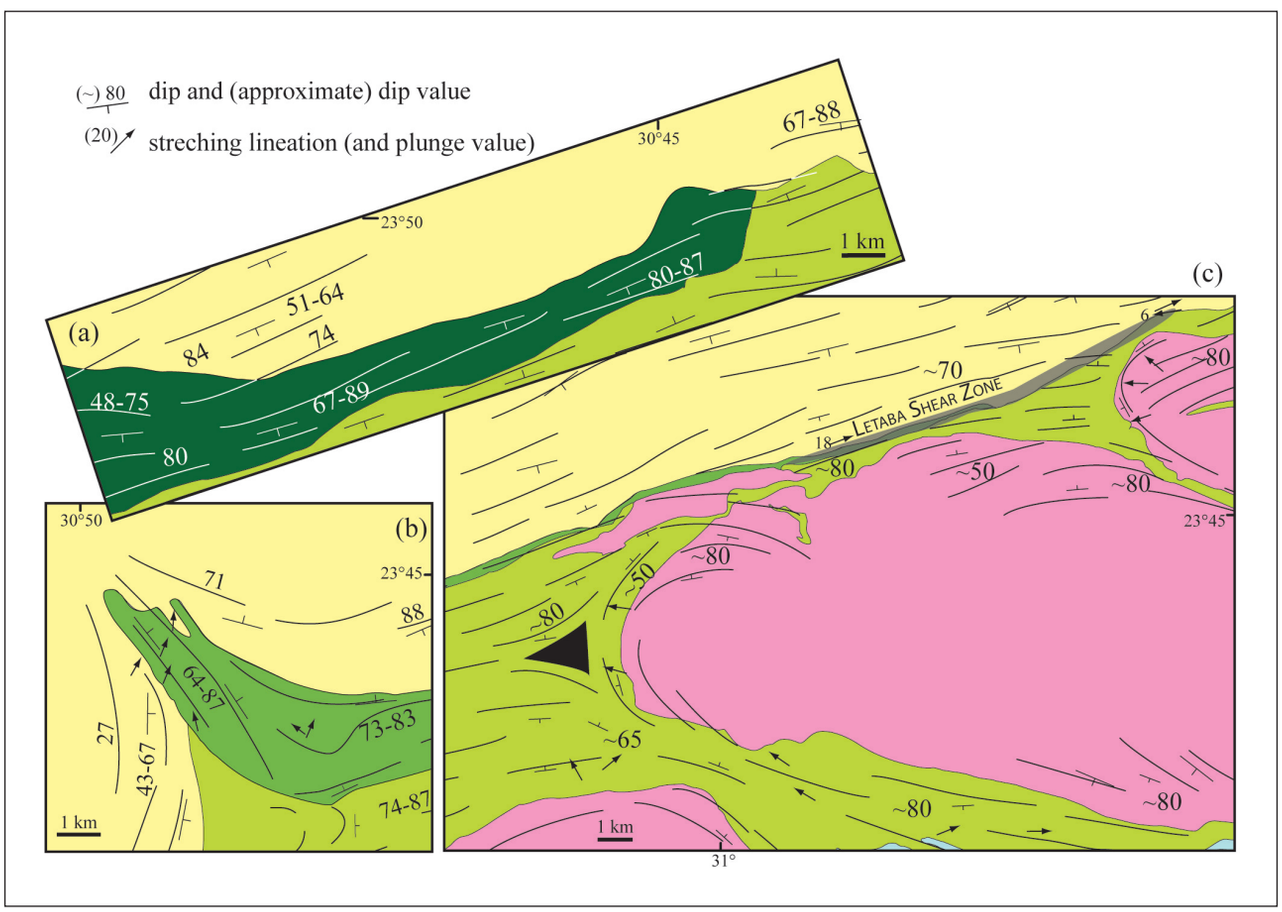

Figure 6. *Insets from Figure 3 describing the Murchison Belt/basement and Murchison Belt/pluton relationships: (**a**) the Hartbeest salient, other examples noted in Figure 3 (**b**) the northern contact, other examples noted † in Figure 3 (**c**) the Baderoukwe gneiss and arms of the belt (black triangle: triple point) For the figure legend, see Figure 3. After maps from Vearncombe et al. (1992), the 1:250 000 maps of Tzaneen (1985) and Pilgrim's Rest (1986), and for (c) see Minnitt and Anhaeusser (1992).*

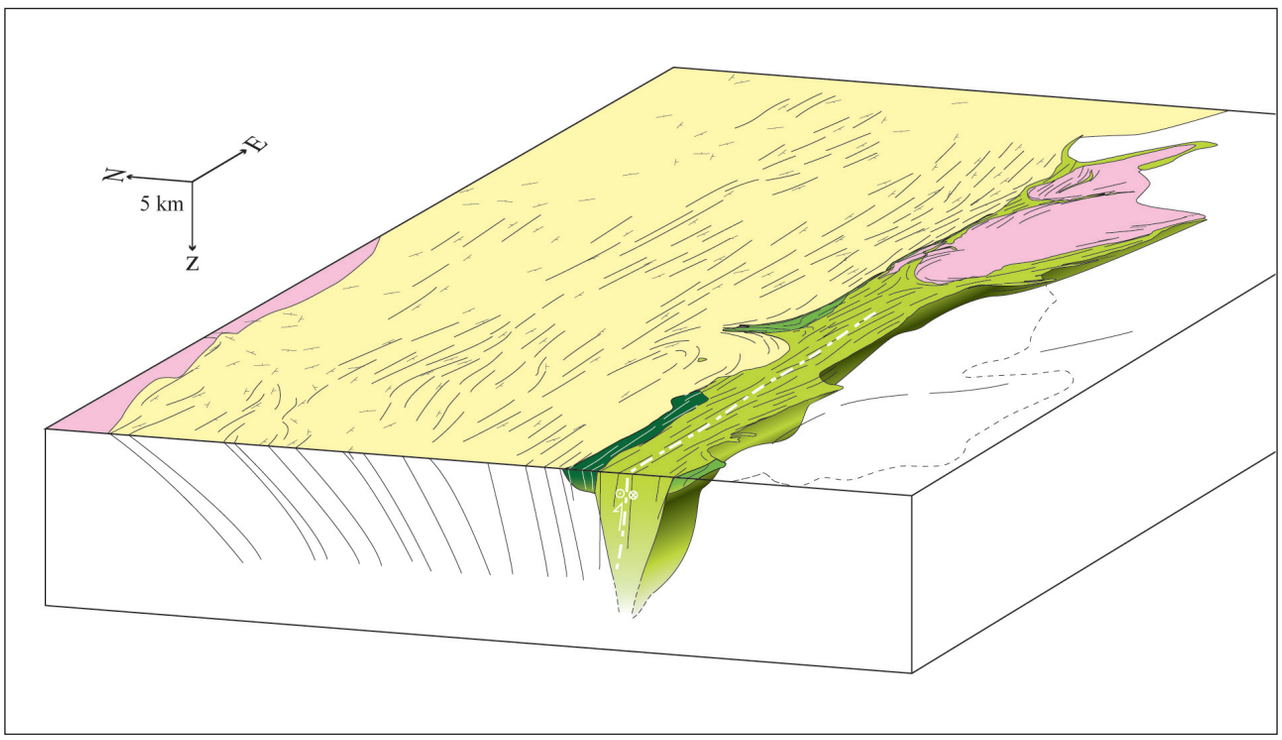

Figure 7. *3-D diagram of the eastern half of the MGB. The depths of the MGB-basement interface are from the gravity and geoelectrical studies from De Beer et al. (1984); no vertical exaggeration. The southern basement has been removed. For the location and figure legend, see Figure 3.*

between the granite margins and the foliations, they argued for a diapiric intrusion. Indeed, foliation trajectories wrap around the contact and locally cut across it (Figure 6c, Minnitt and Anhaeusser, 1992). Furthermore, the foliation tends to define triple points between the concentric fabrics at the contact and the regional ones away from the contact (Figure 6c). Such foliation triple points attest for interference between pluton ballooning and regional deformation (Brun and Pons, 1981; Brun, 1983; Ramsay, 1989).

Further to the south, poorly expressed S-C structures are locally observed along the edges of the muscovite-bearing Lekkersmaak leucogranite. S surfaces are parallel to the granite margin and the regional foliation (Figures 3 and 5). S-C fabrics indicate a progressive deformation starting at high temperature and continuing during subsequent cooling, typical of a syntectonic emplacement (Gapais, 1989).

Discussion

Overall geometry of the MGB

The most notable feature of the MGB is its very narrow and elongate shape. Geophysical data provide constraints on the 3-D geometry of the belt (De Beer et al., 1984). Its average depth is around 4.5 km, with a maximum depth reaching 9 to 12 km near Gravelotte, below the Antimony Line. Furthermore, the bottom of the belt appears to become shallower toward its eastern and western belt terminations. West of Gravelotte, lineations plunge steeply to the east (ca. 70° to 90°), whereas east of Gravelotte, they plunge steeply to the west (ca. 60° to 80°, Vearncombe et al., 1992). Thus, in good agreement with what is described for the belt floor, the finite stretch converges toward a central point at about 9 to 12 km below Gravelotte. Overall, the belt shape mimics that of a pinched keel (Figure 7). The occurrence of steep overturned fold geometries within the belt (Graham, 1974; Vearncombe, 1988), as well as the asymmetric lithological pattern, show that the overall system is asymmetric. Some kinematic indicators showing non-coaxial deformations with overall top-to-the-south motions are consistent with an asymmetric geometry.

On the map, from southwest to northeast, the Rubbervale Formation and the Rooiwater Complex become thinner in the central part of the belt (Figure 3). Vearncombe et al. (1992) observed that this was accompanied by an increase in fabric intensity. This strongly suggests that the shape of the units within the belt may reflect some strain gradients from the southwest belt termination to the belt centre. If so, there would be a correlation between belt depth, belt width, and strain intensity.

Progressive fabric development in the MGB

Where present, kinematic indicators associated with the regional foliation indicate top-to-the-southeast motions. Two areas seem to show different kinematics, namely the Antimony Line and the Letaba Shear Zone. In the Antimony Line, kinematic indicators attest for

components of sinistral strike slip (Figure 4c). However, the stretching lineation is mostly steeply plunging along the Line, as observed in most parts of the belt (Figure 5). This, combined with the limited length of the Line (less than 50 km, Figure 3), thus suggest that horizontal motions remained limited. According to the recent synthesis of Clark and Cox (1996) on relationships between fault length and displacement, horizontal displacements along the Antimony Line might not have exceeded 5 km. In the Letaba Shear Zone, gently plunging lineations do occur in mylonites (Figure 6c) and are associated with sinistral wrenching (Vearncombe, 1987; 1988). Following Clark and Cox (1996), horizontal displacement should have been in the order of 2 km for this 20 to 30 km long shear zone.

The Antimony Line and Letaba Shear Zone are therefore two exceptions when compared to the regional fabrics. They also appear as to have recorded rather late deformations. Indeed, kink-bands, veins and tension gashes cutting across the foliation occur in the Antimony Line (Vearncombe et al., 1988), and pseudotachylites have been reported along the Letaba Shear Zone (Fripp et al., 1980). All these features indicate deformations in upper crustal conditions.

We therefore infer that the deformation history of the rocks from the MGB was marked by distributed horizontal shortening under ductile conditions associated with top-to-the-south-east motions in a transpressive context, followed by strain localization along discrete zones where components of sinistral strike slip have concentrated during the retrograde history of the belt. The Antimony Line and Letaba Shear Zone suggest that strain was localised along zones with preferential fluid transfers or along the basement-belt contacts.

Tectonic implications

The first-order structural features of the MGB are the sub-vertical attitude of both foliations and stretching lineations, rather pervasive and distributed strains, and the strong narrowness of the belt surrounded by rather homogeneous granitoid basement units. Some intrusions affected by the regional fabric cut across both the basement and the belt (e.g. Maranda granodiorite, Figure 3), and consistent fabrics are observed across the basement and the belt (e.g. northern belt boundary, Figure 3). Furthermore, to the north of the belt, there is a progressive southward increase in dip and ordering of the foliation, which suggests some strain gradient in the basement toward the margin of the belt. Within the belt, the different domains show the same dominant fabrics (Figure 3). These features imply that the different domains in and around the belt experienced the same north-northwest-south-southeast horizontal shortening and steeply dipping principal stretching. Thus the belt appears as a zone where different domains were juxtaposed in a convergence context (Vearncombe, 1988) and then squeezed together during ongoing shortening and granite emplacement. In such a model, domains may have different pre-shortening stratigraphic, geochronological, metamorphic, or even tectonic signatures.

The belt basically consists of sedimentary and volcanic metamorphosed rocks and therefore appears as an upper crustal complex buried down within the underlying basement. Overlaps exist between the geochronological zircon ages reported for the belt and its surrounding units (see review in Poujol et al., 2003). This supports the interpretation of a thermally active and deforming crust throughout both the belt and its surroundings. It further suggests a weak crust, where upper crustal rocks may have sunk within underlying weak materials during horizontal shortening. In addition, there is evidence for outcropping contemporaneous felsic metavolcanites and granitoids emplaced during two different periods (Weigel Formation and Harmony granite at ~3.09 Ga, Rubbervale Formation and Baderoukwe granodiorite at ~2.97 Ga, see Poujol et al., 2003). The fact that contemporaneous volcanics and deeper granitic intrusions are now observed at the same structural level also supports our interpretation of a vertical burial of the upper crust.

The structure observed in the Hartebeest salient, at a high angle with the overall belt shortening (Figure 6b), is difficult to interpret in terms of the northwest-southeast shortening. Constrictional strains are reported in the area (Vearncombe, 1988), and Vearncombe et al. (1992) tentatively interpreted its striking geometry as that of a frontal ramp structure. In our view, a more simple interpretation is that the area reflects local effects of relative vertical motions between sediments sinking within possibly buoyant country rocks. Constrictional strains would be consistent with combinations of regional shortening and oblique vertical motions.

From the features above, we infer that regional deformations observed in the MGB support models that involve sagduction of supra-crustal rocks within the underlying crust (Bouhallier et al., 1995; Choukroune et al., 1995; Chardon et al., 1996; Cagnard et al., 2006; Cagnard et al., 2007; Chardon et al., 2009; Gapais et al., 2009). In such models that imply a weak and hot crust, deformations are marked by pop-downs of supra-crustal rocks in a crust undergoing overall distributed horizontal shortening. In the original sagduction models, the first-order driving force was gravity, with heavy greenstone mafic volcanics overlying a light gneissic basement (Choukroune et al., 1995). The bulk density contrast between the MGB and its surrounding gneisses is actually rather low, in the order of 1.07 (De Beer et al., 1984). However, recent experimental studies have demonstrated that the sinking of the upper crust within an underlying weak material is not gravity driven, but only requires a horizontal shortening of the crust (Cagnard et al., 2006). Recently, evidence of sagduction has consistently been reported in greenstone lacking Palaeoproterozoic orogens (see the review of Chardon et al., 2009).

One leucogranitic body, the Lekkersmaak granite, occurs at the southern contact between the belt and the basement (Figure 3). Two-mica granites generally result from partial melting of juvenile sediments (e.g. Zen, 1988; Clemens, 2003). A preliminary Nd isotopic analysis, that yielded model ages (DePaolo, 1981) of 2.83 to 3.01 Ga and εNd(T) values ranging from -1 to 0, support this interpretation for the Lekkersmaak granite (Jaguin et al., 2010). Thus, it can be inferred that the partial melting of buried sediments of the belt at depth is the best candidate for the formation of this leucogranite. Owing to the 9 to 12 km maximum belt depth, our interpretation would be consistent with a rather high thermal gradient, although the burial depth of the presently outcropping rocks is still very poorly constrained.

Time and duration of the deformation

The Lekkersmaak leucogranite was emplaced during late deformation stages at ~2.77 Ga, much later than the emplacement of the granodiorite intrusions at ~2.97 Ga that look somewhat more deformed on the map (Baderoukwe intrusions, Figure 3). These emplacement ages point to a long-lasting deformation history for the MGB. Recently, it has consistently been underlined that contrary to localised deformations, distributed deformations, such as those typical of the weak orogens, imply low local strain rates (Chardon et al., 2009; Gapais et al., 2009). The combination of large strains, as suggested by the structures in the MGB, with low strain rates, would imply a long deformation history.

The Rooiwater Complex provided younger ages: a discordant zircon age at ~2.74 Ga interpreted as a minimum age (Poujol et al., 1996), and a concordant age at ~2.6 Ga (Zeh et al., 2009), for two different lithologies (tonalite and gabbro, respectively). According to the structural data, this Complex seems to be deformed together with the belt, but shows less developed fabrics than other parts in the belt (Vearncombe et al., 1987). Thus, the Rooiwater Complex might have been emplaced in its present position rather late in the deformation history of the belt. However, Zeh et al. (2009) emphasized that the emplacement history of the Rooiwater Complex might have been complex, a feature that has been underlined by the two different ages available so far. This highlights that the maximum duration for the deformation in the MGB remains poorly constrained.

Links with the other belts in the area: Giyani Greenstone Belt, Pietersburg Greenstone Belt, Limpopo Belt

The Giyani and Pietersburg Greenstone Belts (GGB, PGB, respectively) are spatially close the MGB (Figure 1). These belts share the same orientation, and isotopic and geochemical data proved that they belong to a single terrane (Kreissig et al., 2000). Structural studies reported some comparable map-scale geometries and orientations between the three belts, pointing to a northwest-southeast shortening (Figure 1, for GGB: Mc Court and van Reenen, 1992; for PGB: de Wit et al., 1992b). Furthermore, several observations made in the different belts suggest striking analogies with those from the MGB. Thus, the belts are dominated by intense northeast-southeast to east-west sub-vertical or steeply dipping fabrics with some steeply plunging lineations (D2 of the PGB, de Wit et al., 1992b; also D2 of the GGB, de Wit et al., 1992c; Mc Court and van Reenen, 1992). The latter authors even evoked some vertical sheath-like folds on the northern border of the belt.

Intense vertical finite stretching has been reported in the northern part of the Limpopo Belt (Roering et al., 1992; Blenkinsop and Kisters, 2005). The exhumed granulitic crust of the northern Limpopo Belt was interpreted by Blenkinsop and Kisters (2005) as reflecting vertical extrusion.

From these structural analogies, the question arises whether or not the deformation processes that occurred in the Greenstone Belts in the northeastern part of the Kaapvaal craton should be reappraised in the light of the shortening modes that prevailed in hot continental lithospheres.

Conclusions

- Structures of the Murchison Greenstone Belt are marked by northwest-southeast horizontal shortening leading to distributed sub-vertical foliations and steeply plunging stretching lineations.
- Available structural and geophysical data indicate that the belt has an overall keel geometry, with a maximum depth of 9 to 12 km.
- The tectonic style of the Murchison Greenstone Belt is consistent with sagduction models of supracrustal rocks within a hot lithosphere (see Chardon et al., 2009).
- The main granitoid intrusions along the belt appear to be syn- to late-tectonic.
- Leucogranite intrusions are tentatively interpreted as the result of the melting of sediments buried during sagduction.
- Available ages on the intrusions suggest a long-lasting tectonic history.
- Structures of other belts in the region, such as the Limpopo Belt, the Pietersburg or Giyani Greenstone Belts should perhaps be reappraised in the light of models of compression of hot lithospheres.

Acknowledgements

Julian Vearncombe and Marteen de Wit are acknowledged for their helpful and constructive reviews of the manuscript. The authors thank S. Block for constructive discussions during field work. This work was funded by the CNRS-INSU "Action incitative". J.J. was supported by a PhD grant from the French Research Ministry and obtained funding from the Region of Bretagne to attend the 5th IAS. We also thank Richard W. Allmendinger and collaborators for providing the Stereonet software free of charge.

References

Anhaeusser, C.R. and Wilson, J.F., 1981. The granitic-gneiss greenstone shield: South Africa. In: D.R. Hunter (Editor), Precambrian of the Southern Hemisphere, 423–453.

Anhaeusser, C.R., 2006. A reevaluation of Archean intracratonic terrane boundaries on the Kaapvaal Craton, South Africa: Collisional suture zones? In: W.U. Reimold and R.L. Gibson (Editors.), Processes on the Early Earth, Geological society of America, Special Paper, 405, 193–210.

Barton, J.M., 1984. Timing of ore emplacement and deformation, Murchison and Sutherland Greenstone Belts, Kaapvaal craton. In: R. Foster (Editor), Gold 82: the geology, geochemistry and genesis of gold deposits, A.A. Balkema, Rotterdam, 629–644.

Block, S. and Moyen, J.-F., 2011. The Murchison greenstone belt, South Africa: Accreted silvers with contrasting metamorphic conditions. Abstract, 23rd Colloquium of African Geology, University of Johannesburg and Council for Geosciences, South Africa, 52p.

Blenkinsop, T. and Kisters, A., 2005. Steep extrusion of late Archaean granulites in the Northern Marginal Zone, Zimbabwe: evidence for secular change in orogenic style. In: D. Gapais, J.-P. Brun and P.R. Cobbold (Editors), Deformation Mechanisms, Rheology and Tectonics: from Mineral to the Lithosphere, Geological society, London, Special Publication, 243, 193–204.

Bouhallier, H., Chardon, D. and Choukroune, P., 1995. Strain patterns in Archaean dome-and-basin structures: The Dharwar craton (Kamataka, South India). Earth and Planetary Science Letters, 132, 57–75.

Brandl, G., Cloete, M. and Ahnaeusser, C.R., 2006. Archean Greenstones Belts. In: M.R. Johnson, C.R. Anhaeusser and R.J. Thomas (Editors), The Geology of South Africa, Geological Society of South Africa/Council for Geoscience, South Africa, 9–56.

Brandl, G., Jaeckel, P. and Kröner, A., 1996. Single zircon age for the felsic Rubbervale Formation, Murchison greenstone belt, South Africa. South African Journal Geology, 99, 229–234.

Brandl, G. and Kröner, A., 1993. Preliminary results of single zircon studies from various Archaean rocks of the Northeastern Transvaal. In: Extented. Abstract. 16th International Colloquium of African Geology, Mbabane, Swaziland, 54–56.

Brun, J.-P., 1983. Isotropic points and lines in strain fields. Journal of Structural Geology, 5, 321–327.

Brun, J.-P. and Pons, J., 1981. Strain patterns of pluton emplacement in a crust undergoing non-coaxial deformation, Sierra Morena, Southern Spain. Journal of Structural Geology, 3, 219–229.

Cagnard, F., Brun, J.-P. and Gapais, D., 2006. Modes of thickening of analogue weak lithospheres. Tectonophysics, 421, 145–160.

Cagnard, F., Gapais, D. and Barbey, P., 2007. Collision tectonics involving juvenile crust: The example of the southern Finnish Svecofennides. Precambrian Research, 154, 125–141.

Chardon, D., Choukroune, P. and Jayananda, M., 1996. Strain patterns, décollement and incipient sagducted greenstone terrains in the Archaean Dharwar craton (south India). Journal of Structural Geology, 18, 991–1004.

Chardon, D., Gapais, D. and Cagnard, F., 2009. Flow of ultra-hot orogens: A view from the Precambrian, clues for the Phanerozoic. Tectonophysics, 477, 105–118.

Choukroune, P., Bouhailler, H. and Arndt, N.T., 1995. Soft lithosphere during periods of Archean crustal growth or crustal reworking. In: Coward, M.P., Ries, A.C. (Editors), Early Precambrian Processes. Geological Society, Special Publication, 95, 67–86.

Choukroune, P., Ludden, J.N., Chardon, D., Calvert, A. J. and Bouhallier, H., 1997. Archean crustal growth and tectonic processes: a comparison of the Superior province, Canada and the Dhawar Craton, India. In: J.-P. Burg and M. Ford (Editors). Orogeny Through Time, Geological Society, Special Publication, 121, 63–98.

Clark, R.M. and Cox, S.J.D., 1996. A modern regression approach to determining fault displacement-length scaling relationships; Journal of Structural Geology, 18, 147–152.

Clemens, J.D., 2003. S-type granitic magmas - petrogenetic issues, models and evidence, Earth Science Reviews, 61, 1–18.

De Beer, J.H., Stettler, E.H., Duvenhage, A.W.A., Joubert, S.J. and De Raath, C.J., 1984. Gravity and geoelectrical studies of the Murchison greenstone belt, South Africa. South African Journal of Geology, 87, 347–359.

DePaolo, J.D., 1981. Trace element and isotopic effects of combined wallrock assimilation and fractional crystallization. Earth and Planetary Science Letters, 53, 189–202

de Wit, M.J., de Ronde, C.E.J., Tredoux, M., Roering, C., Hart, R.J., Armstrong, R.A., Green, R.W.E., Peberdy, E. and Hart, R.A., 1992a. Formation of an Archaean continent. Nature, 357, 553–562.

de Wit, M.J, Jones, M.J. and Buchanan, D.L, 1992b. The geology and tectonic evolution of the Pietersburg Greenstone Belt, South Africa. Precambrian Research, 55, 123–153.

de Wit, M.J., van Reenen, D. and Roering, C., 1992c. Geologic observations across tectono-metamorphic boundary in the Babangu area, Giyani (Sutherland) Greenstone belt, South Africa. Precambrian Research, 55, 111–122.

Fripp, R.E.P., van Nierop, D.A., Callow, M.J., Lilly, P.A., and du Plessis, L.U., 1980. Deformation in part of the Archean Kaapvaal Craton, South Africa. Precambrian Research, 13, 241–251.

Gapais, D., 1989. Shear structures within deformed granites: Mechanical and thermal indicators. Geology, 17, 1144–1147.

Gapais, D., Cagnard, F., Gueydan, F., Barbey, P. and Ballèvre, M., 2009. Mountain building and exhumation processes through time: inferences from nature and models. Terra Nova, 21, 188–194.

Geological Survey of South Africa, 1985. Map of Tzaneen (n° 2330), 1/250 000 edition.

Geological Survey of South Africa, 1986. Pilgrim's Rest (n° 2430), 1/250 000 edition.

Good, N. and de Wit, M., 1997. The Thabazimbi-Murchison Lineament of the Kaapvaal Craton, South Africa: 2700 Ma of episodic deformation. Journal of the Geological Society, 154, 93–97.

Graham, R.H., 1974. A structural investigation of the southern part of the Limpopo belt and the adjacent Kaapvaal Craton, South Africa. In: 18th Annual Report of the Research Institute of African Geology, University of Leeds, U.K., 63–69.

Hamilton, W.B., 1998. Archean magmatism and deformation were not products of plate tectonics. Precambrian Research, 91, 143–179.

Henderson, D.R., Long, L.E., Barton, J.M., 2000. Isotopic ages and chemical and isotopic compositions of the Archaean Turfloop batholith, Pietersburg granite–greenstone terrane, Kaapvaal Craton, South Africa. South African Journal of Geology, 103, 38–46.

Jaguin, J., Moyen, J.-F., Boulvais, P. and Poujol, M., 2010. Mid-Archean granites south of the Murchison Greenstone Belt, South Africa: the oldest large biotite-muscovite leucogranite bodies. Abstract. In: I.M. Tyler and Knox Robinson (Editors), Abstract, Fifth International Archean Symposium, Geological Survey of Western Australia, Perth, Australia, 78pp.

Kramers, J.D., McCourt, S. and van Reenen, D.D., 2006. The Limpopo Belt. In: M.R. Johnson, C.R. Anhaeusser and R.J. Thomas (Editors), The geology of South Africa, Geological Society of South Africa and council for Geoscience, 209–236.

Kröner, A., Jaeckel, P. and Brandl, G., 2000. Single zircon ages for felsic to intermediate rocks from the Pietersburg and Giyani greenstone belts and bordering granitoid orthogneisses, northern Kaapvaal Craton, South Africa. Journal of African Earth Sciences, 30, 773–793.

Kreissig, K., Nägler, T.F., Kramers J.D., van Reenen D., Smit, A., 2000. An isotopic and geochemical study of the northern Kaapvaal Craton and the Southern Marginal Zone of the Limpopo Belt: are they juxtaposed terranes? Lithos, 50, 1–25.

Maiden, K.J., 1984. Metamorphic features of the Maranda J Copper-Zinc deposit, Murchison Greenstone Belt, Transvaal. Transaction to the Geological Society of South Africa, 87, 335–345.

Marshak, S., 1999. Deformation style way back when: thoughts on the contrasts between Archean/Paleoproterozoic and contemporary orogens. Journal of Structural Geology, 21, 1175–1182.

McCourt, S., 1995. The crustal architecture of the Kaapvaal between 3.5 and 2.0 Ga. Mineralium Deposita, 30, 89–97.

McCourt, S and van Reenen, D.D., 1992. Structural geology and tectonic setting of the Sutherland Greenstones Belt, Kaapvaal Craton, South Africa. Precambrian Research, 55, 93–110.

Minnitt, R.C.A. and Anhaeusser, C.R., 1992. Gravitational and diapiric structural history of the eastern portion of the Archean Murchison greenstone belt, South Africa. Journal of African Earth Sciences, 15, 429–440.

Pearton, T.N. and Viljoen, M.J., 1986. Antimony mineralization in the Murchison Greenstone Belt – An overview. In: C. R. Anhaeusser and S. Maske (Editors), Mineral Deposits of Southern Africa, Geological Society of South Africa, 293–320.

Poujol, M., 1997. Etude U-Pb et Pb-Pb de la Murchison Greenstone Belt et du bassin aurifère d'Evander, Afrique du Sud : implications pour l'évolution du Kaapvaal Craton. Ph.D. thesis (unpublished), University of Montpellier II, France, 247p.

Poujol, M., 2001. U-Pb isotopic evidence for episodic granitoid emplacement in the Murchison greenstone belt, South Africa. Journal of African Earth Sciences, 33, 155–163.

Poujol, M., 2007. An overview of the pre-mesoarchean rocks of the Kaapvaal Craton, South Africa. In: M. Van Kranendonk, R.H. Smithies and V.C. Bennett (Editors), Developments in Precambrian Geology: Earth s Oldest Rocks, 15, 453–463.

Poujol, M., Robb, L.J., Anhaeusser, C.R. and Gericke, B., 2003. A review of the geochronological constraints on the evolution of the Kaapvaal Craton, South Africa. Precambrian Research, 127, 181–213.

Poujol, M. and Robb, L.J., 1999. New U-Pb zircon ages on gneisses and pegmatites from south of the Murchison Greenstone belt, South Africa. South African Journal of Geology, 102, 93–97.

Poujol, M., Robb, L.J., Respaut, J.-P. and Anhaeusser, C. R., 1996. 3.07-2.97 Ga Greenstone Belt formation in the northeastern Kaapvaal Craton: implication for the origin of the Witwatersrand Basin. Economic Geology, 91, 1455–1461.

Ramsay, J.G., 1989. Emplacement kinematics of a granite diaper: the Chindamora batholith, Zimbabwe. Journal of structural Geology, 11, 191–210.

Robb, L.J., Brandl, G., Anhaeusser, C.R., and Poujol, M., 2006. Archaean granitoid intrusions. In: M.R. Johnson, C.R. Anhaeusser and R.J. Thomas (Editors), The geology of South Africa, Geological Society of South Africa/Council for Geoscience, South Africa, 57–94.

Roering, C., van Reenen, D.D., Smit, C.A., Barton Jr, J.M., de Beer, J.H., de Wit, M.J., Stettler, J.F., van Schalkwyk, J.F., Stevens, G. and Pretorius, S., 1992. Tectonic model for the evolution of the Limpopo Belt. Precambrian Research, 55, 539–552.

South African Committee for Stratigraphy, 1980. Chapter 2.3: The Murchison Sequence, In: Stratigraphy of South Africa, part 1: Lithostratigraphy of the Republic of South Africa, South West Africa/Namibia and the Republics of Bophuthatswana, Transkei and Venda. South Africa Geological Survey Handbook, 8, 45–52.

Schwarz-Schampera, U., Terblanche, H. and Oberthür, T., 2010. Volcanic-hosted massive sulfide deposits in the Murchison greenstone belt, South Africa. Mineralium Deposita, 45, 113–145.

van Eeden, O.R., Partridge, F.C., Kent, L.R. and Brandt, J.W., 1939. The mineral deposits of the Murchison Range east of Leydsdorp. Memoir of the Geological Survey of South Africa, 36, 172p.

Vearncombe, J.R., 1988. Structure and metamorphism of the Archean Murchison Belt, Kaapvaal Craton, South Africa. Tectonics, 7, 761–774.

Vearncombe, J.R., 1991. A possible Archaean Island Arc in the Murchison Belt, Kaapvaal Craton, South Africa. Journal of African Earth Sciences, 13, 299–304.

Vearncombe, J.R., Barton, J. M., Cheshire, P.E., De Beer, J.H., Stettler, E.H., and Brandl, G., 1992. Geology, geophysics and mineralization of the Murchison Schist Belt, Rooiwater Complex and surrounding granitoids, Memoir of the Geological Survey of South Africa, 81, 139p.

Vearncombe, J.R., Barton, J.M. and Walsh, K.L., 1987. The Rooiwater Complex and associated rocks, Murchison granitoid-greenstone terrane, Kaapvaal Craton. South African Journal of Geology, 90, 361–377.

Vearncombe, J.R., Cheshire, P.E., De Beer, J.H., Killick, A.M., Mallinson, W.S., McCourt, S. and Stettler, E.H., 1988. Structures related to the Antimony line, Murchison schist belt, Kaapvaal craton, South Africa. Tectonophysics, 154, 285–308.

Viljoen, M.J., van Vuuren, C.J.J., Pearton, T.N., Minnitt, R.C.A., Muff, R. and Cillier, P., 1978. The regional geological setting of the mineralization in the Murchison Range with particular reference to Antimony. Geological Society of South Africa, Special Publication, 4, 55–76.

Windley, B.F., 1992. Uniformitarism today: plate tectonics is the key to the past. Journal of the Geological Society, 150, 7–19.

Zeh, A., Gerdes, A. and Barton, J.M., Jr., 2009. Archean Accretion and Crustal Evolution of the Kalahari Craton - the Zircon Age and Hf Isotope Record of Granitic Rocks from Barberton/Swaziland to the Francistown Arc. Journal of Petrology, 50, 933–966.

Zen, E. (1988). Phase relations of peraluminous granitic rocks and their petrogenetic implications, Annual Review of Earth and Planetary Sciences, 16, 21–51.

Editorial handling : L.D. Ashwal

On notera que le complexe du Rooiwater, d'après cette étude, est déformé en cohérence avec la ceinture même si ses roches n'expriment que peu de fabrique. Ceci concorde bien avec son âge précoce et sa participation à l'amalgamation des terrains (reévalués dans l'article #1). La compétence des roches du complexe (gabbros, amphibolites, granites) suffit à expliquer sa faible déformation.

LES APPORTS DU METAMOPRPHISME. Dès 1939, van Eeden et al. reconnaissent l'existence d'unités de degrés métamorphiques différents à l'intérieur même de la ceinture de roches vertes de Murchison. L'article #1 a montré que le Rooiwater n'est pas un socle pour la ceinture puisqu'il est contemporain de la mise en place de la Formation de Rubbervale. À ce titre, le contact entre les deux, en faciès différent, ne peut qu'être tectonique (faille, cisaillement). Pour les mêmes raisons, c'est aussi le cas du contact entre la Formation de La France et les schistes de Murchison. L'étude de Block et al. (2012, en annexe) quantifie ces constrastes métamorphiques.

Article en annexe "The Murchison Greenstone Belt, South Africa: accreted slivers with contrasting metamorphic conditions"

Schistes verts. La zone centrale des schistes de Murchison (appellation de Vearncombe 1988, équivalent de l'ensemble Weigel-Leysdorp-Mulati-MacKop) atteind un faciès schiste vert à amphibolite inférieur dans des conditions Pression-Température maximales de 5.6 ± 0.6 kbar et 570°C pour un échantillon vers le sud, tandis qu'un échantillon dans le prolongement de l'Antimony Line atteint 1.3–2.8 kbar à 340–370°C. La formation de Rubbervale est en facies schiste vert.

Amphibolites. Trois unités séparées sont en facies amphibolitique. La formation de La France (schistes alumineux, pic à 8–9 kbar, 600–650°C), pour laquelle deux âges sont reportés, séparés de 160 Ma : le premier ca 2.92 Ga serait un âge minimum et le second, vers 2.74 Ga, pourrait marquer une réactivation. L'unité de Silwana montre un pic à 8.7–10 kbar et 630–670°C. Enfin, le complexe du Rooiwater, intrusion mafique et felsique, contient des paragénèses à grenat-hornblende-plagioclase et des petites zones de cisaillements retromorphosées en schiste vert.

Synthèse

La ceinture de Murchison semble illustrer le paradoxe thermique archéen : les déformations distribuées, potentiellement sagdutantes, sont cohérentes avec une croûte chaude alors que le métamorphisme témoigne d'un gradient comparable aux zones orogéniques phanérozoïques. Plus précisément, on peut relever un point d'incohérence entre les deux études : tandis que la première argumente pour une déformation distribuée responsable des fabriques homogènes entre unités, la seconde met en évidence la juxtaposition d'unités métamorphiques distinctes, ce qui implique des mouvements verticaux relatifs localisés. Deux hypothèses émergent :

- Soit ces deux phénomènes sont synchrones : la juxtaposition tectono-métamorphique accomode le raccourcissement crustal de façon localisée à

l'intérieur la ceinture et en bordure quand en parallèle le développement d'une fabrique subverticale accomode le raccourcissement de façon distribuée à l'échelle régionale.

- Soit ces deux phénomènes sont diachrones : la déformation distribuée précède la déformation localisée. Il faut alors accoler des unités présentant exactement la même fabrique pour avoir des fabriques homogènes entre les unités tectoniques : ceci parait moins probable. La déformation distribuée est donc vraisemblablement synchrone ou postérieure à la juxtaposition des unités.

Les datations montrent que les mises en place des roches des différentes unités sont synchrones vers 2.97 Ga (magma du complexe de Rooiwater 2965 ± 6, volcanites de la Rubbervale) ou du moins contemporaines (sédiments de La France Formation et de MacKop/Mulati, article #1 et références incluses). Donc l'âge du métamorphisme est postérieur à 2.97 Ga. En outre, un dyke du pluton de Baderoukwe recoupe les amphibolites de Silwana, les schistes de Murchison et est folié dans leur contact cisaillé (2964 ± 5 Ma, Block et al. 2012). Cela permet de suggérer que la juxtaposition des unités de Silwana et de Murchison, et a fortiori le métamorphisme schiste vert et amphibolitique, se déroulent avant 2964 ± 5 Ma dans la partie nord. Enfin, si l'on considère que les amphibolites de Silwana et le complexe du Rooiwater sont génétiquement corrélés (hypothèse de Vearncombe et al. 1992), alors l'ensemble du métamorphisme au nord se déroule entre 2965 ± 6 Ma et 2964 ± 5 Ma. Autrement dit, ces formations sont synchrones dans l'erreur des âges.

Au sud l'âge minimal du pic métamorphique est fournit par une monazite au sein d'un dysthène à 2923 ± 11 Ma, tandis que la majorité des âges sont à 2754 ± 11 Ma et difficiles à interpréter. Enfin, le pluton de Baderoukwe, daté à 2965 ± 6 Ma (voir article #3), est synchrone de la déformation distribuée.

Ainsi, l'accrétion des blocs sud et nord est contemporaine du métamorphisme amphibolitique des unités Rooiwater et Silwana (article #1), ce qui soutient l'hypothèse d'une subduction à vergence nord. Cette accrétion et son raccourcissement horizontal sont accomodés par la déformation localisante de la juxtaposition des unités métamorphiques différentes. Par ailleurs, ce raccourcissement crustal est aussi accomodé par une déformation distribuée qui débute contemporainement ou rapidement après la juxtaposition métamorphique vers 2.97 Ga, peut-être le signe d'une étape de vraie collision. La déformation distribuée se prolonge ensuite (article #2 ; voir aussi chapitre 6 article #4 et Conclusions chapitre 9-A). Enfin, il faut noter que l'Antimony Line n'est pas une zone de déformation ou de saut métamorphique majeur : cet aspect sera détaillé dans l'article #4.

Chapitre 3 — Histoire géologique du craton du Kaapvaal

Les grands événements qui affectent le craton du Kaapvaal sont susceptibles d'être enregistrés dans la ceinture. À l'inverse, ce travail et en particulier les données géochronologiques et pétrogénétiques, contribue à préciser l'histoire du craton, par exemple l'interaction entre la ceinture de roches vertes de Murchison et le bassin du Witwatersrand dans l'article #1. Ceci sera discuté dans les différents articles et synthétisé dans la discussion au chapitre 9. Ce chapitre propose donc un cadre général de l'histoire géologique du craton du Kaapvaal.

En premier lieu ce chapitre s'intéresse à la construction du "proto"-craton par l'intermédiaire de l'histoire de ses terrains à granitoïdes et ceintures de roches vertes, entre 3.6 et 3.0 Ga, la ceinture de Murchison n'étant qu'une des nombreuses ceintures du craton du Kaapvaal; ensuite les dépôts volcano-sédimentaires du centre du craton et la ceinture du Limpopo font l'objet d'une revue succincte. Enfin nous présenterons brièvement les évènements tardifs majeurs perturbants le craton. En l'absence d'indications contraires, les informations et références associées sont tirées du livre Geology of South Africa (Geological Society of South Africa 2006), en particulier des chapitres 2 pour les ceintures de roches vertes (Brandl et al. 2006) et 3 pour les granitoïdes (Robb et al. 2006).

A — Cadre général

L'enregistrement géologique dans le craton du Kaapvaal et dans la ceinture du Limpopo s'étale sur plus d'1 Ga. Les affleurements archéens sont reconnus au nord de l'Afrique du Sud (figure 3–1), et les données géophysiques (sismologie, gravimétrie et magnétisme) ont permis de délimiter les contours du craton (de Wit et al. 1992a et références incluses). Sa surface est d'environ 1.2 10^6 km^2, pour une épaisseur de croûte de 37 km, à laquelle il faut associer une racine lithosphérique épaisse (*SCLM : sub-continental lithospheric mantle*) jusqu'à environ 350 km. De plus, ces données géophysiques montrent que le craton est constitué d'une mosaïque de petits blocs, détaillée dans de Wit et al. (1992a). Ces sous domaines ont des âges différents et structurent le craton. Le plus vieux d'entre eux, l'Ancient Gneiss Complex, est formé de gneiss de composition TTG cristallisés vers 3.64 Ga et modifiés vers 3.50 puis 3.43 Ga, et on y trouve également des zircons jusqu'à 3.7 Ga. Il est considéré comme le noyau primordial du craton.

Figure 3–1 (page suivante): *Carte géologique de l'Afrique du Sud (Reimold et Gibson 2005) et échelle stratigraphique associée (Hunter et al. 2006).*

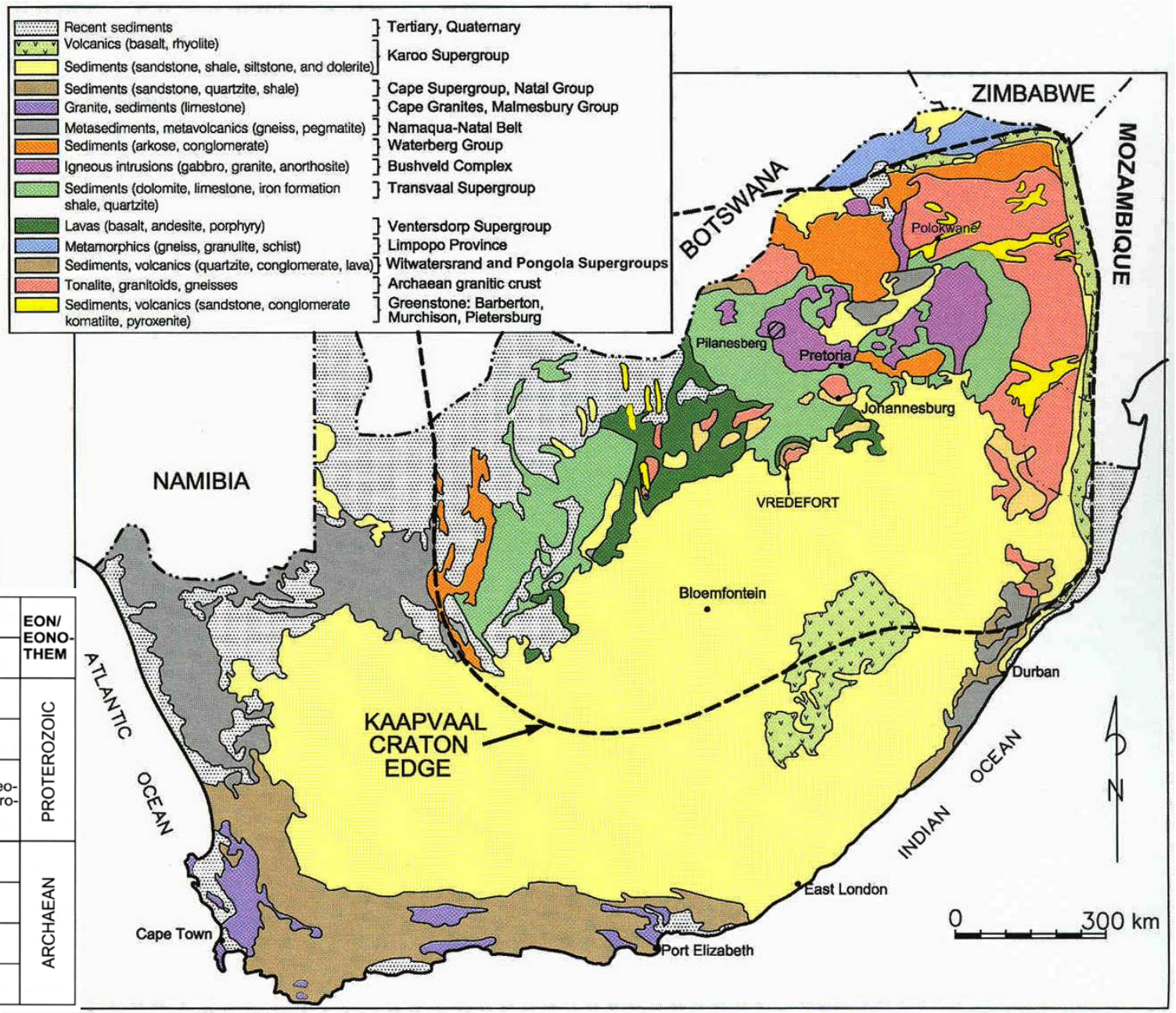

Ma	ERA/ERATHEM				EON/ EONOTHEM
	SACS		SPS		
545	Namibian		Neoproterozoic		PROTEROZOIC
1 000	Namaquan [1]	Mokolian	Mesoproterozoic		
1 600	Kheisian [1]		Palaeoproterozoic [2]	Palaeoproterozoic	
2 050	Vaalian		Eoproterozoic [2]		
2 500			Neoarchaean		ARCHAEAN
2 650	Randian				
2 800			Mesoarchaean		
3 080	Swazian				
3 200			Palaeoarchaean		
3 600			Eoarchaean		

B — Construction : les ceintures de roches vertes archéennes et leurs granitoïdes

La géologie générale des ceintures de roches vertes (CRV) et de leurs terrains granitoïdiques a fait l'objet du chapitre 2. Les CRV d'Afrique du Sud ont la particularité d'être nombreuses (figure 3–2), et certaines sont précoces (Barberton).

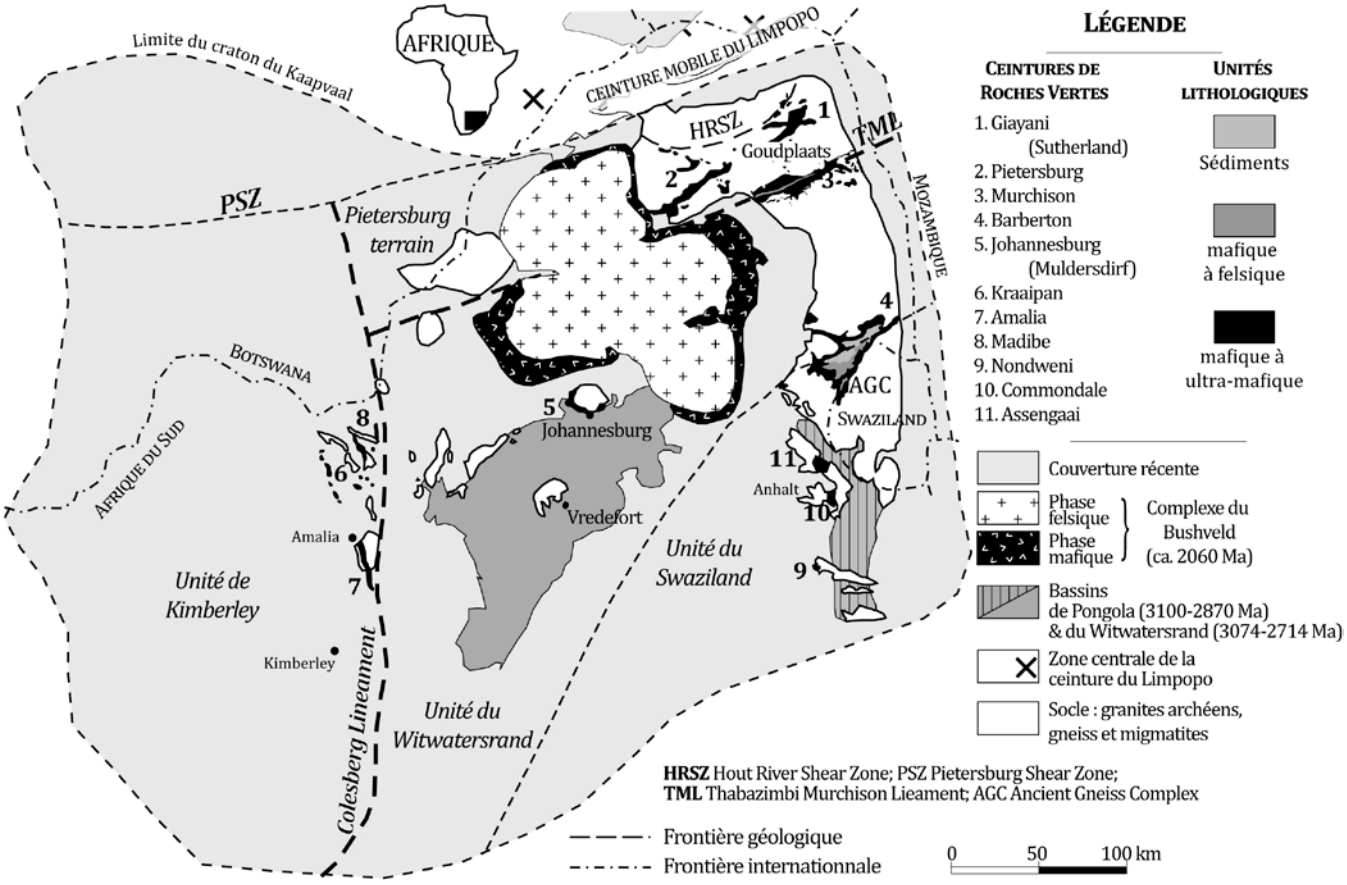

Figure 3–2 : *Craton du Kaapvaal (modifiée d'après Poujol 2007) incluant la répartition du socle et des ceintures de roches vertes sud-africaines. Noter les deux groupes d'orientations des ceintures : Nord-Nord-Est pour les ceintures de l'est et du nord-est du craton, et Nord-Sud pour celles de l'ouest du craton. Ces orientations sont globalement parallèles aux limites de terrains, soulignant le lien génétique entre la formation des ceintures et les collision-accrétion de blocs.*

- ***ZONE SUD-EST.*** Alors que la CRV de Barberton affleure remarquablement, plus au sud, les CRV ne sont que rarement visibles sous les sédiments postérieurs.

BARBERTON. Le terrain à granites et ceinture de roches vertes de Barberton est sûrement le plus étudié parmi les terrains sud-africains, et un des plus connus mondialement. En effet, il est à la fois très ancien (3.5-3.1 Ga) et particulièrement bien préservé. La ceinture de roches vertes de Barberton constitue l'un des modèles des CRV en général.

La pile volcano-sédimentaire atteindrait 20 km. Elle comprend en position inférieure le groupe d'*Onverwacht*, composé de volcanites ultra-mafiques (dont de nombreuses komatiites) mafiques, rarement acides, ainsi que de quelques sédiments déposés en milieu marin (3.55-3.29 Ga). Ce groupe est surmonté par celui de *Fig Tree*, composé de sédiments détritiques terrigènes et de quelques dacites (3.26–3.22 Ga). Il s'est déposé en contexte marin (profond pour le terrain du nord, peu profond pour celui du sud). Enfin, le groupe de *Moodies* rassemble des sédiments alluviaux, fluviaux et tidaux, conglomératiques à argileux (3.35-3.21 Ga).

Parallèlement, les roches magmatiques associées à la ceinture se sont formées lors de plusieurs épisodes tectoniques (le nombre varie selon l'importance accordée par chacun des auteurs):

- 3.55-3.46 Ga : dépôt des laves basales du Groupe d'Onverwacht, et mise en place du protolithe d''un gneiss TGG (3.51 Ga) — en contexte océanique extensif ou d'arc ou de plateau océnique (cette dernière est l'hypothèse privilégiée).
- 3.47-3.41 Ga : dépôt des laves acides du groupe d'Onverwacht et cristallisation des intrusions équivalentes de nombreux gneiss TTG juvéniles, relativement petits, souvent intrusifs dans la ceinture (3.47-3.44 Ga) — en contexte analogue à une celui d'une subduction
- 3.26-3.22 Ga (culmine à 3.23 Ga) : intrusion de grands batholithes TTG, mais aussi de granites potassiques; leur origine est une croûte plus évoluée que dans le cas des roches précédentes. Cette phase correspond à l'amalgamation des terrains nord-ouest et sud-est ainsi que de l'*Ancient Gneiss Complex*. C'est aussi la phase tectono-métamorphique principale, dont les conditions peuvent atteindre 1.2–1.5 GPa pour 600–650°C (Moyen et al. 2006).

De nombreux fragments de ceintures de roches vertes sont reconnus juste au sud de Barberton. Les fragments de **Weergevonden** et **Shapenburg**, proches de la CRV de Barberton, seraient des restes de cette dernière, en particulier de ses termes inférieurs (Onverwacht et Fig Tree).

ASSEGAAI, DE KRAALEN, COMMONDALE. Les fragments d'Assegaai, de De Kraalen et de Commondale forment un amas plus au sud observables à la faveur de fenêtres dans les sédiments jurassiques. Leurs successions volcano-sédimentaires montrent des rapports laves/sédiments très variables, et chacune d'entre elles est dénommée « formation ». Cependant il existe de nombreuses similarités entre ces fragments. La pétrologie des laves est ultra-mafique à mafique, celle des sédiments est détritique (pélite à conglomérats), chimique (formations de fer nombreuses) et on observe quelques niveaux calc-silicatés. Toutes ces roches se sont déposées en contexte marin peu profond. Plusieures phases de déformation sont observées dans les différents fragments, de style plissants voir de nappes. Le métamorphisme est en faciès amphibolitique (bas à haut) rétromorphosé en faciès schiste vert sur l'ensemble du

fragment de Commondale ou seulement le long de zones de cisaillements tardives (Assegai, De Kraalen).

NONDWENI-ILANGWE. Sur la bordure sud-est du craton, le groupe de Nondweni réunit plusieurs affleurements accessibles sous la couverture sédimentaire, dont les deux majeurs de Nondweni et d'Ilangwe. Ces deux groupes sont constitués d'unités tectoniques empilées de laves ultra-mafiques et mafiques, de rares coulées de composition intermédiaire à rhyolitique et de sédiments très divers (cherts, BIF, quartzites, conglomérats, évaporites, stromatolithes). Les roches d'Ilangwe sont en faciès amphibolitique développé lors de plissements, puis en faciès schiste vert lors d'une phase déformation produisant des plis verticaux. La zone de Nondweni est, elle, en faciès schiste vert, le grade amphibolitique étant limité aux pourtours des plutons. Les contraintes géochronologiques sont rares, une coulée de Nondweni a été datée à 3.41 Ga.

Peu de datations sont disponibles sur les CRV au sud de Barberton. On retiendra surtout le caractère intrusif de la suite trondhjemitique d'Anhalt, indiquant une formation de ces CRV avant 3.29-3.25 Ga. Vers 3.1 Ga, l'intrusion exclusivement de grands batholithes de granites potassiques (anorogéniques) marque la fin de l'activité tectono-métamorphique de la région sud. Deux renouveaux magmatiques post-tectoniques (post-Pongola) forment un assemblage nord-sud de plutons au sud de la CRV de Barberton sur une centaine de kilomètres. Le premier est potentiellement de type S (basse teneur en Ca) vers 2.86-2.82 Ga, le second est de type I (haute teneur en Ca) entre 2.74 et 2.69 Ga.

- **ZONE CENTRALE.** Deux CRV de taille modeste apparaissent dans le cœur et au nord du bassin du Witwatersrand, dans le bloc du Witwatersrand.

DOME DE JOHANNESBURG. Les restes de ceinture au nord du dôme sont des xénolithes d'amphibolites massives et de schistes ultra-mafiques de tailles modestes. Au sud, les affleurements sont plus continus, ils constituent pour l'essentiel un complexe ultra-mafique serpentinisé (dunite-pyroxénite…) mais on y trouve aussi des basaltes (tholeiitiques à komatiitiques). Cet assemblage serait analogue à une ophiolite moderne. Un gneiss TTG à 3.34 Ga contenant ces xénolithes du nord fournit un âge minimum de la CRV. Il précède une tonalite à 3.20 Ga. Ces deux phases sont recoupées par des granodiorites potassiques vers 3.12-3.11. Cette succession semble similaire à celle du terrain de Barberton, les deux zones pourraient appartenir au même ensemble est-ouest.

DOME DE VREDEFORT. La croûte retournée par l'impact éponyme donne accès au soubassement du bassin du Witwatersrand (voir ci-dessous). Comme dans le dôme de Johannesburg, il apparait d'une part des restes de taille limitée de CRV sous forme de xénolithes et d'autre part une séquence plus significative, la formation des Greenlands. Les premiers sont des xénolithes de pélites, des formations sédimentaires, des gneiss

mafiques, le tout à haut grade dans des granulites-migmatites. La formation des Greenlands est faite de basaltes (ultramafiques) et de BIF, en faciès schiste vert moyen. Les gneiss du dôme sont datés à 3.09 Ga (mais cela pourrait être l'âge du migmatisme).

- ***ZONE NORD-EST.*** Quatre ceintures beaucoup plus significatives se groupent dans le nord-est du craton : la ceinture de Polokwane (anciennement Pietersburg), de Giyani (anciennement Sutherland), de Rhenosterkoppies et de Murchison (figure 3–3). Elles sont séparées de la ceinture de Barberton par le grand batholithe potassique de Nelspruit mis en place vers 3.10 Ga. Ces CRV sont orientées NE à ENE dans l'ensemble, avec des digitations autour des "dômes" (sauf pour la CRV limitée de Rhenosterkoppies). Les CRV de Polokwane, de Giyani et de Rhenosterkoppies pourraient avoir été un seul et même ensemble, mais cela reste spéculatif. L'amalgamation de ces terrains est discutée dans l'article #1. Le tableau 1 présente une synthèse des âges de la zone incluant les données récentes de cette thèse et de la thèse d'O. Laurent.

POLOKWANE/PIETERSBURG. La ceinture affleure en deux parties, une au nord-est et une au sud-ouest de Polokwane, qui présentent des différences dans la séquence sédimentaire, la chimie des laves, la déformation et le degré métamorphique. Sa pile volcano-sédimentaire est dite "lithotectonique", c'est-à-dire qu'elle correspond pour partie au moins à un empilement structural dont l'épaisseur est de 7 km au maximum. L'unité basale est dominée par les roches volcaniques ultra-mafiques à mafiques, l'unité sommitale (formation d'Uitkyk) par des métasédiments clastiques, et la séquence basale serait répétée tectoniquement dessus. La première est représentée d'une part par des serpentinites et des schistes à talc-carbonates-chlorite-tremolite (le caractère intrusif ou extrusif n'est pas clairement établi), d'autre part par des roches mafiques de type amphibolites (actinote-hornblende) dont les protolithes sont majoritairement des basaltes tholéitiques et parfois des basaltes komatiitiques, des gabbros et des péridotites. On trouve aussi quelques roches felsiques intercalées (rhyolithes et porphyres de quartz) dans la zone SO, ainsi que des formations de fer en boudins. Peu d'âges sont disponibles, seulement un âge imprécis à 3.46 ± 0.1 Ga pour une amphibolite. Reposant en discordance sur cette unité, la formation d'Uitkyk est restreinte à la zone SO. Les conglomérats, quartzite et arénites dominent sur les argilites, et la séquence correspond à un bassin d'avant-pays (cône alluvial, rivières en tresses). L'âge de dépôt est contraint entre 2.88 (Zeh et Gerdes, 2012) et 2.69 Ga.

La déformation est hétérogène, la zone NE expose communément de belle foliations tandis que la zone SO expose souvent des roches massives et seulement quelques roches foliés associées à des zones de cisaillements. Deux phases de déformations sont reconnues. À la première est attribuée la formation de plis à axes est-ouest au SO, et au NE à axes nord-est-sud-ouest avec foliation pénétrative associée. La deuxième phase est plus localisée avec des chevauchements à vergence nord, elle daterait de 2800 Ma. Enfin des cisaillements décrochants senestres tardifs sont reportés. Le métamorphisme de la zone est hétérogène latéralement et polyphasé. Une

première phase M1 a une composante hydrothermale importante et est en faciès schiste vert au SO et amphibolite inferieur au NE, où il est associé au développement de la foliation. Une seconde phase métamorphique M2 est en bas grade (schiste vert), restreint à la formation d'Uitkyk, et des conditions plus profondes sont localement observées (intrusions).

La CRV de Pietersburg est recouverte en discordance angulaire par le groupe de Wolkberg, qui a au moins 2650 Ma. Elle est bordée au nord de gneiss non-migmatitiques granodioritiques–tonalitiques, intrusifs dans la ceinture, datés entre 2940 et 2870 Ma. Les granites méridionaux apparaissent en *dome-and-keel* (ceinture dans des synclinaux entre les dômes de granitoïdes). Ils seraient intrusifs dans la CRV mais les contacts sont cisaillés. Parmis eux le granite de Turfloop a 2780 Ma et une phase du Groot Letaba gneiss dans la CRV a 2885 Ma.

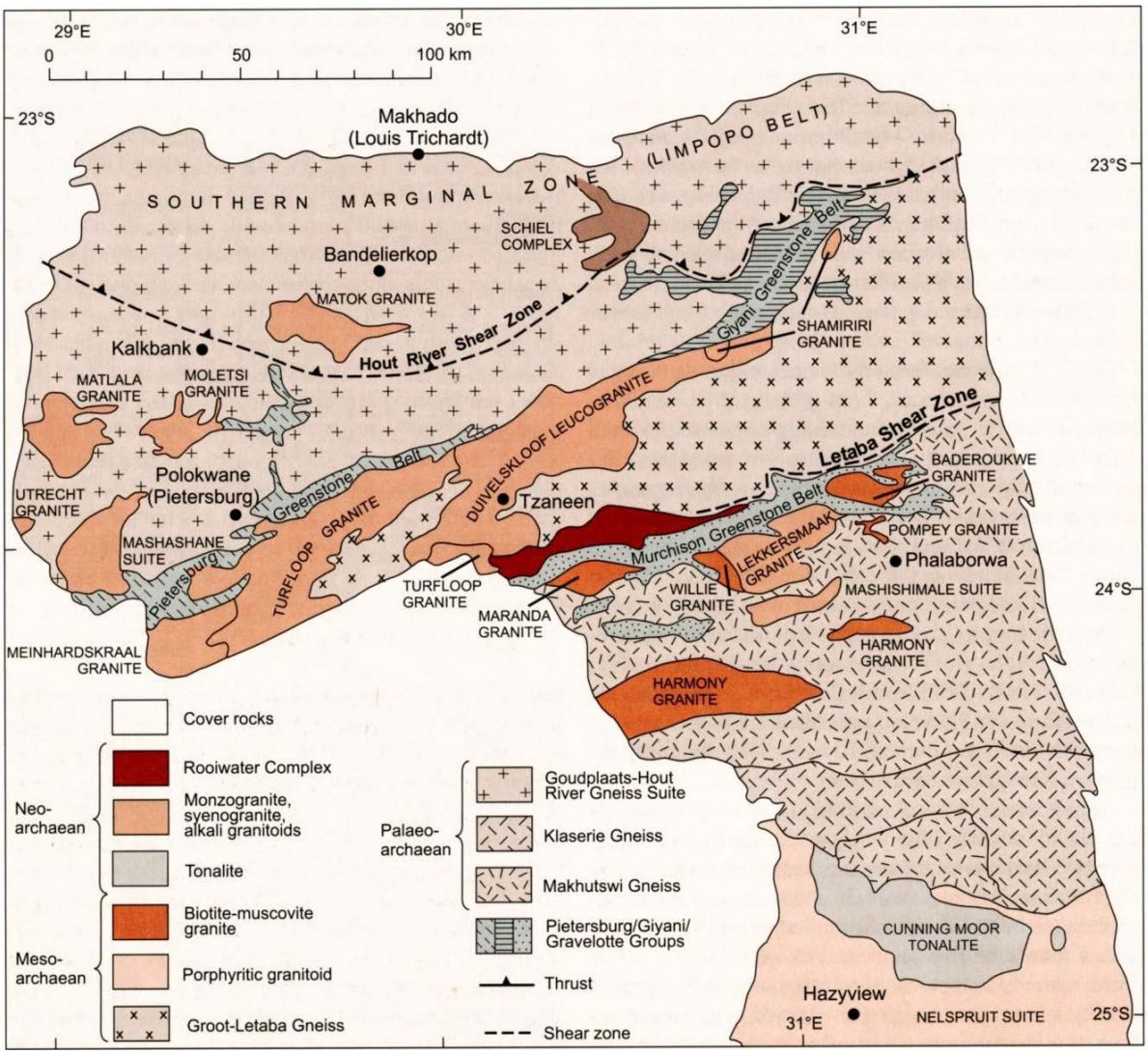

Figure 3–3 : *carte du nord-est du craton du Kaapvaal comprenant les gneiss, les plutons et les Ceintures de Roches Vertes (Robb et al. 2006).*

GIYANI/SUTHERLAND. La ceinture de Giyani est localisée juste au sud de la zone de cisaillement de la rivière Hout (*Hout River Shear Zone*), zone mylonitique verticale qui limite la zone marginale sud de la ceinture du Limpopo. C'est une séquence volcano-sédimentaire fine (3 km au maximum) et fragmentaire, où les roches ultra-mafiques dominent encore. Celles-ci comprennent une intrusion de dunite altérée (*Leonde intrusion*), des serpentinites, des schistes à talc-chlorite-hornblende-trémolite dont le protolithe était des basaltes komatiitiques; les roches mafiques sont des amphibolites issues de basaltes tholéitiques. Les rares volcanites felsiques (rhyolites) sont altérées (enrichissement sodique), les métasédiments sont localement en séquence épaisse (conglomérats, quartzites, pélites, formations de fer, dolomite). Une méta-andésite a fourni un âge de 3.20 Ga, un porphyre de quartz folié recoupant le litage est daté à 2.87 Ga.

La schistosité est nette, de direction NE et à pendage modéré à sub-vertical vers le nord-ouest ou le sud-est. On trouve des zones de cisaillements parallèles à la fabrique à pendage nord-est qui indiquent une cinématique inverse vers le sud, et des zones mylonitiques à pendage sud et cinématique nord. Cette CRV est interprétée comme une écaille allochtone mise en place lors du chevauchement vers le nord. Elle serait tectonisée par la suite avec des chevauchements à cinématique vers le sud, éventuellement en lien avec des mouvements décrochants tardifs notamment sur la bordure nord (cisaillement mylonitique). Le métamorphisme varie de schiste vert à amphibolitique inférieur vers le nord-est, mais il peut être absent dans certains sédiments. L'empreinte amphibolitique à l'approche du terrain Limpopo est attribuée à la deuxième phase de déformation.

La CRV de Giyani est entourée de gneiss migmatitiques, en contact tectonique. De même, les granites du sud sont peu déformés dans la masse mais les contacts avec la CRV sont cisaillés.

RHENOSTERKOPPIES. La ceinture de Rhenosterkoppies est une petite succession tectono-stratigraphique. Les roches mafiques sont des amphibolites, interprétées comme des volcanites tholéitiques. Les roches ultra-mafiques sont des roches altérées : serpentinites, pyroxénites et divers schistes à talc-antigorite-trémolite-chlorite. Les niveaux sédimentaires comprennent des formations de fer, des quartzites et des roches calc-silicatées. Les roches de la CRV sont plissées au cours d'un premier événement, associé à un mouvement chevauchant vers le nord. La CRV prend ensuite la forme d'un anticlinal plat d'axe est-ouest, replissé lors d'une phase ultérieure. Une zone de cisaillement est supposée dans la CRV. Le métamorphisme est en faciès schiste vert supérieur dans le centre et amphibolite supérieur au nord. Ce dernier serait potentiellement imputable au chevauchement secondaire vers le sud des granulites de la zone marginale sud de la ceinture de la Limpopo, avant de se rétromorphoser en contexte schiste vert avec des fluides aquo-carboniques. La CRV est entourée du gneiss de Goudplaats-Hout sauf sur sa partie occidentale où elle est intrudée par le granite de Moletsi.

Les dépôts volcano-sédimentaires des CRV sont diachrones et les successions différentes (par exemple la formation d'Uitkyk), ce qui implique que chaque ceinture a une histoire au moins en partie indépendante.

MURCHISON. La ceinture de Murchison est bien plus au sud que les trois CRV décrites précédemment, entre la limite sud du gneiss de Goot-Letaba et la limite nord de celui de Makhutswi. Elle est décrite dans les contextes géologiques des articles, particulièrement dans l'article #2.

LE SOCLE NORD. La suite gneissique de Goudplaats-Hout inclue (1) au nord de la zone de cisaillement de la rivière Hout, des faciès de haut grade de la zone marginale sud de la ceinture de Limpopo, et (2) au sud de cette zone de cisaillement, le socle de bas grade au nord des ceintures de Polokwane et de Giyani. Ce terme recouvre donc des gneiss variés, complexes, tant en texture, en couleur, en structure qu'en composition.

Au nord, il est composé de lits de migmatite et de granite leucocrate anatectique. Le premier est à hornblende-biotite et il a une composition de granodiorite, le second, à composition de monzogranite-tonalite, proviendrait de la fusion déshydratée du premier. On y trouve des enclaves de gneiss tonalitiques foliés, probablement issues du terrain de haut grade au nord. Vers la CRV de Polokwane, c'est un gneiss gris homogène à grain moyen à biotite, avec localement des leucosomes d'anatexie. À l'est de la CRV de Rhenosterkoppies, deux phases grises (migmatite et non-migmatique) montrent une gamme d'âges entre 2940 et 2870 Ma. Vers la CRV de Giyani, le gneiss est leucocratique, à grain est moyen. Il est associé à des phases mineures, litées grises, datées à 3282 et 3274 Ma. Leur composition varie de monzogranite à granodiorite. Enfin, vers Goudplaats, les gneiss gris migmatitiques sont précoces (plissés) et dominants par rapport aux phases leucocratiques. Un de ces gneiss gris a été daté à 3333 Ma. Ils ont des compositions de TTG. D'après le peu d'âges disponibles, ce gneiss est plus vieux que les CRV de Giyani, de Polokwane et de Rhenosterkoppies, il représenterait donc le socle de ces CRV.

Cependant, une étude géochronologique récente (Oscar Laurent, comm. pers.) trouve uniquement des âges < 3.2 Ga dans ce gneiss (héritage entre 3.1-3.2 Ga, activités magmatiques à environ 2.95 et 2.83 Ga). Ce gneiss ne serait donc pas un "socle" à proprement parler (voir discussion chapitre 11). En conséquence, il fournit peu de contraintes sur l'âge minimum des CRV.

LE "SOCLE" SUD. Le gneiss de Groot-Letaba englobe les lithologies variées situées au sud des CRV de Polokwane et de Giyani et au nord de la CRV de Murchison. Ce sont des mélanges de tonalite et de trondhjémite essentiellement et un peu de gneiss lités. Ils sont souvent migmatitiques, et les quelques données géochronologiques montrent des activités à 3171 Ma, vers 3100-3000 Ma et 2780-2620 Ma (cette dernière donnée est apparemment sans signification). Les roches peuvent être massives localement,

mais le plus souvent elles sont déformées (foliées, plissées). Des enclaves de CRV dans ce gneiss sont notées, sans précisions sur la localisation ou la nature (donc sans pouvoir supposer d'une origine).

Encore plus au sud (c'est-à-dire au sud de la CRV de Murchison), deux gneiss sont différenciés, celui de Makhutwsi et celui de Klaserie. Le gneiss de Makhutwsi est composite, migmatitique, lité et plissé. Il serait de composition TTG. Il est recoupé par un réseau de filons de gneiss tonalitique homogène. L'âge du gneiss proprement dit est 3.23 Ga tandis que ces phases plus jeunes seraient entre 3.12 et 3.06 Ga. Des enclaves de roches mafiques et sédimentaires y sont abondantes. Le gneiss de Klaserie serait chimiquement un équivalent du gneiss de Makhutwsi qu'il intrude.

LES PLUTONS. Le tableau 1 présente une synthèse des âges de la zone. Ces gneiss sont percés de nombreux plutons au nord comme au sud. Ils ont une forme assez ronde au nord dans le gneiss de Goudplaats-Hout, et souvent une forme allongée NE-SO au sud. Ils sont très divers géochimiquement depuis des compositions TTG jusqu'à des plutons de type S. Ces intrusions sont bien mieux datées que les gneiss environnants. Elles montrent une activité magmatique très prolongée sur plus de 400 Ma. En effet, on distingue des épisodes magmatiques à 3.09-3.06, 2.97-2.92, 2.85-2.83, 2.77-2.76 et 2.69 Ga (voir par exemple l'article #1 et le *geological setting* de l'article #2), notamment sur les bordures sud des CRV. Ce spectre d'âges et de compositions est presque entièrement retrouvé dans le terrain granitoïdique de la Murchison. Toutefois, les données de cette thèse permettent de réévaluer la géochronologie de la région : l'importance de la phase à 2.97-2.92 Ga est renforcée dans les articles #1, 3 et 5 et discutée dans le chapitre 7; la caractérisation du magmatisme vers 2.82-2.77 Ga fait l'objet du chapitre 8. Ces deux épisodes ainsi que les plutons à 3.09-3.06, 2.85-2.83, et 2.69 sont intégrés à l'histoire régionale du nord du Kaapvaal dans le chapitre 9.

Les plutons peuvent fournir des contraintes temporelles sur le dépôt des CRV, et les déformations dans les terrains à granites et ceintures de roches vertes. On notera donc :

- Le granite de Moletsi, intrusif dans la CRV de Rhenosterkoppies, est aujourd'hui daté à environ 2680 Ma, et on ne lui décrit pas de déformation
- Le gneiss trondjémitique de Melkboomfontein, intensément folié, est intrusif dans le sud de la CRV de Polokwane à 2853 ± 20 Ma ; dans le nord le gneiss de Goudplaats-Hout est intrusif dans la ceinture et serait daté entre 2940 et 2870 Ma.
- Un porphyre de quartz folié est intrusif à 2874 Ma dans la CRV de Giyani tandis qu'une pegmatite non-déformée est datée à 2632 ± 53 Ma (mais la méthode Rb-Sr n'est pas toujours fiable)
- Beaucoup de plutons sont intrusifs dans la ceinture de Murchison ; celui reconnu comme le plus vieux est le pluton de Baderoukwe, déformé, aujourd'hui daté à 2965 Ma.

- ***ZONE OCCIDENTALE.*** Les ceintures de Kraaipan, d'Amalia et de Madibe sont situées à l'ouest du craton. Elles affleurent peu sous les laves du Ventersdorp ou les sédiments Khalahari. Elles sont réunies stratigraphiquement dans le groupe de Kraaipan. D'orientation NNO-SSE, elles se composent de bandes étroites parallèles avérées (Kraaipan) ou supposées par la géophysique (Amalia). Elles sont donc parallèles à l'anomalie magnétique de Colsberg, une structure géophysique principale du craton située moins de 30 km vers l'est, qui sépare le block de Kimberley du bloc du Witwatersrand. À ces dernières CRV peut donc être ajoutée la ceinture isolée au sud de Marydale qui est également à l'est de l'anomalie.

AMALIA. La ceinture d'Amalia est constituée de laves mafiques à ultra-mafiques (basaltes tholeitiques à komatiitiques), de formations de fer et de sédiments clastiques et de schistes à talc-chlorite (mafique). Son âge reste ambiguë, car si elle est intrudée à l'est par de jeunes granodiorites de 2.88 Ga, des âges plus récents (2.75 Ga ; Poujol et al. 2005) sur les roches de la ceinture remettent en cause cette relation. Ces roches présentent des plis mais la déformation principale est pervasive et fortement pentée. Elle a été suivie d'un cisaillement dextre. Le métamorphisme associé à la déformation principale est en faciès schiste vert supérieur à amphibolitique inférieur. Cette épisode de déformation correspondrait à la formation d'un (arrière) arc. La ceinture d'Amalia est accolée à l'ouest à des gneiss TTG.

KRAAIPAN. La ceinture de Kraaipan montre 3 bandes. La pile volcano-sédimentaire est dominée par des laves mafiques à ultra-mafiques (basaltes tholéiitiques à komatiitiques) avec de rares passées plus felsiques (rhyolitiques) ; des formations sédimentaires (formations ferrugineuses, schistes, sédiments clastiques, cherts). Peu d'études ont été menées sur la déformation de la zone, et seules quelques brèches sont reportées. Le métamorphisme est variable, souvent en schiste vert mais localement les roches n'ont atteint que de très bas grade ou au contraire le faciès amphibolitique inférieur. Seules les coulées felsiques ont fourni une contrainte sur l'âge vers 3.10-3.07 Ga. Les affleurements de socle sont particulièrement rares dans la zone de Kraaipan. Des TTG gneissiques avec des xénolites de CRV datés à 3.01 Ga fournissent un âge minimum de la ceinture. Les phases magamatiques de granodiorites-quartz-monzonite en grands plutons foliés à 2.91-2.88 Ga suivies de granites post-tectoniques à 2.79 Ga (suite de Gaborone, qui s'étend bien au-delà vers le nord) fournissent un âge maximum.

MADIBE (d'après Poujol et al. 2008 et références incluses). La ceinture de Madibe, la plus à l'est, est constituée d'une succession volcanique (ultramafique à calco-alcalin) et sédimentaire (BIF) sur 3 km de large, déposée entre 3.04 et 3.08 Ga. Cette sucession est attribuée au fonctionnement d'un arc volcanique. La déformation est intense, elle présente une fabrique à fort pendage et la ceinture est délimitée des roches grantioïdiques par des failles. Le métamorphisme y est similaire à la ceinture d'Amalia, i.e. schiste vert supérieur à amphibolite inférieur.

Enfin, les granitoïdes de cette zone ressemblent en âge (3.08, 2.94-2.91-2.87-2.80 Ga ; Poujol et al. 2002) et en composition aux phases observées dans le nord-est du craton et illustrent une grande phase d'accrétion d'arc (TTG) et de collision sur la bordure Ouest (Poujol et al. 2008).

Le **DOME DE MAKOPPA** présente très peu de roches, qui sont des amphibolites des BIF et des schistes à talc. Cependant, la succession de gneiss TTG vers 3.03-3.01, puis granite potassiques à 2.89 et 2.80-2.78 Ga la rapprocherait des terrains des ceintures occidentales.

MARYDALE. Enfin, la ceinture de Marydale se trouve sur la limite sud-ouest du craton. D'orientation NE-SO, elle s'entend sur près de 100 km. Elle est dominée par des laves de basaltes tholéitiques, tandis que des passées de laves intermédiaires à felsiques et des sédiments sont moins fréquents. Ces sédiments sont clastiques (toute granulométrie) et quelques formations de fer et des calcaires. La séquence correspondrait à un contexte intra-continental, vers 2.99 Ga (datation imprécise à ±0.1 Ga du sommet de la pile). Le métamorphisme est en faciès schiste vert, localement amphibolitique. Il est associé à la phase précoce de la déformation produisant plis et foliation. Une zone de cisaillement verticale recoupe la ceinture et les granitoïdes environnants. Seulement deux plutons sont observés dans la zone, tout deux étant intrusifs dans la CRV. Ils sont décrits comme des granites leucocratiques à 2 micas (Bt-Ms). Le premier folié est daté à 3.11-2.93 Ga et 2.72 Ga selon les échantillons, le second à 2.85 Ga.

Tableau 1 (page suivante) : *Compilation des ages U-Pb ou Pb-Pb de la zone nord-est du craton du Kaapvaal.*

Methode: (A) Pb-Pb zircon evaporation; (B) U-Pb zircon LA-ICPMS; (C) U-Pb zircon ID-TIMS (D) Roche totale Pb-Pb (D) U-Pb titanite.

References: (1) Brandl et Kröner, 1993 (2) Zeh el al. 2009 (3) Henderson 2000 (4) Poujol et al. 1996 (5) Poujol 2001 (6) Brandl et al. 1996 (7) Poujol et Robb, 1999 (8) Jaguin et al. 2012 (article #3) (9) Laurent et al. submitted (10) Kröner et al. 2000 (11) Walraven 1981 (12) de Wit et al. 1993 (13) Burger et Walraven 1979 (14) SACS 1980 (15) Byron et Barton 1990 (16) Zeh et Gerdes 2012 (17) Walraven 1989 (18) Zeh et al. en prep (article #1) (19) Jaguin et al. en prep (article #6) (20) Jaguin et al. accepté (article #5). Erreurs à 2σ.

Unit name (pluton, formation...)		Sample nature	Age (Ma)	Method	Ref	Interpretation
Limpopo Belt and its plutons	Hugomont	Bt-granite	2658 ± 65	D?	13	Crystallisation
	Matok Igneous Complex	Bt-granite	2688 ± 8	B	9	Crystallisation
		Bt-Hb-granodiorite	2680 ± 9	B	9	Crystallisation
		Px-diorite ("enderbite")	2686 ± 7	B	9	Crystallisation
		granite	2679 ± 7	B	2	Crystallisation
Hout River Shear Zone						
Goudplaats-Hout River gneiss suite and its plutons	Matlala Pluton	Bt-Ep-granite	2703 ± 14	B	9	Crystallisation
		Bt-granite	2693 ± 7	B	9	Crystallisation
		Bt-Hb-granodiorite	2693 ± 8	B	9	Crystallisation
	Moletsi Pluton	Bt-granite	2688 ± 10	B	9	Crystallisation
		Bt-granite	2685 ± 7	B	9	Crystallisation
	Rhenosterkoppies sequence		> than the intrusive 2.69 Ga Moletsi granite			
	Hout River Gneiss	migmatitic tonalite gneiss	3333 ± 5	A	1	Crystallisation
		Bt-leucocratic gneiss	2810.6±0.4	A	10	gneiss precursor
		tonalitic gneiss	2886 ± 4	A	1	Crystallisation
		leucogneiss	2885 ± 4	A	1	Crystallisation
		potassic granite	2976 ± 84	B or C	11	Crystallisation
		?	2761 ± 80	B or C	14	Crystallisation
		Merini gneiss	2931 ±8	B	2	Crystallisation
		Migmatitic tonalite gneiss	2953 ± 13	B	9	Crystallisation
			3125 ± 43	B	9	*Inherited*
		Granite dyke cross-cutting HRG-1	2836 ± 11	B	9	Crystallisation
			2941 ± 25	B	9	*Inherited*
			3189 ± 41	B	9	*Inherited*
	Hout River Gneiss	tonalitic gneiss	3282.6 ± 0.4	A	10	Crystallisation
	Mashashane Pluton	Leucogranite	2681 ± 10	B	9	Crystallisation
		Bt-Hb-granodiorite	2678 ± 7	B	9	Crystallisation
		Uitloop granite	2679 ± 8	B	2	Crystallisation
			2687 ± 2	C	12	Crystallisation

Ysterberg Shear Zone						
The Giyani and Pietersburg Belts	Pietersburg sequence		> than the Melkboomfontein gneiss and 2.87-2.94 Ga gneisses			
		basal amphibolite	3455 ±128?	D	15	volcanic deposition
		Uitkyk sediments	2879 ± 9	B	16	max age of deposition
		metaquartz porphyre	2949.7 ± 2	A	10	volcanic deposition
	Giyani sequence		> than the cross-cutting 2.87 Ga porphyre			
		feldspar porphyre	2874.1 ± 0.2	A	10	volcanism
		meta-andesite	3203.3 ± 0.2	A	10	volcanic deposition
Groot-Letaba gneiss suite and its plutons	Melkboomfontein gneiss	granitoid	2958 ± 2	C	12	intrusif in the PGB sequence
		trondhjemitic 2 micas gneiss	2853 ± 19	A	10	min age of crystallisation
		migmatitic granodiorite	3170.5 ± 0.3	A	10	migmatic precussor
	Turfloop	porphyritic granodiorite	2777 ± 10	C	3	Crystallisation
		porphyritic granodiorite	2763 ± 15	E	3	Crystallisation
			2782± 13	B	2	Crystallisation
		monzogranite	2765 ± 7	C	4	Crystallisation
	Duiwelskloof "batholith"	Bt-granite	2841 ± 10	B	9	Magmatic
			2936 ± 22	B	9	*Inherited*
			3121 ± 32	B	9	*Inherited*
		Migmatitic granodiorite gneiss	2941 ± 13	B	9	Magmatic
		Bt-granite	2776 ± 10	B	9	Magmatic
			2983 ± 44	B	9	*Inherited*
			3126 ± 41	B	9	*Inherited*
	Groot Letaba	migmatitic tonalitic gneiss	2953 ± 60	A	10	gneiss precursor
			3171 ± 6	A	1	Crystallisation
			2784 ± 8	B	2	Crystallisation
			2839 ± 8	B	2	Crystallisation
		Bt-granite	2856.2 ± 8.8	B	unpublished	Crystallisation

Murchison-Thabazimbi Lineament						
	Rooiwater complex	Hornblende tonalite	2611 ± 10	B	2	min age of crystallisation
			2740 ± 4	C	4	min age of crystallisation
			2961 ± 150	D?	13	Crystallisation
			2965 ± 6 Ma	B	18	Crystallisation
The Murchison Belt (MGB)	ubbervale Formatio	dacite	2969 ± 20	C	5	deposition
		rhyolite	2965.2 ± 1.4	A	6	deposition
	MacKop Formation	meta-conglomerates	3076 ± 4	C	5	maximum age of deposition
		xenocrits	*3168 ± 11*	*C*	*4*	*age of a source*
	Weigel Formation	felsic volcanic	3087 ± 21	C	4	deposition
	Mulati	quartzite	2979 ± 7 Ma	C	18	maximu age of deposition
	La France Formation	aluminous schist	2986 ± 12	C	18	maximum age of deposition
Makhutswi gneiss and its plutons	Baderoukwe	trondjemite gneiss	2966.2 ± 2.9	B	8	Crystallisation
			3018 ± 15	C	5	min age of crystallistation
	Malati Pump mine	granodiorite	2964 ± 6	B	8	Crystallisation
	Maranda	granodiorite	2901 ± 20	C	4	min age of crystallistation
		albititic plug	2920	B	20	Crystallisation
	pegmatite		2848 ± 58	C	7	Crystallisation
	Lekkersmaak	peraluminous granite	2795 ± 8	B	2	Crystallisation
			2775 ± 6	B	19	Crystallisation
	unnamed	porphyritic phase in Lekkersmaak	2690 ± 65	B or C	17	Crystallisation
	unnamed	porphyritic Bt-granite in Lekkersmaak	2741 ± 9	B	19	Crysatlisation
	Willie	peraluminous granite	2820 ± 38	C	5	Crystallisation
			2817 ± 10	B	19	Crystallisation
	Discovery	granite	2969 ± 17	C	5	Crystallisation
	Mashishimale	peraluminous granite	2671 ± 8	B	2	Crystallisation
			2698 ± 21	C	5	Crystallisation
	Harmony	Bt-Ms granodiorite	3091 ± 5	C	7	Crystallisation
	Makhustwi	tonalitic gneiss	3063 ± 12	C	7	Crystallisation
			3112 ± 5	A	1	Crystallisation
			3118 ± 5	A	1	Crystallisation
		tonalitic gneiss	3078 ± 6	A	1	Crystallisation
	Makhustwi (French Bob)	trondjemite and tonalitic gneiss	3228 ± 12	C	4	Crystallisation

- **SYNTHESE.** Les terrains à granitoïdes et ceintures de roches vertes sud-africains se forment sur une large gamme de temps. On notera que les granitoïdes se mettent en place sur une péridode de 3.6 à 2.5 Ga, deux fois plus longue que celle des ceintures de roches vertes (de 3.5 à 3.0 Ga).

Les granitoïdes montrent une grande variété chimique depuis des TTG (> 3.1 Ga) jusqu'aux granitoïdes alcalins (monzo-syeno-granites), en passant par quelques plutons qui seraient de type S. Ils correspondent à la formation de la croûte (juvénile puis recyclée, voir chapitre 1), notamment par fusion de matériel mafique à intermédiaire pour les TTG. Ils constituent des arcs magmatiques souvent étroitement associés aux CRV. Ces dernières ont des lithologies similaires entre elles (souvent termes volcaniques mafiques basaltiques en base et sédimentaires et/ou volcaniques plus acides en haut). Ceci indique plutôt un contexte océanique, rarement continental (CRV de Nondwegi). Ce sont par la suite des objets avec plusieurs phases de déformation (plis et parfois nappes) et des caractéristiques métamorphiques variables.

Les terrains sont également diachrones et permettent de reconstituer la formation du craton (pour les détails et références, voir les synthèses de Wit et al. 1992a et Poujol et al. 2003). Un noyau regroupant les terrains de Barberton et l'Ancient Gneiss Complex se forme entre 3.6-3.25 Ga. Le terrain du KwaZulu Natal (CRV de Nondweni et environnantes) s'amalgame à ce premier vers 3.2 Ga. Ces deux zones sont stables vers 3.0 Ga, alors que les terrains du nord-est et de la zone marginale sud de la Limpopo s'agglomèrent sur ce proto-craton entre 3.2 et 2.8 Ga selon les rares données. Les ceintures centrales pourraient se rapprocher de cette étape (CRV du Vredefort) ou de l'étape Barberton (CRV de Johannesburg). Enfin, les informations fragmentaires des CRV du centre et de l'ouest indiqueraient une accrétion vers 3.1-2.9 Ga.

C — Cratonisation : les bassins volcano-sédimentaires archéens

Bumby et al. (2012) présentent une synthèse récente et largement illustrée des bassins sud-africains et de leurs évolutions. Ces accumulations sédimentaires marquent l'amalgamation et une certaine stabilisation de la région sud puis centrale et enfin nord (la cratonisation n'étant pas un phénomène synchrone). Cette sédimentation est à la base du découpage stratigraphique de la figure 3-1 : les premiers dépôts sur le socle (Dominion) posent la limite Swazien-Randien ; le bassin Transvaal délimite le Randien du Vaalien (figure 3–1).

DOMINION. Le groupe de Dominion est une fine accumulation d'une suite bimodale de laves mafique-intermédiaires et felsiques avec des passées clastiques mineures. Le sommet de pile s'est déposé à 3074 ± 6 Ma. Il résulterait soit d'un volcanisme de marge active (proximal ou plus en arrière-pays), soit d'un volcanisme lié à un amincissement lithosphérique (voire rift).

WITWATERSRAND. Le bassin du Witwatersrand s'est déposé entre ~2.97 et ~2.73 Ga (figure 3-2). Il est connu pour être le plus important gisement d'or mondial (voir

encart ci-dessous). Le super-groupe du Witwatersrand, d'environ 5 à 8 km d'épaisseur, est divisé en 2 groupes : le groupe inférieur de West Rand, et le groupe supérieur de Central Rand. Chacun d'eux correspond à un système sédimentaire distinct :

- le groupe de West Rand, composé d'argilites et parfois de grès, s'est déposé en environnement marin peu profond et sub-tidal (épicontinental) après 2.97 Ga. Ce contexte pourrait être la marque de la subsidence thermique à la suite du volcanisme de Dominion.
- le groupe de Central Rand, dominé par des quartzites et des conglomérats à uranium et or avec seulement quelques argilites, s'est déposé en environnement fluvial dans un bassin d'avant-pays après 2.90 Ga. Cet avant-pays se développe en réponse à la convergence du craton de Kaapvaal et du craton du Zimbabwe, et l'accrétion de terrains à l'ouest, au nord-est et au nord. L'alimentation de ce bassin notemment par les ceintures de roches vertes de Pietersburg et de Murchison est discutée dans l'article #1.

Métallogenèse de l'or dans le bassin du Witwatersrand

Ce bassin est un gisement historique de l'Afrique du Sud, à tel point que la plus grande ville, Johannesburg, s'y est installée. Il en a été extrait près de 40% de l'or mondial. Pourtant, la métallogenèse de l'or n'est toujours pas complètement comprise. Le débat tourne autour de la part respective des processus syngénétiques (sédimentaires) et épigénétiques (hydrothermalisme ; revue dans Frimmel et al. 2005).

Historiquement, le premier modèle proposé est celui du placer : l'or est érodé du sous-bassement du bassin et aussi des terrains à granites et ceinture de roches vertes et l'ensemble est déposé proximalement sous forme de conglomérats. Mais dans les années 1990, des auteurs ont souligné l'aspect hydrothermal de l'or à petite échelle, ainsi que des évidences de migration de fluides et d'altération dans les niveaux aurifères. Cette opposition trouverait aujourd'hui un consensus dans un modèle de placer modifié. Ce voisin est donc un exemple d'objet minéralisé chimérique, comme le sont nombre de provinces métallogéniques majeures. Cette question est adressée dans le cas de l'*Antimony Line* dans la partie II et discutée dans les conclusions générales.

PONGOLA. Le super-groupe de Pongola désigne la séquence volcanique et sédimentaire de près de 10 km d'épaisseur affleurant au sud-est du craton du Kaapvaal (figure 3–2). Il correspond au développement, entre 2.98 et 2.86 Ga, sur le craton stabilisé d'un bassin continental (sédiments fluviaux) puis d'un rifting (sédiments et laves bimodales associées) et enfin d'un bassin marin (sédiments clastiques et calcaires). Ces deux groupes pourraient être corrélés aux groupes de Dominion et du West Rand.

VENTERSDORP. Le super-groupe Ventersdorp (figure 3–1) représente une importante accumulation de laves (> 4.5 km) essentiellement sur le centre du craton, ce qui en fait une « grande province magmatique » (*Large Igneous Province*). Le dépôt a commencé en discordance sur le bassin du Witwatersrand vers 2.73 Ga et s'est terminé

vers 2.64 Ga, durant une tectonique globalement extensive. Il est constitué de conglomérats basaux et sommitaux mineurs, séparés par des basaltes et andésites d'affinité mantélique. La pétrogenèse de ces laves indique la fusion du manteau, vraisemblablement dans un panache mantellique.

TRANSVAAL. Les dépôts du Transvaal reposent en discordance sur les roches sous-jacentes dans un bassin au nord du craton et l'autre vers l'ouest (figure 3–1). Les groupes basaux variés ("*protobasinal*") formés en contexte extensif seraient en fait à rapprocher du super-groupe de Ventersdorp. La partie inférieure du bassin du Transvaal est un bassin intra-cratonique à sédimentation clastique (fluvial) puis de plate-forme carbonatée. La partie supérieure montre l'alternance de phases intracratoniques et de rifting, à dépôts respectivement argileux marins et continentaux (quelques passées de basaltes et d'andésites).

La couverture sédimentaire du Transvaal cachète dans le nord-est du craton les terrains à granites et ceintures de roches vertes (figure 3–3), leurs structures majeures et leur métamorphisme. Elle impose donc un âge minimum, en particulier son groupe de Wolkberg dont le dépôt aurait commencé vers 2.66-2.68 Ga. La fin du dépôt de ce bassin est datée vers 2.19 Ga.

D — La ceinture orogénique de Limpopo

La ceinture orogénique de Limpopo est une zone 200 km de large de gneiss granulitiques entre les cratons du Kaapvaal et de Zimbabwe (figure 3–4). Elle représente une orogénèse de collision entre ces cratons. D'abord vue comme tardi-archéenne (ca 2.8-2.6 Ga, et donc décrite comme la première chaine de type moderne), la documentation d'âges protérozoïques (ca 2.0 Ga) remet en question la chronologie de sa formation. Cela souligne la complexité de cette zone polyphasée dont les évènements tectono-métamorphiques s'étalent sur plus de 600 Ma. Elle est divisée en 3 zones : la zone centrale, la zone marginale sud et la zone marginale nord, séparées entre elles et des cratons adjacents par des cisaillements d'échelle continentale.

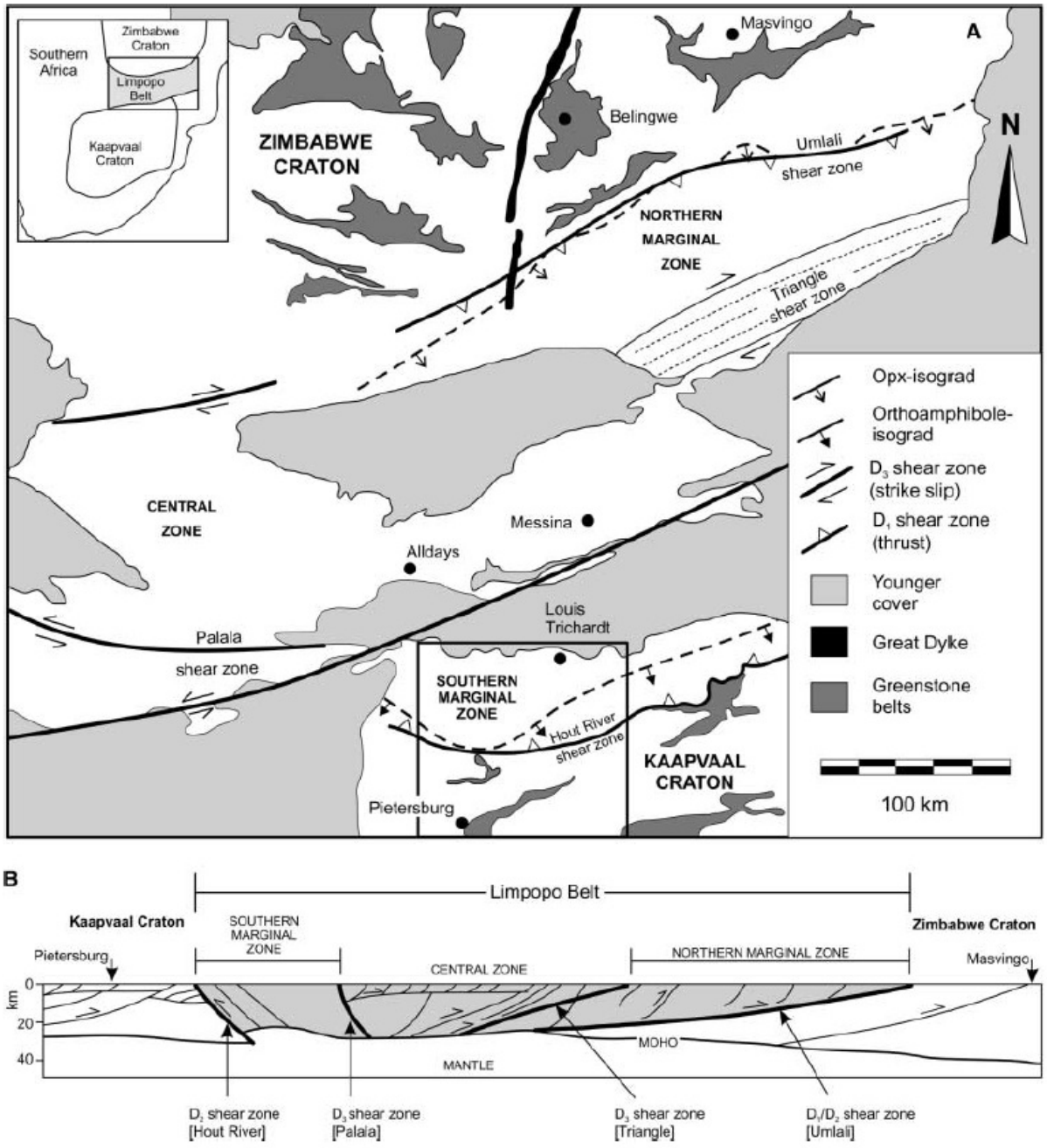

Figure 3–4 : *Carte géologique simplifiée de la ceinture de Limpopo et coupe sismique interprétée. Noter le chevauchement fortement penté de la zone marginale sud sur le craton du Kaapvaal. La ceinture de Murchison est située à l'extrème sud-est de la carte. D'après van den Berg et Huizenga 2001, et références incluses).*

La zone marginale sud est constituée d'un mélange tectonique de gneiss volcano- et para-dérivés (pélitique, mafique, ultra-mafique) et orthodérivés (orthogneiss enderbitiques), le tout intrudé par des granitoïdes (par exemple le pluton de Matok, tableau 1). La zone nord a une fabrique gneissique de direction E-O à ENE, parcourue de zones de cisaillements inverses fortement pentées vers le nord. Ces fabriques s'aplatissent vers la *Hout River Shear Zone* (encart dans figure 3–4). La partie septentrionale a atteint des conditions d'au moins 820°C et 8.5 kbar vers 2.69 Ga, tandis que la partie méridionale est rétromorphosée-réhydratée à des conditions inférieures à 600°C et 4-6 kbar, potentiellement lors du chevauchement sur le craton

du Kaapvaal vers 2.67 Ga. Ce terrain est l'équivalent de haut grade des terrains du nord-est du craton du Kaapvaal, qu'il chevauche le long de la *Hout River Shear Zone*.

La zone centrale est constituée d'un mélange de roches d'origine majoritairement sédimentaire et de roches d'origine magmatique (felsique et mafique), et des intrusifs TTG plissés. Elle s'étend au nord de la zone de cisaillement sub-verticale de Palala. Sa structure interne est assez chaotique, avec des fabriques N-S et E-O et des plis fermés. Les datations indiquent que deux événements métamorphiques en faciès granulitique se sont succédé, à 2. 56-2.69 Ga et à 2.02-2.00 Ga. L'origine de ce bloc est à rechercher dans le craton du Zimbabwe.

La zone marginale nord est faite d'orthogneiss de composition diorite-TTG ("vrais" chanorkite-enderbite) et de rares méta-basites et méta-BIF. Elle commence au nord de la *Triangle Shear Zone*, zone de décrochement à pendage sud. Elle chevauche le craton du Zimbabwe le long du *North Marginal Thrust,* qui a fonctionné entre 2.58 et 2.62 Ga. Dans sa partie nord, le métamorphisme syn-magmatique est daté vers 2.55-2.60 Ga, donc synchrone du chevauchement. Cette zone est sûrement l'équivalent partiellement fondu (recyclé) du sud du craton du Zimbabwe. En revanche, vers le contact avec la zone centrale, le métamorphisme est amphibolitique, associé à une intensification du cisaillement et est daté entre 1.93 et 2.00 Ga.

Il n'existe pas encore de modèle synthétique sur la formation de cet orogène expliquant à la fois la chronologie et les conditions tectono-métamorphiques des différents terrains. Des modèles privilégient la collision tardi-archéenne suivie d'un orogène transpressif au protérozoïque. D'autres argumentent en faveur d'une collision oblique protérozoïque, impliquant des restes de terrains granulitiques archéens.

E — Evénements géologiques postérieurs

Vers 2.0 Ga, après la sédimentation du Transvaal et l'orogénèse Limpopo, un magmatisme intra-plaque ponctuel s'exprime sous la forme de complexe mafique lité et d'essaims de filons associés et d'intrusions alcalines. C'est la phase terminale de «l'ère vaalienne» (figure 3–1).

LE COMPLEXE DU BUSHVELD. La province magmatique du Bushveld est la plus grande intrusion mafique litée (*LIP*) au monde, s'étendant sur 65000 km^2 sous forme de trois lobes (figure 3–2). Dans son ensemble, elle correspond à un magmatisme intraplaque provoqué par la remontée de manteau entre 2061 et 2054 Ma (Scoates et Friedmann 2012). Elle est composée principalement d'une épaisse suite de roches mafiques diverses, la suite de Rustenburg : norite, gabbro-norite, anorthosite, pyroxénite, diorite. Ce sont des cumulats précipités à partir de liquides basaltiques, produits par la fusion partielle du manteau. Des termes plus felsiques sont représentés par les suites de Rooiberg (volcanites: rhyolithe-dacite-andésite), de Rashoop ("granophyre") et de Lebowa (granite alcalins à hornblende-biotite, de type A). La suite de Rooiberg, précoce, est co-magmatique de la suite Rustenburg (Hatton et Schweitzer

1995). La suite de Lebowa provient de la fusion de la croûte moyenne provoquée par les intrusions basiques (Hill et al. 1996).

LE COMPLEXE DE PHALABORWA. Le complexe de Phalaborwa est une triple intrusion annulaire. Il est constitué de roches alcalines (phoscorite, sövite) formées à partir de magmas silicatés et carbonatés, cristallisées à 2060 Ma. Ces roches représentent la racine d'un volcan ultramafique de carbonatite, formé par la fusion partielle du manteau enrichi, potentiellement en lien avec l'activité relative au complexe du Bushveld.

LE COMPLEXE DE SCHIEL. Ce complexe est aussi une intrusion annulaire multiple. Il est constitué de roches silicatées alcalines (syenogabbro, syenite, quartz syenite, granite). Il semble bien synchrone des deux complexes précédemment évoqués, malgré un âge peu précis à 2059 +35/-36 Ma. Des granites calc-alcalins du même âge se trouvent également dans la zone marginale sud de la ceinture de la Limpopo.

A 2023 ± 4 Ma, une météorite impacte le bassin du Witwatersrand et forme le dôme de Vredefort.

Après cette activité magmatique, le craton est principalement affecté par des cycles de collision formant des "ceintures mobiles" et de fragmentation des continents, essentiellement les bordures sud et ouest du craton. La province du Kheis est l'expression sud-africaine de la ceinture « Ubendian » lors de la collision des cratons Kaapvaal–Zimbabwe et le craton de Congo (1.8-2.0 Ma, groupe d'Olifantshoek). Le continent se fracture jusqu'au rifting (1.6-1.2 Ga ; on notera le complexe alcalin de Pilanesberg à 1.2 Ga au Nord de la CRV de Giyani). La ceinture du Namaqua–Natal (1.2-1.0 Ga) marque la formation du supercontinent Rhodinia. Vers 700 Ma, la Rhodinia se fragmente à nouveau avant que la collision panafricaine (600–550 Ma) ne forme le Gondwana, influençant l'Afrique du Sud seulement dans la région du Cap (granites). Il s'ensuit la formation de la ceinture du Cap (*Cape Fold Belt* ; 500-350 Ma) et le dépôt des sédiments du Karoo. La fragmentation gondwanienne est associée à la mise en place des trappes du Karoo (180 Ma ; dont les reliefs Lebombo à l'est de la CRV de Murchison en bordure du craton).

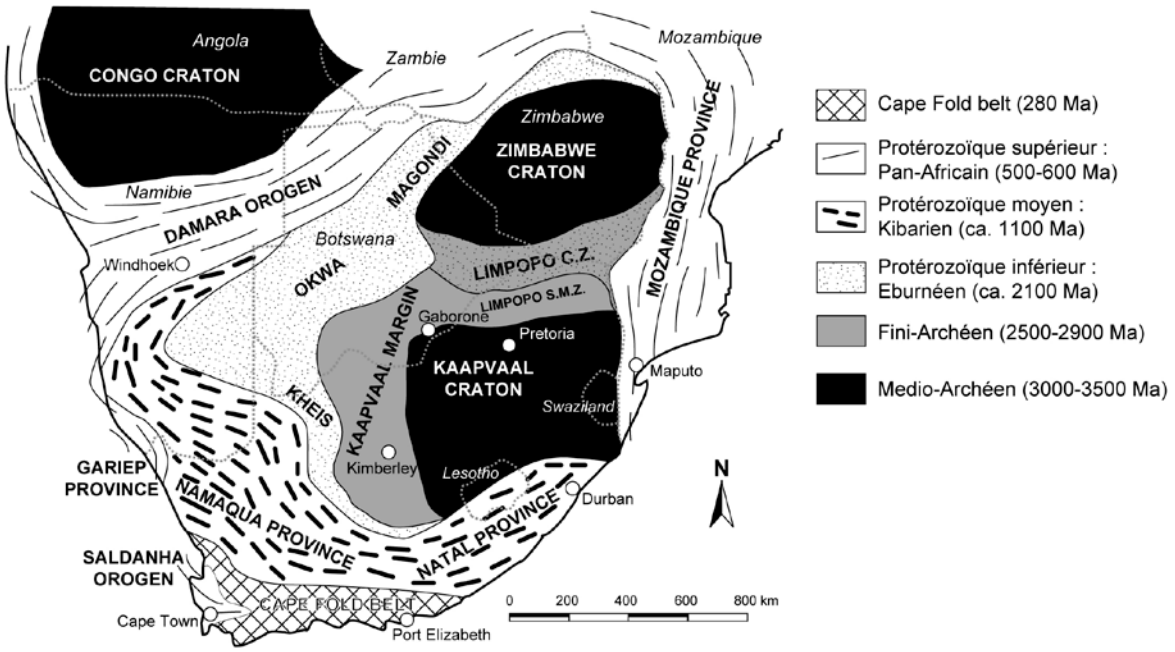

Figure 3–5 : *Schéma structural du sud de l'Afrique montrant les différentes ceintures mobiles post-archéennes (Moyen comm. pers.).*

Des intrusions de kimberlite, parfois diamantifères, percent le craton du Kaapvaal en s'échelonnant de 1.9 Ga à 70 Ma.

Chapitre 4 — Métallogénie : le cas des fluides et des magmas

Ce chapitre présente des généralités sur les minéralisations en métaux. Tout d'abord, un bref aperçu des relations géodynamiques et des évolutions séculaires des minéralisations montre qu'il existe des contrôles géologiques de premier ordre sur celles-ci. Il s'agit ensuite de poser les généralités sur les processus à l'origine des minéralisations en métaux, en se concentrant uniquement sur les deux grandes familles qui seront discutées dans la partie II, c'est-à-dire ceux impliquant les magmas et les fluides hydrothermaux. Par ailleurs, le rôle des zones de cisaillement met en exergue le contrôle structural sur les minéralisations. Puis une revue des minéralisations en antimoine mondiales permet de cerner l'originalité de la minéralisation de la ceinture de roches vertes de Murchison. Enfin, la problématique des datations de ces objets particuliers est détaillée. Les parties A, B et C sont largement inspirées du livre de L. Robb Introduction to ore-forming processes (2005) et le lecteur y est renvoyé pour les références additionnelles.

A — Relations géodynamiques et évolutions séculaires

Les associations de métaux et les types de gisements ont des affinités pétrologiques (et géochimiques) fortes (voir partie B-). Ces affinités sont le reflet des conditions géodynamiques (e.g. Mitchell et Garson 1981 ; Kerrich et al. 2005). Les gisements de cuivre porphyriques illustrent très bien cette notion : sur la figure 4–1, ces gisements sont intiment liés aux zones de subduction (type andines) actuelles ou passées. Bien d'autres couples contextes géodynamique-métaux ont été caractérisés depuis (revue dans Kerrich et al. 2005 ; Robb 2005 ; Groves et al.2005).

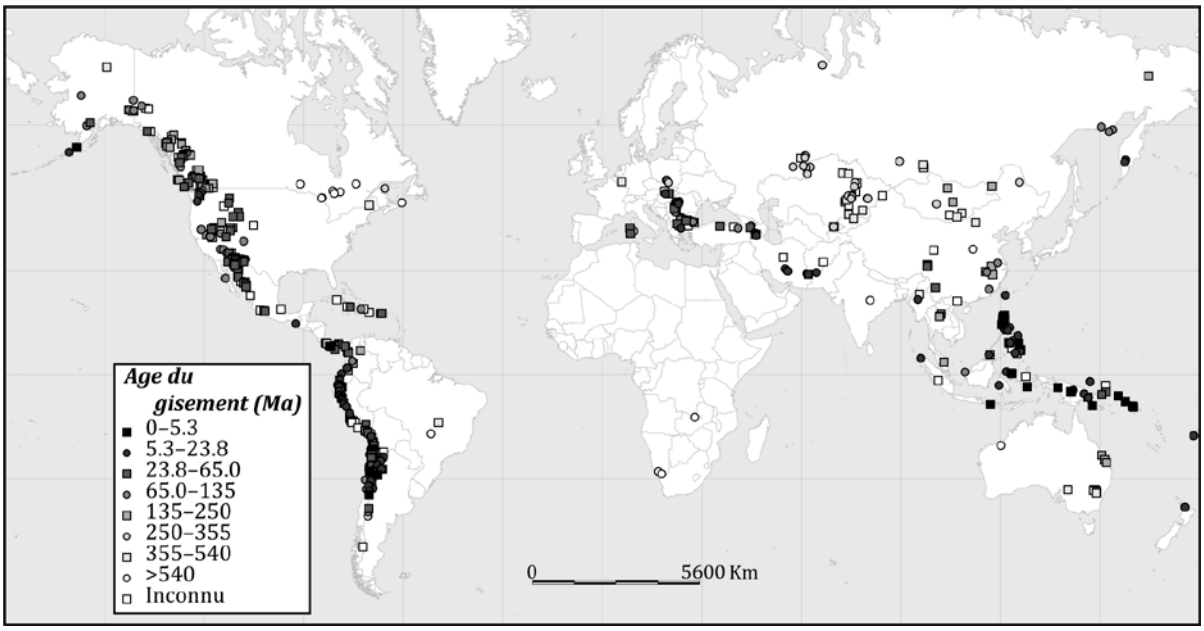

Figure 4–1 : *Carte mondiale des gisements de porphyres de cuivre, classés par âges (USGS, Singer et al. 2002). Noter (1) la série de gisements majeurs dans les Andes, surtout depuis le Crétacé, (2) celle cénozoïque dans l'arc indonésien, et (3) les gisements mésozoïques dispersés dans l'Himalaya. Ainsi, les principaux gisements sont dans les croûtes continentales à l'aplomb des zones desubductions. La relation subduction-gisements de cuivre a été reconnue très tôt après la formulation de la théorie de la tectonique des plaques (historique dans Sillitoe et Perellò, 2005).*

Puisque la géodynamique et la pétrologie présentent une évolution séculaire, à la même époque, des auteurs (Meyer 1981, 1988 ; Veizer 1989 ; Barley et Groves 1992 ; Kerrich et al. 2005 ; Groves et al. 2005) présentent l'évolution séculaire des gisements (figure 4–2). Cette figure souligne que chaque éon (Archéen, Protérozoïque et Phanérozoïque) a ses spécificités métallogéniques, qualitatives et quantitatives. Ainsi, les cratons archéens sont concentrés en nombreuses associations métalliques (par exemple Au, Cr-Ni-Ti-PGE, estimations dans de Wit et Thiard, 2005). Un des exemples illustré sur la figure 4–2 est l'or, dont 60% de la production cumulée vient de roches archéennes. Ce pourcentage se répartit entre les gisements dits *orogéniques* ou *en filons* (typiquement dans les ceintures de roches vertes) à hauteur de 18%, et le seul gisement du bassin du Witwatersrand, à hauteur de 40% (l'or de ce dernier provenant sûrement ultimement des ceintures de roches vertes, Frimmel 2005). Pour expliquer cette évolution, les causes invoquées résident dans les variations séculaires de la géologie terrestre (Robb, 2005). L'occurrence d'un gisement est soumise à la conjoncture d'une ou plusieurs de ces causes :

- la tectonique et l'activité des panaches (la géodynamique d'une manière générale; par exemple la fragmentation des continents et les gisements de sulphures volcanogéniques massifs, figure 4–2)
- la composition des enveloppes externes (par exemple le faible taux d'O_2 atmosphérique avant 2.2 Ga et les gisements d'uraninite sédimentaires)

- le flux de chaleur (par exemple la formation des komatiites à l'Archéen et les gîtes sulfurés à Ni-Cu associés)
- la préservation des gisements (par exemple préservation des bassins carbonatés et gisements *Mississippi Valley type*).

Figure 4–2 : *Distribution des types de gisements majeurs au cours du temps (d'après Kerrich et al. 2005, référence incluses et dans le texte)*

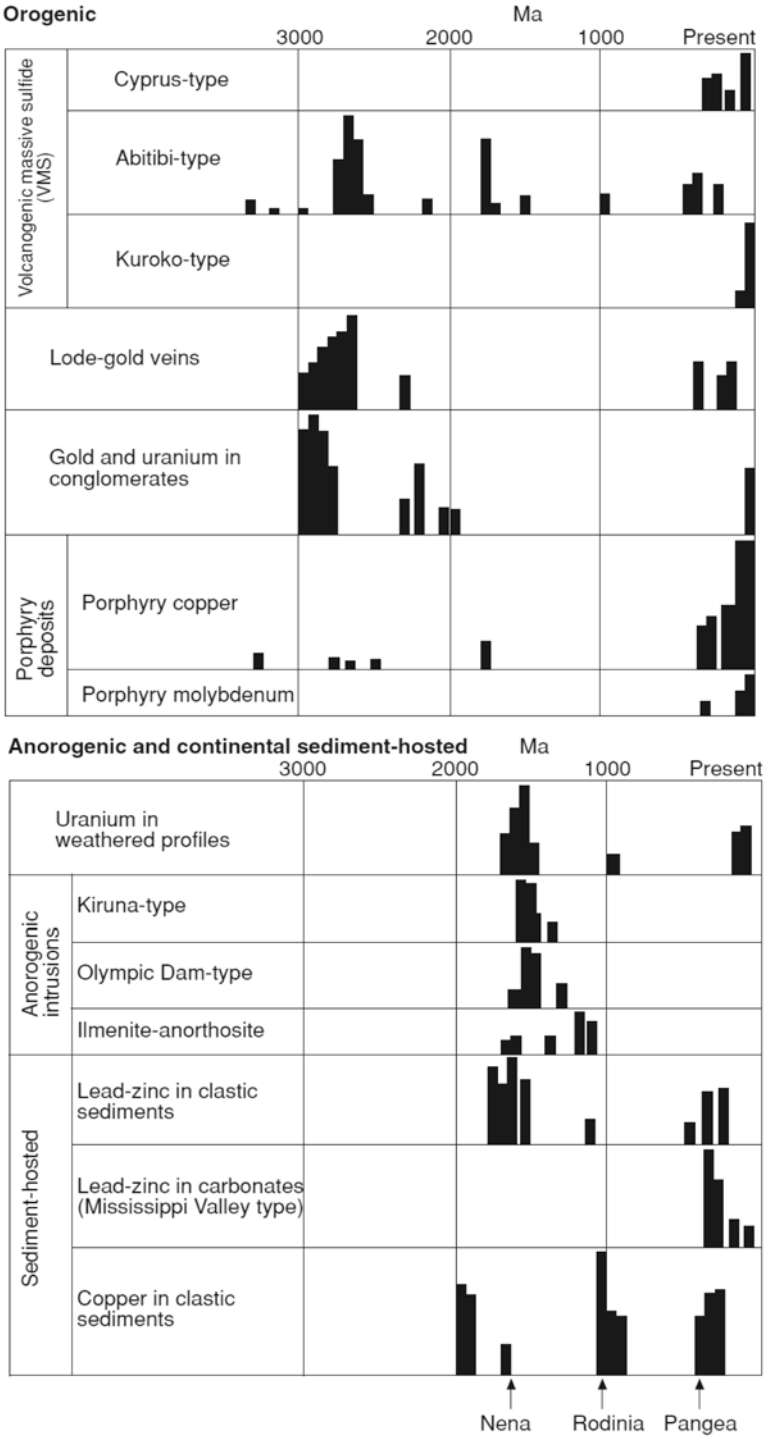

Ces causes sont interdépendantes : de façon simpliste, la tectonique est contrôlée par le flux de chaleur (dont celui lié aux panaches) tandis qu'elle joue sur la préservation. L'abondance de métaux à l'Archéen serait donc imputable au cumul de conditions propices : une atmosphère réductrice, un flux de chaleur élevé (voir chapitre 1), un mode tectonique différent de l'actuel (voir chapitre 2) et une préservation des cratons (voir chapitre 1 et 3). Il faut cependant noter que, dans le détail, les cratons possèdent chacun une empreinte métallogénique légèrement différente (de Wit et Thiart 2005). Comme une minéralisation peut être l'expression d'un contexte spécifique, la variabilité métallogénique inter-craton pourrait être la marque de la variabilité des processus géodynamiques.

B — Rôles des fluides hydrothermaux et des magmas

La métallogénie est la science des gisements, c'est-à-dire qu'elle étudie les zones de concentration anormalement élevée en une substance, communément un métal. Intrinsèquement, la métallogénie s'intéresse donc à des phénomènes extrêmes d'enrichissement à partir de traces, soit qu'ils impliquent des processus particuliers (anormaux), soit qu'ils résultent de processus communs, mais dont la combinaison est peu probable. Pour autant, les gisements ne sont pas exempts de classifications, certaines descriptives et d'autres plus interprétatives en fonction :

- de la roche porteuse et des suites métalliques (e.g. Chappel et White 1974)
- à plus grande échelle, des sites géodynamiques (voir partie A- ; Meyer 1988 ; Groves et al. 2005)
- de la température de formation ou du niveau structural (Lindgren 1933 ; Emmons 1936 ; Guilbert et Park 1986)
- des processus génétiques (Meyer 1981 ; Misra 2000)

La figure 4–3 est une représentation semi-quantitative de l'origine des gisements, autrement dit une classification suivant les processus génétiques. Ce type de classification présente le désavantage d'être soumis à l'interprétation de chaque gisement particulier (il ne classe donc pas les gisements pour lesquels la genèse n'est pas comprise, et il ne prend pas directement en compte l'évolution ou la modification de ces gisements). Cependant, la compréhension croissante des systèmes minéralisateurs, surtout ces vingt dernières années, gomme ces inconvénients. De plus, par définition, elle est attachée au processus géologiques sous-jacents aux minéralisations et c'est donc une perspective privilégiée pour une approche géologique générale. Dans ce cadre, la figure 4–3 met bien en évidence la forte participation des fluides hydrothermaux et, dans une moindre mesure, des magmas dans la métallogenèse. Nous allons donc définir ce que l'on entend par fluide et par magma. Lorsque l'on reporte quelques grands systèmes minéralisés, il n'y a pas de différence brusque entre les deux processus : il faut garder à l'esprit que les deux forment un continuum métallogénique.

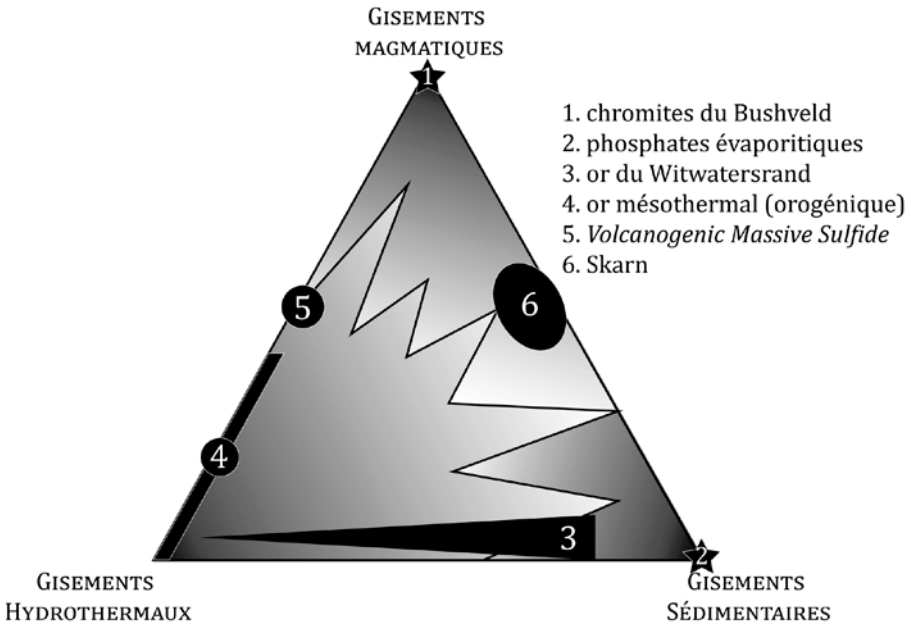

Figure 4—3 : *Diagramme triangulaire évaluant la part des différents contextes des minéralisations (d'après Robb, 2005). Quelques exemples de gisements et types de gisements sont reportés pour l'illustrer.*

- ***PROCESSUS MAGMATIQUES.*** Les grands processus à l'origine des minéralisations magmatiques sont ceux qui régissent classiquement la pétrogenèse de ces roches, mais à des degrés ou dans des conditions particuliers, et parfois quelques processus anormaux. La fusion d'une roche produit un magma, donc un liquide silicaté à haute température constitué majoritairement d'ions SiO_4^+, plus ou moins polymérisés (visqueux), et d'éléments additionnels (pricipalement Fe, Mg, Na, Ca, K, Al). Très rarement, le magma est carbonaté et cristallise sous forme de carbonatites (exemple dans le chapitre 3-E).

HERITAGE, FUSION PARTIELLE. Les liquides basaltiques se forment par la fusion partielle de péridotite mantellique, tandis que les liquides granitiques sont issus dans la majorité des cas de la fusion partielle de matériel crustal continental ou océanique (quand ils ne proviennent pas de la différenciation de liquide mafique). Or, d'une façon caricaturale, ces deux types de protolithes sont différents chimiquement : leurs compositions vont être héritées dans les liquides, en éléments majeurs comme en traces (lois de substitutions) et selon les réactions de fusions précises mises en jeu.

Ainsi les roches mafiques sont riches en Fe, Mg et en éléments traces comme Ni, V, Co, Cr, Pt (figure 4–4). Par exemple, la substitution du Mg par le Ni dans l'olivine produit une corrélation positive forte dans les roches mafiques, ce qui fait des komatiites, roches magnésiennes par excellence, de bons objets de départ pour les minéralisations nickélifères. À l'inverse, les roches granitiques sont plus riches en incompatibles majeurs (par exemple K, Na, Al) et en éléments traces comme U, Th, Li,

W, F, REE, Nb (figure 4–4). Ainsi, dans le leucogranite de Rössing en Namibie, la fusion d'un sédiment particulièrement enrichi en U (> 10 ppm) semble nécessaire à la viabilité de ce gisement d'U. Cette notion d'héritage semble être indispensable dans les gisements, sans être suffisante à elle seule dans la grande majorité d'entre eux. En effet, ce gisement de Rössing est aussi possible car la fusion partielle n'est efficace pour induire une minéralisation que sur des éléments très incompatibles et pour de faibles taux de fusion.

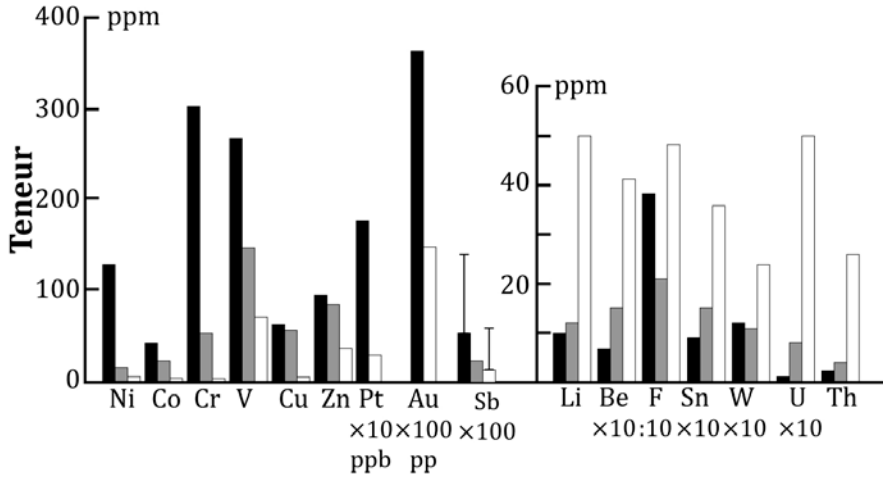

Figure 4—4 : *Histogrammes des concentrations en éléments choisis de basaltes (noirs), andésites (gris) et rhyolites (blanc) non-minéralisés. À gauche les éléments ont une affinité pour les roches mafiques, à droite pour les granitoïdes. L'antimoine aurait une légère préférence pour les magmas basaltiques (Robb 2005 et références incluses).*

CRISTALLISATION FRACTIONNEE. La cristallisation fractionnée des magmas s'avère être impliquée plus souvent dans les minéralisations magmatiques. Ce phénomène produit des minéraux néo-cristallisés et un liquide différencié en conséquence, qui s'enrichit en éléments incompatibles. Dans le cas de liquides mafiques peu visqueux, les cristaux denses sédimentent en formant des cumulats sous l'effet de la gravité (figure 4–5 ; en réalité la dynamique des chambres magmatiques est plus complexe, impliquant entres autres des courants convectifs ou la diffusion thermique et chimique). Par exemple le complexe mafique du Skaergaard comprend un niveau de sulfures, avec des inclusions d'alliage Au-Pd. Ceux-ci sont restreints à ses cumulats de fin de cristallisation, c'est-à-dire lorsque le S, Au et Pd, incompatibles jusqu'alors, sont concentrés dans le liquide résiduel.

Dans le cas des liquides acides, plus visqueux de plusieurs ordres de grandeur, on peut observer dans certains plutons une zonation concentrique (différentiation croissante vers le cœur). Cette dernière est attribuée à une progression de la cristallisation, produisant la séparation physique des phases. Le gisement en Sn de Zaaiplaats (granite du complexe du Bushveld) est un exemple où de la cassitérite cristallise dans la zone apicale lorsqu'un très fort degré de cristallisation fractionnée est atteint. Comme dans la fusion partielle, ces exemples « purs » sont rares, d'autres phénomènes s'ajoutent à la cristallisation fractionnée pour rendre compte de concentrations anormales en éléments.

CONTAMINATION. Un des objets minéralisés les plus documentés est le complexe du Bushveld, et plus précisément sa partie mafique. Parmi ses cumulats se trouvent au moins 14 niveaux de chromite dont l'un peut être suivi sur plus de 160 km. Irvine a proposé en 1977 un modèle pour expliquer, non pas l'occurrence, mais la quantité et la concentration anormale de ce minéral. Il invoque l'introduction dans le système basaltique évolué soit de magmas plus primitifs, soit de composants siliceux (par exemple l'encaissant crustal). Le mélange perturbe la thermodynamique du système qui précipite les chromites en masse. Cette contamination (mélange de magma ou assimilation) est invoquée de la même manière pour les chromitites podiformes ophiolitiques (figure 4–5).

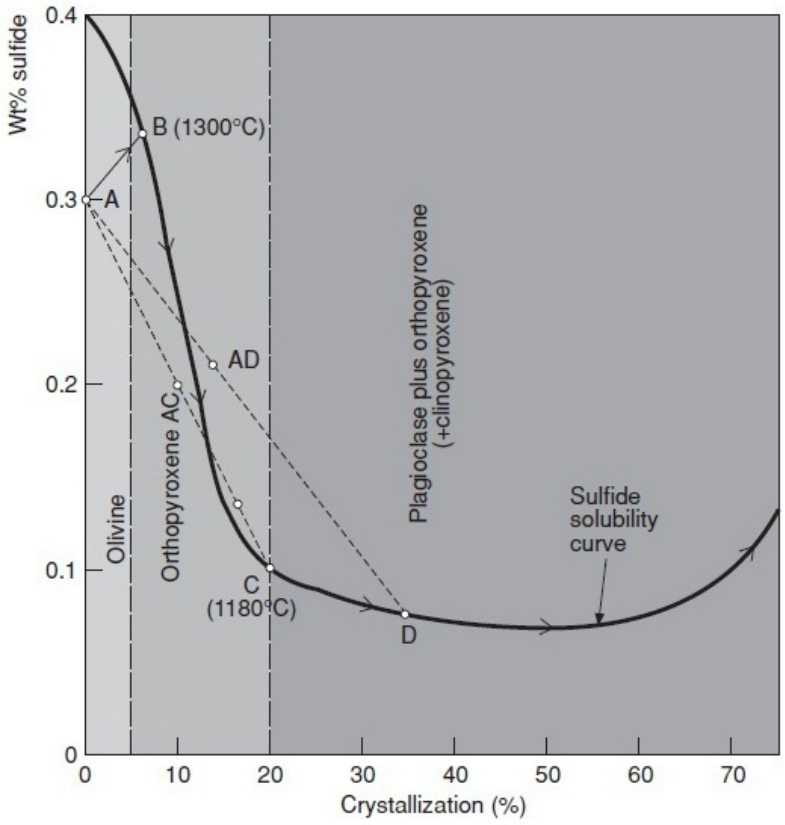

Figure 4—5 : *Illustration des processus magmatiques et de leur combinaison. Variation de la solubilité du sulfure au cours de la cristallisation fractionnée dans un magma mafique type Bushveld (d'après Robb 2005, tiré de Naldrett et von Grünewaldt 1989). De A à B, l'olivine est extraite par cristallisation fractionnée, impliquant la diminution de FeO dans le liquide et une baisse de la solubilité du S ; parallèlement, le sulfure (incompatible) est enrichi dans le liquide résiduel ; en B se forment des globules de liquide sulfuré en proportion cotectique, et ce jusqu'à C, voir D. Si le liquide C est injecté par un magma A et forme le mélange AC, alors il est sous le seuil de solubilité du sulfure et les globules disparaissent. Si le liquide D est injecté par un magma A et forme le mélange AD, le sulfure est insoluble et forme une fraction importante de liquide sulfuré immiscible. Le même principe est applicable aux chromites.*

IMMISCIBILITE. L'immiscibilité des liquides est un processus qui consiste en la séparation physique de deux phases liquides. L'immiscibilité silicate-oxyde des magmas alcalins serait rare et n'est pas prouvée comme métallogène. Au contraire, la

formation d'une phase sulfurée est plutôt commune au cours de l'évolution d'un liquide mafique. En effet, la saturation en sulfure est atteinte dès lors que, à partir d'une concentration en S dans le magma augmentée par la cristallisation fractionnée, la concentration en FeO diminue (précipitation d'olivine par exemple) ou la fO_2 (fugacité en oxygène) augmente (figure 4–5). De plus, la saturation est favorisée si la concentration en sulfure augmente par contamination (mélange de magma, assimilation, figure 4–5). Alors, des globules sulfurés se forment et ce type de liquide a de très fortes affinités pour les métaux chalcophiles (Ni, Cu, Co, Au, Pt). Pour atteindre la qualité de gisement, ces globules doivent rester en quantité limitée (pour concenter les métaux), interagir efficacement avec le liquide silicaté (pour prélever les métaux), et s'accumuler de façon non disséminée. C'est le cas des gisements Ni-Cu dans les komatiites de Kambala en Australie, où ces métaux ont été prélevés dans une phase sulfurée tôt dans la séquence de cristallisation, à la faveur d'une saturation en sulfure précoce lors de l'assimilation des sulfures de l'encaissant.

- ***PROCESSUS HYDROTHERMAUX.*** Des espèces volatiles, au premier rang desquelles l'eau et le dioxyde de carbone, sont communes dans les différentes enveloppes de la Terre, depuis l'hydrosphère jusque dans les roches de la croûte et du manteau (à l'exception du noyau). Un fluide hydrothermal fait donc référence à l'accumulation d'une ou de plusieurs de ces espèces volatiles en une phase à part entière, interagissant avec les roches (i.e. impliquée dans la dissolution, la précipitation et l'altération des minéraux).

En terme de volumes, l'eau est répartie entre l'eau externe, dominée à 98% par l'océan (1400×10^6 km^3, Berner et Berner 1996), l'eau interne du manteau (3 à 6 fois la masse des océans, Ahrens, 1989 ; Ringwood, 1975), et l'eau interne de la croûte (teneur de 2% pds, Wedepohl 1995). Ces volumes interagissent entre eux dans le cadre du cycle de l'eau interne (e.g. Ohtani 2005, cycle de l'eau « profonde », Berner et Berner 1996, cycle de surface) lors des processus d'enfouissement, de subduction, d'infiltration, de fusion et de dégazage des magmas. Les isotopes stables des éléments constitutifs des fluides (O, C, H) ont largement démontré leur utilité dans la compréhension des réservoirs et de leurs processus (flux) dès les années 1970 (e.g. Taylor 1978). Ainsi, les fluides aqueux sont catégorisés selon 4 grands réservoirs génétiques (figure 4–6a): eau météorique, eau connée, eau magmatique, eau métamorphique dont les signatures isotopiques sont illustrées en figure 4–6a.

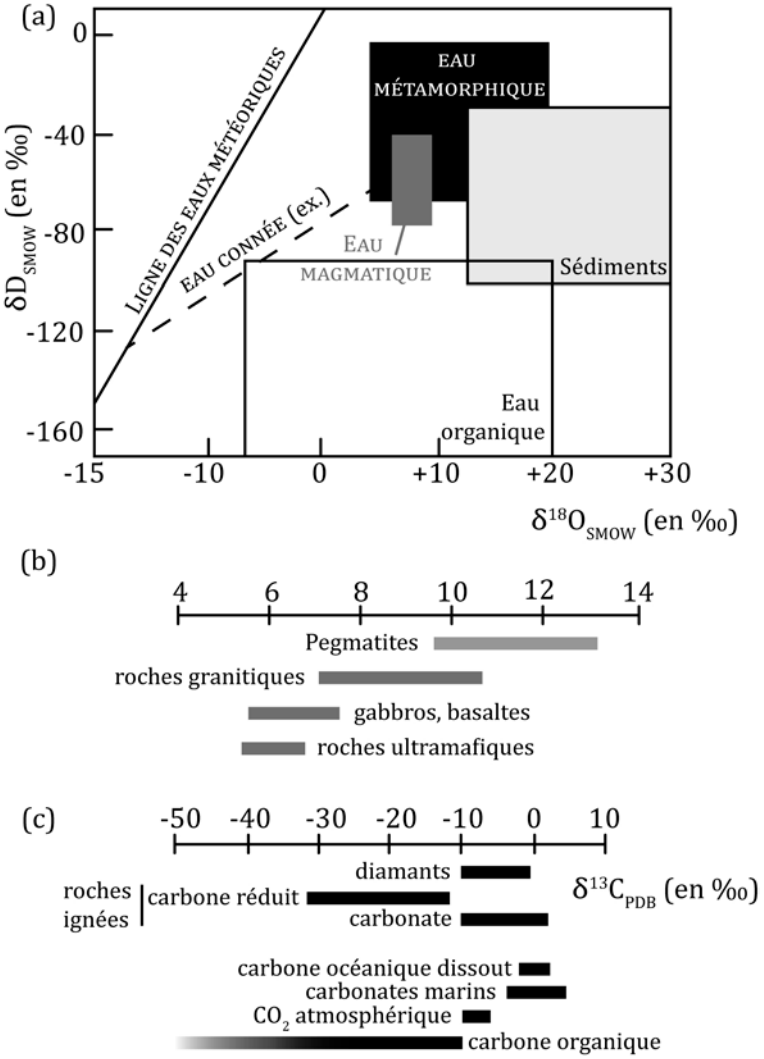

Figure 4—6 : *(a) Diagramme δD-δ¹⁸O et les signatures des réservoirs fluides (en gras majuscule). SMOW : Standard Mean oceanic Water, composition de l'océan. Pour le détail, voir texte. (b) signatures δ¹³C des réservoirs de carbone (modifiée d'après Misra 2012)*

FLUIDES METEORIQUES ET OCEAN. Les fluides météoriques correspondent aux eaux impliquées dans les phénomènes atmosphériques, donc de surface ou infiltrés : océan, glaces des calottes, eaux de pluie, de ruissellement, de lac, de nappes. Au vu de son volume et de sa position centrale dans le cycle externe de l'eau, la signature isotopique de ce système est imposée par l'océan. Les compositions des fluides dérivés (pluie, glaces, lac) obéissent alors aux lois de fractionnement isotopique lors des changements d'état dans des conditions de basse température, donc très sensibles à celle-ci.

L'atmosphère archéenne était beaucoup plus riche en CO_2 (31% vs 0.03% aujourd'hui) mais comme le CO_2 et H_2O sont immiscibles à basse pression, les fluides météoriques sont en fait des fluides aqueux incorporant des ions HCO_3^- dissous. Na^+ K^+ Ca^{2+} Mg^{2+}, Cl^- et SO_4^{2-} sont les solutés communs de ces eaux, jusqu'a 3.5 % pds pour l'eau de mer alors que les pluies en contiennent 3 à 4 ordres de grandeur moins.

La présence de l'océan est avérée par les dépôts sous-marins de sédiments et de laves dès 3.8 Ga et même fortement supposée dès 4.3 Ga à partir des isotopes de l'oxygène de zircons (Mojzsis et al. 2001). Sa composition semble constante autour de 0±2‰ au cours des temps géologiques (discussion dans Muelenbach 1998).

L'explication de cette constance tient au fait que ce volume d'eau interagit essentiellement avec la croûte océanique à la ride, qui est de composition constante au cours des temps géologiques, et selon des réactions métasomatiques et à des températures comparables à l'actuel (Muelenbach et Clayton 1976). Par ailleurs, les températures de surface donc les compositions isotopiques des eaux non-océaniques sembleraient équivalentes à l'actuel. On notera ici que les $\delta^{13}C$ des carbonates marins archéens (Veizer 1989) sont autours de 1.5 ±1.5 ‰, témoignant que le cycle externe est déjà en place.

Les implications métallogéniques directes des fluides météoriques concernent soit des processus superficiels (sédimentaires, altérations supergènes) soit des processus plus crustaux dès lors que ces fluides pénètrent dans la croûte (voir partie C). L'exemple le plus connu est celui des VMS (Volcanogenic Massive Sulfide) dans lequel l'eau de mer infiltre la croûte océanique le long des failles à la ride, se réchauffe, et réagit avec cette croûte en lessivant des éléments, notamment des métaux (Fe Cu Zn Mn) et en déposant d'autres éléments. En remontant vers la surface, ce fluide hydrothermal précipite des sulfures de ces métaux.

FLUIDES CONNES. Les fluides connés sont les fluides enfermés dans la porosité des sédiments. Ils proviennent de l'eau météorique mais s'équilibrent avec les sédiments, et ce au fur et à mesure de l'enfouissement (augmentation P-T). L'eau liée des minéraux est expulsée dès le début de la diagénèse et peut s'ajouter aux premiers fluides. Isotopiquement, les fluides connés représentent donc un intermédiaire entre les fluides météoriques et métamorphiques. Ces fluides ont des compositions variables selon le bassin et peuvent être très salés (jusqu'à 400‰ pds NaCl eq., Hanor 1979). Leur évolution séculaire est liée à l'évolution séculaire des types de bassins (plate-forme carbonatés, séquence argileuses…).

Ils peuvent être directement impliqués dans les minéralisations. Le cas typique est celui des dépôts de type Mississippi (MVT) : au Missouri, USA, le gisement de Viburnum Trend est un bassin carbonaté dont les fluides connés sont mis en mouvement par gravité lors de l'orogénèse varisque 200 Ma après le dépôt. Ils déposent alors des sulfures de Pb-Zn.

FLUIDES MAGMATIQUES. Les fluides magmatiques représentent les fluides issus des magmas. L'eau est incorporée dans les magmas lors de la fusion des minéraux hydratés (le rôle de l'eau sur la fusibilité des protolithes magmatiques est d'ailleurs crucial). Il n'existe finalement pas d'exemple naturel de magma strictement anhydre, avec un minimum de 0.9% pds H_2O dans les komatiites (Shimizu et al. 2001) et à l'opposé, la fusion de la muscovite peut facilement incorporer 7% pds H_2O dans un magma granitique. Soit par diminution de la pression (exolution dite de "première ébullition"), soit par cristallisation fractionnée (eau et dioxyde de carbone sont des composés incompatibles, "deuxième ébullition"), le magma devient saturé et une phase fluide s'en sépare. De part les types de sources, la densité des magmas et le caractère incompatible

de l'eau, les fluides magmatiques sont beaucoup plus reliés aux magmas granitoïdiques qu'aux magmas basiques.

Le dioxyde de carbone serait moins concentré d'un ordre de magnitude par rapport à l'eau, même si certains auteurs plaident pour la possibilité de former des fluides magmatiques riches en CO_2 (Burrow et Spooner 1987). H_2O et CO_2 ont cependant des comportements différents dans la gamme de conditions P-T magmatiques : la solubilité du CO_2 est beaucoup plus basse dans les magmas, et donc se sépare à des pressions plus hautes que H_2O lors de l'ascension des magmas dans la croûte. La solubilité du CO_2 est plus importante (4 à 5 fois) dans les magmas alcalins que felsiques. Au premier ordre, la composition élémentaire d'un fluide magmatique suit celle du magma dont il est extrait : Si sous forme de H_4SiO_4, métaux alcalins sous forme d'ions Na^+ et K^+, c'est-à-dire qu'on y retrouve les éléments incompatibles enrichis dans le magma évolué. Ils sont accompagnés de Ca^{2+}, Mg^{2+}, Fe^{2+}. L'anion principal est le Cl^-, suivi de HS^-, HCO_3^- SO_4^{2+}. À 10 kbar-650°C, la quantité de soluté dans ces fluides est expérimentalement de 9%, en proportion du liquide eutectique granitique (Burnham 1967) et ces fluides peuvent donc précipiter des objets minéralogiquement identiques à un granite (pegmatites). À 2 kbar, la quantité de soluté est d'environ 0.7% pds, et le rapport Si/(Na+K) augmente : les fluides magmatiques précipitent des veines de quartz vers la surface.

La composition isotopique en oxygène d'un magma est imposée par sa source et modifiée par la différenciation qu'il subit (par exemple +1‰ en $\delta^{18}O$ par augmentation de 3% pds de SiO_2 pour un granite, Tartèse et Boulvais, 2010). Pour un même contexte de formation, les magmas "mantelliques" ont les mêmes signatures isotopiques, quel que soit leur âge, car le manteau n'a pas varié isotopiquement. Ainsi, les magmas primaires issus du manteau ont des signatures mantelliques (5.7-7.5‰, komatiites, basaltes, gabbros, Lahaye and Arndt 1996), la signature des TTG et des adakites est la même (Bindeman et al. 2005). Au contraire, le passage d'un régime d'extraction mantellique à un régime de recyclage de la croûte continentale (c'est-à-dire le changement fondamental de la source des magmas, voir chapitre 1) change la signature des magmas (ex sanukitoïde *versus* TTG, King et al. 1998). Or la signature est transmise aux fluides magmatiques formés à l'équilibre avec les magmas à haute température. Cependant, les variations sont de l'ordre de 3‰ en isotopes de l'oxygène, au premier ordre les fluides magmatiques restent donc constants au cours de l'évolution de la Terre.

Ces fluides magmatiques sont directement responsables de nombreux types de minéralisations en métaux. Une des raisons principales est que les métaux initialement dans le magma se partitionnent nettement en faveur des fluides aqueux (cas général), en s'associant avec des anions dits ligants, comme avec les sulfures dans les liquides immiscibles sulfurés. Deux exemples l'illustrent :

- Les gisements pegmatitiques (Sn, W, B, F, P, Li, Cs, Ta, Nb). Ces objets matérialisent des fluides assez primaires, même si les conditions exactes de

leurs formations ne sont pas totalement élucidées (considérations métastables). À Manitoba au Canada, la pegmatite de Tanco à Li-Cs-Ta cristallise de 700°C à 300 °C à partir d'un fluide aqueux (98 mol% d'H_2O, étude des inclusions fluides, Thomas et al. 1988).

- Les gisements porphyriques à Cu-Mo. Ces minéralisations sont intiment associées à des roches d'affinité calc-alcaline de zone de subduction type andine (magma type I) formées par fusion d'un protolithe amphibolitique ± biotite. Quand ces magmas atteignent la croûte supérieure, les éléments Cu et Mo s'échappent dans les fluides magmatiques pour lesquels ils ont une plus forte affinité. La quantité d'eau, la profondeur de mise en place et le degré de cristallisation contrôlent ensemble la balance Cu/Mo.

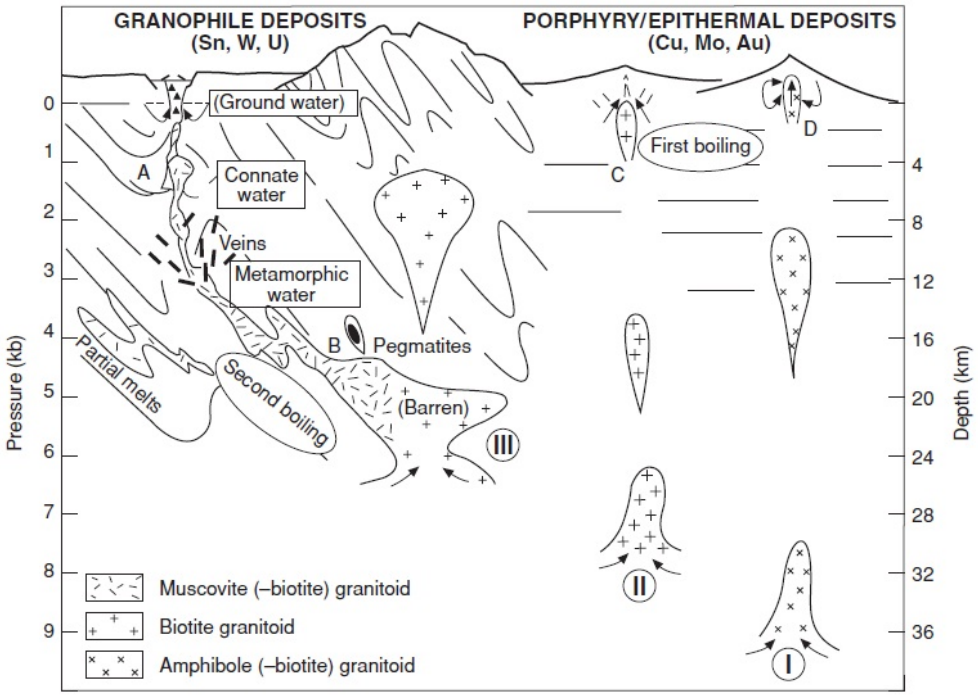

Figure 4—7: *Modèle de Strong liant la nature du granitoïde, le style de mise en place et les caractéristiques métallogéniques (Robb 2005 d'après Strong 1988).*

FLUIDES METAMORPHIQUES. Les fluides métamorphiques sont produits par la déshydratation et la décarbonatation des roches lors de l'augmentation de la pression et de la température. En effet, dans le métamorphisme (ca >200°C), les réactions qui impliquent des phases hydratées (phyllosilicates, amphiboles) réagissent en formant des phases anhydres (ou moins hydratées) et de l'eau ("défavorisés" dans les systèmes cristallins vers les hautes températures car ils ont une forte entropie). De même, l'oxydation du graphite et la décarbonatation des minéraux carbonatés libèrent du CO_2. Ces fluides sont donc produits dans le métamorphisme prograde. Dans une roche donnée, ces réactions se produisent par paliers déclenchant des pics de production de fluides (ex. Stevens et al. 1997, figure 4—8a).

Les fluides métamorphiques sont composés d'H_2O et CO_2 (et de CH_4 mineur, en conditions réductrices). En particulier, le fluide est à $H_20>CO_2$ du faciès schiste vert à

amphibolite inférieur, CO_2>H_2O en facies granulitique. La composition élémentaire est très variable, en fonction des roches desquelles le fluide est extrait, des réactions impliquées et du degré métamorphique (exemple de roche ultramafique, figure 4–8b). On notera surtout que, sauf interaction avec des niveaux évaporitiques, la quantité de soluté est faible dans ces fluides (< 10% pds équivalent NaCl) relativement à l'eau de mer et aux saumures magmatiques. La variabilité élémentaire est aussi reconnue isotopiquement ($\delta^{18}O$=+5 à +20‰, figure 4–6) car la signature dépend elle aussi du protolithe et des fractionnements mis en jeu (réaction et température). Ainsi, les fluides métamorphiques ont des compositions isotopiques recouvrant celles des fluides magmatiques (figure 4–6).

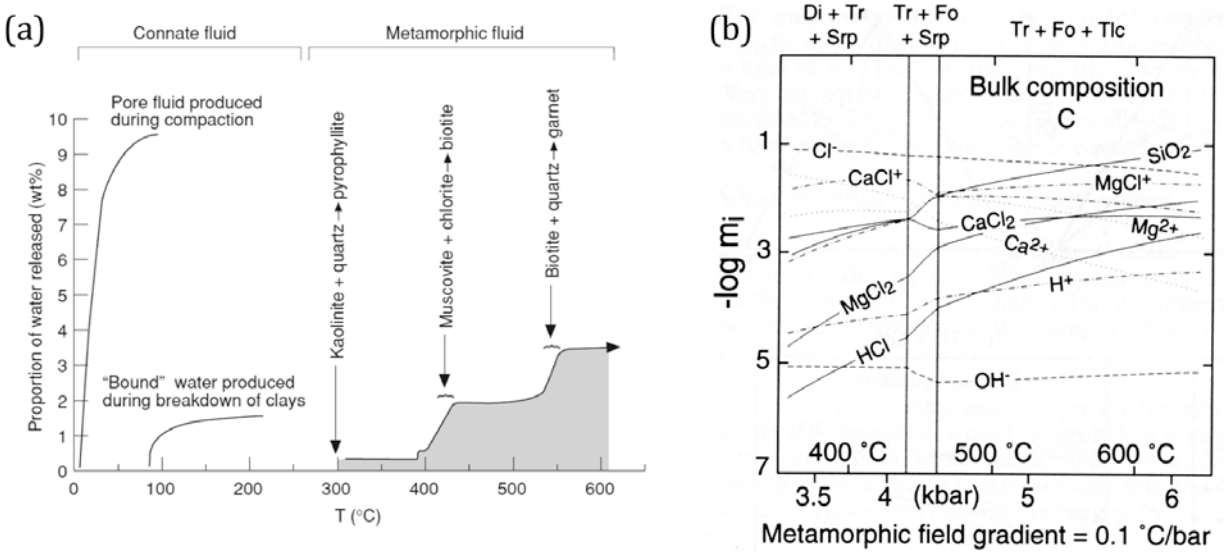

Figure 4–8 : *(a) Production des fluides par pics au cours du métamorphisme prograde (exemple du bassin du Witwatersrand, Steven et al. 1997). (b) Évolution théorique (calcul thermodynamique) au cours du métamorphisme de la composition d'un fluide en espèces dissoutes en équilibre avec une roche ultramafique. Di diopside Tr trémolite Srp serpentine Fo forstérite Tlc talc (Eugster et Baumgartner 1987).*

Leur évolution séculaire est théoriquement rattachée à celle de la croûte et des températures régnant dans celle-ci (gradient géothermique). La croûte évolue peu en $\delta^{18}O$ dans son ensemble (voir fluides magmatiques). Les gammes de température, si elles varient au cours des temps géologiques (voir paradoxe thermique à la fin du chapitre 2), n'ont que peu de répercussions isotopiques dans ces hautes températures. Il ne doit donc pas y avoir une évolution séculaire symptomatique de ce type de fluides.

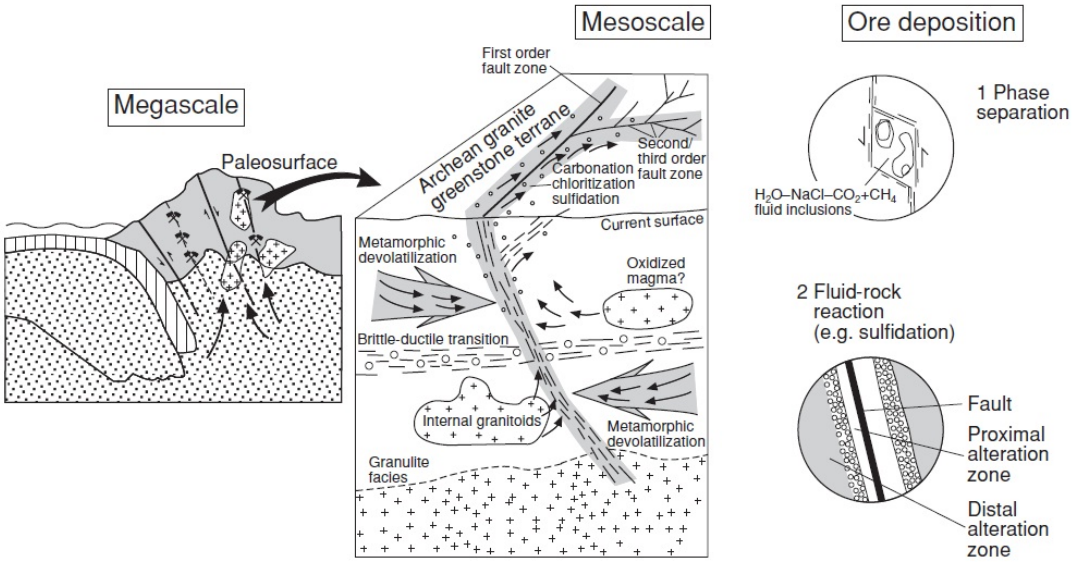

Figure 4—9 : *modèle synthétisant la formation des gisements d'or orogéniques. Le rôle des fluides météoriques et magmatiques est encore sujet à débat, toutefois, il est clairement établi aujourd'hui que la majorité des fluides est métamorphique (figure de Robb 2005, d'après Hagemann et Cassidy 2000).*

Enfin, peu de types de gisements sont exclusivement attribués à des fluides métamorphiques : le seul exemple significatif est celui des gisements d'or orogéniques, aussi nommé or en filon (lode-gold). Ce ne sont pour autant pas les moindres puisque 60% de l'or dans le monde en provient (directement, et indirectement par l'or du bassin du Witwatersrand). La figure 4–9 illustre la formation de ces gisements. Lors d'une collision et du métamorphisme régional associé, les fluides métamorphiques infiltrent des cisaillements crustaux des ceintures de roches vertes et des orogènes. Ils y concentrent l'or qui précipite dans des veines de quartz ± carbonate par séparation de phase et/ou par réaction avec l'encaissant.

- Les tailles relatives des réservoirs fluides ont été différentes à l'Archéen, puisque les espèces volatiles suivent la différenciation de la Terre. Par exemple, la Terre « profonde » était plus hydratée comme l'indique des évidences de liquides ultramafiques hydratés (Williams et Hemley 2001). Les relations entre les réservoirs (flux) ont elles aussi été modifiées : flux manteau-croûte et diminution de la croissance crustale, flux manteau atmosphère et diminution de la longueur des rides. Pourtant, il ne semble pas exister de réservoir spécifiquement archéen d'un point de vue isotopique en oxygène ou en carbone ou chimique (de Ronde et al. 1997), et les processus régissant les réservoirs fluides sont universels (par exemple métamorphisme, fusion, infiltration).

PRECIPITATION DES METAUX. Les fluides sont métallogéniques car d'une manière générale la plupart des métaux sont partitionnés préférentiellement dans le fluide aqueux où la présence de ligants (Cl^- ou HS^- SO_4^{2-} OH^-, HCO_3^-) augmente la solubilité des métaux. Cependant, les métaux dissous n'y sont qu'à l'état de traces. Comme pour les processus magmatiques, des phénomènes additionnels sont nécessaires pour atteindre la saturation des complexes métal-ligant et précipiter de façon concentrée un métal. Basiquement, ces complexes sont déstabilisés par la modification des conditions thermodynamiques du fluide. Évidement, les fluides naturels minéralisateurs résultent souvent de la combinaison des processus évoqués ci-après.

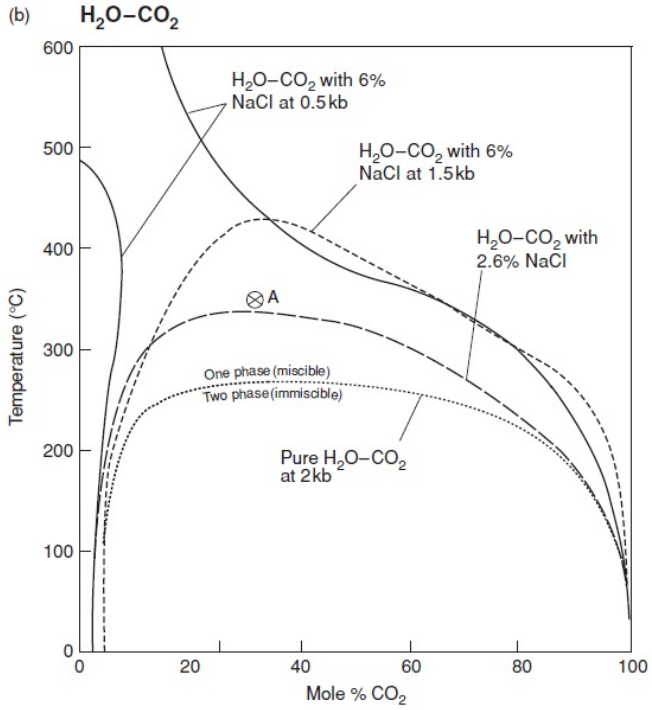

Figure 4–10 : *Diagramme de phase H_2O-CO_2. Les solvus sont perturbés par la salinité de la solution. (Robb 2005 d'après Brown 1998).*

Ainsi, une simple baisse de la température permet souvent d'atteindre la saturation. Ce processus s'applique surtout aux complexes chlorés dans des conditions épithermales, par exemple dans les VMS. Dans des conditions épithermales également, la diminution de la pression provoque l'apparition dans le fluide supercritique d'une phase vapeur ("*boiling*"). Le soufre passe préférentiellement dans cette dernière, déstabilisant ainsi les complexes sulfurés. C'est par exemple le cas des gisements d'or épithermaux (Cook et Simmons 2000). De même, la phase résiduelle est enrichie en sels et voit son pH augmenter, ce qui peut précipiter également les complexes chlorés. De la même manière qu'il existe des séparations de phases entre liquide silicaté magmatique et phase aqueuse (paragraphe fluides magmatiques), le CO_2 peut se séparer d'un fluide. La miscibilité entre l'eau et le CO_2 augmente avec la température, ces deux espèces devenant totalement miscibles à environ 265°C et 1,5-2 kbar (Takenouchi et Kennedy 1964). En dessous de ce solvus, l'apparition d'une phase riche en CO_2 et d'une phase riche en H_2O (démixion) modifie la stabilité des complexes. C'est un processus susceptible d'apparaitre dans des conditions plus mésothermales lors des chutes de pression épisodiques dans le modèle de valve de Sibson (1987) et invoqué

dans les gisements d'or orogéniques. Inversement, le mélange de fluides différents implique une modification drastique de stabilité des complexes métaux-ligant dans le mélange (météorique-magmatique par exemple) et force la précipitation des complexes métalliques. Ce serait un phénomène courant des gisements superficiels comme par exemple dans le gisement d'oxyde de fer, de cuivre et d'or d'Olympic Dam (Haynes et al. 1995) ou dans le cas des skarns (précipitation de galène, sphalérite chalcopyrite tardive liée à des fluides météoriques).

Métasomatose. Fréquemment, la circulation d'un fluide altère la roche encaissante. Les réactions impliquées modifient aussi la composition du fluide. Elles sont diverses et fonction de multiples paramètres (e.g. Reed 1997) : la composition initiale de la roche encaissante, celle du fluide, les conditions physiques (pression-température, porosité) et l'évolution de l'interaction fluide/roche. Deux grandes catégories de réactions jouent un rôle prépondérant sur la précipitation des complexes métal-ligant : les oxydoréductions qui changent la fugacité en O_2 (fO_2) et S_2 (fS_2), et les réactions acide-base qui changent le pH. Quelques exemples de réactions métasomatiques avec l'encaissant sont présentées ci-dessous. Elles peuvent par exemple influencer la solubilité de l'or (Figure 4–11) :

- A-A', exemple d'acidification d'un fluide : la chloritisation des feldspaths

$$2NaAlSi_3O_8 \text{ (albite)} + 4Mg^{2+} \text{ (aq)} + 2(Fe,Al)^{3+} \text{ (aq)} + 10H_2O \text{ (aq)} \rightarrow Mg_4(Fe,Al)_2Si_2O_{10}(OH)_8 \text{ (chlinochlore)} + 4SiO_2 + 2Na^+ \text{ (aq)} + \mathbf{12H^+} \text{ (aq)}$$

- B-B', exemple de neutralisation d'un fluide: échange d'H^+ contre cation métallique alcalin

$$\mathbf{2H^+} \text{ (aq)} + 2NaAlSi_3O_8 \text{ (albite)} \rightarrow 2SiO_2 + 2Na^+ \text{ (aq)} + Al_2Si_4O_{10}(OH)_2 \text{ (pyrophyllite)}$$

- B-B'', exemple de réduction d'un fluide : hématisation

$$8FeO \text{ (roche)} + SO_4^{2-} \text{ (aq)} + 2H^+ \text{ (aq)} \rightarrow 4Fe_2O_3 \text{ (hematite)} + \mathbf{H_2S \text{ (aq)}}$$

Le métasomatisme est donc une preuve de paléo-circulations (avec la présence de veine). En pratique, la terminologie des métasomatoses rend compte des produits finaux et donc des réactions en jeu : par exemple carbonatation, silicification, séricitisation, albitisation. L'intensité des interactions fluides-roches est fonction des réactions mais surtout du rapport fluide/roche : ce rapport synthétise à quel point le fluide (ou la roche) a dominé le système géochimiquement et physiquement (thermique, pression de fluide).

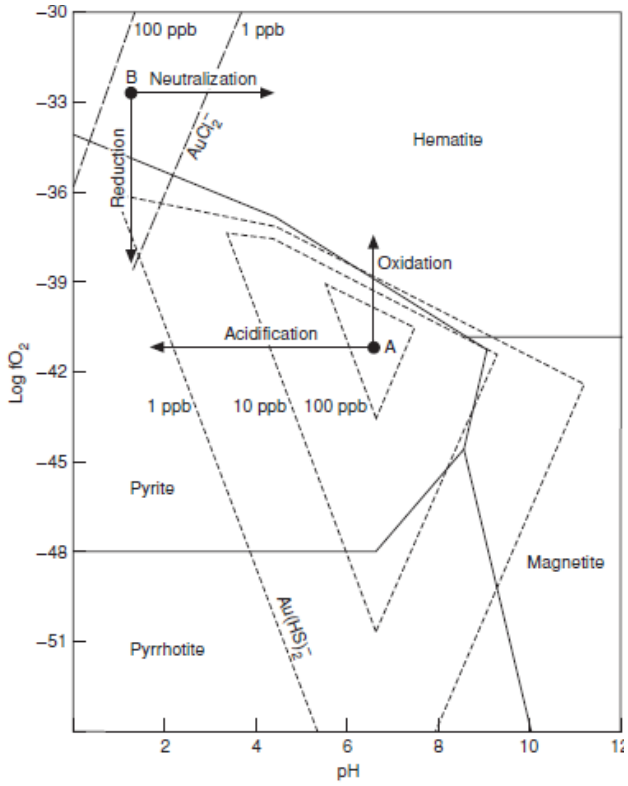

Figure 4–11 : Stabilités des complexes $AuCl^{2-}$ et $Au(HS)_2$ en fonction du pH et de l'oxydation (fugacité en oxygène) du fluide (d'apès Robb 2005)

C — Mobilités et zones de cisaillements

Les fluides aquo-carboniques sont très peu visqueux, on parle même de *fluides supercritiques* pour décrire leur comportement intermédiaire entre liquide et vapeur. Les magmas sont visqueux, voire très visqueux dans le cas des magmas acides et les mélanges magmas + cristaux. Leur rhéologie respective est certes différente, mais les fluides et les magmas sont tous des fluides au sens physique, et donc capables de se déplacer. Mais pour se déplacer et donc transporter et redistribuer les éléments dont ceux des minéralisations, il faut deux conditions. Tout d'abord il faut qu'il y ait un moteur. Naturellement, ces phases sont moins denses que leur encaissant crustal. La mobilité est aussi exacerbée par des moteurs correspondant physiquement à des gradients thermiques et/ou de pression : gravité (relief), compaction, échauffement/refroidissement, pompage sismique (Garven et Raffensperger 1997). Ensuite il faut qu'il existe un chemin de percolation, une connectivité. Cela peut être auto-provoqué dans le cas de surpression de fluide mais ce n'est valable que pour des pressions lithostatiques minimes, c'est-à-dire près de la surface.

La déformation joue alors un rôle essentiel dans cette connectivité. Elle diminue la taille de grain et augmente la porosité des roches. Quand les structures sont localisées (failles et zones de cisaillement ductile) elles constituent des drains pour les fluides (revue dans McCaig 1997). La déformation peut même être active sur la circulation quand, en régime compressif, le mouvement le long de plans cisaillants provoque des sous-pressions dans les irrégularités du plan : c'est le phénomène de pompage sismique (figure 4–12 ; Sibson 1987). C'est un processus invoqué par exemple dans les gisements d'or orogéniques (voir figure 4–9).

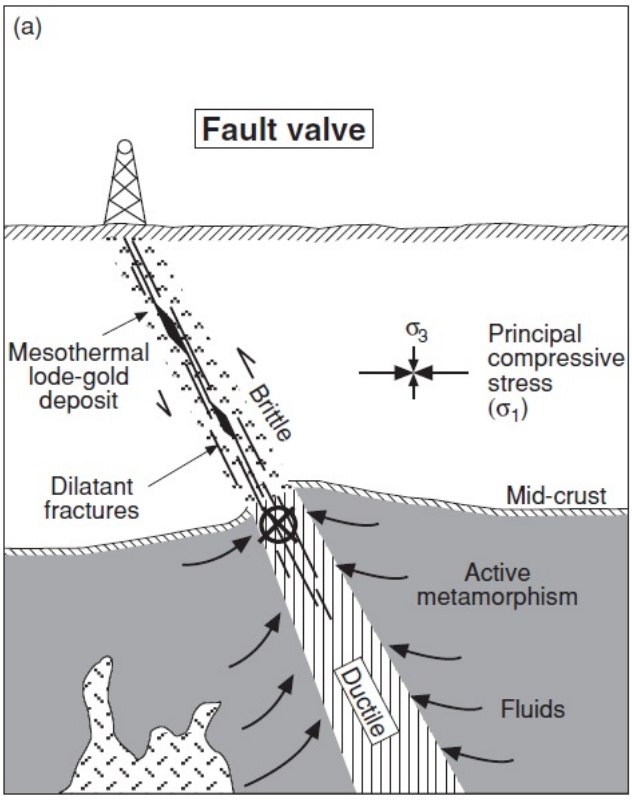

Figure 4–12 : *shéma de principe du pompage sismique sur une structure crustale compressive (Robb 2005 d'après Sibson 1987).*

Ainsi, des fluides sédimentaires peuvent infiltrer la croûte *per descendum* jusqu'à 10-15km de profondeur (par exemple Boiron et al. 2003 ; synthèse dans McCaig 1997). À l'inverse, les fractures sont indispensables à la remontée des magmas selon Clemens et Mawer (1992). Les zones de cisaillement sont donc les lieux de passage privilégiés des magmas et des fluides, de leur rencontre, et donc des transports et des précipitations d'élements associés.

D — Dater et caractériser les minéralisations

CARACTERISATION ET DATATION. L'intérêt économique des zones minéralisées stimule la production de données rendant accessible les échantillons, la géométrie 3D des objets (obtenue par prospection géophysique, de mines, de forages), mais aussi par des analyses géochimiques. Par exemple, les connaissances sur la géologie du craton du Kaapvaal sont apportées en partie grâce aux investigations menées dans le cadre de prospection de ressources minérales. La caractérisation consiste ensuite à comprendre le processus minéralisateur, idéalement dans son ensemble :

- la(les) source(s) des différents constituants (métal, fluide, magmas)
- le transport
- le moteur du système
- les conditions physico-chimiques lors du dépôt du minerai (P, T, contraintes, état d'oxydation fO_2, pH)

- le fonctionnement interne du système (vitesses et durées des processus, variabilité)
- l'âge du dépôt

Les outils nécessaires impliquent tous les domaines de la géologie. Les études structurales sont importantes, surtout dans le cas des fluides (voir C- ; articles #2 et #4). Comme une minéralisation consiste en une concentration anormale en un élément, c'est la géochimie qui est l'outil central dans le cadre de ce travail (articles #3, #4, #5) mais aussi d'une manière générale pour les minéralisations endogènes. Il s'agit d'abord de quantifier les compositions élémentaires et isotopiques de la minéralisation, de la roche et de ses minéraux (elle s'appuie donc sur la pétrologie). À partir de cette documentation, la géochimie permet alors de s'attacher à 3 grands axes pour caractériser la minéralisation :

(i) le **traçage** (du magma, de la roche, des éléments, du fluide)
(ii) les **interactions fluide-roche** (cas des minéralisations fluides)
(iii) l'**âge** des objets (géochronologie)

Sans faire une revue exhaustive, il n'existe pas de systématique entre la méthode employée et les applications qu'elle peut avoir. Par exemple, la mesure des isotopes de l'oxygène peut contraindre l'origine d'un fluide ou bien les interactions fluide-roche, les systèmes isotopiques radiogéniques peuvent avoir des applications de tracage et/ou de datation.

La datation fait partie intégrante de la caractérisation générale d'une minéralisation. Déterminer l'âge d'une minéralisation permet de contraindre le processus minéralisateur lui-même. Si les phénomènes magmatiques, métamorphiques, tectoniques ou sédimentaires locaux sont documentés, la datation permet de rattacher (ou non) le fonctionnement du système minéraliateur à l'un d'eux et de discuter des liens de cause à effet. De plus, le phénomène minéralisateur daté complète l'histoire géologique d'une zone et souligne par exemple un pic d'activité.

DATER LES MINERALISATIONS. Il est finalement rarement possible de dater directement le minerai (méthode Re-Os, Mao et al. 2002 ; gisements d'uranium). Il s'agit alors d'établir un lien génétique entre un objet datable et la minéralisation.

Par définition, les minéralisations magmatiques sont co-génétiques de leur magma. Les magmas différenciés, enrichis en U-Th, fournissent aisément des minéraux datables (typiquement U-Pb sur zircon). Cependant, la datation peut s'avérer plus compliquée pour les magmas basiques. On peut alors cibler des phases dans l'auréole de contact développée dans l'encaissant (e.g. Buick et al. 2001).

Ainsi, les phases mafiques du complexe du Bushveld, par exemple, étaient datées à ± 27 Ma jusqu'en 1991 (2061 ± 27 Ma), puis par encadrement grâce aux âges obtenus sur les phases felsiques du complexe jusqu'en 1997 (2054 ± 2 Ma, 2060 ± 2 Ma). En 2001 le développement de la technique U-Pb sur titanite à permis de dater l'altération

hydrothermale de l'encaissant (Buick et al. 2001), mais ce n'est qu'en 2008 que Scoates et Friedman fournissent des âges directs.

Dans le cas des minéralisations hydrothermales, le minerai peut avoir co-précipité avec une phase datable (le zircon cristallise par exemple jusqu'à des températures aussi basses que 300°C). Dans le cas contraire, une difficulté supplémentaire tient au fait que les fluides étant mobiles, il existe souvent une distance significative entre la minéralisation et son origine. C'est justement dans ce cas que la caractérisation de la minéralisation apporte des contraintes pour la datation :

- l'âge de l'encaissant.
- l'âge de l'altération de l'encaissant.
- l'âge de la déformation.
- l'âge de la source d'un élément.
- l'âge du moteur.

De part la physique qui les gouverne, les systèmes isotopiques radiogéniques sont intrinsèquement des chronomètres. Classiquement, la géochronologie des roches endogènes repose sur le concept de température de fermeture d'un minéral ou d'une roche pour un système radiométrique donné : l'âge mesuré est le temps écoulé depuis son dernier passage sous cette température (ou directement depuis la cristallisation si la température de fermeture lui est supérieure). Récemment, Villa (2010) et Tartèse et al. (2011) insistent sur l'influence des fluides sur les chronomètres. Tartèse et al. (2011) mettent en particulier en évidence l'influence différentielle selon les systèmes (radiogéniques et minéraux), qui implique que la géochronologie des systèmes altérés doit être interprétée avec la caractérisation chimique et texturale des phases.

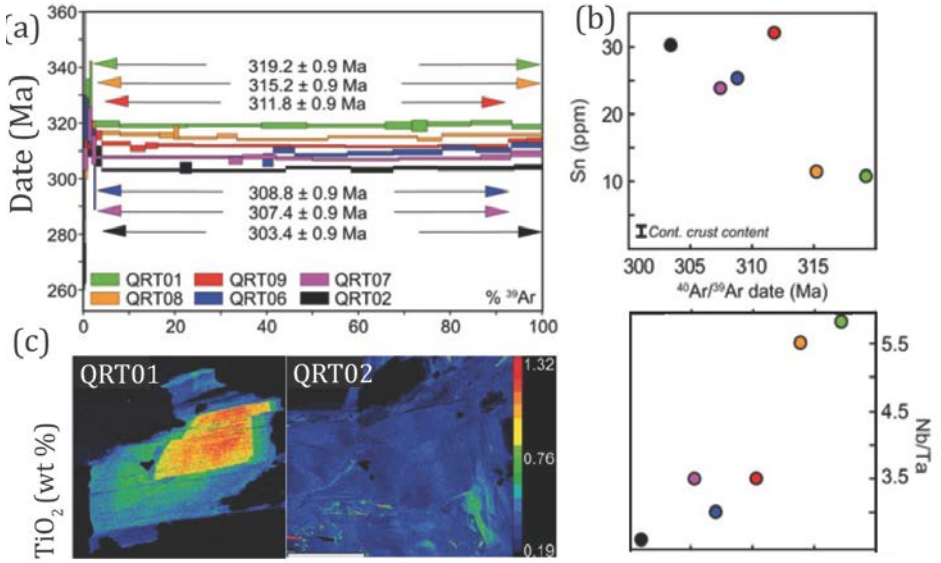

Figure 4–13 : *Influence des fluides sur la datation Ar-Ar (Tartèse et al. 2011). (a) Les ages apparents des muscovites sont liées en (b) à la chimie de la roche en métaux et en (c) aux textures mêmes des muscovites.*

E — Minéralisations en antimoine

UTILISATIONS, ECONOMIE (sources : Ward 1998 ; Butterman et Carlin 2004 et références incluses). Sa forme métallique pure est friable et donc l'antimoine n'est que très peu utilisé tel quel. L'antimoine a deux applications principales. Dans la première (20% de la consommation mondiale), il est associé en alliage avec le plomb ou l'étain, où il en augmente la résistance et ralenti la corrosion : il est utilisé dans divers objets comme les batteries, les munitions, les roulements à métaux, les tuyaux résistants à la corrosion, les soudures, les gaines de câbles, les intérieurs de cuves. Dans la deuxième, il est utilisé sous forme de trioxyde comme retardateur de flammes (60%) par exemple pour les textiles, dans la fabrication de plastiques (PVC, PET), de caoutchouc. Il trouve des applications dans les semi-conducteurs, dans l'industrie du verre et dans la peinture.

En 2010, le principal pays producteur est la Chine, suivie de l'Afrique du Sud, la Bolivie et la Russie (environ dans les mêmes proportions). Les réserves sont elles aussi détenues surtout par la Chine, puis la Russie, la Bolivie et au 5e rang l'Afrique du Sud (pour laquelle l'Antimony Line est le principal producteur). La demande mondiale en Sb s'accroit tandis que la Chine a le monopole de production et donc de l'offre (90%). En conséquence, le marché de l'antimoine est tendu et les institutions européennes et britanniques qualifient ce métal de critique (au même titre que les Terres Rares, par exemple ; European Union 2011, British Geological Survey 2011).

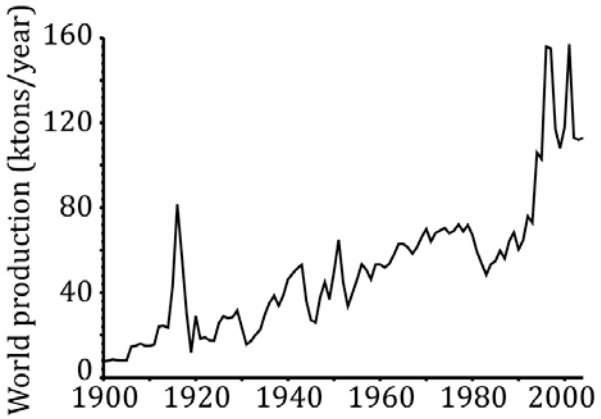

Figure 4–14 : *production d'antimoine mondiale (Butterman et Carlin 2004)*

- **MINERALISATIONS.**

GEOCHIMIE. Le clarke de l'antimoine serait de 0.2 g/t[1] (0.2 ppm), soit 2 ordres de grandeur de plus que l'or, 1 ordre de grandeur de moins que l'arsenic (Figure 4–4; Robb 2005). De numéro atomique 51, l'antimoine forme avec le silicium, le germanium, l'arsenic et le tellure un groupe intermédiaire entre les métaux et les non-métaux. Deux

[1] Chiffre cité par Robb (2005), Butterman et Carlin de l'USGS (2004) et le site www.mineralinfo.fr (partenaire du BRGM, http://www.mineralinfo.org/substance/Antimoine/SbDCE.pdf), mais sans référence directe associée.

états d'oxydation existent, Sb(III) et Sb(V), en phase aqueuse la forme prédominante est le Sb^{3+} (Robb 2005). Dans la classification acide-base de Lewis, il fait partie des métaux intermédiaires, c'est-à-dire qu'il est aussi bien associé à des ligants "doux" (HS^-, H_2S, $S_2O_3^{2-}$ etc) qu'à des ligants « forts » (OH^-, CO_3^{2-}, SO_4^{2-} etc) : les complexes stables sont $Sb(OH)_3$ à l'état oxydé, et $HSb_2S_4^-$ dans les fluides concentrés en sulfures (Robb 2005). Il est décrit comme chalocophile, précipitant sous forme de stibine la plupart du temps (*stibnite* en anglais Sb_2S_3), parfois sous forme de sulfosels ($X_aSb_bS_c$, X = Fe, Pb, Cu,…). Des oxydes d'antimoine sont produits par dégradation en surface.

Dans les roches magmatiques, il montrerait légèrement plus d'affinité pour les roches basaltiques que rhyolitiques (figure 4–4) mais il n'y a pas de minéralisations en Sb rapportées dans les roches magmatiques. Les gisements d'antimoine sont hydrothermaux, ceci dit, ils montrent une certaine diversité qui n'a pas encore fait l'objet de synthèse exhaustive.

Repartition temporelle et spatiale. de Wit et Tiard (2005) quantifient que, comme nombre de métaux, les gisements Sb-Sn sont plus fréquents (par unité d'espace) dans les roches archéennes que dans les roches post-archéennes. Cependant, deux biais doivent être soulignés dans cette étude : premièrement le lien entre le Sb et le Sn n'est pas systématique et un découplage des deux fausserait les conclusions sur le Sb seul ; deuxièmement, comme souligné dans l'étude, il peut exister un biais d'exploration entre les zones cratoniques réputées métallifères et les zones non cratoniques. À l'opposé, des auteurs comme Kerrich et al. (2005) ou Goldfarb et al. (2005) regroupent l'antimoine avec le mercure dans la catégorie des gisements épizonaux épithermaux. Or Groves et al. (2005) soulignent le déficit de dépôts epithermaux archéens en général, les zones superficielles ayant d'autant moins de chance d'être préservées qu'elles sont vieilles. Des minéralisations à antimoine sont reconnues tout d'abord sur quelques cratons archéens : Zimbabwe (e.g. Buchhholz et al. 2007) ; Ylgarn (e.g. Hagemann et Luders 2003), Pilbara (e.g. Huston et al. 2002); Superior Province (e.g. Powell et Patison 1997) et Kaapvaal (e.g. van Eeden et al. 1939). La chaine hercynienne au sens large comprend aussi de nombreux dépôts étudiés : Massif Central (e.g. Bellot et al. 2003), Massif Armoricain (e.g. Bailly et al. 2000), Appalaches canadiennes (Normand et al. 1996, Kontak et al. 1996). Un autre groupe de minéralisations se distinguent, celles liées à la cordillère américano-andine depuis le Canada (Nesbitt et al. 1989) jusqu'à la Bolivie (Dill 1998) en passant par le Mexique (Soyatal, White 1948). Enfin, les gisements les plus productifs et potentiellement les plus grands sont en Chine (province de Hunan, e.g. Peng et al. 2003). Les âges des gisements sont donc très variables et ne montrent pas de tendance à long terme.

Processus. Quand elles sont datées, les minéralisations à Sb sont épigénétiques, déconnectées de l'âge de la roche encaissante. Elles sont filoniennes (e.g. Massif Central) ou stratiformes (e.g. gisement de Xikuangshan, Peng et al. 2003). Les deux morphologies pourraient être continues verticalement (Pellisionnier 1997 et références incluses, Dill 1998). De plus, elles se rencontrent dans des lithologies très différentes depuis des complexes ultramafiques (Buchholz et al. 2007) jusqu'à des

turbidites (Huston et al. 2002) et des carbonates sédimentaires (e.g. gisements de Xikuangshan). Cela suggèrerait que, d'une manière globale, la chimie de la roche encaissante et les processus métasomatiques associés n'ont pas ou peu d'influence sur la précipitation de l'antimoine. Toutefois des zones d'altération sont rapportées par Bucholz et al. (2007) et Dill (1998), tandis que les gisements stratiformes sont souvent associés à des séquences carbonatées : dans ces cas, la lithologie pourrait jouer un rôle sur la précipitation de stibine.

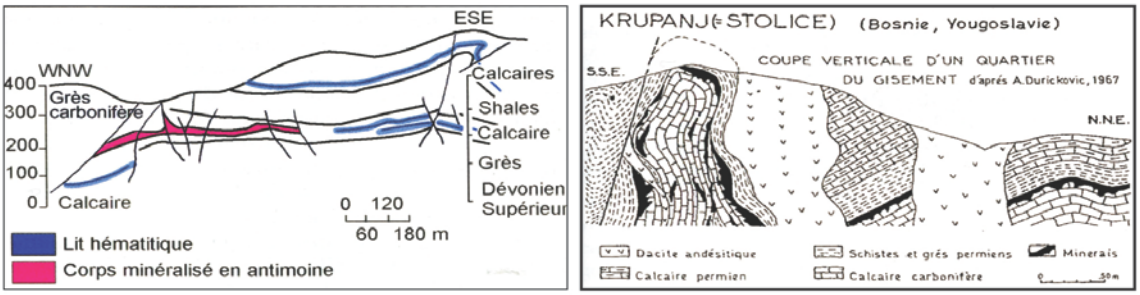

Figure 4–15 : *Gisements stratiformes carbonatés. A gauche, gisement chinois de gisement Xikuangshan, à droite gisement de Stolice (Pelissonier 1997, et références incluses).*

Dill (1998) propose une classification des gisements basée sur deux sites (andin et carpathe). Le *Type I* est mésothermal, localisé dans des zones de cisaillement où ont circulé des fluides crustaux tandis que le *Type II* est épithermal en amas (« stockwork »), enrichi en Bi, As, Ag, Hg, et relié aux activités magmatiques (volcaniques) acides à intermédiaires. Cependant, cette étude repose essentiellement sur la morphologie et s'applique mal aux autres gisements. Par exemple, Sb est communément précipité avec Au, As, Ag, Hg, W et aussi avec des élements chalcophiles comme Pb, Zn, Cu, qui ne sont pas intégrés dans la classification de Dill (1998).

Il existe néanmoins un paramètre commun entre les gisements d'antimoine, à savoir la relativement basse température de formation (Figure 4–16 ; e.g. Nesbitt et al. 1989 ; Williams-Jones et Normand 1997). L'association Sb-Hg souligne le contrôle de la solubilité de ces métaux par les basses températures (Goldfarb et al. 2005). Ceci est illustré relativement aux autres métaux par Emmons (1936) puis Guilbert et Park (1986) qui reconstruisent une veine "virtuelle" pour mettre en évidence la séquence paragénétique en fonction de la profondeur crustale (leur modèle s'applique aux métaux complexés par des sulfures). L'antimoine apparait dans la zone épithermale entre l'or (plus chaud) et le mercure (plus froid) ainsi qu'à des niveaux mésothermaux avec le Cu et As. Concrètement (voir discussion dans l'article #4), les gisements antimonifères se forment vers 150-300°C (épithermaux à sub-mésothermaux), donc à des profondeurs faibles (e.g. Nesbitt et al. 1989), ou comme phase tardive de la séquence paragénétique (e.g. Buchholz et al. 2007), ou encore dans les zones distales des sources de chaleur.

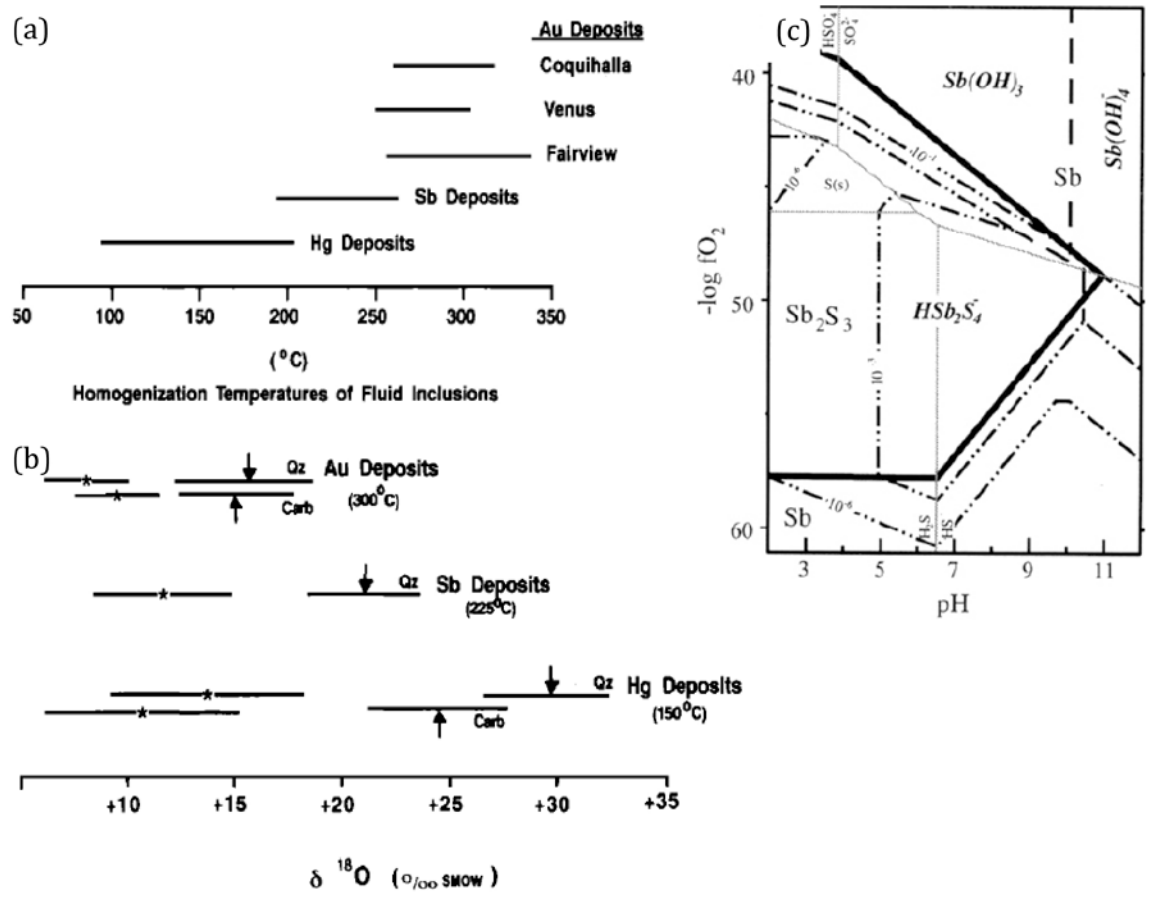

Figure 4-16 : *Données indiquant les conditions de faibles températures prévalant dans les minéralisations en Sb du de la cordillère canadienne (a) températures d'homogénisation des inclusions fluides (b) signatures isotopiques (Nesbitt et al. 1989 et références incluses). (c) Diagramme thermodynamique fO_2-pH du système Sb-S-O-H pour ce type de température (à 150°) et une concentration de 0.1 m de S. indiquant les stabilités des phases (d'après Guillemette et William-Jones 1993).*

Les fluides minéralisateurs ont une origine crustale, i.e. métamorphique-magmatique comme par exemple dans le craton du Ylgarn (Hagemann et Luders 2003) ou dans les gisements hercyniens-acadiens (Kontack et al. 1996). Ils montrent parfois une composante météorique (Nesbitt et al. 1989) ou plus vaguement de surface (Buchholz et al. 2007, Bellot et al. 2003). Le paramètre généralement invoqué pour expliquer la précipitation dans les gisements est la chute de la température (e.g. Bellot et al. 2003) dont la cause pourrait être le mélange avec des fluides froids de surface. Dans de rares études, les chutes de pression sont aussi invoquées (Bailly et al. 2000), par exemple au cours de la déformation en déclenchant une démixion du fluide (Hagemann et Luders 2003).

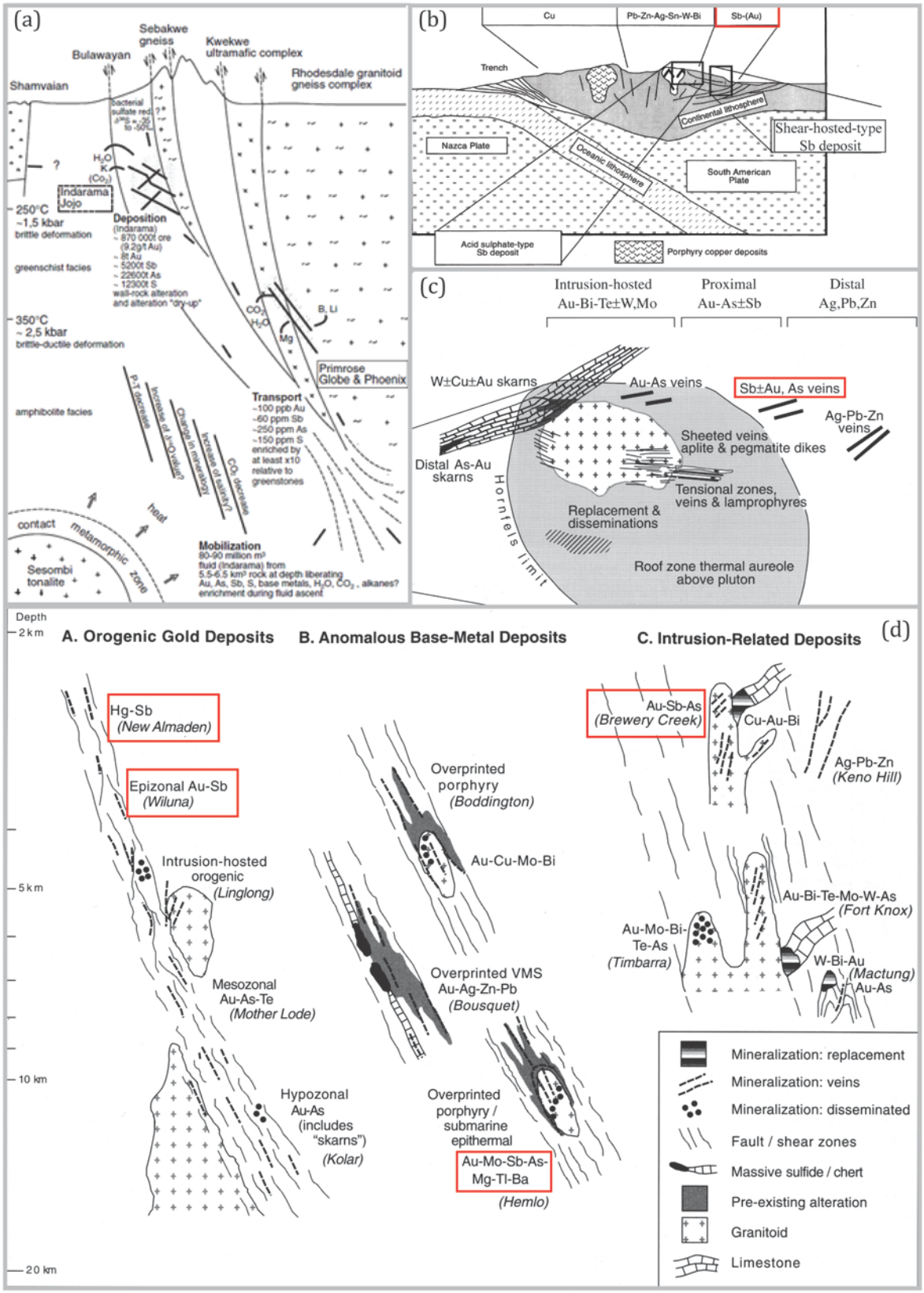

Figure 4–17 : *différents modèles de minéralisation en antimoine (encadré en rouge). (a) Système minéralisateur Au-Sb de la ceinture de Midlands (Zimbabwe Buchholz et al. 2007). (b) Un des modèles synthétiques des orogènes récents, de Dill (1998), ici dans une zone de cisaillement. (c) Occurrence de veines à Sb-Au-As près d'un pluton (Hart et al. 2002) (d) Modèle du « continuum crustal » de Groves (2003) dans des zones de cisaillement orogéniques.*

SYNTHESE & QUESTIONS

Le chapitre 4 montre en filigrane que les processus minéralisateurs sont variés, qu'ils impliquent une succession de processus, et que chacun d'entre eux peut être complexe. Pour ce qui est des minéralisations en antimoine au niveau mondial, elles sont clairement hydrothermales et épigéniques, stratiformes dans des piles de carbonates sédimentaires, mais le plus souvent mises en place en association avec des structures liées à des périodes orogéniques où elles sont épithermales.

Dans le cas de la ceinture de Murchison, l'antimoine est essentiellement présent dans une zone verticale carbonatée, l'*Antimony Line*. Dès 1984, Boocock et al. confirment le caractère structural du gisement. Les auteurs ont proposé des modèles métallogéniques bien différents, attribuant la minéralisation à des processus syngénétiques volcanogéniques (Minnitt 1975 ; Muff et Saager 1979 ; Ileri 1973; Viljoen et al. 1978), ou bien à des processus épigéniques hydrothermaux (Viljoen et al. 1978) ; dans ce dernier cas, l'origine supposée du fluide est variée, liée à l'intrusion des granites (Hausmann, 1959; van Eeden et al., 1939, Kedda 1992), ou provenant du manteau (Boese, 1964), ou encore de fluides associés au métamorphisme (« sécrétions latérales », Pearton 1980, Wilson et Viljoen 1986 ; Boese 1964 ; Pearton et Viljoen 1986).

Ces études, en se focalisant sur l'un ou l'autre des aspects de la minéralisation, se sont révélées infructueuses pour proposer un modèle complet (Viljoen et al 1978). Pearton et Viljoen (1986) synthétisent ces travaux et proposent que la minéralisation de l'antimoine est semblable à celle que l'on observe dans les gisements aurifères orogéniques, c'est-à-dire par des fluides métamorphiques dans une zone cisaillante. Cependant, même si leur modèle satisfait les observations, nous soulignerons le manque de données sur les fluides et la chronologie des événements pour le valider. Certes, la ceinture a été étudiée depuis, essentiellement lors des travaux menés par Vearncombe (cartographiques, structuraux et sur le complexe du Rooiwater : Vearncombe et al. 1987 ; Vearncombe 1988 ; Vearcombe et al. 1988 ; Vearncombe 1991 ; Vearncombe et al. 1992) et de travaux géochronologiques (Poujol et al. 1996 ; Poujol et Robb 1999 ; Poujol 2001). Cependant ces études n'ont pas définitivement contraint l'histoire de la minéralisation.

L'objectif dans ce travail est dès lors de comprendre la minéralisation en antimoine dans la ceinture de roches vertes de Murchison. Pour l'atteindre, la méthodologie suivie s'attache à aborder la métallogénie en l'intégrant dans l'histoire géologique de la ceinture, autrement dit en utilisant des outils géologiques généraux. Ce travail est entamé par les articles #1 et #2 qui posent de nouvelles bases concernant l'accrétion crustale et l'évolution tectono-métamorphique de la ceinture de roches vertes de Murchison. Dans la suite du manuscrit, d'autres informations pétrologiques, géochronologiques et géochimiques complèteront l'histoire du magmatisme, de la déformation et de l'altération hydrothermale. C'est en effet dans ce cadre global que

l'on peut contextualiser la minéralisation elle-même, par exemple les carcactéristiques structurales depuis l'échelle de *l'Antimony Line* jusqu'aux veines, l'histoire thermique de la zone, et les datations des événements géologiques. Aussi, les questions à adresser peuvent être formulées :

- **Comment décrire le ou les événements minéralisateurs en antimoine ? Cela revient à tenter de quantifier leurs âges respectifs, leur(s) origine(s) (magma, fluide et métal), la part de chacun, et le rôle de la déformation. Ces questions s'inscrivent dans la problématique du modèle géodynamique pour ce terrain (ceinture et granitoïdes), en particulier il faut cerner comment l'*Antimony Line* et sa minéralisation se rattachent à cette l'histoire.**

PARTIE II

MINERALISATION EN ANTIMOINE DE LA CEINTURE DE ROCHES VERTES DE MURCHISON

Genèse et datations de deux épisodes minéralisateurs

Chapitre 5 — Magmatisme à 2.97 Ga et minéralisation en or – antimoine

Le bilan sur les minéralisations en antimoine mondiales au chapitre 4-E souligne qu'or et antimoine sont souvent associés, par exemple dans les gisements de la cordillère canadienne, de la chaîne varisque ou dans les cratons archéens du Zimbabwe et du Yilgarn. C'est aussi le cas dans la ceinture de roches vertes de Murchison. Ce chapitre est un court article qui s'intéresse au cas d'une petite mine d'or abandonnée dans le prolongement Est de l'Antimony Line, à Malati Pump. Il illustre l'utilité de la géochronologie sur la compréhension des systèmes minéralisateurs depuis l'échelle de la mine jusqu'à celle de la ceinture.

En effet, il repose sur la datation U-Pb sur zircon de l'intrusion granodioritique de la mine et sur la datation Pb-Pb des sulfures de la minéralisation aurifère. Ces résultats démontrent que l'or, et minoritairement l'antimoine associé, sont génétiquement reliés à l'intrusion de ce granitoïde. En outre, l'appartenance de ce pluton à un batholithe de 2.97 Ga intrusif dans l'Antimony Line, le batholithe de Baderoukwe, suggère que cette interprétation peut être extrapolée à l'Antimony Line, c'est-à-dire que la minéralisation à antimoine–or de l'Antimony Line pourrait avoir été initialement générée par ce magmatisme. Enfin, les âges similaires de la minéralisation en Cu-Zn-Pb dans les laves de la formation de Rubbervale (Copper-Zinc Line) semblent signaler un système minéralisateur commun.

Cependant, depuis la parution de cette étude, la mesure des signatures Hf des zircons de la Rubbervale indique une extraction mantellique (article #1). Cette origine n'est pas cohérente avec celle du batholithe de Baderoukwe, d'affinité TTG (donc d'extraction crustale). À la suite de cet article, nous réévalurons donc, à la lumière de ces données, le lien entre le batholithe de Baderoukwe et les volcanites de Rubbervale, et par extension le lien entre la minéralisation de la Copper-Zinc Line, l'or du Baderoukwe et l'Antimony Line.

Article #3

"Metallogeny of precious and base metal mineralization in the Murchison Greenstone Belt, South Africa: indications from U–Pb and Pb–Pb geochronology"

Publié à *Mineralium Deposita*, 2012, issue 7, vol. 47, p. 739-747

Résumé en français

La ceinture de roches vertes de Murchison (3.09-2.97 Ga) est un métallotecte majeur de la zone nord du craton du Kaapvaal (Afrique du Sud) puisqu'elle renferme plusieurs gisements de métaux précieux et de métaux de base. Au cœur de ce métallotecte se trouve l'Antimony Line, s'étirant en direction ENE sur plus de 35 km de long, qui contient une série de gisements de Sb-Au. Au nord de l'Antimony Line, portée

par des roches volcaniques felsiques, la Copper-Zinc Line consiste elle aussi en une série de petits gisements de Cu-Zn de type amas sulfurés massifs (VMS, Volcanogenic Massive Sulfides) mis en place vers 2.97 Ga.

Dans cette étude nous apportons de nouvelles données sur la mine d'or de Malati Pump, située à l'extrême Est de l'Antimony Line. Les cristallisations de la granodiorite de Malati Pump et de la granodiorite de Baderoukwe sont datées à 2964 ± 7 Ma et 2970 ±7 Ma respectivement (méthode U-Pb sur zircon), tandis que la pyrite associée à la minéralisation en or fournit un âge de 2967 ± 48 Ma.

Par conséquent, la mise en place de la granodiorite, la cristallisation de la pyrite et la minéralisation en or semblent contemporaines à environ 2.97 Ga. Cela suggère donc (i) que les minéralisations majeures (orogénique en Au-Sb et volcanogénique en Cu-Zn) sont contemporaines au sein de la ceinture de Murchison ; (ii) que la formation de la minéralisation méso- à épithermale en Au-Sb à un niveau structural peu profond s'est accompagnée de l'extrusion sous-marine de roches volcaniques felsiques à l'origine des minéralisations en Cu-Zn associées.

Miner Deposita (2012) 47:739–747
DOI 10.1007/s00126-012-0422-7

LETTER

Metallogeny of precious and base metal mineralization in the Murchison Greenstone Belt, South Africa: indications from U–Pb and Pb–Pb geochronology

J. Jaguin · M. Poujol · P. Boulvais · L. J. Robb · J. L. Paquette

Received: 13 February 2012 / Accepted: 8 May 2012 / Published online: 26 May 2012

Abstract The 3.09 to 2.97 Ga Murchison Greenstone Belt is an important metallotect in the northern Kaapvaal Craton (South Africa), hosting several precious and base metal deposits. Central to the metallotect is the Antimony Line, striking ENE for over 35 km, which hosts a series of structurally controlled Sb–Au deposits. To the north of the Antimony Line, hosted within felsic volcanic rocks, is the Copper–Zinc Line where a series of small, ca. 2.97 Ga Cu–Zn volcanogenic massive sulfide (VMS)-type deposits occur. New data are provided for the Malati Pump gold mine, located at the eastern end of the Antimony Line. Crystallizations of a granodiorite in the Malati Pump Mine and of the Baderoukwe granodiorite are dated at 2,964±7 and 2,970±7 Ma, respectively (zircon U–Pb), while pyrite associated with gold mineralization yielded a Pb–Pb age of 2,967±48 Ma. Therefore, granodiorite emplacement, sulfide mineral deposition and gold mineralization all happened at ca. 2.97 Ga. It is, thus, suggested that the major styles of orogenic Au–Sb and the Cu–Zn VMS mineralization in the Murchison Greenstone Belt are contemporaneous and that the formation of meso- to epithermal Au–Sb mineralization at fairly shallow levels was accompanied by submarine extrusion of felsic volcanic rocks to form associated Cu–Zn VMS mineralization.

Keywords Gold mineralization · VMS deposit · Antimony Line · Kaapvaal Craton · Murchison range · South Africa

Editorial handling: H. Frimmel

J. Jaguin (✉) · M. Poujol · P. Boulvais
Campus de Beaulieu Géosciences Rennes,
UMR CNRS 6118, OSUR, Université Rennes 1,
35042 Rennes Cedex, France
e-mail: justine.jaguin@gmail.com

L. J. Robb
Department of Earth Sciences, University of Oxford,
South Parks Road,
Oxford OX1 3AN, UK

J. L. Paquette
UMR CNRS 6524, Laboratoire Magmas et Volcans,
63038 Clermont-Ferrand Cedex, France

Introduction

The 3.09 to 2.97 Ga Murchison Greenstone Belt (MGB; Poujol et al. 1996) represents one of a number of Archaean volcano-sedimentary belts within the Kaapvaal Craton and is located in the northeastern portion of the craton (a in Fig. 1), approximately 200 km north of the Barberton Greenstone Belt (BGB).

The MGB is well known for its numerous precious and base metal deposits, including: (1) Sb and Au mineralization along a central structural lineament, the *Antimony Line* (AL); (2) massive sulfide-style Cu–Zn mineralization associated with acid volcanic rocks along the northern margin of the belt; and (3) beryl–emerald mineralization associated with granitoid intrusions along the southern margin.

The present study focuses on the Malati Pump Mine (also referred to as the Malati Store), which is a small granodiorite-hosted gold deposit along the AL and aims to: (1) date the Au mineralization by U–Pb and Pb–Pb isotopic determinations on zircon and pyrite, respectively; and (2) assess the role that granitoids played in that system. The dating provides additional insights into the metallogenic system at the scale of the MGB.

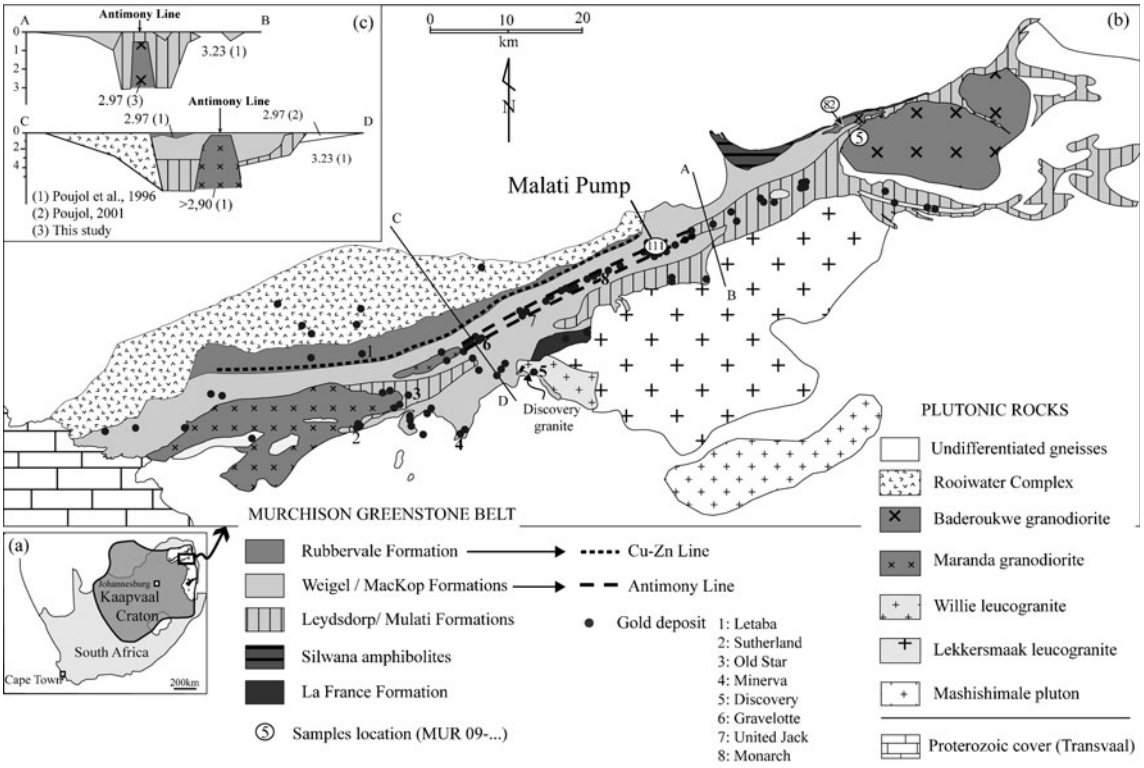

Fig. 1 *Inset* (*a*) shows the location of the Murchison Greenstone Belt in the Kaapvaal Craton. (*b*) Simplified geological map of the MGB (modified after SACS 1980; Vearncombe et al. 1992; gold deposits from Ward and Wilson 1998). *Inset* (*c*) shows cross-sections from the geophysical survey undertaken by de Beer et al. (1984), with available ages (in Ga)

Geological setting

The east-northeast-trending MGB comprises folded (e.g. Graham 1974; Vearncombe et al. 1992), complexly deformed metavolcanic and metasedimentary rocks intruded by diverse Archaean granitic gneisses. Intense deformation and lack of definitive relationships have, in the past, prevented the recognition of a volcano-sedimentary stratigraphy (Vearncombe 1988), although, more recently, based on available geochronological data, Poujol (2001) proposed a stratigraphic column for the MGB successions. The undated Leydsdorp and Mulati Formations are a mafic to ultramafic succession along the southern flank of the MGB. In the centre of the belt, the ca. 3.09 Ga Weigel Formation (Poujol et al. 1996) comprises mafic to felsic volcanic rocks and volcaniclastic sedimentary rocks and hosts the AL. Felsic sedimentary rocks (MacKop Formation) have a minimum age of 3,076±4 Ma (Poujol et al. 1996). Intermediate to felsic lavas, pyroclastic rocks, quartz–feldspar porphyries and the mineralized "Copper–Zinc Line" constitute the Rubbervale Formation, deposited between 2,974 and 2,963 Ma ago along the northern flank of the MGB (Brandl et al. 1996; Poujol et al. 1996; Poujol 2001; Schwarz-Schampera et al. 2010).

The Baderoukwe granodioritic gneiss was emplaced syntectonically along the eastern side of the MGB (Minnitt and Anhaeusser 1992). The Discovery granite located along the southern contact of the MGB was dated at 2,969±14 Ma (Poujol 2001). The Maranda granodiorite, at the western extremity of the AL, was emplaced at a minimum age of 2,901±20 Ma (Poujol et al. 1996). The peraluminous Lekkersmaak granite intruded the southern margin of the MGB at 2,795±8 Ma (Zeh et al. 2009). The final magmatic event in this region is represented by the Mashishimale pluton, emplaced to the south of the belt and dated at ca. 2.67 Ga (Poujol 2001; Zeh et al. 2009).

Migmatites and orthogneisses of Tonalite–Trondhjemite–Granodiorite (TTG) affinity occur both to the north (Groot-Letaba gneiss) and to the south (Makhutswi gneiss) of the MGB. Rocks from the Groot-Letaba gneiss have been dated at 3,171±6 Ma (Brandl and Kröner 1993), 3170.5±0.3 Ma (Kröner et al. 2000), 2,839±8 Ma, (Zeh et al. 2009) and 3,063±12 Ma for the Makhutswi gneiss (Poujol and Robb 1999). Finally, to the south of the MGB, the Harmony granite yielded an age of 3,091±5 Ma, contemporaneous with the age of the Weigel Formation (Poujol and Robb 1999).

The MGB represents an important metallotect because it hosts several styles of mineralization; Sb–Au (+As, W, Hg) are the most frequent associations found within hydrothermal mineralized systems in the AL (Vearncombe et al. 1992; Viljoen et al. 1978). In addition, Cu–Zn mineralization in the Rubbervale Formation occurs in volcanogenic massive sulfide systems

(Schwarz-Schampera et al. 2010 and references therein). Finally, emerald mineralization occurs to the south of the MGB (Groat et al. 2008).

Cu–Zn massive sulfide mineralization of the Copper–Zinc Line

The massive base metal sulfide mineralization of the Copper–Zinc Line is located in the southern part of the Rubbervale Formation, along a zone between tuffaceous rhyolite and overlying pelitic metasedimentary rocks (Terblanche and Lewis 1995). The mineralization is of a felsic VMS type of syngenetic origin (Taylor 1981; Terblanche and Lewis 1995; Schwarz-Schampera et al. 2010), like those observed in many Archaean terranes. The 12 known deposits are typically small deformed lenses (500–1,000 m long, 500 m wide) that are Zn-rich (up to 27 %) with subordinate Cu (0.4 %) and variable Pb, Au and Sb. They are closely associated with felsic volcanic centres (Schwarz-Schampera et al. 2010). The deposits are hosted in dacitic to rhyolitic volcanic rocks and were dated by U–Pb evaporation technique on zircon grains, yielding ages between 2974.8±3.6 and 2963.2±6.4 Ma (Schwarz-Schampera et al. 2010).

Antimony mineralization along the Antimony Line

Very significant Sb mineralization occurs within the MGB. The production of Sb from the Consolidated Murchison mine reached 25,000 t (15,000 metal) in 1951, and by 1986, total Sb production in the MGB represented 18 % of the world production (Pearton and Viljoen 1986; Ward 1998). The MGB is estimated to have an indicated resource of 7.4 million tons at 2.47 % for Sb (Metorex Limited 2011).

Antimony mineralization occurs in the form of stibnite and berthierite associated with pyrite and arsenopyrite, mainly in quartz–carbonate veins. Mineralization occurred intermittently along the entire length of the 35 km long, 250 m wide Antimony Line, the latter representing an upper-crustal shear zone (Vearncombe et al. 1988; Jaguin et al. 2012); the ores are characterized by strong metamorphic remobilization, but although broadly orogenic in character, their detailed metallogenesis is still poorly understood. Archaean Sb deposits are a rare phenomenon, which implies that either this style of mineralization is characterized by an unusual set of processes and/or that they were poorly preserved. Au is also commonly associated with the Sb mineralization, which suggests that both elements were enriched during the same mineralization processes (Pearton and Viljoen 1986).

Gold mineralization

Gold in the MGB has been mined from 89 deposits over the past century (Fig 1), most of which have now been worked out. Some 27 of these deposits show a strong association with Sb: 32 t of Au were recovered from the MGB, with two thirds as a by-product of Sb production (Ward and Wilson 1998).

The model established for gold deposits of the BGB has been applied to the MGB with a classification into three groups (Saager and Köppel 1976):

1. massive stratabound deposits that could be of exhalative origin, such as Letaba, Gravelotte, Monarch and United Jack mines;
2. disseminated sulfide ores in veinlets of Na-rich porphyry; they could either be secretions from the country rock at the time of granite emplacement (Viljoen et al. 1969, 1970) or subvolcanic equivalents of the VMS, with gold being concentrated during differentiation (Saager 1973, 1974); and
3. gold-rich quartz veins, such as the Old Star mine, that would have formed from late volatile emanations of granites or metamorphic mobilization from the country rocks (Saager 1973, 1974; Viljoen et al. 1969, 1970).

Saager and Köppel (1976) suggested that granites played an important role in the mineralization in the BGB, but that they could not be considered as the ultimate source of the gold. More recently, Vearncombe et al. (1992) classified the gold mineralization from the MGB into seven different types: (1) mineralization associated with stibnite and berthierite in carbonaceous rocks (AL); (2) mineralization associated with arsenopyrite and pyrite in ferruginous cherts and banded iron formation; (3) disseminated sulfides in chlorite, amphibolitic or talcose schists; (4) Au-bearing pyrite and other sulfides in shear zones; (5) quartz veins spatially related to shear zones; (6) zones with minor quartz veining and disseminated pyrite; and (7) disseminated auriferous pyrite within albitized granodiorite intrusions.

Several small, now albitized, TTG intrusions were emplaced along the AL into the Weigel Formation. Ward and Wilson (1998) listed similar albitized bodies associated with gold mineralization in other parts of the MGB (Discovery Shaft, Minerva, Sutherland mines, type 7 of Vearncombe's classification). Moreover, they indicated that 25 of the gold deposits are spatially associated with granitoid intrusives or granite–gneiss contacts. Kedda (1992) studied gold mineralization associated with albitized felsic intrusions that he related to deuteric and post-magmatic fluids. The mineralization is characterized by an atypical Au–Mo–W–Be–B–Sb–Hg paragenesis associated with a mesothermal (250–350°C) temperature regime. Stable isotopes, as well as fluid inclusion data, indicate an intimate relationship between Au–Sb and the granites as well as a fluid homogeneity on a regional scale (Kedda et al. 1990; Kedda 1992).

Characteristics of the mineralization at Malati Pump Mine

The mineralization at Malati Pump is essentially Au-rich with only minor Sb. Gold (up to 3 g/t) is found in quartz–tourmaline–pyrite veins near the apex of the granodiorite pluton and is related to fine disseminated pyrite in the wall rock and as visible and microscopic inclusions in the pyrite (Kedda 1992). The exposed intrusion is a cupola zone of an underlying granodioritic body intruded along the AL (Fig. 2; Kedda 1992; de Beer et al. 1984). The granodiorite intruded quartz–chlorite schists of the Weigel Formation and was, in turn, intruded by a late (Palaeoproterozoic or Mesozoic) dolerite dyke (Kedda et al. 1990). It is an S-shaped body, 50 m in diameter (Vearncombe et al. 1992). The cupola has undergone albitization, carbonation, sulfidation, tourmalinization and silicification, at about 250°C (Kedda 1992). The hosting schists underwent silicification, sericitization, carbonation and sulfidation and display quartz veins, some carrying gold. Quartz vein stockworks have been reported in the granodioritic body (Kedda 1992), which may represent the equivalent of the quartz-veined zones associated with oxidized sulphides of Vearncombe et al. (1992).

Results: petrography and age determinations

Petro-geochronology of the intrusions: U–Pb dating of the Malati Pump and Baderoukwe granodiorites

Zircon grains were separated using standard techniques. Handpicked zircon grains were cast in epoxy mounts, imaged and analysed by LA-ICP-MS in the Magmas et Volcans Laboratory (Clermont-Ferrand, France). Additional information on the analytical procedure can be found in Poilvet et al. (2011).

The Baderoukwe gneiss (Fig. 1b, samples 5 and 82) is a coarse-grained biotite–trondhjemite, altered in some places (with secondary albite, epidote, titanite, white mica). The samples provided stubby to elongated zircon grains, with luminescent core and visible oscillatory zoning (Fig. 3a, inset). They have low Pb contents (24–136 ppm; Table 1) and variable U contents (34–243 ppm). Four concordant analyses provide a Concordia date (Ludwig 1998) of 2,961.9±9.4 Ma (MSWD=0.019). Twenty analyses out of 17 grains give a similar upper intercept date of 2,967.3±6.7 Ma with a lower intercept at 76±140 Ma (MSWD=10.1).

Sample MUR 09-111 was collected from the Malati Pump Mine (Fig. 1b, locality 111). It is an albitized granodiorite comprising coarse-grained albite (An 0–2) and quartz. Minor phases include Fe–Mg–Ca–carbonates, rutile, tourmaline, white mica and sulfides (mostly pyrite, pyrrhotite, arsenopyrite). The sample provided homogeneous, weakly luminescent, elongated zircon grains with low Pb contents (10–227 ppm) and variable U contents (12–982 ppm). Ten analyses out of eight grains give an upper intercept date of 2,963.8±6.6 Ma (MSWD=5.3) if the lower intercept is anchored to 0±100 Ma (Fig. 3b).

Mineralization: Pb–Pb dating of pyrite

Pyrite grains were extracted from the Malati Pump Mine granodiorite and from the host quartz–chlorite schists of the Weigel Formation. The sample provided two types of minerals. Type 1 is a typical, cream-coloured, euhedral pyrite, whereas type 2 corresponds to reddish euhedral pseudomorphs of haematite after pyrite. The fractions were carefully selected under a binocular microscope, washed in acetone and dissolved in a Savilex beaker. Lead was separated and purified on an ion exchange resin and the isotopic ratios measured on a VG Sector mass spectrometer (University of Montpellier II, France). Additional information on the analytical procedure can be found in Poujol et al. (1999).

On a $^{206}Pb/^{204}Pb$-$^{207}Pb/^{204}Pb$ diagram (Fig. 3c), the two types of minerals plot in different positions. Type 1 pyrite defines a restricted range of values, whilst type 2 hematite displays more radiogenic values. Type 1 pyrite, together with previous data (Vearncombe et al. 1992), as well as pyrite from the intruded felsic schist of the Weigel Formation, define a Pb–Pb secondary isochron which yields a date of 2,967±48 Ma (MSWD=2) with a μ_1=7.84 (Fig. 3d). The more radiogenic type 2 hematite does not provide any meaningful age.

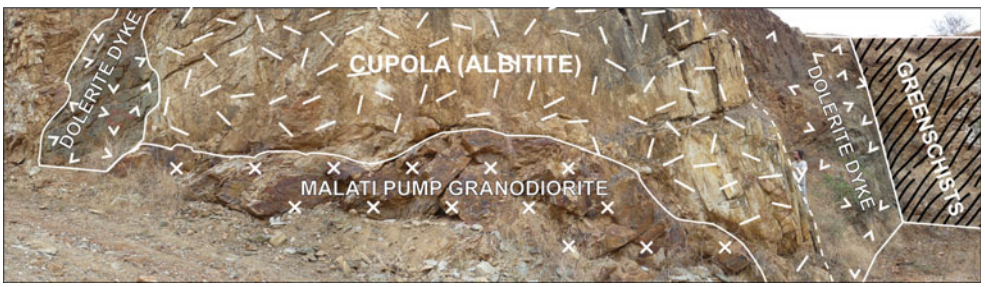

Fig. 2 Quarry face in the Malati Pump Mine showing the geometry of the different rock types (man to the *right* for scale)

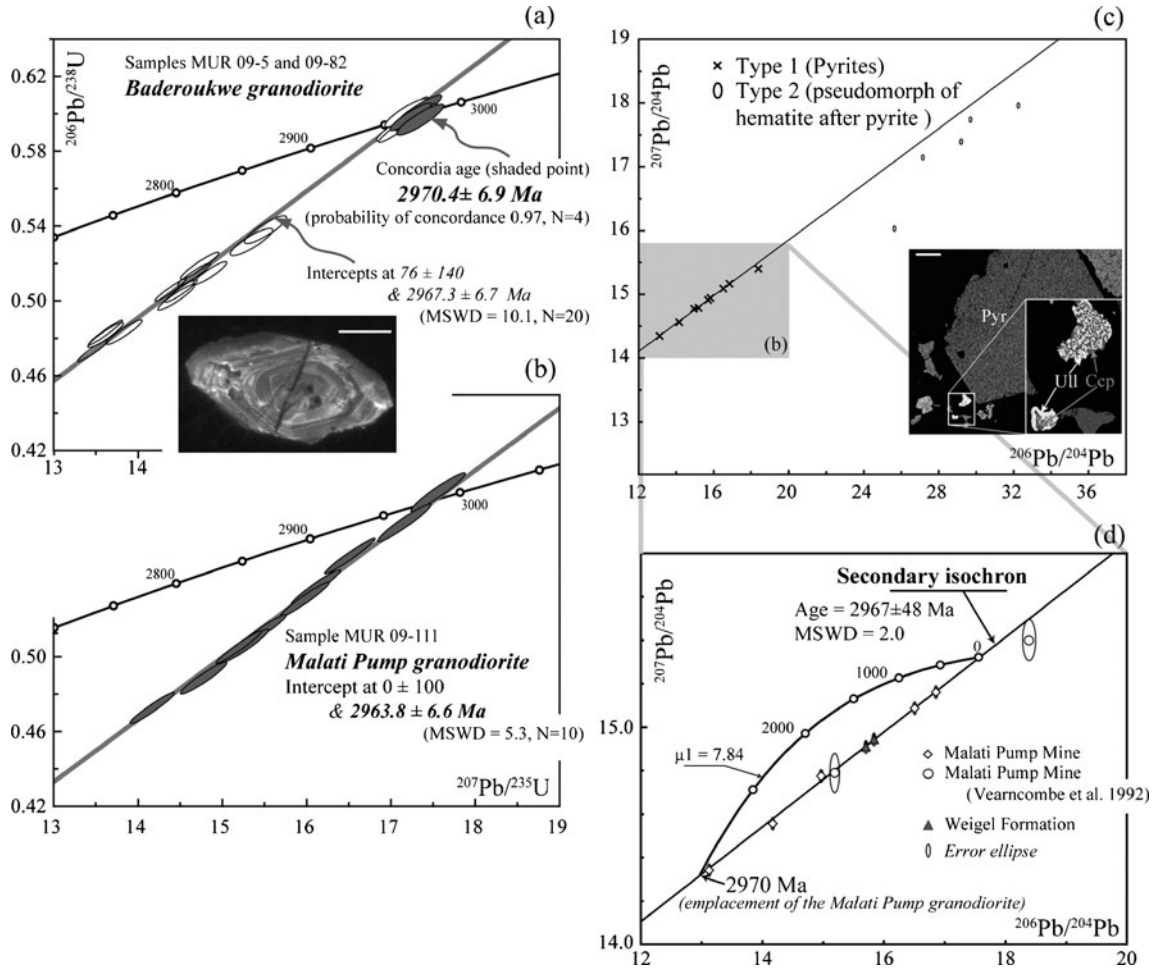

Fig. 3 Geochronological diagrams. (*a*) Concordia diagram for the Baderoukwe granodiorite. *Inset* CL image of a zircon grain from sample MUR 09-5, with oscillatory zoning (*bar scale*, 100 μm). (*b*) Concordia diagram for the Malati Pump granodiorite. (*c*) Pb–Pb diagrams for pyrite and haematite grains from the Malati Pump Mine and Weigel Formation displaying two populations with distinct isotopic Pb signature. *Inset* SEM image of the Malati Pump granodiorite showing the association between pyrite (*Pyr*) with mingled chalcopyrite (*Ccp*) and ullmanite (*Ull*; *bar scale*, 100 μm). (*d*) Isochron for the pyrite population (type 1). Isoplot software (Ludwig 2000)

Discussion and conclusions

The Baderoukwe Batholith

The U–Pb dates obtained for the Malati Pump (2,964± 7 Ma) and the Baderoukwe (2,970±7 Ma) granodiorite plutons are identical within error (Fig. 3a and b). They are interpreted as dating the emplacement age of the granodiorite. Therefore, these two granodiorite bodies are regarded as part of the same large-scale batholith, now referred to as the Baderoukwe Batholith. Following geophysical evidence (de Beer et al. 1984), this batholith is likely to be present all along the AL (Fig. 1c). Moreover, the 2.97 Ga Discovery granite (Poujol 2001) demonstrates that the Baderoukwe Batholith could possibly be extended to the south of the MGB. The Maranda granodiorite to the west of the AL has a minimum age of 2.90 Ga and could therefore eventually represent the western extremity of the Baderoukwe Batholith. In addition, the ca. 2.97 Ga volcanic rocks of the Rubbervale Formation are identical in age with the emplacement of the Baderoukwe Batholith, suggesting that they might represent its extrusive equivalent. This is further confirmed by the fact that they share similar calc-alkaline affinities (Zeh et al., in preparation).

Age of the mineralization

The Pb–Pb date of 2,967±48 Ma is interpreted as the age of the pyrite crystallization. This sulfidation is therefore comparable in age (within error) to the emplacement of the Baderoukwe Batholith. As shown in Fig. 3c, pyrite includes, or is associated with, various other Sb–As–Cu–Co–Zn sulfides. Moreover, Kedda (1992) demonstrated a direct genetic link between pyrite and the Au–Sb mineralization

Table 1 LA-ICP-MS U–Pb isotope data for zircon

Sample name		Chemistry		Ratios							Ages			Concordance (%)
		U (ppm)	Pb (ppm)	$^{207}Pb/^{235}U$	Error	$^{206}Pb/^{238}U$	Error	Rho	$^{207}Pb/^{206}Pb$	Error	$^{235}U/^{207}Pb$	$^{238}U/^{206}Pb$	$^{207}Pb/^{206}Pb$	
Baderoukwe granodiorite	MUR 09-05	115	80	17.530	0.210	0.5874	0.0068	0.97	0.2165	0.0023	2,964	2,979	2,955	101
		75	*52*	*17.680*	*0.223*	*0.5885*	*0.0068*	*0.91*	*0.2178*	*0.0025*	*2,973*	*2,983*	*2,965*	*101*
		41	*29*	*17.693*	*0.230*	*0.5835*	*0.0068*	*0.89*	*0.2199*	*0.0027*	*2,973*	*2,963*	*2,980*	*99*
		120	71	15.833	0.208	0.5245	0.0060	0.87	0.2160	0.0024	2,867	2,718	2,973	91
		51	29	15.042	0.186	0.5052	0.0059	0.94	0.2193	0.0025	2,818	2,636	2,951	89
		186	110	15.665	0.206	0.5178	0.0059	0.87	0.2189	0.0027	2,857	2,690	2,976	90
		243	136	14.762	0.181	0.4882	0.0056	0.93	0.2194	0.0027	2,800	2,563	2,975	86
		77	43	13.913	0.175	0.4680	0.0055	0.93	0.2150	0.0023	2,744	2,475	2,948	84
		218	120	13.909	0.165	0.4692	0.0054	0.97	0.2156	0.0025	2,744	2,480	2,944	84
		149	80	14.137	0.175	0.4695	0.0054	0.93	0.2183	0.0025	2,759	2,481	2,969	84
	MUR 09-82	*57*	*37*	*17.649*	*0.202*	*0.5848*	*0.0061*	*0.91*	*0.2189*	*0.0025*	*2,971*	*2,968*	*2,972*	*100*
		51	*33*	*17.582*	*0.202*	*0.5851*	*0.0061*	*0.91*	*0.2179*	*0.0025*	*2,967*	*2,969*	*2,966*	*100*
		40	26	17.525	0.207	0.5872	0.0062	0.89	0.2165	0.0025	2,964	2,978	2,955	101
		68	45	17.423	0.186	0.5785	0.0058	0.94	0.2184	0.0024	2,958	2,943	2,969	99
		42	27	17.404	0.195	0.5792	0.0060	0.92	0.2179	0.0024	2,957	2,945	2,966	99
		86	49	14.694	0.151	0.4921	0.0049	0.96	0.2165	0.0023	2,796	2,580	2,955	87
		64	37	15.168	0.167	0.5011	0.0051	0.92	0.2195	0.0025	2,826	2,619	2,977	88
		58	33	14.976	0.160	0.5004	0.0050	0.94	0.2171	0.0024	2,814	2,615	2,959	88
		105	58	14.820	0.159	0.4916	0.0050	0.94	0.2186	0.0024	2,804	2,578	2,971	87
		123	66	13.752	0.146	0.4593	0.0046	0.95	0.2171	0.0023	2,733	2,437	2,960	82
	Mean	98	58											92
Malati Pump albitite	MUR 09-111	203	133	16.509	0.242	0.5541	0.0079	0.97	0.2160	0.0024	2,907	2,842	2,951	96
		341	219	15.193	0.223	0.5052	0.0072	0.97	0.2181	0.0024	2,827	2,636	2,967	89
		118	80	17.158	0.257	0.5720	0.0082	0.96	0.2175	0.0025	2,944	2,916	2,962	98
		231	150	15.476	0.230	0.5137	0.0074	0.96	0.2185	0.0024	2,845	2,673	2,969	90
		164	106	15.975	0.237	0.5307	0.0076	0.97	0.2183	0.0024	2,875	2,744	2,968	92
		251	147	14.171	0.212	0.4726	0.0068	0.96	0.2175	0.0025	2,761	2,495	2,962	84
		114	79	17.557	0.265	0.5885	0.0085	0.95	0.2164	0.0025	2,966	2,983	2,954	101
		171	110	16.107	0.241	0.5372	0.0077	0.96	0.2174	0.0024	2,883	2,772	2,962	94
		186	108	14.779	0.225	0.4886	0.0071	0.95	0.2193	0.0026	2,801	2,565	2,976	86
		172	105	15.265	0.232	0.5060	0.0073	0.95	0.2188	0.0025	2,832	2,639	2,972	89
	Mean	195	124											92

Errors are listed at 1σ

Data in italics were used to calculate the concordia age

Table 2 ID-TIMS Pb–Pb isotope data for pyrite and hematite

Sample name	$^{208}Pb/^{204}Pb$[a]	$^{207}Pb/^{204}Pb$[a]	$^{206}Pb/^{204}Pb$[a]	Pb (ppm)	U
Malati Pump Mine (Au)					
Pyr 2 Aut	32.905	14.346	13.117	–	
Pyr 2 ter Aut	36.083	15.089	16.504	4.5	600 ppb
Pyr 3 TV	34.623	14.56	14.163	–	
Pyr 2 bis	36.238	14.776	14.961	9.4	
Pyr 1	37.638	15.165	16.846	–	
Pyr M ox	39.671	17.463	29.263	4.6	
Pyr MH ox	37.39	16.291	26.004	8.8	
Pyr Am ox	42.031	18.039	32.323	16	
Pyr MD ox	40.527	17.8	29.752	4.3	
Pyr 3 bis ox.	42.037	18.203	31.462	16	1.4 ppm
Pyr 3 red ox	47.992	17.15	27.162	–	

[a]Data are accurate to at least 0.15 % for $^{206}Pb/^{204}Pb$ and $^{207}Pb/^{204}Pb$ and 0.20 % for $^{208}Pb/^{204}Pb$

because gold is found within hydrothermal pyrite. Therefore, granodiorite emplacement, sulfide mineral deposition and gold mineralization are considered contemporaneous.

Some pyrite grains (type 2) were altered to hematite, suggesting that an oxidizing fluid circulated within the system. The U content in the type 2 haematite is higher than in the type 1 pyrite (1.4 ppm versus 600 ppb) and its Pb–Pb signature is, consequently, more radiogenic. This demonstrates that the fluid responsible for the oxidation consistently carried more U and/or radiogenic Pb. Unfortunately, this oxidation event was not datable (Fig. 3c and Table 2) and could be either close to, or much younger than, 2.97 Ga. This distinct fluid may eventually have partially remobilized Au.

Model for the Au mineralization and implications regarding other deposits of the MGB

This study demonstrates for the first time that several different styles of mineralization in the MGB are contiguous and related to a period of magmatism that witnessed, at 2.97 Ga, coeval emplacement of granodioritic (TTG) intrusions and a calc-alkaline-type magma extrusion. Central to this study has been the Malati

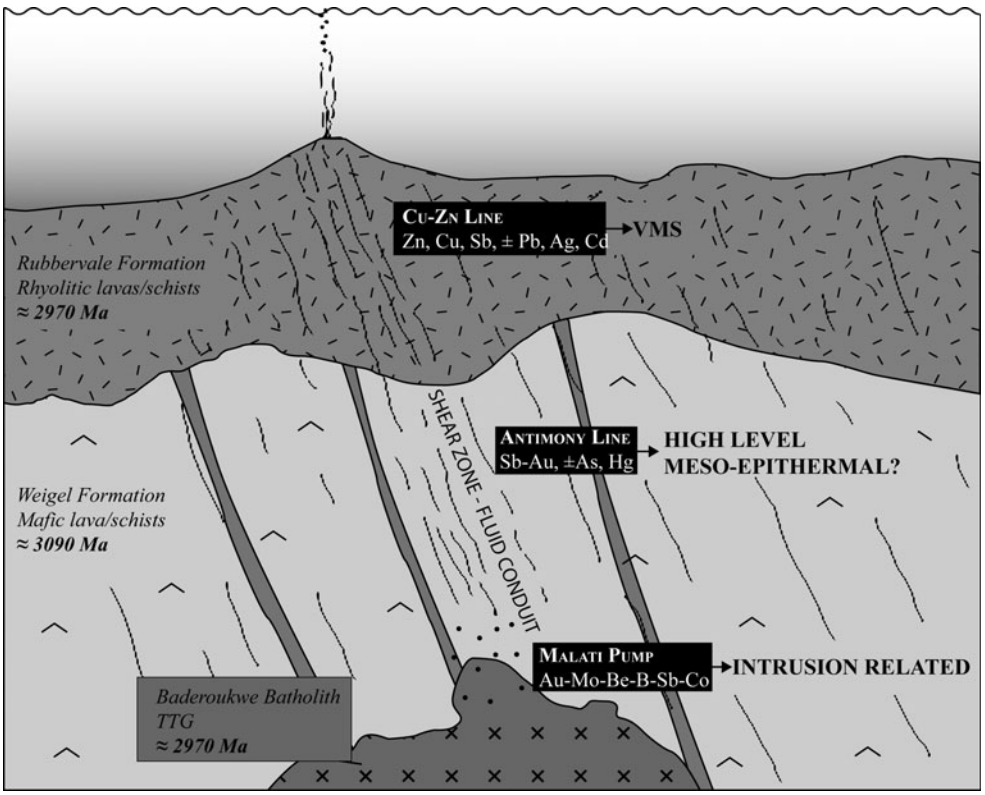

Fig. 4 Sketch for the MGB metallogenic system as proposed in this study

Pump intrusion with its Au mineralization and associated Sb–As–Hg metal suite that is perhaps more reminiscent of a high-level epithermal setting than of a mesothermal origin (e.g. Nesbitt and Muehlenbachs 1989). In addition to the Malati Pump intrusion, the entire AL is decorated with numerous small TTG-type intrusions (Pearton and Viljoen 1986; Kedda 1992), geophysical evidence for which suggests a spatial link at depth and the possible existence of a larger batholith (de Beer et al. 1984). A continuum of Au–Sb mineralization, as described for example in Groves et al. (2003) and Nesbitt and Muehlenbachs (1989), is a feature of the AL, and in this regard, it seems likely that this system can be related in its entirety to a single system where heat input and fluid flow were at least in part directly related to TTG emplacement at 2.97 Ga (Fig. 4).

This study also shows that the Rubbervale Formation and its syngenetic VMS-style Cu–Zn mineralization (Schwarz-Schampera et al. 2010) are contemporaneous and directly related to the emplacement of the Baderoukwe Batholith, again at circa 2.97 Ga. Consequently, the calc-alkaline rocks of the Rubbervale Formation are likely the extrusive equivalents of a major TTG-type intrusive event, here termed the Baderoukwe Batholith. It is therefore suggested (1) that the major styles of orogenic Au–Sb and the VMS-style Cu–Zn mineralization in the MGB are contemporaneous and (2) that the formation of meso- to epithermal Sb–Au mineralization at fairly shallow intrusive levels was accompanied by the extrusion of felsic volcanic rocks in a subaqueous shallow marine environment to form associated Cu–Zn VMS mineralization, all at circa 2.97 Ga. A close spatial relation between, on one side, VMS deposits plus their extrusive host rocks and, on the other side, intrusive magmatic–hydrothermal system has not often been described in Archaean settings (Franklin et al. 2005). It should also be noted that the beryl–emerald mineralization occurring along the southern margins of the MGB and spatially associated with the intrusion of the Discovery granite might have also occurred at 2.97 Ga, the age of the latter intrusion. In light of these data, we recognize the MGB as a major metallotect that has been underexplored for precious and base metal mineralization. Our data suggest that a new exploration strategy should be employed in the region, recognizing the Baderoukwe Batholith as the central geological feature that is spatially and secularly related to substantial and varied styles of mineralization. In particular, the structures that have played a key role along and into which phases of the Baderoukwe Batholith have been emplaced should remain the object of concerted exploration targeting in this region.

Acknowledgments This work was funded by the National Institute of Sciences of the Universe (CNRS-INSU "Action Incitative", France). We acknowledge C. Anhaeusser and J. Vearncombe for their comments. Thanks are also due to Bernd Lehmann and Hartwig Frimmel for editorial handling.

References

Brandl G, Kröner A (1993) Preliminary results of single zircon studies from various Archaean rocks of the Northeastern Transvaal. Extended abstracts. In: Mabuza M, Maphalala R (eds) 16th Colloquium on African Geology. Geological Survey of Mines Department, 14–16th September 1993, Mbabane, Swaziland, pp 54–56

Brandl G, Jaeckel P, Kröner A (1996) Single zircon age for the felsic Rubbervale Formation, Murchison Greenstone Belt, South Africa. S Afr J Geol 99:229–234

de Beer JH, Stettler EH, Duvenhage AWA, Joubert SJ, Raath CJ (1984) Gravity and geoelectrical studies of the Murchison Greenstone Belt, South Africa. Trans Geol Soc S Afr 87:347–359

Franklin JM, Gibson HL, Jonasson IR, Galley AG (2005) Volcanogenic massive sulfide deposits. In: Hedenquist W, Thompson JFH, Goldfarb RJ, Richards JP (eds) Econ Geol 100th anniversary volume. Society of Economic Geologists, Littleton, CO, pp 523–560

Graham RH (1974) A structural investigation of the southern part of the Limpopo belt and adjacent Kaapvaal Craton, South Africa. Research Institute of African Geology Annual Report 18, pp 63–69

Groat LA, Giuliani G, Marshall DD, Turner D (2008) Emerald deposits and occurrences: a review. Ore Geol Rev 34:87–112

Groves DI, Goldfarb RJ, Robert F, Hart CJR (2003) Gold deposits in metamorphic belts: overview of current understanding problems, future research, and exploration significance. Econ Geol 98:1–29

Jaguin J, Gapais D, Poujol M, Boulvais P, Moyen J-F (2012) The Murchison Greenstone Belt (South Africa): a general tectonic framework. S Afr J Geol 115:65–76

Kedda SW (1992) Geochemical and stable isotope studies of gold bearing granitoids in the Murchison Schist Belt, North Eastern Transvaal. Unpublished MSc thesis, University of the Witwatersrand, 241 pp

Kedda SW, Robb LJ, Meyer FM, Verhagen BT (1990) Gold mineralization associated with albitized felsic intrusions in the Murchison Greenstone Belt, South Africa. Extended abstracts. In: Glover JE, Ho SE (eds) Third International Archaean Symposium. Geol Society of Australia, 17–21 September 1990, Perth, Australia

Kröner A, Jaeckel P, Brandl G (2000) Single zircon ages for felsic to intermediate rocks from the Pietersburg and Giyani greenstone belts and bordering granitoid orthogneisses, northern Kaapvaal Craton, South Africa. J Afr Earth Sci 30:773–793

Ludwig KR (1998) On the treatment of concordant uranium–lead ages. Geochim Cosmochim Acta 62:665–676

Ludwig, KR (2000) Isoplot/Ex: a geochronological toolkit for Microsoft Excel Berkeley Geochronology Center, Berkeley

Meteorex Limited (2011) Mine operations statistics, gold & antimony. Fact Sheet 2. http://www.metorexgroup.com/fact_sheet_02.htm. Accessed 19 March 2012

Minnitt RCA, Anhaeusser CR (1992) Gravitational and diapiric structural history of the eastern portion of the Archaean Murchison Greenstone Belt, South Africa. J Afr Earth Sci 15:429–440

Nesbitt BE, Muehlenbachs K (1989) Geology, geochemistry, and genesis of mesothermal lode gold deposits of the Canadian Cordillera—evidence for ore formation from evolved meteoric water. Econ Geol Mon 6:553–563

Pearton TN, Viljoen MJ (1986) Antimony mineralization in the Murchison Greenstone belt—an overview. In: Anhaeusser CR, Maske S (eds) Mineral deposits of Southern Africa. Geological Society of South Africa, Johannesburg, pp 293–320

Poilvet JC, Poujol M, Pitra P, Van den Driessche J, Paquette JL (2011) The Montalet granite, Montagne Noire, France: an early Permian syn-extensional pluton as evidenced by new U–Th–Pb data on zircon and monazite. CR Geosci 343:454–461

Poujol M (2001) U–Pb isotopic evidence for episodic granitoid emplacement in the Murchison Greenstone Belt, South Africa. J Afr Earth Sci 33:155–163

Poujol M, Robb LJ (1999) New U–Pb zircon ages on gneisses and pegmatite from south of the Murchison Greenstone Belt, South Africa. S Afr J Geol 102:93–97

Poujol M, Robb LJ, Respaut JP, Anhaeusser CR (1996) 3.07–2.97 Ga greenstone belt formation in the northeastern Kaapvaal Craton: implications for the origin of the Witwatersrand Basin. Econ Geol 91:1455–1461

Poujol M, Robb LJ, Respaut JP (1999) U–Pb and Pb–Pb isotopic studies relating to the origin of gold mineralization in the Evander Goldfield, Witwatersrand Basin, South Africa. Precambrian Res 95:167–185

S.A.C.S. (1980) The Murchison sequence. In: Kent LE (ed) Stratigraphy of South Africa, Part 1. Lithostratigraphy of the Republic of South Africa, South West Africa/Namibia and the Republics of Bophuthatswana, Transkei and Venda. Handbook Geological Survey South Africa, pp 45–52

Saager R (1973) Metallogenese präkambrischer Goldvorkommen in den vulkano-sedimentären Gesteinskomplexen (greenstone belts) der Swaziland Sequenz in Südafrika. Geol Rundschau 62:888–901

Saager R (1974) Geologische und geochemische Untersuchungen an primären und sekundären Goldvorkemmen im frühen Präkambriun Südafrikas: Ein Beitrag zur Deutung der primären Herkunft des Goldes in der Witwatersrand Lagerstätte. Universität Heidelberg, 150 pp

Saager R, Köppel V (1976) Lead isotopes and trace elements from sulfides of Archaean greenstone belts in South Africa—a contribution to the knowledge of the oldest know mineralizations. Econ Geol 71:44–57

Schwarz-Schampera U, Terblanche H, Oberthür T (2010) Volcanic-hosted massive sulfide deposits in the Murchison Greenstone Belt, South Africa. Miner Deposita 45:113–145

Taylor RS (1981) Volcanogenic copper–zinc sulfide deposits of the Murchison greenstone belt, northeastern Transvaal. Unpublished PhD thesis, University of Durham, 361 pp

Terblanche HK, Lewis RD (1995) An overview of the Maranda base metal mine. Extended abstracts. In: Barton JM and Copperthwaite YE (eds) Centennial Geocongress. Geological Society of South Africa, 3–7 April 1995, Johannesburg, South Africa, pp 111–114

Vearncombe JR (1988) Structure and metamorphism of the Archean Murchison Belt, Kaapvaal Craton, South Africa. Tectonics 7:761–774

Vearncombe JR, Cheshire PE, de Beer JH, Killick AM, Mallinson WS, McCourt S, Stettler EH (1988) Structures related to the Antimony Line, Murchison Schist Belt, Kaapvaal Craton, South Africa. Tectonophysics 154:285–308

Vearncombe JR, Barton JM, Cheshire PE, de Beer JH, Stettler EH, Brandl G (1992) Geology, geophysics and mineralization of the Murchison Schist Belt, Rooiwater complex and surrounding granitoids. Geol Surv S Af Mem 81:139

Viljoen RP, Saager R, Viljoen MJ (1969) Metallogenesis and ore control in the Steynsdorp Goldfield, Barberton Moutain Land, South Africa. Econ Geol 64:778–797

Viljoen RP, Saager R, Viljoen MJ (1970) Some thoughts on the origin and processes responsible for the concentration of gold in early Precambrian of southern Africa. Miner Deposita 5:164–180

Viljoen MJ, Van Vuuren CJJ, Pearton TN, Minnit RCA, Muff R, Cilliers P (1978) The regional geological setting of mineralization in the Murchison range with particular reference to antimony. In: Verwoerd WJ (ed) Mineralization in metamorphic terranes. Geological Society of South Africa Special Publication 4, pp 55–86

Ward JHM (1998) Antimony. In: Wilson MGC, Anhaeusser CR (eds) The mineral resources of South Africa. Council for Geoscience, pp 59–65

Ward JHW, Wilson MGC (1998) Gold outside the Witwatersrand Basin. In: Wilson MGC, Anhaeusser CR (eds) The mineral resources of South Africa. Council for Geoscience Handbook 16, Pretoria, South Africa, pp 350–386

Zeh A, Gerdes A, Barton JM (2009) Archean accretion and crustal evolution of the Kalahari Craton—the zircon age and Hf isotope record of granitic rocks from Barberton/Swaziland to the Francistown arc. J Petrol 50:933–966

Commentaires additionnels

LES SULFURES. Nos échantillons de l'albitite de Malati Pump permettent d'observer les relations entre la pyrite et divers métaux. Sur la figure 5–1, les sulfosels d'As, Sb, Ni et Cu sont inclus dans les grains de pyrite en (a) et (b) tandis qu'ils montrent des textures en (c) et (d) qui laisseraient à penser qu'une partie des sulfosels pourraient être des phases tardives et/ou remobilisées. S'il n'a pas été possible de confirmer les observations de Kedda (1992) reliant l'or à la pyrite, les inclusions à As-Sb vont dans ce sens, car ces métaux sont communément associés à l'or.

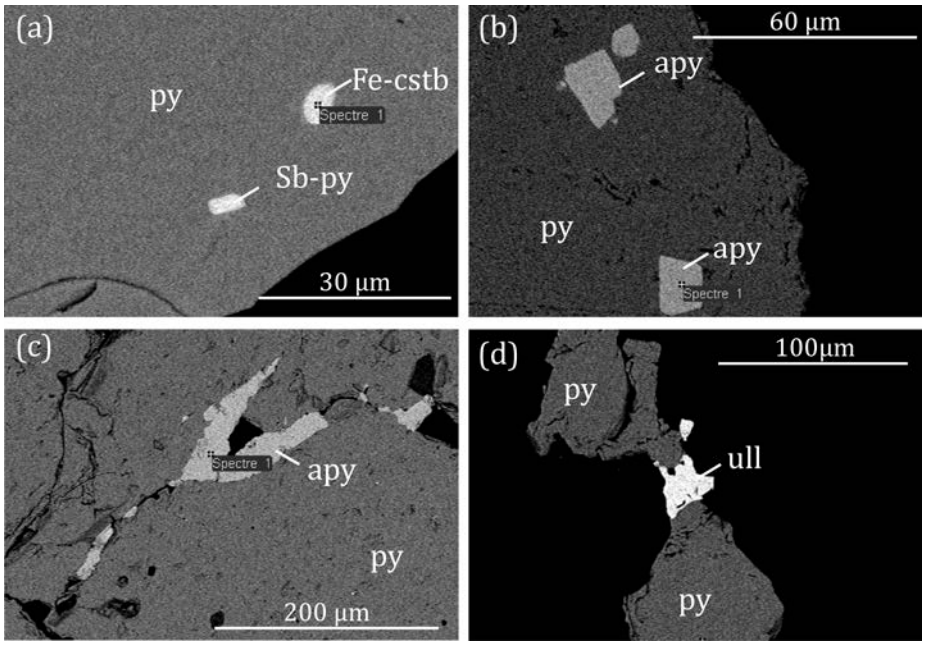

Figure 5–1 : *Photos au MEB des sulfures de la granodiorite de Malati Pump. (a) inclusions dans la pyrite (py) de pyrite antimonifère (Sb-py, $Fe_{0.99}Sb_{0.01}S$) et de chalcostibine ferrifère (Fe-cstb $Cu_{2.63}Sb_{1.08}Fe_{0.54}S_4$). (b) inclusions dans la pyrite d'arsenopyrite (apy, $Fe_{0.94}$ $As_{0.79}$ S). (c) grains d'arsenopyrite le long d'une fracture dans une pyrite. (d) ullmanite (ull, $Ni_{0.73}Co_{0.29}Sb_1S_1$) entre deux grains de pyrite.*

Par ailleurs, Kedda (1992) propose une séquence paragénétique dans laquelle les sulfures sont postérieurs à l'albitisation. Pourtant, les textures dans nos échantillons suggèrent le contraire (figure 5–2). Cette chronologie est cohérente avec la chronologie fournie par nos âges, à savoir les âges des pyrites présentés dans l'étude (vers 2.97 Ga) et l'âge de l'albitisation vers 2.8 Ga (article #5). De plus, dans cet article #3, nous reportons les interprétations de Kedda (1992) concernant la température d'albitisation vers 250°C. Dans l'article #5, nos propres données indiquent que la formation des albitites s'est faite au minimum à 250°C, voire même à des températures significativement supérieures (350°C) pour la circulation de fluide dans l'*Antimony Line* (chapitre 7, article #4).

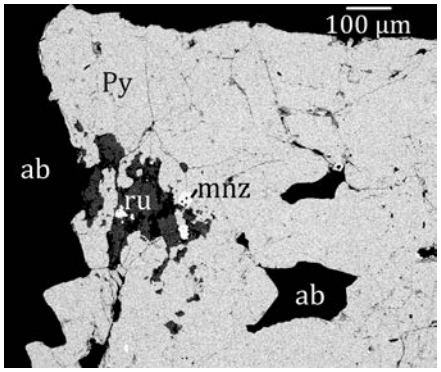

Figure 5–2 : *Altération des sulfures par la paragénèse d'albitisation albite-rutile-monazite (ab, ru, mnz, extrait de la figure 8, article #5).*

UN EVENEMENT, DEUX PETROGENESES. Le magmatisme à 2.97-2.92 Ga comprend le batholithe du Baderoukwe (article #3), les protolithes des albites, potentiellement le pluton de Maranda (article #5), le granite de Discovery (Poujol 2001), la tonalite de Free State du complexe du Rooiwater (article #1) et les volcanites de la Rubbervale (Brandl et al. 1996; Poujol et al. 1996; Poujol 2001; Schwarz-Schampera et al. 2010). Leur contemporanéité pose la question de leur éventuel lien génétique, et donc de la pétrogenèse de ces roches, qui, par ailleurs, contraindra la géodynamique de cet épisode vers 2.97 Ga.

Les roches plutoniques du Rooiwater et les volcanites de Rubbervale sont génétiquement liées entre elles vues les relations intrusives de terrain, les études géochimiques (Vearncombe 1991) et l'origine mantellique commune (Hf sur zircon, article #1). Les gabbros lités du complexe (Novengilla suite) représentent des cumulats, la suite de Free State des phases felsiques plus différenciées, et les rhyolites de la Rubbervale les produits extrusifs de l'un ou l'autre (Vearncombe et al. 1987). L'ensemble est issu de la fusion du manteau (ou éventuellement d'une croûte océanique très jeune). Enfin, les spectres de terres rares des zircons ne montrent pas d'influence de fluide, ce qui suggère que le contexte de la fusion partielle devait être extensif plutôt que proche d'un panneau plongeant.

L'article #5 expose les caractéristiques chimiques du pluton de Baderoukwe. Nous y argumentons que le Baderoukwe est peu altéré et que les échantillons MUR 09-5a et MUR 09-6 représentent donc correctement le magma du Baderoukwe. Le pluton est acide ($SiO_2 \approx 70\%$ pds), pauvre en ferromagnésiens ($Fe_2O_3+MgO+MnO+TiO_2 < 3.5$ % pds), riche en Na par rapport au K (fort rapport Na_2O/K_2O = 1.7-2.6 soit Na/K mol. = 2.6-4.0). Dans le triangle des feldspaths (O'Connor 1965), il se positionne entre le champ des granites et des trondhjémites. Par ailleurs, les Terres Rares dessinent un spectre fractionné avec un rapport $(La/Yb)_N$ = 28-42, surtout imputable aux faibles teneurs en HREE (Yb < 1ppm) et sans anomalie en Eu. Ainsi, le pluton de Baderoukwe correspond bien à une TTG. Cette affinité TTG est assortie d'une origine crustale à partir de roches basiques (chapitre 2). Le rapport Sr/Y relativement faible et les teneurs en Nb et Ta élevées le rapprocherait de TTG formées à faibles ou moyennes pressions (10-15 kbar, Moyen 2011). Ansi, conformément à l'article #1, nous proposons que ce pluton est issu de la fusion partielle d'une croûte basique subductée. Les données Sm-Nd (dans les albitites du Baderoukwe) montrent des signatures $\varepsilon Nd_{2.97}$

$_{Ga}$ super-chondritiques (1.14-3.39) et des T_{DM} associés proches de l'âge de cristallisation (article #5). Ces signatures marquent l'extraction depuis un matériel légèrement appauvri comme un manteau primitif, un manteau appauvri, ou une croûte océanique jeune. Le T_{DM} proche de l'âge de cristallisation est assorti d'une erreur d'environ 13 Ma si les seules erreurs isotopiques sont prises en compte, et 100 Ma en y ajoutant celle sur l'âge. Il ne peut donc pas discriminer l'âge précis d'extraction mantellique, mais suggère que la croûte subductée avait au maximum 100 Ma lors de la fusion partielle qui a formé le magma du Baderoukwe. De cela, il apparait que, à 2.97 Ga, la phase d'amalgamation des terrains nord et sud est liée à deux systèmes magmatiques mis en place en parallèle mais génétiquement distincts.

IMPLICATIONS METALLOGENIQUES. Si le Baderoukwe est syn-compression, la Rubbervale (et le complexe du Rooiwater) se forment au contraire en extension. Les deux systèmes sont donc spatialement distincts. Les deux minéralisations, en or et VMS, mettent en jeu des vecteurs différents : le premier est un magma ou un fluide magmatique lié au Baderoukwe (Article #3 ; minéralisation dans veines à quartz-tourmaline), le second est de l'eau de mer (avec interaction éventuelle avec le système magmatique Rubbervale, Schwarz-Shampera et al. 2010). Ainsi, le contexte tectonique, le magmatisme et les fluides dépeignent deux systèmes minéralisateurs physiquement séparés.

Pourtant, l'étude de Schwarz-Schampera et al. (2010) souligne que les minerais de la VMS contiennent de l'antimoine et de l'or. Soit la cause est postérieure à cette étape, c'est-à-dire que les minerais seraient contaminés par exemple pendant le métasomatisme mais cela n'est pas cohérent avec leur faible degré d'altération (Schwarz-Schampera et al. 2010), soit la cause est intrinsèque à cette étape. Pearton (1980) a montré l'enrichissement en antimoine des schistes mafiques de la Weigel, schistes qui doivent avoir le même âge que les volcanites de la Weigel datés par Poujol et al. (1996).

- Alors une première hypothèse est que le système hydrothermal des VMS s'est enrichi lors de la traversée de ces roches ; mais au moment du développement des VMS la Rubbervale n'est peut-être pas accolée à la Weigel.
- Alternativement, l'antimoine peut être issu du magma lui-même comme le sont parfois les métaux dans les VMS (Franklin et al. 2005), c'est-à-dire qu'il serait ici hérité du manteau.

Nous privilégions cette dernière hypothèse car elle unifie l'origine supposée de l'Sb dans les volcanites mafiques de la Weigel (Pearton 1980) et de la Rubbervale.

D'autre part, l'étude de Muff et Saager (1979) décrit les minerais de l'Antimony Line avec une composante Cu-Zn-Pb-Co. Ainsi, les deux systèmes ne sont pas indépendants en termes de suite métallique même si ce sont deux systèmes séparés. Quoiqu'il en soit, l'antimoine dans la pyrite à 2.97 Ga à Malati Pump confirme la présence de ce métal dans les roches de la Weigel précocement. Cette phase constituerait donc une remobilisation d'un enrichissement de fond.

Chapitre 6 — L'Antimony Line, une zone de circulation de fluides crustaux minéralisateurs

Le chapitre précédent insiste sur une phase minéralistrice en or-antimoine à 2.97 Ga liée à l'intrusion du batholithe de Baderoukwe. Pourtant, la minéralisation en antimoine telle qu'elle existe et qu'elle est exploitée aujourd'hui dans l'Antimony Line ne se trouve ni dans ni autour des plutons, ce n'est donc pas une minéralisation de nature porphyrique. Elle est restreinte à une zone de cisaillement verticale l'Antimony Line, où se développent des corps minéralisés. Les minerais sont en particulier portés par des veines de quartz-carbonate qui se développent pendant la déformation.

Ainsi, la minéralisation est d'origine hydrothermale. Pour caractériser les fluides à l'origine de ce type d'objets géologiques, deux outils complémentaires ont montré leur efficacité : les isotopes stables qui renseignent sur les conditions de l'interaction fluide-roche (origine des fluides, température d'interaction, rapports fluide-roche), et les inclusions fluides qui en fossilisant des microquantités de fluide donnent accès à la chimie du fluide et aux conditions pression-température lors des circulations.

Article #4

"Stable isotopes (C, O) and fluid inclusion study of quartz-carbonates veins from the Antimony Line, Murchison Greenstone Belt"

Soumis à *American Journal of Science*

Résumé en français

Les zones de deformation localisées constituent des chemins préférentiels pour les circulations de fluides. C'est aussi le cas des régions où la déformation est distribuée comme par exemple la ceinture archéenne de roches vertes de Murchison (craton du Kaapvaal, Afrique du Sud). La région est caractérisée par une déformation distribuée, mais la ceinture inclue une structure fragile-ductile à mouvement inverse, l'Antimony Line, qui contient plusieurs corps minéralisés en antimoine-or. De grandes quantités de fluides minéralisateurs ont circulés dans cette structure comme en témoignent l'abondance de roches métasomatisées et les veines minéralisées.

Cette étude souligne tout d'abord le contôle lithologique sur la localisation de la circulation de fluides le long de cette structure et l'adoucissement de la structure par les fluides. Afin de mieux comprendre le système minéralisateur, nous présentons des données isotopes stables (oxygène et carbone), associées à une étude des inclusions fluides dans les veines minéralisées de quartz-carbonate, ainsi que l'analyse chimique de carbonates et des datations par méthode ^{40}Ar-^{39}Ar sur des grains de fuchsite associés aux veines.

L'étude des inclusions de fluides caractérise trois types de fluides dominés par des compositions à H_2O-CO_2 et minoritairement à CH_4-N_2. Les mesures microthermométriques indiquent des gammes de pression-température lors de la précipitation dans les conditions ambiantes du métamorphisme, vers 350-450°C, 200-300 MPa. Les carbonates sont riches en Fe et Mg et montrent des spectres de terres rares plats pour les terres rares moyennes et lourdes et légèrement appauvris pour les terres rares légères. Ainsi, ils sont équilibrés avec les lithologies encaissantes. Au premier ordre, nos données isotopiques sont homogènes à l'échelle de l'Antimony Line ($\delta^{18}O_{quartz}$ = 10.9-14.3‰). En detail, de petites différence dans les valeurs du $\delta^{18}O$ pour les quartz et les carbonate existent selon le site d'échantillonage. Ces différences sont probablement dues à des variations mineures de la température et/ou de la géochimie des roches encaissantes le long de l'Antimony Line. La combinaison des données isotopiques stables et inclusions fluides permet d'identifier une origine métamorphique des fluides minéralisateurs. Enfin, nous présentons une synthèse géologique de l'histoire de la ceinture de Murchison en y intégrant la métallogénie de l'Antimony Line, qui est comparable à des gisements "d'or en filon" (*orogénique gold*).

STABLE ISOTOPES (C, O) AND FLUID INCLUSION STUDY OF QUARTZ-CARBONATE VEINS FROM THE ANTIMONY LINE, MURCHISON GREENSTONE BELT

Jaguin J.[a], Boulvais P.[a], Poujol M.[a], Gapais D.[a], Boiron M.-C.[b], Briant N.[a]

[a] *Géosciences Rennes, UMR CNRS 6118, OSUR, Université de Rennes 1, Campus de Beaulieu, 35042 Rennes CEDEX, France. E-mails:* justine.jaguin@gmail.com*, philippe.boulvais@univ-rennes1.fr, marc.poujol@univ-rennes1.fr, denis.gapais@univ-rennes1.fr*

[b] *Université de Lorraine, G2R, CNRS, Boulevard des Aiguillettes, BP 70239, 54506 Vandoeuvre-les-Nancy, France. E-mail: marie-christine.boiron@univ-lorraine.fr*

ABSTRACT

Zones of localized deformation represent a preferential path for fluid circulations. This is also true in areas affected by a distributed deformation such as the Archean Murchison Greenstone Belt (Kaapvaal Craton, South Africa). The region is marked by distributed deformations, but the Belt hosts a reverse brittle-ductile structure marked out by several antimony-gold ore-bodies, defining the so-called Antimony Line. Large flows of mineralizing fluids during deformation are obvious along the structure through the abundance of metasomatic rocks and mineralized veins.

This study emphasizes the lithological control on fluid flow localization along with the softening of the structure by fluids. In order to gain a better understanding on the mineralizing system, we produce a stable isotope dataset (oxygen and carbon) combined with a fluid inclusions study on the mineralized quartz-carbonate veins, as well as chemical analyses of carbonates and some ^{40}Ar-^{39}Ar dating on fuchsite associated with the veins.

The fluid inclusion study specifies three types of fluid inclusions of H_2O-CO_2-dominated fluids plus minor CH_4-N_2. Microthermometric measurements indicate pressure-temperature of precipitation in metamorphic ambient conditions at about 350-450°C, 200-300 MPa. Carbonates are Fe-Mg-rich and are characterized by flat MREE and HREE patterns, with slight depletions in LREE. They are thus equilibrated with the host-rocks lithologies. At the first-order, our isotopic data are homogeneous at the scale of the Antimony Line ($\delta^{18}O_{quartz}$ = 10.9-14.3‰). In details, subtle differences in the $\delta^{18}O$ values for quartz and carbonate exist depending on the sampling sites, likely due to minor temperature and/or host rocks geochemistry variations along the Antimony Line. Taken together, fluid inclusions and stable isotopes data point to a metamorphic origin for the fluids responsible for the mineralization. Finally, we present an overview of the Murchison Greenstone Belt geological history by integrating the antimony metallogeny of the Antimony Line, which, overall, can be compared to an orogenic gold deposit.

INTRODUCTION

In orogens, fluids circulate particularly in zones affected by localized deformation (faults, shear zones) which act as preferential paths. This has been demonstrated by numerous studies, dealing with terrains of different ages: the Phanerozoic metamorphic core complex of North America Cordillera (for example Nesbitt and others, 1986), the Proterozoic Mt Isa Block of Australia (for example Oliver, 1995), the Archean craton of Abitibi (for example Kerrich, 1986). On the other hand, ancient orogenic zones of Archaean or Paleoprotrozic age, often tend to exhibit distributed deformation patterns across large areas (see reviews by Chardon and others, 2009 and Gapais and others, 2009). Fluid flows, which are most of the time synchronous with deformation (mechanical details in Sibson, 1994), should be more diffuse in such ancient terranes.

The Murchison Greenstone Belt (Kaapvaal Craton, South Africa; fig. 1) represents an example of these ancient terranes where deformation is distributed throughout the belt as well as in adjacent gneisses and plutons (Jaguin and others, 2012a). The Murchison belt also exhibits in its core a localized reverse brittle-ductile structure known as the "Antimony Line", marked by the occurrence of numerous antimony and associated gold deposits (Wilson-Moore, 1896, Vearncombe and others, 1988). The Antimony Line has never been described as a boundary between geological formations. Indeed, there are no metamorphic, petrological nor structural differences described across the Antimony Line, an observation which underlines that this structure cannot be considered as a major tectonic break at the scale of the belt (see also Jaguin and others, 2012a). Nevertheless, large fluid flows are obvious in this narrow and elongate vertical feature, with the presence of abundant metasomatic rocks and mineralized veins (for example Pearton and Viljoen, 1986). The question that arises at the scale of the belt is therefore the explanation behind the apparent paradox between the localized flow path and the distributed strain pattern.

Here, we provide a comprehensive oxygen and carbon stable isotopes dataset together with fluid inclusion data, chemical analyses and some ^{40}Ar-^{39}Ar dating, especially on mineralized veins, in order to better constrain the fluid-rock interaction regime. We highlight he lithological control on flow localization, give first order characteristics of the mineralizing fluid flow event(s) (chemistry and origin of the fluid, heterogeneity between sites), and integrate all these data it in a broader geological history.

GEOLOGICAL SETTING

The Murchison Greenstone Belt (MGB)

The MGB (fig. 1) is a narrow belt trending east-northeast, 10 to 15 km wide, 140 km long and 4.5 to 9 km deep (de Beer and others, 1984). It is located 220 km north of the Barberton Greenstone Belt and 70 km south of the Limpopo Belt (fig. 1, inset).

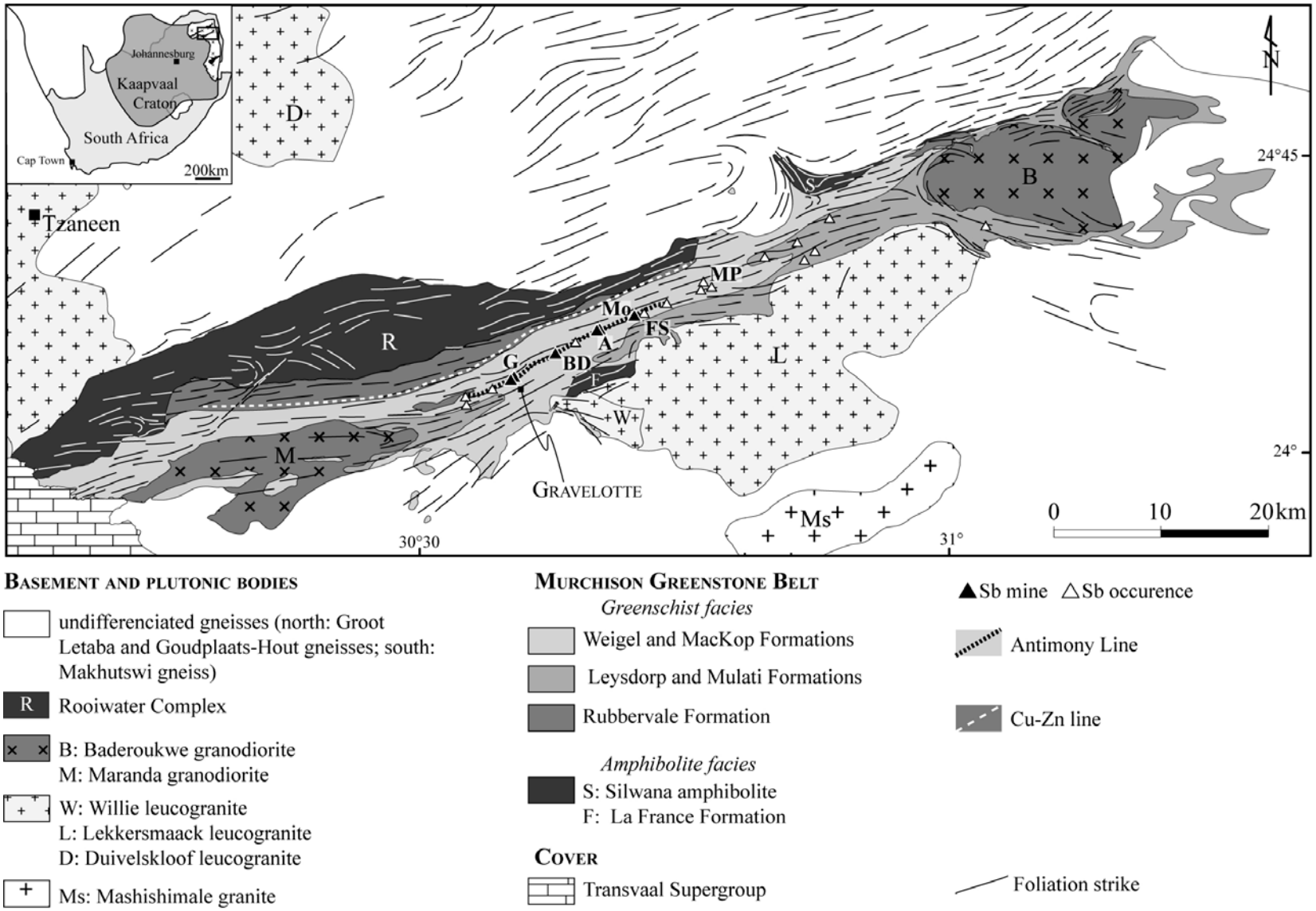

Fig. 1: *Geological map of the Murchison Greenstone Belt (modified after Vearncombe and others, 1992 and the 1:250 000 map of Tzaneen, Geological Survey of South Africa, 1985) and foliation trajectories of the region (Jaguin and others, 2012a). Antimony Line and its main deposits from Pearton and Viljoen (1986). Sampling sites: G = Old Gravelotte mine, Gravelotte shaft; BD = Beta decline; AS = Athens shaft; Mo = Monarch mine and hill; FS = Free State mine; MP = Malati Pump mine.*

The sedimentary and volcanic sequence of the MGB (Gravelotte Group) was divided into Formations by the South African Committee for Stratigraphy (SACS 1980, fig. 1). These volcano-sedimentary formations were deposited between ca. 3.09 Ga (Weigel Formation) and 2.97 Ga (Mulati, La France and Rubbervale Formation; Zeh and others, in prep.; Poujol and others, 1996). These formations are described here from South to North. The metapelites and quartzites of the La France Formation have a maximum deposition age of deposition of 2986 ± 12 Ma (Zeh and others, in prep.). The mafic to ultramafic successions of the Leydsdorp and Mulati Formations occupy the rest of the southern flank to the east and west. The meta-arenites of the MacKop Formation found in the eastern portions of the MGB deposited with a maximum age of 3076 ± 4 Ma (Poujol and others, 1996). To the northeast, the Silwana Amphibolite unit (Vearncombe, 1988) is made of hornblende-biotite schists and gneisses of unknown ages. To the north, the Rubbervale Formation is made of intermediate to felsic lavas and tuffs deposited ca 2.97 Ga ago (Brandl and others, 1996; Poujol and others, 1996; Poujol 2001; Schwarz-Schampera and others, 2010). This formation hosts the "Cu-Zn Line", a large volcanic-hosted massive sulfide (VHMS) district (Schwarz-Schampera and others, 2010). In this study, we focus on the largest domain of the belt, comprising the mafic to felsic volcanic rocks, BIF, quartzite and conglomerates of the Weigel Formation and associated carbonated rocks, see section *The Antimony Line*). These rocks deposited between 3087 ± 21 Ma (for some felsic volcanites) and 2979 ± 7 Ma (maximum age of deposition for a quartzitic schist, Zeh and others, in prep.).

Magmatic activity is diverse and protracted in the area: ca 3.2 and 3.06 Ga tonalite-trondhjemite gneisses (French Bob Mine Granite, Poujol and others, 1996; Makhutwsi gneiss, Poujol and Robb, 1999, respectively); ca 2.97-2.92 Ga tonalite-granodiorite plutons (Discovery Granite, Poujol, 2001; Baderoukwe batholith, Jaguin, and others, 2012b; Free State tonalite of the Rooiwater layered igneous complex, Zeh and others, in prep.; Maranda granodiorite, Jaguin and others, accepted); 2.85-2.78 Ga pegmatite and granites (Groot Letaba orthogneiss, Zeh and others, 2009; pegmatitic dykes, Poujol and Robb, 1999; Willie granite, Poujol 2001; Lekkersmaak leucogranite, Zeh and others, 2009; Turfloop and Duivelskloof batholiths, Henderson and others, 2000); 2.70 Ga granite (Mashishimale pluton, Poujol, 2001; Zeh and others, 2009).

Ages of syn-kinematic granitoids (2.97 to 2.77 Ga) suggest a long-lasting tectonic process. The ductile deformation is distributed at the regional scale, both within the belt and in the northern bounding gneisses (Jaguin and others, 2012a). It is expressed by a regional sub-vertical foliation at a low angle to the belt strike, bearing steeply plunging lineations (Graham, 1974; Viljoen and others, 1978; Vearncombe and others, 1988; Jaguin and others, 2012a) in and around the MGB. Superposed fold structures are also common (Graham, 1974; Maiden, 1984; Maiden and Boocock, 1987; Vearncombe, 1988; Vearncombe and others, 1988), with east-northeast to east-west trending folds, steep axial planes and shallowly to steeply plunging axes. Two shear zones, the Letaba shear zone and the Antimony Line, accommodated more localized deformation, most likely at a late, upper crustal stage (Jaguin and others, 2012a). Metamorphism of the MGB rocks is generally of greenschist- to lower-amphibolite-

facies grade (P–T conditions of 1.3–2.8 kbar at 340-370°C and 5.6 ±0.6kbar at 570 °C, Block and others, 2012). The Silwana amphibolites, the La France Formation and the Rooiwater Complex (Vearncombe, 1988; Block and others, 2012) were metamorphosed under amphibolite-facies conditions with maximum P–T estimates for the former two near 8.7–10 kbar and 600–670 °C.

Quartz veins are widespread in all the units besides the Antimony Line zone, from infra-centimetric to decametric veins. They can be found in iron formations (quartz-sulfide ± gold), metapelites (quartz-kyanite), quartzites, biotite-schists (quartz-muscovite) or at the pluton/belt boundaries. Pegmatites are also common along the southern border. Veins throughout the belt and its immediate surroundings attest to regional-scale fluid flows.

The Antimony Line and its Antimony Mines

The Antimony Line is a planar, sub-vertical and discordant structure in the central part of the Weigel Formation, which constitutes a localized structure at the scale of the belt (Vearncombe and others, 1988; Jaguin and others, 2012a). In details, it is a brittle-ductile reverse shear zone (northern units overriding the southern ones; Vearncombe and others, 1988).

Sb-mineralization is intermittently developed along the Antimony Line (fig. 2): the exploited deposits (mines) span over a distance of 15 km, but all the known occurrences cover a distance of 55 km (Pearton and Viljoen, 1986). The sustainable production of Sb in the Antimony Line mines exists since World War I and, at the peak of production in 1986, represented 18% of the world production (Pearton and Viljoen, 1986; Ward, 1998). It is still valuable today with indicated resource estimated at 7.4 million tons at 2.47 % Sb (Meteorex Limited, 2011). Around the Antimony Line, the Weigel Formation consists of quartz-muscovite ± chlorite schist (Pearton and Viljoen, 1986). The Antimony Line itself is characterized by chloritic talcose schist, grading to fuchsitic quartz-carbonate rocks toward the mineralized centers (detailed description in Pearton and Viljoen, 1986). These talc schists are proposed to be derived from komatiites (Pearton, 1980). The mineralization is restricted to quartz-carbonate veins and appears rarely disseminated in host rocks (Pearton and Viljoen, 1986). The ore bodies are lensoid, up to several hundred meters in length, with a vertical extension exceeding their strike (Pearton and Viljoen, 1986; fig. 2). The bodies, which are parallel to the foliation, consist of a dense network of quartz-carbonate, Sb-minerals veins. The veins are surrounded by alteration zone made of talc quartz-carbonate-chlorite schists with fuchsite as a characteristic mineral of the alteration halo. Together with quartz and Ca-Mg-Fe carbonates, the veins contain minor albite, chlorite and tourmaline. Antimony sulfides are mainly stibnite (Sb_2S_3) and berthierite ($FeSb_2S_4$), with a total of about 40 mineral species (Fe, Au, Hg, As, Cu, Zn, Ni; Muff and Saager, 1979).

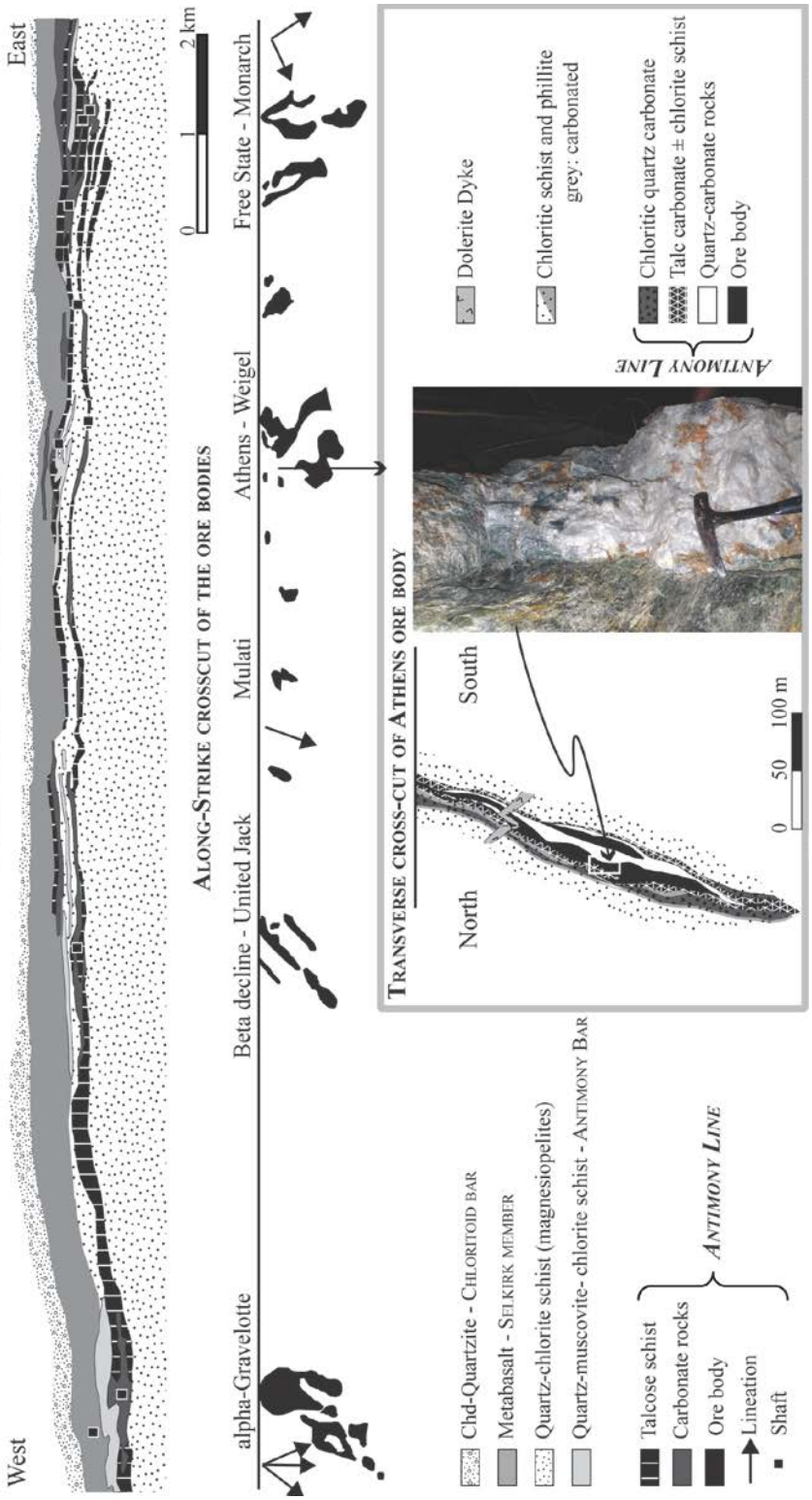

Fig. 2: *Map of the AL area and associated along-strike crosscut (Pearton and Viljoen, 1986; slightly modified after Wilson and Viljoen, 1986; lineations from Boocock and others, 1984, Vearncombe and others, 1988 and Abbot and others, 1986). Transversal crosscut across the AL in the Athens ore body, after Wilson and Viljoen (1986). Picture from the Athens shaft showing a talc-carbonate-chlorite schist hosting a boudinaged quartz-carbonate-stibnite vein.*

Operating mines along the Antimony Line run from the Alpha-Gravelotte ore body to the west to the Monarch-Free State ore body to the east (fig. 2; description hereinafter from synthesis of Ward, 1998). The westernmost site is historically the principal producer of Sb in the form of stibnite (minor pyrite, gersdorffite, ullmanite, berthierite). Ore bodies are associated with a steeply west-southwest-plunging fold, especially in cymoidal structures in a quartz-carbonate lens. Our samples originate from the disused Old Gravelotte decline as well as from cores from the Main Shaft (fig.

2). Further east, the United Jack ore body provided samples from its deep extension in the Beta decline (the ore body plunges 45° WSW). Ore is mainly under the form of stibnite with minor gold, arsenopyrite and berthierite. The next sampled site, the Athens-Weigel ore body, is today the main producer for gold and antimony. Samples come from the deepest zone, namely the Athens body. The plunge of the ore-body switches to 45° east-northeast in this area. Again, stibnite is the main antimony ore with minor pyrite, arsenopyrite and berthierite. The Monarch-Free State ore body, the easternmost working mine on the Antimony Line, has been sampled both in the Monarch and Free State shafts. The ore-hosting lens plunges 65° to the ENE and carries a more complex mineralogy with berthierite, gersdorffite, ullmanite and gold. Further to the East, the Malati Pump mine is somewhat different from the other sampling sites. Indeed, this site is a disused gold mine with only minor Sb, where gold was found in apical veins around an albitized granodioritic plug (Kedda, 1992; Jaguin and others, 2012b, Jaguin and others, accepted). In this locality, samples have been collected in either the disused quarry itself or from drilled cores. Seven quartz veins coming from outside the Antimony Line complete the samples set and will be used as a regional referential.

ANALYTICAL TECHNIQUES

Stable Isotopes on Carbonates and Silicates

Carbon and oxygen isotopes from quartz-carbonate veins were analyzed in the isotopes laboratory of University of Rennes 1. For quartz, about 7 mg of handpicked grains were finely crushed in a boron carbide mortar. O_2 was produced from minerals by reaction with BrF_5 in Ni tubes at 670°C over night (after the method of Clayton and Mayeda, 1963). During extraction O_2 was converted to CO_2 by reaction with hot graphite, and analyzed using a VG SIRA 10 triple collector instrument. Long-term analysis of NBS 28 standard ($\delta^{18}O$ = 9.58‰) gave a mean value of 9.3 ± 0.1‰ and measured values have thus been corrected accordingly. The uncertainty is estimated to be 0.2‰.

For carbonate, about 12 mg of material were handpicked and crushed. The powder was reacted with anhydrous phosphoric acid (H_3PO_4) in sealed vessels at 90°C over 2 to 3 days (or 50°C over night for calcitic veins). The $\delta^{13}C$ data have been corrected by adding 0.1‰ following the analyses of the in-house standard material provided by Prolabo Rennes. The $\delta^{18}O$ calculation requires a good estimate of the chemical composition of the carbonate minerals, which determines the experimental fractionation coefficient between CO_2 and carbonate $\alpha_{Carb\text{-}CO2}$, given the chemical variations of the carbonates. The chemical composition of the carbonate minerals were measured by SEM analysis on thin sections and, when various carbonate phases were observed in one sample during SEM imaging, proportions of the respective phase have been estimated for the α calculation. The coefficient $\alpha_{carb\text{-}CO2}$ was calculated for each sample using the coefficient of the end-members carbonates taken from the literature weighted by each carbonate abundance (at 90°C, $\alpha_{Calcite–CO2}$=1.00818, $\alpha_{Magnesite–}$

$_{CO2}$=1.00947: Das Sharma and others, 2002; $\alpha_{Dolomite-CO2}$=1.00932, $\alpha_{Ankerite-CO2}$=1.00926, $\alpha_{Siderite-CO2}$=1.00908: Rosenbaum and Sheppard, 1986; $\alpha_{Rhodocrosite-CO2}$=1.00756: Böttcher, 1996). The average uncertainties on isotopic compositions are 0.1‰ for C and ± 0.2‰ for O.

Fluid Inclusions

Microthermometry and Raman analysis of fluid inclusions have been carried out at the G2R laboratory in Nancy (France). Seven thick sections were selected to inventory and classify fluid inclusion types. Microthermometric characterization of the fluids was performed on wafers using a Fluid Inc stage. Fluid inclusions used for the calibration were a pure CO_2 natural standard fluid inclusion from Camperio (triple point at -56.6°C) and H_2O-NaOH synthetic fluid inclusions (ice melting temperature at -0.4°C). The accuracy at high temperatures is 2°C. Salinity is expressed as % NaCl weight equivalent (wt.% NaCl eq., Bodnar, 1993).

Molar fractions of CO_2, CH_4, N_2 and H_2S were determined in individual fluid inclusions using a DILOR–LABRAM Raman spectrometer. The bulk composition and molar volumes were computed using the P-V-T-X properties of individual inclusions in the C-O-H-N-S system (Dubessy, 1984; Dubessy and others, 1989; Thiéry and others, 1994; Bakker, 1997). Isochores were calculated using the Zhang and Frantz (1987) equation of state for aqueous fluid inclusions, and using the program of Bakker (1999) based on the Bowers and Helgeson (1983) equation of state for the C-H-O-N-NaCl system for aqueous-carbonic fluid inclusions.

Several types of fluid inclusions were distinguished and their notation follows the nomenclature of Boiron and others (1992). This notation is based on the bulk homogenization temperature of the fluid inclusions and the nature of the fluid components. In this study, fluid inclusions composed by a liquid and a vapor phase, are noted L because the homogenization is in the liquid phase (L+V→L). Depending on their composition, the letter w (for water) or c (for CO_2) is added. Observed fluid inclusions are aqueous fluid inclusions (Lw), carbonic inclusions (Lc, when no water is visible by optical observation) and aqueous-carbonic fluid inclusions, Lc-w or Lw-c. Fluid inclusions with one or more solids, are respectively noted Lw-s. Fluid inclusions are noted Lw-(c) when the presence of CO_2 is only determined using Raman micro-spectroscopy.

Major and Minor Whole Carbonate Chemistry

Nine representative samples have been selected for a comprehensive chemical analysis. Rocks were crushed in a boron carbide mortar until a fine powder was obtained. The SARM laboratory (CRPG-CNRS, Nancy, France) performed the chemical analyses using $LiBO_2$ fusion and acid dissolution by ICP-AES for major elements and ICP-MS for trace elements. Whole carbonate chemical compositions are reported in table 1, together with the detection limits. Analytical uncertainties depend on the

content and more details can be found in Carignan and others (2001) and on the laboratory webpage (http://helium.crpg.cnrs-nancy.fr/SARM/pages/roches.html).

Sample		**MUR 09-99**	**MUR 09-46**	**MUR 09-48**	**MUR 09-33**	**MUR 09-37**	**MUR 09-28**	**MUR 09-27**	**MUR 09-53**	**MUR 09-32**
site	*DL*	Gravelotte	Beta decline	Beta decline	Athens	Athens	Monarch	Monarch	Monarch	Free State
species		**Fe-dolomite**	**Fe-magnesite**	**Fe-dolomite**	**Fe-dolomite**	**Fe-magnesite**	**Fe-dolomite**	**Fe-dolomite**	**Fe-dolomite**	**Fe-magnesite**
CaO	*0.035*	28.19	0.90	23.71	24.48	1.80	25.42	28.12	28.95	4.95
MgO	*0.02*	17.70	33.68	21.26	14.64	30.28	19.08	17.26	18.97	31.85
Fe_2O_3	*0.01*	4.52	17.92	5.10	10.80	19.71	4.53	6.40	3.39	11.01
MnO	*0.0005*	0.31	0.33	0.13	0.64	0.47	0.12	0.32	0.11	0.21
SiO_2	*0.5*	4.22	bdl	5.32	7.12	2.04	7.25	3.42	2.51	5.79
Al_2O_3	*0.02*	*bdl*	*bdl*	0.27	0.16	*bdl*	0.03	0.04	*bdl*	0.17
Na_2O	*0.03*	0.05	0.04	0.21	0.06	*bdl*	0.06	0.05	0.04	0.13
K_2O	*0.01*	0.01	*bdl*	*bdl*	0.05	*bdl*	*bdl*	*bdl*	*bdl*	*bdl*
TiO_2	*0.001*	*bdl*	0.002	*bdl*	0.00	*bdl*	*bdl*	0.001	*bdl*	*bdl*
P_2O_5	*0.05*	*bdl*	*bdl*	*bdl*	*bdl*	*bdl*	*bdl*	*bdl*	*bdl*	0.05
L.O.I.		44.20	46.01	44.03	41.01	44.51	42.99	43.61	45.51	44.95
Total		99.19	98.88	100.02	98.96	98.81	99.48	99.21	99.49	99.11
La	*0.06*	1.597	*bdl*	0.835	0.682	*bdl*	1.268	1.824	1.073	0.138
Ce	*0.1*	5.063	0.135	3.195	2.21	*bdl*	4.521	6.645	4.378	0.59
Pr	*0.008*	0.828	0.02	0.601	0.359	0.018	0.817	1.137	0.838	0.118
Nd	*0.03*	4.179	0.124	3.478	1.78	0.109	4.584	6.057	4.887	0.696
Sm	*0.007*	1.39	0.066	1.72	0.811	0.055	2.114	2.837	2.109	0.327
Eu	*0.004*	0.706	0.039	0.858	1.025	0.076	1.158	1.836	1.308	0.134
Gd	*0.02*	2.029	0.114	2.586	1.23	0.077	3.233	4.756	2.713	0.534
Tb	*0.004*	0.375	0.022	0.48	0.229	0.015	0.621	0.948	0.504	0.107
Dy	*0.007*	2.784	0.186	3.353	1.387	0.12	4.316	6.268	3.577	0.75
Ho	*0.001*	0.635	0.055	0.734	0.268	0.033	0.914	1.285	0.801	0.174
Er	*0.003*	1.855	0.224	2.205	0.742	0.13	2.628	3.614	2.42	0.555
Tm	*0.005*	0.274	0.057	0.342	0.106	0.03	0.389	0.527	0.385	0.093
Yb	*0.003*	1.852	0.509	2.301	0.76	0.296	2.524	3.472	2.519	0.716
Lu	*0.001*	0.281	0.097	0.339	0.112	0.064	0.34	0.48	0.382	0.121
Y	*0.4*	18.66	1.665	21	7.123	1.041	26.23	37.85	23.52	4.964
Sb	*0.1*	144	46.7	180	6.49	7.15	24.5	19.3	38.2	55.8
As	*1.1*	1.92	461	10.4	10.1	5.42	2.60	19.8	33.1	157
V	*0.45*	24.8	11.7	12.2	7.31	3.88	4.94	7.80	14.2	13.0
Cr	*4*	20.5	39.9	64.5	36.2	23.7	37.7	37.9	84.1	82.7
Co	*0.35*	1.05	20.2	1.40	1.59	31.3	1.55	1.24	3.34	20.2
Ni	*4.5*	11.8	239	33.5	21.9	240	26.4	19.2	45.1	231
Cu	*4.5*	34.68	*bdl*	*bdl*	*bdl*	12.1	*bdl*	*bdl*	21.2	*bdl*
Zn	*14*	*bdl*	70.0	24.2	30.3	52.0	23.4	20.0	15.2	37.2
Pb	*0.9*	*1.29*	*bdl*	*bdl*	12.0	*bdl*	*bdl*	*bdl*	5.6	*bdl*
Cd	*0.12*	*bdl*	*bdl*	*bdl*	0.39	*bdl*	*bdl*	*bdl*	0.23	*bdl*
Ga	*0.2*	*bdl*	*bdl*	*bdl*	0.50	*bdl*	*bdl*	0.23	*bdl*	0.22
Ge	*0.11*	*bdl*	*bdl*	*bdl*	*bdl*	*bdl*	0.13	*bdl*	*bdl*	*bdl*
W	*0.2*	0.22	0.74	0.58	*bdl*	*bdl*	0.21	0.44	*bdl*	0.27
Cs	*0.15*	*bdl*	*bdl*	0.16	0.27	*bdl*	*bdl*	*bdl*	*bdl*	*bdl*
Rb	*0.3*	0.40	0.39	0.39	1.64	*bdl*	*bdl*	0.32	*bdl*	*bdl*
Sr	*1.4*	242	11.4	230	1004	24.9	406	547	298	40.1
Ba	*1.5*	10.2	14.9	33.0	37.0	7.60	5.81	13.0	20.3	9.82
U	*0.03*	*bdl*	*bdl*	*bdl*	*bdl*	*bdl*	*bdl*	0.03	*bdl*	*bdl*

major elements in wt%, minor elements in ppm. DL: detection limit. bdl: below detection limit. L.O.I.: lost on ignition

Table 1: *Chemical compositions of carbonate from selected veins along the Antimony Line. REE patterns illustrated on figure 5.*

Fuchsite ^{40}Ar-^{39}ArDating

Fuchsite grains coming from the Monarch (MUR 09-26) and Free State mines (MUR 09-31) schists were dated by the ^{40}Ar-^{39}Ar dating method at the University of Rennes 1 Argon laboratory.

The fuchsite separates were wrapped in Al foils to form small packets (11 × 11 mm) that were stacked up with other samples to form a pile within which packets of fluence monitors were inserted every 10 samples. The irradiation standard was amphibole Hb3gr (Turner and others, 1971; Roddick, 1983; Jourdan and others, 2006; Jourdan and Renne, 2007; 1081.0 ± 1.2 Ma according to Renne and others, 2010 and 2011). This pile was irradiated at the McMaster reactor (Hamilton, Canada) in the 5C location for 133.5 hr (total fluence of 8×10^{18} n.cm^{-2}). The sample arrangement within the irradiation allowed to monitor the flux gradient with a precision of 0.2 %.

Step-heating analyses of fuchsite grains were performed with a CO_2 laser probe. The experimental procedure was described by Ruffet and others (1991, 1995). The five argon isotopes and the background baselines were measured in eleven cycles, in peak-jumping mode. Blanks were performed routinely each first or third/fourth run, and subtracted from the subsequent sample gas fractions. All isotopic measurements are corrected for K, Ca and Cl isotopic interferences, mass discrimination and atmospheric argon contamination. Apparent age errors are plotted at the 1σ level and do not include the errors on the $^{40}Ar^*/^{39}Ar_K$ ratio and age of the monitor and decay constant. The errors on the $^{40}Ar^*/^{39}Ar_K$ ratio and age of the monitor and decay constant are included in the final calculation of the (pseudo-)plateau age error margins or for apparent ages individually cited. Analyses were performed on a Map215® mass spectrometer.

It is commonly considered that a plateau is obtained when calculated $^{40}Ar^*/^{39}Ar_K$ ratios of at least three consecutive steps, comprising a minimum of 70 % of the ^{39}Ar released, agree within 1 or 2σ error bars with the weighted mean calculated $^{40}Ar^*/^{39}Ar_K$ ratio of the plateau segment. Pseudo-plateau ages can be defined with less than 70% of the ^{39}Ar released. All ages are displayed at the 1σ level.

Analytical data, parameters used for calculations (isotopic ratios measured on K, Ca and Cl pure salts; mass discrimination; atmospheric argon ratios; J parameter; decay constants…) and reference sources are available in supplementary data repository.

QUARTZ-CARBONATE VEINS

Petrography

Veins in the Antimony Line appear as stockworks. Most of the veins are commonly several cm in width, sometimes infra-centimetric, and rarely exceed 1 m in width. Some are boudinaged (fig. 3A, B and C) or sheared in the foliation (fig. 3G). This type of veins can be considered as early with respect to deformation. Other veins consist of tension cracks in competent lithologies, perpendicular to the foliation (fig.

3E, J and fig. 4B), or open-space filling in pre-existing veins (fig. 4A and C). These latter veins are thus coeval with deformation. Finally, some late veining is illustrated by veins cross-cutting foliation (fig. 3F, H and 4G). As a whole, veining can be thus considered as synkinematic.

The veins are most often quartz- and carbonate-bearing (table 2). Sample MUR 09-102 is an exception as it is pure calcite. Veins contain variable proportion of quartz and carbonate, from 1% to 90% volume of carbonate, with no clear correlation with the nature of the immediate host rock. At the vein scale, quartz and carbonate seem synchronous (epitaxic carbonate in quartz, fig. 3F, H; euhedral carbonate with quartz, fig. 3B). At a microscale, they seem somewhat diachronic: the quartz often postdates carbonate by cutting it (fig. 4D) or by filling space in carbonate boudins (fig. 4C). On the opposite, carbonate may crystallize after quartz, in the neck of quartz boudins (fig. 4A), as micro-tension cracks (fig. 4B) across quartz grain joint or is found cross-cutting quartz grains (fig. 4F). Sb-sulfides (stibnite, berthierite, ullmanite) seem more often associated with quartz precipitation (fig. 4C and D) than with carbonate (fig. 4A). Within the veins and in the immediate host rock, the paragenesis includes very often chlorite (fig. 4A), talc, tourmaline, epidote (fig. 4F), fuchsite (fig. 3F and I), sometimes biotite (in reaction rims, fig. 4G) and albite.

Fig. 3 (next page): *Mine and hand sample pictures of veins. A Athens shaft: quartz- (and minor carbonate-) boudinaged veins, and locally slightly folded (F). B sample MUR 09-18 (Monarch): boudinaged vein in a chloritoschist, with carbonate minerals in periphery (C) and quartz in the center (Q). C sample MUR 09-36 (Athens shaft): chlorite-talc schist displaying boudinaged cm-scale nodules of carbonate minerals (C) and cross-cutting quartz zone (Q); note the tension crack of quartz, pyrite and stibnite to the right (TC).D MUR 09-99 (Gravelotte shaft) quartz-carbonate vein including stibnite (Stb) and fuchsite (Fu) E Beta decline: vertical massive layer (within schistose talc zone) with a set of horizontal tension cracks filled by quartz-carbonate assemblage (sample MUR 09-48) F MUR 09-43 (Old Gravelotte mine): schistose fuchsite-rich rock and cross-cutting veins made of quartz in the centre (Q) and epitaxic carbonate (C) G MUR 09-50 (Beta decline): foliated, carbonated, talc-chlorite schist with a quartz-carbonate vein crosscutting the foliation and also shifted between syn-foliation shear planes H MUR 09-32 (Free State decline): vein made of epitaxic, typical orange carbonate (C1), white carbonate (C2) and quartz (Q), with a tourmaline-rich host schist. I Free State mine: wide vein made of quartz (white), carbonate (orange) and fuchsite (green) (sample MUR 09-47). Foliation is almost in the plane of the picture, the vein cuts across it and is foliated.J Beta decline: zoned tension gashes of stibnite (Stb) and quartz (Q).*

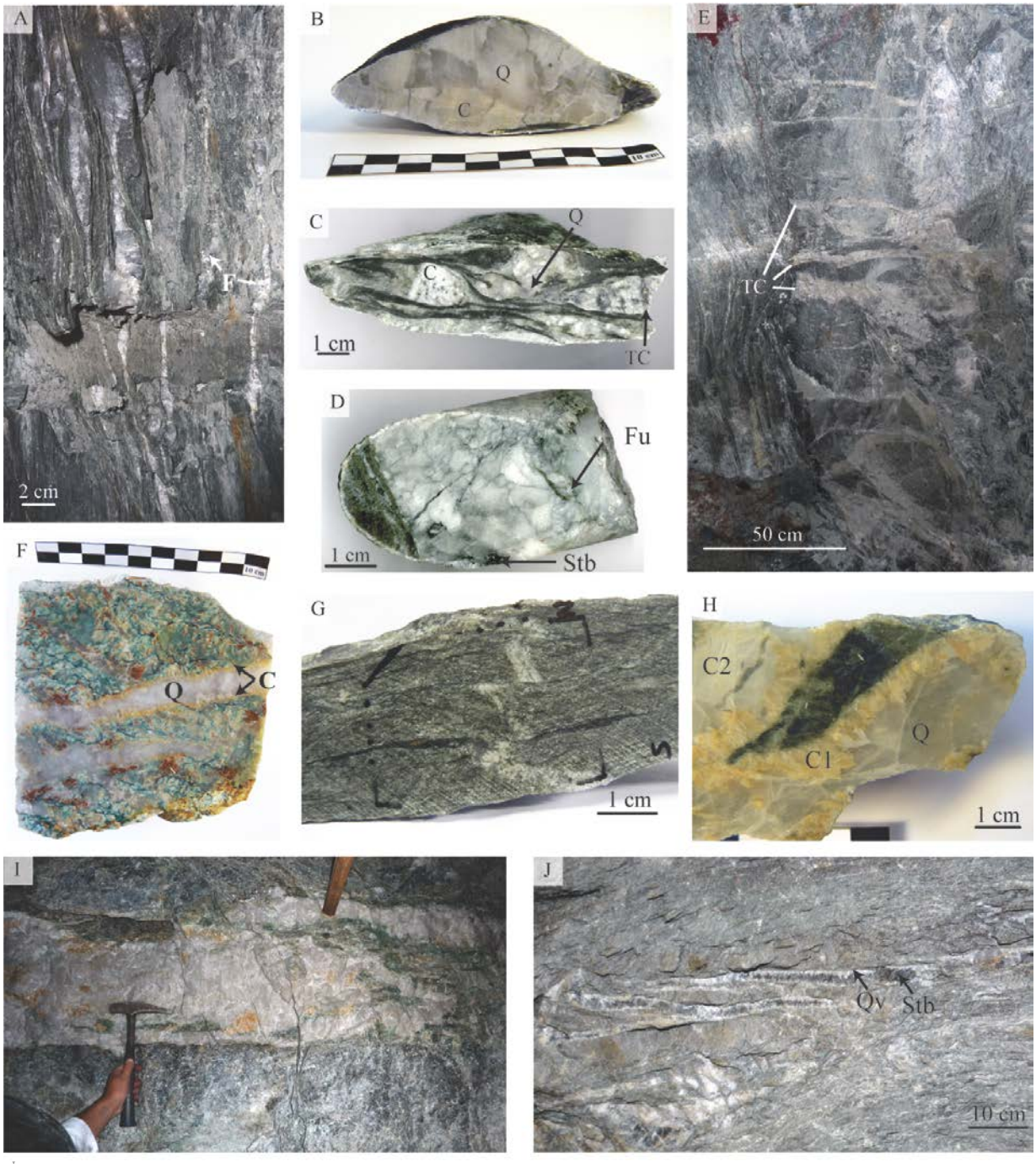
A
F
2 cm
B
Q
C
C
Q
C
1 cm
TC
D
Fu
1 cm
Stb
E
TC
50 cm
F
Q
C
G
1 cm
H
C2
Q
C1
1 cm
I
J
Qv
Stb
10 cm

Fig. 4 (next page): *Thin section pictures of veins. Bar scale 500µm. A MUR 09-105 (Gravelotte): quartz-chlorite schist and vein. The vein is made of boudinaged quartz, and at the neck sulfide and associated carbonate. Note chlorite within the vein. B MUR 09-95 cross-polar light: example of carbonate (micro tension-cracks) clearly cross-cutting quartz. C MUR 09-36: in chlorite schist, vein parallel to foliation is made of two carbonate assemblages that separate a space where stibnite and quartz are elongate parallel to foliation, displaying a tension gash. D MUR 09-99: a carbonate mineral is split in two by a quartz-stibnite veinlet that is also associated with new, euhedral, clear carbonate. E MUR 09-94 sulfide can be altered by a chlorite-quartz foliated paragenesis. F MUR 09-104: in a vein, quartz divides an epidote crystal. Both are cut across by carbonate. G MUR 09-90B carbonate and minor quartz vein at high angle to foliation of the chloritic host rock. Along the vein and within it, there is biotite, slightly reoriented.*

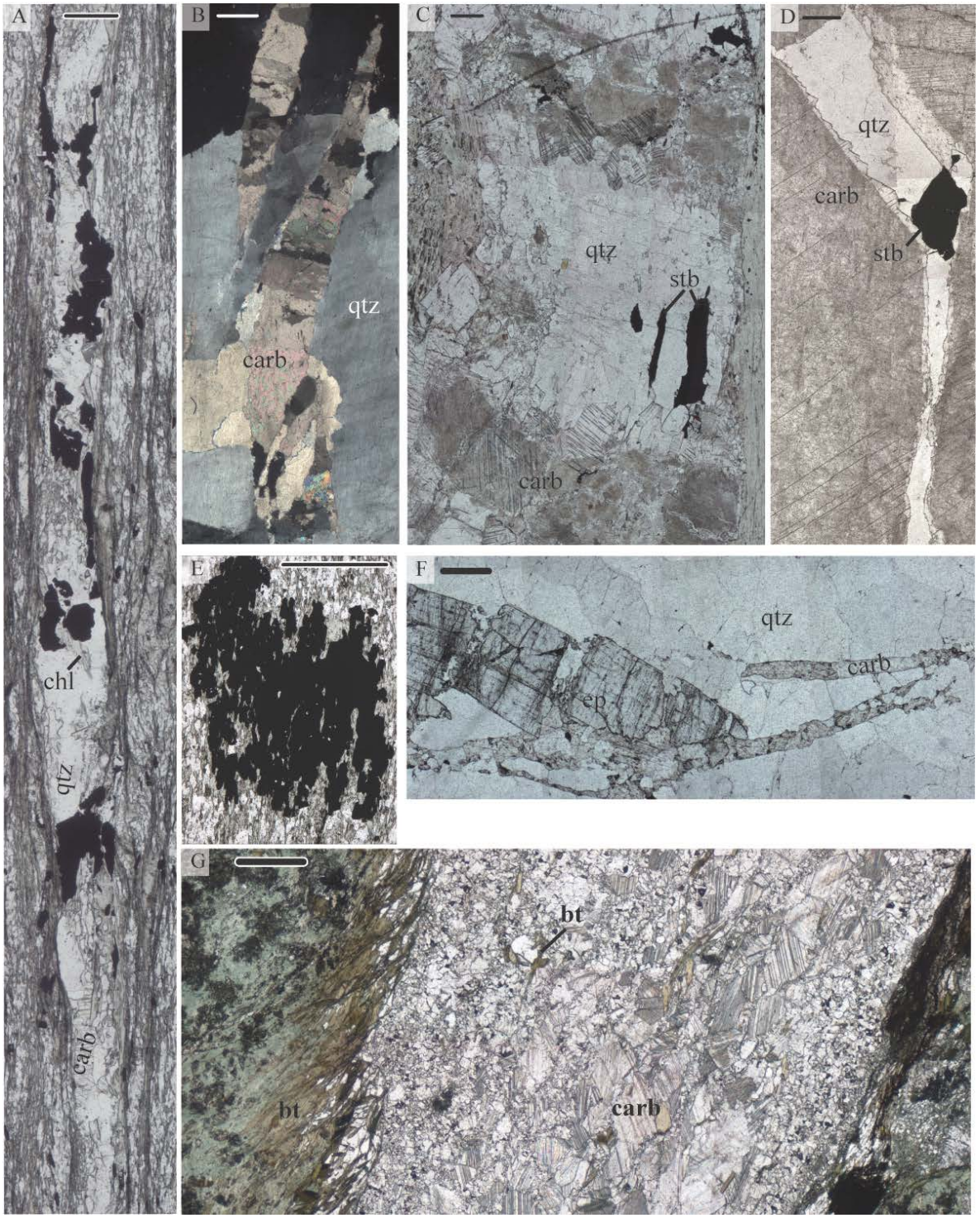

Chemical Composition of the Carbonate Fraction

Carbonates in the Antimony Line veins are mostly under the form of ferroan dolomite and ferroan magnesite (in equal proportion), sometime of calcite and rarely of ankerite (table 1 and 2). Magnesite incorporates up to 27 mol.% of siderite, while dolomite incorporates at least 14 and up to 32 mol% of ankerite. These phases are sometimes mingled. In the Malati Pump quarry, carbonates are only under the form of calcite and ankerite.

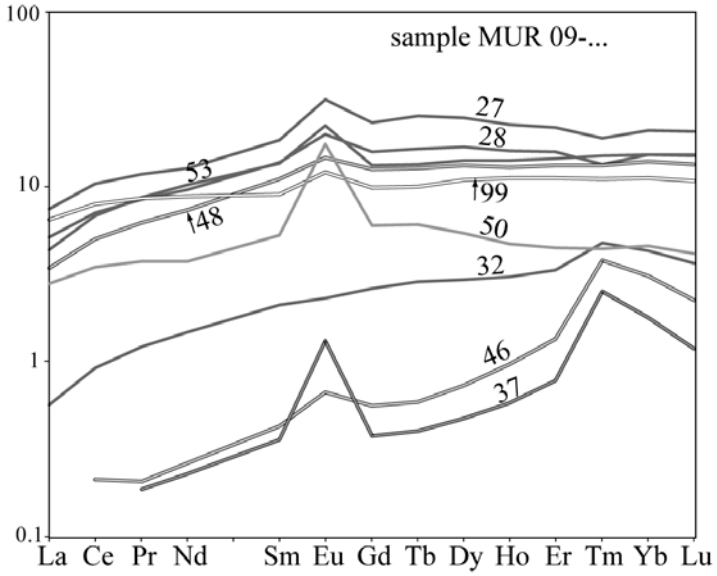

Fig. 5: *Rare Earth Elements pattern for the studied veins (Evansen, 1978).*

The Rare Earth Element (REE) distribution of representative carbonates is reported in figure 5. The carbonates display flat MREE and HREE patterns, with slight depletion in LREE. A Eu positive anomaly is present in most samples. Most samples are 10 times the chondrite values, with the notable exception of samples MUR 09-32, 09-46 and 09-37 that yield much lower content. The metal content of carbonates is variable from one sample to another (table 1), but Sb and As are systematically enriched (up to 180 ppm Sb), while other base metals have erratic contents (low Cu, Pb, Ga and Ge versus high Ni, Cr and Zn).

Fuchsite ^{40}Ar-^{39}ArDating

The two analyzed fuchsite grains yield distinct age spectra with slightly distinct ages. Fuchsite MUR 09-31 from the Free State mine displays a staircase-shaped age spectrum. It allows calculating two pseudo-plateau ages at 2005.4 ± 2.4 Ma and 2024.0 ± 1.9 Ma, respectively in the low and high temperature steps (fig. 6). Such shape could be related to various causes, such as losses of radiogenic ^{40}Ar by diffusion (Turner and others, 1971) or mixing between distinct mineral phases with distinct ages due to partial recrystallization or neocrystallization. The age spectrum of fuchsite MUR 09-26 from the Monarch mine favors the second hypothesis. Despite high apparent ages in the first 30% of $^{39}Ar_K$ degassing, probably related to a slight recoil effect, it allows calculating a plateau age at 2006.1 ± 2.3 Ma, interpreted as a crystallization age. This age is fully concordant with the low temperature pseudo-plateau age of the previous fuchsite and suggests that sample MUR 09-31 experienced a partial recrystallization at ca 2005 Ma of an older ca 2025 Ma fuchsite phase.

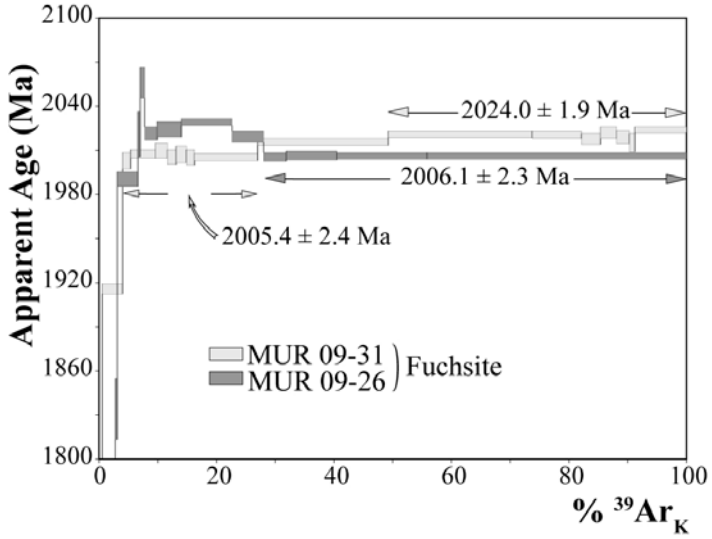

Fig. 6: *^{40}Ar-^{40}Ar age spectrum of fuchsite.*

STABLE ISOTOPE

At a regional scale, the $\delta^{18}O$ values of the quartz veins are rather homogeneous and span only over 3.6 delta units (10.6-14.3‰, table 2, fig. 7). At the scale of the Antimony Line, this oxygen isotope range narrows down to 3.3‰ (10.9-14.3‰), while carbonates display wider and globally lower $\delta^{18}O$ values (from 8.8 to 13.9‰, fig. 7) than the associated quartz. The $\delta^{13}C$ values in carbonates vary from -8.5 to -2.6‰ (fig. 8), which is slightly wider but consistent with the data from Smith (1986; $\delta^{13}C$ = -6.5 to -4‰) and consistent with the limited data (n=4) of Kedda (1992; $\delta^{13}C$ = -7 to -5.5‰) obtained on comparable materials from the Antimony Line.

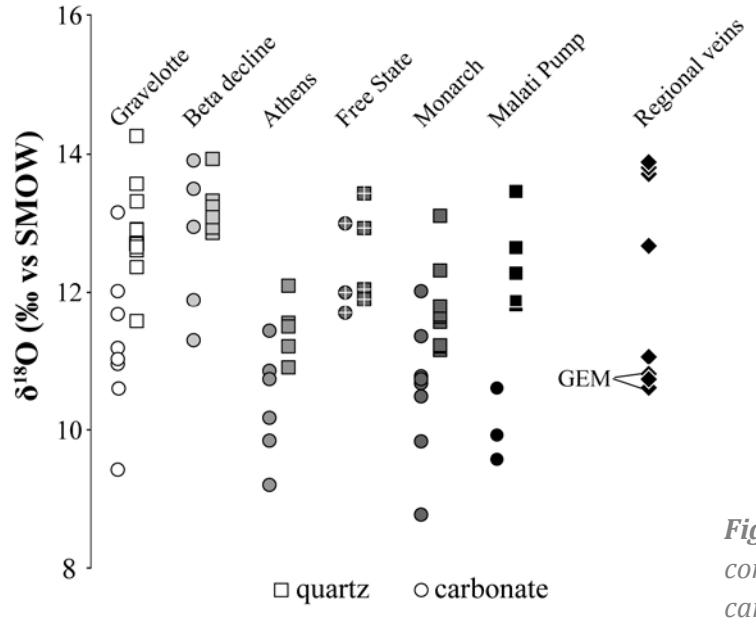

Fig. 7: *Oxygen isotopic compositions of quartz and carbonates in Sb-mine veins and regional veins.*

Sample	site	carbonate				quartz	
			$\alpha^{18O}_{(CO_2\text{-}Carb)}$	$\delta^{13}C$ (‰)	$\delta^{18}O$ (‰)	$\delta^{18}O$ (‰)	$\Delta^{18}O_{Qz\text{-}Carb}$ (‰)
MUR 09-42	Gravelotte - Old decline					13.6	
MUR 09-43	Gravelotte - Old decline	Fe-magnesite	1.00943	-4.70	13.2	13.3	0.1
MUR 09-93	Gravelotte - Shaft	NA				12.9	
MUR 09-94	Gravelotte - Shaft	ankerite	1.00914	-5.08	11.2	12.4	1.2
MUR 09-95	Gravelotte - Shaft	Fe-dolomite	1.00926	-4.95	10.6	12.6	2.0
MUR 09-96	Gravelotte - Shaft	calcite	1.00931	-5.32	11.0		
MUR 09-99	Gravelotte - Shaft	Fe-dolomite	1.00919	-4.66	9.4	11.6	2.2
MUR 09-102	Gravelotte - mine	calcite	1.00822	-7.38	12.0		
MUR 09-103	Gravelotte - mine	calcite	1.00937	-3.96	11.0	12.7	1.7
MUR 09-104	Gravelotte - mine	calcite	1.00819	-2.59	11.7	12.7	1.0
MUR 09-09	Gravelotte - city	dissolved (wheathered)				14.3	
MUR 09-10	Gravelotte - city	dissolved (wheathered)				12.9	
MUR 09-46	Beta decline	Fe-magnesite	1.00937	-5.25	13.5	13.3	-0.2
MUR 09-47	Beta decline	Fe-magnesite (40%) + Fe-dolomite (60%)	1.00932	-4.90	13.0	13.1	0.1
MUR 09-48	Beta decline	Fe-magnesite (10%) + Fe-dolomite (90%)	1.00923	-5.67	11.9	13.2	1.3
MUR 09-49	Beta decline	NA				12.9	
MUR 09-50	Beta decline	Fe-dolomite	1.00931	-6.06	11.3	12.9	1.7
MUR 09-51	Beta decline	calcite	1.00819	-4.87	13.9	13.9	0.0
MUR 09-33	Athens Shaft	ankerite	1.01052	-5.62	10.9	12.1	1.2
MUR 09-35	Athens Shaft	calcite (10%) + ankérite (90%)	1.00910	-5.64	9.2	10.9	1.7
MUR 09-36	Athens Shaft	Fe-dolomite (early, as boudin)	1.00924	-3.23	10.2		
		Fe-magnesite (late, as massive vein)	1.00938	-5.85	10.7	11.2	0.5
MUR 09-37	Athens Shaft	Fe-magnesite	1.00935	-6.74	11.4	11.5	0.1
MUR 09-38	Athens Shaft	Fe-dolomite	1.00931	-5.31	9.9	11.6	1.7
MUR 09-18	Monarch	Fe-dolomite (early, as boudin)	1.00927	-4.71	9.8	11.6	1.8
			carbonate-free late quartz vein -->			11.7	
MUR 09-19	Monarch	NA				12.3	
MUR 09-20	Monarch	Fe-magnesite	1.00936	-4.74	10.7	11.2	0.5
MUR 09-22	Monarch	NA				11.6	
MUR 09-23	Monarch	Fe-dolomite	1.00924	-5.09	8.8	11.2	2.4
MUR 09-24	Monarch					11.7	
MUR 09-27	Monarch	Fe-dolomite	1.01051	-5.39	10.5	11.7	1.2
MUR 09-28	Monarch	Fe-magnesite	1.00937	-4.43	12.0	11.8	-0.2
		Fe-dolomite	1.00932	-4.85	10.8	11.8	1.0
MUR 09-52	Monarch - vicinity of mine	Fe-dolomite	1.00918	-5.16	10.7	11.2	0.5
MUR 09-53	Monarch - vicinity of mine	Fe-dolomite	1.00923	-7.52	11.4	13.1	1.7
MUR 09-29	Free State decline	NA				13.4	
MUR 09-30	Free State decline	Fe-magnesite	1.00939	-8.10	12.0	12.9	0.9
MUR 09-31	Free State decline	Fe-magnesite	1.00940	-8.49	13.0	11.9	-1.1
MUR 09-32	Free State mine	Fe-magnesite (50%) + Fe-dolomite (50%)	1.00925	-6.09	11.7	12.1	0.4
MUR 09-12	Malati Pump mine					13.5	
MUR 09-90 A	Malati Pump mine	calcite	1.00820	-4.60	9.6	11.8	2.2
MUR 09-90 B	Malati Pump mine	calcite		-5.65	9.7	11.9	2.2
MUR 09-90 C	Malati Pump mine	calcite	1.00937	-4.71	9.9	12.3	2.4
MUR 09-91	Malati Pump mine	ankerite	1.00910	-8.06	10.6	12.7	2.1
MUR 09-110	Selati game reserve					11.1	
MUR 09-68	South-east border					13.7	
MUR 09-71	South-east border					12.7	
MUR 09-76	Gravelotte Emerald Mine					10.6	
MUR 09-77	Gravelotte Emerald Mine					10.8	
MUR 09-86	Witkop hill					10.7	
MUR 09-17	Bawa arm quartzite			*late quartz vein -->*		13.8	
				syn-folial quartz vein -->		13.9	

Table 2: *Isotopic compositions of veins in the Murchison Greenstone Belt with special emphasis on the Antimony Line. See text for details.*

In detail, some differences in the $\delta^{18}O$ values of quartz and carbonate exist depending on the sampling sites along the Antimony Line. In Athens and Monarch mines, the $\delta^{18}O$ values are quite low ($\delta^{18}O$quartz<12.3‰, excepted one high value of 13.1‰); on the contrary, Gravelotte, Beta decline and Free State mines have higher $\delta^{18}O$ ($\delta^{18}O$quartz>12.1‰, excepted one low value of 11.6‰). Noteworthy, the Malati Pump site shows peculiar signatures, with low $\delta^{18}O$carbonate but high $\delta^{18}O$quartz. Nevertheless its C and O isotope signatures cover the same range than the other Antimony Line samples, albeit this site is an unusual deposit, Au- rather than Sb-dominated. However, excluding Malati Pump site, it is not possible to correlate these features with a peculiar location within the Antimony, nor with the host rock parageneses, the depth, the presence or absence of fuchsitization in the host rocks or the carbonate mineralogy.

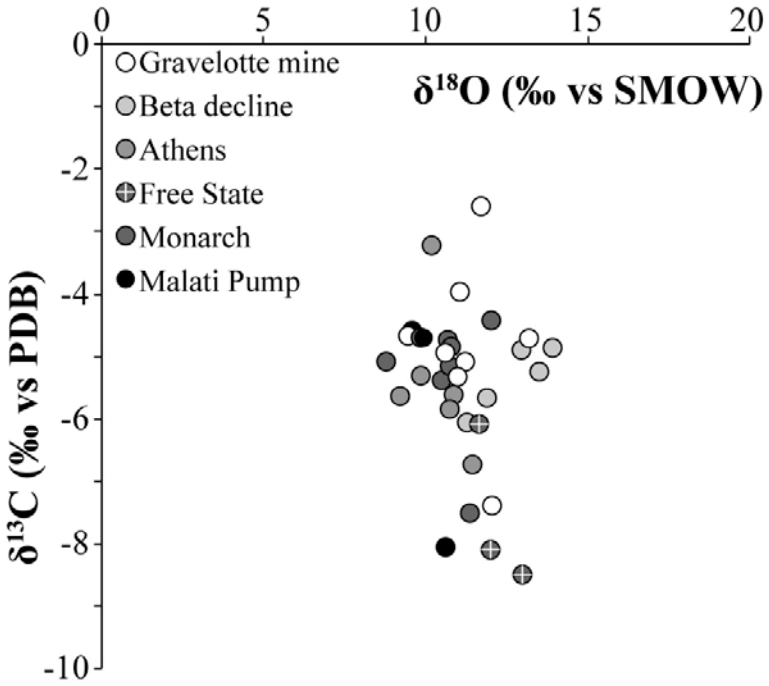

Fig. 8: *Carbon and oxygen isotopic compositions of carbonates from Sb-mine veins.*

For quartz-carbonate veins, the $\Delta^{18}O_{quartz\text{-}carbonate}$ spans from -1.1 to 2.4‰ (table 2). For most of data, the $\Delta^{18}O$ is positive, which is consistent with equilibrium fractionation between these two phases. The variable fractionation nevertheless reflects a very wide range of unrealistic apparent temperature of equilibrium, from about 120°C up to 930°C (respectively for $\Delta^{18}O_{quartz\text{-}dolomite}$ = 2.4 ‰ and 0.2 ‰, Zheng, 1999). Indeed, there is no correlation between the apparent temperature and the mineralogy of the veins or the type of host rocks. At low apparent temperature, either biotite (MUR 09-90C) or chlorite (MUR 09-23) is observed in veins, but this is true as well at high apparent temperature (biotite in MUR 09-46 and chlorite in MUR 09-28). The negative values, which clearly indicate isotopic disequilibrium between quartz and carbonate, are found in different mines. Again, no systematic correlation between isotopic disequilibrium and mineralogy or relative chronology can be drawn.

FLUID INCLUSIONS

Several types of inclusions have been recognized in the studied samples (table 3, fig. 9), either in quartz or in carbonate. Fluid inclusions are rather small, mostly 5 to 10 µm in size, and sometime up to 30µm. They are found either isolated or along planes. There are monophasic (liquid), two (liquid + vapor) or three (liquid + vapor + solid) phasic at room temperature.

- Aqueous carbonic fluid inclusions (Lc-w): they are observed either in quartz and carbonate from the veins associated with Sb mineralization. They display two phases at room temperature (H_2O liquid + volatile liquid phase, fig. 9D, E). The percentage of the H_2O phase (flw) is highly variable (20 to 80%, table 3, fig. 9D) but most of the Lc-w inclusions show flw around 40 to 50%. The melting temperature of CO_2 ($TmCO_2$) ranges from -58.9 to -56.6 °C with a mode around -57°C. The homogenization temperature of CO_2 ($ThCO_2$) occurs to the liquid phase in temperatures ranging from 0.1 to 13.6°C with a mode at 6°C. Melting temperature of clathrate (Tm Cl) is observed between 2.6 and 6.5°C (mode at 5°C). The melting temperature of ice (Tm ice) ranges from -11.4 to -3.5°C. However, most of the Tm ice values are comprised between -5 to -7°C. Homogenization temperatures (Th) are observed from 280°C to up to 350°C. Numerous fluid inclusions decrepitated in the range of 320-350°C. Raman analyses showed that CO_2 is the main component of the volatile phase and is always higher than 86.5 mol.% (most of the data show CO_2 content in between 94 and 97 mol.%). The CH_4 content ranges from 0.7 to 4.3 mol.% but can reach in some cases up to 8 mol.%. N_2 contents are mostly observed in the range of 0.4 to 4.2 mol.% and some data are measured up to 10 mol.%. Traces of H_2S have been observed. Bulk compositions of these inclusions show relatively variable content in H_2O and CO_2 + CH_4+ N_2 (table 4) due to the large range of liquid/volatile ratio (20 to 80%).
- Carbonic inclusions: Lc inclusions were observed in quartz from the quartz veins closed to the Sb minerals (fig. 9A, B). They can be found isolated or as planes (fig. 9B). They are monophasic at room temperature. $TmCO_2$ ranges from -58 to -56.7 °C with a mode around -57°C. $ThCO_2$ occurs to in the liquid phase in the range of -3.8 to 4°C. The Raman analyses showed that the compositions of the volatile phase are very similar to that of the Lc-w inclusions. The CO_2 contents range from 90 to 98 mol.%. CH_4 and N_2 contents are range from 0.6 to 5 mol.% and 1.2 to 5.6 mol.% respectively.
- Aqueous inclusions Lw-(c), Lw-(c)-s, Lw-s or Lw are scattered or were observed along planes in the same quartz crystal than the Lc and Lc-w inclusions (fig. 9C, F). Tm ice range from -1.7 to -12.8°C and the corresponding salinity is comprised between 3 and 16.7 wt.% eq. NaCl (Bodnar, 1993). Two ranges of Th have been obtained for these inclusions. A part of the Lw-(c), Lw-(c)-s, Lw-s inclusions display Th ranging from 280 up to 350°C. Small Lw fluid inclusions show Th in the range 150 to 200°C. Lw-(c)-s and Lw-(c) show traces of gas. For most of them, the composition of the volatile phase is comparable to

those of the Lc-w and Lc inclusions, for example CO_2 in the range of 99.8 to 91 mol.%, CH_4 when detected from 0.2 to 3.3 mol.% and N_2 from 0.2 to 7.7 mol.%. In some of these inclusions, the CO_2 content is lower (around 70 mol.%) and CH_4 content increases up to 25 mol.%. N_2 content is between 5 to 10 mol.%. Solid has been identified as nahcolite ($NaHCO_3$, fig. 8G) by Raman spectroscopy with the typical bands at 1041 and 1265 cm^{-1}. HCO_3^- and dissolved CO_2 have been determined in the liquid phase.

Sample	Occurrence	Type of fluid inclusions		Microthermometry (°C)					volatile phase (mol.%)		
			flw	Tm CO_2	Th CO_2	Tm Cl	Tm ice	Th	CO_2	CH_4	N_2
MUR09-43[1], MUR09-18	quartz and carbonate veins	aqueous-carbonic inclusions	20 to 80%	-58.9 to -56.6	0.1 to 13.6 (L)	2.6 to 6.5	-11.4 to -3.5	280 to >350			
MUR09-93, MUR09-36		Lc-w	mostly 40-50% :	-57 (45)	6 (45)	5 (12)	-5 to -7 (44)	300 (12)	94 - 97	0.7 - 4.3	0.4 - 4.2
MUR09-93, MUR09-36	quartz veins	carbonic inclusions	0%	-58 to -56.7	-3.8 to 4 (L)						
MUR09-43		Lc		-57 (6)	- (6)				90 - 98	0.6 - 5	1.2 - 5.6
MUR09-48, MUR09-18	quartz veins	aqueous inclusions	70 to 90 %				-12.8 to -1.7	150 to 200			
MUR09-93, MUR09-36		Lw-(c), Lw, Lw-(c)-s, Lw-s					- 7 (34)	280 to >350	91 - 99.8	0.2 - 3.3	0.2 - 7.7
MUR09-99, MUR09-43								- (30)	70	up to 25	5-10

[1]: see table 4

Table 3: *Summary of the microthermometric data from the different types of fluid inclusions and chemical compositions of the volatile phase obtained by Raman spectroscopy. For each microthermometric parameter, range (first line), mode (second line) and number of measurements (in brackets) are given. For nomenclature of the fluid inclusion type, see text. Flw: fraction of the aqueous liquid. Tm CO_2: melting temperature of CO_2, Th CO_2: homogenization temperature of the volatile phase, Tm Cl: melting temperature of clathrate, Tm ice: melting temperature of ice, Th: homogenization temperature. L: Liquid.*

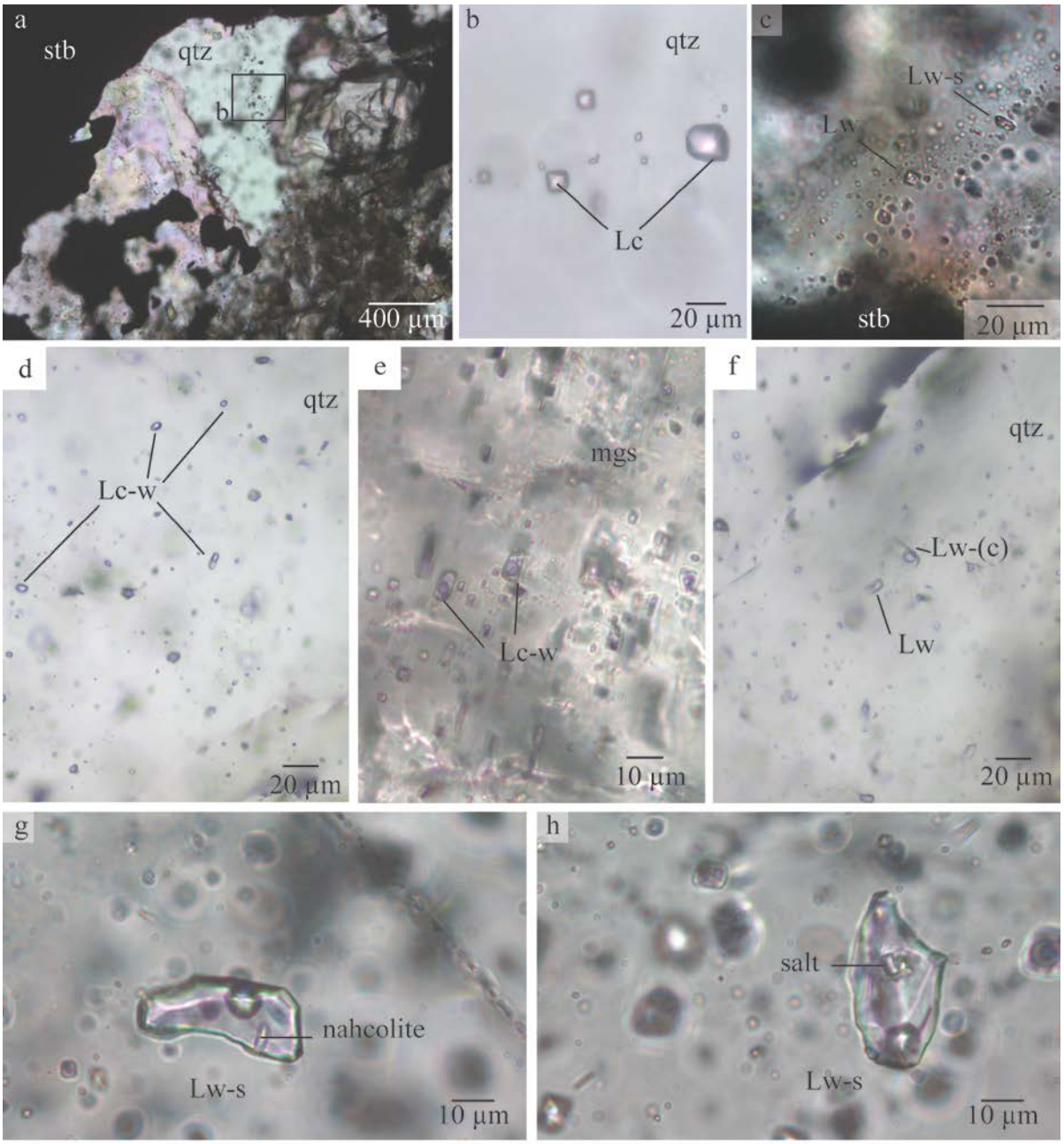

Fig. 9: *Microphotographs of the different fluid inclusions observed in the studied samples. (a) association of carbonic fluid inclusions with stibnite (stb) and quartz, sample MUR 09-36B. (b) zoom of (a) showing carbonic fluid inclusions Lc in quartz (qtz). (c) small Lw and Lw-s aqueous fluid inclusions in planes in quartz crystal close to stibnite. (d) aqueous-carbonic inclusions Lc-w in quartz showing variable H_2O/volatile ratios, sample MUR 09-43 (see table 4 for details). (e) aqueous-carbonic inclusions Lc-w in magnesite (mgs), sample MUR 09-36B. (f) aqueous inclusions with trace of gas Lw-(c) in quartz, sample MUR 09-43 (see table 3 for details). (g) and (h) aqueous inclusions with solid phase Lw-s (nahcolite) in quartz, sample MUR 09-18.*

DISCUSSION

Interaction between Fluid Circulation and Deformation

The Antimony Line and its veins have developed during deformation as illustrated by the synkinematic character of the veins. Kinematics of the shear zone consists of a top-to-the-south reverse movement (for example Vearncombe and others, 1988, Jaguin and others, 2012a) and horizontal planes of tension cracks and vertical boudinage attest to vertical stretch. At a larger scale, Viljoen and others (1978) noted a regional structural control of the mineralization on the basis of ore bodies plunges (toward the west in the western part of the Antimony Line and toward the east in the eastern part, fig. 2). Indeed, in the general kinematic context of the shear zone, the ore bodies appear as large tension gashes (parallel to the foliation and perpendicular to the stretching lineation), confirming a regional structural control of the metallogenic system.

More precisely, the Antimony Line has developed immediately south of the *Chloritoid bar-Selkirk member-Antimony bar* triad (fig. 2, Pearton and Viljoen, 1986). In the central part of the Weigel Formation, regular occurrences of low ridges made of quartz-muscovite-chloritoid schists, locally ferruginous, and of quartzites and conglomerates, is known as the *Chloritoid bar*. To the south, a layer of metabasalts is known as the *Selkirk member* (Pearton and Viljoen, 1986, tholeitic to magnesian-rich basalts) and further south, the *Antimony Bar* is made of quartzites and quartz-muscovite schists found as discontinuous lenses. The rest of the Weigel Formation is broadly composed of quartz-chlorite or quartz-muscovite schists (magnesiopelites). Pearton and Viljoen (1986) explained that the *Antimony Bar* lenses create a competency contrast, hence allowing and enhancing fluid penetration and carbonation. We further point out that there must have been a positive feed-back on the structure development thereafter because (1) fluids are expected to induce important softening during shearing (for example Barnes and others, 2004), (2) rocks, that were probably komatiites in origin (Pearton, 1980), have been altered by the fluids into incompetent talcose schist rocks in the Antimony Line, (3) while lenses of massive metasomatic carbonate rocks crystallized, providing again competency contrasts. The late brittle fracturing of carbonate bodies induced the formation of traps for ore-forming fluids (Boocock and others, 1984), at lower temperature and higher P_{CO2} (Pearton, 1980). Fluid-induced effects boosted minor primary competency contrasts, providing further localization of the deformation and fluid circulation. This evolution explains how such a localized structure without large displacements developed in a broad region of distributed deformation.

Characteristics of the Sb-Mineralizing Fluid

Temperature estimate

Quartz is the best mineral to characterize the Sb-mineralizing fluid properties, notably because Sb precipitation as sulfides seems to be associated with quartz

precipitation (see above, fig. 3J, fig. 4C and D). Indeed, the erratic behavior of the $\Delta^{18}O_{quartz\text{-}carbonate}$ values indicates that the two minerals are not in isotopic equilibrium. Quartz, unlike carbonate, is resistant to the post-crystallisation effects of alteration, associated with either late fluid circulation or deformation. The more constant values found for the quartz veins in the Antimony Line (10.9-14.3‰) relative to the carbonate (8.8-13.19‰) confirm that point.

The schistosed host rocks show variable parageneses, but they very often present the same mineralogy than the crosscutting veins. Furthermore, halos are rare, with the notable exception of the fuchsite occurrence at some of the sampling sites. Therefore, the host rocks must have been in thermal equilibrium with the fluids. The homogeneity of quartz isotopic composition on a large scale likely indicates a narrow range of precipitation temperature, otherwise a concomitant variation in temperature and fluid isotopic composition would have been required in order to produce the same isotopic signature, which appears unlikely. A major inference is that paragenesis in wall rocks is relevant to estimate the temperature of precipitation. Indeed, the coexistence of chlorite and biotite points to greenschist facies conditions. Among the observed phases, the talc-carbonate (dolomite) equilibriums in several samples point to a maximum temperature of around 450°C (Bucher and Grapes, 2011). Conversely, chloritoid occurrences require temperature higher than 400°C (in pure KFMASH or CFMASH systems, Bousquet and others, 2008). Thus, the temperature of fluid-related alteration was likely in the range 400-450°C.

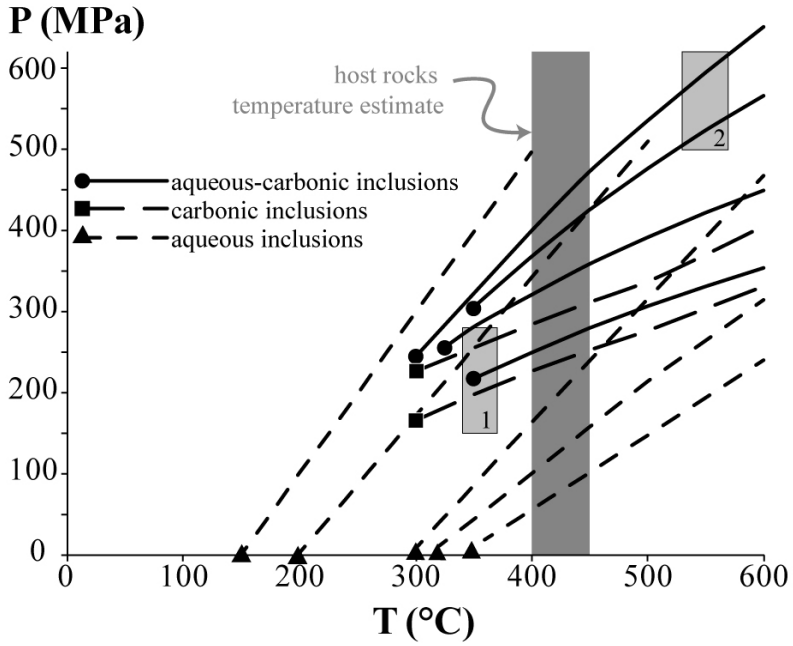

Fig. 10: *Isochores calculated from fluid inclusions data. Grey boxes are P-T metamorphic fields determined on rocks from the Murchison schists in the western vicinity of the Antimony Line for number 1 and along the southern border of the belt for number 2 (Block and others, 2012).*

This estimate is consistent with the fluid inclusion data (table 3 and table 4). Indeed, the homogenization temperatures have been measured mainly in the range 280-350°C. Isochores calculated (fig. 10) indicate that (aqueous)-carbonic inclusions formed at a minimum pressure of 160 MPa and at a minimum temperature of 350°C. P-T estimates of a sample from the Antimony Line vicinity (number 1 in fig. 10, Block and others, 2012) are in a good agreement with the base of these isochors, with a minimum

temperature of 350°C and a pressure of 200-300 MPa. The aqueous fluid inclusions with high Th cannot be formed under the same conditions. If they were formed concomitantly with carbonic and aqueous-carbonic inclusions, it would have required temperature higher than 450°C at 300 MPa. These high temperatures neither agree with the host rocks paragenesis nor with any of the two metamorphic temperature estimates of Block and others (2012). Alternatively, they could have formed at 350-400°C but under lower pressure (50-100 MPa).

Origin of the fluid

From this temperature range (350-450°C) and quartz composition range, the $\delta^{18}O_{H2O}$ value calculated is between 5.0 and 11.3‰ (using the fractionation factor of Zheng, 1993). This signature is characteristic of a metamorphic origin for the fluid, although a magmatic origin cannot be completely ruled out. It is also consistent with the oxygen isotope signature of crustal fluid calculated for the associated albitites in the Antimony Line (Jaguin and others, accepted). The sulfur isotope composition of antimony ores and pyrite in the Monarch mine is $\delta^{34}S = 2.6 \pm 0.7$‰ (Pearton and Viljoen, 1986). These authors interpreted such values as consistent with a magmatic origin in a broad sense (exhalative, hydrothermal, or remobilized magmatic for example by dissolution of the volcano-sedimentary sulfides). However, the REE distribution of carbonate with typical LREE depletion indicates that the fluid underwent a strong, if not complete, equilibration with meta-(ultra)basic rocks (fig. 5).

	microthermometry (°C)					volatile phase (mol.%)			bulk composition (mol.%)				
Inclusions	**Tm CO_2**	**Th CO_2 (L)**	**Tm Cl**	**Tm ice**	**Th**	**CO_2**	**CH_4**	**N_2**	**H_2O**	**CO_2**	**CH_4**	**N_2**	**NaCl**
43-1	-57.9	11.5	2.6	-4.2	291	96.6	1.6	1.8	74.1	20.5	0.4	0.3	4.7
43-2	-57	7.1	3.8	-7.3	326	96.7	1.9	1.4	37.2	58.6	1.0	1.1	2.1
43-3	-57.4	6.4	5.3	-6.2	309	96	2.4	1.6	59.8	35.8	0.9	0.6	2.9
43-6	-58.2	8.7	6.5	-9.2	decripated	96.8	2.3	0.9	51.0	45.7	1.0	0.4	1.9
43-7	-59.5	6.3	5.3	-8.8	>340	94.9	3.3	1.9	21.5	74.7	2.3	0.5	1.0
43-8	-58	6.3	4.4	-10.3	decripated	97.4	3	0.6	59.6	36.2	0.9	0.2	3.1
43-9	-58.3	6	5.8	-9.1	>360	96.6	2.8	0.5	60.0	36.5	0.6	0.4	2.5
43-10	-57.7	5.2	4.9	-8.8	>350	96.7	1.5	1.9	59.7	35.7	0.6	1.0	3.0
43-11	-57.5	4.8	4.2	-5.7	decripated	95.6	1.5	2.9	49.6	45.4	1.5	0.9	2.6
43-12	-58.5	6.7	3.7	-8.3	decripated	97.4	1.6	1	67.4	27.9	0.4	0.5	3.8

Table 4: *Bulk chemical compositions obtained by Raman microprobe spectroscopy and corresponding microthermometric data of aqueous-carbonic (Lc-w) fluid inclusions from sample MUR 09-43. $TmCO_2$: melting temperature of CO_2, Th CO_2: homogenization temperature of the volatile phase, Tm Cl: melting temperature of clathrate, Tm ice: melting temperature of ice, Th: homogenization temperature. L: Liquid.*

The various vein samples enclose three different types of fluids inclusions (table 3), with a large range of salinity (up to 16.7% in aqueous fluid inclusions). We therefore propose that a parental aqueous-carbonic fluid undergone unmixing into two fluids, one mainly carbonic and the other one mainly aqueous, the latter carrying traces of the same gases and sequestering salts (some nahcolite). Complementary or alternatively, unmixing could have occurred deeper and be followed by heterogeneous entrapment (Diamond, 1994), accounting for the variable water/volatile ratios in sample MUR 09-43. Regardless of the exact process, the dominant CO_2 compositions found in most of the fluid inclusions point to a metamorphic origin as already suggested by the stable isotope data. In that case relatively higher CH_4 proportion in aqueous fluid inclusions may result from the interaction with reducing host rocks. The sodium of the nahcolite solid echoes with the Na mobility documented for the albitite in the Antimony Line (Jaguin and others, accepted). The bicarbonate component of the nahcolite must be somehow related to the carbonation of the Antimony Line rocks. Carbonate bodies and veining developed during the same deformation process, so the HCO_3^--fluid in veins was likely responsible for the carbonation of the host rocks. Thus the chemistry of the fluid inclusions supports intense exchange with the hosting lithologies. As a whole, the mineralizing fluid equilibrated in the conditions of regional metamorphism. Nevertheless, the aqueous fluid inclusion type with lower Th and low salinity (250°C, table 3) may also be related to mixing with a cold and dilute fluid. This could be the sign for the involvement of a surficial fluid in addition to the metamorphic contribution. However, the oxygen isotope composition of quartz and carbonates did not record this involvement, which has thus to be confirmed further.

Finally, the carbon isotope compositions of the carbonates span over 5.6‰, which likely indicates two sources for the carbon (Smith, 1986). The lower value (down to -8.5‰) requires a deep source of CO_2 (Smith, 1986). Whether the CO_2 came directly from the degassing of the mantle or from the magma during emplacement (as suggested by Smith, 1986) or indirectly from the remobilization of carbon from the carbonate-rich altered see-floor (Groves and others, 1988), cannot be resolved in this study. We cannot exclude that part of the low $\delta^{13}C$ values may be due to the decarbonation effects of the allochthonous altered see-floor carbonate during the metamorphic stage. The higher value at - 2.6 ‰ may reflect the involvement of seawater or the input of marine carbonate-derived carbon (around 0‰), supporting the hypothesis that some surficial fluids may have been involved.

Circulation mode

During the early-to-late veining evolution, the fluid isotopic signature appears to be constant (table 2, fig. 7, and section *Origin of the fluid* above). This homogeneity together with the occurrence of strongly metasomatized rocks in the Antimony Line, confirm that the fluid is dominant in the mineralizing system along the Antimony Line (as suggested for example by Vearncombe and others, 1988).

Nevertheless, the little variations observed between the studied sites (fig. 7) might point to the influence ofthe local hosting lithologies with which the fluid partially equilibrated. These lithologies do not vary significantly from a mine to the other (detailed on maps of Vearncombe and others, 1992), but some variation in their relative proportion (for example felsic *versus* basic rocks) or their specific geochemistry may account for these different signatures. Such site-related isotopic peculiarities were already pointed out by Jaguin and others (accepted) for the carbonate fraction of metasomatic albitites from the same zone. Another hypothesis is that, from the same fluid, veins have precipitated at higher temperature in Monarch and Athens sites than in other sites, in order to get the observed lower $\delta^{18}O$ values (table 2). A variation from 350 to 450°C produces a decrease of 1.9‰ in the quartz oxygen signature, and thus is able to explain, at least to some extent, these discrepancies.

The unmixing (or mixing) processe(s) evoked in the section "origin of the fluid" are critical. Indeed both processes lower sulfur activity and are able to trigger stibnite precipitation (Guillemette and Williams-Jones, 1993). Pressure variations during cracking and veining (the "valve system" of Sibson and others, 1988) may have favored unmixing of metamorphic fluids and/or pumping and mixing of surficial fluid with metamorphic deeper fluid, as interpreted by Kontak and others (1996) in the case of the Meguma antimony deposit in Canada.

Comparison between the Antimony Line and Orogenic Gold Deposits

Common points

Pearton and Viljoen (1986) reviewed the studies published in the seventies and early eighties dealing with the metallogeny of the Antimony Line. They highlighted (1) the metamorphic-metasomatic nature of the rocks in the Antimony Line and (2) the structural control of competent lithologies on the Sb-deposits. They concluded that the Antimony Line shared characteristics with lode-gold, orogenic style deposits (as previously suggested by Viljoen and others, 1978). From our study and through the compilation of orogenic gold deposits characters by Goldfarb and others (2005), further common points can be summarized as follow.

- **Greenschist P-T conditions**. The 350-450°C and 200-300 MPa conditions of the Antimony Line zone (veins formation and host rock alteration) are enclosed in the range of orogenic gold deposits; they correspond to a mesozonal context (in the metallogenic sense of Gebre-Mariam and others, 1995). The observed gangue minerals (quartz, carbonate, albite, fuchsite, chlorite, tourmaline, biotite, pyrite and arsenopyrite) are also observed under these conditions in greenstone belts lithologies.
- **Fluid properties**. Based on the samples studied for fluid inclusions, the mineralizing Sb-fluid is very similar in composition to those encountered in orogenic gold deposits: H_2O-CO_2 fluid with trace amounts of CH_4, N_2 and H_2S, variable H_2O/CO_2, low to moderate salinity (table 3). Alike orogenic gold fluid,

the Sb-fluid is also thermally equilibrated with its host rocks and the Fe-Mg-Ca nature of carbonate reflects some chemical equilibration. Finally, the $\delta^{18}O_{quartz}$ values in this study are similar to most of those found in Archean lode gold deposits worldwide (11-14‰) as reported in the synthetic diagram of figure 11. Our interpretation of a metamorphic origin, with maybe some surficial fluid involvement, for the Sb-fluid (5.0-11.3‰) is in a good agreement with an orogenic deposit model (see also Boiron and others, 2003).

- **Structural control**. The important structural control depicted here for the Sb-deposits, in a semi-brittle-ductile mode, is a common (and even critical) parameter with in orogenic gold deposits. Consistently with the latter, the Antimony Line is a second or third order structure, albeit a first order fluid path.

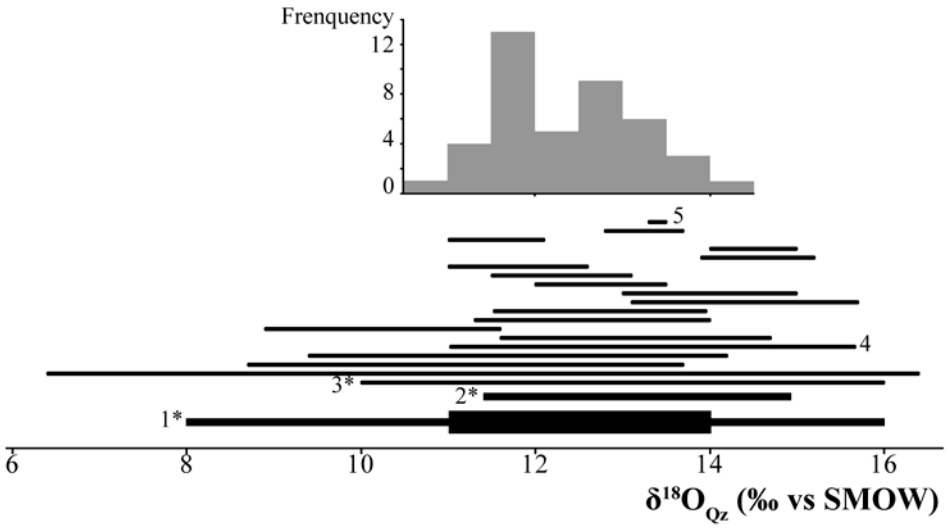

Fig. 11: *$\delta^{18}O$ of quartz from Archean lode gold deposits worldwide compare to our data from Antimony Line quartz veins (table 2). * Compilation of data from 1: Groves and Foster (1998), 2: Kerrich (1989) 3: Roberts (1987); individual deposits datasets from 4: Fyon and others (1983), 5: Golding and Wilson (1983), and all other from Gosselin and Dubé (2005) and ref. therein.*

The comparison suggests that some of the Antimony Line characteristics can fit the interpretations drawn for classical orogenic lode gold deposits. In this way, the somewhat regular spacing between deposits (fig. 1 and 2) might well correspond to fluid flow cells; the intrusive granitoid plugs in the shear zone might have further played a structural role in partitioning the deformation; as suggested above, variations in the $\delta^{18}O_{quartz}$ values may reflect litho-geochemical variations. Finally, our difficulty to (i) be unequivocal between magmatic *versus* metamorphic origin for the fluid (despite the fact that we favor the latter), (ii) identify clear carbon and sulfur sources, (iii) specify the role of magma in the Sb enrichment (Jaguin and others, 2012b), are all issues that are also encountered when trying to construct metallogenic models for orogenic gold deposits.

The nearby greenstones belts of Pietersburg (Polokwane) and Giyani host gold mineralization (review in Ward and Wilson, 1998). In the Pietersburg greenstone belt, the main gold mineralization is hosted in sub-vertical shear zones striking east-west, in quartz-carbonates-sulfide veins or in mafic talcose schists within amphibolite lenses. In the Giyani greenstone belt, gold is mainly hosted in quartz or carbonate within a ductile shear zone dipping toward the north, especially along the northern boundary of the belt where hosting lithologies are biotite-chlorite-tourmaline. The mineralization appears broadly similar in style to the Antimony Line deposit, thus reinforcing the idea that the Antimony Line is comparable to classic orogenic gold deposits found in greenstone belts.

Differences: why antimony rather than gold?

Conversely, some differences exist between the two types of deposits. First, the lithological succession in the vicinity of the Antimony Line is possibly more ultramafic than in other greenstone belts. Indeed, Mg- or Cr- phases are widespread in the gangue (talc, fuchsite), carbonates in the veins tend to be poorer in Ca compared to other gold deposits (magnesite dominates, although calcite exists), and talc-schist and carbonate (in alteration halos around the deposit centers) are Mg-and Cr-rich and Ca-poor (Viljoen and others, 1978). Secondly, the carbonation is anomalously strong (Viljoen and others, 1988), indicating a large time-integrated CO_2 input. The above differences may explain the unusual metal balance where Sb>Au, Hg, As (minor Zn-Cu-Pb, Ni-Cr, Muff and Saager, 1979) which is the obvious difference between the Antimony Line and orogenic gold deposits.

Generally, antimony deposits formed at cool 150-300°C (hypogene) conditions, that is at shallow depths (for example Nesbitt and others, 1989) and/or in a distal context relative to heat source and/or during a late phase (for example Buchholz and others, 2007). The main reason why Sb is found in a low-temperature context is that at temperature higher than 350°C, Sb is highly soluble and stibnite can only precipitate if Sb is highly enriched (thousands of ppm in the Fe-Sb-S-O system, William-Jones and Normand, 1997). It has to be noticed that, however, some Sb deposits may experience higher temperature of circulation: in the Haut Allier (Massif Central, France, 280-400°C, Bellot and others, 2003), in Lake George (Canada, 300-420°C; review in William-Jones and Norman, 1997 and Normand and others, 1996), in West Gore Sb-Au Deposit (Meguma Terrane, Nova Scotia, Canada, 350-495°C, Kontak and others, 1996). Nevertheless, these deposits were never formed at temperatures higher than 350°C, and thus the temperature-control process inferred by William-Jones and Normand (1997) may still be valid. In the case of the Antimony Line, to understand how mineralization may have occurred at such high temperatures, a first hypothesis is that the presence of Mg instead of Fe in the Fe-Sb-S-O system may change the solubility conditions for the Sb. This would be consistent with the tenuous link observed between ultramafic lithologies and Sb-anomalies in worldwide Sb deposits (Hagemann and Lüders, 2003; Huston and others, 2002, Normand and others, 1996; William-Jones and Normand, 1997). A second hypothesis is that the primary enrichment (see below)

concentrated Sb in the Antimony Line, so that the metamorphic fluid would have been easily saturated in Sb and could haveprecipitatedstibnite at higher temperature.

The Antimony mineralization and the Antimony Line in frame of the Murchison Greenstone Belt history

An early background enrichment of the MGB

Pearton (1980) indicated strong Sb-enrichment in the greenstones lithologies: magnesiopelites (mafic-to-ultramafic sedimentary rocks) of the Weigel Formation are 45 times richer than classical shales and metabasalts of the Mulati Formation are 10 times enriched. Mafic magmatic-related process(es), including inheritance, may result in Sb-enrichment of these rocks (and of sedimentary rocks derived from them) at ca 3.09 Ga (Poujol and others, 1996).

A 2.97-2.92 Ga granodiorite-related Au-Sb-mineralization

Many authors have proposed a magmatic origin nor the Sb mineralization, prior to its syntectonic metamorphic redistribution. A syngenetic volcanic origin has been preferred for a long time (Muff and Saager, 1979, Minnitt, 1975, Viljoen and others, 1978) but an older model involving a deeper, magmatic origin (van Eeden and others, 1939; Boese, 1964, see also Kedda, 1992; Ileri, 1973) was recently re-evaluated (Jaguin and others, 2012b; see also detailed discussion in Jaguin and others, accepted). The former study presents a meso- to epithermal granodiorite-related scenario for Au (and minor Sb) mineralization in the Malati Pump gold mine at 2.97 Ga, and suggests that it may be extrapolated to the entire Antimony Line deposits. It is possible that Au and Sb were remobilized from the surrounding pre-enriched host rocks during this 2.97 Ga event.

Further dating showed that the Antimony Line, at least as a structure, existed in the belt history as early as 2.97-2.92 Ga (Jaguin and others, 2012b, Jaguin and others, accepted). Noteworthy, little localized movement was accommodated by this structure despite its long history.

The ca 2.8 Ga Orogenic Sb-mineralization

Along the Antimony Line, the granodioritic Baderoukwe-related magmas emplaced at ca 2.97-2.92 Ga and these rocks have been strongly albitized at ca. 2.8 Ga by crustal fluids (ages obtained on monazite grains crystallized during albitization; Jaguin and others, 2012b, Jaguin and others, accepted). As albitization was concomitant with Sb-enrichment, the orogenic-style of Sb-mineralization can be dated at ca 2.8 Ga. This event is of regional importance and related to both magmatism and metamorphism (for details see part *Geological Setting*).

The metamorphic ore-forming fluid was at least partly extracted from the greenstone belt lithologies, from which it must have remobilized and concentrated antimony as previously argued by Pearton and Viljoen (1986). The occurrence of this

set of deposits at quite deep conditions has allowed for the preservation of the Archean Sb-deposit, which is rare for typically shallow-level metal such as Sb (Groves and others, 2005).

The ca 2.0 Ga ages

Finally, fuchsite ages correspond either to recrystallisation of much older fuchsite or relate to new crystallization very late in the belt history. The shape of MUR 09-31 fuchsite spectrum could be related to various causes, such as loss of radiogenic ^{40}Ar by diffusion (Turner and others, 1971) or mixing between distinct mineral phases with distinct ages due to partial recrystallisation or neocrystallization. MUR 09-26 plateau age is fully concordant with the low temperature pseudo-plateau age of previous fuchsite and suggests that sample MUR 09-31 experienced a partial recrystallization at ca 2005 Ma of an older, at least 2025 Ma, fuchsite phase. As this mineral is related to the metamorphic-deformation-circulation processes (fig. 3F and I, fig. 4C), we suggest that recrystallisation may have reset a much older fuchsite phase. This interpretation is consistent with interpretations of monazite dating of the albitites along the Antimony Line. Indeed, scarce monazite grains have been dated at ca 2.0 Ga (Jaguin and others, accepted), an age that has was also interpreted as resulting from late recrystallisation fluid-related process(es). Additionally, titanite in the Baderoukwe batholith depicted ca 1.94 Ga U-Pb upper intercepts age (Jaguin and others, accepted). All the three dates may be related to fluid flow. Besides, this late event may be responsible (at least in part) for the quartz-carbonate oxygen isotope disequilibrium in the veins hosted in the Antimony Line.

Here, fuchsite dating at ca 2.0 Ga reinforces the 'two major event' hypothesis proposed in Jaguin and others (accepted). Accordingly, both types of minerals may have recrystallized during the event responsible for the thermic overprint of the Kaapvaal Craton and the associated emplacement of the nearby Bushveld and/or Phalaborwa complexes at ca 2.0 Ga (Buick and others, 2001; Reischmann, 1995, respectively). In any case, this young, possibly fluid-related event (Good and de Wit, 1997) had limited or even no effects on the mineralization.

CONCLUSIONS

In the core of the Weigel Formation, primary stratigraphic and competency contrasts have switched deformations from distributed to localized, a process thereafter maintained by fluid-driven secondary contrasts (softening versus carbonate crystallizing). Nevertheless, little movements have been accommodated on the Antimony Line likely because this vertical shear zone was in an unfavorable orientation geometry to accommodate the regional prevailing stress field (high- angle with respect to the horizontal shortening direction), or maybe in an unfavorable position in core of the belt (Sibson and others, 1988).

The Antimony Line-hosted mineralization is an orogenic-style deposit emplaced ca 2.8 Ga ago during the metamorphic and second magmatic climax of the Murchison

Greenstone Belt. During regional metamorphism, a H_2O-CO_2crustal fluid, likely escaped from lateral lithologies, was trapped in the Antimony Line at temperatures near 350-450°C and precipitated antimony sulfides. The occurrence of an important antimony concentration in the Antimony Line may be related to a previous enrichment associated with early magmatism and/or deposition under particular thermodynamics parameters, like the high Mg content associated with mafic to ultra-mafic lithologies. A late, ca 2.0 Ga (fluid-related?) event had little influence on the Sb-deposit itself.

ACKNOWLEDGMENTS

We thank chief geologist Colin Willson as well as Consolidated Murchison Mine Co. for their overall technical support, especially for opening their mines and for the access to their core yard. Maxime Casez is thanked for the preliminary study of the fluid inclusions by microthermometry. This paper benefited from discussions with Pr. Laurence Robb and Pr. Romain Bousquet. This work was funded by the CNRS-INSU "Action incitative" program.

Supplementary table: ^{40}Ar-^{39}Ar dating parameters.

REFERENCES

Abbot, J.E., van Vuuren, C.J.J., and Viljoen, M.J., 1986, The Alpha Gravelotte antimony ore body, Murchison Greenstone Belt, *in* Anhaeusser C.R., Maske, S., editors, Mineral Deposits of Southern Africa. p. 321-332.

Bakker, R.J., 1997, Clathrates: Computer programs to calculate fluid inclusion V-X properties using clathrates melting temperatures: Computer and Geosciences, v. 23-1, p. 1-18

Bakker, R.J., 1999, Adaptation of the Bowers and Helgeson (1983) equation of state to the H_2O-CO_2-CH_4-N_2-NaCl system: Chemical Geology, v. 154, p. 225-236

Barnes, J.D., Selverstone, J., and Sharp, Z.D., 2004, Interactions between serpentine devolatilisation, metasomatism and strike-slip strain localisation during deep crustal shearing in the Eastern Alps: Journal of Metamorphic Geology, v. 22, p. 283–300.

Bellot, J.P, Lerouge, C., Bailly, L., Bouchot, V., 2003, The Biards Sb-Au–Bearing Shear Zone (Massif Central, France): An Indicator of Crustal-Scale Transcurrent Tectonics Guiding Late Variscan Collapse: Economic Geology, v. 98, p. 1427-1447

de Beer, J.H., Stettler, E.H., Duvenhage, A.W.A., Joubert, S.J., and De Raath, C.J., 1984, Gravity and geoelectrical studies of the Murchison greenstone belt, South Africa: South African Journal of Geology, v. 87 (3), p. 347-359.

Block, S., Moyen, J.-F., Zeh, A., Poujol, M., Jaguin, J., and Paquette, J.-L., 2012, The Murchison Greenstone Belt, South Africa: accreted slivers with contrasting metamorphic conditions: Precambrian Research, in press, doi: 10.1016/j.precamres.2012.03.005.

Bodnar, R. J., 1993, Revised equation and table for determining the freezing point depression of water-sodium chloride solutions: Geochimica et Cosmochimica Acta, v. 57, p.683-684.

Boese, R., 1964, Die Antimoglanzgänge von Gravelotte in der Murchison Range on Nordost-Transvaal, PhD thesis, University of Hamburg, Germany.

Boiron, M.-C., Essarraj, S., Sellier, E., Cathelineau, M., Lespinasse, M., Poty, B., 1992, Geometric and genetic relationships between cathodoluminescent microstructural domains in quartz and fluid inclusions: Application to the reconstruction of Au-ore fluid chronology: Geochimica et Cosmochimica Acta, v. 56, p. 175-185.

Boiron, M.C., Cathelineau, M., Banks, D.A., Fourcade, S., Vallance, J., 2003, Mixing of metamorphic and surficial fluids during the uplift of the Hercynian upper crust: consequences for gold deposition: Chemical Geology, v. 194, p. 119-141

Boocock, C.N., 1984, Ore genesis along the Antinomy Line, Murchison Range, North-eastern Transvaal: M.Sc. thesis, University of the Witwatersrand, South Africa, 193p

Böttcher, M.E., 1996, $^{18}O/^{16}O$ and $^{13}C/^{12}C$ fractionation during the reaction of carbonates with phosphoric acid: effects of cationic substitution and reaction temperature: Isotopes in Environmental and Health Studies, v. 32, p. 299-305.

Bousquet R., Oberhänsli R., Goffé B., Wiederkehr M., Koller F., Schmid S. M., Schuster R., Engi M., Berger A. and Martinotti G., 2008, Metamorphism of metasediments in the scale of an orogen: A key to the Tertiary geodynamic evolution of the Alps, *in* Siegesmund, S., Fügenschuh, B. and Froitzheim, N., editors, Tectonic Aspects of the Alpine-Dinaride-Carpathian System: Geological Society, London, Special Publications, v. 298, p. 393-412.

Bowers, T.S., Helgeson, H.C., 1983, Calculation of the thermodynamic and geochemical consequences of non-ideal mixing in the system H_2O-CO_2-NaCl on phase relation in geological systems: Equation of state for H_2O-CO_2-NaCl fluids at high pressure and temperature: Geochimica et Cosmochimica Acta, v. 47, p. 1247-1275.

Brandl, G., Jaeckel, P. and Kröner, A., 1996, Single zircon age for the felsic Rubbervale Formation, Murchison greenstone belt, South Africa: South African Journal of Geology, v. 99(3), p.229-234.

Bucher, K. and Grapes, R., 2011, Petrogenesis of metamorphic rocks: Berlin Heildelberg, Springer, 8th edition, 428p.

Buchholz P., Oberthür T., 2007, Multistage Au-As-Sb Mineralization and Crustal-Scale Fluid Evolution in the Kwekwe District, Midlands Greenstone Belt, Zimbabwe: A Combined Geochemical, Mineralogical, Stable Isotope, and Fluid Inclusion Study: Economic Geology, v. 102, p. 347-378.

Carignan, J., Hild, P., Mevelle, G., Morel, J., and Yeghicheyan, D., 2001, Routine Analyses of Trace Elements in Geolgical Samples using Flow Injection and Low Pressure On-Line Liquid Chromatography Couples to ICP-MS: A Study of Geochemical Reference Materials BR, DR-N, UB-N, AN-G and GH: Geostandards Newsletter, v. 25 (2-3), p. 187-198.

Chardon, D., Gapais, D., and Cagnard, F., 2009, Flow of ultra-hot orogens: A view from the Precambrian, clues for the Phanerozoic: Tectonophysics, v. 477, p. 105-118.

Clayton, R.N., and Mayeda, T.K., 1963, The use of bromine pentafluoride in the extraction of oxygen from oxides and silicates for isotopic analysis: Geochimica et Cosmochimica Acta, v. 27, p.48-52.

Diamond L.W, 1994, Introduction to phases relations of the CO_2-H_2O fluid inclusions: Short course Fluid inclusions in minerals: methods and applications, *in* De Vivo and Frezzotti, editors, Virginia Tech, p. 131-158.

Dubessy, J., 1984, Simulation des équilibres chimiques dans le système C-O-H, Conséquences méthodologiques pour les inclusions fluides, Bulletin de Mineralogy, v. 107, p. 155-168.

Dubessy, J., Poty, B., and Ramboz, C., 1989, Advances in C-O-H-N-S: fluid geochemistry based on micro Raman spectrometric analysis of fluid inclusions: European Journal of Mineralogy, v. 1, p. 517-534.

Evensen, E., Hemilton, P.J., and O'Nions, R.K., 1978, Rare-earth abundances in chondritic meteorites: Geochimica et Cosmochimica Acta, v. 42 (8), p. 1199-1212.

Fyon, J.A., Crocket, J.H., and Schwarz, H.P., 1983, Application of Stable Isotope Studies to Gold Metallogeny in the Timmins-Porcupine Camp, *in* Ontario Geosciences Research Grant Program, Grant No. 49, Ontario Geological Survey Open File Report no 5464,182 p.

Gapais, D., Cagnard, F., Gueydan, F., Barbey, P., and Ballèvre, M., 2009, Mountain building and exhumation processes through time: inferences from nature and models: Terra Nova, v. 21, p. 188-194.

Gebre-Mariam, M., Hagemann, S.G., and Groves, D.I., 1995, A classification scheme for epigenetic Archean lode-gold deposits: Mineralium Deposita, v. 30, p. 408–410.

Geological Survey of South Africa, 1985, Map of Tzaneen (n° 2330), 1/250 000 edition.

Goldfarb, R.J., Baker, T., Dubé, B., Groves, D.I., Hart, C.J. R., and Gosselin, P., 2005, Distribution, Character, and Genesis of Gold Deposits in Metamorphic Terranes *In* Hedenquist, J. W., Thompson, J.F.H., Goldfarb, R.J., Richards, J.P., editors, Economic Geology 100th anniversary volume, p. 407-450

Golding, S.D., and Wilson, A.F., 1983, Geochemical and Stable Isotope Studies of the No. 4 Lode, Kalgoorlie, Western Australia: Economic Geology, v. 78, p.438-450

Good, N., and De Wit, M. J., 1997, The Thabazimbi-Murchison Lineament of the Kaapvaal craton, South Africa: 2700 Ma of episodic deformation: Journal of the Geological Society, v. 154, p. 93-97.

Gosselin, P., and Dubé, B. 2005, Gold deposits of the world: distribution, geological parameters and gold content, *in* Geological Survey of Canada, Open File 4895, 2005; 271pp; doi:10.4095/220379

Graham, R.H., 1974, A structural investigation of the southern part of the Limpopo belt and the adjacent Kaapvaal Craton, South Africa, *in* University of Leeds, Annual Report of the Research Institute of African Geology, 18th, p.63-69.

Groves, D.I., Golding, S.D., Rock, N.M.S., Barley, M.E., and McNaughton, N.J., 1988, Archean carbon reservoir and their relevance to the fluid source for gold deposits: Nature, v. 331, p. 254-257

Groves, D.I., and Foster, R.P., 1998, Archean lode gold deposits, *in* Foster, R.P, editor, Gold metallogeny and exploration, p. 63-103

Groves, D.I., Condie, K.C., Goldfarb, R.J., Kronsky, J.M.A., and Vielreicher, R.M., 2005, Secular Changes in Global Tectonic Processes and Their Influence on the Temporal Distribution of Gold-Bearing Mineral Deposits: Economic Geology, v. 100, p. 203–224

Guillemette, N., and William-Jones, A.E., 1993, Genesis of the Sb-W-Au deposits at Ixtahuacan, Guatemala: evidence from fluid inclusions and stable isotopes: Mineralium Deposita, v. 28, p. 167-180

Henderson, D.R., Long, L.E., and Barton, J.M., 2000, Isotopic ages and chemical and isotopic composition of the Archaean Turfloop Batholith, Pietersburg granite - greenstone terrane, Kaapvaal Craton, South Africa: South African journal of geology, v. 103(1), p.38-46.

Huston, D.L., Blewett, R.S., Keillor, B., Standing, J., Smithies, R.H., Marshall, A., Mernagh, T.P., and Kamprad, J., 2002, Lode Gold and Epithermal Deposits of the Mallina Basin, North Pilbara Terrain, Western Australia: Economic Geology, v. 97 (4), p. 801-818.

Jaguin, J., Gapais, D., Poujol, M., Boulvais, P., and Moyen, J.-F., 2012a, The Murchison Greenstone Belt (South Africa): a General Tectonic Framework: South African Journal of Geology, v. 115, (1), p. 65-76.

Jaguin, J., Poujol, M., Boulvais, P., Robb, L.J., and Paquette, J.-L., 2012b, Metallogeny of precious and base metal mineralization in the Murchison Greenstone Belt, South Africa: Indications from U-Pb and Pb-Pb geochronology: Mineralium Deposita, v. 47, p. 739-747.

Jaguin J., Boulvais, P., Poujol, M., Bosse, V., Paquette, J.-L., Vilbert, D., accepted, Albitization in the Antimony Line, Murchison Greenstone Belt (Kaapvaal Craton): a geochemical and geochronological investigation: Lithos.

Jourdan, F., Verati, C., Féraud, G., 2006, Intercalibration of the Hb3gr $^{40}Ar/^{39}Ar$ dating standard: Chemical Geology, v. 231, p. 77–189.

Jourdan, F., Renne, P.R., 2007, Age calibration of the Fish Canyon sanidine$^{40}Ar/^{39}Ar$ dating standard using primary K-Ar standards: Geochimimica et Cosmochimica Acta, v. 71, p. 387-402.

Kedda, S.W., 1992, Geochemical and stable isotope studies of gold bearing granitoids in the Murchison Schist Belt, North Eastern Transvaal, *in* M. Sc, University of the Witwatersrand.

Kerrich, R., 1986, Fluid infiltration into fault zones: Chemical, isotopic, and mechanical effects: Pure and Applied Geophysics, v. 124(1-2), p.225-268.

Kerrich, R., 1989,Geochemical evidence on the source of fluids and solutes for shear zones hosted mesothermal Au Deposits, *in* Bursnall, J.T., editor, Mineralization and Shear zones, Geological association of Canada, Short Course Notes, v. 6, p. 129-198

Kontak, D.J., Horne, R.J., and Smith, P.K., 1996, Hydrothermal Characterization of the West Gore Sb-Au Deposit, Meguma Terrane, Nova Scotia, Canada: Economic Geology, v. 91, p. 1239-1262

Maiden, K.J., 1984, Metamorphic features of the Maranda J Copper-Zinc deposit, Murchison Greenstone Belt, Transvaal: Transaction to the geological society of South Africa, v. 87, p. 335-345.

Maiden, K.J., and Boocock, C.N., 1987, Deformational and metamorphic features of Antimony ores of the Murchison Antimony Line, North-Eastern Transvaal: Transaction to the geological society of South Africa, v. 87, p.327-333.

McMillan, P.F., 1989, Raman Spectroscopy in Mineralogy and Geochemistry: Annual Review of Earth and Planetary Sciences, v.17, p. 255–279.

Meteorex Limited, 2011, Mine operations statistics, gold and antimony. 451 Fact Sheet 2. Available at: http://www.metorexgroup.com/fact_sheet_02.htm.

Minnitt, R.C.A., 1975, The geology of the Murchison Range between Quagga Camp area and the Kruger National Park, *in* M.Sc. thesis (unpubl.), University of Witwatersrand, Johannesburg, South Africa.

Muff, R., and Saager, R., 1979, Metallogenic interpretation from a mineragraphic and geostatistic study of Antimony ores of the Murchison Greenstone Belt, South Africa: Special publication of the geological Society of South Africa, v. 5, p.167-179.

Nesbitt, B.E., Murowchick, J.B., and Muehlenbachs, K., 1986, Dual origins of lode gold deposits in the Canadian Cordillera: Geology, v. 14(6), p.506.

Nesbitt, B.E., Muehlenbachs, K., Murowchick, J.B., 1989, Genetic Implications of Stable Isotope Characterisation of Mesothermal Au Deposits and Related Sb and Hg Deposits in the Canadian Cordillera: Economic Geology, v. 84, p. 1489-1506

Normand, C., Gauthier, M., and Jébrak, M., 1996, The Quebec Antimony Deposit: An Example of Gudmundite-Native Antimony Mineralization the Ophiolitic Mélange of the Southeastern Quebec Appalachians: Economic Geology, v. 91, p. 149-163.

Oliver, N.H.S., 1995, Hydrothermal history of the Mary Kathleen Fold Belt, Mt Isa Block, Queensland: Australian Journal of Earth Sciences, v. 42(3), p.267-279.

Pearton, T.N., 1980, The geochemistry of the Carbonate and related rocks of the Antimony Line, Murchison Greenstone Belt, with particular reference to their genesis and to the origin of stibnite mineralization, *in* Ph.D. thesis, University of the Witwatersrand, South Africa.

Pearton, T.N., and Viljoen, M.J., 1986, Antimony mineralization in the Murchison Greenstone Belt - An overview, *in* Anhaeusser C.R., Maske, S., editors, Mineral Deposits of Southern Africa. p. 293-320.

Poujol, M., Robb, L.J., Respaut, J.-P., and Anhaeusser, C.R., 1996, 3.07-2.97 Greenstone Belt Formation in the northeastern Kaapvaal Craton: Implication for the Origin of the Witwatersrand Basin: Economic Geology, v. 91, p.1455-1461.

Poujol, M., 2001, U-Pb isotopic evidence for episodic granitoid emplacement in the Murchison greenstone belt, South Africa: Journal of African Earth Sciences, v. 33(1), p.155-163.

Poujol, M., and Robb, L.J., 1999, New U-Pb zircon ages on gneisses and pegmatite from south of the Murchison greenstone belt, South Africa: South African Journal of Geology, v. 102(2), p.93-97.

Roberts, R.G.,1987,Archean Lode Gold Deposits, *In* Journal of the geological association of Canada, editor, Ore deposits Models#11, 14, p. 37–52

Rosenbaum, J., and Sheppard, S.M., 1986, An isotopic study of siderites, dolomites and ankerites at high temperatures: Geochimica et Cosmochimica Acta, v. 50(6), p.1147-1150.

Schwarz-Schampera, U., Terblanche, H. and Oberthür, T., 2010, Volcanic-hosted massive sulfide deposits in the Murchison greenstone belt, South Africa: Mineralium Deposita, v. 45(2), p.113-145.

Das Sharma, S., Patil, D.J., Gopalan, K., 2002, Temperature dependence of oxygen isotope fractionation of CO2 from magnesite-phosphoric acid reaction: Geochimica et Cosmochimica Acta, v. 66(4), p.589-593.

Renne P.R., Balco G., Ludwig R.L., Mundil R., Min K., 2011, Response to the comment by W.H. Schwarz and other on "Joint determination of (40)K decay constants and (40)Ar*/(40)K for the Fish Canyon sanidine standard, and improved accuracy for (40)Ar/(39)Ar geochronology" by P.R. Renne and other, 2010,Geochimica et Cosmochimica Acta, v. 75, p. 5097-5100.

Renne P.R., Mundil R., Balco G., Min K., Ludwi R.L., 2011, Joint determination of ^{40}K decay constants and $^{40}Ar*/^{40}K$ for the Fish Canyon sanidine standard, and improved accuracy for $^{40}Ar/^{39}Ar$ geochronology: Gechimica Cosmochimica Acta, v. 74, p. 5349–5367.

Roddick, J.C., 1983, High precision intercalibration of $^{40}Ar/^{39}Ar$ standards: Geochimica et Cosmochimica Acta, v. 47, p. 887-898.

Ruffet, G., Féraud, G., Amouric, M., 1991, Comparison of $^{40}Ar/^{39}Ar$ conventional and laser dating of biotites from the North Trégor Batholith: Geochimica et Cosmochimica Acta, v. 55, p. 1675-1688.

Ruffet, G., Féraud, G., Ballèvre, M., Kiénast, J.R., 1995, Plateau ages and excess argon on phengites: a $^{40}Ar/^{39}Ar$ laser probe study of alpine micas (Sesia zone): Chemical Geology, v. 121, p. 327-343

Sibson, R.H., 1994, Crustal stress, faulting and fluid flow: Geological Society, London, Special Publications, v. 78(1), p.69-84.

Sibson, R.H., Robert, F., and Poulsen, K.H., 1988, High-angle reverse faults, fluid-pressure cycling, and mesothermal gold-quartz deposits: Geology, v. 16, p. 551-555

Smith, H. S., 1986, Evidence from ^{13}C and ^{18}O isotopes in carbonates minerals for the origin of fluids in Archeaen greenstone belt, metamorphic and mineralization processes: Extended abstracts, Geocongress1986 Johannesburg (Geological Society of South Africa), p. 341-344.

South African Committee for Stratigraphy, 1980, The Murchison Sequence, *in* Stratigraphy of South Africa, part 1: Lithostratigraphy of the Republic of South Africa, South West Africa/Namibia and the Republics of Bophuthatswana, Transkei and Venda. p. 45-52.

Thiéry, R., Vidal, J., and Dubessy, J., 1994, Phase equilibria modelling applied to fluid inclusions: Liquid-vapour equilibria and calculation of the molar volume in the CO_2-CH_4-N_2 system, Geochimica et Cosmochimica Acta, v. 58, p. 1073-1082.

Turner, G., Huneke J.C., Podosek F.A., Wasserburg G.J., 1971, $^{40}Ar/^{39}Ar$ ages and cosmic ray exposure age of Apollo 14 samples: Earth Planetary Science Letters, v. 12, p.19-35.

Van Eeden, O.R., Partridge, F.C., Kent, L.R., and Brandt, J.W., 1939, The mineral deposits of the Murchison Range east of Leydsdorp: Memoir of the geological survey of South Africa, v. 36,p. 172.

Vearncombe, J.R., 1988, Structure and metamorphism of the Archean Murchison Belt, Kaapvaal Craton, South Africa: Tectonics, v. 7(4), p.761-774.

Vearncombe, J.R., Cheshire, P.E., de Beer, J.H., Killick, A.M., Mallinson, W.S., McCourt, S., and Stettler, E.H., 1988, Structures related to the Antimony line, Murchison schist belt, Kaapvaal Craton, South Africa: Tectonophysics, v. 154 (3-4), p. 285-308.

Vearncombe, J.R., Barton, J.M., Cheshire, P.E., de Beer, J.H., Stettler, E.H., and Brandl, G., 1992, Geology, geophysics and mineralization of the Murchison Schist Belt, Rooiwater Complex and surrounding granitoids: Memoir of the Geological survey of South Africa no 81.

Viljoen, M.J.,van Vuuren, C., Pearton, T.N., Minnitt, R.C.A., Muff, R., and Cillier, P., 1978, The regional geological setting of the mineralization in the Murchison Range with particular reference to Antimony, *in* Verwoerd, W. J., editor, Mineralization in metamorphic terranes. p. 55-76.

Ward, J.H.W., 1998, Antimony, *in* Wilson, M. and Anhaeusser, C. R., Council for Geoscience, editors, The mineral resources of South Africa, Pretoria, South Africa, p. 59-65.

Ward, J.H.W., Wilson, M.G.C., 1998,Gold outside the Witwatersrand Basin, *in* Wilson, M. and Anhaeusser, C. R., Council for Geoscience, editors, The mineral resources of South Africa, Pretoria, South Africa, p. 350-386.

William-Jones, A. E., Normand, C., 1997, Controls of mineral parageneses in the system Fe-Sb-S-O: Economic Geology, v. 92, p. 308-324

Wilson-Moore, C., 1896, The economic importance of the Murchison Range: Transaction to the Geological Society of South Africa, v. 1, p.51-75.

Willson, C., and Viljoen, M.J., 1986, The Athens Antimony ore body, Murchison Greenstone Belt, *in* Anhaeusser, C.R. and Maske, S., editors, Mineral Deposits of Southern Africa, Geological Society of South Africa, Johannesburg, p. 333-338.

Zeh, A., Gerdes, A., and Barton, J.M., 2009,Archean Accretion and Crustal Evolution of the Kalahari Craton - the Zircon Age and Hf Isotope Record of Granitic Rocks from Barberton/Swaziland to the Francistown Arc: Journal of Petrology, v. 50(5), p. 933-966.

Zeh, A., Jaguin, J., Poujol, M., Boulvais, P., Hallot, E., Block, S., and Paquette, J.-L., (in prep), Juvenile crust formation in the northeastern Kaapvaal Craton at 2.97 Ga – Implications for Archean crust-mantle evolution, terrane accretion, and the Witwatersrand gold source.

Zhang, Y.G., Frantz, J.D., 1987, Determination of the homogeneization temperatures and densities of supercritical fluids in the system NaCl-KCl-$CaCl_2$-H_2O using synthetic fluid inclusions, Chemical Geology, v. 64, p. 335-350.

Zheng, Y.-F., 1993, Calculation of oxygen isotope fractionation in anhydrous silicate minerals. Geochimica et Cosmochimica Acta, v. 57 (5), p. 1079-1091.

Chapitre 7 — Dater la minéralisation : le proxy des albitites

Le chapitre 4-D a abordé la problématique de la datation des circulations de fluides. Dans la zone de l'Antimony Line, les roches encaissantes sont des roches mafiques et ultramafiques métasomatisées et fortement déformées. Un des minéraux d'origine métasomatique, la fuchsite, est datable mais s'est révélée être sensible à un événement tardif vers 2.0 Ga (article #4). Aussi, cibler d'autres minéraux datables s'est avéré difficile dans les roches encaissantes. Celles-ci sont en effet pauvres en éléments incompatibles tels que l'uranium et le thorium rendant la précipatation de minéraux datables par la méthode U-Th-Pb très difficile voire impossible. Egalement, une tentative de datation par Sm-Nd des veines de carbonates elles-mêmes s'est révélée infructueuse du fait de difficultés rencontrées pour la mise en solution des carbonates ferrifères.

Néanmoins, la zone de circulation renferme des roches dérivées de granitoïdes et métasomatisées en albitites. Ainsi, nous avons focalisé sur ces roches susceptibles de nous apporter des contraintes chronologiques sur la circulation de fluides dans l'Antimony Line. Elles font l'objet de l'article suivant. Il s'agit de renseigner leur lien génétique avec la circulation à l'origine de la précipitation de l'antimoine dans les veines, et de dater leur formation.

Article #5

"Albitization in the Antimony Line, Murchison Greenstone Belt (Kaapvaal Craton): a geochemical and geochronological investigation"

Accepté avec révisions modérées à *Lithos*[2]

Résumé en français

La ceinture de roches vertes de Murchison (3.09-2.97 Ga) est une des ceintures volcano-sédimentaires archéennes du craton du Kaapvaal (Afrique australe). Parmi les différents gisements de cette ceinture, une série de gîtes à Sb-(±Au) se concentre dans une structure majeure fragile-ductile altérée en quartz-carbonate, l'Antimony Line. Cette Antimony Line est donc clairement associée à la circulation de fluides hydrothermaux.

Dans cette étude, nous nous concentrons sur les albitites qui parcourent l'Antimony Line. Les investigations petro-géochimiques indiquent que l'albitisation se développe aux dépends de protolithes granodioritiques lors d'interactions à rapports fluide/roches élevés, et que l'albitisation s'accompagne d'un enrichissement en antimoine. Les isotopes de l'oxygène sur les albitites révèlent un fluide hydrothermal

[2] Accepted on october the 15th. The manuscript presented here is the original version as submitted initially.

albitisant d'origine crustale. La géochronologie sur zircon et monazite identifie une cristallisation magmatique à 2.97-2.92 Ga, événement déconnecté de l'altération hydrothermale vers 2.8 Ga, et potentiellement un épisode jeune vers 2.0 Ga.

Ces données soulignent une probable minéralisation primaire associée au magmatisme vers 2.97-2.92 Ga, suivie d'une mobilisation secondaire vers 2.80 Ga en conditions métamorphiques provoquant un enrichissement en Sb dont la mobilisation a peut-être duré jusque 2.0 Ga.

ALBITIZATION IN THE ANTIMONY LINE, MURCHISON GREENSTONE BELT (KAAPVAAL CRATON): A GEOCHEMICAL AND GEOCHRONOLOGICAL INVESTIGATION

Accepted with moderate revison in Lithos

Justine Jaguin[1]*, Philippe Boulvais[1], Marc Poujol[1], Valérie Bosse[2], Jean-Louis Paquette[2], David Vilbert[1]

1: Université de Rennes 1Géosciences Rennes - UMR CNRS 6118 OSUR, 35042 Rennes Cedex, France

2: Université Blaise Pascal, UMR CNRS 6524, Laboratoire Magmas et Volcans, 63038 Clermont-Ferrand Cedex, France

**Corresponding author: justine.jaguin@univ-rennes1.fr Tel.: +33(0)223233081 Fax: +33(0)223236097*

ABSTRACT

The 3.09-2.97 Ga Murchison Greenstone Belt is one of several Archean volcano-sedimentary belts within the Kaapvaal Craton in southern Africa. Among the diverse ore deposits found within the belt, a Sb-(±Au) set of deposits are located in a major quartz-carbonate altered brittle-ductile structure known as the Antimony Line. The Antimony Line is thus clearly related to hydrothermal fluid circulation.

In this study we focus on albitites that run along the Antimony Line. Petrological and geochemical investigation indicate that albitization developed at the expense of a granodioritic protoliths under high fluid/rock ratios and also that Sb enrichment was concomitant to albitization. Oxygen isotopes on albitites point to a crustal origin for the hydrothermal fluid responsible for the albitization process. Geochronology on zircon and hydrothermal monazite identifies a 2.97-2.92 Ga magmatic crystallization event, disconnected from a ca 2.8 Ga hydrothermal alteration, and a potentially younger event around 2.0 Ga. These data highlight a likely magmatic-related primary mineralization at 2.97-2.92 Ga, followed by a secondary metamorphic-related mobilization event around 2.80 Ga leading to a Sb-enrichment that may have lasted until 2.0 Ga.

Keywords: *Murchison Greenstone Belt, antimony, albitization, Archean, Kaapvaal Craton*

INTRODUCTION

Albitization is a rather common phenomenon mostly because sodium dissolves very easily in natural fluid, and thus becomes mobile at the scale of the entire crust. It is therefore a widespread fluid-rock interaction process consisting in the replacement of potassium and calcium by sodium. It takes place in various geological contexts:

magmatic (granitic rocks by deuteric fluid: Recio et al., 1997; Hecht et al., 1999); sedimentary (siltstones or sandstone by basinal brines: Kalsbeek, 1992; van de Kamp and Leake, 1996, respectively); orogenic (as retrograde crustal fluid infiltration, Munz et al., 1994; in extensional zones as circulation of surface waters in the upper crust, Boulvais et al., 2007). It also occurs at various geological times: from the Phanerozoic (Poujol et al., 2010; Carten, 1986) to the Proterozoic (Kaur et al., 2012; Cuney et al., 2012; Munz et al., 1994) up to the Archean (Witt 1992; Robert and Kelly, 1987).

During this fluid-rock metasomatic process leading to albitization, some metals are also mobile. It is quite common therefore to found metallic mineralization associated with albitites. This is for example well documented in uranium deposits (Ukraine, Cuney et al., 2012; Guyana, Alexandre, 2010, and references therein). Some examples are also reported for Sn-W mineralization (Charoy and Pollard, 1989; Costi et al., 2002; Cheilletz and Giuliani, 1982) and *Iron Oxides Gold Copper*-type deposits (review in Williams et al., 2005). This holds for gold deposits too, for example in the Superior and Yilgarn Provinces (review in Robert et al., 2005), in western Africa (Béziat et al., 2008), in Australia (Witt, 1992), and in the Murchison Greenstone Belt (South Africa), where Jaguin et al. (2012b) recently dated gold mineralization in an albitized granodiorite.

Albitites in the Murchison Greenstone Belt (MGB) developed at the expense of magmatic plugs that were emplaced along a mineralized structure, the so-called Antimony Line, right in the core of the belt (Fig. 1). The Antimony Line is an unusual Sb-Au-As-Hg Precambrian set of deposits (e.g. Pearton and Viljoen, 1986). At the first order, there is a spatial relationship between the antimony mineralized zone and the albitized intrusions. In this paper, we expose a comprehensive petrological, geochemical, and geochronological dataset for the albitized plugs found within the Antimony Line and their unaltered equivalents. This dataset allows us to discuss the potential genetic links between albitization and antimony mineralization and to improve our knowledge of the belt by providing new insights into its global metallogenetic system. We show that (i) in the MGB, there is an intense albitization of the granodioritic intrusions located in the Antimony Line; (ii) these albitites are enriched in Sb and (iii) the albitization alteration process took place several tens of millions of years after the magmatic emplacement (2.97-2.92 Ga) and possibly relates to successive fluid flow events within the belt from ca. 2.8 Ga down to ca. 2.0 Ga.

GEOLOGICAL SETTING

The MGB and surrounding granitoids

The MGB is a ENE trending, narrow, deeply rooted, strongly deformed and metamorphosed sequence of volcano-sedimentary rocks (e.g. Vearncombe, 1988, Jaguin et al., 2012a, Block et al., 2012) exposed between a northern and a southern granitoid-gneissic basements and intruded by a variety of Archean granitoids (Lekkersmaak granite for example, Fig. 1b).

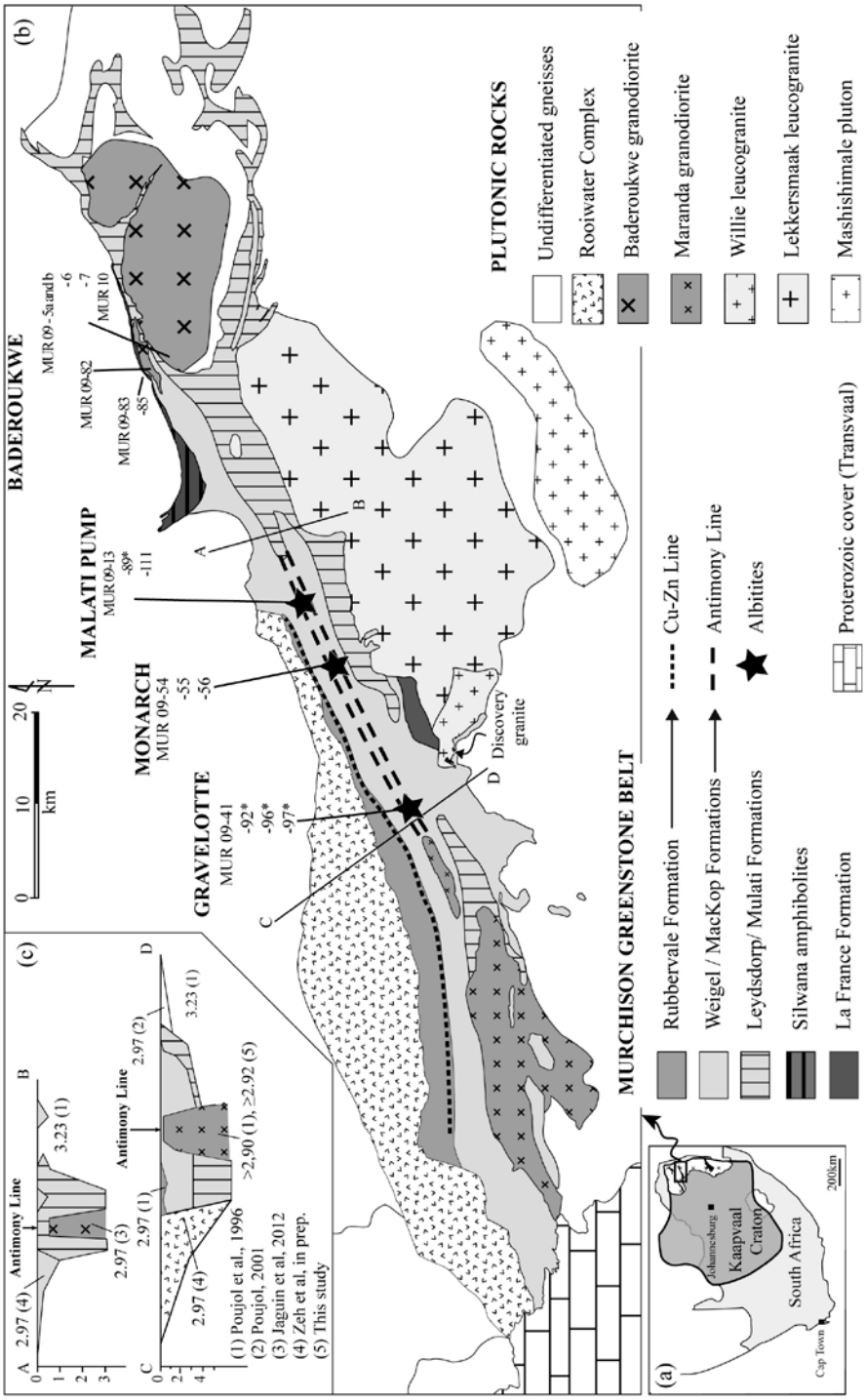

Figure 1: *Inset (a) shows the location of the Murchison Greenstone Belt in the Kaapvaal Craton. (b) Simplified geological map of the Belt, its surrounding granitoids and the Antimony Line (modified after SACS 1980 and Vearncombe et al. 1992), with sampling sites reported (* for core). Inset (c) shows cross-cuts from the geophysical study of de Beer et al. (1984), with available ages (Ga).*

The South African Committee for Stratigraphy (SACS, 1980) assigned all the various volcanic and sedimentary rocks of the MGB to the generic name of Gravelotte Group, subsequently divided into Formations described here from roughly south to north (Fig. 1b). The *La France Formation* is a small area in the south-centre part of the belt, made of metapelites with a maximum age of deposition of 2986 ±12 Ma (Zeh et al, in prep.). The *Leydsorp and Mulati Formations*, represented by mafic-to-ultramafic successions of unknown age, occupy the rest of the southern flank. The largest domain, comprising the mafic to felsic volcanics and volcanoclastic sediments of the *Weigel Formation* and the meta-arenites of the *MacKop Formation* occupies the central portion of the MGB. The maximum age of deposition for the *MacKop Formation* is defined at

3076 ± 4 Ma (youngest detrital zircon of Poujol et al., 1996) and 2979 ± 7 for the *Weigel Formation* (Zeh et al, in prep.). Some felsic volcanics from the *Weigel Formation* have been consistently dated at 3087 ± 21 Ma (Poujol et al., 1996). To the North, the *Rubbervale Formation* comprises intermediate to felsic lavas and tuffs deposited at 2.97 Ga (Brandl et al., 1996; Poujol et al., 1996; Poujol, 2001; Schwarz-Schampera et al., 2010). It hosts the "Cu-Zn Line" a large volcanic-hosted massive sulfide (VHMS) district (see Schwarz-Schampera et al., 2010). The *Silwana Amphibolite unit* located to the northeast of the MGB (not described by SACS but by Vearncombe, 1988) is a 300 m wide slice made up of hornblende and biotite schists and deformed amphibolite gneisses. Finally, the *Rooiwater Complex* (van Eeden et al., 1939) in the northwestern part of the MGB is a 2.97 Ga layered igneous complex (Zeh et al., in prep.) of gabbros-anorthosites, amphibolites and tonalite that is up to 7.5 km wide (e.g. Vearncombe et al. 1987).

Most of the MGB Formations have been affected by a lower greenschist grade metamorphism with the exception of the Silwana unit, *La France Formation* and the *Rooiwater Complex* (Vearncombe, 1988; Block et al., 2012) that underwent metamorphism in the amphibolite facies.

The belt is surrounded by granitoids spreading both in time (over 300 Ma) and composition (granodiorite to leucogranite). The different magmatic nomenclature refers to the most usual terms of the literature but should be handle with caution. The French Bob Mine Granite, cropping out to the south of the MGB, is the oldest granitic rock (tonalitic to trondhjemitic gneiss) with an age of 3228 ± 12 Ma (Poujol et al., 1996). The southern basement crystallization was also dated at 3063 ± 12 Ma on migmatitic gneiss (Makhutswi gneiss, Poujol and Robb, 1999). This age overlaps with the age of ca. 3.09 obtained for the *Weigel Formation* (Poujol et al., 1996). Then several plutonic bodies intruded the MGB around 2.97 Ga: the Discovery Granite (2969 ± 14 Ma; Poujol, 2001), the Malati Pump granodiorite (2964 ± 7 Ma, Jaguin et al., 2012b), the Baderoukwe pluton (2969 ± 12 Ma, Jaguin et al., 2012b), the Free State granite (2966 ± 9 Ma, Zeh et al., in prep.). All these ages are similar to the deposition age of the volcanic rocks from the Rubbervale Formation (see above). Finally, a minimum crystallization age of 2901 ± 20 Ma was proposed for the Maranda granodiorite (Fig.1; Poujol et al., 1996). In the literature, some intrusives rocks of unknown age are located into the Antimony line and termed *beresite* (Boese, 1964; Pearton, 1978), meaning ms-granite of uncertain genesis, *granite-like bodies* (Muff and Saager, 1979), *granodiorite* (Vearncombe et al., 1988; Kedda, 1992) or albitites (Pearton, 1980; see part 2.4.). Around 2.8 Ga, another period of important magmatic activity is illustrated by the emplacement of the Groot Letaba orthogneiss protolith to the north of the MGB (2839 ± 8 Ma, Zeh et al., 2009), and to the south of the belt with crystallizations of: (i) pegmatitic dykes intrusive into the Makhutswi gneiss (2848 ± 58 Ma, (Poujol and Robb, 1999); (ii) the Willie Granite (2820 ± 38 Ma, Poujol, 2001; 2817 ± 10 Ma, pers. unpubl. data); and (iii) the Lekkersmaak leucogranite (2795 ± 8 Ma, Zeh et al., 2009, 2777 ± 10 Ma, Jaguin unpubl. data). To the north west of the MGB, along the northern margin of the Rooiwater Complex, the Turfloop granodiorite (and probably its eastern

continuation known as the Duivelskloof granite) is 2778 ± 10 Ma old (Henderson et al., 2000). A last episode of magmatic activity took placed around 2.7 Ga with the emplacement of the Mashishimale granite (2698 ± 21 Ma, Poujol, 2001; 2671 ± 8 Ma, Zeh et al., 2009).

The Antimony Line and its Sb mineralization

The MGB is famous for being an important metallotect, hosting Cu-Zn VMS-type deposits, as well as emerald mineralizations, a rare Hg deposit, and the Antimony Line (AL, Wilson-Moore, 1896), hosting discontinuous Sb deposits (e.g. early investigations of Hall, 1912, van Eeden et al., 1939, Hausmann, 1959).

The AL corresponds to a narrow, ENE-trending deformation zone in the centre of the *Weigel Formation*. It is a brittle-ductile structure that acted as a fluid conduit, with a reverse movement and some sinistral component (Vearncombe et al., 1988, Jaguin et al., 2012a). Although described as stratiform in the past (Muff and Saager, 1979), the mineralized line is actually oblique to some iron lithologies belonging to the *Weigel Formation* (Vearncombe et al., 1988). Petrologically, the AL is a 250m wide zone of alteration surrounded by chlorite-schists. This alteration is broadly concentric ranging from talcose schists to various massive pinched-and-swell quartz-carbonate schists (Pearton and Viljoen, 1986; Muff and Saager, 1979). The latest constitute the host rocks for the Sb mineralization, where Sb-sulfides (stibnite Sb_2S_3 and Ni-rich berthierite $(NiFe)Sb_2S_4$, Muff and Saager, 1979) are found in cm-scale sulfide-veinlets or in quartz-carbonate veins (e.g. Maiden and Boocock, 1987).

Several metallogenic models have been proposed to account for the presence of this Sb mineralization within the AL. They are based on various arguments, from structural to geochemical. Pearton and Viljoen (1986 and references therein), based on an exhaustive synthesis, proposed a model involving a structurally-controlled metamorphic mobilization, i.e. similar to that of an orogenic gold deposit ('lode' gold, see also (Willson and Viljoen, 1986), and Vearncombe et al., 1988). For others, there was an earlier mineralization event, either linked to syngenetic volcanic exhalative fluids (Ileri, 1973; Muff and Saager, 1979; Minnitt, 1975; Viljoen et al., 1978), mantellic-derived fluids (Boese, 1964), or magmatic fluids (van Eeden et al., 1939). While ages for other types of deposits in the MGB are bracketed around 2.97 Ga (possibly 2.97 emeralds, Robb and Robb, 1986, Poujol, 2001; Cu-Zn VMS types, Schwarz-Schampera et al., 2010; gold, Jaguin et al., 2012b), the age of the Sb mineralization remains unknown.

Albitite rocks along the AL

The overall MGB shape was imaged by the geophysical (gravity and electrical) study of de Beer et al. (1984). Especially, the high contrast between granitoid and mafic rock densities allowed these authors to model the depth of the Belt. Cross-section depicted in Fig. 1c show that plugs of granitoids-like material underlie the entire AL and are probably connected at depths with the Baderoukwe and Maranda plutons cropping-out to the west and to the east of the AL respectively (Fig. 1b). This was

partially confirmed by Jaguin et al. (2012b), who demonstrated that both the Malati Pump Mine granodiorite and the Baderoukwe pluton (now both referred to as the *Baderoukwe batholith)* were emplaced 2.97 Ga ago.

At the surface, along strike of the AL, several of these plugs, up to tens of meters large, are found to be albititized (Malati Pump quarry, Monarch mine, Athens Shaft, Old Gravelotte gold mine, Pearton, 1980; Pearton and Viljoen, 1986; Vearncombe et al., 1988; Kedda, 1992). These albitites were first described as magmatic rocks (a tonalitic type granite, van Eeden et al., 1939, Pearton, 1978). Later, authors invoked a metamorphic-hydrothermal process by differentiation of a quartz-feldspar rock (Muff and Saager, 1979), or by carbonation of a non-magmatic Na-rich rock (Pearton, 1980; Pearton and Viljoen, 1986). Their 'close association' with the antimony mineralization was interpreted by the latter authors as reflecting only a hydrothermal overprint of the deposits. Vearncombe et al. (1988) focused on their structural characteristics: they conclude that these plugs were emplaced after the main deformation and mineralization events but before the last stages of deformation. These authors also invoke unpublished results from boreholes in the Old Gravelotte albitite indicating that the albitite was secant to the ore body, was posterior to the main deformation phase cleavage and that stibnite and berthierite occurred in the quartz-rich margin of the intrusive, as well as stibnite mineralization from the Maranda pluton itself (west of the MGB, Fig. 1b). In brief, it seems that albitites are connected with the Baderoukwe and Maranda plutons, but there is, to our knowledge, no study that focussed on the albitization process along the AL itself and that discussed the potential relationship between albitization and antimony mineralization.

Sampling

Albitites have been collected in three mines along the AL (Fig. 1b, Table1). The westernmost sampling site is also the largest antimony deposit of the belt, Gravelotte (the so-called 'Alpha-Gravelotte mining complex'). Further east, samples from the 'Monarch-Free State complex' were found on a hill a few tens of meters north of the Monarch operation site. Finally the Malati Pump mine is somewhat different as it was a gold mine. It represents the easternmost albitites reported so far, and was sampled in this study in an old quarry. The rock samples were collected in abandoned mines (MUR 09-41 in the Old Gravelotte mine; MUR 09-13 and MUR 09-111 in the Malati Pump quarry) and from surface outcrops (MUR 09-54 to MUR 09-56, Monarch mine vicinity), while others were collected from drilled cores (Table 1). Fresh samples from the flat-lying Baderoukwe pluton have been collected in its northwestern side along a road under construction at the time of the field work (Fig. 1, MUR 09-5,-6, -7, MUR 10). Another sample (MUR 09-82) was picked from the northern slice of the pluton to the south of the Witkop hill. It would have been precious to sample the Maranda intrusion, the western equivalent of the Baderoukwe pluton, but access was not possible because

of the development of heavily fenced game farms and reserves. Some major elements whole rocks data are nevertheless available in Vearncombe et al. (1992).

Sample	site	description	latitude	longitude
MUR 09-5a	Baderoukwe pluton	coarse-grained Bt-granitoid	23°45'30.8"	30°59'44.5"
MUR 09-5b		coarse-grained Bt-Ms granitoid		
MUR 09-6		medium-grained, deformed granitoid		
MUR 09-7		idem, with quartz vein		
MUR 10		coarse-grained, slightly green, altered granitoid	23°45'46.9"	30°59'40.2"
MUR 09-82		Ms-rich highly deformed granitoid	23°45'4.1"	30°58'29.8
MUR 09-83		albitized, quartz-veined, porous rock		
MUR 09-85		coarse-grained, quartz-veined, granitoid	23°44'50.4"	30°58'12.6"
MUR 09-13	Malati Pump	deformed albitite	23°51'31.7"	30°36'19.2"
MUR 09-111		porous albitites		
MUR 09-89A		albitite with quartz vein	core	
MUR 09-89B		albitite with quartz, carbonate, pyrite	core	
MUR 09-89C		coarse-grained albitite	core	
MUR 09-89D		coarse-grained albitite	core	
MUR 09-54	Monarch	fine-grained albitite		
MUR 09-55		fine-grained albitite	23°53'7.7"	30°42'50.5"
MUR 09-56		deformed albitite		
MUR 09-41	Gravelotte	silicified albitite	23°56'23.1"	30°36'28.7"
MUR 09-92		albitite with quartz, carbonate, pyrite, muscovite	core	
MUR 09-96		albitite with muscovite	core	
MUR 09-97		idem, close to the border	core	

Table 1: *Sampling and localization.*

PETROGRAPHY

Protolith (Baderoukwe pluton)

Hand samples of the Baderoukwe pluton have a leucocratic (MUR 09-5a) to hololeucocratic color (MUR 09-5b, -6, -7). Rocks are undeformed (MUR 09-5a, -5b, -7) to slightly deformed (MUR 09-06). In the northern slice, sample MUR 09-82 is muscovite-rich, which draws irregular foliation plans around quartz-feldspar nodules.

Protolith samples display two types of textures, from coarse-grained equigranular (size of grains around 1.5 mm, MUR 09-5a, Fig. 2a) to a bimodal-size texture made of quartz-feldspars nodules embedded in a fine-grained (< 150µm) groundmass of quartz-feldspar (MUR 09-5b, 6 and 7, Fig. 2b).

Feldspar minerals are largely dominated by Na-rich plagioclase (Table 3, Fig. 4) whereas orthoclase is very rare (only one grain observed in MUR 09-5b). MUR 09-5b feldspar is albite to oligoclase ($An_{0.16-18.23}$). Albite s.s. is present in MUR 09-5a ($An_{1.88-9.22}$) and MUR 09-82 ($An_{0.77-6.37}$). No difference between cores and border was detected during microprobe analysis despite the widespread optical observations of the cores (Fig. 2a and b). Feldspar grains often show irregular edges when found in contact with the fine-grained matrix (Fig. 2b). Feldspar is altered in epidote (saussuritization) and

sericite (sericitization), with the cores being more altered than the borders (Fig. 2a). Quartz displays an undulose extinction. Dark-brown biotite is always present (Fig. 2a, b and c), with titanite (Fig2a and c) and zircon. It is often associated in clusters with muscovite of the same size, plus epidote (Fig. 2b and c). Muscovite is also found isolated in the groundmass. Fig. 5 indicates that muscovite composition of sample MUR 09-5a has a narrow, low-Ti range, and thus is restricted to the "secondary" field of Miller et al. (1981). For sample MUR 09-5b, muscovite also displays a low Na content (around 10 mol%), but the range of compositions encompasses both the "primary" and the "secondary" fields (Fig. 5). The abundant muscovite of sample MUR 09-82 is limited to a small compositional range around the limit between the two fields.

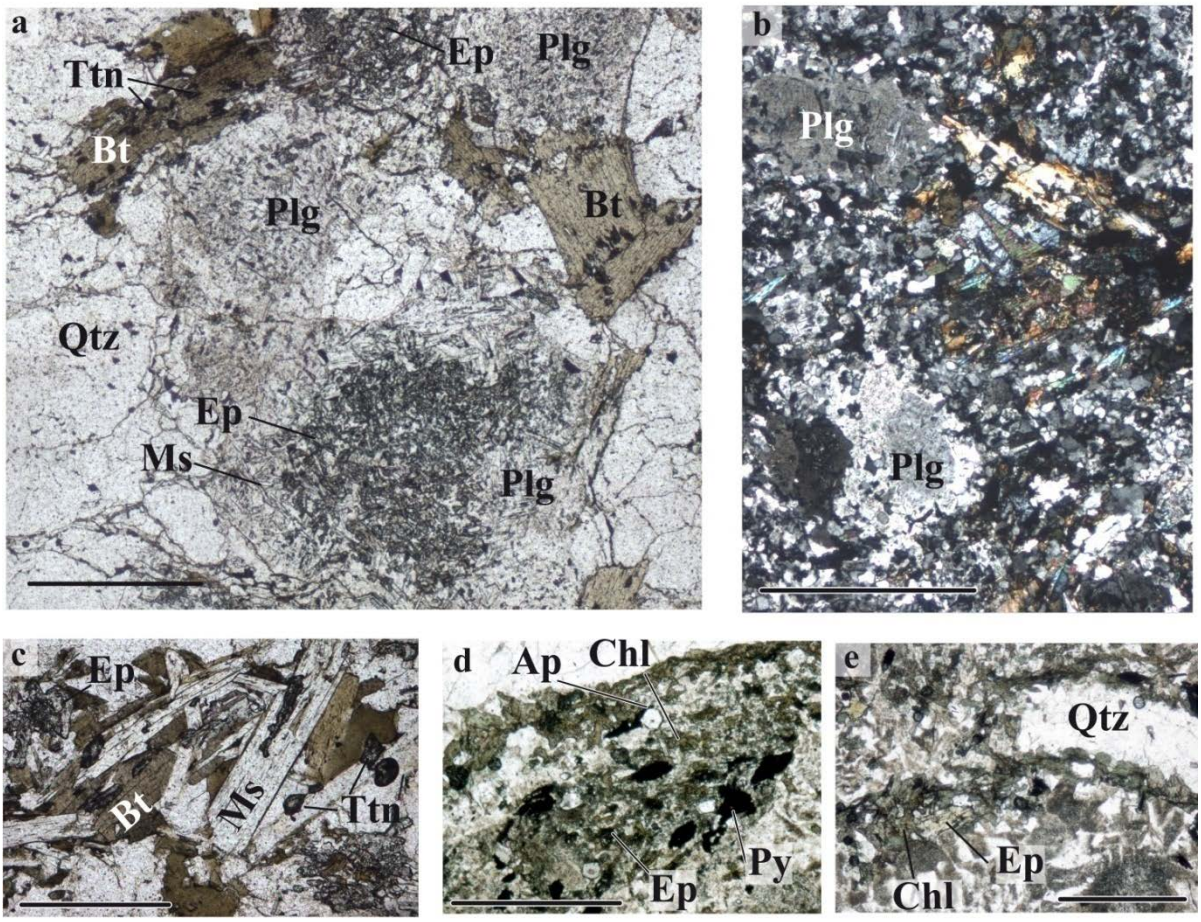

Figure 2: *Pictures of the Baderoukwe pluton. (a) Freshest aspect of the Baderoukwe pluton with quartz-feldspar and biotite. Note the more saussuritized core of plagioclase (MUR 09-5a; bar scale 1 mm). (b) Texture often consists of porphyric quartz and feldspar grains in fine-grained quartz-feldspar groundmass (MUR 09-5b; bar scale 1 mm). (c) Biotite and muscovite are isolated or associated in clusters together with titanite and epidote (MUR 09-5a, bar scale 500 µm). (d) Pseudomorphs after feldspar (?) of chlorite + epidote + pyrite + apatite (MUR 10, bar scale 500 µm). (e) Same sample, example of quartz dissolution with chlorite precipitation, the latter is associated with epidote (bar scale 500 µm).*

Sample MUR 10 is a quite peculiar sample. It is made up of up to 5mm large feldspar and veinlets of quartz, which indicate significant silicification. Pseudomorphs, likely after feldspar, consist of a greenschist facies association (chlorite epidote, plus

apatite, pyrite and quartz and/or feldspar; Fig. 2d). Myrmekitic zones separate quartz from feldspar, and are cross-cut by a chlorite-epidote assemblage (Fig. 2f).

Besides, two altered rocks have been sampled right to the north of the northern slice (MUR 09-83 and 85; Fig. 1b). They bear quartz veins that crosscut a quartzo-feldpathic groundmass (fine grained for MUR 09-83, or larger grain for MUR 09-85), that carries an epidote + chlorite-biotite + muscovite assemblage.

Albitites

In the field, albitites are recognized by their powdery, matt, yellowish altered aspect (MUR 09-13, -41, -54, -55, -56, and 111). Cores samples have a fresher, grayish color. They are hololeucocratic, apart from MUR 09-89C and D that show a slightly green color. Cm-scale quartz veins (MUR 41, 55, 89A, 111) or quartz patches (MUR 09-89A, -B) are common, and MUR 09-92 exhibits muscovite-veins in the form of a mm-wide dense network.

In thin sections, apart from quartz veins, most of the rocks are made up of up to 95% of albitic fedlspar (anorthite content maximum is $An_{2.2}$, Fig. 4). Albitites show three types of textures. (i) Albite grains can be millimetric porphyric (Fig. 3a) associated with quartz with an undulose extinction, this latter exhibiting dissolution figures (Fig. 3d). These dissolution figures are filled with a groundmass made of fine-grained albite plus minor quartz (Fig. 3c and d, Monarch samples and MUR 09-13 from Malati Pump). (ii) Albite can simply form large continuous grains (Fig. 3e, Malati Pump samples MUR 09-89A-D and MUR 09-111). (iii) Sometime (MUR 09-97) one can observed numerous small neoformed albite grains replacing a large feldspar grain (inset in Fig. 3a); in this case, two-elements twinning can even be preserved.

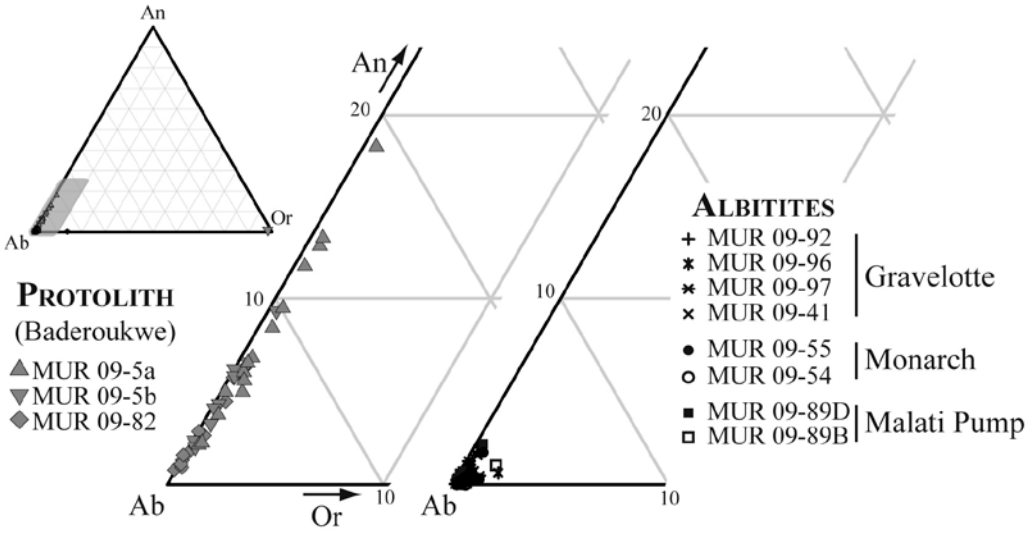

Figure 4: *Feldspar composition ternary diagram from EMP measurements. The maximum An content in feldspar for Baderoukwe protolith is 18.23, against 2.2 for albitites.*

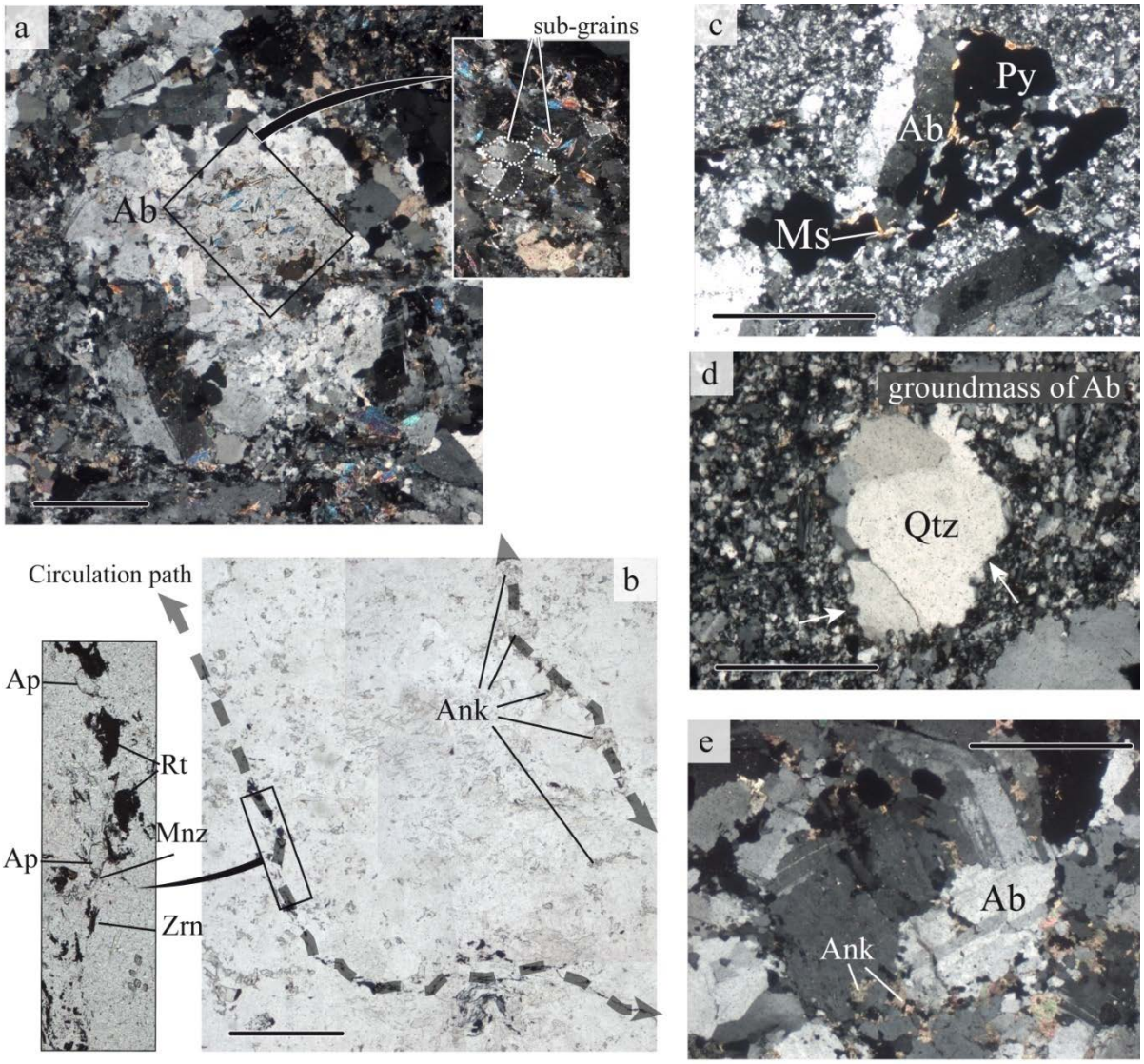

Figure 3: *Pictures of the Albitites. (a) Albitite MUR 09-97 has porphyric pseudomorphs after feldspar of sub-grains albite. Also contained muscovite and carbonates (crossed polars light, bar scale 1 mm). (b) Same view, planed polars light. Around this albite are circulation zones embodied in paragenesis of ankerite + rutile + apatite + zircon + monazite. (c) Texture can take the form of porphyric albite in albite-quartz groundmass. Pyrite suffered albitization and muscovitisation (MUR 09-54, crossed polars light, bar scale 1 mm). (d) The porphyric minerals display dissolution figures (white arrows) into quartz (MUR 09-55, crossed polars light, bar scale 500 µm) (e) in Malati Pump, samples are made of massive albite with ankerite in joints around it (MUR 09-89A, crossed polars light, bar scale 1 mm).*

Ca-Mg-Fe carbonate is often present, mostly fine-grained around albite and is dolomitic to ankeritic in composition (FeO 1.7 to 12.0 wt%, Table 3, Fig. 3b and e). Rarely, siderite is present in fractures (MUR 09-89B) and calcite is observed as diffuse veins (MUR 09-96). Sulfides are widespread (pyrite-pyrrhotite, Fig. 3c) and oxides are rare (one hematite grain observed, MUR 09-41). Rutile and phosphates (apatite, monazite, xenotime), zircons (see 7.1) and sometimes tourmaline are commonly associated, along circulation paths around the albite grains (Fig. 2b inset), as well as filling dissolution zones of sulfides. Muscovite is present in variable proportions (rare

in MUR 09-54 and 55, MUR 09-89A and B). Where abundant, it forms either veinlets crosscutting the albite grains (MUR 09-92 and MUR 09-41) or diffuse impregnation in association with chlorite (MUR 09-13). With the exception of the Monarch site, muscovite has a wide range of compositions with a significant Na-enrichment (Fig. 5).

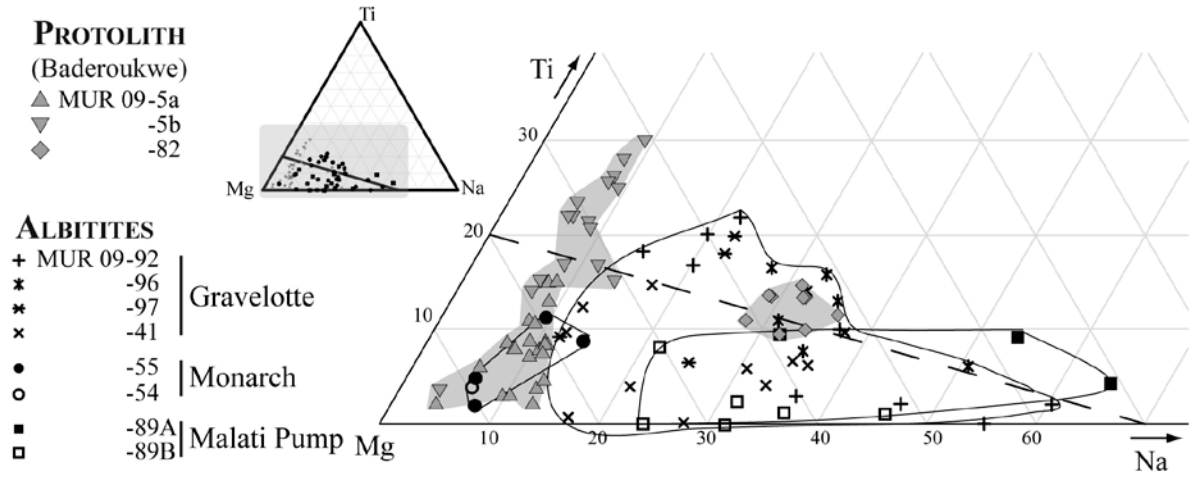

Figure 5: *Muscovite ternary composition diagram after Miller et al (1981). Up to the dashed line is the field of primary (magmatic) muscovite; down is the field of secondary muscovite.*

ANALYTICAL PROCEDURES

Rocks were crushed first in a steel jaw crusher then in an agate mortar until a fine powder was obtained. The SARM laboratory (CRPG-CNRS, Nancy) performed the chemical analyses using $LiBO_2$ fusion and acid dissolution by ICP-AES for major elements and ICP-MS for trace elements. Whole rock chemical compositions are reported in Table 2, together with detection limits. Analytical uncertainties depend on the content and more details can be found in Carignan et al. (2001).

Mineral compositions were measured in thin section on a SX-100 CAMECA electron microprobe (EMP) at the *Laboratoire Magmas et Volcans* (Clermont-Ferrand) using 15kV accelerating voltage.

	PROTOLITH (Baderoukwe)			ALBITITES						
location	North-western		North slice	**Malati Pump**	**Monarch**			**Gravelotte**		
sample	MUR 09-5a	MUR 09-5b	MUR 09-82	MUR 09-89A-D	MUR 09-54	MUR 09-55	MUR 09-41	MUR 09-92	MUR 09-96	MUR 09-97
Plagioclase	*n=10*	*n=15*	*n=11*	*n=23*	*n=1*	*n=15*	*n=16*	*n=6*	*n=7*	*n=22*
SiO_2	67.73	66.64	68.75	69.51	73.79	69.09	69.21	68.51	69.26	68.66
Al_2O_3	20.42	21.00	20.23	19.67	19.38	19.70	19.60	20.27	19.75	19.79
CaO	0.93	1.65	0.57	0.10	0.02	0.07	0.09	0.10	0.21	0.09
Na_2O	10.93	10.59	11.15	11.67	9.61	11.60	11.44	11.10	11.61	11.43
K_2O	0.07	0.09	0.05	0.05	0.05	0.07	0.04	0.43	0.06	0.04
Total	100.07	99.96	100.75	101.00	102.86	100.53	100.38	100.40	100.89	100.01
					Structural formula based on 8 oxygen atoms					
Si	2.96	2.92	2.98	3.00	3.09	3.00	3.00	2.98	2.99	2.99
Al	1.05	1.08	1.03	1.00	0.96	1.01	1.00	1.04	1.01	1.02
Ca	0.04	0.08	0.03	0.00	0.00	0.00	0.00	0.00	0.01	0.00
Na	0.93	0.90	0.94	0.98	0.78	0.98	0.96	0.94	0.97	0.97
K	0.00	0.00	0.00	0.00	0.00	0.00	0.00	0.02	0.00	0.00
					End-member feldspar, mole %					
orthose	0	0	0	0	0	0	0	3	0	0
albite	95	92	97	99	100	99	99	97	99	99
anorthite	4	8	3	0	0	0	0	0	1	0
Muscovite	*n=23*	*n=16*	*n=9*	*n=9*	*n=1*	*n=4*	*n=12*		*n=8*	*n=4*
SiO_2	47.39	47.55	46.66	47.29	48.87	47.99	48.82		47.51	47.09
TiO_2	0.39	1.27	0.57	0.15	0.24	0.37	0.29		0.48	0.67
Al_2O_3	30.11	29.48	34.00	34.32	30.91	31.79	32.06		33.79	31.56
FeO	3.41	3.09	1.89	1.61	1.88	2.03	1.54		2.04	3.58
MnO	0.04	0.05	0.02	0.02	0.00	0.01	0.01		0.01	0.01
MgO	2.14	2.22	1.30	1.06	2.95	2.31	1.44		1.06	1.65
Na_2O	0.20	0.19	0.55	0.50	0.17	0.20	1.31		0.78	0.39
K_2O	11.18	11.02	10.43	10.27	11.17	9.79	9.73		10.29	10.58
Total	94.86	94.87	95.41	95.24	96.20	94.50	95.21		95.97	95.52
					Structural formula based on 11 oxygen atoms					
Si	3.22	3.22	3.11	3.14	3.24	3.21	3.23		3.15	3.17
Ti	0.02	0.06	0.03	0.01	0.01	0.02	0.01		0.02	0.03
Al	2.41	2.36	2.67	2.69	2.41	2.51	2.52		2.64	2.50
Fe	0.19	0.18	0.11	0.09	0.10	0.11	0.09		0.11	0.20
Mn	0.00	0.00	0.00	0.00	0.00	0.00	0.00		0.00	0.00
Mg	0.22	0.22	0.13	0.11	0.29	0.23	0.14		0.10	0.17
Na	0.03	0.03	0.07	0.06	0.02	0.03	0.16		0.10	0.05
K	0.97	0.95	0.89	0.87	0.94	0.84	0.83		0.87	0.91
Carbonates				*n=19*	*n=7*	*n=10*			*n=7*	*n=14*
CO_2				44.86	39.20	46.40			39.59	44.37
CaO				28.59	1.96	30.91			59.33	29.36
MgO				12.92	5.61	20.09			0.13	12.58
FeO				12.64	50.92	2.33			0.50	13.04
MnO				0.71	1.04	0.13			0.22	0.54
Total				99.73	98.74	99.86			99.77	99.90
						Structural formula based on 6 oxygen atoms				
C				1.84	1.82	1.84			1.73	1.85
Ca				1.16	0.08	1.18			2.50	1.18
Mg				0.73	0.35	1.07			0.02	0.70
Fe				0.40	1.79	0.07			0.01	0.41
Mn				0.02	0.04	0.00			0.01	0.02
						End-member Carbonate, mole %				
calcite				50	4	51			99	51
magnesite				31	16	46			0	30
siderite				17	79	3			1	18
rhodochrosite				1	2	0			0	1

Table 3: *Minerals composition. Average electron microprobe analyses (wt. %) and corresponding structural formulae (apfu).*

Sr and Sm-Nd isotopes analyses were performed on 100 mg of rock powders using the 7-collectors Finningan MAT-262 mass spectrometer available at Geosciences Rennes. Powders were dissolved twice with a mixture of concentrate HF – HNO_3 acids. After five days of digestion, the solution was evaporated to dryness and then taken up

in 6 N HCl acid for two days. They were then dried and taken up with concentrated HCl 2.5N and loaded on cationic exchange chromatography using AG50W – X8 resin to collect the REE fractions on one hand and Sr and Rb on the other hand. The REE fractions were then purified and Sm and Nd isolated using a secondary column loaded with Eichrom Ln resin. Sr was separated with the Spec resin. Sr and Sm-Nd concentrations were measured by isotope dilution using ^{84}Sr and $^{149}Sm/^{150}Nd$ spikes, respectively. All samples were spiked before dissolution. During the analytical session, measurements of the AMES Nd standard gave a mean $^{143}Nd/^{144}Nd$ ratio of 0.511957 ± 3 (n=18), and analyses of the NBS-987 Sr standard yielded a mean $^{87}Sr/^{86}Sr$ ratio of 0.710183 ± 10 (n =18). Blanks values for Nd and Sr were < 300 pg. Model ages and εNd are calculated using the decay constant $\lambda = 6.54\ 10^{-12}\ y^{-1}$ and Goldstein et al.'s (1984) parameters.

Oxygen and carbon isotope analyses (Table 2 and 5) were carried out in Géosciences Rennes. For silicates analyses, about 7 mg of whole rock powder were crushed and reacted with BrF_5 in Ni tubes at 670°C over night (after the method of Clayton and Mayeda, 1963). It was then converted to CO_2 by reaction with hot graphite, and analyzed using a VG SIRA 10 triple collector instrument. Long-term analysis of NBS 28 standard ($\delta^{18}O$ = 9.58‰) gave a mean value of 9.3 ± 0.1‰. Measured values have thus been slightly corrected. The carbonate fraction of albitites was reacted with anhydrous phosphoric acid (H_3PO_4) in sealed vessels at 50°C over night. The chemical composition of the carbonate fraction was either measured by electron microprobe or estimated using SEM analysis. It was then used to estimate the experimental fractionation coefficient of each sample together with the coefficient of end-members carbonates taken from the literature (at 50°C, $\alpha_{Cal-CO2}$=1.00936, $\alpha_{Magnesite-CO2}$=1.01160: Das Sharma et al., 2002; $\alpha_{Dol-CO2}$=1.01066, $\alpha_{Ank-CO2}$=1.01061, $\alpha_{Siderite-CO2}$=1.01046: Rosenbaum and Sheppard, 1986; $\alpha_{Rhodocrosite-CO2}$=1.00756: Böttcher, 1996). The average uncertainties on isotopic compositions are 0.1‰ for C in carbonate, about 0.2‰ for O in carbonate and about 0.2‰ for oxygen whole rock composition.

Zircon grains were dated by in-situ LA-ICP-MS either *in context* in thin sections or as separated grains mounted in epoxy mounts. For the latter, a classic mineral separation procedure has been applied. Rocks were crushed, the powder fraction (<250 µm) has been concentrated in heavy minerals by Wilfley table and heavy liquids methods. Magnetic minerals were then removed with an isodynamic Frantz separator. Grains were carefully handpicked under a binocular microscope, embedded in epoxy mounts and polished. They were imaged by cathodoluminescence (CL) using a Reliotron CL system. Additional zircon and all the monazite grains were spotted in thin sections. U–Th–Pb analyses were carried out by in situ LA-ICPMS at the *Laboratoire Magmas et Volcans* in Clermont-Ferrand, France. For zircon analyses, we used ablation spot diameters of 26 µm (mount MUR 09-54, thin section MUR 09-89B and C), 20µm (mounts MUR 09-41, MUR 09-97, MUR 09-111) and down to 11µm (thin sections MUR 09-41, MUR 09-54 and MUR 09-92) with a repetition rate of 3 Hz. Data were corrected for U–Pb and Th–Pb fractionation and for the mass bias by standard bracketing with repeated measurements of the GJ1 zircon standard (Jackson et al., 2004). For monazite

dating, settings were 7µm, 1Hz and data were corrected using the Moacir standard (Gasquet et al., 2010). Further information on the instrumentation and the analytical technique is detailed in Hurai et al. (2010). For titanite, setting were 26µm, 3Hz and data were corrected using the Lillebukt Alkaline Complex standard (Pedersen et al., 1989). Data reduction was carried out with the GLITTER® software package developed by the Macquarie Research Ltd. Ages and diagrams were generated using Isoplot/Ex (Ludwig, 2000).

GEOCHEMICAL RESULTS

Protolith (Baderoukwe)

Three out of the four Baderoukwe pluton samples cover a narrow compositional range for major elements (Table 2), with a slightly peraluminous character (1.0<A/CNK<1.1). These samples display classical granodioritic to tonalitic compositions (Fig. 6a). The SiO_2 content of the North-western samples is between 70 and 72 wt. %, whereas a strong SiO_2 increase is documented in sample MUR 09-83, consistently with the observed silicification in thin section (see also the peculiar position of this sample in Fig. 6a), and sample MUR 09-82 shows a significant SiO_2 depletion (North slice; see position in Fig. 6a). The ranges of alkali and calcium contents are small (Na_2O+K_2O = 7.0 wt. %, CaO = 2.0 wt%) with Na/K_{mol} greater than 2.57, this ratio reaching a value of 18 in sample MUR 09-85, an undoubtedly characteristic of some alteration, likely albitization (Fig. 6a). The Rare Earth Elements (REE) distribution of the North-western samples are typical of Archean granitoid (Martin, 1994), with strongly fractionated pattern, HREE <10 ppm and no significant Eu anomaly (Fig. 6b). The two altered protolith samples have lower REE contents but this depletion is not accompanied by clear intra-REE fractionation. These two last samples also display much lower contents in other trace elements when compared to the North-western and North slice samples, with the notable exception of Co and Cu. The mobile elements Ba and Cs display erratic contents within the entire population. The oxygen isotope composition of the unaltered protolith is homogeneous between 8.2 and 8.4‰, which are classical values for granitic bodies, whereas the altered protolith shows a significant $\delta^{18}O$ decrease ($\delta^{18}O$ = 5.5 and 6.7‰, Table 2 and Fig. 6d). These two last samples have unradiogenic Sr and Nd signatures (at 2.97 Ga, I_{Sr} = 0.701 and 0.705, εNd = 2.4 and 3.2; Table 4).

Table 2 (next page): *Whole rocks geochemistry: major and trace element plus isotopic oxygen whole rock composition.*

		PROTOLITH (Baderoukwe)						ALBITITES				
location		North-western			North slice	Altered Protolith		**Malati Pump**		**Monarch**	**Gravelotte**	
sample MUR-		09-5a	09-6	10	09-82	09-83	09-85	09-13	09-111	09-55	09-41	09-97
	Detection limit											
SiO_2	*0.5*	70.52	72.03	70.14	61.66	94.29	71.57	70.71	69.42	75.04	77.09	67.41
TiO_2	*0.001*	0.30	0.22	0.31	0.24	0.05	0.26	0.36	0.66	0.10	0.21	0.24
Al_2O_3	*0.02*	14.89	14.86	15.03	22.64	3.08	16.12	15.22	15.39	13.53	13.85	16.05
Fe_2O_3	*0.01*	2.35	1.44	2.44	1.32	0.51	0.97	3.15	4.47	0.74	1.08	1.62
MnO	*0.0005*	0.04	0.02	0.04	0.00	0.01	0.02	0.01	0.01	0.00	0.01	0.03
MgO	*0.02*	0.79	0.67	0.85	0.44	0.14	0.09	1.25	0.19	0.39	0.56	0.77
CaO	*0.035*	2.42	1.81	1.94	0.27	0.44	2.45	0.04	0.07	0.53	bdl	1.77
Na_2O	*0.03*	4.94	4.50	5.54	6.94	1.04	7.14	4.83	8.23	7.67	3.14	8.08
K_2O	*0.01*	1.89	2.66	1.62	3.27	0.40	0.60	1.40	0.13	0.07	2.67	0.69
P_2O_5	*0.05*	0.14	0.08	0.15	bdl	bdl	0.06	bdl	0.10	bdl	bdl	0.10
L.O.I.[1]		1.12	1.20	1.53	2.14	0.42	0.85	2.67	1.46	1.31	1.92	3.09
Total		99.41	99.48	99.58	98.92	100.37	100.12	99.63	100.15	99.38	100.53	99.84
$\delta^{18}O$[2]		8.3	8.4	8.1	8.2	6.7	5.5	11.9	10.4	11.1	11.6	10.4
La	*0.06*	27.41	23.50	30.29	20.63	2.280	6.522	20.85	20.41	3.653	14.32	15.17
Ce	*0.1*	47.47	37.78	56.89	39.42	4.379	14.14	39.36	41.99	7.826	25.10	27.91
Pr	*0.008*	5.412	4.297	6.408	4.120	0.524	1.722	4.368	5.119	0.980	2.757	2.963
Nd	*0.03*	19.04	14.04	21.83	13.81	1.909	6.418	15.59	19.77	3.880	9.624	10.31
Sm	*0.007*	3.071	2.108	3.357	2.230	0.370	1.403	3.124	4.137	0.821	1.524	1.767
Eu	*0.004*	0.859	0.596	0.943	0.700	0.121	0.582	0.882	1.236	0.257	0.438	0.503
Gd	*0.02*	2.328	1.389	2.385	1.571	0.308	1.287	2.697	3.991	0.637	1.150	1.331
Tb	*0.004*	0.305	0.185	0.323	0.193	0.046	0.206	0.427	0.631	0.089	0.152	0.188
Dy	*0.007*	1.549	0.922	1.659	0.881	0.264	1.172	2.537	3.939	0.448	0.814	0.993
Ho	*0.001*	0.276	0.155	0.287	0.132	0.048	0.208	0.483	0.799	0.079	0.142	0.166
Er	*0.003*	0.742	0.416	0.791	0.332	0.137	0.587	1.354	2.276	0.236	0.407	0.454
Tm	*0.005*	0.103	0.057	0.110	0.047	0.020	0.084	0.203	0.351	0.033	0.057	0.066
Yb	*0.003*	0.660	0.374	0.728	0.320	0.143	0.609	1.367	2.371	0.225	0.375	0.429
Lu	*0.001*	0.101	0.056	0.112	0.051	0.023	0.094	0.212	0.380	0.037	0.058	0.065
Y	*0.4*	8.577	4.655	3.923	9.337	1.496	6.226	14.50	22.98	2.514	4.446	5.290
Sb	*0.1*	bdl	bdl	bdl	bdl	0.30	bdl	**6.97**	**23.9**	**21.9**	**1003**	**17.1**
As	*1.1*	bdl	bdl	bdl	bld	bld	bld	2.53	bdl	25.7	18.6	161
V	*0.45*	23.1	12.3	23.7	27.8	9.33	17.0	47.5	49.7	2.90	32.5	24.2
Cr	*4*	35.2	31.5	30.3	16.1	87.1	20.1	35.7	14.7	39.3	31.5	25.8
Co	*0.35*	5.15	3.33	5.28	3.70	1.78	1.01	2.99	2.99	1.17	2.43	4.33
Ni	*4.5*	12.6	16.2	13.8	10.4	11.6	5.23	13.9	7.31	11.0	21.7	9.85
Cu	*4.5*	13.7	10.5	13.8	12.6	18.5	13.6	7.01	15.8	60.0	9.80	38.6
Zn	*14*	57.8	28.6	61.3	18.7	1.50	bdl	53.8	29.5	bdl	bdl	bdl
Ga	*0.2*	19.6	17.4	19.8	31.6	4.05	18.5	18.3	13.6	9.59	16.0	21.1
Ge	*0.11*	0.77	0.78	0.75	0.73	0.23	0.56	0.93	0.69	0.83	1.21	0.91
Sn	*0.4*	0.94	1.36	1.08	1.51	bdl	0.87	1.58	bdl	bdl	0.61	1.20
W	*0.2*	bdl	bdl	bdl	4.61	bdl	0.22	1.49	6.51	1.37	1.91	1.40
Cs	*0.15*	2.03	5.58	0.81	1.09	bdl	0.33	0.60	bdl	bdl	2.64	1.08
Rb	*0.3*	63.7	94.5	47.6	82.1	11.6	18.4	37.8	3.11	0.76	89.7	24.6
Sr	*1.4*	395	305	358	450	63.6	232	73.1	64.7	97.1	35.4	107
Ba	*1.5*	429	527	373	1014	64.0	141	190	38.3	20.6	503	184
Zr	*0.8*	128	116	137	113	18.3	57.1	139	202	52.8	83.7	97.2
Nb	*0.06*	5.77	3.99	5.06	4.92	0.78	12.0	6.30	7.65	0.71	2.28	4.05
Ta	*0.015*	0.60	0.61	0.56	0.48	0.15	2.23	0.91	0.86	0.07	0.26	0.49
Hf	*0.03*	3.40	3.27	3.59	3.49	0.52	1.96	3.83	4.99	1.59	2.40	2.75
Th	*0.02*	4.08	5.86	4.17	3.34	0.41	1.89	4.52	2.65	0.57	3.04	3.54
U	*0.03*	1.04	1.47	0.98	0.82	0.36	2.51	1.55	0.98	0.27	0.61	1.17
Pb	*0.9*	9.11	13.1	8.95	8.50	1.57	42.0	2.17	3.77	1.20	28.6	1.42

Oxide contents in wt.%. Trace element in ppm. bdl : below detection limit. [1] L.O.I. Loss on Ignition. [2] Whole rock silica analyses

Albitites

Albitites samples display rather high SiO_2 contents, between 67 and 77 wt. %. They plot outside the field of classical igneous rocks. Besides silicification for two of them (MUR 09-13 and 41), their main feature is their enrichment in sodium, visible in high $Na/(K+Ca)_{mol}$ ratios up to 64 for sample MUR 09-111 (Fig. 6c and d). Their REE patterns differ significantly from the Baderoukwe ones, by an increase in HREE content and a less fractionated REE pattern ($(La/Lu)_N$ down to 5.5). They do not show any Eu anomaly. Some major and trace elements behave randomly in the various samples (e.g. Fe, Ti, Ni, Cu, Zn, Pb; Table 2). Nevertheless, some LIL elements such as Th, U, Nb, Ta, Zr and Hf present contents that are comparable with the ones found for the unaltered protolith, whereas mobile elements such as Rb, Cs and Ba tend to be depleted in the albitites. The main difference between the albitites and the protolith is the metals Sb-As-W (±Mo, ±Cd) content. None of them are detected in the Baderoukwe pluton, whereas albitites are enriched in these elements, for example up to 1003 ppm for Sb (Fig. 6c).

	location	sample	Sm (ppm)	Nd (ppm)	$^{147}Sm/^{144}Nd$	$^{143}Nd/^{144}Nd$	εNd [1] at 2.97 Ga	T_{DM} [2] (Ma)	Rb [3] (ppm)	Sr [3] (ppm)	$^{87}Rb/^{86}Sr$	$^{87}Sr/^{86}Sr$	I_{Sr} [4] at 2.97 Ga
PROTOLITH (Baderoukwe)		**MUR 09-83**	0.370	1.909	0.110791	0.511076	2.36	2982	11.58	63.64	0.5273	0.7234	0.7007
		MUR 09-85	1.403	6.418	0.129690	0.511491	3.23	2911	18.37	232.10	0.2292	0.7154	0.7055
ALBITITES	Malati Pump	**MUR 09-13**	2.867	15.179	0.114144	0.511077	1.14	3097	37.75	73.12	1.5026	0.7683	0.7036
		MUR 09-111	3.740	18.954	0.119264	0.511291	3.39	2903	3.11	64.65	0.1390	0.7129	0.7069
	Monarch	**MUR09-55**	0.799	3.875	0.124532	0.511381	3.11	2926	0.76	97.09	0.0225	0.7029	0.7020
	Gravelotte	**MUR 09-41**	1.466	9.143	0.096867	0.510812	2.60	2969	89.71	35.40	7.5147	0.9623	(0.6386)
		MUR 09-97	1.619	9.761	0.100229	0.510823	1.52	3056	24.56	107.10	0.6655	0.7387	0.7101

1: $^{143}Nd/^{144}Nd_{CHUR} = 0.512638$; $^{147}Sm/^{144}Nd$ CHUR = 0.1967; ^{147}Sm: $\lambda = 6.54 \times 10^{-12}$. 2: Goldstein et al 1984. 3: mesured by ICP-MS. 4: I_{Sr} = initial $^{87}Sr/^{86}Sr$; ^{87}Rb $\lambda = 1.42 \times 10^{-11}$;

Table 4: *Radiogenic Sm-Nd and Rb-Sr isotopes.*

$\delta^{18}O$ values of Ca-Mg-Fe carbonates (Table 5) range from 11.2 to 13.5 ‰ except for sample MUR 09-55 that show a much higher value (20.7-20.8 ‰). Their carbon isotope signature seems to be site-dependent, with -9.9 to -9.3 ‰ in Malati Pump mine, -6.1 ‰ in Monarch samples and -5.3 to -4.9 ‰ in Gravelotte. Albitites whole rocks display a narrow range of oxygen signatures (10.4-11.9 ‰). Sr data are somewhat variable, with $I_{Sr}(T)$ varying from 0.710 down to 0.702, with the exception of one meaningless value of 0.6386. Also, $\varepsilon_{Nd}(T)$ are consistent between 1.1 and 3.4, and compare well with the values of the unaltered protolith.

Sample	nature	$\delta^{18}O$[1] (‰ SMOW)	$\delta^{13}C$ (‰ PDB)
MUR 09-89A	Ankerite > Dolomite	11.8-12.7	-9.6
MUR 09-89B	Ankerite ≈ Dolomite	11.7-12.8	-9.9
MUR 09-89C	Ankerite >> Dolomite, Siderite	11.5-11.8	-9.5
MUR 09-89D	Dolomite-Ankerite	13.5	-9.3
MUR09-55	Dolomite >> Ankerite	20.7-20.8	-6.1
MUR 09-92	Ankerite >> Dolomite	11.6-12.2	-5.1
MUR 09-96	Calcite	11.2	-5.3
MUR 09-97	Ankerite >> Dolomite	11.6-12.1	-4.9

[1] *Isotopic composition ranges from chemical carbonate compositions correction*

Table 5: *Isotope composition of the carbonate fraction from albitite rocks.*

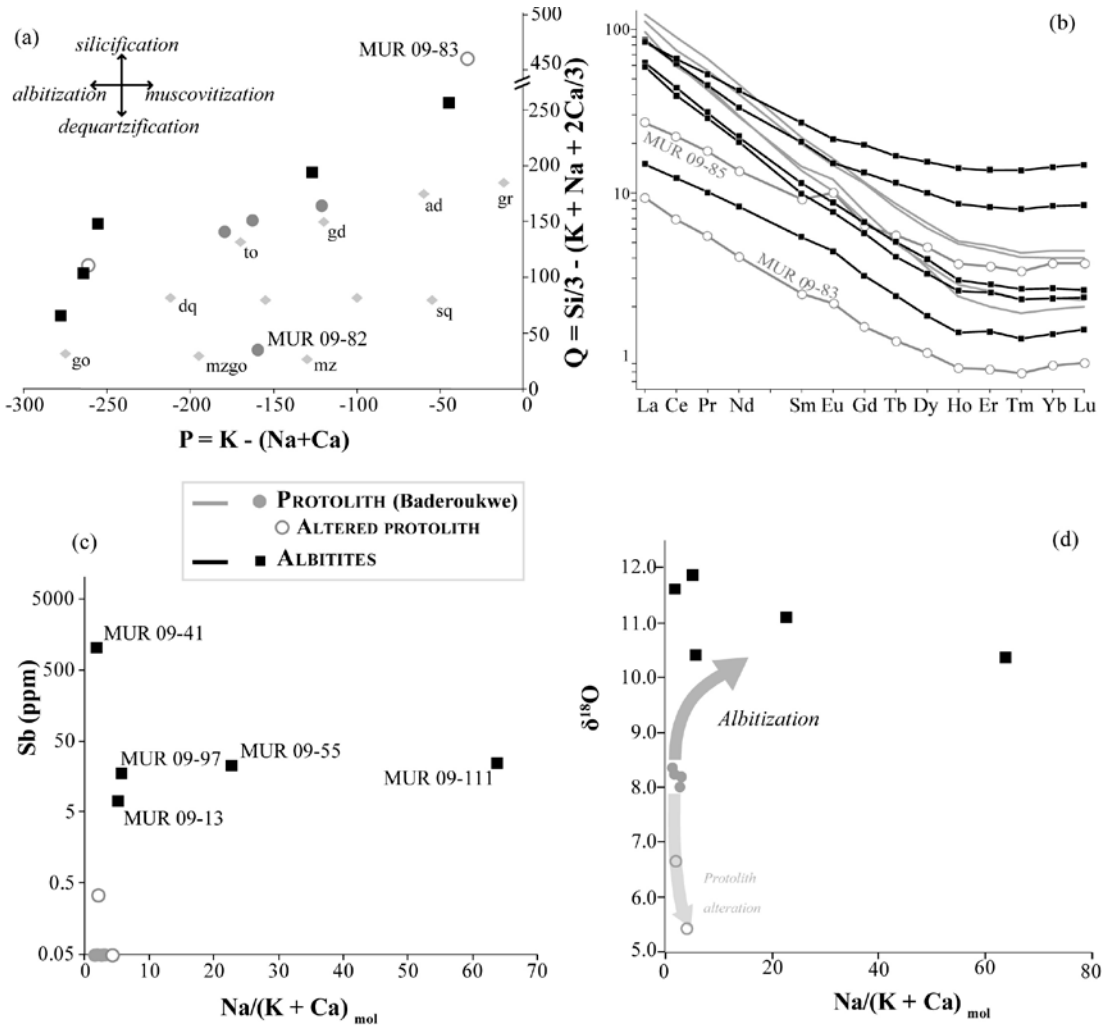

Figure 6: *Geochemical diagrams of the albitites compared to the protolith (Baderoukwe) and its altered samples. (a) Chemical diagram of Debon and Lefort (1983), with Q and P in mmol proportion; grey diamonds for regular igneous rocks gr = granite ad = adamelitte gd = granodiorite to = tonalite (mz)dq = quartz (monzo)diorite (mz)go = (monzo)gabbro sq = quartz syenite (q)mz = (quartz) monzonite. (b) Chondrite-normalized Rare-Earth-Elements (REE) pattern (chondrite values from Evensen et al 1978). (c) Diagram of Sb content versus Na/(K+Ca) (molar proportion). (d) $\delta^{18}O$ whole rocks oxygen isotopic composition (‰ SMOW) versus Na/(K+Ca) (molar proportion).*

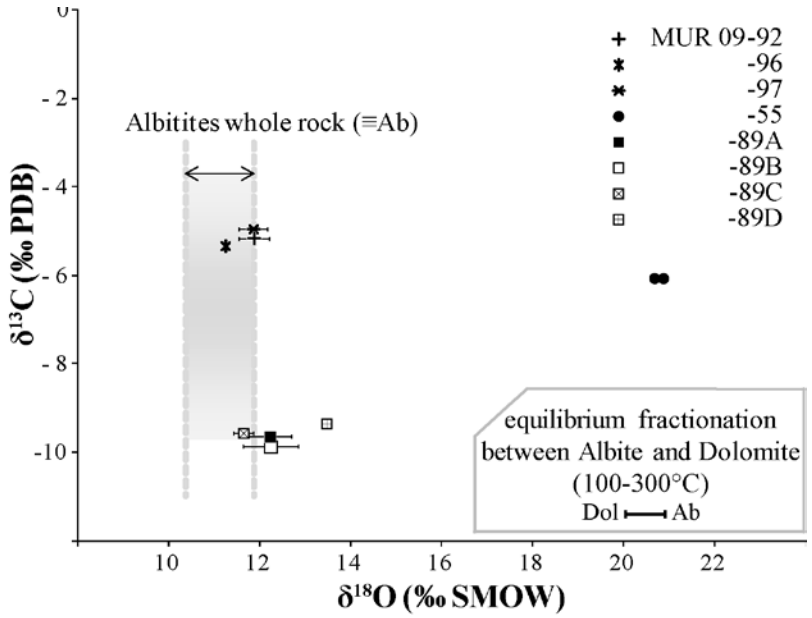

Figure 7: *Diagram of oxygen and carbon isotopes composition of carbonate (symbols) and albitites (grey range). Dolomite-albite fractionation is calculated using data in Zheng et al (1993).*

MONAZITE, ZIRCON AND TITANITE DATING

Petrography of these minerals

Zircon grains have been dated from minerals separates as well as from thin sections in the albitites (Table 6). They occur in various contexts, either enclosed within large albite grains (Zr1 in MUR 09-41, Fig. 8d) or within the groundmass (Fig. 2b). Most of the time, zircon grains are euhedral (Fig. 8a, d) and sometimes they display oscillatory zoning (Fig. 8a, c, d). Some zircon grains have patchy textures (Fig. 8b) or display complex and unusual circumvolution-like relationship between core and overgrowth (Fig. 8c).

Monazite grains were often small (10µm, Fig. 8f) with rare medium-size grains (80µm, Fig. 8h) and yield highly variable Th/U ratio (0.2 to 224, Table 7). They are found sometime isolated in albite grains, but most of the time they are associated with circulation pathways where quartz or albite are present or in association with rutile-apatite-zircon assemblages (Fig. 2b, inset). In sample MUR 09-92, most of the monazite grains are found in fluid circulation veinlets dominated by muscovite. They are also found enclosed in altered pyrite, with rutile and xenotime (MUR 09-89A, Fig. 8f) or as "overgrowths" around pyrite grains (MUR 09-92, Fig. 8h). These petrological observations indicate that monazite was associated to the mineral reactions related to the albitization process.

In the Baderoukwe samples, titanite grains are found mostly in and around biotite grains as an alteration phase (Fig. 2a and c, Table 8, Fig. 8g).

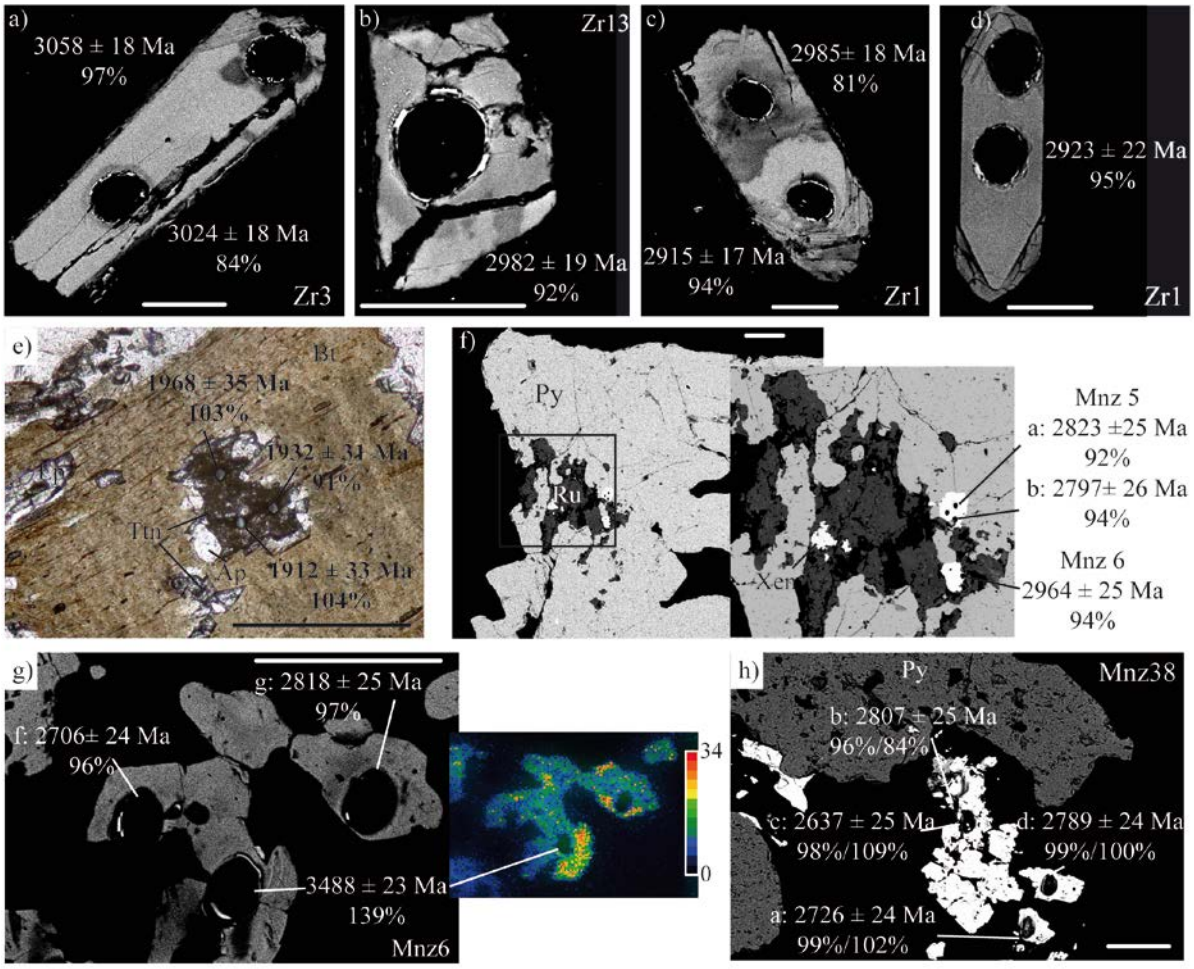

Figure 8: *Pictures of dated phases. (a) to (d) SEM (back scattered) images of zircon grains from MUR 09-41 sample (bar scale 50 µm) (a) grain with homogeneous core and some oscillatory zoning along the top border. (b) Grain with patchy texture. (c) Grain with two zones (core and overgrowth?) with circumvolution-like relationship. White circles are for data noted # in Table 5 (d) Grain with homogeneous core and some oscillatory zoning along the top left border.(e) Titanite (Ttn) plus apatite (Ap) enclosed in biotite (Bt) (bar scale 250 µm). (f) to (h) Monazite grains (f) SEM back scattered image of pyrite (Py) grain with altered zone filled by rutile (Ru) xenotime (Xen) and monazite 5 and 6 (MUR 09-89A, bar scale 200 µm) (g) SEM back scattered image, large spreading of date within a same cluster can be related to Th enrichment. Inset: EMP map of Th (MUR 09-89B, bar scale 50 µm) (h) SEM back scattered image of monazite in cluster, coating a pyrite (MUR 09-92, bar scale 50 µm).*

Geochronological data

Zircon

Zircon data acquired in this study from the albitite samples are reported in Figure 9 (a to d). On these diagrams, the age of the Baderoukwe batholith (Jaguin et al., 2012b) is indicated by a black star. The first striking point is that they do not define a simple trend in the Concordia diagrams. They rather plot in a discordant position with apparent $^{207}Pb/^{206}Pb$ dates ranging from 3058 down to 2837 Ma. They also clearly display lower Th/U ratios than in Malati Pump (Table 6; mean Th/U in Malati Pump

0.748; 0.343 in this study), although these values are still too high to be attributed to a metamorphic origin.

MUR 09-97 and MUR 09-54 do not provide any meaningful age (Fig. 9c and d). Sample MUR 09-92 yields a poorly constrained date of 2944 ± 42 Ma (MSWD=46) (Fig. 9a) due to the large scattering of the data and their overall high discordancy. This date could be tentatively compared to the age of ca 2.97 Ga found for the Baderoukwe batholith (Jaguin et al., 2012b). Data from sample MUR 09-41 are also rather scattered (Fig. 9b). Two main trends can be observed however. A group of eight discordant data (shaded ellipses) define a discordia with an upper intercept date of ca 3051±25 Ma (MSWD=3.6), while twenty-one analyses (black ellipses) yield a $^{207}Pb/^{206}Pb$ date of 2922 ± 8 Ma (MSWD=0.66). The remaining data either fall in between these two main trends or point to older apparent dates.

Titanite

Nine data acquired directly in a thin section yield a discordia with an upper intercept date of 1939 ± 46 Ma (Fig. 9e). Although poorly constrained (MSWD=6), this date is confirmed by the mean $^{207}Pb/^{206}Pb$ date of 1936 ± 41 Ma (MSWD=2.1).

Monazite

Monazite radiogenic data for the albitite samples displays a complex behavior as illustrated on Fig. 9f. Plotted in the ^{206}Pb-^{238}U vs ^{207}Pb-^{235}U concordia diagram, the data are scattered in a concordant to slightly discordant position. At the first order, the positions of the data can be explained in terms of a crisis polygon (Fig. 9f), defined by three apices at ca 2800, 2000 Ma and zero, respectively. Inside this polygon, the data imprecisely cluster around 2.8, 2.6, 2.4, 2.2 Ga. The 2.8 Ga group is found in every sample (and site), and two dates can be independently calculated at 2793 ± 24 Ma (MUR 09-92) and 2784 ± 21 Ma (MUR 09-89; Fig. 9g) while the apparent 2.6, 2.4 and 2.2 Ga groups are not found in each sample. As these two dates of 2793 ± 24 and 2784 ± 21 Ma are similar within error, we calculate a global $^{207}Pb/^{206}Pb$ date of 2791 ± 12 Ma for this group of 35 data (MSWD=2.1; Fig. 9h).

Table 6 (next page): *Geochronological dating of zircon from albitites.*

	Sample	grain-spot	Chemistry Pb (ppm)	U (ppm)	Th/U	Isotopic ratios $^{207}Pb/^{235}U$	error	$^{206}Pb/^{238}U$	error	ρ	$^{207}Pb/^{206}Pb$	error	Ages ^{235}U-^{207}Pb	^{238}U-^{206}Pb	^{207}Pb-^{206}Pb	±	Conc[1] %
Gravelotte	MUR 09-41	1-up	114	215	0.423	13.795	0.169	0.4536	0.0053	**0.951**	0.2206	0.0024	2736	2411	2985	18	81
		1-down	**179**	**300**	**0.329**	**15.377**	**0.183**	**0.5280**	**0.0061**	**0.969**	**0.2112**	**0.0022**	**2839**	**2733**	**2915**	**17**	**94**
		1-#1	**97**	**157**	**0.346**	**16.161**	**0.174**	**0.5443**	**0.0054**	**0.919**	**0.2153**	**0.0024**	**2886**	**2801**	**2946**	**18**	**95**
		1-#2	**89**	**150**	**0.232**	**15.617**	**0.169**	**0.5392**	**0.0053**	**0.914**	**0.2100**	**0.0023**	**2854**	**2780**	**2906**	**18**	**96**
		1-#3	109	201	0.191	14.528	0.179	0.4887	0.0051	**0.842**	0.2156	0.0027	2785	2565	2948	20	87
		1-#4	**51**	**80**	**0.306**	**16.382**	**0.182**	**0.5637**	**0.0056**	**0.892**	**0.2108**	**0.0024**	**2899**	**2882**	**2911**	**18**	**99**
		1-#5	**48**	**76**	**0.275**	**16.311**	**0.182**	**0.5636**	**0.0056**	**0.888**	**0.2099**	**0.0024**	**2895**	**2882**	**2905**	**19**	**99**
		1-#6	**81**	**124**	**0.310**	**16.888**	**0.187**	**0.5707**	**0.0056**	**0.889**	**0.2146**	**0.0025**	**2929**	**2911**	**2941**	**18**	**99**
		1-#7	98	153	0.329	16.495	0.189	0.5575	0.0055	**0.860**	0.21456	0.0025	2906	2856	2940	19	97
		1-#8	**90**	**141**	**0.316**	**16.221**	**0.188**	**0.5580**	**0.0055**	**0.850**	**0.21082**	**0.0025**	**2890**	**2858**	**2912**	**19**	**98**
		1-#9	135	384	0.244	9.673	0.115	0.2774	0.0028	**0.832**	0.25289	0.0031	2404	1578	3203	19	49
		1-#10	**79**	**125**	**0.292**	**16.492**	**0.197**	**0.5599**	**0.0055**	**0.826**	**0.21363**	**0.0026**	**2906**	**2866**	**2933**	**20**	**98**
		2-core	112	215	0.347	13.697	0.172	0.4506	0.0053	**0.932**	0.2204	0.0025	2729	2398	2984	18	80
		3-core	89	157	0.292	15.092	0.185	0.4841	0.0056	**0.951**	0.2261	0.0025	2821	2545	3024	18	84
		3-border	146	210	0.351	18.499	0.228	0.5810	0.0068	**0.948**	0.2309	0.0026	3016	2953	3058	18	97
		4-core	130	196	0.342	17.436	0.214	0.5545	0.0065	**0.947**	0.2280	0.0025	2959	2844	3038	18	94
		4-border	329	956	0.295	10.033	0.120	0.2293	0.0027	**0.966**	0.3174	0.0034	2438	1331	3557	16	37
		5-border	118	190	0.381	16.261	0.197	0.5161	0.0060	**0.954**	0.2285	0.0025	2892	2683	3041	17	88
		5-core	152	275	0.334	14.440	0.175	0.4740	0.0055	**0.954**	0.2209	0.0024	2779	2501	2987	17	84
		6-border	**93**	**160**	**0.300**	**14.911**	**0.185**	**0.5129**	**0.0060**	**0.938**	**0.2108**	**0.0024**	**2810**	**2669**	**2912**	**18**	**92**
		6-core	100	177	0.333	14.501	0.181	0.4682	0.0055	**0.932**	0.2246	0.0026	2783	2476	3014	18	82
		8	111	148	0.331	19.346	0.240	0.6362	0.0074	**0.935**	0.2205	0.0025	3059	3174	2984	18	106
		9-core	125	197	0.383	16.315	0.200	0.5277	0.0061	**0.941**	0.2242	0.0025	2895	2732	3011	18	91
		9-border	**147**	**239**	**0.353**	**15.625**	**0.190**	**0.5364**	**0.0062**	**0.946**	**0.2112**	**0.0023**	**2854**	**2768**	**2915**	**18**	**95**
		10-core	171	260	0.312	17.227	0.218	0.5522	0.0064	**0.920**	0.2263	0.0026	2948	2834	3026	18	94
		10-border	**115**	**190**	**0.297**	**15.604**	**0.193**	**0.5338**	**0.0062**	**0.932**	**0.2120**	**0.0024**	**2853**	**2758**	**2921**	**18**	**94**
		11-core	79	124	0.311	16.818	0.210	0.5382	0.0062	**0.925**	0.2266	0.0026	2925	2776	3028	18	92
		11	**152**	**251**	**0.411**	**15.197**	**0.191**	**0.5173**	**0.0060**	**0.921**	**0.2131**	**0.0025**	**2828**	**2688**	**2929**	**18**	**92**
		12-core	**139**	**232**	**0.328**	**15.160**	**0.189**	**0.5250**	**0.0061**	**0.924**	**0.2094**	**0.0024**	**2825**	**2720**	**2901**	**18**	**94**
		13	95	152	0.329	16.179	0.204	0.5326	0.0062	**0.917**	0.2203	0.0026	2888	2753	2983	19	92
		14-core	145	293	0.357	12.476	0.167	0.4262	0.0050	**0.878**	0.2123	0.0027	2641	2288	2923	20	78
		14-border	**180**	**316**	**0.329**	**14.435**	**0.183**	**0.4943**	**0.0057**	**0.910**	**0.2118**	**0.0025**	**2779**	**2589**	**2919**	**19**	**89**
		15-core	123	214	0.413	14.574	0.187	0.4829	0.0056	**0.899**	0.2189	0.0026	2788	2540	2973	19	85
		15-border	**121**	**198**	**0.329**	**15.532**	**0.200**	**0.5263**	**0.0061**	**0.897**	**0.2140**	**0.0026**	**2848**	**2726**	**2936**	**19**	**93**
		16-core	174	313	0.400	14.847	0.195	0.4367	0.0051	**0.886**	0.2466	0.0030	2806	2336	3163	19	74
		17-core	96	196	0.235	12.474	0.162	0.4309	0.0050	**0.888**	0.2099	0.0025	2641	2310	2905	19	80
		18	103	179	0.374	14.473	0.190	0.4826	0.0056	**0.882**	0.2175	0.0027	2781	2539	2962	20	86
		19	100	168	0.324	16.374	0.225	0.4623	0.0055	**0.860**	0.2569	0.0033	2899	2450	3228	20	76
		20-core	**135**	**218**	**0.312**	**15.564**	**0.202**	**0.5377**	**0.0062**	**0.885**	**0.2099**	**0.0025**	**2850**	**2774**	**2905**	**19**	**95**
		20-border	199	386	0.299	13.512	0.177	0.4245	0.0049	**0.880**	0.2308	0.0028	2716	2281	3058	19	75
		21-core	**113**	**190**	**0.302**	**15.075**	**0.198**	**0.5193**	**0.0060**	**0.876**	**0.2105**	**0.0026**	**2820**	**2696**	**2910**	**20**	**93**
		22-	152	268	0.431	15.872	0.213	0.3895	0.0045	**0.867**	0.2955	0.0037	2869	2121	3447	19	62
		23-core	**120**	**187**	**0.409**	**16.020**	**0.212**	**0.5397**	**0.0062**	**0.871**	**0.2153**	**0.0027**	**2878**	**2782**	**2946**	**20**	**94**
		23-border	321	819	0.309	11.375	0.151	0.2589	0.0030	**0.870**	0.3186	0.0040	2554	1484	3563	19	42
		1-core	***79***	***130***	***0.273***	***15.862***	***0.205***	***0.5417***	***0.0055***	***0.791***	***0.2123***	***0.0029***	***2869***	***2791***	***2923***	***22***	***95***
		1-border	*274*	*600*	*0.430*	*12.886*	*0.156*	*0.3456*	*0.0034*	***0.819***	*0.2704*	*0.0034*	*2671*	*1914*	*3308*	*20*	*58*
		4	*109*	*268*	*0.516*	*11.292*	*0.150*	*0.2757*	*0.0029*	***0.781***	*0.2970*	*0.0042*	*2548*	*1570*	*3455*	*22*	*45*
		3-core	*237*	*420*	*0.484*	*16.192*	*0.202*	*0.3968*	*0.0039*	***0.796***	*0.2960*	*0.0039*	*2888*	*2154*	*3449*	*20*	*62*
		3-border	*238*	*436*	*0.604*	*16.681*	*0.207*	*0.3258*	*0.0032*	***0.792***	*0.3713*	*0.0049*	*2917*	*1818*	*3797*	*20*	*48*
		8	*40*	*132*	*0.356*	*8.626*	*0.138*	*0.1931*	*0.0022*	***0.714***	*0.3240*	*0.0056*	*2299*	*1138*	*3589*	*26*	*32*
		9	*261*	*1156*	*0.324*	*6.365*	*0.082*	*0.1483*	*0.0015*	***0.758***	*0.3113*	*0.0043*	*2027*	*891*	*3527*	*21*	*25*
		9	*105*	*221*	*0.314*	*12.255*	*0.178*	*0.3848*	*0.0040*	***0.709***	*0.2309*	*0.0036*	*2624*	*2099*	*3059*	*24*	*69*
		17	*257*	*544*	*0.511*	*12.455*	*0.182*	*0.3576*	*0.0036*	***0.685***	*0.2525*	*0.0039*	*2639*	*1971*	*3201*	*24*	*62*
	MUR 09-92	*2-core*	*106*	*299*	*0.177*	*8.939*	*0.100*	*0.3414*	*0.0033*	***0.870***	*0.1899*	*0.0022*	*2332*	*1894*	*2741*	*19*	*69*
		3	*172*	*563*	*0.450*	*7.313*	*0.084*	*0.2710*	*0.0027*	***0.853***	*0.1957*	*0.0024*	*2150*	*1546*	*2791*	*20*	*55*
		5	*63*	*264*	*0.331*	*5.415*	*0.068*	*0.2170*	*0.0022*	***0.803***	*0.1810*	*0.0024*	*1887*	*1266*	*2662*	*22*	*48*
		5	*4*	*24*	*0.535*	*4.411*	*0.137*	*0.1666*	*0.0028*	***0.536***	*0.1921*	*0.0064*	*1714*	*993*	*2760*	*54*	*36*
		23	*76*	*403*	*0.442*	*4.380*	*0.052*	*0.1676*	*0.0017*	***0.821***	*0.1895*	*0.0024*	*1709*	*999*	*2738*	*21*	*36*
		14	*80*	*159*	*0.416*	*12.989*	*0.155*	*0.4435*	*0.0044*	***0.827***	*0.2124*	*0.0027*	*2679*	*2366*	*2924*	*20*	*81*
		14	*105*	*219*	*0.305*	*12.110*	*0.137*	*0.4296*	*0.0041*	***0.853***	*0.2044*	*0.0024*	*2613*	*2304*	*2862*	*19*	*80*
		17	*55*	*346*	*0.336*	*3.742*	*0.052*	*0.1444*	*0.0015*	***0.738***	*0.1879*	*0.0028*	*1581*	*870*	*2724*	*24*	*32*
		25	*78*	*358*	*0.355*	*4.847*	*0.069*	*0.1984*	*0.0020*	***0.723***	*0.1771*	*0.0027*	*1793*	*1167*	*2626*	*25*	*44*
		15	*75*	*401*	*0.280*	*3.774*	*0.046*	*0.1757*	*0.0017*	***0.789***	*0.1557*	*0.0020*	*1587*	*1044*	*2410*	*22*	*43*
		16	*301*	*1019*	*0.534*	*6.557*	*0.074*	*0.2623*	*0.0025*	***0.831***	*0.1813*	*0.0022*	*2054*	*1501*	*2665*	*20*	*56*
		36-core	*80*	*167*	*0.329*	*12.427*	*0.148*	*0.4245*	*0.0041*	***0.808***	*0.2123*	*0.0027*	*2637*	*2281*	*2923*	*20*	*78*
		29	*120*	*279*	*0.419*	*10.584*	*0.127*	*0.3686*	*0.0035*	***0.798***	*0.2082*	*0.0027*	*2487*	*2023*	*2891*	*21*	*70*
		29	*78*	*666*	*0.174*	*2.402*	*0.031*	*0.1098*	*0.0011*	***0.744***	*0.1586*	*0.0022*	*1243*	*672*	*2440*	*24*	*28*
		24	*67*	*176*	*0.321*	*9.701*	*0.124*	*0.3421*	*0.0033*	***0.764***	*0.2056*	*0.0028*	*2407*	*1897*	*2871*	*22*	*66*
		26	*18*	*92*	*0.162*	*3.981*	*0.071*	*0.1803*	*0.0020*	***0.617***	*0.1601*	*0.0031*	*1630*	*1069*	*2456*	*32*	*44*
		22	*24*	*116*	*0.111*	*4.841*	*0.073*	*0.1907*	*0.0019*	***0.679***	*0.1841*	*0.0030*	*1792*	*1125*	*2690*	*26*	*42*
		31	*70*	*248*	*0.250*	*6.795*	*0.088*	*0.2525*	*0.0024*	***0.742***	*0.1951*	*0.0027*	*2085*	*1452*	*2786*	*23*	*52*
		32	*101*	*486*	*0.616*	*4.406*	*0.058*	*0.1770*	*0.0017*	***0.725***	*0.1805*	*0.0026*	*1714*	*1051*	*2658*	*24*	*40*
		20	*80*	*196*	*0.335*	*9.785*	*0.129*	*0.3506*	*0.0034*	***0.729***	*0.2023*	*0.0029*	*2415*	*1938*	*2845*	*23*	*68*
		20	*14*	*75*	*0.226*	*3.969*	*0.062*	*0.1750*	*0.0018*	***0.647***	*0.1645*	*0.0028*	*1628*	*1039*	*2503*	*28*	*42*
		10	*71*	*126*	*0.470*	*14.028*	*0.180*	*0.4731*	*0.0045*	***0.734***	*0.2150*	*0.0030*	*2752*	*2497*	*2944*	*23*	*85*
		11	*40*	*104*	*0.392*	*9.368*	*0.131*	*0.3313*	*0.0032*	***0.698***	*0.2050*	*0.0031*	*2375*	*1845*	*2867*	*25*	*64*
	MUR 09-97	1-core	121	241	0.184	12.919	0.200	0.4653	0.0067	**0.936**	0.2014	0.0024	2674	2463	2837	19	87
		2-border	140	271	0.409	13.310	0.207	0.4622	0.0067	**0.933**	0.2088	0.0025	2702	2449	2896	19	85
		3-border	86	169	0.351	13.129	0.206	0.4529	0.0066	**0.925**	0.2102	0.0025	2689	2408	2907	19	83
		4-core	10	12	4.780	8.989	0.155	0.3740	0.0056	**0.864**	0.1743	0.0025	2337	2048	2599	24	79
		3-core	162	281	0.267	15.186	0.240	0.5273	0.0077	**0.923**	0.2088	0.0025	2827	2730	2896	20	94
Monarch	**MUR 09-54**	1-core	220	1041	0.190	6.128	0.089	0.1975	0.0028	**0.964**	0.2250	0.0025	1994	1162	3017	18	39
		1-border	198	2039	0.541	2.181	0.032	0.0811	0.0011	**0.960**	0.1951	0.0022	1175	503	2785	18	18
		2-core	251	1140	0.264	6.253	0.090	0.2010	0.0028	**0.964**	0.2257	0.0025	2012	1181	3021	18	39
		3-core	88	231	0.186	10.973	0.160	0.3743	0.0052	**0.955**	0.2127	0.0024	2521	2050	2926	18	70
		3-border	7	11	0.326	15.258	0.254	0.4965	0.0072	**0.868**	0.2229	0.0032	2832	2599	3002	23	87

All errors are 1σ. In italic, *in situ* zircon grains analyses; in bold and shaded, data in black and in grey ellipses on Fig 9b, respectively.

	Sample	grain - spot	Chemistry (ppm) Pb	Th	U	Th/U	Isotopic ratios $^{207}Pb/^{235}U$	error	$^{206}Pb/^{238}U$	error	ρ	$^{207}Pb/^{206}Pb$	error	$^{208}Pb/^{232}Th$	error	Ages (Ma) ^{235}U-^{207}Pb	$^{238}U/^{206}Pb$	^{207}Pb-^{206}Pb	±	^{232}Th-^{208}Pb	Conc[1] %
Gravelotte	MUR 09-41	10b	2209	19339	494	39	9.968	0.165	0.4473	0.0056	0.762	0.1617	0.0026	0.11327	0.0012	2432	2383	2473	27	2169	96
		2b	900	7654	157	49	13.373	0.223	0.4817	0.0061	0.761	0.2014	0.0033	0.11883	0.0013	2706	2535	2838	26	2270	89
		5	669	5643	78	73	11.067	0.268	0.4420	0.0068	0.634	0.1816	0.0045	0.12265	0.0014	2529	2360	2668	40	2338	88
		10a	405	3215	101	32	10.865	0.195	0.4653	0.0061	0.736	0.1694	0.0030	0.12346	0.0014	2512	2463	2552	29	2353	97
		13b	3137	26033	450	58	11.356	0.184	0.4617	0.0057	0.756	0.1784	0.0029	0.12372	0.0013	2553	2447	2638	26	2358	93
		2c	941	7269	271	27	11.780	0.183	0.4851	0.0059	0.786	0.1762	0.0027	0.12417	0.0014	2587	2549	2617	25	2366	97
		2a	1230	8582	507	17	12.415	0.208	0.5022	0.0064	0.758	0.1793	0.0029	0.12669	0.0014	2636	2623	2647	27	2411	99
		13a	4169	29170	1151	25	14.119	0.214	0.5254	0.0063	0.791	0.1949	0.0029	0.13562	0.0015	2758	2722	2784	24	2571	98
		20b	728	5251	161	33	11.807	0.238	0.4272	0.0061	0.704	0.2005	0.0040	0.1387	0.0015	2589	2293	2830	32	2625	81
	MUR 09-92	35	831	8796	92	96	7.596	0.136	0.3950	0.0051	0.717	0.1395	0.0025	0.10666	0.0012	2184	2146	2221	30	2048	97
		13	1017	9913	144	69	8.001	0.132	0.3693	0.0048	0.796	0.1572	0.0024	0.10741	0.0012	2231	2026	2425	26	2062	84
		11a	2609	25227	265	95	6.644	0.113	0.3655	0.0048	0.776	0.1319	0.0021	0.10753	0.0012	2065	2008	2123	28	2064	95
		11c	307	2933	32	92	5.955	0.180	0.3364	0.0056	0.547	0.1284	0.0039	0.10882	0.0013	1969	1869	2077	53	2088	90
		12	376	3375	32	107	7.451	0.197	0.3788	0.0060	0.596	0.1427	0.0038	0.11604	0.0013	2167	2071	2260	45	2219	92
		31b	660	6352	60	106	7.542	0.268	0.4006	0.0073	0.515	0.1366	0.0050	0.11776	0.0013	2178	2172	2184	62	2250	99
		38c	1673	14162	211	67	12.183	0.184	0.4957	0.0062	0.823	0.1782	0.0025	0.12685	0.0014	2619	2595	2637	23	2414	98
		23	102	845	10	82	8.411	0.407	0.4220	0.0099	0.486	0.1446	0.0072	0.12696	0.0015	2276	2270	2283	84	2416	99
		27b	267	1996	40	50	10.045	0.236	0.4535	0.0068	0.642	0.1607	0.0038	0.13773	0.0016	2439	2411	2463	39	2608	98
		38b	1954	13464	305	44	12.036	0.197	0.4416	0.0057	0.790	0.1977	0.0031	0.15493	0.0017	2607	2358	2807	25	2911	84
		31a	89	760	13	61	11.434	0.318	0.4477	0.0075	0.601	0.1852	0.0053	0.1301	0.0015	2559	2385	2700	46	2472	88
		32c	1003	7503	384	20	13.926	0.217	0.5146	0.0062	0.777	0.1963	0.0030	0.13449	0.0015	2745	2676	2795	25	2551	96
		34b	2478	14529	1412	10	13.869	0.215	0.5158	0.0062	0.772	0.1950	0.0030	0.13877	0.0015	2741	2681	2785	25	2627	96
		38a	2356	18600	125	149	13.602	0.210	0.5244	0.0066	0.819	0.1881	0.0027	0.14061	0.0016	2722	2718	2726	24	2659	100
		32d	1422	10081	523	19	14.153	0.225	0.5288	0.0065	0.766	0.1941	0.0030	0.1421	0.0016	2760	2736	2778	25	2686	99
		34a	1462	6974	1189	6	14.295	0.221	0.5297	0.0064	0.775	0.1957	0.0030	0.14247	0.0016	2770	2740	2791	25	2692	98
		34c	1474	7672	1012	8	14.554	0.226	0.5303	0.0064	0.770	0.1991	0.0030	0.14253	0.0016	2787	2743	2819	25	2693	97
		32a	1906	12879	712	18	14.373	0.218	0.5357	0.0065	0.800	0.1946	0.0028	0.14278	0.0016	2775	2766	2781	24	2698	99
		10a	2889	20285	492	41	14.964	0.220	0.5429	0.0070	0.883	0.2000	0.0026	0.14283	0.0016	2813	2795	2826	21	2698	99
		32b	1519	10985	422	26	13.939	0.215	0.5306	0.0064	0.783	0.1905	0.0029	0.14624	0.0016	2746	2744	2747	24	2759	100
		38d	3628	25980	153	170	14.525	0.225	0.5389	0.0067	0.805	0.1955	0.0029	0.14809	0.0017	2785	2779	2789	24	2791	100
		30b	7470	45762	2281	20	15.482	0.231	0.5498	0.0067	0.819	0.2042	0.0029	0.14892	0.0017	2845	2825	2860	23	2806	99
		8b	326	2204	29	77	14.706	0.516	0.5414	0.0113	0.593	0.1970	0.0071	0.15571	0.0018	2796	2789	2802	58	2925	100
		21	45	364	77	5	1.896	0.061	0.1113	0.0018	0.504	0.1236	0.0041	0.11397	0.0014	1080	680	2009	57	2181	34
		11b	95	123	551	0.2	3.771	0.066	0.1835	0.0025	0.763	0.1491	0.0025	0.05408	0.001	1587	1086	2335	28	1065	47

Table 7: *Geochronological dating of monazite from albitites.*

Gravelotte	MUR 09-97	16	393	3228	194	17	7.413	0.113	0.3764	0.0048	0.843	0.1429	0.0020	0.11079	0.0013	2163	2059	2262	24	2124	91
		12i	5753	48733	1755	28	13.095	0.198	0.4947	0.0062	0.826	0.1920	0.0027	0.11216	0.0012	2687	2591	2760	23	2149	94
		10b	769	6686	118	57	9.712	0.193	0.4116	0.0059	0.714	0.1712	0.0033	0.11745	0.0013	2408	2222	2569	32	2245	87
		10c	1661	14467	163	89	10.953	0.171	0.4646	0.0060	0.829	0.1710	0.0025	0.11904	0.0013	2519	2460	2568	24	2273	96
		12g	2566	19713	686	29	13.194	0.192	0.5268	0.0065	0.849	0.1817	0.0025	0.11996	0.0013	2694	2728	2669	22	2290	102
		12h	2125	15296	540	28	13.496	0.202	0.5073	0.0063	0.835	0.1930	0.0027	0.1294	0.0014	2715	2645	2768	23	2460	96
		12d	3982	30917	381	81	13.913	0.212	0.5108	0.0065	0.842	0.1976	0.0028	0.12989	0.0014	2744	2660	2806	23	2468	95
		12d	3089	23031	767	30	8.487	0.133	0.3455	0.0044	0.817	0.1782	0.0026	0.13138	0.0015	2285	1913	2636	24	2495	73
		12a	4906	32894	1150	29	15.092	0.221	0.5435	0.0069	0.867	0.2014	0.0027	0.14185	0.0016	2821	2798	2838	22	2681	99
		12b	2175	13682	659	21	14.338	0.213	0.5180	0.0066	0.858	0.2008	0.0027	0.14747	0.0017	2772	2691	2833	22	2780	95
Monarch	MUR 09-54	16	305	2348	171	14	8.500	0.147	0.3980	0.0051	0.737	0.1550	0.0026	0.11167	0.0013	2286	2160	2402	28	2140	90
		17c	557	3218	641	5	8.080	0.129	0.4029	0.0050	0.776	0.1455	0.0022	0.11447	0.0013	2240	2182	2294	26	2191	95
		17a	237	1440	188	8	9.273	0.156	0.4431	0.0056	0.750	0.1518	0.0024	0.12478	0.0014	2365	2365	2367	27	2377	100
		3a	373	2595	195	13	10.476	0.192	0.4406	0.0057	0.712	0.1725	0.0030	0.12578	0.0015	2478	2353	2582	29	2395	91
		17b	425	2142	401	5	12.669	0.203	0.4689	0.0058	0.778	0.1961	0.0030	0.13047	0.0015	2655	2479	2794	25	2479	89
		8	1577	10277	565	18	14.000	0.247	0.5309	0.0069	0.734	0.1913	0.0032	0.13749	0.0016	2750	2745	2754	27	2604	100
		9	1381	8830	460	19	14.457	0.241	0.5191	0.0066	0.759	0.2021	0.0032	0.14139	0.0016	2780	2695	2843	26	2673	95
		18	318	2134	85	25	10.764	0.203	0.4723	0.0063	0.703	0.1654	0.0030	0.14293	0.0016	2503	2494	2511	30	2700	99
		4	124	754	41	18	9.750	0.251	0.4557	0.0070	0.596	0.1553	0.0040	0.14634	0.0018	2412	2420	2405	43	2761	101
		3b	355	1806	125	14	18.207	0.343	0.5767	0.0077	0.711	0.2291	0.0041	0.1756	0.0021	3001	2935	3046	28	3270	96
	MUR 09-55	3a	91	738	28	26	10.600	0.271	0.4231	0.0066	0.606	0.1818	0.0046	0.11348	0.0014	2489	2274	2669	41	2173	85
		4b	113	721	92	8	8.751	0.182	0.3991	0.0055	0.657	0.1591	0.0032	0.11498	0.0014	2312	2165	2446	33	2200	88
		3b	792	6277	346	18	7.774	0.151	0.3925	0.0052	0.679	0.1437	0.0026	0.11622	0.0014	2205	2134	2272	31	2222	94
		4a	322	2214	182	12	8.532	0.168	0.3864	0.0052	0.676	0.1602	0.0030	0.12108	0.0014	2289	2106	2458	31	2310	86
		5a	1000	7790	343	59	9.017	0.140	0.4177	0.0055	0.853	0.1567	0.0022	0.1231	0.0014	2340	2250	2420	23	2346	93
		7c	286	1580	253	95	12.585	0.186	0.4659	0.0061	0.879	0.1960	0.0026	0.12445	0.0015	2649	2465	2793	21	2371	88
		5b	190	1360	89	52	9.087	0.187	0.4253	0.0062	0.706	0.1550	0.0031	0.12593	0.0015	2347	2285	2402	33	2397	95
		7b	553	3201	414	53	11.485	0.165	0.4730	0.0061	0.896	0.1762	0.0022	0.13017	0.0015	2563	2497	2617	21	2473	95
		7a	263	1561	196	53	11.415	0.173	0.4440	0.0058	0.867	0.1866	0.0025	0.13053	0.0015	2558	2368	2712	22	2480	87
		3c	393	2501	178	14	10.579	0.206	0.4698	0.0062	0.678	0.1633	0.0030	0.13841	0.0017	2487	2483	2491	30	2620	100
		8	887	6527	66	99	12.804	0.271	0.4895	0.0068	0.654	0.1897	0.0038	0.14347	0.0017	2665	2569	2740	33	2710	94
		6	140	331	200	41	13.600	0.205	0.5263	0.0069	0.876	0.1875	0.0025	0.15284	0.0018	2722	2726	2721	22	2875	100

Malati Pump	8	1728	13681	227	60	14.302	0.216	0.4850	0.0059	0.812	0.2139	0.0031	0.1286	0.0014	2770	2549	2935	23	2445	87
	6	3972	31744	224	142	16.393	0.263	0.5459	0.0069	0.789	0.2178	0.0034	0.13117	0.0014	2900	2808	2964	25	2491	95
	1b	999	9474	151	63	9.519	0.195	0.4217	0.0059	0.689	0.1637	0.0033	0.12055	0.0014	2389	2268	2495	34	2301	91
	20a	2301	20320	273	74	9.147	0.130	0.4159	0.0049	0.828	0.1595	0.0022	0.11344	0.0012	2353	2242	2450	23	2172	92
	1c	1601	9484	159	60	11.290	0.191	0.4479	0.0059	0.773	0.1828	0.0030	0.19602	0.0022	2547	2386	2679	27	3618	89
	19b	834	6738	70	96	13.223	0.286	0.4892	0.0071	0.675	0.1960	0.0043	0.12589	0.0013	2696	2567	2793	36	2397	92
MUR 09-89A	5a	3401	27924	170	165	13.579	0.211	0.4932	0.0061	0.795	0.1996	0.0030	0.12765	0.0014	2721	2585	2823	25	2428	92
	20b	1421	10819	123	88	12.916	0.210	0.4868	0.0061	0.770	0.1924	0.0031	0.1328	0.0014	2674	2557	2763	26	2520	93
	2	1448	9999	498	20	14.049	0.199	0.5089	0.0061	0.840	0.2003	0.0027	0.13329	0.0014	2753	2652	2828	22	2529	94
	19a	2145	16197	188	86	13.374	0.189	0.5068	0.0060	0.838	0.1913	0.0026	0.13374	0.0014	2706	2643	2754	22	2537	96
	5b	2460	18714	89	211	13.730	0.222	0.5067	0.0064	0.778	0.1965	0.0031	0.13909	0.0015	2731	2643	2797	26	2632	94
	22	1435	10375	198	52	14.239	0.207	0.5203	0.0063	0.828	0.1985	0.0027	0.14133	0.0015	2766	2701	2814	22	2672	96
	21	378	2792	15	185	15.087	0.377	0.5393	0.0087	0.644	0.2030	0.0052	0.14376	0.0016	2821	2780	2850	41	2715	98
	6c	893	6773	136	50	13.337	0.285	0.4986	0.0073	0.689	0.1940	0.0041	0.13289	0.0015	2704	2608	2777	34	2522	94
	6f	1306	9964	234	43	12.769	0.201	0.4984	0.0062	0.787	0.1858	0.0028	0.13335	0.0015	2663	2607	2706	24	2530	96
	6b	1673	12490	131	96	13.616	0.206	0.5176	0.0065	0.827	0.1908	0.0027	0.13986	0.0016	2723	2689	2749	23	2646	98
MUR 09-89B	6h	2279	17442	78	224	13.405	0.231	0.5084	0.0065	0.743	0.1913	0.0032	0.14223	0.0016	2709	2650	2753	27	2688	96
	11a	1527	11040	173	64	14.375	0.249	0.5312	0.0067	0.725	0.1963	0.0033	0.14261	0.0016	2775	2747	2796	27	2695	98
	6g	2820	21036	137	154	14.498	0.238	0.5283	0.0067	0.767	0.1990	0.0031	0.14484	0.0016	2783	2735	2818	25	2734	97
	6d	1140	7310	208	35	14.810	0.244	0.5494	0.0071	0.784	0.1955	0.0031	0.15323	0.0017	2803	2823	2789	25	2882	101

All errors are 1σ. Shaded in grey, data used to calculate ages in Fig 9h.

Table 8: *Geochronological dating of titanite from albitites.*

		Chemistry		Isotopic ratios							Ages (Ma)				
	Sample	Pb (ppm)	U (ppm)	$^{207}Pb/^{235}U$	error	$^{206}Pb/^{238}U$	error	ρ	$^{207}Pb/^{206}Pb$	error	^{235}U-^{207}Pb	^{238}U-^{206}Pb	^{207}Pb-^{206}Pb	±	Conc[1] %
Baderoukwe	**MUR 09-5a**	22	22	6.184	0.113	0.3713	0.0057	**0.832**	0.1208	0.0024	2002	2036	1968	35	103
		25	29	5.105	0.082	0.3127	0.0043	**0.852**	0.1184	0.0021	1837	1754	1932	31	91
		12	13	5.801	0.100	0.3594	0.0051	**0.823**	0.1171	0.0022	1947	1979	1912	33	104
		37	81	2.585	0.046	0.1613	0.0023	**0.799**	0.1162	0.0023	1296	964	1899	34	51
		19	20	5.856	0.105	0.3694	0.0052	**0.786**	0.1150	0.0022	1955	2027	1879	35	108
		9	22	2.533	0.065	0.1512	0.0028	**0.723**	0.1215	0.0035	1282	908	1978	50	46
		19	33	3.551	0.074	0.2074	0.0032	**0.733**	0.1242	0.0029	1539	1215	2017	40	60
		14	20	4.173	0.087	0.2437	0.0037	**0.719**	0.1242	0.0029	1669	1406	2017	40	70
		34	153	1.298	0.029	0.0826	0.0013	**0.692**	0.1139	0.0028	845	512	1863	43	27

All errors are 1σ.

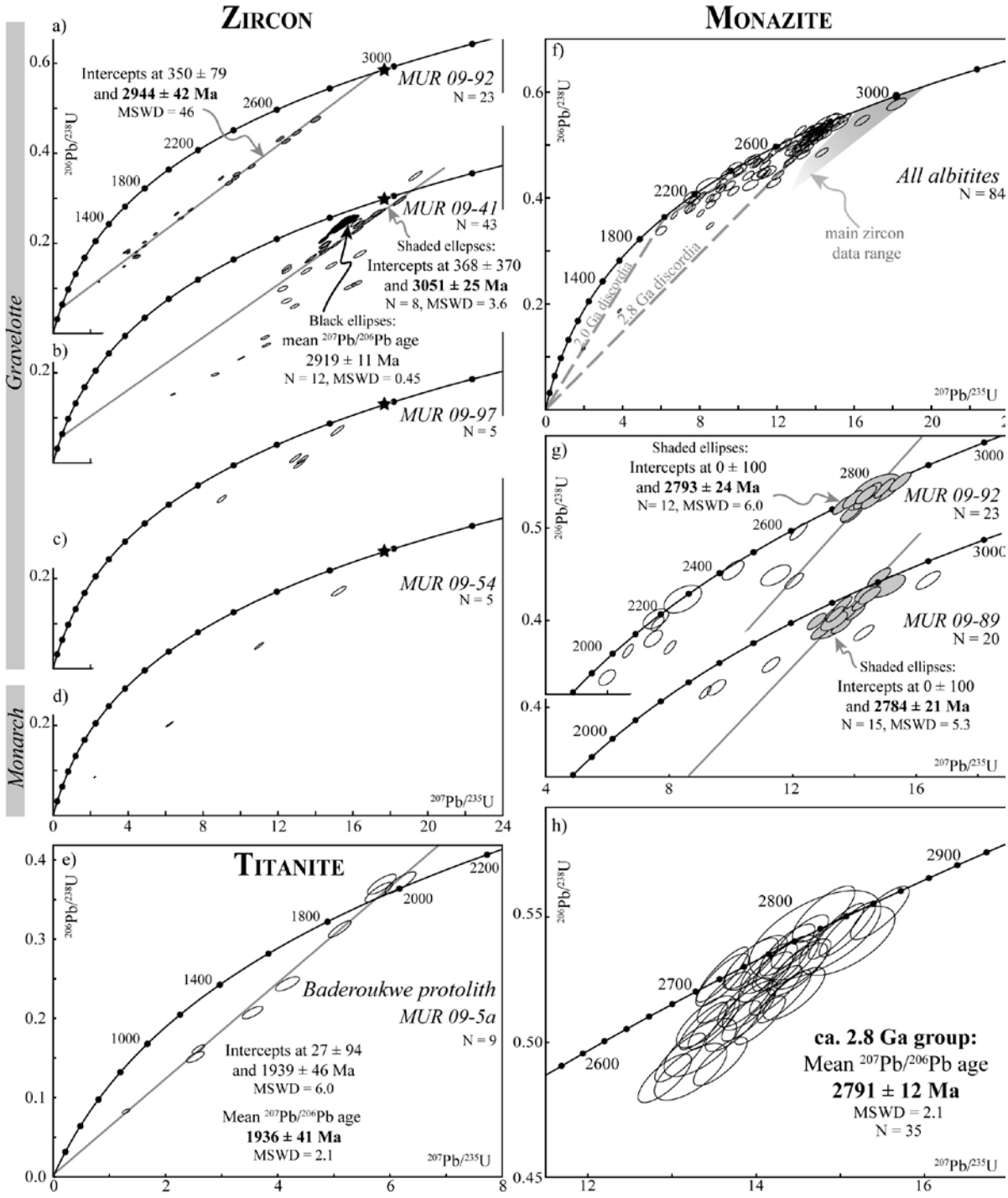

Figure 9: *Concordia (U-Pb) diagrams of albitites. Zircon dating of sample (a) MUR 09-92, (b) MUR 09-41, (c) MUR 09-97 and (d) MUR 09-54. Black star is the Baderoukwe batholith age for comparison. (e) Dating of secondary titanite from the protolith. Monazite dating (f) from all albitites of the Antimony Line and insets for (g) samples MUR 09-92 and MUR 09-89 and (h) the ca 2.8 Ga cluster.*

Geochemical characterization of the monazite grains

In order to shed some light on the complex behavior of the monazite encountered in the albitites, we decided to perform EMPA analyses in all the samples. One hundred spot analyses were performed, with the systematic measurement of 13 elements (Si, P, Y, Ca, La, Ce, Pr, Nd, Sm, Gd, Th Pb and U). All analyses demonstrate that

the monazite grains are Ce-La-Nd monazite with limited brabandite or huttonite substitution (Fig. 10b). Chemical variations are generally moderate within a grain or a cluster of grain, although rare zones presenting a Pb or a Pb and Th enrichment can be observed (Fig. 8g). Th is rather low as expected in hydrothermal monazite but is also highly variable ($0 < ThO_2 < 8.8$ wt %, Supplementary Data Table 1). REE are also variable with an inverse correlation between the LREE and the MREE (Fig. 10a). Unfortunately, there is no clear correlation between the chemistry and the apparent age of the monazite grains. Rather, the monazite compositions seem to show some trends that are site dependant (Fig. 10b).

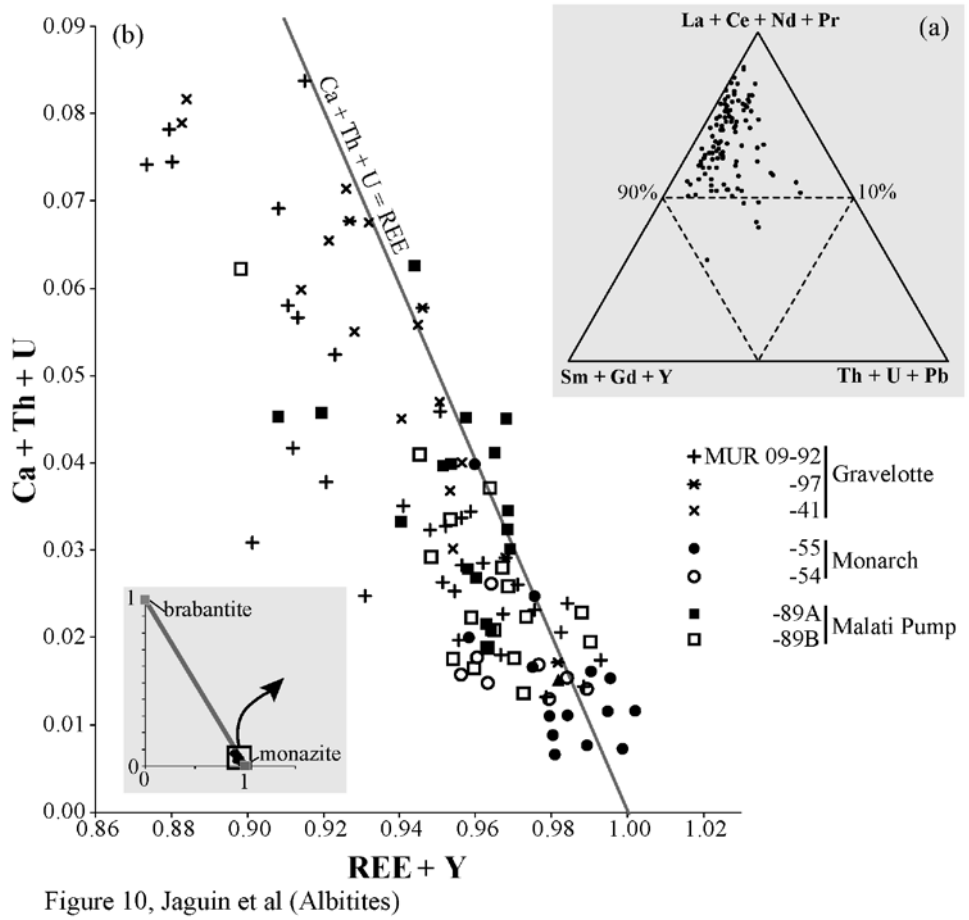

Figure 10, Jaguin et al (Albitites)

Figure 10: *Chemistry of monazite grains (structural formulae based on 4 oxygen atoms). (a) LREE-MREE-Th + U + Pb ternary plot of all data (b) Ca + Th + U versus REE + Y diagram, inset shows pure brabandite and monazite compositions, and their substitution along the grey line.*

DISCUSSION

It is clear at this stage that the albitites from the Antimony Line are enriched in Sb when compared to their unaltered protolith. In the Malati Pump Mine, granodiorite emplacement, sulfide mineral deposition and gold mineralization all happened at ca. 2.97 Ga (Jaguin et al., 2012b). As antimony is associated with gold, a magmatic origin for the antimony can be suggested. On the other hand, the Baderoukwe pluton, which was not altered into albitite, lacks the presence of Sb as well as the associated by-products As, Hg ± W. This is therefore in favor for an alteration origin for the Sb

enrichment in the albitites. This is confirmed by the clear correlation that exists between the Sb enrichment and the $\delta^{18}O$ increase from the protolith to the albitites (Fig. 6c and 6d), a typical characteristic of a fluid-rock interaction. Moreover, albitization and mineralization share two specificities: there are both (i) fluid-related (see 7.2.2) and (ii) restricted to the Antimony Line. Therefore, we argue that albitites were Sb-enriched during the alteration rather than during the magmatic history. Thus, we now aim at characterizing the process of albitization itself and then discuss how this study could bring some information on the Sb mineralization in the Antimony Line.

Characteristics of albitization

Identification of the protolith: the Baderoukwe-albitites connection

When rocks undergo a strong alteration by fluids, it is very useful to identify their protolith as the chemical and isotopic differences between the two lithologies provide information on the elements mobility, which in turn allows for a mass balance calculation (e.g. Boulvais et al., 2007) and to discuss the origin of the fluids. Unfortunately, it was not possible to get unaltered samples in the close vicinity of the albitite plugs from the Antimony Line, which argues in a favor of a large amount of fluids involved in the alteration process. Nevertheless, geophysics data in the studied area link the albitites and the pluton (Fig. 1c). The Baderoukwe batholith can be thus be considered as a probable protolith for the albitites samples.

Several arguments converge towards this assumption. First, the REE patterns of some of the albitites mimic those of the Baderoukwe intrusion (Fig. 6b), which argues for a common source, as do the Nd isotope signatures (Table 4). Therefore, albitites cannot be seen as pure products of carbonated-related alteration as suggested by Pearton and Viljoen (1986) and Pearton (1980). Second, zircon dating emphasizes that most of the albitite plugs and the Baderoukwe share the same age (2.97 Ga; Fig. 9a to d). In details, the Malati Pump and one of sample from Gravelotte Mine (MUR 09-92) crystallization age is defined at ca. 2.97 Ga (Jaguin et al., 2012b and Fig. 8a respectively). Zircon data from the other Gravelotte samples and from the Monarch Mine are less straightforward. The 2.92 Ga cluster of data in sample MUR 09-41 could indeed reflect the age of a second magmatic event as it is very unlikely that this cluster of twelve data is an artefact. In the region, there are at least two other locations where magmatic ages around 2.92 Ga have been found; some 2917± 27 Ma old pegmatite to the south of the MGB (Kruger et al., 1998) and the Maranda granite, at the western termination of the Antimony Line with a minimum age of 2901±20 Ma (Fig. 1; Poujol et al., 1996). In the light of our data, we thus propose that the Maranda batholith was emplaced around 2.92 Ga and developed satellite intrusions in both the Gravelotte and the Monarch sites.

Unfortunately, it was not possible to sample the Maranda granite during our sampling. Vearncombe et al. (1992) described a plug of the Maranda granite (within the

belt) as a strongly altered sodic (up to 7.9% Na_2O) biotite-muscovite alkali feldspar rock, where carbonate minerals are present. Therefore we believe that the Maranda batholith compared better to the albitites group than to the Baderoukwe. We can nevertheless underline the fact that all the studied albitites were enriched in Na and depleted in Ca and K relative to the Baderoukwe protolith during the alteration. They were consistently depleted in some alkali (Rb, Cs) and alkali-earths (Sr, Ba) trace elements, and enriched in some metals (Sb-As-W).

Some samples from the Baderoukwe pluton show evidence of interaction with fluids; these are sample MUR 09-82 from the North slice and what we called altered-protoliths in Table 2 (samples MUR 09-83 and MUR 09-85). Sample MUR 09-82 is desilicifed while MUR 09-83 is highly silicified. Silica mobility is an ubiquitous characteristic of albitization (Cathelineau, 1986). So it may be questioned if these samples do not represent complementary alterations associated with the albitization documented in the Antimony Line. Two independent evidences argue against this hypothesis. First, if any, these altered samples show a decrease for the $\delta^{18}O$ values while we found an increase of this value for the albitites samples (Fig. 6d). Second, none of these samples is enriched in Sb; rather they are enriched in Co and Cu. Thus, if these samples do show some alteration related to some fluid-rock interaction, the related event is distinct from the one studied in this paper (Sb-related albitization). We suggest that they underwent an interaction with fluids with a low $\delta^{18}O$ signature able to carry transition metals; this could correspond to a metamorphic fluid in partial to total equilibrium with ultramafic to mafic lithologies that are common in the Murchison Greenstone Belt. An interesting point at this stage is that some ca 2 Ga titanites were found in the Baderoukwe pluton. We can therefore propose that these titanites grew in response to the circulation of these low $\delta^{18}O$ potentially metamorphic fluids around 2.0 Ga. The final information that can be deduced from the specific alteration of some Baderoukwe samples is that the albitization seems geographically confined to the Antimony Line, which reinforces the idea that the study of the albitites may provide information on the Sb mineralization itself.

Fluid-rock interaction properties

The fluid-rock interaction occurred on a regional scale, at P-T conditions typical of greenschist facies (between 250 and 400°C) as deduced from the alteration mineralogy in the thin sections. This is in accordance with the estimation of Block et al. (2012), who proposed that metamorphism in the MGB reached greenschist facies conditions in the Antimony Line vicinity, (1.3-2.8 kbar at 340-370°C). The fluid-rock interaction also occurred under large fluid/rock ratios. This is first suggested in thin sections because the rock presents a great percentage of pure albite and because textures are typical of fluid-rock interactions (e.g. porphyric albite after feldspar, dissolution figures, Fig. 2a; Engvik et al., 2006). Major elemental mobilities involving Si, Na, K and Ca confirm theses observations. Also, the fluid-rock interaction involved an externally-derived fluid. The increase in $\delta^{18}O$ from 8.1 – 8.4‰ in the protolith up to 10.4 – 11.9 ‰ in the albitites shows that the albitizing fluid was not in equilibrium

with the initial magmas. Rather, if we consider that the fluid responsible for the albitization was able to isotopically buffer the rock, one can estimate the $\delta^{18}O$ range between 4.5 ‰ (water in equilibrium with the albitite with 10.5‰ at 250°C, using the fractionation factor of Zheng, 1993) and 9.5‰ (in equilibrium with the albitite with 10.5‰ at 400°C). This range may correspond to crustal fluids derived from dehydrated lithologies more or less mixed with some low-$\delta^{18}O$ fluids derived from the surface, possibly sea-water. No clear information on the fluid origin, via the source of the elements transported, can be derived from the radiogenic isotopic systems because the compositions measured in the albitites are very closed to that of their protolith (Table 4).

Besides, widespread carbonatation between the albite grains is visible in thin section. It implies the introduction of a CO_2-bearing fluid phase. In Fig. 7, the carbonate phase displays equal or higher $\delta^{18}O$ values than the albitite whole rock, which can be approximated as the value for the albite. This is the indubitable sign for isotopic disequilibrium between the two mineral species, as albite should have a $\delta^{18}O$ value higher than carbonate (see insert in Fig. 7 where we used dolomite as the most common carbonate in the albitites samples). This discrepancy necessary involves the late infiltration of a fluid under distinct conditions, either from another source with higher $\delta^{18}O$ value or implying a common fluid but carbonate precipitation at lower temperatures. Both events could have occurred simultaneously. Interestingly, the carbonate developed in association with rutile, apatite, monazite and xenotime (Fig. 3b). It is thus possible that the slight HREE fractionation (Fig. 6b) could be related to the appearance of one of these phases, CO_3^{2-} anionic molecules having played the role of a complexing agent for HREE. LREE were not fractionated during alteration processes (albitization and carbonatation).

Zircon and sulphides may represent the best relics of the pre-albitization history in the studied rocks, even if most of them are perturbed, as zircon grains in the albitites rarely display concordant isotopic data (Fig. 9 a to d). Sulphides are almost certainly the carrier of the Sb-As-W metal enrichment, so they likely underwent recrystallization process during the alteration. Nevertheless, as they still display a restricted range in $\delta^{34}S$ values, it seems that they preserve their original magmatic signature (Kedda, 1992).

Timing of albitisation vs. timing of Sb-mineralization

Monazite dating and interpretation(s)

Monazite grains are petrographically related to albitization-muscovitisation and/or carbonation and thus constitute a suitable target to date the alteration. Monazite dates spread within a “crisis polygon” (Fig. 9f) mostly along the concordia curve between ca. 2.8 and 2.0 Ga. They thus do not show any magmatic age (2.97-2.92 Ga), as recorded by the zircon grains (Fig. 9a to d). We can therefore exclude a

magmatic-related fluid event as the main albitization process. Rather, the monazite dates distribution in Fig. 9f can be explained either by a 'two major events scenario' or by a 'multiple events scenario'. The *'multiple events'* scenario is based on almost-concordant clusters in the concordia diagram. They seem to clusters at 2.8 Ga (very few older, maybe magmatic in origin), but also at 2.6 Ga, 2.4 and 2.2 Ga. This would indicate a story with multiple, likely fluid-related, events for these rocks, starting at 2.8 Ga. The history of the belt is protracted and therefore is consistent with this hypothesis. Each date cluster however is difficult (if not impossible) to interpret, as they are not precise. The *'two major events'* hypothesis is bracketed between two ages: 2.8 Ga, as found on many monazite grains and the ca. 2.0 Ga, age found for the titanite grains. If we consider that the monazite grains first grew at 2.8 Ga and that their isotopic systems were perturbed at ca. 2.0 Ga, one can explain the position of the remaining grains as fitting along a discordia linking these two end-members, the remaining, more discordant, data showing a subsequent recent Pb-loss. Arguments in favor on this hypothesis are (i) the almost continuous record of apparent $^{207}Pb/^{206}Pb$ dates between 2.8 and ca. 2.0 Ga; (ii) the documentation of a regional 2.8 Ga event (Rooiwater complex, 2795 Ma alteration/metamorphism, Zeh et al., in prep.; Lekkersmaak, Duivelskloof and Willie pluton and associated pegmatites emplacements; Zeh et al., 2009, Henderson et al., 2000, Poujol, 2001 and Poujol and Robb, 1999 respectively; metamorphic age data, Block et al., 2012 and (iii) the better agreement between the ^{232}Th-^{208}Pb age *vs* ^{207}Pb-^{206}Pb dates for the 2.8-2.7 Ga monazite grains than for the "younger" monazite grains. In this scenario, the lower intercept age is not precise, and possible driving-events can range from burying under the Transvaal sediments at ca. 2.2 Ga (Burger and Coertze, 1973-74), to a thermic overprint related to emplacement of the nearby Bushveld and/or Phalaborwa complexes at ca 2.0 Ga (Buick et al., 2001; Reischmann, 1995, respectively). It is also noteworthy to point out that numerous Rb/Sr ages obtained on biotite and/or phlogopite around 2.0 Ga have been obtained within the MGB (unpublished data cited in Vearncombe et al., 1992), but also to the north (Barton and van Reenen, 1992) and south (Kruger et al 1998). Although we cannot completely rule out the first scenario involving multiple events, we favor the second scenario and propose that the main albitization event in the Antimony Line took place 2.8 Ga ago followed by a second (fluid-flow related?) event ca 2.0 Ga ago. This ca 2.8 Ga event, as already pointed out by Poujol (2001), corresponds to a major event at the scale of the Kaapvaal Craton as granitoids in the Pietersburg and Giyani greenstone belts to the north (de Wit et al., 1993; Kröner et al., 2000), S-type plutons in Swaziland to the east (Meyer et al., 1994), or the Schweizer-Reneke granite (Robb et al., 1992), Mosita adamellite (Poujol et al., 2002) and Rooibokvlei granodiorite (Anhaeusser and Poujol, 2004) to the west of the Craton were also dated around 2.8 Ga.

Insights into the Sb mineralization model

In the MGB, a major magmatic event has been documented at 2.97 Ga: (i) Rubbervale Formation (Poujol et al., 1996) (ii) Baderoukwe pluton (Jaguin et al.,

2012b) (iii) Rooiwater granitoid (Zeh et al., in prep) (iv) Discovery granite (Poujol, 2001). Besides, several mineralizing events have been characterized as closely magmatic-related around 2.97 Ga: (i) the Rubbervale VMS deposits (Schwarz-Schampera et al., 2010); (ii) the granodiorite-hosted gold (Jaguin et al., 2012b); (iii) the Rooiwater vanadium-titanium magnetite layers (sub-economic, Reynolds, 1986; Zeh et al., in prep); (iv) the emerald deposits (Robb and Robb, 1986; Grundmann and Morteani, 1989). Therefore, in the MGB, the association between mineralization and magmatism appears to be quite strong. But antimony has an original place among all the belt deposits, as there is no consensual model for its formation. In particular, only few authors favor a magmatic origin (Kedda, 1992; Ileri, 1973). Some arguments support this 'magmatic connection': gold and antimony are often found together within the Antimony Line and a gold-bearing granodiorite (carrying little antimony mineralization) to the east of the AL has been dated at 2.97 Ga (Jaguin et al., 2012b); this granodiorite is part of a large body that runs along the entire AL (de Beer et al., 1984); antimony mineralization are found closely associated with this body. In this study, we confirm that this body was emplaced 2.97 Ga ago and may be a little after (2.92 Ga) in its westernmost part.

Yet, Pearton and Viljoen, (1986), Vearncombe et al. (1988) and Willson and Viljoen (1986) rather proposed that the main Sb mineralizing event was roughly synchronous with the metamorphic event, i.e. an orogenic-style of the AL, although Vearncombe et al. (1992) subsequently did not exclude the fact that it could be synchronous with the emplacement of the granodioritic body. This is consistent with long lasting activity later recognised in the area. Poujol et al. (1996) obtained a minimum age of 2.90 Ga for the emplacement of the Maranda granite and Block et al. (2012) pointed to a late tectono-thermal event around 2.75 Ga in the area. Our data on zircon and monazite point to a dichotomy between magmatism and alteration, with the magmatic emplacement dated around 2.97 – 2.92 Ga and the main alteration event dated around 2.80 Ga (upper cluster of monazite data; Fig. 9h). From this study, it is clear that the albitite are enriched in Sb when compared to the unaltered protolith (Fig. 6c). This demonstrates that the Sb found in the albitites was remobilized from an older primary mineralization or enrichment. As the albitization (and therefore the Sb enrichment) is dated at ca. 2.8 Ga, this means that the first mineralization or enrichment event happened prior to 2.8 Ga. Consequently, the late ca 2.75 Ga tectono-metamorphic event documented by Block et al. (2012) cannot be responsible for the primary mineralizing event. This demonstrates also that the alteration event (that induced albitization) was able to mobilize some antimony from the primary mineralization. Some 800 Ma after, the discrete event documented around 2.0 Ga may also have induced another episode of Sb mobility to some extent. So, we conclude that the ages obtained on monazite do not yield the primary Sb mineralization event, but that they rather document events of secondary Sb mobilization in the Murchison Greenstone Belt. Our data together with data from Jaguin et al. (2012b) and Kedda (1992) seem to indicate that the main mineralization event was probably synchronous with the emplacement of the granodiorite body 2.97 Ga ago. Whether this is true or not,

at least two main remobilization events have been recorded within the Antimony Line that have perturbed most of the primary indicators, preventing to propose any definitive model. But, from a mining point of view, it looks like the antimony was never transported far away from its original location.

CONCLUSIONS

The main conclusions of this study are as follows:

- All intrusives within the Antimony Line underwent intense albitization
- Sb-mobility is associated with this albitization
- Oxygen isotopes alteration associated with albitization points to a crustal fluid
- Monazite and zircon U-Pb data show that this Sb-enrichment is a secondary mobilization, likely from a magmatic-related primary mineralization at 2.97 Ga. Secondary mobilization occurred mainly around 2.80 Ga and may have lasted until at least 2.0 Ga.

ACKNOWLEDGMENTS

We thank Consolidated Murchison Mine Co. and especially the chief geologist Colin Willson, for opening their mine premises, giving us access to their core yard and for their overall technical support. This work was funded by the 'Action Incitative' Programm (CNRS-INSU).

REFERENCES

Alexandre, P., 2010. Mineralogy and geochemistry of the sodium metasomatism-related uranium occurrence of Aricheng South, Guyana. Mineralium Deposita 45 (4), 351-367, doi: 10.1007/s00126-010-0278-7.

Anhaeusser, C., and Poujol, M., 2004. Petrological, geochemical and U-Pb isotopic studies of Archaean granitoid rocks of the Makoppa Dome, northwest Limpopo Province, South Africa. South African Journal of Geology 107, 521-544.

Barton, J.M., and van Reenen, D.D., 1992. The significance of Rb-Sr ages of biotite and phlogopite for the thermal history of the Central and Southern Marginal Zones of the Limpopo belt of southern Africa and the adjacent portions of the Kaapvaal Craton. Precambrian Research 55, 17-31.

de Beer, J.H., Stettler, E.H., Duvenhage, A.W.A., Joubert, S.J., and De Raath, C.J., 1984. Gravity and geoelectrical studies of the Murchison greenstone belt, South Africa. South African Journal of Geology 87 (3), 347-359.

Béziat, D., Dubois, M., Debat, P., Nikiéma, S., Salvi, S., and Tollon, F., 2008. Gold metallogeny in the Birimian craton of Burkina Faso (West Africa). Journal of African Earth Sciences 50 (2-4), 215-233, doi: 10.1016/j.jafrearsci.2007.09.017.

Block, S., Moyen, J.-F., Zeh, A., Poujol, M., Jaguin, J., and Paquette, J.-L., 2012. The Murchison Greenstone Belt, South Africa: accreted slivers with contrasting metamorphic conditions. Precambrian Research (in press) doi: 10.1016/j.precamres.2012.03.005.

Boese, R., 1964. Die Antimoglanzgänge von Gravelotte in der Murchison Range on Nordost-Transvaal. PhD thesis, University of Hamburg.

Boulvais, P., Ruffet, G., Cornichet, J., and Mermet, M., 2007. Cretaceous albitization and dequartzification of Hercynian peraluminous granite in the Salvezines Massif (French Pyrénées). Lithos 93 (1-2), 89-106, doi: 10.1016/j.lithos.2006.05.001.

Brandl, G., Jaeckel, P., and Kröner, A., 1996. Single zircon age for the felsic Rubbervale Formation, Murchison greenstone belt, South Africa. South African Journal of Geology 99 (3), 229-234.

Buick, I.S., Maas, R., and Gibson, R., 2001. Precise U-Pb titanite age constraints on the emplacement of the Bushveld Complex, South Africa. Journal of the Geological Society 158, 3-6.

Burger, A.J., and Coertze, F.J. Age determinations - April 1972 to march 1974 . Annual Geological Survey of South Africa 10, 135-141.

Böttcher, M.E., 1996. $^{18}O/^{16}O$ and $^{13}C/^{12}C$ fractionation during the reaction of carbonates with phosphoric acid: effects of cationic substitution and reaction temperature. Isotopes in Environmental and Health Studies 32, 299-305.

Carignan, J., Hild, P., Mevelle, G., Morel, J., and Yeghicheyan, D., 2001. Routine Analyses of Trace Elements in Geolgical Samples using Flow Injection and Low Pressure On-Line Liquid Chromatography Couples to ICP-MS: A Study of Geochemical Reference Materials BR, DR-N, UB-N, AN-G and GH. Geostandards Newsletter 25 (2-3), 187-198.

Carten, R.B., 1986. Sodium-Calcium Metasomatism: Chemical, Temporal, and Spatial Relationships at the Yerington, Nevada, Porphyry Copper Deposit. Economic Geology 81, 1495-1519.

Cathelineau, M., 1986. The Hydrothermal Alkali Metasomatism Effects on Granitic Rocks: Quartz Dissolution and Related Subsolidus Changes. Journal of Petrology 27 (4), 945-965.

Charoy, B., and Pollard, P.J., 1989. Albite-Rich, Silica-Depleted Metasomatic Rocks at Emuford, Northeast Queensland: Mineralogical, Geochemical, and Fluid Inclusion Constraints on Hydrothermal Evolution and Tin Mineralization. Economic Geology 84, 1850-1874.

Cheilletz, A., and Giuliani, G., 1982. Role de la Déformation du Granite dans la Genèse des Episyénites Feldspathiques des Massifs de Lovios-Geres (Galice) et des Zaer (Maroc Central). In : Mineral Deposits of Southern Africa 17, 387-400.

Clayton, R.N., and Mayeda, T.K., 1963. The use of bromine pentafluoride in the extraction of oxygen from oxides and silicates for isotopic analysis. Geochimica et Cosmochimica Acta 27, 48-52.

Costi, H.T., Dall'Agnoll, R., Borges, R.M.K., Minuzzi, O.R.R., and Teixeira, J.T., 2002. Tin-Bearing Sodic episyenites Associated with the Proterozoic, A-Type Agua Boa Granite, Pitinga mine, Amazonian Carton, Brazil. Gondwana Research 5 (2), 435-451.

Cuney, M., Emetz, A., Mercadier, J., Mykchaylov, V., Shunko, V., and Yuslenko, A., 2012. Uranium deposits associated with Na-metasomatism from central Ukraine: A review of some of the major deposits and genetic constraints. Ore Geology Reviews 44, 82-106, doi: 10.1016/j.oregeorev.2011.09.007.

Das Sharma, S., J, P.D., and Gopalan, K., 2002. Temperature dependence of oxygen isotope fractionation of CO2 from magnesite-phosphoric acid reaction. Geochimica et Cosmochimica Acta 66 (4), 589-593, doi: 10.1016/S0016-7037(01)00833-X.

Debon, F., Lefort, P., 1983. A chemical–mineralogical classification of common plutonic rocks and associations. Transactions of the Royal Society of Edinburgh: Earth Sciences 73, 135–149.

van Eeden, O.R., Partridge, F.C., Kent, L.R., and Brandt, J.W., 1939. The mineral deposits of the Murchison Range east of Leydsdorp. Memoir of the geological survey of South Africa 36, 172.

Engvik, A.K., Korneliussen, A., and Austrheim, H., 2006. Mineralogical evolution during albitisation and scapolitisation of the Ødegården metagabbro, Bamble, South Norway. Geophysical Research Abstract 8.

Evensen, E., Hemilton, P.J., O'Nions, R.K., 1978. Rare-earth abundances in chondritic meteorites. Geochimica et Cosmochimica Acta, 42 (8), 1199-1212.

Gasquet, D., Bertrand, J.-M.J.-Mi., Paquette, J.-L. ean-L., Lehmann, J., Ratzov, G., De Ascencao Guedes, R., Tiepolo, M., Boullier, A.-M., Scaillet, S., and Nomade, S., 2010. Miocene to Messinian deformation and hydrothermal activity in a pre-Alpine basement massif of the French western Alps: new U-Th-Pb and argon ages from the Lauziere massif. Bulletin de la Societe Geologique de France 181 (3), 227-241, doi: 10.2113/gssgfbull.181.3.227.

Goldstein, S.L., O'Nions, R.K., and Hamilton, P.J., 1984. A Sm-Nd isotopic study of atmospheric dusts and particulates from major river systems. Earth and Planetary Science Letters 70, 221-236.

Grundmann, G., and Morteani, G., 1989, Emerald mineralization during regional metamorphism: the Habachtal (Austria) and Leydsdorp (Transvaal, South Africa) deposits. Economic Geology 84, 1835-1849.

Hall, A., 1912. The Geology of Murchison Range and District Geological Survey of South Africa. Memoir of the Geological Survey of South Africa 6, 186.

Hausmann, S.G., 1959. A mineralogical investigation of the Letaba copper-zinc ores and the Monarch Cinnabar deposits located in the Murchison Range of the Eastern Transvaal. PhD thesis, University of the Witwatersrand, Johannesburg.

Hecht, L., Thuro, K., Plinninger, R., and Cuney, M., 1999, Mineralogical and geochemical characteristics of hydrothermal alteration and episyenitization in the Königshain granites, northern Bohemian Massif , Germany. International Journal of Earth Sciences 88, 236-252.

Henderson, D.R., Long, L.E., and Barton, J.M., 2000. Isotopic ages and chemical and isotopic composition of the Archaean Turfloop Batholith, Pietersburg granite - greenstone terrane, Kaapvaal Craton, South Africa: South African journal of geology 103 (1), 38-46, doi: 10.2113/103.1.38.

Hurai, V., Paquette, J.-L., Huraiová, M., and Konečný, P., 2010. U–Th–Pb geochronology of zircon and monazite from syenite and pincinite xenoliths in Pliocene alkali basalts of the intra-Carpathian back-arc basin. Journal of Volcanology and Geothermal Research 198 (3-4), 275-287, doi: 10.1016/j.jvolgeores.2010.09.012.

Ileri, S., 1973. Genesis and fabric study of stibine ores at the Murchison Range, South Africa. PhD thesis (unpubl.) Columbia University, New York.

Jackson, S.E., Pearson, N.J., Griffin, W.L., and Belousova, E.A., 2004. The application of laser ablation-inductively coupled plasma-mass spectrometry to in situ U–Pb zircon geochronology. Chemical Geology 211 (1-2), 47-69, doi: 10.1016/j.chemgeo.2004.06.017.

Jaguin, J., Gapais, D., Poujol, M., Boulvais, P., and Moyen, J.-F., 2012a. The Murchison Greenstone Belt (South Africa): a General Tectonic Framework: South African Journal of Geology 115 (1), 65-76, doi: 10.2113/gssajg.115.1.65.

Jaguin, J., Poujol, M., Boulvais, P., Robb, L.J., and Paquette, J.-L., 2012b, Metallogeny of precious and base metal mineralization in the Murchison Greenstone Belt, South Africa: Indications from U-Pb and Pb-Pb geochronology. Mineralium Deposita (in press), doi: 10.1007/s00126-012-0422-7.

Kalsbeek, F., 1992. Large-scale albitisation of siltstones on Qeqertakavsak island, northeast Disko Bugt, West Greenland. Chemical Geology 95, 213-233.

van de Kamp, P.C., and Leake, B.E., 1996. Petrology, geochemistry, and Na metasomatism of Triassic-Jurassic non-marine clastic sediments in the Newark, Hartford, and Deerfield rift basins, northeastern USA. Chemical Geology 133, 89-24.

Kaur, P., Chaudhri, N., Hofmann, A.W., Raczek, I., Okrusch, M., Skora, S., Baumgartner, L.P., and Fu, M.-planck-institut, 2012. Two-Stage, Extreme Albitization of A-type Granites from Rajasthan , NW India. Journal of Petrology (in press), 1-30, doi: 10.1093/petrology/egs003.

Kedda, S.W., 1992. Geochemical and stable isotope studies of gold bearing granitoids in the Murchison Schist Belt, North Eastern Transvaal. MsC thesis, University of the Witwatersrand.

Kruger, F.J., Kamber, B.S., and Harris, P.D., 1998. Isotopic peculiarities of an Archaean pegmatite (Union Mine, Mica, South Africa): Geochemical and geochronological implications. Precambrian Research 91, 253-267.

Kröner, A., Jaeckel, P., and Brandl, G., 2000. Single zircon ages for felsic to intermediate rocks from the Pietersburg and Giyani greenstone belts and bordering granitoid orthogneisses, northern Kaapvaal Craton, South Africa. Journal of African Earth Sciences 30 (4), 773-793, doi: 10.1016/S0899-5362(00)00052-X.

Ludwig, K., 2000. Isoplot/Ex: a geochronological toolkit for Microsoft Excel. Berkeley Geochronology Center special publication.

Maiden, K.J., and Boocock, C.N., 1987. Deformational and metamorphic features of Antimony ores of the Murchsion Antimony Line, North-Eastern Transvaal. Transaction to the geological society of South Africa 87, 327-333.

Martin, H., 1994. The Archean Grey Gneisses and the Genesis of Continental Crust, in: Condie, K.C. (ed.), Archean Crustal Evolution, Elsevier, 205–259.

Meyer, F.M., Robb, L.J., Reimold, W.U., and de Bruiyn, H., 1994. Contrasting low- and high-Ca granites in the Archean Barberton Mountain Land, Southern Africa. Lithos 32 (1-2), 63-76, doi: 10.1016/0024-4937(94)90021-3.

Miller, C.F., Stoddard, E.F., Bradfish, L.J., and Dollase, W.A., 1981. Composition of plutonic muscovite: genetic implications. Canadian Mineralogist 19, 25-34.

Minnitt, R.C.A., 1975. The geology of the Murchison Range between Quagga Camp area and the Kruger National Park, M.Sc. thesis (unpubl.) University of Witwatersrand, Johannesburg.

Muff, R., and Saager, R., 1979. Metallogenic interpretation from a mineragraphic and geostatistic study of Antimony ores of the Murchsion Greenstone Belt, South Africa. Special publication of the geological Society of South Africa 5, 167-179.

Munz, I.A., Wayne, D., and Austrheim, H., 1994. Retrograde fluid infiltration in the high-grade Modum Complex, South Norway: evidence for age, source and REE mobility. Contributions to Mineralogy and Petrology 116, 32-46.

Pearton, T.N., 1978. The Geology and geochemistry of the Monarch Ore Body and Environs, Murchison Range, North-Eastern Transvaal, in: Verwoerd, W.J. (ed.), Mineralization in metamorphic terranes. Geological Society of South Africa, Special publication n° 4, 77-86.

Pearton, T.N., 1980. The geochemistry of the Carbonate and related rocks of the Antimony Line, Murchison Greenstone Belt, with particular reference to their genesis and to the origin of stibnite mineralization. PhD thesis, University of the Witwatersrand.

Pearton, T.N., and Viljoen, M.J., 1986. Antimony mineralization in the Murchison Greenstone Belt - An overview, in: Anhaeusser, C.R. and Maske, S. (eds.), Mineral Deposits of Southern Africa, 293-320.

Pedersen, R.B., Dunning, G.R., and Robins, B., 1989. U–Pb ages of nepheline syenite pegmatites from the Seiland Magmatic Province, N Norway, in: Gayer, R.A. (ed.), The Caledonide Geology of Scandinavia, London, 3-8.

Poujol, M., 2001. U-Pb isotopic evidence for episodic granitoid emplacement in the Murchison greenstone belt, South Africa. Journal of African Earth Sciences 33 (1), 155-163.

Poujol, M., Anhaeusser, C., and Armstrong, R.A., 2002. Episodic granitoid emplacement in the Archaean Amalia-Kraaipan terrane, South Africa: confirmation from single zircon U-Pb geochronology. Journal of African Earth Sciences 35 (1), 147-161.

Poujol, M., Boulvais, P., and Kosler, J., 2010. Regional-scale Cretaceous albitization in the Pyrenees : evidence from in situ U – Th – Pb dating of monazite, titanite and zircon. Journal of the Geological Society London 167, 751-767, doi: 10.1144/0016-76492009-144.

Poujol, M., and Robb, L.J., 1999. New U-Pb zircon ages on gneisses and pegmatite from south of the Murchison greenstone belt, South Africa. South African Journal of Geology 102 (2), 93-97.

Poujol, M., Robb, L.J., Respaut, J.-P., and Anhaeusser, C.R., 1996. 3.07-2.97 Greenstone Belt Formation in the northeastern Kaapvaal Craton: Implication for the Origin of the Witwatersrand Basin. Economic Geology 91, 1455-1461.

Recio, C., Fallick, A.E., Ugidos, J.M., and Stephens, W.E., 1997. Chemical characterization of multiple fluid-granite interaction processes in the episyenites of Avila, Central Iberian Massif, Spain. Chemical Geology 143, 127-143.

Reischmann, T., 1995. Precise U/Pb age determination with baddeleyite (ZrO_2): a case study from the Phalaborwa Igneous Complex, South Africa. South African Journal of Geology 98, 1-4.

Reynolds, I.M., 1986. Vanadium-bearing titaniferous iron ores of the Rooiwater Complex, North-eastern Transvaal, in: Anhaeusser, C.R. and Maske, S. (eds.), Mineral Deposits of Southern Africa, Geological Society of South Africa, Johannesburg, 451-460.

Robb, L.J., Davis, D.W., Kamo, S.L., and Meyer, F.M., 1992. Ages of altered granites adjoining the Witwatersrand basin with implications for the origin of gold and uranium. Nature 357, 677-680.

Robb, L.J., and Robb, V.M., 1986. Archean pegmatite deposits in the North-Eastern Transvaal, in: Anhaeusser, C.R. and Maske, S. (eds.), Mineral Deposits of Southern Africa, Geological Society of South Africa, Johannesburg, 437-449.

Robert, F., and Kelly, W.C., 1987. Ore-Forming Fluids in Archean Gold-Bearing Quartz Veins at the Sigma Mine, Abitibi Greenstone Belt, Canada. Economic Geology 82, 1464-1482.

Robert, F., Poulsen, K. howard, Cassidy, K.F., and Hodgson, C.J., 2005. Gold metallogeny of the Superior and Yilgarn Cratons, in: Economic Geology 100th Anniversary Volume, 1001-1033.

Rosenbaum, J., and Sheppard, S.M., 1986. An isotopic study of siderites, dolomites and ankerites at high temperatures. Geochimica et Cosmochimica Acta 50 (6), 1147-1150, doi: 10.1016/0016-7037(86)90396-0.

Schwarz-Schampera, U., Terblanche, H., and Oberthür, T., 2010. Volcanic-hosted massive sulfide deposits in the Murchison greenstone belt, South Africa. Mineralium Deposita 45 (2), 113-145, doi: 10.1007/s00126-009-0266-y.

South African Committee for Stratigraphy, 1980. The Murchison Sequence, in Stratigraphy of South Africa, part 1: Lithostratigraphy of the Republic of South Africa, South West Africa/Namibia and the Republics of Bophuthatswana, Transkei and Venda 45-52.

Vearncombe, J.R., 1988. Structure and metamorphism of the Archean Murchison belt, Kaapvaal Craton, South Africa. Tectonics 7 (4), 761-774.

Vearncombe, J.R., Barton, J.M., Cheshire, P.E., de Beer, J.H., Stettler, E.H., and Brandl, G., 1992. Geology, geophysics and mineralization of the Murchison Schist Belt, Rooiwater Complex and surrounding granitoids. Memoir of the Geological survey of South Africa n° 81.

Vearncombe, J.R., Barton, J.M., and Walsh, K.L., 1987. The Rooiwater Complex and associated rocks, Murchison granitoid-greenstone terrane, Kaapvaal Craton. South African Journal of Geology 90 (4), 361-377.

Vearncombe, J.R., Cheshire, P.E., de Beer, J.H., Killick, A.M., Mallinson, W.S., McCourt, S., and Stettler, E.H., 1988. Structures related to the Antimony line, Murchison schist belt, Kaapvaal craton, South Africa. Tectonophysics 154 (3-4), 285-308.

Viljoen, M.J., van Vuuren, C., Pearton, T.N., Minnitt, R.C.A., Muff, R., and Cillier, P., 1978. The regional geological setting of the mineralization in the Murchison Range with particular reference to Antimony, in: Verwoerd, W.J. (ed.), Mineralization in metamorphic terranes, 55-76.

Williams, P.J., Barton, M.D., Johnson, D.A., Fontboté, L., De Haller, A., Mark, G., Oliver, N.H.S., and Marschik, R., 2005. Iron Oxide Copper-Gold Deposits: Geology, Space-Time Distribution, and Possible Modes of Origin. in: Economic Geology 100th Anniversary volume, 371-406.

Willson, C., and Viljoen, M.J., 1986. The Athens Antimony ore body, Murchison Greenstone Belt, in Anhaeusser, C.R. and Maske, S. (eds.), Mineral Deposits of Southern Africa, Geological Society of South Africa, Johannesburg, 333-338.

Wilson-Moore, C., 1896. The economic importance of the Murchison Range: Transaction to the Geological Society of South Africa 1, 51-75.

de Wit, M.J., Armstrong, R.A., Kamo, S., and Erlank, A., 1993. Gold-bearing sediments in the Pietersburg Greenstone Belt, age equivalents of the Witwatersrand Supergroup sediments, South Africa. Economic Geology 88 (5), 1242-1252.

Witt, W.K., 1992. Porphyry intrusions and albitites in the Bardoc–Kalgoorlie area, Western Australia, and their role in Archean epigenetic gold mineralization: Canadian Journal of Earth Sciences 29 (8), 1609-1622.

Zeh, A., Gerdes, A., and Barton, J.M., 2009. Archean Accretion and Crustal Evolution of the Kalahari Craton--the Zircon Age and Hf Isotope Record of Granitic Rocks from Barberton/Swaziland to the Francistown Arc: Journal of Petrology 50 (5), 933-966, doi: 10.1093/petrology/egp027.

Zeh, A., Jaguin, J., Poujol, M., Boulvais, P., Hallot, E., Block, S., and Paquette, J.-L., (in prep). Juvenile crust formation in the northeastern Kaapvaal Craton at 2.97 Ga – Implications for Archean crust-mantle evolution, terrane accretion, and the Witwatersrand gold source.

Zheng, Y.-F., 1993. Calculation of oxygen isotope fractionation in anhydrous silicate minerals. Geochimica et Cosmochimica Acta 57 (5), 1079-1091.

Supplementary data table 1: Monazite composition from electron microprobe analyses. Structural formula base on 4 oxygen atoms.

Données additionnelles et commentaires

DATATIONS DE LA MONAZITE. En dépit de l'analyse exhaustive des monazites à la microsonde et au LA-ICP-MS, la relation entre la chimie et l'âge apparent des grains de monazite demeure complexe.

Ainsi, des variations chimiques sont discrètes mais détectables comme sur la Figure 10 ou sur la Figure 8–1 ci-contre, mais ne sont corrélées qu'avec les sites. Ces différences suggèrent que les éléments constitutifs de la monazite (notamment les terres rares) sont hérités du protolithe ou de la zone encaissante immédiate, et qu'ils sont donc peu mobiles à l'échelle de l'Antimony Line.

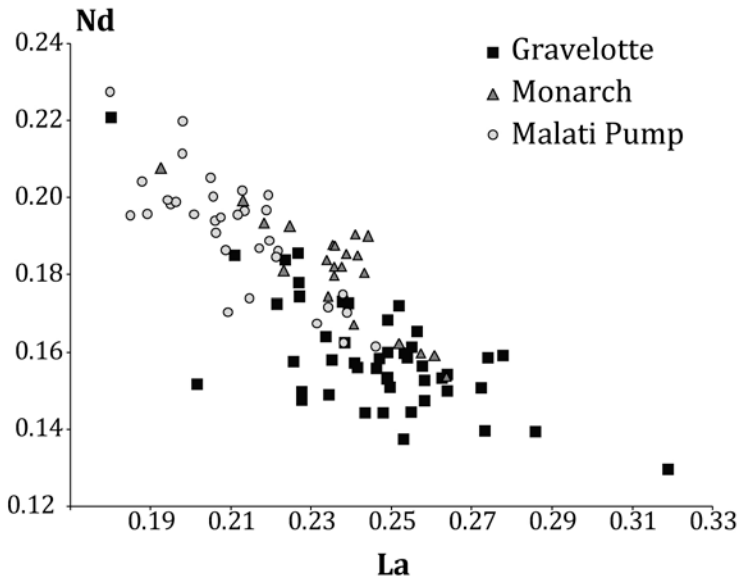

Figure 8–1 : *Composition en Nd en fonction du La, en formule structurale pour 4 O.*

Sur la Figure 8–2, les petites monazites sont davantage susceptibles de montrer des âges jeunes. Cette tendance n'est pas due à un phénomène de diffusion car le plomb diffuse peu dans la monazite (Smith et Giletti 1997). Deux explications, non antagonistes, peuvent expliquer cette distribution. Ces petits grains ont proportionnellement plus de surface en contact avec le milieu extérieur, et auraient enregistré plus efficacement des perturbations tardives dues à des interactions avec des fluides. Alternativement ils ont été analysés quasiment en totalité donc les bordures qui enregistreraient mieux les recristallisations tardives auraient pu contribuer proportionnellement plus au signal isotopique. Ce comportement souligne que l'événement vers 2.0 Ga est une perturbation mineure puisqu'il n'est vraiment détecté qu'à condition qu'une taille de grain faible participe aux analyses.

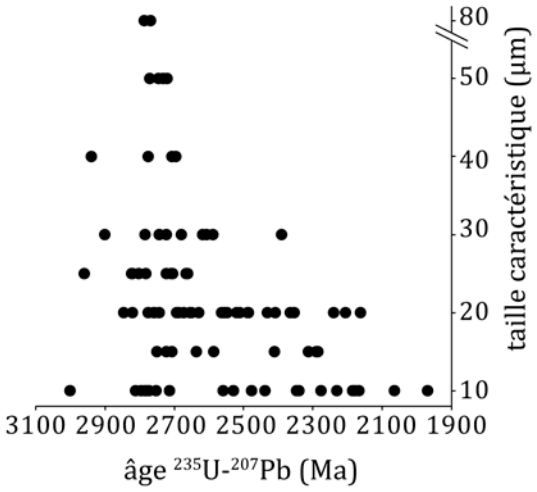

Figure 8–2 : *Taille caractéristique des grains de monazite (c'est-à-dire la dimension la plus petite) en fonction de l'âge ^{235}U-^{207}Pb.*

LE PLUTON DE MARANDA. La partie du pluton de Maranda[3] affleurant dans la ceinture est une roche à quartz, feldspaths alcalins, biotite et muscovite et elle est albitisée (66.49 % d'albite en norme CIPW, Vearncombe et al. 1992). Les seules données disponibles sur le corps principal sont celles fournies par les cartes géologiques au 1/250 000 où le pluton est décrit comme "granite leucocratique à muscovite". En l'absence de données pétrologiques ou géochimiques plus précises sur ce dernier, le lien génétique entre le Baderoukwe et le Maranda est impossible à établir catégoriquement. La géochronologie pointe un diachronisme potentiel de 50 Ma entre les deux. Cependant, leur aspect cartographique (alignés et intrudés dans la ceinture), la géophysique et le lien géochimique entre le Baderoukwe et les albitites suggèrent fortement que ce sont des intrusions associées. Il semble raisonnable de postuler que l'intrusion de Maranda et de Baderoukwe forment un batholite multiple de nature TTG.

ALBITISATION. L'albitisation s'étend un peu au delà de l'Antimony Line : un échantillon au nord du Baderoukwe (MUR 09-85) et un échantillon du complexe du Rooiwater (voir description à la suite de l'article #1) sont albitisés. Cela souligne que l'albitisation est un phénomène très commun d'interaction fluide-roche, principalement du fait que le sodium est très soluble dans les fluides, et donc mobile à l'échelle crustale où il remplace le potassium et le calcium. Par ailleurs, le premier échantillon est dans la zone de cisaillement tardive de la Letaba (Table 2 et Figure 6) et le deuxième dans ce qui apparait sur notre carte des foliations (Figure 3 de l'article #2) comme une zone de cisaillement NE-SO senestre dans le complexe. Ces deux échantillons renforcent encore le lien entre les zones de cisaillement et les circulations de fluides, mais ne sont pas associés à une mobilité de Sb.

[3] Dans ce travail le pluton de Maranda fait référence au corps tel que délimité par les cartes de Tzaneen (1985) et de Pilgrim's Rest (1986) et reporté sur les cartes de ce travail, et non pas seulement au petit affleurement auquel Vearncombe se réfère (e.g. Vearncombe et al. 1992).

Régionalement, dans la ceinture de Pietersburg, de Wit et al. (1992b) rapportent que l'albitisation des roches est commune, et Ward et Wilson (1998) précisent qu'un pluton est particulièrement albitisé (Roodepoort). De même, dans la ceinture de Giyani, Brandl et al. (2006) décrivent des volcanites felsiques à forte altération sodique. Or, les commentaires additionnels à l'article #4 présentaient les minéralisations en or des ceintures de roches vertes de Polokwane et Giyani. De là, il semble qu'une investigation similaire à celle développée ici dans l'article #5 soit nécessaire dans ces ceintures. Dans un premier temps, il faudrait évaluer le lien entre ces altérations, vraisemblablement hydrothermales, et les minéralisations en or. Si le lien est établi, il faudrait alors, dans un second temps, cibler préférentiellement les protolithes acides pour dater l'épisode minéralisateur.

Cet article #5 identifie une phase hydrothermale majeure vers 2.8 Ga. L'article #4 propose que la circulation hydrothermale ait eu lieu en conditions du métamorphisme schiste vert supérieur dans l'Antimony Line (unité de Murchison). Par conséquent, dans le cœur de la ceinture de Murchison, au moins une partie du métamorphisme-métasomatisme date de 2.8 Ga et est diachrone du métamorphisme amphibolitique-schiste vert au nord (2.97 Ga, voir commentaires à la suite de l'article #2). De plus, cet âge à 2.8 Ga démontre que la déformation est active bien après l'accrétion des terrains nord et sud même si elle est mineure sur l'Antimony Line. Enfin, cet âge semble contemporain de la mise en place du granite de Lekkersmaak, au sud de la ceinture, objet du chapitre suivant.

Chapitre 8 — Le leucogranite de Lekkersmaak

Ce chapitre sur le leucogranite de Lekkersmaak est présenté sous la forme d'un article en préparation ; quelques données isotopiques restent à acquérir, notamment avant soumission.

L'étude suit deux axes. Les granites de type S sont rares dans l'évolution de la croûte archéenne et sont soit de taille limitée, soit présentant un caractère peralumineux et/ou un âge douteux. La suite granitique de Lekkersmaak (intrusions de Lekkersmaak et Willie) est donc candidate au titre du plus vieux leucogranite de taille significative et représente un objet inhabituel qu'il s'agit de caractériser. Le deuxième axe saisit l'opportunité de l'existence de ce pluton alumineux exceptionnel pour appliquer une nouvelle méthode de modélisation géochimique. Cette partie du travail a été engagée en collaboration avec Jean-François Moyen (Université Jean Monnet, St Etienne). Le but est d'estimer les apports de cette méthode pour contraindre les conditions de genèse des magmas (sources, pression, température).

La première partie de cette étude précise la pétrologie, la minéralogie, la géochimie et la géochronologie de la suite de Lekkersmaak au sud de la ceinture de Murchison. Les échantillons sont constitués de quartz, plagioclase, orthose, biotite, muscovite et occasionnellement de grenat. La suite est de type S sur le plan des éléments majeurs (A/CNK=1.06 à 1.13, $Na_2O+K_2O \approx 8.3$ pds %). Elle montre des signatures isotopiques en oxygène basses et aux variations restreintes ($\delta^{18}O$=8.2-8.7 ‰ vs. SMOW). Les spectres de Terres Rares recouvrent une gamme limitée en Terres Rares légères, mais très large en Terres Rares lourdes. La géochronologie U-Pb sur zircon date à 2774.5 ± 6.8 Ma la cristallisation pour le pluton du Lekkersmaak et à 2817.0 ± 10 Ma la cristallisation du pluton de Willie, confirmant ainsi que ce dernier est une phase distincte précoce.

La modélisation de la fusion partielle suit ici une méthode nouvelle car au lieu d'utiliser des approches semi-quantitatives classiques, elle utilise la construction de pseudo-section (ici grâce au logiciel de thermodynamique, PERPLE_X), pour déterminer les phases, leurs proportions et leurs compositions (y compris du liquide) à partir d'un protolithe choisi, et ce en chaque point de l'espace pression-température. Les données extraites servent ensuite à recalculer les teneurs en éléments traces du liquide en prenant en compte les phases accessoires riches en Terres Rares. Les modèles reproduisent correctement, à partir de protolithes sédimentaires, les teneurs en éléments majeurs du pluton de Lekkersmaak pour des gammes de Pression-Température géologiquement raisonnables. Des résultats préliminaires soulignent naturellement le rôle du grenat dans la composition du liquide en éléments traces. Une phase finale de modélisation est encore nécessaire avant la soumission de l'article pour exploiter le potentiel de ces résultats.

Article #6 THE OLDEST PERALUMINOUS GRANITES: PETROLOGY, GEOCHEMISTRY AND GEOCHEMICAL MODELING. EXAMPLE FROM THE LEKKERSMAAK SUITE, SOUTH AFRICA

In preparation for *Precambrian Research*

Jaguin J.[a], Moyen J.-F.[b], Poujol M.[a], Boulvais P.[a], Paquette, J.-L.

a: Géosciences Rennes, Université de Rennes 1, France; justine.jaguin@univ-rennes1.fr

b: Laboratoire Magmas et Volcans, Université Jean Monnet, Saint Etienne, France

INTRODUCTION

S-type granites are formed by the recycling of continental crust, especially terrigenous sedimentary material, and are characterized by high alkali and aluminium contents (e.g. Clemens and Vielzeuf 1987, Clemens 2003). Early Archaean S-type granites are rare, while they become common, although in minor proportion, during the Neoarchaean and the Archaean-Proterozoic transition. Indeed, the accumulation of sizeable detrital sequences necessary to produce such magmas, thereafter buried and heated, represent a combination of processes that may have not been common during the Archean.

S-type granites are reported from the Eastern Superior Province (2.70 -2.64 Ga; Bourne and Danis 1987; Ducharne et al., 1997; Feng and Kerrich 1992; Machado et al., 1990; Bédard and Ludden 1997), the Western Superior Province (2.65-2.69; Larbi et al., 1999; Day and Weiblen 1986; Goad and Cerny 1981), the western Dhawar craton (ca 2.56 Ga; Dhoundial et al., 1987 Sarvothaman and Leelanandam 1987), the Brazilian Shield (Stokes, 1991), the Baltic Shield (2.6-2.7 Ga Kulikov et al., 1986). In the Kaapvaal Craton, several S-type occurrences are reported so far: a 2.71 Ga old leucogranite to the southeast (McCourt et al., 2000), to the east and northeast S-type granites are also described but with doubtful old age (3.07 Ga, Maphalala and Kröner 1993; Trumbull 1993) or younger (2.86-2.78 Ga) and an unconfirmed S-type affinity (Meyer et al., 1994, Henderson et al., 2000), or as clasts in youger sequence (3.57-3.30 Ga, Sanchez-Garrido et al. 2011). Finally S-type affinity gneisses and migmatites are found in the Limpopo Belt (2.69-2.57 Ga, Kröner et al., 1999; Jaeckel et al., 1997; Kreissig et al., 2001) and in Wyoming the oldest known S-type granite reported so far (3.1 Ga, Grace et al. 2006). In this study, we focus on the large (430 km^2) ca. 2795 ± 8 Ma old Lekkersmaak and 2820 ± 38 Ma Willie leucogranites (Anhaeusser et al., 2007, Zeh et al., 2009, Poujol 2001), which crop out to the south of the Murchison Greenstone Belt in the Kaapvaal Craton and stand for the first true sizeable S-type pluton.

Constraining the petrogenesis of the Lekkersmaak suite (source and P-T melting conditions) is therefore crucial to explain its formation. For this purpose, this study is divided into two main parts. First, we document the petrology, mineralogy (mineral

composition), geochemistry (elementary, Sr and Nd isotopes, O isotopes) and geochronology of the Lekkersmaak pluton. Then, we develop an original geochemical modelling. Usually, geochemical modelling based on trace elements is semi-quantitative disconnected from thermodynamic information (mineral stabilities, proportions during melting). Yet, thermodynamic models of mineral stabilities during crustal melting are now available. Here we propose a comprehensive model for the melting of aluminous metasediments and generation of leucogranites melts, taking into account thermodynamic constraints and able to predict both major and trace elements compositions. Finally, we specify the source and P-T conditions at the origin of the Lekkersmaak and Willie magmas.

GEOLOGICAL SETTING: THE MURCHISON GREENSTONE AND GRANITOIDS TERRAIN

The Murchison Granitoids Greenstone Terrain is located in the northeastern part of Kaapvaal craton (Fig. 1a), 70 km to the south of the Limpopo Belt limit (Hout River Shear Zone), and the Giyani and Pietersburg Greenstone Belts. The Thabazimbi-Murchison Lineament (TML, Du Plessis, 1990) is a craton-scale geophysical feature (Vinnik et al., 1995). Its exact location around the Murchison belt remains unclear (Fripp et al., 1980, de Wit et al., 1992a; Anhaeusser, 2006; Zeh et al., in prep). Nevertheless the TML broadly separates the 3.17-3.0 Ga northern Groot-Letaba gneiss from the 3.22-3.06 Ga southern Makhutwsi gneiss (Brandl and Kröner 1993, unpublished data cited in Robb et al., 2006 and Poujol et al., 1996, Brandl and Kröner 1993, respectively).

Between these TTG gneisses, the Murchison Greenstone Belt is a narrow (10-15 km) and deeply rooted (4 km, 9 km maximum, de Beer et al., 1984) east-northeast trending volcano-sedimentary sequence. The surrounding granitoids, which were emplaced over a priod of 300 Ma present variable geochemical compositions ranging from granodiorite to leucogranite. Dating of synkinematic intrusions, fluid circulations and metamorphic overprints indicate that the tectonic history of the terrain was protracted between 2.97 Ga and ca. 2.80 Ga (e.g. Vearncombe, 1988, Jaguin et al., 2012a, Block et al., 2012).

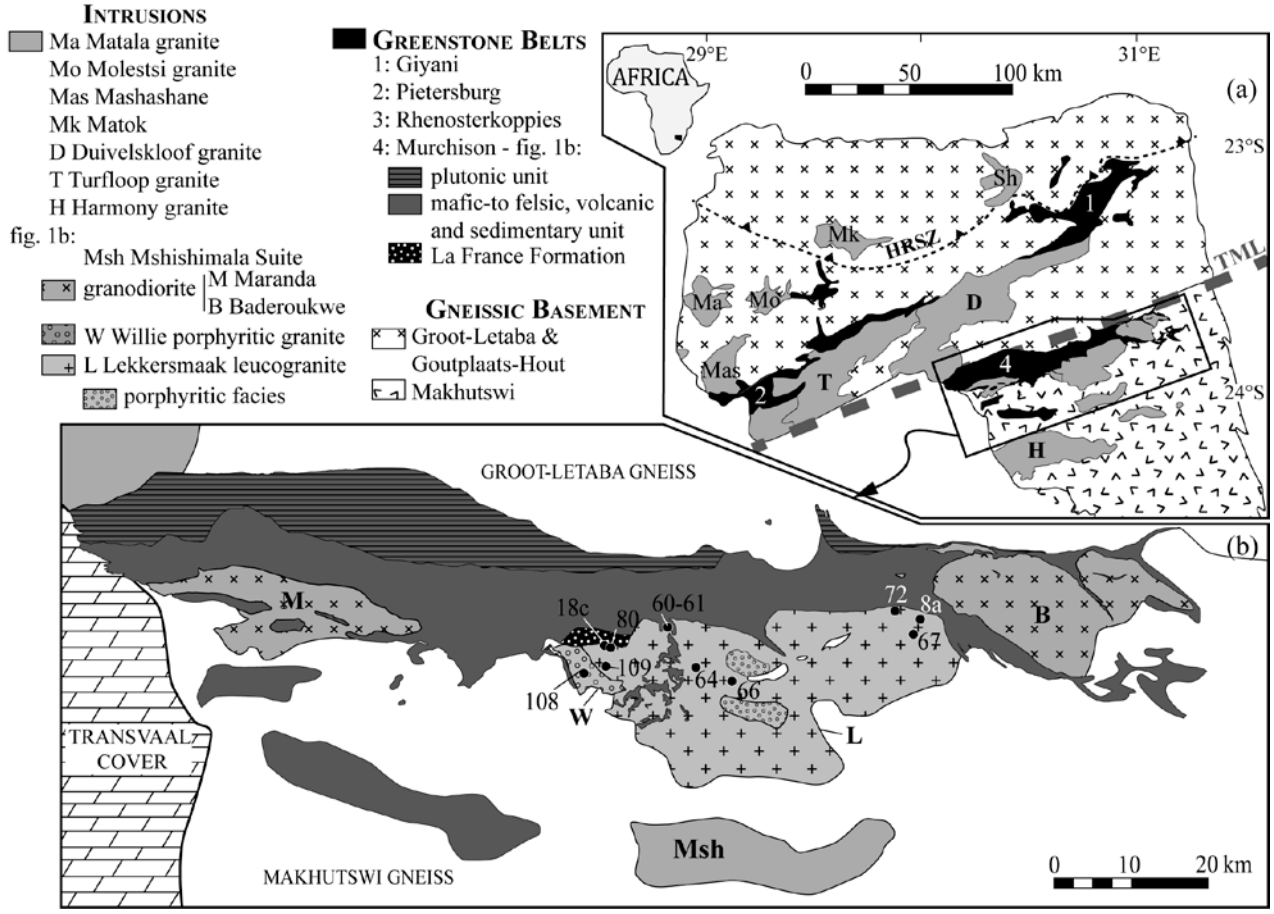

Figure 1: *(a) Map of the northeastern Kaapvaal craton after Robb et al., 2006. TML: Thabazimbi-Murchison Lineament. HRSZ: Hout River Shear Zone (b) Map of the Murchison Granite Greenstone Belt Terrain. Only the La France Formation is identified within the volcano-sedimentary sequence. On Lekkersmaak and Willie plutons, the reported number are sampling sites corrresponding to samples MUR 09-xx. Belt limits are from Vearncombe et al. (1992); basement and intrusive are from 1:250 000 map of Tzaneen (Geological Survey of South Africa 1985) and Pilgrim's Rest (1986); mapping of the Willie pluton and western part of the Lekkersmaak plutons are from Ian Kramers (pers. comm).*

Although the exact age remains unknown, the deposition of the Murchison Belt started prior to 3.09 Ga with the deposition of the mafic and ultramafic komatiitic Mulati and Leydsorp Formations (Poujol, 2001) followed, at 3.09 Ga, by the emplacement of the mafic-to-felsic volcanic rocks of the Weigel Formation (Poujol et al., 1996). This episode was coeval with the intrusion of the Harmony granite and tonalitic phases farther to the south (Fig. 1b; Poujol and Robb, 1999).

At ca. 2.99-2.97 Ga, felsic volcanites of the Rubbervale Formation emplaced to the north (Poujol et al., 1996) while some sedimentary rocks deposited in the center, among which the La France Formation (Zeh et al., in prep; Fig 1b). The La France Formation is a small area in the south-center part of the belt. It comprises quartzites as well as kyanite and staurolite-bearing micaschists, indicating recrystallisation under amphibolite facies conditions (Block et al., 2012). Important plutonic activity of the terrain is now largely documented at 2.97-2.92 Ga (Baderoukwe granodioritic batholith, Jaguin et al., 2012b; Discovery granite, Poujol 2001; Rooiwater gabbro-

diorite complex, Zeh et al., in prep), and may be related to accretion between the northern and the southern terranes (Zeh et al., in prep).

After a magmatic quiescent period, a third period of activity occurred between 2.84 and 2.77 Ga. It comprises the peraluminous Willie and Lekkersmaak granites (Vearncombe et al., 1992) which crystallised at 2820 ± 38 Ma and 2795 ± 8 Ma (Poujol 2001, Zeh et al., 2009 respectively), the Duivelskloof "granite" and related gneissic phase (2841 ± 10 Ma and 2776 ± 10 Ma, Laurent et al., submitted; 2839 ± 8 Ma and 2784 ± 8, Zeh et al., 2009), the granite-granodiorite Turfloop batholith (2777 ± 10 Ma, Henderson et al., 2000), and pegmatitic dykes intrusive into the Makhutswi gneiss (2848 ± 58 Ma, Poujol and Robb, 1999). This activity is contemporaneous with fluid circulation and deformation in the Antimony Line, a structure within the Murchison Belt hosting antimony deposits (Jaguin et al., submitted). Finally to the south of the belt, the Mashishimale pluton, a polyphased bt ± hbl monzogranite (Villaros et al. 2011), is dated at ca 2.67 Ga (Poujol, 2001; Zeh et al., 2009).

SAMPLES

The Lekkersmaak suite corresponds to a two lobe-shape, 40 km long, max. 20 km wide ENE-elongate body (Fig. 1b, Geological Survey of South Africa, map of Tzaneen, 1985; Vearncombe et al., 1992). It includes porphyritic facies in its central part and in its western termination, the so-called "Willie Granite". Basement remnants are present in the core of the intrusive body (white zones in Fig. 1b) probably indicating that the body is thin and present a laccolith-like shape. Finally, the Lekkersmaak intrusion includes in places large enclaves or rafts of mafic lithologies (grey zones in Fig. 1b).

The poor outcrop conditions together with the recent development of fenced game farms prevented an optimal observation and sampling of the plutons. Nevertheless, we managed to collect samples from east to west and from edge to core for the Lekkersmaak intrusion (Fig. 1b), together with one sample from the Willie granite. Samples are light-grey to yellow leucocratic rocks (Fig. 2). Their mineralogy consists of quartz with undulosed extinction, plagioclase (commonly zoned, sometimes poecilitic, and sometimes pervasively sericitized), orthose and microcline, dark biotite, muscovite (Fig. 2d). Garnet was found only in sample MUR 09-67. Epidote and titanite are common accessory minerals, often associated with biotite (Fig. 2e) and other accessory minerals such as sulphide, apatite and zircon. Texturally, most of the pluton is a medium- (MUR 09-67, Fig. 2a) to coarse-grained (MUR 09-108) equigranular facies, but in some place porphyritic facies occurs (cm-long orthose, MUR 09-66A, Fig. 2b). Samples MUR 09-60, 61 and 80 have a slightly gneissic aspect that consists of diffuse quartz appearance and anisotropic orientation of the biotite grains. MUR 09-72 is a foliated rock (Fig. 2c) collected along the margin of the belt. Tourmaline-pegmatite rocks are observed in some place in the margin (close to MUR 09-60 sample site) or in the core of the body (close to MUR 09-64 sample site). MUR 09-63 is made of poecilitic plagioclase and quartz, very rare muscovite but abundant chlorite associated with

opaque minerals. It shows veinlets of quartz-plagioclase with some myrmekitic textures. Sample MUR 09-64 is a coarse-grained leucocratic rock, devoided of muscovite and biotite but made of poecilitic plagioclase and quartz, the latter forming diffuse pseudo-veins, as well as some apatite and epidote.

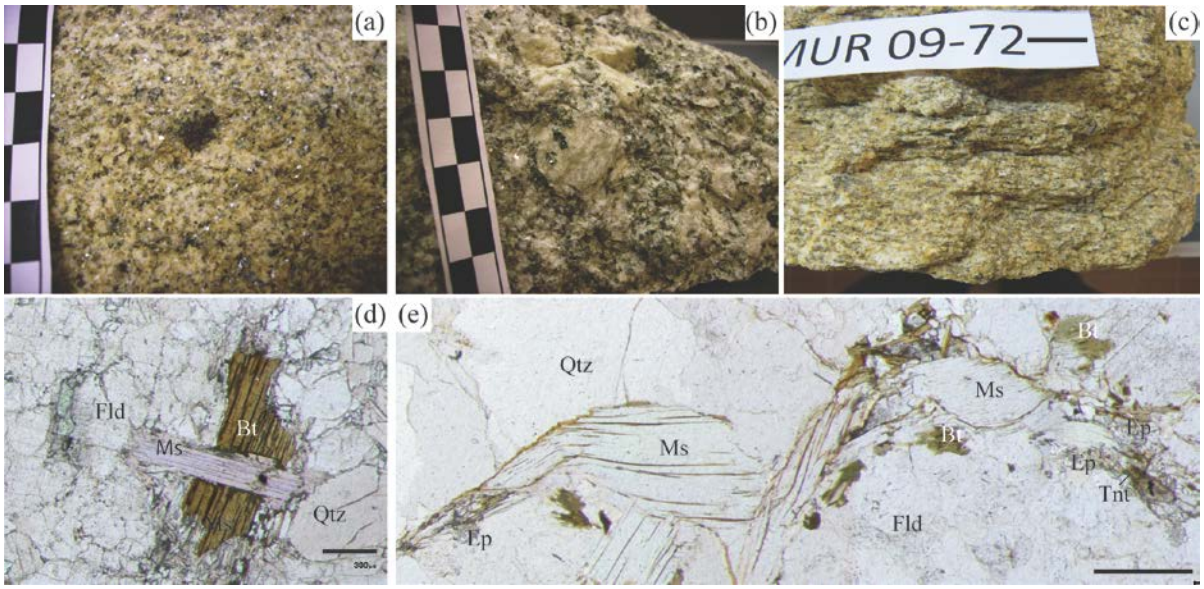

Figure 2: *Pictures of the Lekkersmaak and Willie rocks. Hand samples of: (a) medium-grained, equigranular biotite-muscovite quartzo-feldspatic rock with a rare example of garnet (MUR 09-67); (b) biotite-rich, muscovite-poor porphyritic facies with cm-large feldspar (MUR 09-66); (c) outer, foliated sample (MUR 09-72, bar scale 2 cm). Thin section picture of: (d) intergrowth of biotite and muscovite (sample MUR 09-80, bar scale 600 µm); (e) thin section picture of large muscovite grains (Ms), in place sheared, along with a fine grained matrix of biotite (Bt) + epidote (Ep) + titanite (Tnt) (MUR 09-108, Willie granite, bar scale 400 µm).*

ANALYTICAL PROCEDURES

Mineral and whole rock elementary composition

Mineral compositions were measured in thin section on a SX-100 CAMECA electron microprobe (EMP) at the Laboratoire Magmas et Volcans (Clermont-Ferrand) using 15kV accelerating voltage.

For whole rock composition, rocks were crushed first in a steel crusher then in an agate mortar until a fine powder was obtained. The SARM laboratory (CRPG-CNRS, Nancy, France) performed the chemical analyses using $LiBO_2$ fusion and acid dissolution by ICP-AES for major elements and ICP-MS for trace elements. Whole rock chemical compositions are reported in Table 1, together with detection limits. Analytical uncertainties depend on the content and can be found on the SARM webpage (http://helium.crpg.cnrs-nancy.fr/SARM/pages/roches.html).

Nd and Sr isotope systematics

Sr and Sm-Nd isotopes analyses were performed on 100 mg of rock powders using the 7-collectors Finningan MAT-262 mass spectrometer available at Geosciences

Rennes. Powders were dissolved twice with a mixture of concentrate HF – HNO_3 acids. After five days of digestion, the solution was evaporated to dryness and then taken up in 6N HCl acid for two days. They were then dried and taken up with concentrated HCl 2.5N and loaded on cationic exchange chromatography using AG50W–X8 resin to collect the REE fractions on one hand and Sr on the other hand. The REE fractions were then purified and Sm and Nd isolated using a secondary column loaded with Eichrom Ln resin. Sr was separated with the Spec resin. Sm-Nd concentrations were measured by isotope dilution using a $^{149}Sm/^{150}Nd$ spike. Samples were spiked before dissolution. During the analytical session, measurements of the AMES Nd standard gave a mean $^{143}Nd/^{144}Nd$ ratio of 0.511957 ± 3 (n=18), and analyses of the NBS-987 Sr standard yielded a mean $^{87}Sr/^{86}Sr$ ratio of 0.710183 ± 10 (n =18). Blanks values for Nd and Sr were < 300 pg and therefore considered as negligeable. $^{87}Rb/^{86}Sr$ was calculated using Rb and Sr contents from ICP-MS measurements and a ^{87}Rb abundance of 27.8346 %. I_{Sr} was calculated using the decay constant λ = 1.42 10-11 y^{-1}. Model ages and εNd were calculated using the decay constant λ = 6.54 10-12 y^{-1} and the parameters of Goldstein et al. (1984).

Oxygen isotope systematics

Oxygen isotope whole rocks analyses (Table 1) were carried out in Geosciences Rennes. About 7 mg of whole rock powder were reacted with BrF_5 in Ni tubes at 670°C over night (after the method of Clayton and Mayeda, 1963). It was then converted to CO_2 by reaction with hot graphite, and analyzed using a VG SIRA 10 triple collector instrument. Long-term analysis of NBS 28 standard ($\delta^{18}O$ = 9.58‰) gave a mean value of 9.3 ± 0.1‰. Measured values have thus been slightly corrected. The average uncertainty on oxygen isotope composition is 0.2‰.

U-Pb zircon dating

Zircon grains were dated by in-situ LA-ICP-MS analyses on separated grains mounted in epoxy mounts. A classic mineral separation procedure has been applied. Rocks were crushed, the powder fraction (<250 µm) has been concentrated in heavy minerals by Wilfley table and heavy liquids methods. Magnetic minerals were then removed with an isodynamic Frantz separator. Grains were carefully handpicked under a binocular microscope, embedded in epoxy mounts and polished. They were imaged by cathodoluminescence (CL) using a Reliotron CL system. U–Pb analyses were carried out by in situ LA-ICPMS at the Laboratoire Magmas et Volcans in Clermont-Ferrand, France. We used ablation spot diameters of 26 µm with a repetition rate of 3 Hz. Data were corrected for U–Pb fractionation and for the mass bias by standard bracketing with repeated measurements of the GJ1 zircon standard (Jackson et al., 2004). Further information on the instrumentation and the analytical technique is detailed in Hurai et al. (2010). Data reduction was carried out with the GLITTER® software package developed by the Macquarie Research Ltd. Ages and diagrams were generated using Isoplot/Ex (Ludwig, 2000).

GEOCHEMICAL MODELLING

The method for thermodynamic modelling comprised 2 steps. The first step aimed at producing major elements compositions of the melt and of residual phases in equilibrium with the former. We compiled major elements composition of a given protolith (metasediments). We added 6 wt.% of H_2O to the actual composition, because of dehydration of sediments during metamorphism. We determined this value from the models to account for H_2O saturation at any temperature above the solidus. We used Holland and Powell (1998) internally consistent thermodynamic database. This database is exploited in the program PERPLE_X (e.g. Connolly, 2009) to calculate the proportions and compositions of phases in any given points of the P–T space, and among the phases is the melt.

The next step aimed at extrapolating trace elements contents of the melt from the previous modelling. In a separate spreadsheet, we input protolithic contents C_0 of each *i* trace elements. We calculated the trace element content of the melt C_l^i generated using each *j* major phase proportions (X_j) in equilibrium, combined with published partition coefficients (Kd), for each P–T node:

$$C_l^i = \frac{C_0^i}{D^i + F \times (1 - D^i)} \text{ and } D^i = \sum_j^{for\ i} Kd_j^i \times X_j$$

In addition, the trace element calculation takes into account accessory phase proportion. These proportions were calculated from saturation of zircon (Watson and Harrison, 1983), monazite (Montel, 1993) and xenotime (Montel, 1996). Any Zr, LREE (+Th) or HREE in excess beyond melt saturation was used to build respectively zircon, monazite and xenotime, that were added to the residuum and element partitioning coefficient were corrected accordingly. The process was iterated until the model was stable (i.e contents of trace elements and abundance of phases converged to a constant value). We finally plotted the results using the GCDkit software (Janousek et al., 2006).

PETROLOGIC, GEOCHEMICAL AND GEOCHRONOLOGICAL CHARACTERIZATION

Mineral composition

We performed EMP analyses on samples (Table 1) representative of the variability of facies and mineralogy of the intrusions (east and west lobes, core and border of the Lekkersmaak and the Willie sample). K-feldspar crystals (microcline in thin section), absent in the Willie sample and rare in the other samples, are highly potassic (ca. $Or_{94\text{-}98}$; Fig. 3a). Plagioclase grains are common, with albite to slightly oligoclase composition (maximum $An_{15.1}$; Fig. 3a). Plagioclase grains show very little zoning, with only a decrease of 1-2% of the anorthite content toward the edge.

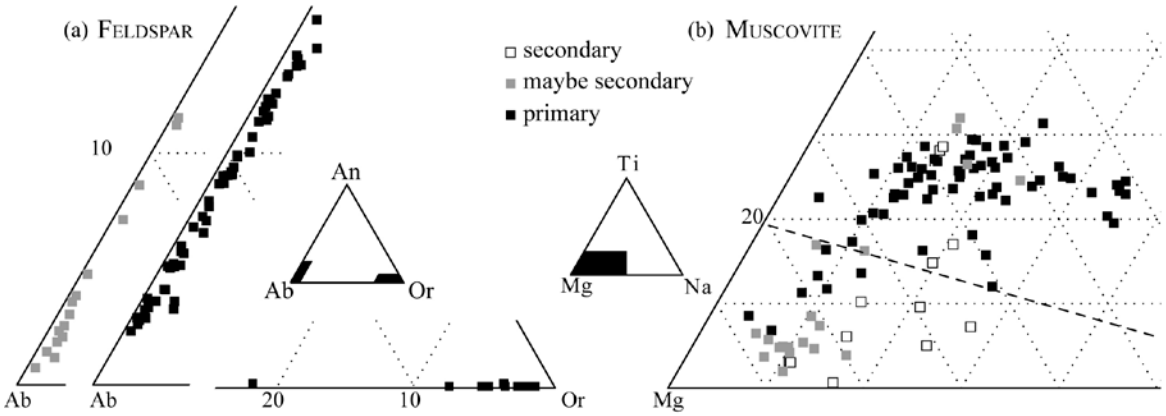

Figure 3: *Mineral composition. (a) End-member ternary diagram of feldspar. (b) Chemical ternary diagram of muscovite. Dashed line separates the field of primary plutonic muscovite composition (top) from the field of secondary muscovite (after Miller et al., 1981). "Secondary", "maybe secondary" and "primary" terminology refer to textural criteria such as size distribution, dissolution figures, association with secondary minerals (epidode, titanite), or association with shear zones.*

Many muscovite grains have a magmatic composition, falling in the primary, high-Ti field of Miller et al. (1981; Fig 3b). Some samples have both magmatic and secondary muscovite in variable proportion. Garnet in sample MUR 09-67 is Mn-rich almandine with the global composition $Alm_{66}Sps_{29}Pyp_5$.

Major and trace elements

Table 2 presents the chemical composition of samples from the Lekkersmaak and the Willie granites. Major elements are reported in Harker diagrams on Fig. 4 together with a database of S-type plutons of various ages and locations (Moyen pers. comm.). The Willie sample (MUR 09-108) is indistinguishable from the Lekkersmaak ones and consequently not labelled individually. The samples are rich in silica (SiO_2 between 72.6 and 75.8 wt.%) and lay on the differentiated side of the peraluminous compositional trend. Samples are rich in alkalis ($Na_2O + K_2O$ = 7.4 to 8.4 wt.%) as most S-types granites. Samples MUR 09-61 and MUR 09-80 show a significant enrichment in Na_2O and a correlative depletion in K_2O (Fig.4). Even excluding these two samples, the samples belong to the sodic-rich, potassic-poor S-type granites. As a whole, the granites have a moderately peraluminous character (A/CNK=1.06 to 1.13; A/NK = 1.16 to 1.24).

Table 1 (next page): *Mineral chemistry of feldspar and muscovite. apfu: atom per formula unit.*

		LEKKERSMAAK GRANITE					WILLIE GRANITE
	sample	MUR 09-61	MUR 09-66	MUR 09-109	MUR 09-67	MUR 09-72	MUR 09-108
K-feldspar		*m=1, n=2*	*m=1, n=1*	*m=5, n=6*	*m=2, n=4*	*n=1*	
	SiO_2	63.81	64.09	64.36	64.57	65.79	
	Al_2O_3	18.49	18.56	18.38	18.43	18.60	
	CaO	0.41	0.25	0.59	0.22	2.47	
	Na2O	16.33	17.00	16.20	16.85	13.69	
	K2O	0.04	0.00	0.00	0.00	0.07	
	SUM	99.08	99.89	99.53	100.06	100.62	
		Structural formula based on 8 oxygen atoms					
	Si	2.98	2.98	2.99	2.99	3.00	
	Al	1.02	1.02	1.01	1.01	1.00	
	Ca	0.00	0.00	0.00	0.00	0.00	
	Na	0.04	0.02	0.05	0.02	0.22	
	K	0.97	1.01	0.96	1.00	0.79	
	SUM	5.01	5.03	5.01	5.01	5.01	
		End-member feldspar, mole %					
	An	0.22	0.00	0.00	0.00	0.33	
	Ab	3.65	2.15	5.24	1.93	21.49	
	Or	96.13	97.85	94.76	98.07	78.18	
plagioclase		*n=18, n=31*	*n=12, n=18*	*m=5, n=10*	*m=7, n=11*	*n=2*	*m=6, n=11*
	SiO2	67.16	66.03	66.00	67.21	66.29	67.4
	Al2O3	20.58	21.26	21.42	20.71	21.61	20.2
	CaO	10.90	10.37	10.28	10.70	10.35	11.1
	Na2O	0.10	0.10	0.10	0.08	0.11	0.1
	K2O	1.19	2.08	2.21	1.25	2.24	0.9
	SUM	99.93	99.83	100.01	99.95	100.60	99.6
		Structural formula based on 8 oxygen atoms					
	Si	2.94	2.90	2.90	2.94	2.89	2.96
	Al	1.06	1.10	1.11	1.07	1.11	1.04
	Ca	0.06	0.10	0.10	0.06	0.10	0.04
	Na	0.93	0.88	0.87	0.91	0.88	0.94
	K	0.01	0.01	0.01	0.00	0.01	0.00
	SUM	4.99	4.99	4.99	4.98	4.99	4.99
		End-member feldspar, mole %					
	An	5.65	9.91	10.57	6.12	10.61	4.16
	Ab	93.79	89.52	88.88	93.45	88.74	95.53
	Or	0.57	0.57	0.55	0.43	0.65	0.31
muscovite		*n=32*	*n=14*	*n=19*	*n=15*		*n=20*
	SiO2	46.46	46.24	45.21	45.22		46.20
	TiO2	0.69	0.72	0.97	0.64		0.84
	Al2O3	31.35	30.63	30.00	32.67		30.12
	FeO	4.07	4.51	4.71	4.28		5.02
	MnO	0.08	0.03	0.05	0.04		0.10
	MgO	1.39	1.42	1.36	0.69		1.69
	Na2O	0.24	0.24	0.26	0.34		0.18
	K2O	11.00	10.83	10.67	10.63		10.84
	SUM	95.29	94.61	93.23	94.51		94.98
		Structural formula based on 11 oxygen atoms					
	Si	3.15	3.16	3.15	3.09		3.16
	Ti	0.04	0.04	0.05	0.03		0.04
	Al	2.51	2.47	2.46	2.63		2.43
	Fe	0.23	0.26	0.27	0.24		0.29
	Mn	0.00	0.00	0.00	0.00		0.01
	Mg	0.14	0.14	0.14	0.07		0.17
	Na	0.03	0.03	0.03	0.04		0.02
	K	0.95	0.95	0.95	0.93		0.95
	SUM	7.05	7.05	7.06	7.05		7.07

Average electron microprobe analyses (wt.%) and corresponding structural formulae (apfu). m: number of grains, n: number of analyses

Figure 4: *Harker diagrams of the Lekkersmaak samples (black squares), plus S-types plutons worldwide (grey, dark grey for Archaean ones).*

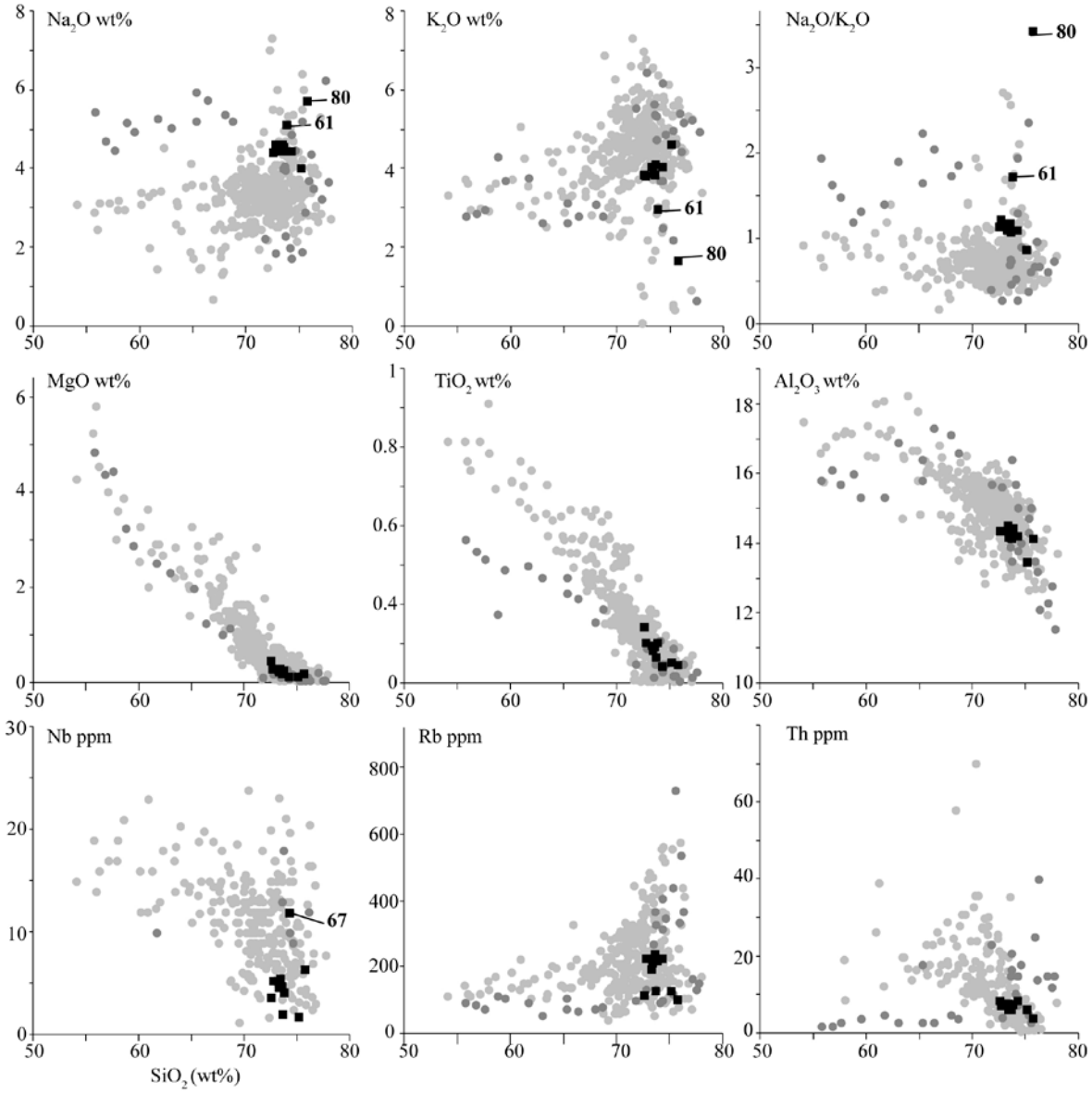

Trace elements contents (like Nb, Th or Rb) appear in the range of magmatic values (Fig. 5). REE elements show enriched LREE (La_N = 69 to 157) and fractionated patterns (La/Yb_N ratios from 10.0 to 80.7, Table 2, Fig. 5). HREE patterns show important variation (Yb_N = 1.1 to 8.3). The Eu anomaly is always negative (Eu/Eu* between 0.42 and 0.90) and some samples (MUR 09-72, MUR 09-108 MUR 18c and MUR 8a) show a small Ce negative anomaly.

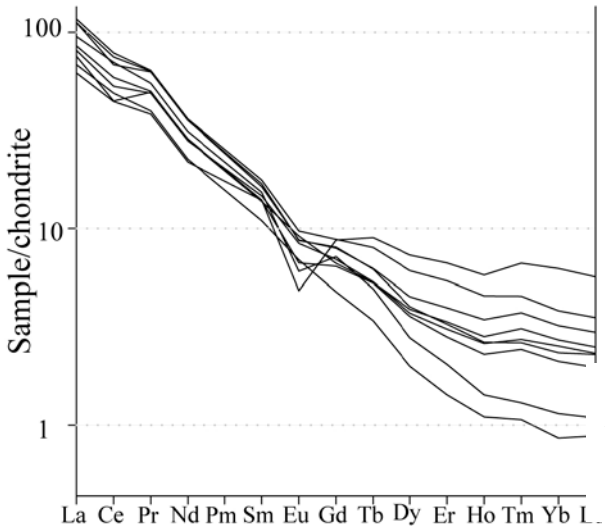

Figure 5: *REE patterns depicting a classic magmatic range of LREE content but a wide variation of HREE content.*

Table 2 (next page): *Whole rock chemistry. Major elements in wt%, trace elements in ppm and δ18O in ‰ vs SMOW. bdl: below detection limit. Errors and detection limits: see Carignan et al., 2001.*

			LEKKERSMAAK GRANITE										WILLIE GRANITE
		sample	MUR 09-60	MUR 09-61	MUR 09-63	MUR 09-66	MUR 09-109	MUR 18c	MUR 09-80	MUR 09-67	MUR 09-72	MUR 8a	MUR 09-108
		Mineralogy	porphyric	porphyric	ms-bt	ms-bt	bt-ms			gt-ms-bt	ms	ms?	Ms-Bt
	Detection limit	Analytical uncertainty											
SiO_2	0.50	< 1%	73.59	73.84	73.68	72.60	73.33	73.43	75.77	74.29	72.76	75.18	73.42
Al_2O_3	0.02	< 1%	14.34	14.43	14.11	14.34	14.49	14.21	14.14	14.21	14.33	13.44	14.15
Fe_2O_3	0.01	< 5%[a]	1.09	1.17	0.86	1.50	1.07	1.07	0.60	0.83	1.08	0.60	0.96
MnO	0.0005	< 10%[b]	0.02	0.03	0.01	0.02	0.03	0.03	0.03	0.02	0.02	0.01	0.02
MgO	0.02	< 10%	0.24	0.25	0.17	0.42	0.25	0.25	0.17	0.10	0.27	0.09	0.21
TiO_2	0.001	< 10%	0.19	0.21	0.13	0.28	0.19	0.19	0.09	0.09	0.21	0.11	0.17
CaO	0.035	< 5%	0.67	0.76	0.87	1.22	0.84	0.96	0.47	0.51	0.87	0.59	0.71
Na_2O	0.03	< 15%[c]	4.52	5.10	4.44	4.38	4.45	4.51	5.69	4.45	4.61	3.98	4.59
K_2O	0.01	< 5%	3.85	2.97	4.09	3.84	4.02	3.93	1.67	4.05	3.79	4.61	3.87
P_2O_5	0.05	> 25%[d]	0.05	0.06	*bdl*	0.15	0.07	0.06	*bdl*	*bdl*	0.06	*bdl*	0.06
LOI [e]		< 5%	0.83	0.81	0.77	0.64	0.84	1.02	0.98	0.69	0.81	0.83	1.00
SUM			99.39	99.63	99.14	99.39	99.58	99.66	99.60	99.24	98.80	99.45	99.15
A/NK			1.24	1.24	1.20	1.26	1.24	1.22	1.27	1.21	1.23	1.16	1.21
A/CNK			1.12	1.11	1.06	1.06	1.10	1.06	1.18	1.13	1.08	1.07	1.09
$\delta^{18}O_{WR}$			8.3	8.5	8.7	8.3	8.4		9.2	8.5	8.3	nd	8.4
La	0.06	< 5%	28.16	37.03	22.60	38.59	31.44	35.78	16.94	20.50	37.02	24.94	26.71
Ce	0.1	< 5%	50.93	64.82	42.37	67.93	60.87	55.86	33.09	38.44	59.13	38.67	45.95
Pr	0.008	< 5%	5.61	7.10	4.46	7.16	6.17	6.54	3.651	4.30	7.04	5.55	5.49
Nd	0.03	< 5%	17.78	22.52	14.18	22.81	19.61	20.98	11.37	13.73	22.44	17.97	17.58
Sm	0.007	< 5%	2.79	3.32	2.22	3.58	2.97	3.10	2.002	2.84	3.43	3.10	2.83
Eu	0.004	< 5%	0.70	0.67	0.53	0.75	0.65	0.62	0.366	0.37	0.67	0.47	0.52
Gd	0.02	< 5%	1.84	2.19	1.32	2.43	1.92	2.09	1.312	2.41	2.22	1.99	1.78
Tb	0.004	< 5%	0.25	0.29	0.16	0.38	0.25	0.28	0.183	0.42	0.29	0.23	0.25
Dy	0.007	< 5%[l]	1.33	1.55	0.69	2.10	1.28	1.47	0.897	2.51	1.37	0.96	1.23
Ho	0.001	< 10%	0.24	0.28	0.10	0.38	0.22	0.25	0.154	0.47	0.23	0.14	0.20
Er	0.003	< 10%[m]	0.64	0.78	0.25	1.02	0.59	0.66	0.397	1.31	0.60	0.32	0.52
Tm	0.005	> 25%[n]	0.09	0.11	0.03	0.14	0.08	0.09	0.058	0.20	0.08	0.04	0.07
Yb	0.003	< 10%	0.60	0.71	0.19	0.84	0.56	0.60	0.39	1.38	0.52	0.25	0.47
Lu	0.001	< 10%[o]	0.09	0.10	0.03	0.12	0.08	0.09	0.056	0.19	0.08	0.04	0.07
Y	0.4	> 25%[h]	7.13	9.66	2.88	11.71	7.08	8.10	4.605	14.88	7.42	3.86	6.42
La/Yb_N			31.8	35.4	80.7	31.0	38.1	40.6	29.3	10.0	48.5	66.8	38.8
Eu/Eu*			0.90	0.72	0.88	0.73	0.78	0.71	0.65	0.42	0.70	0.54	0.66
Cs	0.15	< 10%[g]	10.96	11.54	1.89	3.73	8.72	17.73	7.49	3.02	19.63	4.06	14.91
Rb	0.3	< 5%	240.6	221.4	127.2	118.7	193.0	216.3	102.5	225.0	228.9	131.9	230.40
Ba	1.5	< 5%	721.4	516.4	617.3	933.7	656.6	623.2	275.7	306.6	708.1	344.8	424.90
Sr	1.4	< 5%	312.9	262.8	272.1	483.6	282.1	267.6	217.5	110.7	311.9	159.7	246.00
Be	0.4	> 25%	4.05	3.88	0.84	0.94	3.00	3.53	7.93	2.32	3.92	0.47	3.55
Zr	0.8	< 8%	133.30	137.70	81.08	204.10	135.30	132.20	51.11	70.28	134.20	61.20	99.97
Hf	0.03	< 10%	3.85	3.93	2.57	5.07	3.89	3.63	1.79	2.72	3.74	1.89	3.25
Zr/Hf			34.59	35.00	31.60	40.24	34.75	36.38	28.54	25.89	35.87	32.35	30.73
Nb	0.06	< 10%	4.64	4.12	1.92	3.54	4.56	4.84	6.34	11.77	5.19	1.63	5.39
Ta	0.015	< 15%[i]	1.10	0.79	0.16	0.41	0.72	0.98	1.89	1.40	1.69	0.14	1.12
Nb/Ta			4.22	5.24	12.06	8.67	6.31	4.94	3.36	8.41	3.08	12.01	4.83
Th	0.02	< 10%	6.92	7.51	6.16	8.35	7.15	7.87	3.81	8.30	7.09	6.09	6.29
U	0.03	< 15%	1.74	1.66	0.63	0.95	1.89	3.12	0.94	4.76	1.81	0.98	1.84
Ni	4.5	> 25%	6.73	6.48	7.71	7.20	7.38	17.03	15.89	5.38	25.37	*bdl*	6.37
Cr	4	< 10%	17.69	21.49	54.80	20.46	13.59	14.03	22.01	11.05	17.11	12.48	22.03
Co	0.35	<15%	2.29	2.53	1.07	2.48	2.21	2.14	3.88	1.81	1.51	1.09	1.24
Cu	4.5	> 25%	6.18	*bdl*	*bdl*	*bdl*	*bdl*	7.82	10.76	*bdl*	5.74	*bdl*	5.57
Zn	14	> 25%	38.14	49.85	21.77	39.24	34.67	30.79	16.49	43.58	38.53	17.29	33.64
Pb	0.9	< 5%	18.11	14.51	20.74	21.28	19.06	18.43	16.83	23.92	21.74	24.09	19.64
Bi	0.1	> 25%	0.14	*bdl*	*bdl*	*bdl*	*bdl*	0.21	*bdl*	*bdl*	*bdl*	*bdl*	0.16
Sb	0.1	< 10%	*bdl*	*bdl*	*bdl*	*bdl*	*bdl*	0.11	0.18	*bdl*	*bdl*	*bdl*	*bdl*
As	1.1	> 25%	*bdl*	*bdl*	*bdl*	*bdl*	1.60	2.00	1.94	*bdl*	1.71	*bdl*	*bdl*
W	0.2	> 25%	*bdl*	0.22	*bdl*	*bdl*	0.30	*bdl*	1.10	0.22	*bdl*	*bdl*	0.27
Cd	0.12	> 25%	*bdl*	0.13	*bdl*	*bdl*	*bdl*	*bdl*	*bdl*	*bdl*	*bdl*	*bdl*	*bdl*
Sn	0.4	< 15%	1.63	2.00	1.43	2.53	1.72	2.13	1.66	4.78	1.82	1.23	2.04
V	0.45	> 25%[j]	9.51	9.45	5.89	14.08	8.88	8.68	6.90	3.48	9.32	3.80	7.94
Ga	0.2	< 5%	22.04	21.26	18.04	17.91	22.56	21.21	24.94	24.07	20.22	16.50	28.85
Ge	0.11	> 25%[k]	0.88	0.96	0.69	0.74	0.82	0.81	1.02	1.02	0.94	0.70	1.02
Mo	0.3	> 25%	*bdl*	*bdl*	0.31	*bdl*	*bdl*	0.72	1.45	*bdl*	*bdl*	*bdl*	0.72

ms: muscovite; gt: garnet; WR: whole rock; bdl: below detection limit; nd : undetermined. La/YbN normalized to chondrite (Evansen 1978)

U-Pb geochronology

We dated five samples that account for the petrologic, mineralogic and chemical variabilities of the pluton in terms of facies, muscovite–bearing and muscovite–free samples, muscovite of primary-secondary signature, anomalous chemical features (sodic MUR 09-80). This sampling covers most of the intrusion (eastern and western lobes, border and core, as well as the Willie body).

For each sample, the U-Pb zircon dataset is presented individually in Table 3. In general, zircon grains are primatic. Cathodoluminescence imaging reveals that most of the grains are characterized by a bright "core" with well-defined oscillatory zoning, surrounded by darker rims. Individual $^{207}Pb/^{206}Pb$ dates calculated for each sample from the Lekkersmaak pluton range from 2781± 13 Ma (MUR 09-80; MSWD=0.24) down to 2757 ± 17 Ma (MUR 09-66; MSWD=1.9) Ma and are therefore undistinguishable within error. Therefore we selected the most concordant data and calculated a concordia age of 2774.5 ± 6.8 Ma (MSWD=0.0034, Fig. 6), that we consider as representative of the emplacement age of the Lekkersmaak pluton. This age is confirmed by a weighted average $^{207}Pb/^{206}Pb$ age of 2774.5 ± 6.6 Ma (MSWD=0.43, prob=0.997) calculated for all the data points that are strictly ±5% within concordancy. This age is older than the U-Pb zircon age of 2690 ± 65 Ma previously published by Burger and Walraven (1979) for what was then described as a porphyroblastic biotite granite (sample GJ1032), but is younger than the age of 2795 ± 8 Ma recently published by Zeh et al. (2009) for sample MB1. Both these samples were collected on the southern edge of the Lekkersmaak pluton, but no indications are provided regarding their respective petrology and/or chemistry. As our sampling covers quite an extensive area of the pluton, that the samples chemical and petrological characteristics show a rather good correlation, and because we are sure of their provenance, we consider that the Lekkersmaak magmatic intrusion likely represents one single crystallisation episode at ca 2.75 Ga at the scale of the pluton. We cannot completely rule out, however, that the emplacement of the Lekkersmaak pluton was, at least in part, episodic with the existence of an older and possibly younger intrusive event(s), or that it was intruded by a later phase. This seems to be confirmed by the data obtained on sample MUR 09-64, where the zircon population yields a ^{207}Pb-^{206}Pb mean date of 2741 ± 9 Ma (Table 3) demonstrating the existence of a late (muscovite-free) phase intrusive into the Lekkersmaak granite.

Table 3 (next page): *Zircon dating isotopic data.*

Sample	grain-spot	Chemistry			Isotopic ratios							Ages					
		Pb (ppm)	U (ppm)	Th/U	$^{207}Pb/^{235}U$	error	$^{206}Pb/^{238}U$	error	ρ	$^{207}Pb/^{206}Pb$	error	^{235}U-^{207}Pb	^{238}U-^{206}Pb	^{207}Pb-^{206}Pb	±	Conc[1] %	age[2]
	8-core	*10*	*15*	*2.627*	*14.508*	*0.193*	*0.5436*	*0.0065*	*0.904*	*0.1935*	*0.0024*	*2784*	*2799*	*2772*	*20*	*101*	
	6-core	*20*	*27*	*3.719*	*14.280*	*0.182*	*0.5364*	*0.0064*	*0.933*	*0.1930*	*0.0022*	*2769*	*2769*	*2768*	*19*	*100*	
	4-core	*24*	*34*	*3.633*	*14.924*	*0.189*	*0.5561*	*0.0067*	*0.945*	*0.1946*	*0.0022*	*2810*	*2850*	*2782*	*18*	*102*	
	3-core	43	72	2.608	13.500	0.165	0.5170	0.0061	0.969	0.1894	0.0020	2715	2686	2737	18	98	
MUR 09-66	1-core	16	25	3.653	12.270	0.156	0.4664	0.0056	0.948	0.1908	0.0022	2625	2468	2749	18	90	**2775 ± 21**
	1-border	91	190	0.351	11.444	0.139	0.4426	0.0053	0.979	0.1875	0.0020	2560	2362	2720	17	87	
	14-core	38	71	1.457	11.629	0.155	0.4432	0.0052	0.885	0.1903	0.0023	2575	2365	2745	20	86	
	5-core	21	32	4.239	13.092	0.166	0.4897	0.0058	0.941	0.1939	0.0022	2686	2570	2775	18	93	
	6-border	35	63	2.509	12.147	0.153	0.4563	0.0054	0.942	0.1930	0.0022	2616	2423	2768	18	88	
	8-border	125	255	0.291	11.583	0.145	0.4477	0.0053	0.941	0.1876	0.0021	2571	2385	2722	18	88	
	9-core	42	73	0.618	13.546	0.171	0.5002	0.0059	0.932	0.1964	0.0022	2719	2615	2796	18	93	
	3-core	*21*	*35*	*0.551*	*14.168*	*0.160*	*0.5361*	*0.0056*	*0.921*	*0.1916*	*0.0022*	*2761*	*2767*	*2756*	*18*	*100*	
	4-core	*22*	*36*	*0.594*	*14.313*	*0.164*	*0.5349*	*0.0055*	*0.904*	*0.1940*	*0.0022*	*2771*	*2762*	*2776*	*19*	*99*	
	6-core	*56*	*80*	*1.062*	*14.347*	*0.154*	*0.5381*	*0.0053*	*0.927*	*0.1933*	*0.0021*	*2773*	*2775*	*2771*	*18*	*100*	
	7-core	*46*	*68*	*0.898*	*14.232*	*0.154*	*0.5357*	*0.0053*	*0.917*	*0.1926*	*0.0022*	*2765*	*2765*	*2765*	*18*	*100*	
	8-core	*66*	*105*	*0.512*	*14.272*	*0.152*	*0.5329*	*0.0052*	*0.925*	*0.1942*	*0.0021*	*2768*	*2754*	*2778*	*18*	*99*	
	9-core	*36*	*54*	*0.830*	*14.437*	*0.180*	*0.5376*	*0.0056*	*0.831*	*0.1947*	*0.0025*	*2779*	*2773*	*2782*	*21*	*100*	
	14-core	*41*	*60*	*0.636*	*14.548*	*0.160*	*0.5404*	*0.0051*	*0.865*	*0.1952*	*0.0023*	*2786*	*2785*	*2787*	*19*	*100*	
MUR 09-109	*15-core*	*22*	*32*	*0.638*	*14.430*	*0.166*	*0.5398*	*0.0052*	*0.838*	*0.1938*	*0.0024*	*2778*	*2783*	*2775*	*20*	*100*	**2776.0 ± 6.5**
	16-core	*12*	*18*	*0.408*	*14.572*	*0.176*	*0.5404*	*0.0053*	*0.812*	*0.1955*	*0.0025*	*2788*	*2785*	*2789*	*21*	*100*	
	16-border	*47*	*75*	*0.170*	*14.509*	*0.160*	*0.5410*	*0.0051*	*0.852*	*0.1945*	*0.0024*	*2784*	*2788*	*2780*	*20*	*100*	
	1-core	36	58	0.890	14.028	0.157	0.5274	0.0055	0.937	0.1929	0.0021	2752	2731	2767	18	99	
	2-core	24	40	0.656	14.031	0.159	0.5236	0.0055	0.921	0.1943	0.0022	2752	2715	2779	18	98	
	2-border	209	393	0.078	13.740	0.146	0.5191	0.0053	0.962	0.1920	0.0020	2732	2695	2759	17	98	
	11-border	77	125	0.674	13.275	0.142	0.4994	0.0048	0.896	0.1927	0.0022	2699	2611	2765	19	94	
	12-core	24	37	0.620	14.007	0.158	0.5187	0.0051	0.863	0.1958	0.0024	2750	2694	2791	20	97	
	5-core	66	96	0.827	14.866	0.160	0.5583	0.0056	0.931	0.1931	0.0021	2807	2859	2768	18	103	
	13	204	267	0.426	20.150	0.212	0.6172	0.0058	0.896	0.2367	0.0027	3099	3099	3098	18	100	
	15-core	*27*	*39*	*0.636*	*14.577*	*0.183*	*0.5387*	*0.0059*	*0.873*	*0.1961*	*0.0024*	*2788*	*2778*	*2794*	*20*	*99*	
	7	48	74	0.488	15.209	0.185	0.5663	0.0066	0.952	0.1946	0.0021	2828	2893	2781	18	104	
	10	9	13	0.597	15.643	0.208	0.5891	0.0069	0.878	0.1924	0.0024	2855	2986	2763	21	108	
	12-core	18	28	0.575	13.887	0.179	0.5204	0.0059	0.878	0.1933	0.0024	2742	2701	2771	20	97	
MUR-09-80	14-core	84	126	0.672	13.952	0.161	0.5213	0.0056	0.929	0.1939	0.0022	2747	2705	2776	18	97	**2781.8 ± 6.7**
	16	63	78	0.992	15.292	0.178	0.5666	0.0059	0.898	0.1956	0.0023	2834	2894	2790	19	104	
	18	136	193	0.186	15.553	0.174	0.5794	0.0059	0.907	0.1946	0.0022	2850	2946	2782	19	106	
	19-core	50	67	0.462	15.478	0.177	0.5745	0.0059	0.891	0.1954	0.0023	2845	2926	2788	19	105	
	21	63	79	0.826	14.919	0.169	0.5549	0.0056	0.884	0.1950	0.0023	2810	2846	2785	19	102	
	5-core	84	137	0.373	16.211	0.204	0.5617	0.0068	0.959	0.2092	0.0023	2889	2874	2899	18	100	
	2-border	*97*	*176*	*0.175*	*14.280*	*0.211*	*0.5333*	*0.0072*	*0.905*	*0.1942*	*0.0024*	*2791*	*2818*	*2771*	*18*	*102*	
	2-core	15	26	0.615	13.638	0.213	0.5103	0.0070	0.879	0.1939	0.0026	2723	2657	2772	20	96	
MUR 09-72	3-core	39	60	0.833	14.541	0.220	0.5429	0.0073	0.888	0.1943	0.0025	2819	2874	2779	19	103	**2779 ± 19**
	7-core	80	138	0.374	13.526	0.181	0.5108	0.0065	0.948	0.1920	0.0022	2717	2660	2760	18	96	
	7-border	146	265	0.224	13.350	0.177	0.4959	0.0063	0.953	0.1952	0.0022	2705	2596	2787	18	93	
	12-core	24	36	0.660	14.168	0.204	0.5262	0.0066	0.873	0.1952	0.0026	2761	2725	2787	21	98	
	1-border	*18*	*27*	*0.591*	*15.222*	*0.186*	*0.5612*	*0.0057*	*0.827*	*0.1967*	*0.0025*	*2829*	*2872*	*2799*	*21*	*103*	
	3-core	*9*	*14*	*0.436*	*15.260*	*0.197*	*0.5590*	*0.0057*	*0.791*	*0.1980*	*0.0027*	*2832*	*2863*	*2809*	*22*	*102*	
	4	*22*	*34*	*0.598*	*14.828*	*0.186*	*0.5513*	*0.0055*	*0.796*	*0.1950*	*0.0026*	*2804*	*2831*	*2785*	*21*	*102*	
	5	*51*	*71*	*0.908*	*15.135*	*0.184*	*0.5607*	*0.0055*	*0.804*	*0.1957*	*0.0025*	*2824*	*2870*	*2791*	*21*	*103*	
	6	*33*	*49*	*0.702*	*15.075*	*0.207*	*0.5560*	*0.0068*	*0.893*	*0.1966*	*0.0024*	*2820*	*2850*	*2798*	*20*	*102*	
	6	*36*	*55*	*0.560*	*14.995*	*0.204*	*0.5493*	*0.0067*	*0.898*	*0.1979*	*0.0024*	*2815*	*2822*	*2809*	*20*	*100*	
	7	*31*	*46*	*0.634*	*15.154*	*0.212*	*0.5494*	*0.0068*	*0.878*	*0.2000*	*0.0025*	*2825*	*2823*	*2826*	*20*	*100*	
	8	*15*	*24*	*0.574*	*14.790*	*0.215*	*0.5412*	*0.0067*	*0.854*	*0.1982*	*0.0026*	*2802*	*2788*	*2811*	*22*	*99*	
MUR 09-108	*10-border*	*66*	*101*	*0.461*	*15.226*	*0.207*	*0.5478*	*0.0066*	*0.879*	*0.2015*	*0.0025*	*2830*	*2816*	*2839*	*20*	*99*	**2817.0 ± 10**
	11	*17*	*26*	*0.547*	*15.043*	*0.222*	*0.5426*	*0.0067*	*0.832*	*0.2010*	*0.0028*	*2818*	*2794*	*2835*	*22*	*99*	
	12	*34*	*49*	*0.757*	*14.846*	*0.210*	*0.5446*	*0.0065*	*0.842*	*0.1977*	*0.0026*	*2806*	*2802*	*2807*	*21*	*100*	
	13	*28*	*44*	*0.447*	*14.950*	*0.220*	*0.5461*	*0.0066*	*0.820*	*0.1985*	*0.0027*	*2812*	*2809*	*2814*	*22*	*100*	
	15	*54*	*75*	*0.975*	*14.940*	*0.216*	*0.5368*	*0.0064*	*0.819*	*0.2018*	*0.0028*	*2811*	*2770*	*2841*	*22*	*98*	
	16	*80*	*116*	*0.668*	*15.054*	*0.219*	*0.5477*	*0.0064*	*0.808*	*0.1993*	*0.0028*	*2819*	*2816*	*2820*	*22*	*100*	
	17-border	*119*	*166*	*0.705*	*15.043*	*0.224*	*0.5465*	*0.0064*	*0.788*	*0.1996*	*0.0029*	*2818*	*2811*	*2823*	*23*	*100*	
	9	31	56	0.552	12.506	0.175	0.4550	0.0055	0.871	0.1993	0.0025	2643	2417	2820	21	86	
	2-core	18	23	0.376	23.603	0.341	0.6556	0.0074	0.778	0.2611	0.0039	3252	3250	3253	24	100	
	2-border	22	26	0.651	23.706	0.287	0.6763	0.0068	0.833	0.2542	0.0032	3256	3330	3211	20	104	
	2	24	48	0.724	12.998	0.307	0.5052	0.0116	0.971	0.1866	0.0020	2680	2636	2713	18	97	
	3	28	53	0.787	13.508	0.312	0.5241	0.0119	0.985	0.1869	0.0020	2716	2716	2716	17	100	
	7	11	22	0.601	13.338	0.317	0.5204	0.0119	0.959	0.1859	0.0020	2704	2701	2706	18	100	
	10	41	78	0.862	13.223	0.308	0.5078	0.0114	0.968	0.1888	0.0020	2696	2647	2732	17	97	
	12	21	39	0.923	13.650	0.321	0.5201	0.0117	0.957	0.1903	0.0021	2726	2700	2745	18	98	
	12-border	57	117	0.373	13.699	0.315	0.5266	0.0118	0.970	0.1886	0.0020	2729	2727	2730	17	100	
	13	22	41	0.759	13.752	0.324	0.5225	0.0117	0.954	0.1908	0.0021	2733	2710	2749	18	99	
	14	29	55	0.829	13.355	0.316	0.5145	0.0116	0.950	0.1882	0.0021	2705	2676	2726	18	98	
	15	14	27	0.782	13.216	0.317	0.5020	0.0113	0.939	0.0747	0.0009	2695	2622	2750	18	95	
	16	12	21	0.906	13.953	0.338	0.5313	0.0119	0.929	0.1904	0.0022	2747	2747	2745	19	100	
MUR 09-64	16	17	33	0.736	13.916	0.331	0.5308	0.0118	0.939	0.1901	0.0021	2744	2745	2743	18	100	**2741.1±9.1**
	17	24	46	0.844	13.482	0.322	0.5086	0.0114	0.935	0.1922	0.0022	2714	2651	2761	18	96	
	18	13	27	0.832	12.440	0.310	0.4756	0.0107	0.905	0.1897	0.0022	2638	2508	2739	19	92	
	18	24	48	0.753	13.125	0.320	0.5141	0.0115	0.916	0.1851	0.0021	2689	2674	2699	19	99	
	19	59	121	0.487	13.684	0.322	0.5184	0.0114	0.938	0.1914	0.0021	2728	2692	2754	18	98	
	20	156	359	0.334	12.532	0.295	0.4790	0.0106	0.936	0.1897	0.0021	2645	2523	2739	18	92	
	21	18	35	0.686	14.013	0.340	0.5308	0.0117	0.910	0.1914	0.0022	2751	2745	2754	19	100	
	22-core	48	95	0.946	12.931	0.316	0.4936	0.0109	0.905	0.1900	0.0022	2675	2586	2742	19	94	
	23	36	67	0.796	14.262	0.344	0.5344	0.0117	0.911	0.1935	0.0022	2767	2760	2772	19	100	
	24	15	29	0.697	14.223	0.349	0.5347	0.0118	0.899	0.1929	0.0023	2765	2761	2767	19	100	
	25	58	120	0.663	12.839	0.313	0.4840	0.0106	0.901	0.1924	0.0022	2668	2544	2763	19	92	
	26	89	184	0.460	13.548	0.327	0.5076	0.0111	0.903	0.1936	0.0022	2719	2646	2773	19	95	

1: concordance of ages, only data with concordance > 85%. 2: upper intecept age at 2σ. All other errors at 1σ. In italic data used to calculate concordia ages.

One stricking feature however is the quasi-absence of inheritance shown by the zircon age data spectrum, as only two older ages were found out of 44 analyses (3098 ± 18 Ma and 2899 ± 18 Ma respectively). Furthermore, no inherited cores were identified during the CL imaging. S-type granites are known to typically contain a substantial fraction of inherited cores representative of the heterogeneity of the source (see review in Villaros et al., 2012 for example). Several explanations could be proposed at this stage. This could be due to an analytical bias during the grains selection. Although we cannot completely rule out this hypothesis, all the grain types were selected during the handpicking phase. Another explanation could be that the zircon dated in this study crystallized very late or that the Zr saturation level was very high (such as the one usually encountered in I-type magmas). Alternatively, the source of this S-type granite could have contained very little zircon grains to start with. We can immediately discard the possibility that the source was mostly mafic as it has been demonstrated that a source with more than 10% of mafic material leads to the production of a metaluminous magma (Collins 1998).

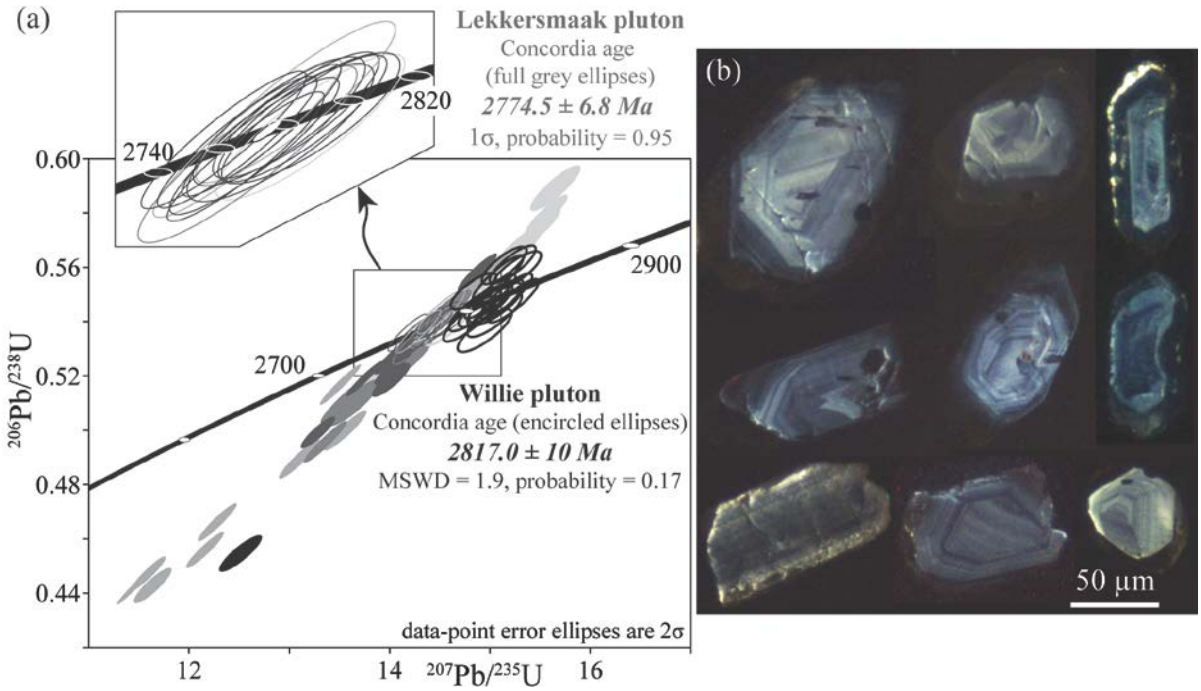

Figure 6: *(a) Concordia diagrams of various samples from the Lekkersmaak pluton (each grey for a sample) and Willie pluton (black). Isoplot software of Ludwig (2000). (b) cathodo-luminescent imaging of zircon grains (the grains three at the bottom are from the Willie sample).*

Zircon grains from the Willie sample look like the Lekkersmaak ones. They provided concordant to sub-concordant isotopic data (Fig. 6). These data allow to calculate a concordant crystallization age of 2817 ± 10 Ma. This age is consistent with an ID-TIMS U-Pb age obtained on single zircon grains at 2820 ± 38 Ma (Poujol, 2001). This confirms that the Willie pluton is significantly older than the Lekkersmaak intrusion. One zircon $^{207}Pb/^{206}Pb$ date of 3253 ± 24 Ma is inherited in the Willie sample. This date is within error with the age of the French Bob Mine granite dated at 3228 ± 12 Ma (Poujol et al., 1996).

Radiogenic isotopes

Isotopic analyses of the Sm-Nd and Sr-Rb systems are presented in Table 4, and the U-Pb ages are used to calculate the I_{Sr} and εNd parameters. εNd values are near-chondritic at the time of crystallisation (1.32 to -1.05) with T_{DM} ages that are 139 to 342 Ma older than the crystallisation age (with the exception of sample MUR 09-80[4]). I_{Sr} show variable values from 0.6824 to 0.7268, most of them being consequently below the BABI value of 0.699 (MUR 09-60, 61, 67, 109 and 108). Such abnormally low values indicate that the Rb-Sr system has been perturbed since crystallization.

sample	Sm (ppm)	Nd (ppm)	$^{147}Sm/^{144}Nd$	$^{143}Nd/^{144}Nd$	εNd [1] at 2.775 Ga	T_{DM} [2] (Ma)	Rb [3] (ppm)	Sr [3] (ppm)	$^{87}Rb/^{86}Sr$	$^{87}Sr/^{86}Sr$	I_{Sr} [4] at 2.78 Ga
MUR 09-60	2.788	17.78	0.090541	0.510680	-0.23	3041	241	313	2.2411	0.7830	0.6929
MUR 09-61	3.316	22.52	0.085884	0.510558	-0.95	3100	221	263	2.4575	0.7919	0.6931
MUR 09-63	2.224	14.18	0.089507	0.510624	-0.96	3100	127	272	1.3590	0.7566	0.7020
MUR 09-66	3.581	22.81	0.087162	0.510576	-1.05	3108	119	484	0.7117	0.7302	0.7016
MUR 09-109	2.974	19.61	0.087780	0.510666	0.49	2982	193	282	1.9928	0.7768	0.6967
MUR 09-67	2.836	13.73	0.119418	0.511288	1.32	2914	225	111	6.0049	0.9237	0.6824
MUR 09-80	2.002	11.37	0.102811	0.509994	-18.12	4492	103	218	1.3734	0.7820	0.7268
MUR 09-108[5]	2.830	17.58	0.093023	0.510671	-0.78	3117	230	246	2.7360	0.8067	0.6950

1: parameters $^{143}Nd/^{144}Nd_{CHUR} = 0.512638$; $^{147}Sm/^{144}Nd$ CHUR = 0.1967; ^{147}Sm: $\lambda = 6.54 \times 10^{-12}$. 2: from Goldstein et al. 1984. 3: mesured by ICP-MS. 4: I_{Sr} = initial $^{87}Sr/^{86}Sr$; ^{87}Rb $\lambda = 1.42 \times 10^{-11}$; 5: εNd and I_{Sr} calculated with t=2817 Ma

Table 4: *Sm-Nd and Rb-Sr isotopic compositions.*

Stable isotope characterization

The oxygen isotope compositions display a very narrow range ($\delta^{18}O$ values from 8.2 to 8.7‰), with the exception of sample MUR 09-80 at a higher value of 9.2‰ (Fig. 8). These signatures are expected for granitic rocks (Taylor and Hugh 1978) but actually low for S-type granites that generally have $\delta^{18}O$ values above 10‰ (e.g. in Himalayan leucogranites, France-Lannord et al., 1988; in Australian batholith, O'Neil et al., 1977).

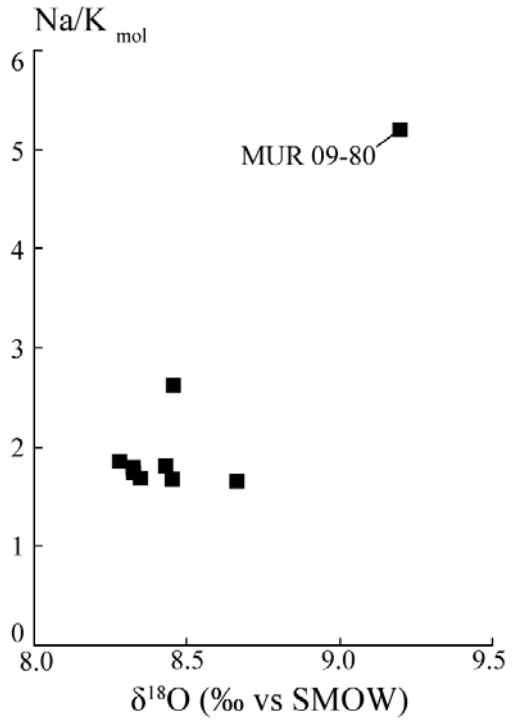

Figure 7: *Na/K mol ratio versus $\delta^{18}O$ whole rock values.*

[4] for which much doubt remains about the $^{143}Nd/^{144}Nd$ value and this sample will be duplicate in a new analytical session

DISCUSSION

S-type character of the Lekkersmaak intrusion

Archaean terranes usually contain very rare S-types plutons. Therefore some unusual geologic conditions (source of the granite, PT conditions of melting) must account for the production of the Lekkersmaak granite to the south of the Murchison Greenstone Belt. Before constraining these conditions, we need to confirm that the peraluminous signature of Lekkersmaak and Willie granites results from magmatic process. We first have to evaluate the level of chemical alteration of the samples. In the region and in particular in the Antimony Line, albitization is the main form of granitoids alteration and is broadly coeval with Lekkersmaak emplacement at ca 2.8 Ga (Jaguin et al., submitted). As an example, sample MUR 09-80 and to a lesser extent sample MUR 09-61 combine several chemical anomalies in Na_2O and K_2O contents, Na_2O/K_2O ratio (Fig. 4), $\delta^{18}O$ (Fig. 7), and Sr-Rb and Sm-Nd isotopic compositions (Table 4). Those features are not associated with any special mineralogical or textural features. It rather indicates a discrete albitization. Once these two samples are excluded, the Na, Ca and K content of other samples are very homogeneous, which argues for an unaltered alkaline signature and ensures the petrological significance of the A/CNK (1.06 to 1.13) and A/NK (1.16 to 1.24) ratios.

On a mineralogical point of view, we targeted white mica because it is a widespread alteration mineral in igneous rocks as well as a magmatic mineralogical indicator of high-aluminum magma. Figure 3b shows that most of muscovite grains fall within the primary magmatic field. Moreover, it is possible to evaluate texturally the primary or secondary origin of muscovite. Textural criteria of secondary muscovite origin are small grain size, association with secondary minerals (epidode, titanite; Fig. 2e) instead of magmatic mineral (biotite, zircon; Fig. 2d) and occurrence in close association with dissolution figures, sheared zones or in recrystallised zones. These mineralogical characteristics correlate well with chemical analyses, i.e., texturally identified secondary-type muscovite fall within the field of secondary muscovite in fig. 3b. From that, we infer that MUR 09-60, MUR 09-80, MUR 09-81 and MUR 8a very likely bear magmatic muscovite (in addition to secondary muscovite) but foliated sample MUR 09-72 is still doubtful regarding that point.

We thus conclude on the basis of mineralogical and geochemical characteristics that the Lekkersmaak suite is a Mg-Fe-Ca poor and moderately peraluminous S-type granite. It differs from classical S-types plutons on several points. First it is on average more sodic and less potassic than typical S-type granites, consistent with the overall poor anorthite content of the plagioclase. Secondly, its high $(La/Yb)_N$ ratio is more similar to Archaean TTG granitoids (> 30) rather than S-types granites or post-archaean granitoids (most S-types in the database used are post-archaean); nevertheless, the measured Eu negative anomaly resembles those of typical S-granites. Finally, the dated zircon grains show almost no inheritance.

Petrogenesis of the Lekkersmaak intrusion

Source of the Lekkersmaak suite

S-type granites result from melting of an immature clastic sedimentary rock. Various constraints help to define the type of sedimentary sequence likely involved. First of all, the Lekkersmaak pluton is large. Assuming a laccolith shape with a thickness versus length ratio of 1:10 and a melting rate of 30 %, the metasedimentary package involved in melting must have represented a volume of about 5700 km^3. It comes from this crude estimate that the genesis of the pluton required the burial of a rather large sedimentary basin.

The Kaapvaal Craton is known to contain such thick sedimentary and pellitic sequences in the Witwatersrand basin, deposited after 3.05-2.97 Ga and prior to 2.74 Ga. In addition to being older than the Lekkersmaak intrusion, Witwatersrand sediments display Sm-Nd signatures consistent with signatures of the Lekkersmaak granite (εNd =-3 to 0 at 2.8 Ga, T_{DM} = 3.35-3.12 Ga; Jahn and Condie 1995). Besides, the $\delta^{18}O$ value of the sediments ($\delta^{18}O$ between 8 and 13‰) show a tendency to become lower as the granulometry gets smaller (Barton et al., 1992; Vennemann et al., 1992, 1996; Jaguin et al., 2010), so that shales are expected to have quite low $\delta^{18}O$ signatures. As a source, it would impose a comparable low $\delta^{18}O$ value of any melt produced, comparable to the one actually measured in the Lekkersmaak samples. Nevertheless, the Witwatersrand basin is now preserved 300 km away from the Lekkersmaak pluton, whereas the Murchison Belt exposed aluminous sedimentary rocks immediately to the north of the Lekkersmaak suite, namely the La France Formation (Fig. 1b). These sediments were produced by erosion of the Barberton and of the Ancient Gneiss terrains (U-Pb and Hf on zircon, Zeh et al., in prep). The rare inherited zircon grains from the Lekkersmaak and Willie plutons (ca 3.25 and 3.10 Ga) fit with the age peaks found for the La France zircon populations (at ca 3.28 and 3.13 Ga). The inherited zircon grain dated at 2.90 Ga may be recycled from a Maranda type of rock.

Accordingly, we used in our modelling two aluminous sediments as potential protoliths for the Lekkersmaak and the Willie granites, a metasediment from the La France Formation (MUR 18D) and a Witwatersrand shale (Roodeport Group, Wronkiewicz and Condie, 1987). Modelling produced granitic liquids with similar major elements distribution than the one measured in the two plutons (Fig. 8), although the model using the Witwatersrand argillites displays isopleths that are more parallels to the P axis at low P for Na, K and N/K ratio than the model using the La France protolith.

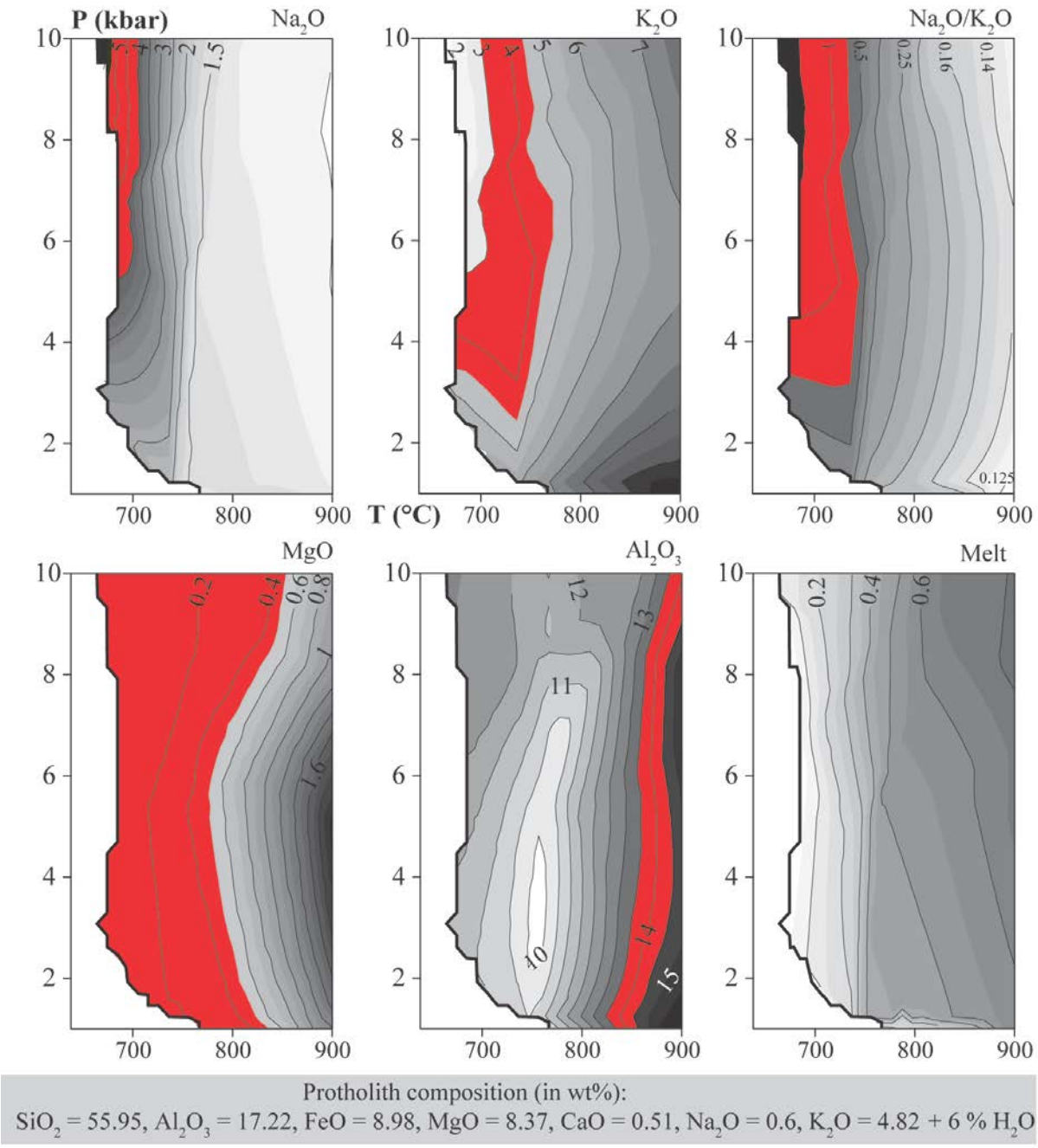

Figure 8: *P-T grid with major element content and melt proportion after modelisation of MUR18D melting. The red areas correspond to Lekkersmaak and Willie content or ratio.*

On the other hand, modelling failed to reproduce the aluminum content found in the two plutons. In the models, the Al_2O_3 content shows a negative correlation with SiO_2 as it is usually observed in S-type granites (Fig. 4), but the melts produced are poorer in Al_20_3 by about 2 wt.% relative to natural granites. Two hypotheses can explain the deficit in aluminum in our models. First, the source of the Lekkersmaak granite may have been more aluminous than the protoliths used for modelling. For example Post Archaean Australian Shales (PAAS) have an Al_2O_3 content of 18.9 wt.% (Taylor and McLennan, 1985), at least 2 wt.% higher than the Al content of the La France schist (Al_2O_3 = 17.2 %) or the Witwatersrand shale (Al_2O_3 = 15.1 wt.%).

Secondly, aluminium may have been preferentialy stored in the residue instead of the melt. In our models, Al is stored in the residue in cordierite (mostly at low P) and garnet (at higher P), plus in minor quantity in sillimanite. Both garnet and cordierite are Fe-Mg phases. The protoliths used for modelling are significantly richer in Fe and Mg than usual shales (FeO + MgO = 15.5 and 16.3 wt.% in our models compared to 9 wt.% maximum for PAAS). Therefore, a Fe and/or Mg rich protolith may produce a modal excess of cordierite or garnet in the residue. Moreover, sequestration of Al in garnet may be amplified by the parameters used in our modelling that set Fe as Fe^{2+}. Indeed, this setting deprives the phases such as garnet in Fe^{3+} so that Al^{3+} may substitute to it. However, garnet measured in our sample has Fe as Fe^{2+} and more generally reduced Fe is the most common form of Fe in S-type granites (Chappell and White, 1974). It is therefore likely that the Lekkersmaak source had a higher Al_2O_3/(FeO + MgO) ratio than the protoliths we tested.

Conditions of partial melting

The Murchison Belt terrain has a protracted tectonic history from 2.97 to 2.78 Ga with two metamorphic episodes dated at 2.97-2.92 and 2.79-2.75 Ga (Block et al., 2012; Jaguin et al., 2012; Jaguin et al., submitted). Tectonic has been attributed to a sagduction process during NE-SW directed horizontal shortening to explain the overall distributed structural pattern found in the belt and in the adjacent granitoids (Jaguin et al., 2012), coeval with localization along shear zones during metamorphic juxtaposition (Block et al. 2012). This sagducting process involved important burial of supracrustal rocks from the belt within the weak underlying rocks. The depth of this downward vertical displacement can reach at the very least 9 km, as shown by the present-day maximum depth of the belt (de Beer et al. 1984).

Besides, staurotide-bearing micaschists as well as quartz-kyanite veins in the La France micaschists evidence medium pressure, medium temperature metamorphism in the belt. Block et al. (2012) estimated for the La France Formation peak P-T conditions of ca. 8–9 kbar, 600–650°C and then decompression toward ca. 5–6 kbar, 580°C. This means that the La France Formation underwent upper amphibolic facies metamorphism. These are metamorphic conditions comparable to phanerozoic-like geothermal gradients which commonly produce partial melting at depth. It is then predictable that, if sediments were buried at deeper levels, the immediate underlying structural level should have experienced partial melting P-T conditions. It follows that the emplacement of the Lekkersmaak intrusion along the southern contact of the belt strongly suggests that it resulted from the melting of lithologies belonging to the belt. Taking into consideration time constrains, this melting process must have happened during the late stage of the tectono-metamorphic history, possibly in relation with the decompression of the La France Formation closer to the surface.

Modelling can help specifying the P-T field for the partial melting. The fact that modelling of two different protoliths led to comparable melts in major elements demonstrates that partial melting buffers the melt composition. This is due to the

involvement of the same partial melting reaction (biotite dehydration-melting in both cases). Yet, condition of melting has to explain two peculiarities of the Lekkersmaak granite: (1) the high Na/K ratio and (2) the $(La/Yb)_N$ large variation. To account for the high Na_2O/K_2O ratio in our models, low temperatures of melting are required (i.e. low partial melting rates, < 720°C) whereas pressure is not well constrained (P = 3.5 to 7 kbar for the La France model and 2-7 kbar for the Witwatersrand model). Noteworthy the Witwatersrand argillite has normal, PAAS-like Na_2O/K_2O ratio (0.30), but the La France metasediments have low Na_2O/K_2O ratio (0.12). In both cases, a low partial melting rate seems sufficient to induce reversal of that ratio toward theLekkersmaak granite values.

Trace elements are useful to bracket the pressure condition. Our models show what is known for a long time, i.e. that the $(La/Yb)_N$ ratio is controlled by garnet in the residue (Fig. 9): HREE content is inversely correlated to garnet modal isopleths, while Lanthanum isopleths remains parallel to the solidus. Values of $(La/Yb)_N$ up to 80 (as those observed in the Lekkersmaak granite) are not reproduced in the La France model. Nevertheless the model displays large $(La/Yb)_N$ gradient (10 to 30) if garnet is present in moderate modal proportion (<10-20% in the La France model, Fig. 9a) and if T varies by ± 50°C and/or P varies by ± 0.5 kbar. This sets the minimum pressure of melting to the apparition of garnet, namely at 5.5-6 kbar (model using La France protolith) or at a much lower pressure of 3 kbar (model using Witwatersrand shale). Combined with the information obtained from the alkali elements, we infer that, if we consider the micaschist from La France Formation as the protolith, partial melting can have occurred at ca 5-7 kbar and 700-740°C.

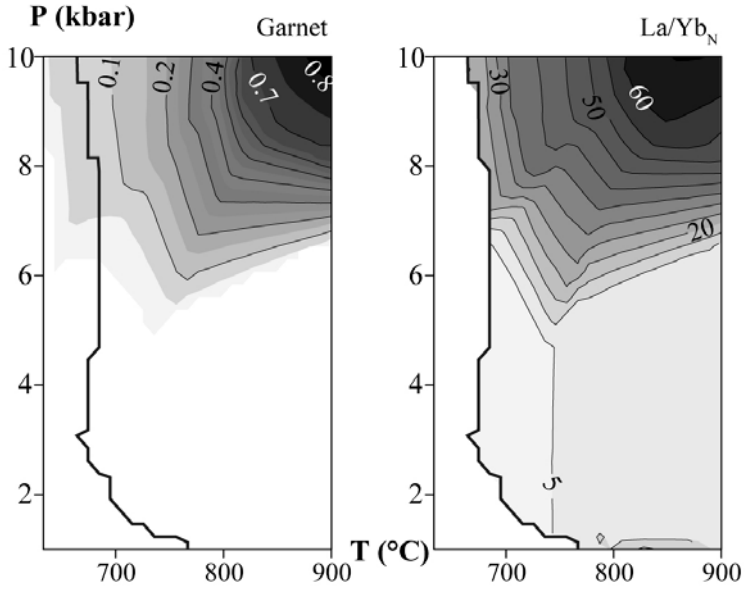

Figure 9: *Proportion of garnet in the residue and La/YbN ratio evolution for the same model as in Fig. 8.*

Therefore, the Lekkersmaak granite seems to have formed form at P-T conditions corresponding to a slightly perturbed geothermal gradient (30-45°C km^{-1}) and from a geochemically classic sedimentary source. The occurrence of such a S-type granite requires two unusual conditions: accumulation of a sizeable aluminous-rich sedimentary basin and subsequently a tectonic context that drives these sediments to sufficient depth, in this case probably sagduction.

A protracted magmatism

The Willie intrusion is dated at 2817 Ga ± 10 Ma and is chemically identical to the Lekkersmaak granite. The Lekkersmaak intrusion age is 2774.5 ± 6.8 Ma. Finally sample MUR 09-64 corresponds to a younger granite (2741 ± 9 Ma) devoided of S-type features: it is muscovite-free, aluminum poor (11.8 wt.%) and with a strong positive europium anomaly (2.08). In summary peraluminous magmatism in the area occurred twice at 2.82 Ga and then 40 Ma later at 2.78 Ga.

The similarities both in term of geochemistry and location shared by the two plutons seem to demonstrate that comparable petrogenetic conditions prevailed for both. The same context was therefore either maintained for 40 Ma or repeated during two separate events. It is doubtful that an uninterrupted melting would have been maintened, all the more that it produced only two crystallisation episodes. It is also doubtful that the same succession of events happened twice. A composite solution is to propose that sub-solidus conditions were maintained for at least 40 Ma but reached the threshold of partial melting only twice. Because the sources of the Willie and Lekkersmaak granite were similar, they cannot have reached the same P-T conditions at the same time. Therefore the similar geochemistry and location suggest that an appropriate source met the appropriate conditions in a dynamic system rather than in a static one. Finally this protracted magmatic activity echoes the long lasting tectonic, metamorphic and granodioritic magmatism history in the Murchison Belt. The geologic history of the belt as a whole may be related to a slow continuous evolution of the area marked by activity pulses (melting, extraction) at different time.

The Turfloop granite was emplaced to the south of the Pietersburg Belt (Fig. 1a) at 2782 ± 13 Ma (Zeh et al., 2009). It may share with the Lekkersmaak granite a S-type affinity (Al_2O_3 = 15 wt.% even if no muscovite is reported so far) and displays strongly fractionnated REE pattern (Henderson et al., 2000). So the peraluminous magmatism is likely of regional extent. The Lekkersmaak and Turfloop granites may eventually have been formed by a similar petrogenetic process. Although the Kaapvaal Craton accumulated sedimentary sequences early (3.05-2.97, 3.2 Ga) and in various contexts (Witwatersrand basin, Barberton Greenstone Belt respectively), burial and melting of sedimentary rocks are so far restricted to the northeast of the Kaapvaal Craton (and Swaziland) where cratonisation was not yet achieved. Yet, the existence of muscovite inclusions in the Jack Hills zircons (and the corresponding high $\delta^{18}O$ values in some Hadean grains, Wilde et al., 2001) suggests that S-type magmas may have been produced as early as 4.2 Ga.

CONCLUSIONS

Our main conclusions are as follow:

- The Lekkersmaak granite is a S-type biotite-muscovite-garnet bearing granite, except that it is sodic in nature and has strongly fractionated REE pattern.
- It formed by the melting of a large immature sedimentary package, eroded from the Kaapvaal Craton and deposited after ca 3.10 Ga.
- The Lekkersmaak granite emplaced 2775 ±5 Ma ago as a single large intrusion.
- The Willie intrusion, a small body located in the western part of the Lekkersmaak granite with which it shares many geochemical characteristics, crystallized earlier at 2817 ± 10 Ma. A protracted peraluminous activity of 40 Ma occurred south of the Murchison Belt.
- The use of the Perple_X software with Holland and Powell thermodynamic database allow to compute of reasonable granite melts both in term of major and trace elements.
- The use of sedimentary sources with different major elements composition did not lead to significantly different granitic melts in term of major element composition but suggests that the source was poor in Fe-Mg relative to Al.
- Partial melting likely occurred in temperatures near solidus with little modal garnet in the residue, in our model at 5-7 kbar, 700-740°C (30-45°C km-1).
- Partial melting was triggered by the burying of sediments during the final tectono-metamorphic stage of the belt

REFERENCES

Barton, J. M., Wenner, D. B. and Hallbauer, D. K., 1992. Oxygen isotopic study of the nature and provenance of large quartz and chert clasts in gold-bearing conglomerates of South Africa. Geology, 20, 1123–1126.

Bédard, L.P. and Ludden, J.N., 1997. Nd-isotope evolution of Archaean plutonic rocks in southeastern Superior Province. Canadian Journal of Earth Sciences, 34, 286-298.

Block, S. and Moyen, J.-F. 2011. The Murchison greenstone belt, South Africa: Accreted silvers with contrasting metamorphic conditions. Abstract In: University of Johanneburg, Council for geosciences, 23rd Colloquium of African Geology, p.52.

Bourne, J. and Danis, D., 1987. A proposed model for the formation of reversely zoned plutons based on a study of the Lacorne Complex, Superior Province, Quebec. Canadian Journal of Earth Sciences, 24, 2506-2520.

Burger A.J., Walraven, F., 1979. Summary of age determinations carried out during the period April 1977 to March 1978. Annal of Geological Survey of South Africa 12: 209-218.

Clayton, R.N., and Mayeda, T.K., 1963. The use of bromine pentafluoride in the extraction of oxygen from oxides and silicates for isotopic analysis. Geochimica et Cosmochimica Acta 27, 48-52.

Clemens, J.D. and Vielzeuf, D., 1987. Constraints on melting and magma production in the crust. Earth and Planetary Science Letters, 86, 287-306.

Clemens, J.D. 2003. S-type granitic magmas—petrogenetic issues, models and evidence. Earth-Science Reviews, 61, 1-18.

Collins W.J. 1998. Evaluation of petrogenetic models for Lachlan fold belt granitoids: implications for crustal architecture and tectonic models. Australian Journal of Earth Sciences, 45, 483–500

Connolly, J. A. D., 2009. The geodynamic equation of state: what and how. Geochemistry, Geo-physics, Geosystem. 10.

Day, W.C. and Weiblen, P.W., 1986. Origin of late Archean granite: geochemical evidence from the Vermilion Granitic Complex of northern Minnesota. Contributions to Mineralogy and Petrology, 93, 283-296.

de Beer, J.H., Stettler, E.H., Duvenhage, A.W.A., Joubert, S.J., and De Raath, C.J., 1984. Gravity and geoelectrical studies of the Murchison greenstone belt, South Africa. South African Journal of Geology 87, 347-359.

Dhoundial, D.P., Paul., D.K., Sarkar, A., Trivedi, J.R., Gopalan, K. and Potts, P.J., 1987. Geochronology and geochemistry of precambrian granitic rocks of Goa, SW India. Precambrian Research, 36 287-302.

Ducharme, Y., Stevenson, R.K. and Machado, N. 1997. Sm–Nd geochemistry and U–Pb geochronology of the Preissac and Lamotte leucogranites, Abitibi Subprovince. Canadian Journal of Earth Sciences, 34, 1059-1071.

Feng, R. and Kerrich, R., 1992. Geochemical evolution of granitoids from the Archean Abitibi Southern Volcanic Zone and the Pontiac subprovince, Superior Province, Canada: Implications for tectonic history and source regions. Chemical Geology, 98, 23-70.

France-Lanord, C., Sheppard, S.M.F. and Fort, P.L., 1988. Hydrogen and oxygen isotope variations in the high Himalaya peraluminous Manaslu leucogranite: Evidence for heterogeneous sedimentary source. Geochimica et Cosmochimica Acta, 52, 513-526.

Geological Survey of South Africa (1985). Map of Tzaneen (n° 2330), 1/250 000 edition.

Geological Survey of South Africa (1986). Pilgrim's Rest (n° 2430), 1/250 000 edition.

Goad, B.E. and Cerny, P. 1981. Peraluminous pegmatitic granites and their pegmatite aureoles in the Winnipeg River District, southeastern Manitoba. The Canadian Mineralogist, 19, 177-194.

Goldstein, SL, O'Nions, RKetHamilton, PJ (1984). A Sm-Nd isotopic study of atmospheric dusts and particulates from major river system. Earth and Planetary Science Letters, vol 70 - 221-236.

Grace, R.L., Chamberlain, K.R., Frost, B.R. and Frost, C.D., 2006. Tectonic histories of the Paleo- to Mesoarchean Sacawee block and Neoarchean Oregon Trail structural belt of the south-central Wyoming Province. Canadian Journal of Earth Sciences, 43, 1445-1466.

Henderson, D.R., Long, L.E. and Barton, J.M., 2000. Isotopic ages and chemical and isotopic composition of the Archaean Turfloop Batholith, Pietersburg granite-

greenstone terrane, Kaapvaal Craton, South Africa. South African Journal of Geology, 103, 38-46.

Holland, T. J. B., Powell, R., 1998. An internally consistent thermodynamic data set for phases of petrological interest. Journal of Metamorphic Geology, 16:309-343.

Hurai, V., Paquette, J.-L., Huraiová, M., and Konečný, P., 2010. U–Th–Pb geochronology of zircon and monazite from syenite and pincinite xenoliths in Pliocene alkali basalts of the intra-Carpathian back-arc basin. Journal of Volcanology and Geothermal Research 198 (3-4), 275-287, doi: 10.1016/j.jvolgeores.2010.09.012.Jaguin et al 2012 tecto

Jackson, S.E., Pearson, N.J., Griffin, W.L., and Belousova, E.A., 2004. The application of laser ablation-inductively coupled plasma-mass spectrometry to in situ U–Pb zircon geochronology. Chemical Geology 211 (1-2), 47-69, doi: 10.1016/j.chemgeo.2004.06.017.

Jaeckel, P. Kröner, A., Kamo, S.L., Brandl, G. and Wendt, J.I., 1997. Late Archaean to early Proterozoic granitoid magmatism and high-grade metamorphism in the central Limpopo belt, South Africa. Journal of the Geological Society, 154, 25-44.

Jaguin, J., Boulvais, P., Poujol, M., Boiron, M.-C. and Cathelineau, M., 2010. Stable Isotope Composition of Quartz-Calcite Veins in the Witwatersrand Basin, South Africa: Implication for Basin-Scale Fluid Circulation. South African Journal of Geology, 113, 169-182.

Jahn, B.M. and Condie, K.C., 1995. Evolution of the Kaapvaal Craton as viewed from geochemical and Sm-Nd analyses of intracratonic pelites. Geochimica et Cosmocimica Acta, 59-11, 2239-2258.

Janoušek, V., Farrow, C.M. and Erban V., 2006. Interpretation of Whole-rock Geochemical Data in Igneous Geochemistry: Introducing Geochemical Data Toolkit (GCDkit). Journal of Petrology, 47, 1255-1259.

Kreissig K., Nägler T.F., Kramers J.D., van Reenen D.D., Smit C.A., 2000, An isotopic geochemical study of the northern Kaapvaal Craton and the Southern Marginal Zone of the Limpopo Belt: are they juxtaposed terranes?, Lithos, 50.

Kröner, A., Jaeckel, P., Brandl, G., Nemchin, A.A. and Pidgeon, R.T. 1999. Single zircon ages for granitoid gneisses in the Central Zone of the Limpopo Belt, Southern Africa and geodynamic significance. Precambrian Research, 93, 299-337

Kulikov, V.S., Kulikova, V.V., Safronova, G.P., Ovchinnkova, L.V., Zudin, A.I., Kazennova, A.D. and Kopylov, V.P. 1986. Archean muscovite rare metal-pegmatite belt at the southeast margin of the Baltic Shield,Transactions (Doklady) of the U.S.S.R. Academy of Sciences: Earth Science Sections 291: 187-191.

Larbi, Y., Stevenson, R., Breaks, F., Machado, N. and Gariépy, C. 1999. Age and isotopic composition of late Archean leucogranites: implications for continental collision in the western Superior Province. Canadian Journal of Earth Sciences, 36, 495-510.

Ludwig, K., 2000. Isoplot/Ex: a geochronological toolkit for Microsoft Excel. Berkeley Geochronology Center special publication.

Machado, N., Gariepy, C., Philippe, S and David, J. 1990. Geochronologie U-Pb du territoire québecois : fosses de l'Ungava et du Labrador, province de Grenville et

sous-provinces de Pontiac et de l'Abitibi. Rapport interimaire, Ministère de l'Energie et des Ressources du Québec, 50p.

Maphalala, R.M. and Kröner, A., 1993. Pb–Pb single zircon ages for the younger Archaean granitoids of Swaziland, southern Africa. In: Ext. Abstr. 16th International Colloquium on African Geology, Mbabane, Swaziland, 201–206.

McCourt, S., Hilliard, P., and Armstrong, R.A., 2000. SHRIMP U–Pb zircon geochronology of granitoids from the western margin of the Kaapvaal Craton: implications for crustal evolution in the Neoarchaean. In: Kisters, A.F.M., Thomas, R.J. (Eds.), Proceedings of the 27th Geocongress, Geol. Soc. S. Afr., Stellenbosch. Journal of African Earth Sciences, 31, 48.

Meyer, F.M., Robb, L.J., Reimold, W.U., and de Bruin, H., 1994. Contrasting low and high Ca granites in the Archaean Barberton Moutain Land, southern Africa. Lithos 32, 63–76.

Miller, C.F., Stoddard, E.F., Bradfish, L.J., and Dollase, W.A., 1981. Composition of plutonic muscovite: genetic implications. Canadian Mineralogist 19, 25-34.

Montel, J.M., 1993. A model for monazite/melt equilibrium and application to the generation of granitic magmas. Chemical Geology, 110, 1-3, p. 127-146.

Moyen, J.F., 2009. High Sr/Y and La/Yb ratios: The meaning of the “adakitic signature”. Lithos 112, 556-574.

O'Neil, J.R., Shaw, S.E. and Flood, R.H., 1977. Oxygen and hydrogen isotope compositions as indicators of granite genesis in the New England Batholith, Australia. Contributions to Mineralogy and Petrology, 62, 313-328.

Poujol M., Robb L.J., Respaut J.P., Anhaeusser C.R., 1996. 3.07–2.97 Ga greenstone belt formation in thenortheastern Kaapvaal Craton: implications for the origin of the Witwatersrand Basin, in Economic Geology, 91 (8), 1455–1461.

Sarvothaman, H. and Leelanandam, C., 1987. Petrography and major oxide chemistry of the Archaean granitic rocks of the Medak area, Andhra Pradesh. Journal of the Geological Society of India, 30, 194-209.

Stokes, T.R., 1991. Le Granite de Xinguara, temoin d'un magmatisme monzogranitique dans l'archeen de l'Amazonie orientale, Bresil. The Xinguara Granite, evidence of monzogranitic magmatism in the Archean of eastern Amazonia, Brazil. PhD thesis, Halifax, Dalhousie University.

Taylor S.R., Hugh P. 1978. Oxygen and hydrogen isotope studies of plutonic granitic rocks. Earth and Planetary Science Letters, 38, 177–210

Taylor, S.R. and McLennan, SM, 1985. The continental crust: Its composition and evolution. Blackwell Scientific (Edition) - 312 p.

Trumbull, R.B. 1993. A petrological and Rb-Sr isotopic study of an early Archean fertile granite-pegmatite system: The Sinceni Pluton in Swaziland. Precambrian Research, 61, 89-116

Vennemann, T.W., Kesler, S.E., Frederickson, G.C., Minter, W.E. and Heine, R.R., 1996. Oxygen Isotope Sedimentology of Gold- and Uranium-Bearing Witwatersrand and Huronian Supergroup Quartz-Pebble Conglomerates. Economic Geology, 91, 322–342.

Vennemann, T. W., Kesler, S. E. and O'Neil, J. R., 1992. Stable isotope compositions of quartz pebbles and their fluid inclusions as tracers of sediment provenance: Implications for gold- and uranium-bearing quartz pebble conglomerates. Geology, 20, 837–840.

Vearncombe, J.R., Barton, J.M., Cheshire, P.E., de Beer, J.H., Stettler, E.H., and Brandl, G., 1992. Geology, geophysics and mineralization of the Murchison Schist Belt, Rooiwater Complex and surrounding granitoids. Memoir of the Geological survey of South Africa n° 81.

Villaros, A., Buick, I. and Stevens, G., 2012. Isotopic variations in S-type granites: an inheritance from a heterogeneous source? Contributions to Mineralogy and Petrology, 163, 243-257.

Villaros, A., et al. 2011. Textural development during cooling of granitic magmas. Seventh Hutton symposium on granites and related rocks, Avila, Spain.

Vinnik L.P., Green R.W.E, Nicolaysen, L.O. 1995. Recent deformations of the deep continental root beneath southern Africa. Nature 375, 50 - 52

Watson E.B., Harrison T.M., 1983. Zircon saturation revisited: temperature and composition effects in a variety of crustal magma types. Earth and Planetary Science Letters, 64-2, 265-304.

Wilde, S.A., Valley, J.W., Peck, W. and Graham, C.M., 2001. Evidence from detrital zircons for the existence of continental crust and ocean on the Earth 4.4 Gyr ago. Nature, 409, 175-178.

Wronkiewicz, D.J. and Condie, K.C., 1987. Geochemistry of Archean shales from the Witwatersrand Supergroup, South Africa: Source-area weathering and provenance. Geochimica et Cosmochimica Acta, 51, 2401-2416.

Zeh, A., Gerdes, A. and Barton, J.M., 2009. Archean Accretion and Crustal Evolution of the Kalahari Craton--the Zircon Age and Hf Isotope Record of Granitic Rocks from Barberton/Swaziland to the Francistown Arc. Journal of Petrology, 50, 933-966.

ANNEXES

Sample	latitude (S)	longitude (E)	
MUR 09-60	23°54'46.7"	30°44'45.3"	western lobe
MUR 09-61			
MUR 09-63	23°55'26.5"	30°47'18.7"	
MUR 09-66	23°55'18.2"	30°49'58"	
MUR 09-109	23°57'40.9"	30°41'55"	
MUR 18c	23°56'45.9"	30°41'30.5"	
MUR 09-80	23°56'36.4"	30°41'58.6"	
MUR 09-67	23°50'15.7"	30°58'58.8"	eastern lobe
MUR 09-72	23°48'55"	30°57'19.6"	
MUR 8a	23°49'02.9"	30°58'59.2"	
MUR 09-108	23°58'20"	30°40'33,6"	Willie pluton

Table 1: *Sampling coordinates.*

Commentaires

Un porteur principal du K et du Rb dans les granites est la muscovite. La mise en évidence de muscovites aux empreintes chimiques secondaires pourrait donc expliquer d'une part la perturbation du système ^{87}Rb-^{87}Sr et d'autre part les datations erratiques ^{40}Ar-^{39}Ar des muscovites en annexe du manuscrit.

La phase magmatique du Lekkersmaak est contemporaine des âges sur monazites vers 2.79 Ga, monazites associées à la circulation hydrothermale minéralisante (article #5).

CHAPITRE 9 – CONCLUSIONS GENERALES

SYNTHESE GEOLOGIQUE, CIRCULATIONS DE FLUIDES ET MOBILITE DES METAUX, PERSPECTIVES

Dans la partie I et surtout la partie II, chacun des six articles et leurs commentaires développent interprétations et discussions des données produites. Sans y revenir dans le détail, cette partie entend proposer une synthèse générale. Dans un premier temps l'histoire géologique la ceinture de roches vertes de Murchison résume l'histoire stratigraphiue, magmatique, métamorphique et tectonique. Cette base géologique permet ensuite d'y intégrer les événements fluides, et en particulier les circulations responsables de mobilités des métaux. Enfin, les avancées que ce travail a fournit dégagent quelques perspectives sur les plans géologique, métallogénique et méthodologique.

A – Histoire géologique du terrain à granitoïdes et ceinture de roches vertes de Murchison

➢ ≥ 3.05 Ga : une Histoire precoce sporadique

Dans ce qui est aujourd'hui la région de Murchison, de rares roches attestent de l'existence d'une croûte antérieure à la ceinture (Tableau 1 au chapitre 3): le gneiss d'affinité TTG de French Bob (3.23 Ga) au sud dans le gneiss de Makhutwsi et un gneiss migmatitique (3.17 Ga) dans le gneiss de Groot-Letaba au nord. Ces deux zones constitueraient donc des socles à l'échelle régionale. Les zircons déposés dans la séquence sédimentaire de la ceinture ont des âges jusqu'à 3.47 Ga mais ils reflètent une croûte continentale recyclée plus au sud (terrains de Barberton et de l'*Ancient Gneiss Complex* ; article #1).

3.12-3.06 Ga. Les roches du socle sud montrent un groupe d'âge vers 3.12-3.06 Ga. Ce sont des gneiss d'affinité TTG, parmi lesquels le granite d'Harmony qui est contemporain des dépôts volcano-sédimentaires de la ceinture (laves mafiques et felsiques de la formation de la Weigel et formation de MacKop, respectivement, figure 9–1). Les âges de nombreux zircons hérités à 3.05-3.09 Ga renforcent l'ampleur de cet épisode (albitite de Gravelotte, granite de Willie, sédiments des Formations de la Weigel, de La France et de Mulati). Poujol et Robb (1999) ont suggéré que le granite d'Harmony et les volcanites de la Weigel témoignaient d'une zone de subduction vers

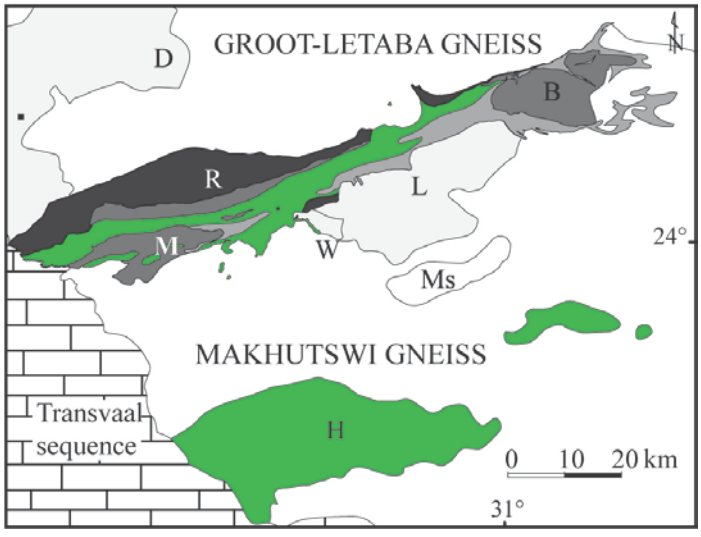

Figure 9—1 : *Carte de la répartition des terrains d'âges 3.12-3.06 Ga (en vert) dans la region de la ceinture de Murchison.*

3.09 Ga. Si cette interprétation est cohérente avec la nature TTG des roches datées de cette période, elle semble plus dure à accorder avec les signatures en Hf des zircons de cette époque. En effet ceux-ci indiquent des âges modèles au moins 200 Ma plus vieux, c'est-à-dire que la croûte subductée à l'origine des TTG auraient au moins 200 Ma (article #1). La nature komatiitique d'une partie des laves de la formation de la Weigel suggère une fusion partielle de matériel mantellique. Par analogie avec la phase suivante à 2.97 Ga, un contexte par exemple dans un arrière-arc peut être proposé (figure 9–2). Cependant, on ne peut pas exclure qu'il n'y avait pas de subduction à l'époque.

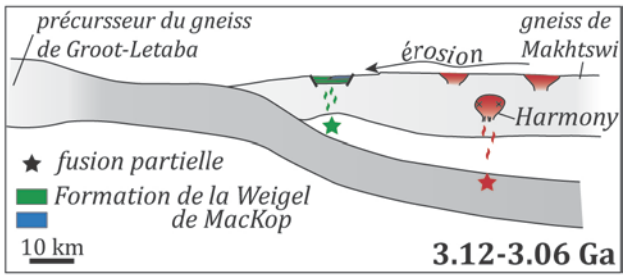

***Figure 9—2** : proposition de contexte géodynamique possible vers 3.12-3.09 Ga (inspiré de Poujol et Robb, 1999)*

➢ 2.99-2.92 Ga: L'episode d'accretion majeur

Des zircons « jeunes » (c'est-à-dire datés à 2.99-2.97 Ga) et concordants sont certes rares, mais ils existent dans les schistes de Murchison (peut-être la Formation de MacKop) et la Formation de La France. Ils posent les âges minimum de ces Formations. Ainsi, le terrain volcano-sédimentaire sud de la ceinture se développe en deux temps, avec une première séquence volcano-sédimentaire vers 3.09 Ga puis une deuxième séquence sédimentaire immédiatement avant l'accrétion des terrains. On peut suggérer qu'une discordance entre la Formation de Weigel et de Mulati existe, mais qu'elle aurait été dissimulée par la déformation forte des roches et les mauvaises conditions d'affleurement.

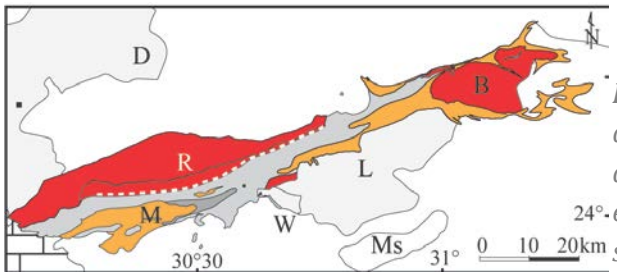

***Figure 9—3 :** carte de la répartition des terrains d'âges 2.97-2.92 Ga dans la region de la ceinture de Murchison. En rouge les terrains dont cet âge est avéré, en orange les terrains dont c'est l'âge suspecté.*

Cette phase est surtout marquée par un magmatisme étendu daté à 2.97 Ga du pluton du Baderoukwe à l'est, du complexe du Rooiwater et des volcanites de la Rubbervale au nord, du Discovery granite au sud et potentiellement du Maranda à l'ouest (figure 9–3). Nous avons argumenté au chapitre 5 que le magmatisme à cette période correspond à deux contextes distincts, une fusion partielle dans un bassin d'arrière arc pour le complexe du Rooiwater et les volcanites de la Rubbervale et une fusion partielle en contexte de subduction pour le batholith du Baderoukwe et

Maranda. Ces deux contextes appartiennent néanmoins au même contexte géodynamique général d'amalgamation des terrains nord et sud.

Les âges très proches entre les sédiments et les pointements du batholithe de Baderoukwe à l'intérieur de la ceinture montrent que ce sont des intrusifs hypo-volcaniques dans les niveaux supérieurs de la croûte. Surtout ce batholithe s'aligne sur un axe est-ouest (article #3), il profite donc surement d'une zone de faiblesse, une "proto-Antimony Line" qui a facilité l'ascension de ces roches près de la surface. On peut émettre l'hypothèse que celle-ci était héritée de l'histoire précoce (i.e. lors de l'extrusion des volcanites de la Weigel).

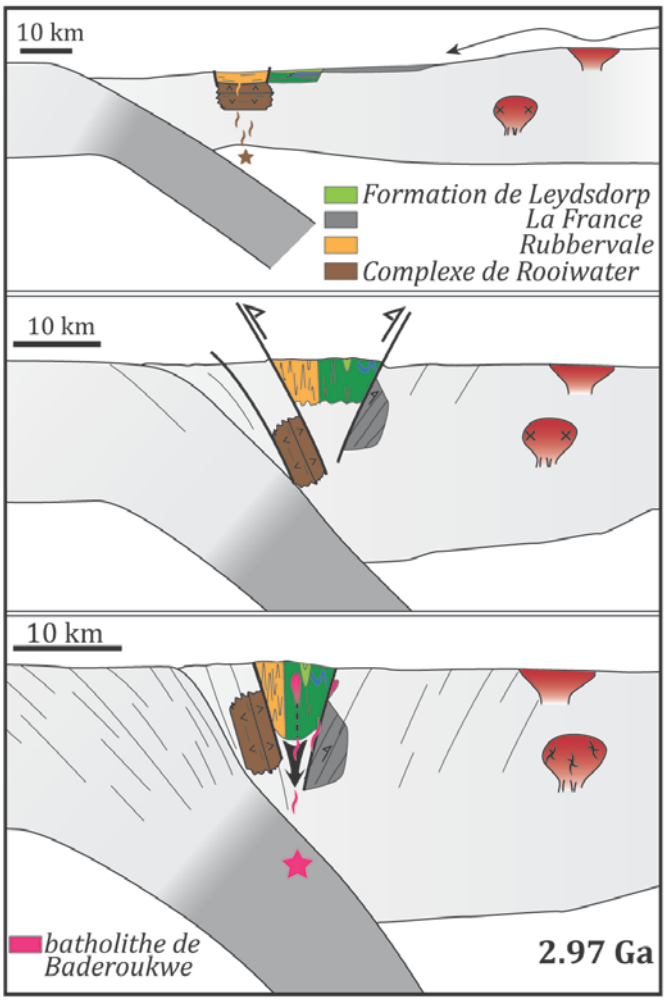

Figure 9—4 : *évolution (de haut en bas) du contexte géodynamique de la ceinture de Murchison vers 2.97 Ga.*

Si le métamorphisme n'est pas daté directement dans le nord de la ceinture, l'article de Block et al. (2012) et les commentaires à la suite de l'article #2 mettent en évidence que le métamorphisme et la juxtaposition des unités métamorphiques datent de 2.97 Ga. Dans le sud (La France) l'âge minimum du pic métamorphique est 2.92 Ga. Le métamorphisme lui-même est imputable à un enfouissement rapide des unités nord selon toute probabilité à cause de la collision des terrains sud et nord (figure 9–4). Par ailleurs le pluton de Baderoukwe par sa forme de dômes lobés intrusif dans les roches de la ceinture s'est mis en place par diapirisme, ce qui est possiblement le cas aussi du

le pluton de Maranda au vu des similarités cartographiques. L'ensemble formerait au premier ordre un motif *dome-and-keel*. Il semble d'après l'article #2 et l'article en annexe qu'à l'échelle régionale la déformation est distribuée, et à l'intérieur de la ceinture est localisée. Il apparait donc que le mode de déformation évolue soit dans le temps rapidement soit dans l'espace d'un mode fragile vers un mode ductile.

A cette période, aucune activité magmatique plus au sud de la ceinture n'a été reconnue, tandis qu'au nord, des gneiss massif de Groot-Letaba (Duivelkloof et de Melkboomfontein) ont des phases aux âges similaires quoique débutant plus tardivement (2.95-2.94 Ga). Ces roches sont contemporaines de volcanites dans la ceinture de Pietersburg (2.95 Ga). Ceci indique que l'activité magmatique est régionale et pourrait se rajeunir vers le nord.

Entre 2.85 et 2.84 Ga, des phases des granites et gneiss de Duivelskloof et Melklboonfontein se mettent en place et ces âges sont retrouvés à proximité de la ceinture de Murchison (2.86-2.84) dans le gneiss de Groot-Letaba, mais les causes de cette activité restent obscures.

➢ 2.82-2.75 Ga : Episode tardi-collision

Cet épisode n'est pas associé à la formation de roches volcano-sédimentaire dans la ceinture elle-même mais il y correspond à une empreinte tectono-métamorphique-métasomatique et à la fin de la construction du socle (intrusion de Lekkersmaak, figure 9–5).

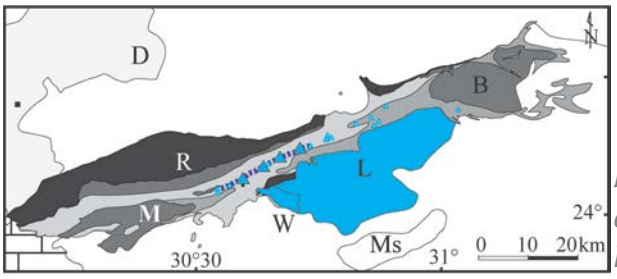

Figure 9—5: *Carte de la répartition des roches d'âges 2.82-2.75 Ga (en bleu) dans la region de la ceinture de Murchison.*

Entre 2.97 Ga et 2.78 Ga, le déplacement vertical de la base de la ceinture atteint des profondeurs maximales de 18 km (figure 9–6). En effet, la ceinture sous l'Antimony Line a aujourd'hui une profondeur de 4.5 km et au maximum de 9 km (voir article #2). D'après les estimations sur les inclusions fluides dans l'Antimony Line (article #4), cette zone centrale de la ceinture a vu des pressions vers 3 kbar (9 km). Dans la Formation de La France, les âges vers 2.75 Ga sur les monazites matricielles pourraient correspondre à un épisode métamorphique dans des conditions de pression-température succédant au pic métamorphique (5.5 kbar, 550-600°C). Cette période est donc marquée par un déplacement vertical significatif des roches.

Vers 2.82-2.78 Ga l'enfouissement devient suffisamment important pour induire deux phénomènes. D'une part, la fusion partielle de protolithes fertiles est démontrée par le magmatisme granitique de type S de Lekkersmaak et de Willie à 2.82 et 2.78 Ga.

Il traduit que l'enfouissement de roches supra-crustales est dynamique et maintenu sur une longue période (42 Ma, article #6).

D'autre part, l'enfouissement provoque la déshydratation métamorphique à l'origine de circulation de fluides (voir section suivante B-). À 2.79 Ga, la circulation de fluides dans l'Antimony Line est équilibrée avec les roches encaissantes vers 2-3 kbar et 350-450°C (article #4). L'albitisation discrète dans le complexe du Rooiwater pourrait y être associée également.

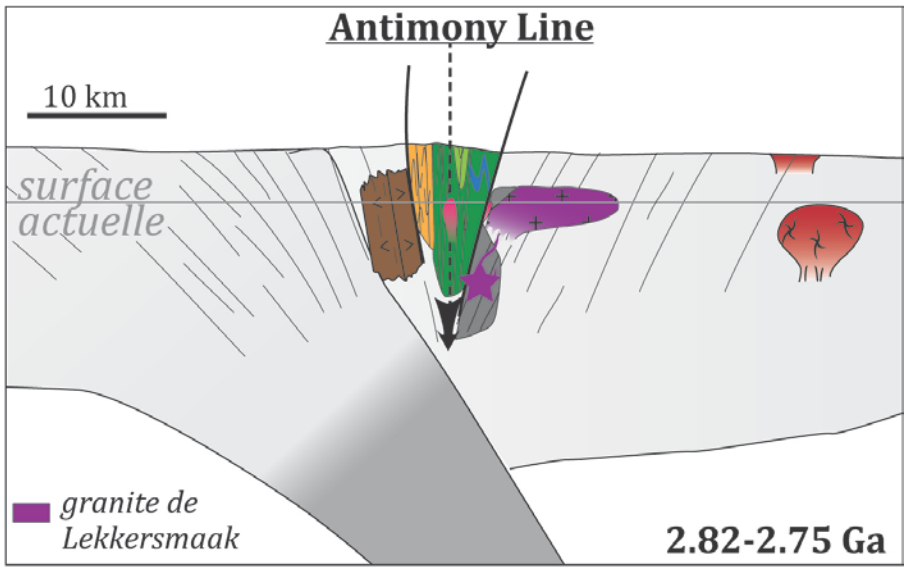

Figure 9—6 : *contexte géodynamique de la ceinture de Murchison vers 2.8 Ga.*

Ces objets ont des structures syn-métamorphique, syn-circulation ou syn-magmatique qui s'inscrivent dans le mode structural distribué de la ceinture. Les fabriques sub-verticales et les linéations fortement plongeantes des roches de la ceinture traduisent une compression horizontale nord-ouest/sud-est et une composante verticale (article #2). Ainsi, dans ce contexte géodynamique de collision, le champ de déformation est en continuité avec l'épisode précédent. Plus généralement, entre 2.97 Ga et 2.78 Ga, cette déformation n'est pas accommodée sur les structures localisées mais distribuée dans la ceinture et son socle. De tout cela, il apparait que la collision se déroule dans un contexte ductile lors d'un processus de sagduction (article #2).

Le gneiss de Groot-Leta est intrudé par des granites potassiques à 2.77 Ga (Turfloop, Duivelskloof) ce qui pourraient indiquer que la collision s'étend largement dans la région. Vers 2.68-2.69 Ga, la fin de l'histoire magmatique de la région se termine par la mise en place d'un granite au sud de la ceinture de Murchison (Mashishimale) et près de la zone marginale sud de la ceinture de Limpopo (granites de Mashashane, Moletsi, Matlala, Matok).

- **≈ 2.0 Ga : La question des ages jeunes**

Dans la ceinture de Murchison, quelques données géochronologiques sur fuchsite (article #4), sur sphène et sur monazite (article #5) documentent des âges

entre 1.94 Ga et 2.02 Ga. Leur position le long de structures localisées (Antimony Line et près de zone de cisaillement de Letaba au nord du pluton de Baderoukwe ; figure 9–7) suggère que ces minéraux enregistrent une recristallisation par des fluides lors de circulation dans ces structures.

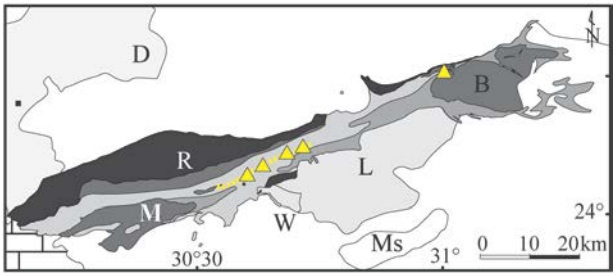

Figure 9—7 : *carte de la répartition des âges d'environ 2.0 Ga (en jaune) dans la region de la ceinture de Murchison.*

La cause de cet événement est à chercher dans la géologie régionale. Dans la région nord-est du craton du Kaapvaal, la période vers 2.0 Ga est une période d'activité majeure avec l'intrusion du Complexe du Bushveld (2.05 Ga) et l'intrusion du complexe carbonatitique de Phalaborwa (2.06 Ga). En dehors de ces objets, dans la région de Murchison, des datations essentiellement de basse température enregistrent des âges vers 2.0 Ga mais dont les interprétations divergent. Barton et Van Reenen (1992) interprètent l'uniformité spatiale de leurs âges comme résultant de l'érosion uniforme du nord de la ceinture de Murchison jusqu'à la ceinture de la Limpopo. Kruger et al. (1998) montrent une influence hydrothermale dans une pegmatite au sud de la ceinture. Enfin, Good et de Wit (1997) datent des muscovites vers 2.0 Ga dans le nord du complexe du Bushveld, le long de la structure crustale du *Thabazimbi-Murchison Lineament*. Qui plus est, ils estiment que cette structure a servi de conduit lors d'une circulation massive de fluides liés à la mise en place du complexe du Bushveld. Nos âges seraient à rapprocher de cette circulation et suggèrent que la réactivation Protérozoique du *Lineament* peut s'étendre plus à l'Est que documenté jusqu'à présent.

B — Circulations de fluides et mobilité des métaux

➢ UNE REDISTRIBUTION LOCALE A 2.97 GA ?

Dans les différents gisements mondiaux, jamais l'antimoine n'est d'origine magmatique. Ainsi, la présence de ce métal à Malati Pump soutient l'hypothèse de Pearton (1980) qu'un enrichissement de fond existait dans les roches volcano-sédimentaires de la Formation de la Weigel.

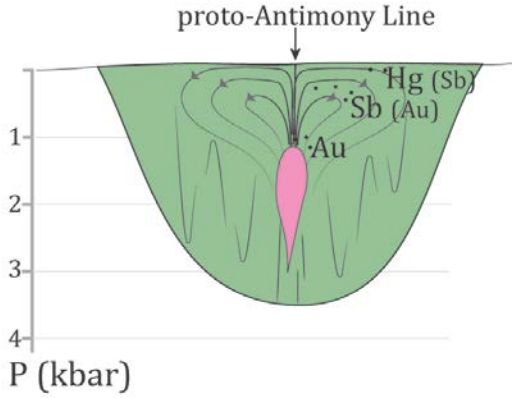

Figure 9—8 : *proposition de modèle métallogénique vers 2.97 Ga lié à l'intrusion de granodiorite (rose) et de circulation de fluides magmatiques (lignes grises) dans la ceinture (vert); inspiré de S. Goldmann (2008)*

Les intrusions de granodiorite se mettent en place dans les roches supra-crustales de la Formation de la Weigel dans une proto-Antimony Line (article #3) donc à des profondeurs faibles (figure 9–8). La remobilisation à 2.97 Ga se passe donc en haut de croûte. À ces profondeurs faibles, le vecteur de remobilisation est un fluide magmatique, surement aqueux. D'après les modèles de continuum de l'or, il existe un gradient or-antimoine-mercure depuis les hautes températures vers les basses températures. Ainsi la domination Au>Sb dans la carrière de Malati Pump tend à suggérer que l'antimoine a été redistribué distalement par rapport à ce pluton, plus haut dans l'Antimony Line (dans les premier km de la croûte) et/ou latéralement.

La suite métallique caractérisée par une domination de l'or a certes été fossilisée à Malati Pump mais les critères géologiques afférents à cette minéralisation ont été perturbé voir effacés par la phase métamorphique. Cette étape magmatique dans l'histoire de la minéralisation restera difficile à caractériser.

➢ LA MINERALISATION METAMORPHIQUE MAJEURE A 2.8 GA

La zone de l'Antimony Line enregistre une circulation de fluides majeure exprimée sous trois formes : la précipitation de veines à quartz-carbonate-sulfures d'antimoine, la métasomatose des roches encaissantes en schistes à talc-carbonate et l'albitisation des intrusions de granodiorites (figure 9–9). Les articles #4 et #5 évaluent les liens entre ces trois phénomènes, mettant ainsi en évidence qu'ils relèvent du même processus génétique. Cette circulation met en jeu des fluides métamorphiques à H_2O-CO_2(-CH_4), dans des conditions de 350-450°C et 2-3 kbar, circulant vers 2.8 Ga (2791 ± 12 Ma, population des monazites des albitites) pendant la déformation.

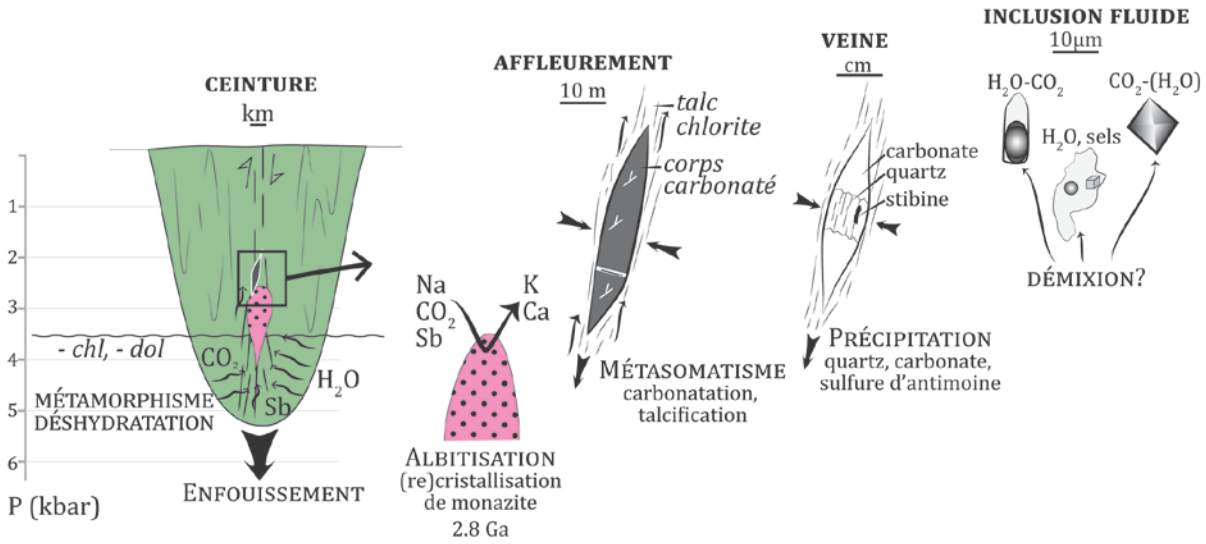

Figure 9—9 : *schéma intégrant à différentes échelle de la minérasation vers 2.8 Ga dans l'Antimony Line.*

Cette circulation est ultimement causée par l'enfouissement des roches de la Formation de la Weigel qui induit un métamorphisme de ces dernières et la déstabilisation de phases hydratées et carbonatées. Comme les fluides sont produits par pulses lors du métamorphisme, et qu'ici le système a vu un grand volume de fluide, la réaction de déshydratation-décarbonatation a dû impliquer la disparition de phases présentent en grande proportion. La circulation dans le niveau structural de la minéralisation est équilibrée avec les roches encaissants, or à ces température les encaissants (et leurs équivalents latéraux loin de l'Antimony Line) contiennent encore des phyllosilicates hydratés stables. Par contre, le métamorphisme a dû atteindre sous l'Antimony Line des températures suffisantes, impliquant par exemple la déstabilisation de la chlorite vers 500-550°C et de la dolomite vers 550°C (figure 9–9).

Ces fluides à H_2O-CO_2(-CH_4) dissolvent une partie de l'antimoine de leur roche source. Soit activement (par pompage sismique) soit par simple anomalie gravitaire, ils sont chenalisés vers l'Antimony Line le long de laquelle ils remontent. Lors de cette remontée, nous avons proposé que la démixion du fluide du fluide provoque la précipitation de sulfures d'antimoine, concomitante avec la formation de quartz et carbonate. La déformation dans l'Antimony Line fournit des pièges structuraux dans lesquels ces phases forment des veines.

La minéralisation métamorphique à 2.8 Ga implique donc une remobilisation à la fois latérale en concentrant l'antimoine de la périphérie vers la structure et verticale par la remontée de fluides.

Enfin, la circulation dans le *Thabazimbi-Murchison Lineament* vers 2.0 Ga ne montre aucun indice de remobilisation.

La surimposition de deux processus dans le cœur de la ceinture a pu être la clé d'un enrichissement dans les proportions observées et contribuer à en faire un gisement de grande ampleur. Le processus tectonique à l'origine du métamorphisme et de la circulation relèverait de conditions caractéristiques de l'Archéen. Pour autant

l'antimoine n'est pas une signature singulière de cette époque et le métamorphisme est un processus universel. En cela, l'Antimony Line n'est pas un gisement typiquement « archéen ».

➢ DESEQUILIBRE GEOLOGIE VERSUS METALLOGENIE

La comparaison entre l'histoire géologique et l'histoire métallogénique en antimoine de la ceinture de Murchison montre un déséquilibre dans l'importance des différents épisodes. La construction géologique de la ceinture et de son terrain de granitoïdes est dominée par la phase d'amalgamation à 2.97 Ga, tandis que la minéralisation en antimoine est dominée par la phase de collision et d'enfouissement vers 2.8 Ga. Plusieurs raisons l'expliquent :

- L'antimoine semble être facilement mobilisable lors de la phase secondaire.
- La nature hydrothermale et 'orogenic gold' du gisement de l'Antimony Line est typiquement tardi-orogénique donc déconnectée de la formation de roches.
- L'histoire très longue de la ceinture (3.07-2.75 Ga) exacerbe ce caractère tardif, car elle permet de distinguer très clairement dans le temps les pics d'activités géologiques.
- Les roches magmatiques acides et les sédiments forment la majorité de la croûte et préservent des minéraux datables résistants. Au contraire, les objets reliés aux fluides représentent un volume limité de roches le long du chemin de circulation. Ces chemins restent des conduits préférentiels lors des circulations perturbatrices ultérieures (dans le cas de l'Antimony Line, vers 2.0 Ga).

C – Perspectives

➢ PERSPECTIVES METALLOGENIQUES

Notre modèle métallogénique de l'Antimony Line peut désormais être confronté aux modèles proposés pour les autres minéralisations de la ceinture de Murchison. Cela permet d'estimer si l'ensemble du métallotecte qu'est la ceinture de Murchison est polyphasé et quelle est l'importance de ces phases.

Dans le gisement d'émeraude dans le sud de la ceinture (le long de la bordure orientale du pluton de Willie), les émeraudes se sont développées dans des schistes à biotite le long du contact avec des filons d'albitite pegmatoïde. La genèse des gemmes est débattue et présente des problématiques similaires à celles qui entourent le gisement de l'Antimony Line (chronologie, origine magmatique ou métamorphique). A partir de la géométrie du gisement et certaines caractéristiques du fluide, certains auteurs proposent une origine magmatique-pegmatitique liée à la mise en place des précurseurs des corps albitiques (Robb et Robb, 1986), du moins pour le début de la cristallisation (Zwann 2006). D'après l'âge du granite de Discovery à proximité ce pourrait être vers 2.97 Ga. À partir de données d'inclusions fluides, de l'isotopie stable et du caractère métasomatique des albitites, d'autres auteurs (Nwe et Morteani 1993 ; Grundmann et Morteani 1989, Groates et al. 2008, G. Giuliani comm. pers.) insistent sur

l'origine métamorphique des émeraudes. L'âge du métamorphisme n'est pas renseigné. Eventuellement les émeraudes pourraient avoir, comme l'Antimony Line, subies deux étapes d'évolution, une première magmatique et une seconde métamorphique.

La Copper-Zinc Line est le deuxième gisement majeur de la ceinture, parallèle à l'Antimony Line. L'extrusion des volcanites acides et le gisement VMS associé sont datés à 2.97 Ga, pendant l'épisode d'amalgamation des terrains (Schwarz-Schampera et al. 2010). Toutefois, deux caractéristiques soulignent une perturbation postérieure de ce gisement (Schwarz-Shampera, comm. pers.). En premier lieu, les corps lenticulaires minéralisés sont fortement boudinés donc ils ont été affectés par une déformation postérieure à la mise en place. Deuxièmement, il y a une altération hydrothermale de la formation de Rubbervale. Cette altération consiste en une paragenèse en facies schiste vert, en la recristallisation de sphalérite et en une remobilisation des minerais chalcopyrite et galène dans des veines. Cependant la remobilisation est de faible échelle, parce que les sulfures de fer et la sphalérite sont réfractaires (ils recristallisent plutôt que d'être remobilisés) et parce que les dômes rhyolitiques abritant les minéralisations restent des objets rigides peu affectés par les circulations de fluides. Ainsi, le gisement de Cu-Zn dans la ceinture de Murchison s'est formé à 2.97 Ga et a été seulement faiblement affecté par les événements ultérieurs comme la circulation de fluides.

- **PERSPECTIVES METHODOLOGIQUES**

Plusieurs méthodes de datations peuvent désormais tester et compléter notre modèle métallogénique. Contrairement à ce qui aurait été attendu dans un projet de métallogénie 'pure', dans ce projet de doctorat nous n'avons pas expertisé en détails les sulfures porteurs de l'antimoine. Pourtant, il existe une méthode de datation qui s'applique aux sulfures et sulfosels, la méthode Rhénium-Osmium. Cette méthode isochrone est basée sur la désintégration du ^{187}Re en ^{187}Os, deux éléments sidérophiles et chalcophiles. Le Re en particulier se substitue au Mo dans la molybdénite, mais la datation est applicable même à des concentrations très basses en Re et Os (10 et 0.03 ppb respectivement, Stein et al. 2000) et donc à de nombreux sulfures. Cet outil a fait ses preuves dans la compréhension de systèmes métallogéniques mondiaux (e.g. Kirk et al. 2002, même métamorphisés, e.g. Selby et al. 2009). Dans l'Antimony Line, une étude géochimique des sulfures a été menée par Muff et Saager (1979) et récemment par Goldmann (non publié, 2008). Aucune molybdénite n'a été reportée mais les concentrations en Mo atteignent 5 ppm voir 503 ppm dans certains minerais (roche totale, Goldmann 2008), ce qui laisse espérer des concentrations suffisantes en Re. L'idéal serait alors de cibler des sulfures d'antimoine, ou du moins de cibler des phases co-génétiques de ces sulfures, qui fourniraient l'âge de la précipitation hydrothermale des minerais.

L'article #4 revient sur la carbonatation intense de l'Antimony Line et il souligne que la formation des veines de quartz-carbonate est hydrothermale et co-génétique de

la précipitation de l'antimoine. Or des carbonates précipités à partir d'un fluide hydrothermal sont datables par la méthode Sm-Nd (par exemple Su et al. 2009). La datation Sm-Nd des carbonates de l'Antimony Line pourrait donc fournir l'âge de la minéralisation hydrothermale. Nous avons tenté technique a été tentée sur une sélection préliminaire de carbonates de veines. Cependant la mise en solution est incomplète dans le cas des carbonates riches en Fe (ankérites, sidérites, dolomites ferrifères). Il faudra reprendre cette datation en sélectionnant un groupe d'échantillons pauvres en Fe et présentant des rapports Sm/Nd les plus variables grâce à une analyse chimique préalable.

Par ailleurs, l'utilisation de la nano-sonde ionique NanoSIMS permettrait l'augmentation de la résolution spatiale des datations. Il serait par exemple théoriquement possible de dater des grains fins (<5-7 µm) des encaissants métasomatisés. Cependant, les minéraux datables par NanoSIMS restent rares (monazite, zircon) dans ces roches. Certes des minéraux pourraient être des cibles alternatives comme le rutile. Nous avons tenté une datation LA-ICP-MS de celui-ci et il est très riche en Pb commun. Néanmoins des études géochronologiques ont montré que la monazite se prête bien à la datation par la NanoSIMS (e.g. Sano et al. 2006, Ayers et al. 2006). Dans les albitites la perturbation des âges des monazites en font des cibles intéressantes pour une datation NanoSIMS. De plus, il est possible de coupler cette datation avec la mesure du $\delta^{18}O$ des monazites par sonde ionique classique pour valider notre interprétation des perturbations radiogéniques (Ayers et al. 2006).

Enfin, des traces de l'événement minéralisateur à 2.97 Ga se trouveraient peut-être loin des zones de perturbation par des fluides secondaires c'est-à-dire loin de l'Antimony Line. C'est peut-être le cas de ce que de rares auteurs (van Eeden et al. 1939, Pearton et Viljoen 1986) reconnaissent comme une *Southern Antimony Line* (une ligne d'anomalies en antimoine) et une *Mercury Line* (mine de mercure à Monarch). Les méthodes évoquées plus haut pourraient suivre un gradient spatial pour tester un éventuel vieillissement des âges en s'éloignant de l'Antimony Line.

➢ PERSPECTIVES GEOLOGIQUES

Les résultats géochronologiques confirment deux éléments concernant la place géologique de la ceinture de Murchison dans la région nord-est du craton du Kaapvaal. Premièrement, le terrain de Barberton et celui de Murchison sont bien géologiquement distincts. La ceinture de Murchison est beaucoup plus jeune et se forme à l'interface entre une zone cratonisée au sud et une zone non-cratonisée au nord. Deuxièmement il semble que les terrains de Pietersburg et de Murchison ont des évolutions communes concernant leur histoire magmatique (figure 9–10), même si les modalités tectoniques diffèrent avec des chevauchements plats en base de ceinture pour les ceintures de Pietersburg et de Giyani (McCourt et van Reenen, 1992 ; de Wit et al. 1992b, de Wit et al. 1992c). Les données pétrologiques, géochronologiques et géochimiques sont encore parcellaires sur les ceintures de Pietersburg, de Giyani et de Rhenosterkoppies et sur

les gneiss de Makhutwsi au sud et du Groot-Letaba au nord. Ces quatre ceintures formeraient un groupe avec une histoire commune. Cependant la ceinture de Murchison diffère de ces trois autres ceintures par l'absence d'influence de la collision de Limpopo. En effet, cette collision est structuralement accommodée par la zone de cisaillement de Hout River et a des effets métamorphiques locaux dans les ceintures de Pietersburg et de Giyani, alors qu'aucun indice ne montre un impact direct dans la région de la ceinture de Murchison. Dès lors il apparait nécessaire d'évaluer plus en détail d'une part l'âge de construction des ceintures et de leur terrain granitique direct (dépôt volcano-sédimentaire, accrétion crustale juvénile) pour déterminer si la construction du nord-est du craton rajeunit vers le nord ; d'autre part l'âge de métamorphisme (et recyclage crustal) de ces ceintures, pour déterminer s'il existe une histoire tectono-métamorphique secondaire commune ou zonée et si la collision des terrains dans la ceinture de Murchison se rapporte à des événements régionaux Limpopo.

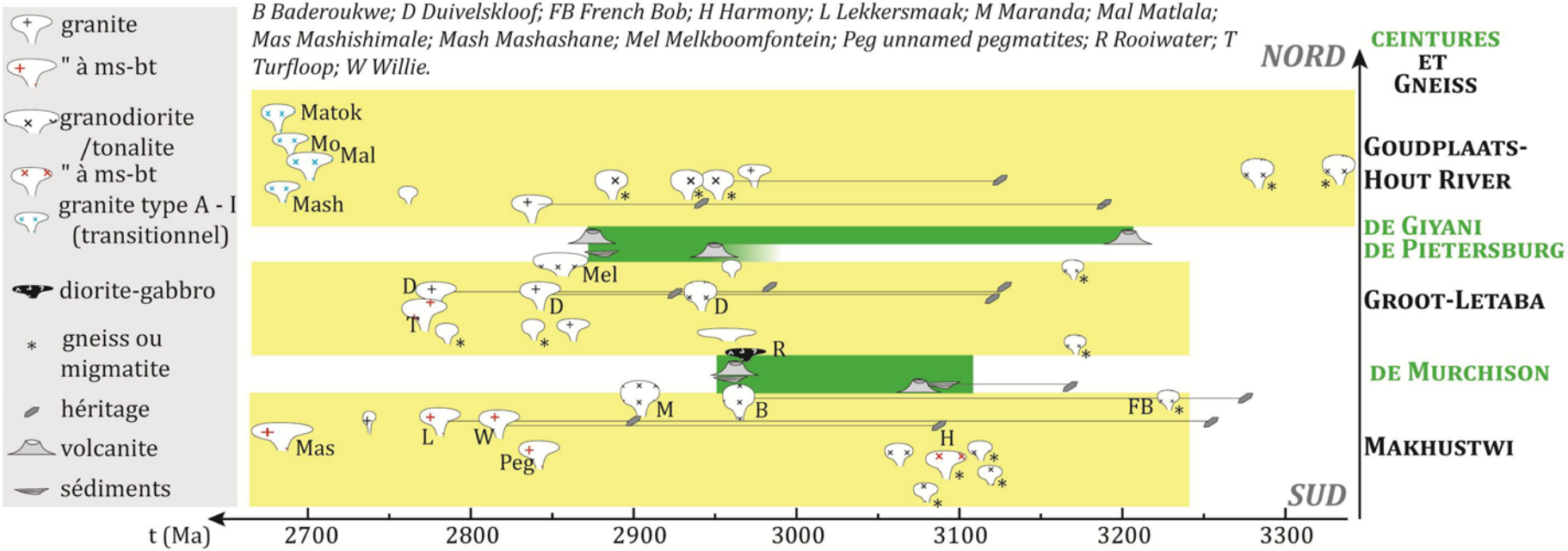

Figure 9-10 : *Compilation des âges des roches plutoniques et des ceintures de roches vertes entre le gneiss de Makhutswi et la ceinture de Limpopo. Les roches sont présentés suivant un axe sud-sud-est/nord-nord-ouest perpendiculaire à la direction des strructures régionales.*

Les granitoïdes associées à la ceinture de Murchison marquent le changement des processus magmatiques depuis une accrétion crustale (TTG) vers du recyclage crustal ultime que sont les granites de type S. Les processus tectoniques précis lors de cette évolution semblent passer de la localisation à la distribution de la déformation. La métallogénie se place dans ce cadre en étant typique des ceinture de roches vertes et mêmes des orogènes récents dans lesquels le métal (Au) est concentré en fin d'histoire géologique pendant l'étape magmato-métamorphique tardive le long de cisaillement. Ainsi la ceinture de Murchison évolue sur 200 Ma depuis une étape de collision d'arc (marquant la suture continentale) vers une étape de collision continentale. De ce point de vue elle est analogue comme nombre de ceintures archéennes à un type 'ceinture de Barberton'.

BIBLIOGRAPHIE

Albarède, F., 1998. The growth of continental crust. Tectonophysics 296-1,2, 1-14.

Anhaeusser, C.R., Mason, R., Viljoen, M.J., Viljoen, R.P., 1969. A Reappraisal of Some Aspects of Precambrian Shield Geology. Geological Society of America Bulletin 80-11, 2175-2200.

Anhaeusser, C.R., 2006. Ultramafic and mafic intrusions of the Kaapvaal Craton In The Geology of South Africa. Johnson, M.R., Anhaeusser, C.R., Thomas, R.J., (Ed.) Geological Society of South Africa, Council for Geoscience (Editions), 95-134

Ahrens, T., 1989. Water storage in the mantle. Nature 342, 122-123.

Armstrong, R.L., 1991. The persistent myth of crustal growth. Australian Journal of Earth Sciences 38, 613-630.

Ayers, J.C., Loflin, M., Miller, C.F., Barton, M.D., Coatch, C.D., 2006. In situ oxygen isotope analysis of monazite as a monitor of fluid infiltration during contact metamorphism: Birch Creek Pluton aureole, White Mountains, eastern California. Geology 34, 653-656.

Bailly, L., Bouchot, V., Bény, C., Milési, J.P., 2000. Fluid inclusion study of stibnite using infrared microscopy: an example from the Brouzils antimony deposit (Vendée, Armorican Massif, France). Economic Geology 95, 221-226.

Barley, M.E., Groves, D.I., 1992. Supercontinent cycles and distribution of metal deposits through time. Geology 20, 291-294.

Barton, J.M., van Reenen, D.D., 1992. The significance of Rb-Sr ages of biotite and phlogopite for the thermal history of the Central and Southern Marginal Zones of the Limpopo Belt of southern Africa and the adjacent portions of the Kaapvaal Craton. Precambrian Research 55, 17-31.

Bellot, J.P., Lerouge, C., Bailly, L., Bouchot, V., 2003. The Biards Sb-Au–Bearing Shear Zone (Massif Central, France): An Indicator of Crustal-Scale Transcurrent Tectonics Guiding Late Variscan Collapse. Economic Geology 98-7, 1427-1447.

Berner, E.K., Berner, R.A., 1987. The Global Water Cycle: Geochemistry and Environment. Prentice Hall, 397p.

Bickle, M.J., Eriksson, K.A., Roberts, D.G., Hastings, D., Chadwick, B., Clarke, A.M., Ziegler, P.A., Osmaston, M.F., 1982. Evolution and Subsidence of Early Precambrian Sedimentary Basins [and Discussion]. Philosophical Transactions of the Royal Society of London, Mathematical and Physical Sciences 305, 225-247.

Bindeman, I.N., Eiler, J.M., Yogodzinski, G.M., Tatsumi, Y., Stern, C.R., Grove, T.L., Portnyagin, M., Hoernle, K., Danyushevsky, L.V., 2005. Oxygen isotope evidence for slab melting in modern and ancient subduction zones. Earth and Planetary Science Letters 235, 480-496.

Bleeker, W., 2004. Towards a 'natural' time scale for the Precambrian—A proposal. Lethaia 37, 219-222.

Bleeker, W., Ernst, R.E., 2006. Short-lived mantle generated magmatic events and their dyke swarms: The key unlocking Earth's palaeogeographic record back to 2.6Ga. In Dyke Swarms – Time Markers of Crustal Evolution, 3-26.

Boese, R., 1964. Die Antimoglanzgänge von Gravelotte in der Murchison Range on Nordost-Transvaal. In PhD thesis, University of Hamburg, 85p.

Boocock, C.N., 1984. Ore genesis along the Antinomy Line, Murchison Range, North-eastern Transvaal. In M.Sc. thesis, University of the Witwatersrand, 193p.

Bowring, S.A.,Williams, I.S., 1999. Priscoan (4.00-4.03 Ga) orthogneisses from northwestern Canada. Contributions to Mineralogy and Petrology 134, 3-16.

Brandl, G., Jaeckel, P., Kröner, A., 1996, Single zircon age for the felsicRubbervale Formation, Murchison greenstone belt, South Africa. South African Journal of Geology 99-3, 229-234.

Brandl, G., Kröner, A., 2003. Preliminary results of sing zircon studies from various Archaean rocks of the north-eastern Transvaal. Abstract of the 16th Colloquium on African Geology, Mbabane, Swaziland 1, 229-234.

Brandl, G., Cloete, M., Anhaeusser, C.R., 2006. Archean greenstone belts. In The Geology of South Africa. Johnson, M.R., Anhaeusser, C.R., Thomas, R.J., (Ed.) Geological Society of South Africa, Council for Geoscience (Editions), 9-56.

British Geological Survey, 2011. Risk list 2012 of mineral commodities http://www.bgs.ac.uk/mineralsuk/statistics/riskList.html

Brown, P.E., 1998. Fluid inclusion modeling for hydrothermal systems. Reviews in Economic Geology 10, 151-171.

Buchholz, P., Oberthür, T., Lüders, V., Wilkinson, J., 2007. Multistage Au-As-Sb Mineralization and Crustal-Scale Fluid Evolution in the Kwekwe District, Midlands Greenstone Belt, Zimbabwe: A Combined Geochemical, Mineralogical, Stable Isotope, and Fluid Inclusion Study. Economic Geology 102, 347-378.

Buick, I.S., Maas, R., Gibson, R., 2001. Precise U–Pb titanite age constraints on the emplacement of the Bushveld Complex, South Africa. Journal of the Geological Society 158, 3-6.

Bumby, A.J., Eriksson, P.G., Catuneanu, O., Nelson, D.R., Rigby, M.J., 2012. Meso-Archaean and Palaeo-Proterozoic sedimentary sequence stratigraphy of the Kaapvaal Craton. Marine and Petroleum Geology 33, 92-116.

Butterman, W.C., Carlin, J.F., Jr. 2004. Mineral Commodity Profiles – Antimony. U.S. Department of the Interior U.S. Geological Survey Open-File Report 03-019.

Burger, A.J., Walraven, F., 1979. Summary of age determinationscarried out during the period April 1977 to March 1978. Annual Geological Survey of South Africa 12, 209-218.

Burnham, C.W., 1967. Hydrothermal fluids in the magmatic stage. In Geochemistry of Hydrothermal Ore Deposits,H.L. Barnes (ed.), Holt, Rinehart,Winston, 34-76.

Burrows, D.R., Spooner, E.T.C.,1987. Generation ofa magmatic H2O-CO2 fluid enriched in Mo, Au and Wwithin an Archaean sodic granodiorite stock, MinkLake, northwestern Ontario. Economic Geology 82, 1931-57.

Byron, C.L., Barton, J.M., 1990. The setting of mineralization in a portion of the Eersteling Goldfield, Pietersburg granite-greenstone terrane, South Africa. South African Journal of Geology 93, 463-472.

Campbell, I., Gill, J., Izuka, T., Allen, C., 2012. What detrital zircons tell us about growth of the continental crust. Abstract. Goldschmidt 2012, Montreal, 412

Cavosie, A.J., Wilde, S.A., Valley, J.W., 2005. A lower age limit for the Archean based on δ18O of detrital zircons. Geochimica et Cosmochimica Acta 69-10 Suppl. 1, Abstract A 391.

Chappell, B.W., White, A.J.R., 1974. Two contrasting granite types. Pacific Geology 8, 173-4.

Chardon, D., Choukroune, P., Jayananda, M., 1996. Strain patterns, décollement and incipient sagducted greenstone terrains in the Archaean Dharwar craton (south India). Journal of Structural Geology 18, 991-1004.

Chardon, D., 1997. Les déformations continentales archéennes - exemples naturels et modélisations thermomécaniques. Thèse de l'Université de Rennes 1, 300p.

Choukroune, P., Ludden, J. N., Chardon, D., Calvert, A. J., Bouhallier, H., 1997. Archaean crustal growth and tectonic processes : a comparison of the Superior Province, Canada, and the Dharwar craton, India. In Orogeny through time.Burg, J.-P., and Ford, M., (Ed.), Geological SocietySpecial Publication 121, 63-98.

Clemens, J.D., Mawer, C.K., 1992. Granitic magma transport by fracture propagation. Tectonophysics 204, 339-360.

Condie, K.C., 1998. Episodic continental growth and supercontinents: a mantle avalanche connection? Earth and Planetary Science Letters 163, 97-108.

Condie, K.C., 2005. TTGs and adakites: are they both slab melts? Lithos 80, 33-44.

Condie, K.C., 2008. Did the character of subduction change at the end of the Archean? Constraints from convergent-margin granitoids. Geology 36, 611-614.

Condie, K.C., Belousova, E., Griffin, W.L., Sircombe, K.N., 2009. Granitoid events in space and time: Constraints from igneous and detrital zircon age spectra. Gondwana Research 15, 228-242.

Cooke, D.R., Simmons, S.F., 2000. Characteristics and genesis of epithermal gold deposits. Reviews in Economic Geology 13, 221–244.

de Almeida, J.A.C., Dall'Agnol, R., de Oliveira, M.A., Macambira, M.J.B., Pimentel, M.M., Rämö, O.T., Guimarães, F.V., Leite, A.A.S., 2011. Zircon geochronology, geochemistry and origin of the TTG suites of the Rio Maria granite-greenstone terrane: Implications for the growth of the Archean crust of the Carajás province, Brazil. Precambrian Research187, 201-221.

de Ronde C.E.J., DeR Channer, D.M., Spooner E.T.C., 1997. Chapter 3.5: Archaean Fluids. In: de Wit M.J. and Ashwal L.D. (Ed.), Greenstone Belts. Oxford Monographs on Geology and Geophysics 35, Oxford Science Publications, Oxford, 309-335.

de Wit, M.J., de Ronde, C.E.J., Tredoux, M., Roering, C., Hart, R.J., Armstrong, R.A., Green, R.W.E., Peberdy, E., Hart, R.A., 1992a. Formation of an Archaean continent. Nature 357, 553-562.

de Wit, M.J., Jones, M.J., Buchanan, D.L., 1992b. The geology and tectonic evolution of the Pietersburg Greenstone Belt, South Africa. Precambrian Research 55, 123-153.

de Wit, M.J., van Reenen, D., Roering, C., 1992c. Geologic observations across tectono-metamorphic boundary in the Babangu area, Giyani (Sutherland) Greenstone belt, South Africa. Precambrian Research 55, 111-122.

de Wit, M.J.,Hart, R.A., 1993. Earth's earliest continental lithosphere, hydrothermal flux and crustal recycling. Lithos 30, 309-335.

de Wit, M.J., Armstrong, R.A., Kamo, S.L., Erlank, A.J., 1993.Gold-bearing sediments in the Pietersburg greenstone belt: ageequivalents of the Witwatersrand Supergroup sediments SouthAfrica. Economic Geology 88, 1242-1252.

de Wit, M.J., Ashwal, L.D., (ed.), 1997. Greenstone Belts. Oxford Monographs on Geology and Geophysics 35, Oxford Science Publications, Oxford, 809p.

de Wit, M.J., Thiart, C., 2005. Metallogenic fingerprints of Archean Cratons. InMineral Deposits and Earth Evolution. McDonald I, Boyce, AJ, Butler IB, Herrigton RJ and Polya DA (ed.),Geological Society of London Special publication 248, 59-70.

Dill, H.G., 1998. Evolution of Sb mineralisation in modern fold belts: a comparison of the Sb mineralisation in the Central Andes (Bolivia) and the Western Carpathians (Slovakia). Mineralium Deposita 33, 359-378.

Dziggel, A., Knipfer, S., Kisters, A.F.M., Meyer, F.M., 2006. P–T and structural evolution during exhumation of high-T, medium-P basement rocks in the Barberton Mountain Land, South Africa. Journal of Metamorphic Geology 24, 535-551.

Emmons, W.H.,1936. Hypogene zoning in metalliferouslodes. Report 1 of the 16th International Geological Congress, 417-32.

Eugster, H.P., Baumgartner, L., 1987. Mineral solubilities and speciation in supercritical metamorphic fluids. Reviews in Mineralogy and Geochemistry 17, 367-403.

European Union 2011, Report lists of 14 critical mineral raw materials. http://europa.eu/rapid/pressReleasesAction.do?reference=MEMO/10/263&format=HTML&aged=0&language=EN&guiLanguage=en

Franklin, J.M., Gibson, H.L., Jonasson, I.R., Galley, A.G., 2005. Volcanogenic massive sulfide deposits. Economic Geology, 100th Anniversary Volume, 523-560.

Frimmel, H.E., Groves, D.I., Kirk, J., Ruiz, J., Chesley, J., Minter, W.E.L., 2005. The formation and preservation of the Witwatersrand goldfields, the largest gold province in the world. Economic Geology 100th Anniversary Volume, 769-797.

Fyfe, W.S., 1978. The evolution ofd the Earth crust: modern plate tectonics to ancient hot spot tectonics? Chemical Geology 23, 84-114.

Garven, G., Raffensperger, J.P., 1997. Hydrogeology and geochemistry of ore genesis in sedimentary basins.In Geochemistry of Hydrothermal Ore Deposits, 3rd edn, H.L. Barnes (Ed.).Wiley, J.,125-190.

Geological Society of South Africa et Council for Geoscience.Johnson, M.R., Anhaeusser, C.R., Thomas, R.J., (Ed.), The Geology of South Africa, 691p.

Goldfarb, R.J., Baker, T., Dubé, B., Groves, D.I., Hart, C.J.R., Gosselin, P., 2005. Distribution, Character and Genesis of Gold Deposits in Metamorphic Terranes. Economic Geology, 100th Anniversary Volume, 407-450.

Goldmann, S., 2008. Antimony-Gold Deposits in the Antimony Line, Murchison Greenstone Belt, Republic of South Africa MsC thesis, Bundesanstalt für Geowissenschaften und Rohstoffe, Hannover, Tgb.-Nr. 11196/08

Good, N., deWit, M.J., 1997. The Thabazimbi-Murchison Lineament of the Kaapvaal Craton, South Africa: 2700 Ma of episodic deformation. Journal of the Geological Society 154-1, 93-97.

Goodwin, A.M., 1981. Archean Plates and Greenstones Belts. In Precambrian plate tectonics 5, A. Kröner (Ed.), 105-135.

Goodwin, A.M., 1991. Precambrian geology. Academic Press, San Diego. 666p.

Groat, L.A., Giuliani, G., Marshall, D.D., Turner, D.,2008. Emerald deposits and occurrences: A review. Ore Geology Reviews 34, 87-112.

Groves, D.I., Barley, M.E., 1994. Archean mineralizations. In: Archean crustal evolution. Condie, K. C. (Ed.) Elsevier, Amsterdam, 461-503.

Groves, D.I., 1993. The crustal continuum model for late-Archaean lode-gold deposits of the Yilgarn Block, Western Australia. Mineralium Deposita 28 366-374.

Groves, D.I., Condie, K.C., Goldfarb, R.J., Kronsky, J.M.A., Vielreicher, R.M., 2005. Secular Changes in Global Tectonic Processes and Their Influence on the Temporal Distribution of Gold-Bearing Mineral Deposits. Economic Geology 100, 203-224.

Grundmann, G., Morteani, G., 1989. Emerald mineralisation during regional metamorphism: the Habachtal (Austria) and Leydsdorp (Transvaal, South Africa)deposits. Economic Geology 84, 1835-1849.

Guilbert, J.M., Park, C.F., 1986.The Geology of Ore Deposits. W.H. Freeman and Co., 985p.

Guillemette, N., William-Jones, A.E., 1993. Genesis of the Sb-W-Au deposits at Ixtahuacan, Guatemala: evidence from fluid inclusions and stable isotopes. Mineralium Deposita 28, 167-180.

Hagemann, S.G., Cassidy, K.F., 2000. Archean orogenic lode gold deposits. Reviews in Economic Geology 13, 9-68.

Hagemann, S.G., Lüders, V., 2003. P-T-X conditions of hydrothermal fluids and precipitation mechanism of stibnite-gold mineralization at the Wiluna lode-gold deposits, Western Australia: conventional and infrared microthermometric constraints. Mineralium Deposita 38, 936-952.

Hamilton, W.B., 1998. Archean magmatism and deformation were not products of plate tectonics. Precambrian Research91, 143-179.

Hanor, J.S., 1979. The sedimentary genesis of hydrothermalfluids. In Geochemistry of Hydrothermal Ore Deposits. H.L. Barnes (Ed.), Wiley-Interscience, 137-172.

Hart, C.J.R, McCoy, D., Goldfarb, R.J., Smith, M., Robert, P., Hulstein, R., Blake, A.A. and Bundtzen, 2002. Geology, exploration and discovery of the Tintina gold province, Alaska and Ykon. Society of economic geologists special publication, 9, 241-274.

Hatton, C.J., Schweitzer, J.K., 1995. Evidence for synchronous extrusive and intrusive Bushveld magmatism. Journal of African Earth Sciences 21, 579-594.

Hausmann, S.G., 1959. A mineralogical investigation of the Letaba copper-zinc ores and the Monarch Cinnabar deposits located in the Murchison Range of the Eastern Transvaal, M.Sc. thesis (unpubl.), Univ. Witwatersrand, Johannesburg, 49p.

Haynes, D.W., Cross, K.C., Bills, R.T., Reed, M.H., 1995. Olympic Dam ore genesis: a fluid-mixingmodel. Economic Geology 90, 281-307.

Henderson, D.R., Long, L.E., Barton, J.M., 2000. Isotopic ages and chemical and isotopic composition of the Archaean Turfloop Batholith, Pietersburg granite - greenstone terrane, Kaapvaal Craton, South Africa: South African Journal of Geology 103, 38-46.

Hill, M., Barker, F., Hunter, D.,Knight, R., 1996. Geochemical Characteristics and Origin of the Lebowa Granite Suite, Bushveld Complex. International Geology Review 38, 195-227.

Hunter, D.R., Johnson, M.R., Anhaeusser, C.R., Thomas, R.J., 2006. Introduction. In The Geology of South Africa. Johnson M.R. Anhaeusser C.R. Thomas R. J. (Ed.), Geological Society of South Africa et Council for Geoscience (Editions), 1-7.

Huston, D.L., Blewett, R.S., Keillor, B., Standing, J., Smithies, R.H., Marshall, A., Mernagh, T.P., Kamprad, J., 2002. Lode Gold and Epithermal Deposits of the Mallina Basin, North Pilbara Terrain, Western Australia. Economic Geology 97, 801-818.

Ileri, S., 1973. Petrographic analysis of naturally and experimentally deformed stibnite.PhD thesis (unpubl.), Columbia University, New York.

Irvine, T.N., 1977. Origin of chromitite layers in theMuskox Intrusion and other stratiform intrusions: anew interpretation. Geology 5, 273-277.

Jahn, B.M., Condie, K.C., 1995.Evolution of the Kaapvaal Craton as viewed from geochemical and Sm-Nd isotopic analyses of intracratonic pelites. Geochimica et Cosmochimica Acta 59, 2239-2258.

Kedda, S.W., 1992. Geochemical and stable isotope studies of gold bearing granitoids in the Murchison Schist Belt, North Eastern Transvaal. MsC thesis, University of the Witwatersrand.

Kerrich, R., Goldfarb, R.J., Richards, J.P., 2005. Metallogenic Provinces in an evolving Geodynamic Framework. Economic Geology, 100th Anniversary Volume,1097-1136.

King, E.M., Valley, J.W., Davis, D.W., Edwards, G.R., 1998. Oxygen isotope ratios of Archean plutonic zircons from granite–greenstone belts of the Superior Province: indicator of magmatic source. Precambrian Research 92, 365-387.

Kirk, J., Ruiz, J., Chesley, J., Walshe, J., England, G., 2002. A Major Archean, Gold-and Crust-Forming Event in the Kaapvaal Craton, South Africa. Science 297, 1856-1858.

Kontak, D.J., Horne, R.J., Smith, P.K., 1996. Hydrothermal characterization of the West Gore Sb-Au deposit, Meguma Terrane, Nova Scotia, Canada. Economic Geology 91, 1239-1262.

Kreissig, K., Nägler, T.F., Kramers, J.D., van Reenen, D.D., Smit, C.A., 2000. An isotopic and geochemical study of the northern Kaapvaal Craton and the Southern Marginal Zone of the Limpopo Belt: are they juxtaposed terranes? Lithos 50, 1-25.

Kröner, A., 1985. Evolution of the Archean Continental Crust.Annual Review of Earth and PlanetarySciences 13, 49.

Kröner, A., 1991. Tectonic evolution in the Archaean and Proterozoic. Tectonophysics 187, 393-410.

Kröner, A., Jaeckel, P., Brandl, G., 2000. Single zircon ages for felsic to intermediate rocks from the Pietersburg and Giyani greenstone belts and bordering granitoid orthogneisses, northern Kaapvaal Craton, South Africa. Journal of African Earth Sciences 30, 773-793..

Kruger, F.J., Kamber, B.S., Harris, P.D., 1998. Isotopic peculiarities of an Archaean pegmatite (Union Mine, Mica, South Africa): Geochemical and geochronological implications. Precambrian Research 91,4, 253-267.

Kusky, T.M., Vearncombe, J.R., 1997. Chapter 2.3: Structural aspects. In de Wit M.J. et Ashwal L.D. (Ed.), Greenstone Belts. Oxford Monographs on Geology and Geophysics n°35, Oxford Science Publications, Oxford 91-124

Kusky, T.M.,Polat, A., 1999. Growth of granite–greenstone terranes at convergent margins, and stabilization of Archean cratons. Tectonophysics 305, 43-73.

Lahaye, Y.,Arndt, N., 1996. Alteration of a Komatiite Flow from Alexo, Ontario, Canada. Journal of Petrology37, 1261-1284.

Lancaster, P.J., Storey, C.D., Hawkesworth, C.J., Dhuime, B., 2011. Understanding the roles of crustal growth and preservation in the detrital zircon record. Earth and Planetary Science Letters 305, 405-412.

Lambert, R.S.J., 1976. Archean thermal regimes, crustal and upper mantle temperatures, and a progressive evolutionary model for the Earth. In Windley, B.F. (Ed.) The Early history of the Earth, Wiley and Sons, London 363-373.

Laurent, O., Martin, H., Doucelance, R., Moyen, J.F., Paquette, J.L.,2011. Geochemistry and petrogenesis of high-K “sanukitoids” from the Bulai pluton, Central Limpopo Belt, South Africa: Implications for geodynamic changes at the Archaean–Proterozoic boundary. Lithos 123, 73-91.

Lindgren, W., 1933. Mineral Deposits. McGraw-Hill, 930p.

Mao, J., Lehmann, B., Du, A., Zhang, G., Ma, D., Wang, Y., Zeng, M., Kerrich, R., 2002. Re-Os Dating of Polymetallic Ni-Mo-PGE-Au Mineralization in Lower Cambrian Black Shales of South China and Its Geologic Significance. Economic Geology 97, 1051-1061.

Martin, H., 1994. The Archean grey gneisses and the genesis of continental crust. In: K. C. Condie (Ed) Archean crustal evolution 6, 205-259.

Martin, H., 1993. The mechanisms of petrogenesis of the Archaean continental crust-comparisonwith modern processes. Lithos 30, 373-388.

Martin, H., Smithies, R.H., Rapp, R., Moyen, J.F., Champion, D., 2005. An overview of adakite, tonalite–trondhjemite–granodiorite (TTG), and sanukitoid: relationships and some implications for crustal evolution. Lithos 79, 1-24.

McCaig, A.M., 1997. The geochemistry of volatile fluid-flow in shear zones. InDeformation-enhanced fluid transport in the Earth's crust and Mantle.Holness, M.B. (Ed.), The Mineralogical Society8,227-266.

McCourt, S., van Reenen, D., 1992. Structural geology and tectonic setting of the Sutherland Greenstones Belt, Kaapvaal Craton, South Africa. Precambrian Research 55, 93-110.

McCulloch, M.T., Bennett, V.C., 1994. Progressive growth of the Earth's continental crust and depleted mantle: Geochemical constraints. Geochimica Cosmochimica Acta 58, 4717-4738.

Meyer, C., 1981. Ore-forming processes in geologic history. Economic Geology, 75th Anniversary Volume, 6-41.

Meyer, C., 1988. Ore deposits as guides to the geologic history of the Earth. Annual Reviews in Earth Planetary Science 16, 147–171.

Minnitt, R.C.A., 1975. The geology of the Murchison Range between nQuagga Camp area and the Kruger National Park.M.Sc. thesis (unpubl.) University of Witwatersrand, Johannesburg.

Misra, K.C., 2012. Introduction to geochemistry: principle and applications. Willey-Blckwell publishing. 438p.

Misra, K.C., 2000.Understanding Mineral Deposits. Kluwer Academic Publishers, 845p.

Mitchell, A.H.G., Garson, M.S., 1981. Mineral Deposits and Global Tectonic Settings. Academic Press, 457p.

Mojzsis, S.J., Harrison, T.M., Pidgeon, R.T., 2001. Oxygen-isotope evidence from ancient zircons for liquid water at the Earth's surface 4,300 Myr ago. Nature 409, 178-181.

Moyen, J.F., 2000. Transition Archéen-Protérozoïque : Exemple de craton du Dharwar, Inde du Sud (Ganite de Closepet et intrusions associées). Thèse de l'Université Blaise Pascal, 502p.

Moyen, J.F., Stevens, G.,Kisters, A., 2006. Record of mid-Archaean subduction from metamorphism in the Barberton terrain, South Africa.Nature 442, 559-62.

Moyen, J.F., 2011. The composite Archaean grey gneisses: petrological significance, and evidence for a non-unique tectonic setting for Archaean crustal growth. Lithos 123, 21-36.

Moyen, J.F., Martin, H., 2012. Forty years of TTG research. Lithos 148, 312-336.

Muehlenbachs, K., Clayton, R.N., 1976. Oxygen Isotope Composition of the Oceanic Crust and Its Bearing on Seawater. Journal of Geophysical Research 81, 4365-4369.

Muehlenbachs, K., 1998. The oxygen isotopic composition of the oceans, sediments and the seafloor. Chemical Geology 145, 263-273.

Muff, R., Saager, R., 1979. Metallogenic interpretation from a mineragraphic and geostatistic study of Antimony ores of the Murchison greenstone Belt, South Africa.Special publication of the Geological Society of South Africa 5, 167-179.

Naldrett, A.J., von Grünewaldt, G., 1989. Associationof platinum-group elements with chromitite inlayered intrusions and ophiolite complexes. EconomicGeology 84, 180-187.

Nesbitt, B.E., Muehlenbachs, K., Murowchick, J.B., 1989. Genetic implications of stable isotope characteristics of mesothermal Au deposits and related Sb and Hg deposits in the Canadian Cordillera. Economic Geology 84, 1489-1506.

Nisbet, E.G.,Cheadle, M.J., Arndt, N.T., Bickle, M.J., 1993. Constraining the potential temperature of the Archaean mantle: A review of the evidence from komatiites. Lithos 30, 291-307.

Normand, C., Gauthier, M., Jebrak, M., 1996.The Quebec antimony deposit; an example of gudmundite-native antimony mineralization in the ophiolitic melange of the southeastern Quebec Appalachians. Economic Geology 91, 149-163.

Nutman, A.P., Friend, C.R.L., Kinny, P.D., McGregor, V.R., 1993. Anatomy of an Early Archean Gneiss complex: 3900 to 3600 crustal evolution in southern West Greenland. Geology 21, 415-418.

Nwe, Y.Y., Morteani, G., 1993. Fluid evolution in the H2O–CH4–CO2–NaCl system during emerald mineralization at Gravelotte, Murchinson greenstone belt, Northeast Transvaal, South Africa. Geochimica et CosmochimicaActa 57, 89-103.

Oberthür, T., Davis, D.W., Blenkinsop, T.G., Höhndorf, A.,2002. Precise U–Pb mineral ages, Rb–Sr and Sm–Nd systematics for the Great Dyke, Zimbabwe —

constraints on late Archean events in the Zimbabwe craton and Limpopo belt. Precambrian Research 113, 293-305.

O'Connor, J.T., 1965. A classification for quartz-rich igneous rocks based on feldspar ratios. U.S. Geological Survey Professionnal Paper525, 79-84.

O'Neil, J., Carlson, R.W., Francis, D., Stevenson, R.K., 2008. Neodymium-142 evidence for Hadean mafic crust. Science 321, 1828-1831.

Ohtani, E., 2005.Water in the Mantle.Elements1, 25-30.

Patchett, J.P., Kouvo, O., Hedge, C.E., Tatsumoto, M., 1982. Evolution of continental crust and mantle heterogeneity: Evidence from Hf isotopes. Contributions to Mineralogy and Petrology 78, 279-297.

Pearton, T.N., 1980. The geochemistry of the Carbonate and related rocks of the Antimony Line, Murchison Greenstone Belt, with particular reference to their genesis and to the origin of stibnite mineralization. PhD thesis, University of the Witwatersrand.

Pellissonier, H., 1997. Réflexions sur la métallogénie. Les ouvrages de l'industrie minérale. 431p.

Peng, J.T.,Hu, R.Z., Burnard, P.G., 2003. Samarium–neodymium isotope systematics of hydrothermal calcites from the Xikuangshan antimony deposit (Hunan, China): the potential of calcite as a geochronometer. Chemical Geology 200, 129-136.

Percival, J.A., 1994. Archean high-grade metamorphism. In Condie, K.C. (Ed.) Archean crustal evolution. Elsevier Amsterdam, 357-410.

Pearton, T.N.,Viljoen, M.J., 1986. Antimony mineralization in the Murchison Greenstone Belt - An overview. In Mineral Deposits of Southern Africa, Anhaeusser, C.R.,Maske, S. (Ed.), 293-320.

Pollack, H.N., 1986. Cratonization and thermal evolution of the Mantle.Earth and Planetary Science Letters 80,175-782.

Poujol, M., Robb, L.J., Respaut, J.P., Anhaeusser, C.R., 1996. Greenstone Belt Formation in the northeastern KaapvaalCraton: Implication for the Origin of the Witwatersrand Basin. Economic Geology 91, 1455-1461.

Poujol, M., Robb, L.J., 1999. New U-Pb zircon ages on gneisses and pegmatite from south of the Murchison greenstone belt, South Africa. South African Journal of Geology 102, 93-97.

Poujol, M., 2001.U-Pb isotopic evidence for episodic granitoid emplacement in the Murchison greenstone belt, South Africa. Journal of African Earth Sciences 33, 155-163.

Poujol, M., Anhaeusser, C.R., Armstrong, R.A., 2002. Episodic granitoid emplacement in the Archaean Amalia-Kraaipan terrane, South Africa : Confirmation from single zircon U-Pb geochronology. Journal of African Earth Sciences 35, 147-161.

Poujol, M., Robb, L.J., Anhaeusser, C.R., Gericke, B., 2003. A review of the geochronological constraints on the evolution of the KaapvaalCraton, South Africa. Precambrian Research 127, 181-213.

Poujol, M., Kiefer, R., Robb, L.J., Anhaeusser, C.R., Armstrong, R.A., 2005. New U-Pb data on zircons from the Amalia greenstone belt Southern Africa: insights into the Neoarchaean evolution of the Kaapvaal Craton. South African Journal of Geology 108, 317-332.

Poujol M., 2007. An overview of the pre-Mesoarchaean rocks of the Kaapvaal Craton, South Africa. In Earth's Oldest Rocks, Serie : Developments in Precambrian Geology15, M. van Kranendonk, R. Smithies and V. Bennett (Ed.), K. Condie (Series Ed.), Elsevier, 453-463.

Poujol, M., Hirner, A.J., Armstrong, R.A., Anhaeusser, C.R., 2008. U-Pb SHRIMP data for the Madibe greenstone belt: implications for crustal growth on the western margin of the Kaapvaal Craton, South Africa. South African Journal of Geology 111, 67-78.

Reed, M.H., 1997. Hydrothermal alteration and its relationship to ore fluid composition. In Geochemistry of Hydrothermal Ore Deposits, H.L. Barnes (Ed.), Wiley, J., 303-366.

Reymer, A., Schubert, G., 1984. Phanerozoic addition rates to the continental crust and crustal growth. Tectonics 3,63-77.

Reimold W. U., Gibson R. L., 2005. Meteorite impact! The danger from space and South Africa's mega-impact, the Vredefort structure. Meteoritics & Planetary Science 40, 1915-1916.

Reynolds, I.M., 1986. Vanadium-bearing Titaniferous iron ores of the Rooiwater complex, North-Eastern Transvaal. In Anhaeusser, Mineral Deposits of Southern Africa, 451-460.

Richter, F.M., 1988. A major change in the thermal state of Earth at the Archean-Proterozoic boundary : consequences for the nature and preservation of the continental lithosphere. Journal of Petrology, Lithosphere special issue, 39-52.

Ringwood, A.E., 1975. Composition and Structure of the Earth's Mantle. McGraw-Hill, New York.

Robb, L.J., Robb, V.M., 1986. Archean pegmatite deposits in the northeastern Transvaal in Mineral deposits of South Africa, Ed Anhaeusser C.R. and Maske S., Geological society of South Africa 1, 437-450.

Robb, L., 2005. Introduction to ore-forming processes. Blackwell publishing, 373p.

Robb, L., Brandl, G., Anhaeusser, C.R, Poujol M., 2006. Archean Granitoid Intrusions In The Geology of South Africa, Johnson, M.R., Anhaeusser C.R., Thomas, R.J. (Ed.), Geological Society of South Africa et Council for Geoscience, 57-94.

SACS (South African Committee for Stratigraphy), 1980. The Murchison Sequence, in Stratigraphy of South Africa, part 1: Lithostratigraphy of the Republic of South Africa, South West Africa/Namibia and the Republics of Bophuthatswana, Transkei and Venda, 45-52.

Sanchez-Garrido, C.J.M.G., Stevens, G., Armstrong, R.A., Moyen, J.F., Martin, H., Doucelance, R., 2011. Diversity in Earth's early felsic crust: Paleoarchean peraluminous granites of the Barberton Greenstone Belt. Geology 39, 963-966.

Sano, Y., Takahata, N., Tsutsumi, Y., Miyamoto, T., 2006.Ion microprobe U-Pb dating of monazite with about five micrometer spatial resolution. Geochemical Journal 40, 597-608.

Schwarz-Schampera, U., Terblanche, H., Oberthür, T., 2010. Volcanic-hosted massive sulfide deposits in the Murchison greenstone belt, South Africa. Mineralium Deposita 45, 113-145,

Scoates, J.S., Friedman, R.M., 2008. Precise age of the platiniferous merenski reef, Bushveld complex, South Africa, by the U-Pb zircon chemical abrasion ID-TIMS technique. Economic Geology 103-3, 465-471.

Selby, D., Kelley, K.D., Hitzman, M.W., Zieg, J., 2009. Re-Os sulfide (bornite, chalcopyrite, and pyrite) systematics of the carbonate-hosted copper deposits at Ruby Creek, Southern Brooks Range, Alaska. Economic Geology 104, 437-444.

Shackleton, R.M., 1995. Tectonic evolution of greenstone belts. Geological Society, London, Special Publications95-1, 53-65.

Shimizu, K., Komiya, T., Hirose, K., Shimizu, N., Maruyama, S., 2001. Cr-spinel, an excellent micro-container for retaining primitive melts – implications for a hydrous plume origin for komatiites. Earth and Planetary Science Letters 189, 177-188.

Sibson, R.H., 1987. Earthquake rupturing as a mineralizing agent in hydrothermal systems. Geology 15, 701-4.

Sillitoe R.H., Perello J., 2005. Andean Copper Province: tectono-magmatic settings, deposit types metallogeny, exploration and discovery. Economic Geology, 100th Anniversary Volume, 845-890.

Smith, H.A., Giletti, B.J., 1997. Lead diffusion in monazite. GeochimicaetCosmochimicaActa 61, 1047-1055.

Smithies, R., Champion, D., Cassidy, K., 2003.Formation of Earth's early Archaean continental crust. Precambrian Research 127, 89–101.

Stein, H.J., Morgan, J.W., Scherstén, A., 2000. Re-Os Dating of Low-Level Highly Radiogenic (LLHR) Sulfides: The Harnäs Gold Deposit, Southwest Sweden, Records Continental-Scale Tectonic Events. Economic Geology 95, 1657-1671.

Stevens, G., Boer, R., Gibson, R.L., 1997. Metamorphism, fluid flow and gold remobilization in the Witwatersrand Basin: towards a unifying model. South African Journal of Geology 100, 363-375.

Strong, D.F., 1988. A review and model for granite related mineral deposits. In Recent Advances in the Geology of Granite-related Mineral Deposits, Taylor R.P. and Strong D.F. (Ed.),Canadian Institute of Mining Metallurgy, Special Volume 39, 424-445.

Su, W., Hu, R., Xia, B., Xia, Y., Liu, Y., 2009.Calcite Sm-Nd isochron age of the Shuiyindong Carlin-type gold deposit, Guizhou, China. Chemical Geology 258, 269-274.

Sylvester, P.J., 1994. Archaean granite plutons. In Archaean crustal evolution,Condie, K.C., (Ed.) Development in Precambrian Geology. Elsevier, Amsterdam 11, 261-314.

Takenouchi, S., Kennedy, G.C., 1964. The binary system H2O-CO2 at high temperatures and pressures. American Journal of Science 262, 1055-1074.

Tartèse, R., Boulvais, P., 2010. Differentiation of peraluminousleucogranites “en route” to the surface. Lithos, 114, 353-368.

Tartèse, R., Ruffet, G., Poujol, M., Boulvais, P., Ireland, T.R., 2011. Simultaneous resetting of the muscovite K-Ar and monazite U-Pb geochronometers: a story of fluids. Terra Nova 23, 390-398.

Taylor, H.P., 1978. Oxygen and hydrogen isotope studies of plutonic granitic rocks.Earth and Planetary Science Letters 38, 177-210.

Taylor, S.R., McLennan, S.M., 1985. The continental crust: Its composition and evolution. Blackwell Scientific Publications 312p.

Taylor, S.R., McLennan, S.M.,1995. The geochemical evolution of the continental crust. Reviews of Geophysics 33, 241-265.

Thomas, A.V., Bray, C.J., Spooner, E.T.C., 1988. A discussion of the Jahns–Burnham proposal for the formation of zoned granitic pegmatites using solid–liquid–vapour inclusions from the Tanco pegmatite, SE Manitoba, Canada. Transactions of the Royal Society Edinburgh: Earth Sciences 79, 299-315.

Van den Berg, R.B., Huizenga, J.H., 2001. Fluids in granulites of the Southern Marginal Zone of the Limpopo Belt, South Africa. Contributions to Mineralogy and Petrology 141-5, 529-545.

Van Eeden, O.R., Partridge, F.C., Kent, L.R., Brandt, J.W., 1939. The mineral deposits of the Murchison Range east of Leydsdorp. Memoir of the geological survey of South Africa 36, 172.

Veizer, J., Jansen, S.L., 1979. Basement and Sedimentary Recycling and Continental Evolution, The Journal of Geology 87, 341-370.

Veizer, J., Laznicka, P., Jansen, S.L., 1989. Mineralization through geologic time: recycling perspective. American Journal of Science 289, 484-524.

Vearncombe, J.R., Barton, J.M., Walsh, K.L., 1987. The Rooiwater Complex and associated rocks, Murchison granitoid-greenstone terrane, Kaapvaal Craton. South African Journal of Geology 90, 361-377.

Vearncombe, J.R., 1988. Structure and metamorphism of the Archean Murchison belt, KaapvaalCraton, South Africa.Tectonics 7, 761-774.

Vearncombe, J.R., Cheshire, P.E., de Beer, J.H., Killick, A.M., Mallinson, W.S., McCourt, S., Stettler, E.H., 1988. Structures related to the Antimony line, Murchison schist belt, Kaapvaalcraton, South Africa. Tectonophysics154, 285-308.

Vearncombe, J.R., 1991. A possible Archaean island arc in the Murchison Belt, Kaapvaal Craton, South Africa. Journal of African Earth Sciences13, 299-304.

Vearncombe, J.R., Barton, J.M., Cheshire, P.E., de Beer, J.H., Stettler, E.H., Brandl, G., 1992. Geology, geophysics and mineralization of the Murchison Schist Belt, Rooiwater Complex and surrounding granitoids. Memoir of the Geological survey of South Africa 81.

Viljoen, M.J., van Vuuren, C., Pearton, T.N., Minnitt, R.C.A., Muff, R., Cillier, P., 1978. The regional geological setting of the mineralization in the Murchison Range with particular reference to Antimony, in Verwoerd, W. J., editor, Mineralization in metamorphic terranes, 55-76.

Villa, I.M., 2010. Disequilibrium textures versus equilibrium modelling: geochronology at the crossroads. In Advances in Interpretation of Geological Processes: Refinement of Multi-scale Data and Integration in Numerical Modelling. Spalla, M.I., Marotta, A.M., Grosso, G., (Ed.), Geological Society of London Special Publication 332, 1-15.

Walraven, F., 1989. The geology of the Pilgrim's rest Explanation of Sheet 2430 (1:250000).Geological Survey of South Africa, 24p.

Walraven, F.,Smith, C.B.,Kruger,F.J.,1991.Age determinations of the Zoetlief Group—a Ventersdorp Supergroup correlative.South African Journal of Geology 94, 220-227.

Ward, J.H.W., 1998. Antimony.InThe mineral resources of South Africa, Pretoria, South Africa, Wilson, M. and Anhaeusser, C. R., (Ed.), Council for Geoscience (edition), 59-65.

Ward, J.H.W., Wilson, M.G.C., 1998. Gold outside the Witwatersrand Basin. InThe mineral resources of South Africa, Pretoria, South Africa, Wilson, M. and Anhaeusser, C. R., (Ed.), Council for Geoscience (edition),350-386.

Wedepohl, H.K., 1995. The composition of the continental crust. Geochimica et Cosmochimica Acta 59-7, 1217-1232.

Wilde, S.A., Valley, J.W., Peck, W.H., Graham, C.M., 2001. Evidence from detrital zircons for the existence of continental crust and ocean on the Earth 4.4 Gyr ago. Nature, 409, 175-178.

Williams, Q.,Hemley, R.J., 2001. Hydrogen in the deep Earth. Annual Review of Earth and Planetary Sciences 29-1, 365-418.

William-Jones, A.E., Normand, C., 1997. Controls of mineral parageneses in the system Fe-Sb-S-O. Economic Geology 92, 308-324.

Wilson, C., Viljoen, M.J., 1986. The Athens antimony ore body, Murchison greenstone belt.Mineral deposits of South Africa 1, 293-320, Anhaeusser C.R. and Maske S. (Ed.), Geological Society of South Africa.

Windley, B.F., 2003. Continental growth in the Proterozoic: a global perspective. Geological Society, London, Special Publications 206, 23-33.

Zeh, A., Gerdes, A., Klemd, R., Barton, J.M., 2008. U-Pb and Lu-Hf isotope record of detrital zircon grains from the Limpopo Belt – evidence for crustal recycling at the Hadean to early-Archean transition. Geochimica et CosmochimicaActa 72, 5304–5329.

Zeh, A., Gerdes, A., Barton, J.M., 2009. Archean Accretion and Crustal Evolution of the Kalahari Craton–the Zircon Age and Hf Isotope Record of Granitic Rocks from Barberton/Swaziland to the Francistown Arc. Journal of Petrology 50, 933-966.

Zeh, A., Gerdes, A., Barton, J.M., Klemd, R., 2010. U-Th-Pb and Lu-Hf systematics of zircon from TTG's, leucosomes, anorthosites and quartzites of the Limpopo Belt (South Africa): constraints for the formation, recycling, and metamorphism of Paleoarchean crust. Precambrian Research 179, 50-68.

Zeh, A., Gerdes, A., Millonig, L., 2011. Hafnium isotope record of the Ancient Gneiss Complex, Swaziland, southern Africa: evidence for Archaean crust-mantle

formation and crust reworking between 3.66 and 2.73 Ga. Journal of the Geological Society of London 168, 953-963.

Zeh, A., Gerdes, A., 2012. U–Pb and Hf isotope record of detrital zircons from gold-bearing sediments of the Pietersburg Greenstone Belt (South Africa)—Is there a common provenance with the Witwatersrand Basin? Precambrian Research 204-205, 46-56.

Zwaan, J.C., 2006. Gemmology, geology and origin of the Sandawana emerald deposits, Zimbabwe. Scripta Geologica 131, 211p.

ANNEXE

Precambrian Research xxx (2012) xxx–xxx

Contents lists available at SciVerse ScienceDirect

Precambrian Research

journal homepage: www.elsevier.com/locate/precamres

The Murchison Greenstone Belt, South Africa: Accreted slivers with contrasting metamorphic conditions

Sylvain Block[a,b,*], Jean-François Moyen[a,b], Armin Zeh[c], Marc Poujol[d], Justine Jaguin[d], Jean-Louis Paquette[a]

[a] Laboratoire Magmas et Volcans, UMR 6524 CNRS, Université Blaise Pascal, Rue Kessler, 63038 Clermont-Ferrand, France
[b] Université Jean Monnet, 23 rue du Dr Paul Michelon, 42023 Saint-Étienne, France
[c] Institut für Geowissenschaften, Altenhöfer Allee 1, D-60438 Frankfurt am Main, Germany
[d] Géosciences Rennes, UMR CNRS 6118, Université de Rennes 1, Campus de Beaulieu, 35042 Rennes CEDEX, France

ARTICLE INFO

Article history:
Received 9 September 2011
Received in revised form 8 March 2012
Accepted 11 March 2012
Available online xxx

Keywords:
Metamorphism
Archaean tectonics
Murchison Greenstone Belt
Kaapvaal craton

ABSTRACT

This paper presents new petrological and geochronological data for the ~3.09–2.92 Ga Murchison Greenstone Belt (MGB), located in South Africa's Kaapvaal Craton, and discusses their geotectonic implications. The MGB is made of three tectono-metamorphic units: the Silwana Amphibolites, the Murchison Unit and the La France Formation. They underwent contrasting clockwise pressure–temperature–deformation (*P–T–D*) histories, and are separated from each other by relatively narrow, high-strain shear zones, with a sinistral, transpressive top-to-the-south movement, consistent with the deformation patterns observed throughout the belt. These patterns are explained by a N–S compressional stress field, affecting the Murchison Belt between 2.97 and 2.92 Ga. Results of new petrological investigations indicate that ultramafic to felsic volcano-sedimentary rocks of the Murchison Unit underwent a greenschist- to lower-amphibolite-facies metamorphism at maximum *P–T* conditions of 5.6 ± 0.6 kbar at 570 °C, along a relatively hot, minimum apparent geotherm of ~30 °C/km. In contrast, the Silwana Amphibolites and the La France Formation were metamorphosed at much higher peak metamorphic conditions of 8.7–10 kbar, 630–670 °C, and 8–9 kbar, 600–650 °C, respectively, and require a colder apparent geotherm of ~20 °C/km. A retrograde, nearly isothermal–decompression *P–T* path followed by isobaric cooling is also inferred for the La France Formation. The timing of the structural–metamorphic overprint is bracketed between 2.97 and 2.90 Ga, which is constrained by U–Pb zircon ages of a syn-deformation granite within the Murchison Unit and the post-deformation Maranda granite, respectively. Monazite and xenotime from La France metapelites yield much younger ages of ca. 2.75 Ga, with few inherited components at 2.92 Ga. They point to a later activation of the MGB, perhaps related with tectono-thermal events in the Rooiwater Complex and the Pietersburg Greenstone Belt. The relatively cold apparent geotherms recorded in the Silwana and La France rocks, the contrasted peak *P–T* conditions between the different units, and the near isothermal decompression of the La France Formation indicate that the Kaapvaal craton crust must have been cold enough to enable significant crustal thickening and strain localisation along narrow shear zones and, as a consequence, fast tectonic juxtaposition of rocks metamorphosed at different crustal depths. These features are similar to those observed along Palaeozoic or modern day, oblique subduction–collision zones, but different to those of hot Archaean provinces. We therefore interpret the MGB as representing part of an oblique collision-zone between two terrains of the Kaapvaal craton: the Witwatersrand and Pietersburg terrains.

1. Introduction

Many tectonic studies on various Archaean cratons have reported structural features in volcano-sedimentary belts that differ from younger Proterozoic and Phanerozoic orogenic belts (e.g. Bouhallier et al., 1993, 1995; Choukroune et al., 1995, 1997; Chardon et al., 1996, 1998, 1999). Linear fold and thrust belts, strain localisation along crustal scale faults, juxtaposition of contrasted metamorphic domains forming "paired metamorphic belts" (e.g., the Mesozoic Ryoke–Sanbagawa belts in Japan, Miyashiro, 1961; Brown, 2010 and references therein), tectonically driven exhumation processes, as well as features that are typical of subduction, such as ophiolites, accretionary prisms and blueschist-facies to

* Corresponding author at: Université Jean Monnet, 23 rue du Dr Paul Michelon, 42023 Saint-Étienne, France. Tel.: +33 621333525.
E-mail address: sylvain.block@gmail.com (S. Block).

0301-9268/$ – see front matter © 2012 Elsevier B.V. All rights reserved.
doi:10.1016/j.precamres.2012.03.005

Ultra-High-Pressure-facies metamorphism, are widely recognised in modern orogens. On the other hand, ubiquitous craton scale shear zones, dome and basin strain patterns, deformation distribution on a regional scale, and the relative homogeneity of erosion levels and metamorphic gradients are characteristic of many Archaean granite–greenstone provinces (Binns et al., 1976; Park, 1982; Chardon et al., 2008, 2009). The description of features in Archaean provinces interpreted to be related to subduction and modern-style accretion tectonics has fed the debate on the onset of plate tectonics and on the evolution of tectonic regimes through time (e.g. Komiya et al., 1999; Kusky et al., 2001; de Wit, 2004; Condie and Kröner, 2008; Cawood et al., 2009); and the recognition of contrasted tectono-metamorphic signatures between modern and Archaean orogens led authors to invoke secular changes in the thermal regime of the Earth as the factor driving the shift from one tectonic style to another (e.g. Komiya et al., 2002; Brown, 2007; Gapais et al., 2009; Sizova et al., 2010). A wide range of models were proposed to account for the features observed in Archaean provinces. An intellectual framework defined by two "end-member" models, with a hot and weak lithosphere in the Archaean as opposed to a cold and strong lithosphere in the Proterozoic and Phanerozoic eras has been widely adopted. However, given the wide variation in the rheological properties of Phanerozoic lithospheres (Watts and Burov, 2003 and references therein), one can expect to be confronted to such geographical disparities in Archaean cratons.

The heat budget of the lithosphere is a major control of its rheological properties, and as a consequence, of the dominant tectonic regime in the crust. Metamorphic rocks record evidence of the pressure and temperature evolution with time, which reflects the thermal environment under which the constituent mineral assemblages equilibrated. Spatial distribution of peak *P–T* conditions provide information on the spatial variation in thermal regimes; hence metamorphic studies are an important tool to investigate the tectonic style of Archaean provinces. Although metamorphic studies, coupled with structural and geochronological constraints, have contributed greatly to our understanding of modern orogenic processes (e.g. Miyashiro, 1961; Ernst, 1973, 1975, 1988; Chopin, 1984; Smith, 1984; Brown, 2009), metamorphism across Archaean granite–greenstone terrains has been comparatively under-studied. Consequently, the lack of well-constrained metamorphic studies has hampered the development of a geodynamic framework for the formation of granite–greenstone terrains. It has also led to the generalisation in the literature of implicit assumptions on Archaean metamorphism, as some observations relevant to specific Archaean provinces are taken to be a general rule.

Most granite–greenstone terrains are reported to have undergone metamorphism along high-temperature, low-pressure apparent geothermal gradients. Metamorphic conditions are generally described as isobaric across hundreds of kilometres, with isotherms parallel to the surface, or as grading progressively from low-grade greenschist–facies to granulite–facies across kilometres–large and hundreds of kilometres–long shear zones, where strain is distributed rather than localised (Grambling, 1986; Collins and Vernon, 1991; Percival, 1994; Percival et al., 1992; Caby et al., 2000). Variations in metamorphic grade in Archaean granite–greenstone terrains are frequently attributed to contact metamorphism linked to the emplacement of granitoid bodies, or as the result of a "crustal overturn" (Van Kranendonk et al., 2002). However, an increasing number of studies provide evidence for disparities in metamorphic patterns between Archaean terrains. High P–low *T* metamorphism (18–20 kbar, 630 °C) is reported from the Indian Bundelkhand Craton at ca. 2.78 Ga (Saha et al., 2011); ca. 2.72 Ga eclogite–facies metamorphism is recorded in the Belomorian belt of Russia (Volodichev et al., 2004; Brown, 2009; Mints et al., 2010). High metamorphic gradients between terrains metamorphosed at different depths, and juxtaposed along planar tectonic structures that localised deformation, are described in the Palaeoarchaean Barberton Greenstone Belt (BGB), in the east of the Kaapvaal craton, South Africa (Kisters et al., 2003; Diener et al., 2005; Moyen et al., 2006) and in the Mesoarchaean Point Lake orogen of the Slave Province, Canada (Kusky, 1991).

This study aims to unravel the tectono-thermal history of the northwestern part of the Archaean Kaapvaal Craton in South Africa. In order to do so, the metamorphic conditions across the Murchison Greenstone Belt, the nature of the contacts between the distinct tectono-metamorphic units, and the timing of the structural–metamorphic and magmatic processes were investigated. By coupling the different information, we intend to bring new insights into the geodynamic evolution that led to the formation of the MGB and to contribute to a broader understanding of Archaean tectonics.

2. Geological setting of the MGB

2.1. Regional context and geochronological constraints

The ENE–WSW trending Murchison Greenstone Belt is one of the volcano-sedimentary belts of the Archaean Kaapvaal craton of South Africa (Brandl et al., 2006; Robb et al., 2006) (Fig. 1). It is situated about 200 km north of the ca. 3.5–3.2 Ga Barberton Greenstone Belt (e.g. Kröner et al., 1991, 1992, 1996; Kamo and Davis, 1994; Dziggel et al., 2002), and about 80 km south of the 3.2–2.8 Ga Giyani Greenstone Belt (Kröner et al., 2000). It extents for ~140 km ENE–WSW, 15–20 km N–S, and is unconformably overlain by the Neoarchaean to Palaeoproterozoic sediments of the Transvaal Supergroup (Burger and Coertze, 1973; Altermann and Nelson, 1998) at its western extremity. Furthermore, it is located along the "Murchison-Thabazimbi Lineament" (Du Plessis, 1990), which is defined on the basis of geophysical data and interpreted to form an important terrain boundary in the northern Kaapvaal craton, separating the Witwatersrand terrain to the south from the Pietersburg terrain to the north (Good and De Wit, 1997; Anhaeusser, 2006; Zeh et al., 2009).

At its northern margin, the supracrustal rocks of the MGB are bounded by the Rooiwater Complex and the Groot Letaba Gneisses. The Rooiwater Complex (Vearncombe et al., 1987) represents a mostly undeformed layered mafic intrusion emplaced at a minimum age of 2.74 Ga (Poujol et al., 1996) and subsequently intruded by mafic dykes at 2.61 Ga (Zeh et al., 2009). Field evidence however suggest that this age may correspond to a late resetting of geochronometers, and the emplacement age of the Rooiwater complex is likely to be significantly older (Vearncombe et al., 1992). The contact between the Rooiwater Complex and the MGB is tectonically reworked (Vearncombe et al., 1992). The Groot Letaba Gneisses (Brandl and Kröner, 1993) comprise a series of locally migmatised dark-grey gneisses, tonalites and trondjhemites. They were mostly emplaced at ca. 3180–3000 Ma, with the exception of some ca. 2885 ± 4 Ma discordant leucogneisses (Brandl and Kröner, 1993). The basement directly to the south of the MGB is made of granitoids (TTGs) of the French Bob's Mine, emplaced 3228 ± 12 Ma ago (Poujol et al., 1996); and by younger intrusive granitoids of ca. 3110–3060 Ma (Brandl and Kröner, 1993; Poujol and Robb, 1999). The southern margin of the MGB was affected by the episodic intrusion of granite plutons and pegmatites of the Voster Suite, at ca. 3020, 2970, 2900, 2820 and 2680 Ma, respectively for the Baderoukwe, Discovery, Maranda, Willie, Mashishimale plutons, and associated intrusions (Fig. 2) (Poujol et al., 1996; Poujol and Robb, 1999; Poujol, 2001; Zeh et al., 2009). Published geochronological data indicate that the supracrustal sequence of the MGB formed over a period of more than 100 Ma, between ca. 3090 and 2970 Ma (Poujol et al., 1996; Poujol, 2001).

Please cite this article in press as: Block, S., et al., The Murchison Greenstone Belt, South Africa: Accreted slivers with contrasting metamorphic conditions. Precambrian Res. (2012), doi:10.1016/j.precamres.2012.03.005

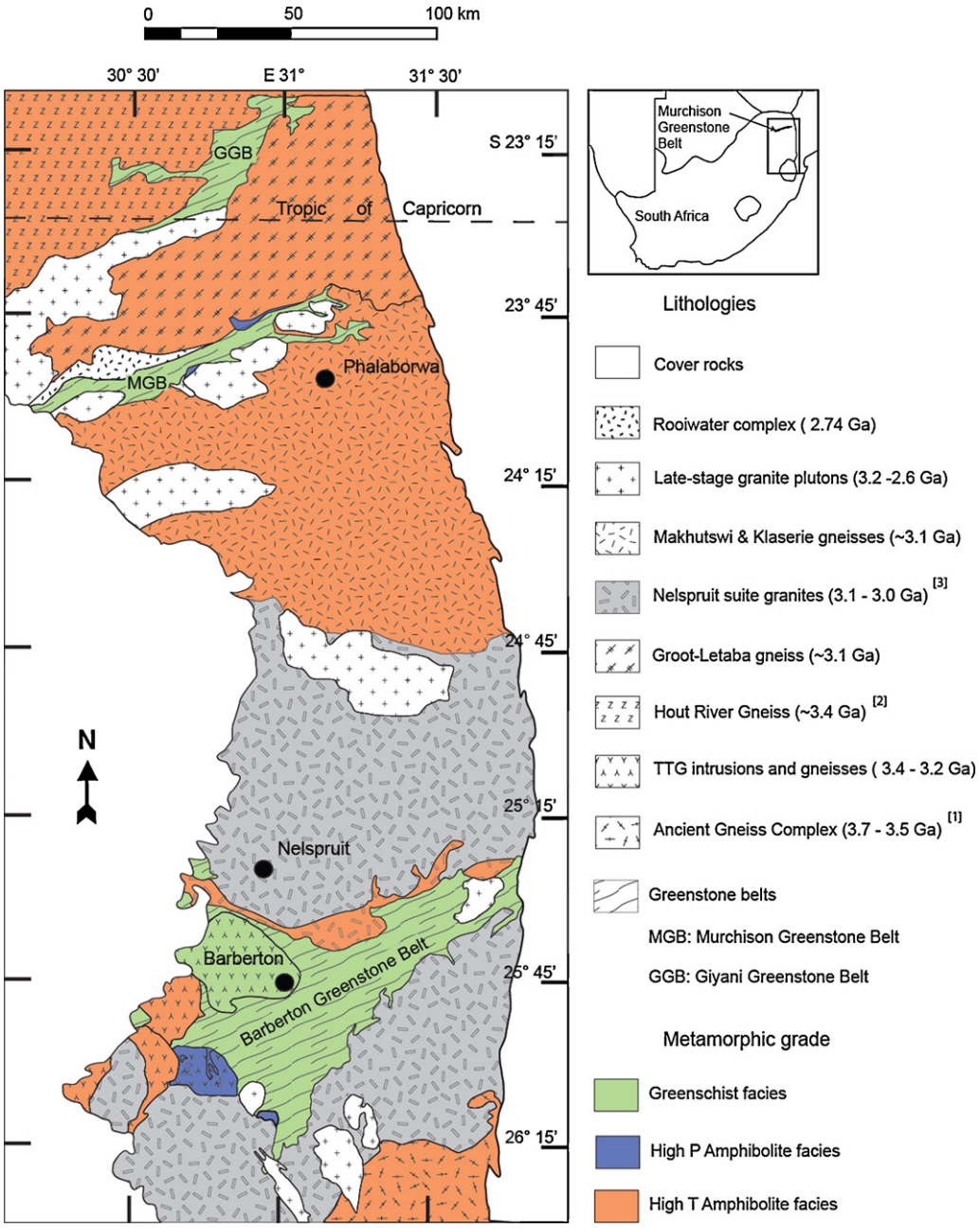

Fig. 1. Simplified geologic map of the north-eastern part of the Kaapvaal craton. Different colours represent domains with different metamorphic grades, inferred from sparse field observations and data from the literature. [1]: Kröner and Tegtmeyer (1994); Compston and Kröner (1988), [2]: Kamo and Davis (1994), [3]: Brandl and Kröner (1993); Kröner et al. (2000). See text for other references.

2.2. Structural–metamorphic units of the MGB

Based on structural and lithological criteria, Vearncombe et al. (1992) subdivided the MGB into four major, ENE–WSW-striking lithostratigraphic domains (Fig. 2):

The largest lithological domain of the MGB, hereafter referred to as the "Murchison Unit", includes the MacKop, Weigel, Leydsdorp and Mulati formations of the South African Committee for Stratigraphy (SACS, 1980) nomenclature. It consists of mafic and ultramafic volcanic rocks along with volcano-sedimentary and sedimentary rocks. The most representative lithologies of the domain are mafic quartz–chlorite and albite–chlorite–actinolite schists, locally pillowed. The volcano-sedimentary rocks are locally interbedded with BIFs and with aluminous quartzites and conglomerates. The clastic sediments form prominent ridges, often corresponding to synform limbs in the central part of the MGB. Massive carbonates and carbonate schists crop out mostly along a high-strain shear zone in the centre of the belt, flanked by quartzite ridges to the north: the Antimony Line (Viljoen et al., 1978; Vearncombe et al., 1988a, 1992), which hosts Sb (±Au) mineralisation. Serpentinite lenses occur in the southern part of the belt. Stratigraphic relationships within this unit remain unclear, as contacts between formations are tectonic in nature (Vearncombe et al., 1992). U–Pb zircon ages provide evidence that the Weigel Formation volcanics were emplaced at ca. 3.09 Ga, while a maximum age of deposition for the MacKop conglomerate was found to be ca. 3.08 Ga old (Poujol et al., 1996).

The Rubbervale Formation is exposed along the northwestern flank of the MGB. It comprises quartz–porphyroclastic schists, along

Please cite this article in press as: Block, S., et al., The Murchison Greenstone Belt, South Africa: Accreted slivers with contrasting metamorphic conditions. Precambrian Res. (2012), doi:10.1016/j.precamres.2012.03.005

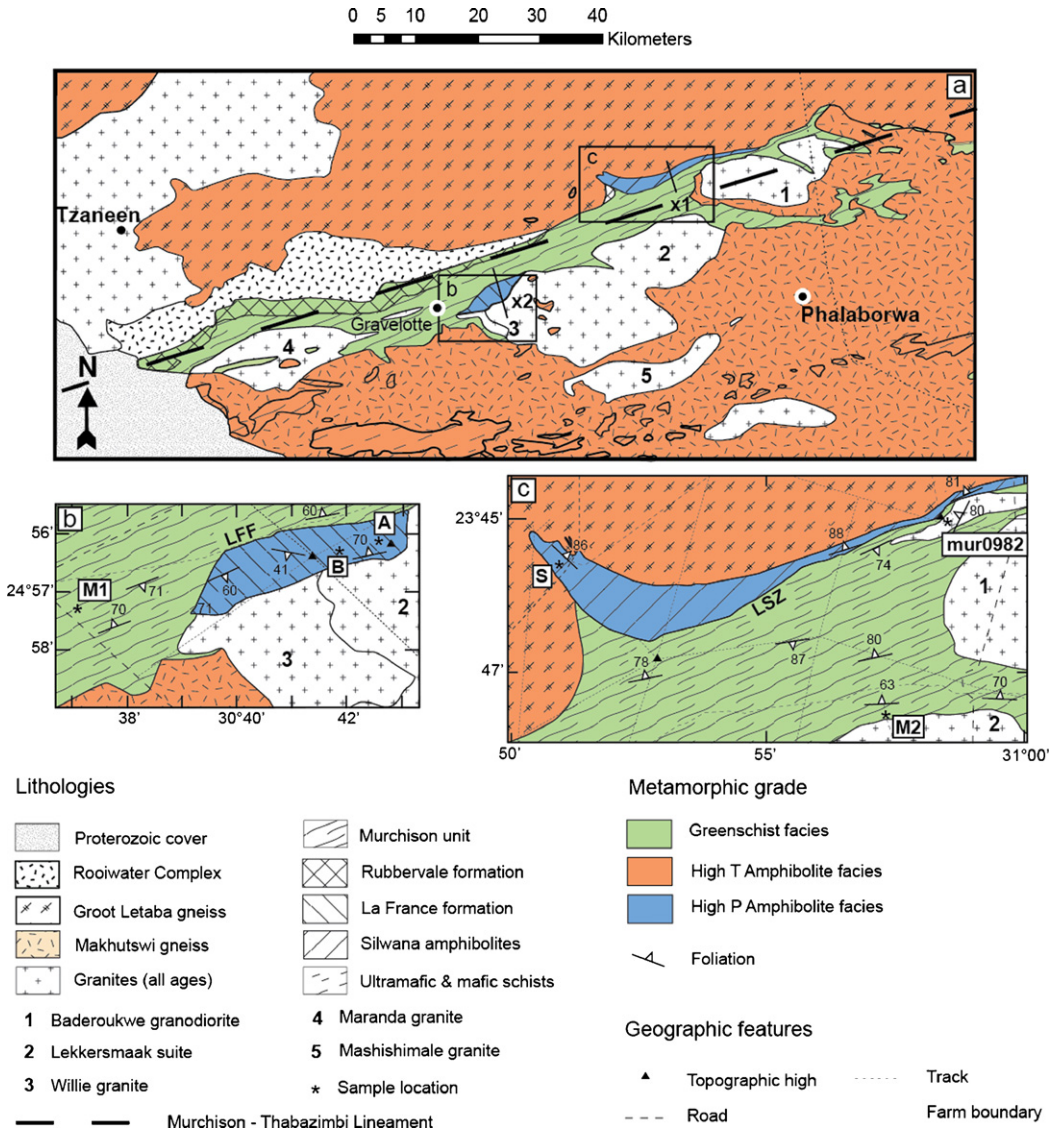

Fig. 2. (a) Simplified geologic and metamorphic map of the Murchison Greenstone Belt and its surroundings. (b, c) Detailed maps with the location of samples (A, B, S, M1, M2 and mur0982) discussed in the text, modified from Vearncombe et al. (1992). The lines marked with x_1 and x_2 correspond to the cross section shown in Fig. 9. LFF = La France Fault, LSZ = Letaba Shear Zone.

with felsic lavas, tuffs and breccias. This formation also hosts the major VMS-type deposit of the so-called 'Cu-Zn' line (Schwartz-Schampera et al., 2010). Emplacement of the Rubbervale formation was dated at ca. 2.97 Ga (Brandl et al., 1996; Poujol et al., 1996; Poujol, 2001).

The third unit, the Silwana Amphibolites (Vearncombe et al., 1992; part of the Rubbervale formation in the SACS terminology), is exposed in the north-eastern part of the MGB, and represent a 0.1–1.5 km wide sliver of amphibolites, rarely garnet-bearing, displaying a centimetric layering.

La France Formation (Vearncombe et al., 1992, SACS terminology) mostly consists of quartzite and kyanite–staurolite–garnet-bearing biotite micaschists.

Vearncombe (1988b) and Vearncombe et al. (1992) stated that the Silwana Amphibolites and the rocks of the La France Formations experienced a higher degree of metamorphism than the rocks of the Murchison Unit and Rubbervale Formation, which together form the core of the MGB (Fig. 2). Metamorphic *P–T* conditions were estimated to be >5 kbar, 550–650 °C for the La France Formation, while field observations qualitatively suggested a higher grade metamorphic conditions in the Silwana Amphibolites compared to the Murchison Unit.

2.3. Contact zones between the units of the MGB

The different units of the MGB are separated from each other by large-scale ductile shear zones. A detailed structural study of the MGB is beyond the scope of this paper and only a brief review of the nature of the contacts is presented here. A description of the regional strain field and the tectonics of the MGB are given in Vearncombe (1988b), Kusky and Vearncombe (1997) and Jaguin et al. (2012).

2.3.1. The Letaba Shear Zone

To the north-east of the MGB, the Letaba Shear Zone (LSZ) separates the Silwana Amphibolites from low-grade, quartz–chlorite and carbonate schists of the Murchison Unit. The contact is very sharp and shows signs of a tectonic melange. The Silwana Amphibolites display a penetrative flattening fabric formed under amphibolite-facies conditions. The cleavage is subvertical and bears

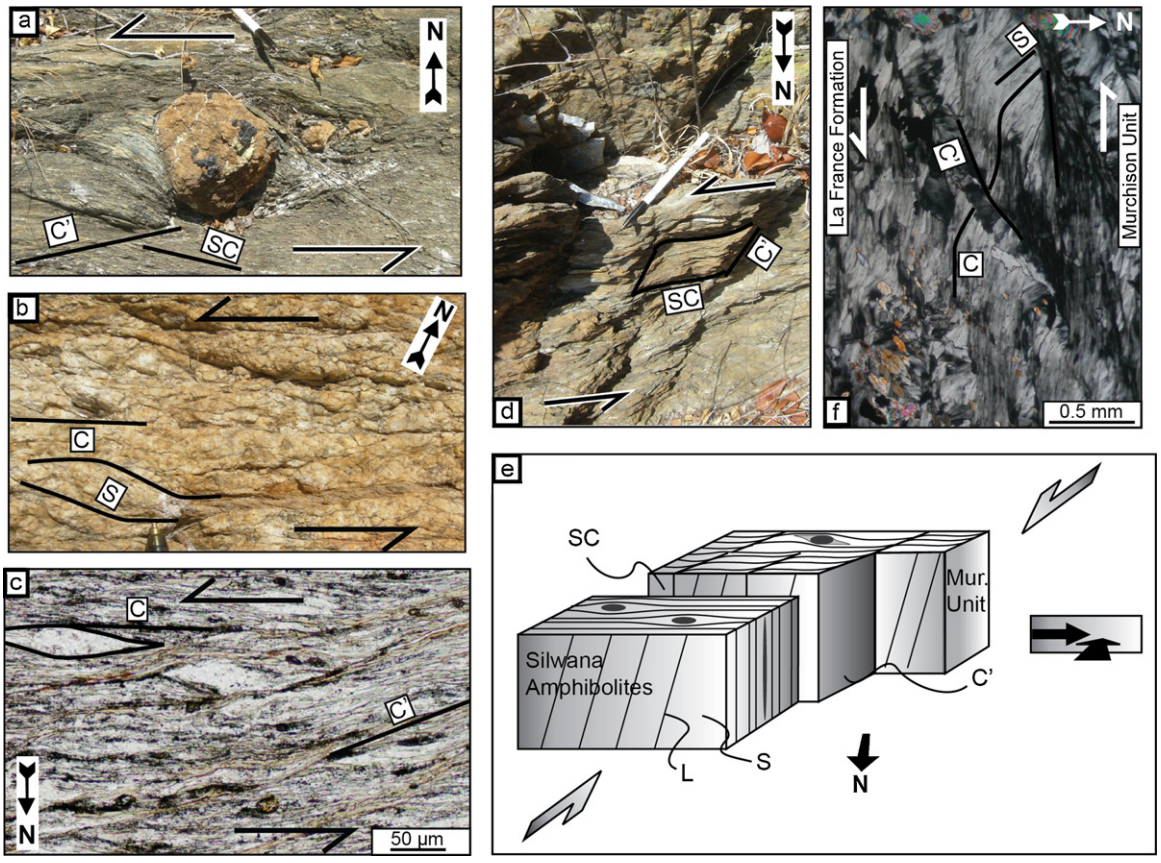

Fig. 3. Fabrics at or near to the sheared contacts between the different terrains of the MGB. (a). Asymmetric pressure shadow zones around a carbonate nodule in a mylonitic carbonate schists of the Murchison Unit, in the Letaba Shear Zone. (b) S–C fabrics in a deformed granite within the Letaba Shear Zone. (c) Microstructures observed in the quartz–chlorite schists of the Letaba Shear Zone include C′ shear bands and mineral fish. (d) S–C–C′ planes in quartz–chlorite schists of the Murchison Unit, in the Letaba Shear Zone. The kinematic indicators in (a–d) provide evidence for sinistral motion along the shear zone. (e) Synopsis of the structures observed along the Letaba shear zone. The flattening fabric in the Silwana amphibolites, that formed under upper-amphibolite facies conditions, occurs in close contact with mylonitised schists of the Murchison Unit, which provide evidence for a sinistral strike–slip under greenschist facies conditions. The latter is interpreted to have occurred in a transpressive setting and was accompanied by a top-to-the-south motion. (f) S–C–C′ fabrics in a chlorite schists of the Murchison Unit, near the contact with the La France Formation, provide evidence for top-to-the-south motion. The C planes are subvertical.

a steep (pitch >75°) easterly plunging mineral elongation lineation. Asymmetric shear sense indicators are rare within this formation: pressure shadow zones around garnet porphyroblasts are symmetrical, and no shear bands were observed in thin sections. Towards the contact with the Silwana Amphibolites, the Murchison Unit schists display a mylonitic microstructure and a significant grain size reduction. The mylonites exhibit an NE–SW cleavage, parallel to the contact between the two formations. The cleavage has a moderate to sub-vertical dip to the south and carries a mineral elongation lineation dipping moderately (pitch > 40°) to the east. Asymmetric shear sense indicators, such as pressure shadow zones around primary carbonate nodules consistently point to a sinistral shear (Fig. 3a). The same shear direction is also reflected by SC–C′-fabrics and extensional crenulation cleavages (Berthé et al., 1979; Platt and Visser, 1980), indicative of stretching parallel to the foliation, which are well developed within the mylonitised quartz–chlorite-schists (Fig. 3c and d). At the "Witkop" locality (near sample mur0982 in Fig. 2), where the relationships between the different units are clearly exposed, a deformed granite intrudes the greenschist-facies mylonites of the Murchison Unit. No contact metamorphism was observed in the quartz–chlorite schists around the granite body. The granite displays well-expressed C–S structures (Fig. 3b). S and C surfaces have a shallow to sub-vertical dip towards the NW, and C surfaces carry a mineral elongation lineation that plunges to the NE. The deformation patterns provide evidence for a sinistral, transpressive setting with a top-to-the-south directed motion (Fig. 3e). The strike–slip component of the finite deformation that is well expressed in the greenschist facies mylonites of the Murchison Unit is not observed in the Silwana Amphibolites.

2.3.2. The "La France Fault"

The La France Formation is separated from the greenschist-facies rocks of the Murchison Unit by a highly deformed zone a few dozen metres wide, hereafter named the "La France Fault". The lithologies in contact with the northern boundary of the La France Formation range from talc schists and serpentinites to chlorite schists containing primary carbonates. Within the shear zone, the schists display open to tight folds with decimetric wavelengths. At least two sets of such folds are found, with axes displaying shallow plunges of 5–10° to the NW and SW respectively. Unfortunately, poor outcrop conditions restricted to exploration trenches, among other constraints, prevented a more extensive study of fold patterns. Mineral elongation lineations on shear-zone-parallel cleavages plunge preferentially to the NE, whereas shear sense indicators, such as mineral fish and asymmetric shadow zones around porphyroblasts, point to a top-to-the-south motion (Fig. 3f). These patterns in combination provide evidence for a sinistral component during a general top-to-the-south reverse faulting, similar to that observed along the Letaba Shear Zone. The latter interpretation is also in agreement with structures observed within the La France formation to the south of the shear zone. The La France schists

Please cite this article in press as: Block, S., et al., The Murchison Greenstone Belt, South Africa: Accreted slivers with contrasting metamorphic conditions. Precambrian Res. (2012), doi:10.1016/j.precamres.2012.03.005

Table 1
Summary of the mineral assemblages and textures developed in the different formations of the MGB.

Terrain	Rock type	Outcrop occurrence	Mineral assemblages	Texture	Sample
La France Formation	Gt–St-bearing micaschist	Bt-schist with thin metamorphic banding, crenulated. Protruding elongated Gt and St	Peak (syn-D_2): Gt + St + Bt + Ms + Q Post-peak: Bt, Hem	Large Gt and St porphyroblasts, thin Bt beds, crenulated.	A
La France Formation	Ky (± St)-bearing micaschist	Bt-schist with thin metamorphic banding. Protruding elongated Ky.	Peak (syn-D_2): Ky + Bt + Ms + Pl ± St ± Ilm ± Ru + Q Retrograde: Bt + Sill + Pl + Crd/Bt + Chl + Ms + St ± Ky Accessory: Mnz, Xno	Large Ky porphyroblasts, elongated parallel to Bt beds. Retrograde Crd, Bt–Chl–Ms simplectite, St	B
Murchison Unit	Act-bearing metabasite	Green metabasite, no pervasive tectonic fabric	Peak: Act + Ab + Chl + Ep + Sph	Garbenscheifer texture: needle-shaped Act, Chl in late shear bands	M1
Murchison Unit	Aluminous quartzite	Fine grained quartzite with well developped metamorphic cleavage, parallel to micaceous bedding	Peak: Gt + Bt + Ms + Q Retrograde: Chl	Thin aligned Ms and Bt beds with small Gt, intercalated with protogranular quartz beds	M2
Silwana Amphibolites	Gt-Hbl-bearing amphibolite	Dark, fine grained, massive "amphibolitic gneiss" with occasional garnet-bearing layers	Peak: Hbl + Pl + Gt + Bt + Ilm + Q Retrograde: Chl, Ep Accessory: Ap, Calc	Equigranular texture with aligned Hbl. Intercalation of Hbl and recristallised Pl and quartz beds. Gt porphyroblasts with Ilm and Hbl inclusions	S

exhibit recumbent folds axial planar to the metamorphic banding, and are affected by crenulations with shallow-plunging axes. These structures are illustrative of a shortening accommodated by reverse faulting.

To the south, the La France Formation is in contact with the 2795 ± 8 Ma Lekkersmaak granite (Zeh et al., 2009) and with the 2820 ± 38 Ma Willie granite (Poujol, 2001), which form part of the Voster Suite. The granites contain micaschist xenoliths derived from the La France Formation. They are mostly undeformed except for occasional shear bands formed under sub-solidus conditions. The field relationships clearly indicate that the Lekkersmaak and Willie intrusions postdate the deformation and metamorphism in the La France Formation.

2.3.3. Other structures

The Antimony Line is a steeply north dipping mineralised shear zone within the Murchison Unit. The dominant fabric consists of isoclinal folds axial-planar to the metamorphic banding, along with S–C planes indicating a top-to-the-south motion. Mineral elongation lineations plunge vertically to moderately eastwards. These structures illustrate a general transpressive, sinistral setting in the Murchison Unit, accompanied by a significant reverse component (Vearncombe et al., 1988a, 1992). They are consistent with the kinematics observed in the Letaba and La France shear zones. At a larger scale, they are in general agreement with the regional-scale sinistral transpressive regime and illustrate deformation localisation in the regional strain field, described in Jaguin et al. (2012).

3. Petrography, fabrics and mineral chemistry

A summary of the main petrographic and textural characteristics of the rocks sampled from the different formations of the MGB is presented in Table 1. Details of analytical techniques used to determine mineral chemistry are given in Appendix A.1.

3.1. La France Formation

Field observations and microstructural studies of quartzites and micaschists of the La France Formation provide evidence that a primary compositional layering S_0 was modified during an early D_1 deformation event, leading to the formation of a composite S_0/S_1 foliation. The S_0/S_1 foliation was subsequently affected by the main D_2 deformation event (Fig. 4b, e). The latter caused the formation of the predominant S_2 fabric that is axial-planar to recumbent folds. The S_2 planes are mostly defined by quartz (Q) ribbons, biotite (Bt), and minor muscovite (Ms). They bear a L_2 mineral elongation lineation. In metapelitic layers syn-deformation staurolite (St), garnet (Gt) and kyanite (Ky) porphyroblasts can additionally be observed, although the latter two are not found together in the same sample (Fig. 4a and c). Plagioclase feldspar (Pl) sillimanite (Sill) and cordierite (Crd) occasionally occur in the kyanite-bearing schists. The S_2 schistose planes were crenulated as a result of a D_3 deformation event, leading to the formation of kinks with a mm- to cm-scale wavelength, and of a crude S_3 cleavage. In kyanite-bearing micaschist, some kyanite, staurolite and chlorite were kinked during D_3 crenulation, while new chlorite, staurolite and muscovite develop in the kink axes (Fig. 4f). The final minerals thus form syn- to post-D_3 assemblages.

The garnet-bearing micaschists display the following peak assemblage:

$$(A): \quad Gt + St + Bt_1 + Ms_1 + Q$$

In these rocks, syn-deformation garnet porphyroblasts with quartz inclusion trails are commonly overgrown by syn-deformation staurolite, with similarly oriented quartz inclusion trails, indicating the successive formation of both minerals during the deformation event D_2 (Fig. 4d). Hematite is always a retrograde phase, which formed along cracks in altered garnet grains, mostly at garnet rims. The peak metamorphic fabric is overgrown by post-deformation biotite (Bt_2) and muscovite (Ms_2). Garnet porphyroblasts show a continuous prograde growth zoning, characterised by increasing X_{Py} (Mg/(Mg + Fe + Ca + Mn)) from 0.05 to 0.09 and Mg# (Mg/(Fe + Mg)) from 0.07 to 0.09, and decreasing X_{Sps} (Mn/(Mg + Fe + Ca + Mn)) from 0.12-0.06 to 0.03 and X_{Grs} (Ca/(Mg + Fe + Ca + Mn)) from 0.07 to 0.06, all from core to rim. Staurolite has Mg# of 0.12–0.14. The Mg# of syn-D_2 biotite (Bt_1) ranges from 0.32 to 0.44 range, while post-D_2 biotite (Bt_2) has Mg# = 0.44, suggesting partial reequilibration of Bt_1. Muscovite (Ms_1 and Ms_2) has low Si of 3.05 a.pf.u. (atoms per formular unit) and a relatively high paragonite component, as is reflected by Na/(Na + K + Ca) = 0.17. Representative mineral compositions are shown in Table 2.

Kyanite-bearing schists (B) provide evidence for the successive formation of different equilibrium assemblages during peak and

Please cite this article in press as: Block, S., et al., The Murchison Greenstone Belt, South Africa: Accreted slivers with contrasting metamorphic conditions. Precambrian Res. (2012), doi:10.1016/j.precamres.2012.03.005

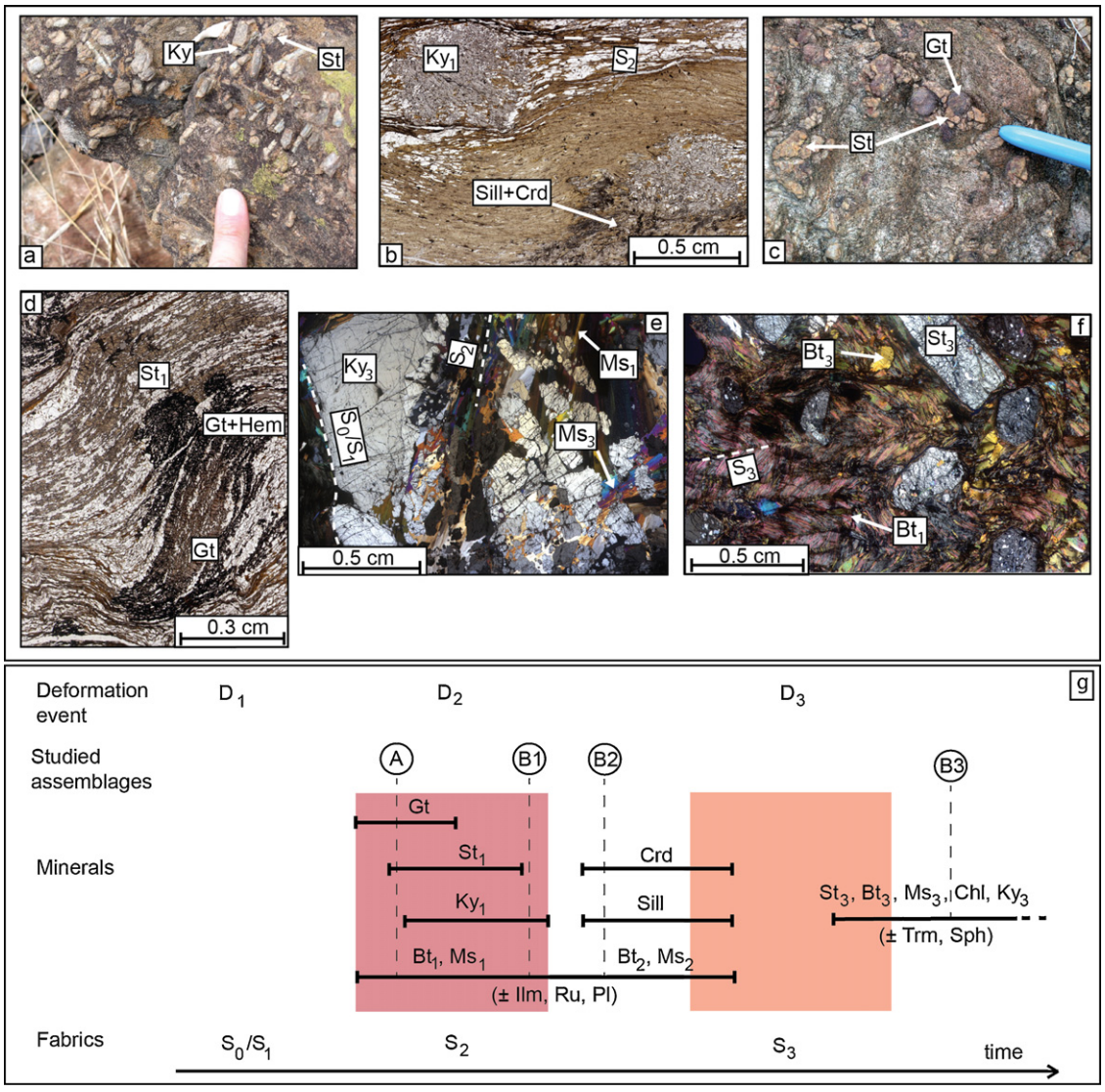

Fig. 4. Petrographic features observed in rocks of the La France formation. (a) Biotite micaschist with protruding staurolite (St) and kyanite (Ky) porphyroblasts. (b) Thin section of a kyanite–staurolite–cordierite-bearing micaschist (sample B). Ky porphyroblasts are surrounded by foliation-parallel biotite and quartz (top), or are overgrown by patches of sillimanite and cordierite. (c) Garnet (Gt)–staurolite-bearing micaschist (sample A). (d) Thin section of sample A showing highly deformed and rotated St and Gt porphyroblasts (syn-D_2), set in a matrix of biotite, muscovite and quartz. Hematite (Hem) occurs along cracks mostly in garnet rims, probably resulting from retrograde alteration. Biotite and muscovite define the syn-D_2 metamorphic banding. (e, f) Thin sections of a Ky–St-bearing schist from the La France formation showing, (e) a compositional layering S_0/S_1 delimiting a kyanite and muscovite-rich layer, with Ky overgrowing the D_2 metamorphic fabric, (f) a crenulated domain, with euhedral staurolite and a crude S_3 cleavage. (g) Synopsis showing the relative temporal relationships between deformation and assemblage formation in the La France Formation (Ilm: Ilmenite, Ru: Rutile, Trm: Tourmaline, Sph: Sphene).

retrograde evolution. The peak metamorphic conditions are illustrated by syn-D_2 kyanite porphyroblasts that commonly contain biotite, muscovite and quartz inclusions. Some rocks additionally bear syn-D_2 staurolite porphyroblasts, produced with kyanite, presumably during the progressive breakdown of chlorite (which completely reacted out). Thus the thin section observations indicate that the following assemblage formed during D_2 deformation at peak pressures (Fig. 4b):

(B1) $Ky_1 + Bt_1 + Pl + Ms_1 + Q \pm St_1$.

The occurrence of prismatic sillimanite, as well as of fibrolite around kyanite indicates that the kyanite-bearing schists crossed the phase transition Ky → Sill. The coexistence of sillimanite and cordierite (Crd) (Mg# = 0.75–0.77; Na = 0.11 a.p.f.u.), which together form patches about 0.5 mm wide, shows furthermore that assemblage (B1) was later (partially) replaced by the assemblage:

(B2) $Sill + Bt_2 + Crd + Pl + Q$.

Subsequently, the cordierite grains were partially replaced by a new generation of micrometric staurolite grains, which are closely intergrown with fine grained, chlorite and symplectitic muscovite. These intergrowth relationships indicate that the final mineral assemblage in the kyanite-bearing schists was:

(B3) $St_3 + Bt_3 + Ms_3 + Chl + Q$.

Retrograde staurolite St_3 generally has higher Mg# of 0.19–0.24 than the prograde and peak metamorphic staurolite St_1, with Mg# of 0.13–0.20. In contrast, biotite from all the successive assemblages (Bt_1 to Bt_3) overlap in compositions, with Mg# = 0.62–0.64, Ti^{vi} = ~0.06. This is interpreted to be the result of widespread chemical reequilibration of biotite composition during

Please cite this article in press as: Block, S., et al., The Murchison Greenstone Belt, South Africa: Accreted slivers with contrasting metamorphic conditions. Precambrian Res. (2012), doi:10.1016/j.precamres.2012.03.005

Table 2
Major element compositions and structural formulae of representative mineral analyses of the peak and retrograde assemblages in lithologies from the La France Formation, Murchison Unit and Silwana Amphibolites.

Sample	A (garnet–staurolite micaschist of the La France Formation)									
Mineral phase	Gt (core)	Gt (core)	Gt(rim)	St (core)	St (rim)	Bt_1	Bt_1	Bt_2	Ms_1	Ms_2
(a) wt%										
Na_2O				b.d.l.	b.d.l.	0.08	0.16	0.22	1.23	1.31
MgO	1.36	1.67	2.21	1.36	1.22	7.39	5.10	8.19	0.42	0.45
Al_2O_3	20.7	20.7	21.0	53.9	54.2	21.6	21.3	19.8	36.6	36.5
SiO_2	36.5	36.7	36.6	26.4	26.3	37.9	36.4	34.8	46.0	45.9
K_2O						7.22	7.50	6.61	9.22	9.46
CaO	2.65	2.07	1.95	b.d.l.	b.d.l.	0.14	0.16	0.08	0.01	0.04
TiO_2				0.22	0.34	0.98	0.65	0.95	0.09	0.07
Cr_2O_3						0.03	0.05	0.03	0.07	0.01
MnO	5.44	3.59	1.17	0.02	0.06	0.01	b.d.l.	b.d.l.	b.d.l.	0.01
FeO	34.2	35.0	37.6	15.7	15.1	16.8	19.4	18.4	1.16	1.04
Total	100.8	100.4	100.4	97.6	97.2	92.1	90.7	89.1	94.8	94.7
Oxygens	12	12	12	48	48	22	22	22	22	22
Si	5.93	5.97	5.93	7.42	7.41	5.76	5.73	5.54	6.11	6.11
Al^{IV}	0.07	0.03	0.07	0.58	0.59	2.24	2.27	2.46	1.89	1.89
Al^{VI}	3.94	3.98	3.90	17.3	17.4	1.70	1.59	1.26	3.84	3.83
Fe^{3+}	0.19	0.03	0.25	0.67	0.55					
Ti				0.05	0.07	0.10	0.11	0.11	0.01	0.01
Cr						0.00	0.00	0.00		
Mg	0.53	0.39	0.33	0.57	0.51	1.58	1.67	1.94	0.08	0.09
Fe^{2+}	4.90	4.87	4.39	3.03	3.00	2.10	2.12	2.45	0.13	0.12
Mn^{2+}	0.16	0.37	0.75	0.01	0.01	0.00				
Ca	0.34	0.39	0.46			0.07	0.02	0.01	0.00	0.01
Na						0.01	0.02	0.07	0.32	0.34
K						1.23	1.39	1.34	1.56	1.61
x[Py]	0.05	0.06	0.09							
x[Alm]	0.75	0.81	0.83							
x[Sps]	0.12	0.06	0.03							
x[Grs]	0.07	0.06	0.06							
*x*Fe[fcel]									0.06	0.06
*x*Mg[mcel]									0.04	0.04
*x*Al[mphen]									0.89	0.90

Sample	B (kyanite-plagioclase micaschist of the La France Formation)											
Mineral phase	Pl	Pl	St_3	St_3	Bt_1	Bt_3	Crd	Crd	Wm_1	Wm_3	Chl	Chl
(b) wt%												
Na_2O	6.65	10.5			0.35	0.21	0.68	0.44	0.36	1.41	b.d.l.	0.03
MgO	0.01	0.02	1.98	2.17	13.26	14.40	9.56	9.68	2.76	1.19	18.8	19.4
Al_2O_3	26.9	21.2	54.1	53.9	19.4	19.2	32.6	32.8	33.1	36.8	22.9	22.7
SiO_2	57.3	66.1	28.9	29.1	36.5	35.2	49.1	49.0	46.6	46.0	25.5	26.0
K_2O	0.04	b.d.l.			9.12	8.40	0.01	0.02	6.02	9.28	0.44	0.68
CaO	8.45	1.99	b.d.l.	b.d.l.	0.04	0.04	0.07	0.03	0.42	0.02	0.10	0.05
TiO_2	0.01	b.d.l.	0.13	0.05	1.09	0.69	0.06	b.d.l.	0.00	0.04	0.02	0.05
Cr_2O_3			0.06	b.d.l.	0.24	0.14					0.05	0.37
MnO	0.01	0.02	0.48	0.42	0.08	0.13	0.19	0.12	0.01	0.02	0.16	0.11
FeO			12.3	12.2	13.9	15.3	5.57	5.41	2.79	1.06	17.3	16.4
Fe_2O_3	b.d.l.	0.06										
Total	99.4	99.8	98.0	97.8	94.0	93.7	97.9	97.4	92.0	95.9	85.2	85.8
Oxygens	32	32	48	48	22	22	18	18	22	22	28	28
Si	10.3	11.6	7.95	8.00	5.47	5.32	5.03	5.03	6.29	6.06	5.30	5.35
Al^{IV}	5.72	4.39	0.05		2.53	2.68	0.97	0.97	1.71	1.94	2.70	2.65
Al^{VI}			17.5	17.5	0.89	0.74	2.97	2.99	3.57	3.77	2.92	2.86
Fe^{3+}			0.49	0.53								
Ti			0.03	0.01	0.12	0.08						0.01
Cr			0.01		0.03	0.02					0.01	0.06
Mg			0.81	0.89	2.96	3.24	1.46	1.48	0.56	0.23	5.84	5.97
Fe^{2+}		0.01	2.34	2.27	1.74	1.94	0.48	0.46	0.32	0.12	3.01	2.82
Mn^{2+}			0.11	0.10	0.01	0.02	0.02	0.01			0.03	0.02
Ca	1.63	0.38			0.01	0.01	0.01		0.06		0.02	0.01
Na	2.32	3.57			0.10	0.06	0.14	0.09	0.10	0.36		0.01
K	0.01				1.74	1.62			1.04	1.56	0.12	0.18
*x*K [Or]	0.00	0.01										
*x*Na [Ab]	0.59	0.90										
*x*Ca [An]	0.41	0.09										
*x*Fe[fcel]									0.14	0.06		
*x*Mg[mcel]									0.25	0.11		
*x*Al[mphen]									0.61	0.83		

Please cite this article in press as: Block, S., et al., The Murchison Greenstone Belt, South Africa: Accreted slivers with contrasting metamorphic conditions. Precambrian Res. (2012), doi:10.1016/j.precamres.2012.03.005

Table 2
(*continued*)

Sample	M1 (greenstone from the Murchison Unit)							
Mineral phase	Act	Act	Chl	Chl	Pl	Pl	Ep	Sph
(c) wt%								
Na_2O					11.7	11.9		
MgO	19.6	19.0	21.5	22.7				
Al_2O_3	1.02	0.96	20.1	20.5	19.6	19.9	21.9	0.69
SiO_2	56.2	55.3	27.5	27.9	67.5	67.4	36.8	30.6
K_2O					b.d.l.	b.d.l.		
CaO	13.0	13.1			0.12	0.20	23.13	29.0
TiO_2	b.d.l.	0.16	b.d.l.	0.16				37.9
Cr_2O_3	0.52	0.18	0.34	0.21				0.26
MnO	0.26	0.23	0.23	0.19				
FeO	8.53	9.70	17.58	17.92				0.41
Fe_2O_3					b.d.l.	0.30	15.0	
Total	99.1	98.6	87.2	89.6	98.8	99.7	96.8	98.8
Oxygens	23	23	28	28	32	32	13	5
Si	7.82	7.79	5.59	5.52	11.9	11.9	3.10	1.01
Al^{IV}	0.17	0.16	2.41	2.48	4.08	4.12		0.03
Al^{VI}			2.39	2.30			2.17	
Fe^{3+}						0.03	0.95	0.01
Ti		0.02		0.02				0.94
Cr	0.06	0.02	0.05	0.03				0.01
Mg	4.06	3.98	6.51	6.69				
Fe^{2+}	0.99	1.14	2.99	2.97		0.01	0.01	
Mn^{2+}	0.03	0.03	0.04	0.03				
Ca	1.94	1.97			0.02	0.04		1.02
Na					4.00	4.04		
K								
*x*K[Or]								
*x*Na[Ab]					0.99	0.99		
*x*Ca[An]					0.01	0.01		
x[cZo] = *x*[Zo]							0.09	
x[Ep]							0.91	
x[Pie]							0.00	

Sample	M2 (garnet-bearing aluminous quartzite of the Murchison Unit)							
Mineral phase	Gt	Gt	Bt	Bt	Chl	Chl	Wm	Wm
(d) wt%								
Na_2O			0.07	0.09	0.04	0.03	0.93	1.06
MgO	2.31	1.80	7.12	7.99	8.85	8.65	0.73	0.81
Al_2O_3	20.9	20.7	16.7	18.0	19.2	18.2	35.7	35.3
SiO_2	36.7	36.4	39.8	36.6	30.0	32.7	46.5	46.6
K_2O			6.77	6.53	1.61	1.62	9.66	9.88
CaO	0.41	0.75	0.78	0.41	0.55	0.69	0.05	0.02
TiO_2			1.16	1.31	0.08	0.04	0.18	0.34
Cr_2O_3			0.15	0.12	0.10	b.d.l.	b.d.l.	0.21
MnO	4.63	6.06	0.16	0.13	0.23	0.32	0.01	0.02
FeO	35.5	34.6	19.9	18.4	27.7	23.5	1.4	1.2
Total	100.4	100.3	92.6	89.6	88.4	85.8	95.1	95.3
Oxygens	12	12	22	22	28	28	22	22
Si	5.95	5.95	6.10	5.79	6.34	6.92	6.17	6.18
Al^{IV}	0.05	0.05	1.90	2.21	1.66	1.08	1.83	1.82
Al^{VI}	3.96	3.93	1.11	1.13	3.13	3.46	3.76	3.70
Fe^{3+}	0.13	0.19						
Ti			0.13	0.16	0.01	0.01	0.02	0.03
Cr			0.02	0.02	0.02			0.02
Mg	0.56	0.44	1.63	1.88	2.79	2.73	0.14	0.16
Fe^{2+}	4.69	4.54	2.54	2.43	4.90	4.16	0.15	0.13
Mn^{2+}	0.64	0.84	0.02	0.02	0.04	0.06		
Ca	0.07	0.13	0.13	0.07	0.12	0.16	0.01	
Na			0.02	0.03	0.02	0.01	0.24	0.27
K			1.32	1.32	0.44	0.44	1.64	1.67
x[Py]	0.09	0.07						
x[Alm]	0.79	0.77						
x[Sps]	0.10	0.14						
x[Grs]	0.01	0.02						
*x*Fe[fcel]							0.08	0.07
*x*Mg[mcel]							0.07	0.08
*x*Al[mphen]							0.85	0.85

Please cite this article in press as: Block, S., et al., The Murchison Greenstone Belt, South Africa: Accreted slivers with contrasting metamorphic conditions. Precambrian Res. (2012), doi:10.1016/j.precamres.2012.03.005

Table 2
(*continued*)

Sample	S (garnet–plagioclase–hornblende amphibolite from the Silwana Amphibolites)										
Mineral phase	Gt (core)	Gt (rim)	Hbl	Hbl in Gt	Bt	Bt	Pl	Pl	Ilm	Chl	Chl
(e) wt%											
Na_2O			2.06	1.67	0.04	0.09	9.69	9.42		0.10	0.09
MgO	1.41	1.54	4.95	3.99	6.00	5.39			0.03	9.98	9.17
Al_2O_3	20.6	20.5	14.0	13.3	16.0	16.3	22.3	22.7	0.00	19.7	14.2
SiO_2	36.9	36.6	40.0	40.2	31.9	31.1	64.5	64.5		25.2	29.5
K_2O			0.56	0.41	6.63	5.23	0.04	0.08		0.13	1.85
CaO	4.94	5.26	10.4	11.0	0.02	0.14	3.55	3.58		0.13	0.24
TiO_2			0.60	0.27	1.90	1.60			52.3	0.63	1.62
MnO	1.97	1.52	0.10	0.15	0.08	0.04	b.d.l.	b.d.l.	0.49	0.06	0.04
FeO	34.9	34.7	24.8	26.2	30.3	33.6			46.9	31.4	30.2
Fe_2O_3							0.08	0.11			
Total	100.7	100.1	97.5	97.2	92.9	93.5	100.1	100.5	99.8	87.3	86.9
Oxygens	12	12	23	23	22	22	32	32	3	28	28
Si	5.97	5.95	6.25	6.3	5.26	5.14	11.4	11.3		5.52	6.50
Al^{IV}	0.03	0.05	1.75	1.67	2.74	2.86	4.63	4.70		2.48	1.50
Al^{VI}	3.89	3.87	0.82	0.80	0.36	0.31				2.62	2.19
Fe^{3+}	0.21	0.27					0.01		0.01		
Ti			0.07	0.03	0.24	0.20			1.00	0.10	0.27
Mg	0.34	0.37	1.15	0.94	1.47	1.33				3.26	3.01
Fe^{2+}	4.50	4.45	3.23	3.46	4.17	4.64		0.01	0.99	5.76	5.57
Mn^{2+}	0.27	0.21	0.01	0.02	0.01	0.01			0.01	0.01	0.01
Ca	0.86	0.92	1.74	1.86		0.02	0.67	0.67		0.03	0.06
Na			0.62	0.51	0.01	0.03	3.31	3.21		0.04	0.04
K			0.11	0.08	1.39	1.10	0.01	0.02		0.04	0.52
x[Py]	0.06	0.06									
x[Alm]	0.76	0.76									
x[Sps]	0.04	0.03									
x[Grs]	0.14	0.15									
*x*K[Or]							0.00	0.00			
*x*Na [Ab]							0.83	0.82			
*x*Ca [An]							0.17	0.17			
*x*Mg [Geik]									0.00		
*x*Fe [Ilme]									0.99		
*x*Mn [Pyro]									0.01		

metamorphic evolution. Prograde muscovite (Ms_1) always shows lower Na/(Na + K + Ca) of 0.08 and higher silica contents (Si = 3.15 a.p.f.u.) than retrograde muscovite (Ms_3), with Na/(Na + K + Ca) = 0.18 and Si = 3.02 a.p.f.u. M./(Na + K + Ca) = 0.08. Retrograde chlorite of assemblage (B3) has Mg# = 0.66–0.69, and high-Al contents of 1.35 a.p.f.u. Plagioclase grains show a wide range of chemical compositions, with X_{An}(Ca/Ca + Na) = 0.09–0.41, and a majority of grains having $X_{An} \sim 0.4$.

In one sample from the same formation, centimetric euhedral kyanite (Ky_3) and staurolite (St_3) crystals overgrow the S_2 metamorphic banding, together with millimetric biotite and muscovite grains (Fig. 4e and f). This assemblage, equivalent to (B3) in more aluminous lithologies, suggests that the Sill → Ky phase transition was crossed during the retrograde evolution of the rock. Furthermore, the retrograde assemblages (B2) and (B3) are characterised by the formation of abundant hydrated minerals, indicating a secondary, H_2O-rich fluid enrichment after peak metamorphism.

3.2. Silwana Amphibolites

The Silwana Amphibolites trend ENE–WSW and show a vertical to steeply north-dipping S_0/S_1 layering defined by modal variations of quartz, plagioclase and hornblende (Hbl) across bands about 10 cm thick. On a smaller scale, the amphibolites develop a planar (S > L), flattening tectonic fabric S_2. The metamorphic banding S_2, is subparallel to the S_0/S_1 layering. It is defined by the alternation of millimetric hornblende-rich and quartz–plagioclase-rich bands. The latter display an equigranular texture, suggesting a relatively high temperature recrystallisation (>500 °C). The S_2 foliation bears a dominant steep easterly dipping mineral lineation L_2 defined by hornblende. At the north-western extremity of the sliver, the strike of the layering changes dramatically from ENE–WSW to NW–SE, with a steep north-easterly dip, while the S_2 foliation carries a steep, north-plunging mineral elongation lineation. It is likely that both the ENE- and NW-trending structures (and related lineations) result from activation of a conjugate shear system. Garnet occurs as an additional phase in rare Al- and Fe-rich layers. Biotite is also present in small proportions (~1 to 2 modal%). Epidote (Ep) is a retrograde phase and frequently formed in cross-cutting veins, in association with carbonates. Chlorite is found in cracks within garnet porphyroblasts. The peak metamorphic assemblage is interpreted to be:

(S) Gt + Hbl + Pl + Bt + Ilm + Q.

The garnet prophyroblasts show a slight prograde growth zoning, as is reflected by increasing X_{Py} (from 0.055 to 0.060, Mg# varies from 0.67 to 0.73) and X_{Grs} (from 0.13 to 0.15), and decreasing X_{Sps} (from 0.04 to 0.03) and X_{Alm}(Fe/(Fe + Mg + Ca + Mn) from 0.77 to 0.76) from core to rim. Garnet contains inclusions of hornblende, quartz and ilmenite. Hornblende inclusions in garnet show some scatter in their chemical composition, with Mg# = 0.21–0.26 and Ca/Na = 3.0–3.6, compared to Mg# = 0.23–0.26 and Ca/Na = 2.8–3.0 for matrix hornblende. Matrix plagioclase has a constant chemical composition, with X_{An} = 0.17. Biotite occurrence is limited, with small grains elongated parallel to hornblende, and some randomly oriented grains occurring around garnet. All matrix biotites show similar compositions with Mg# = 0.22–0.26 and Ti^{vi} = 0.1 a.p.f.u. Retrograde chlorite (Mg# = ~0.36) only formed along cracks in the garnet porphyroblasts.

Please cite this article in press as: Block, S., et al., The Murchison Greenstone Belt, South Africa: Accreted slivers with contrasting metamorphic conditions. Precambrian Res. (2012), doi:10.1016/j.precamres.2012.03.005

3.3. Murchison Unit

Strain distribution in the Murchison Unit is fairly heterogeneous. Minor domains, far from tectonic discontinuities, are almost undeformed, but most rocks displays a pervasive schistose fabric and provide evidence for a poly-phased deformation (Vearncombe, 1988b; Vearncombe et al., 1988a, 1992; Jaguin et al., 2012). Primary sedimentary structures S_0, are only preserved in competent layers. Stratigraphic contacts between the different formations of the Murchison Unit have been completely reworked by tectonic processes during the successive deformation events. A first deformation episode D_1 corresponds to the formation isoclinal folds axial-planar to a S_1 cleavage trending ENE. These isoclinal folds are transposed by E–W trending, S-shaped asymmetric folds, axial planar to a S_2 cleavage, formed during a second deformation event, D_2. However, it is generally difficult to attribute the pervasive cleavages

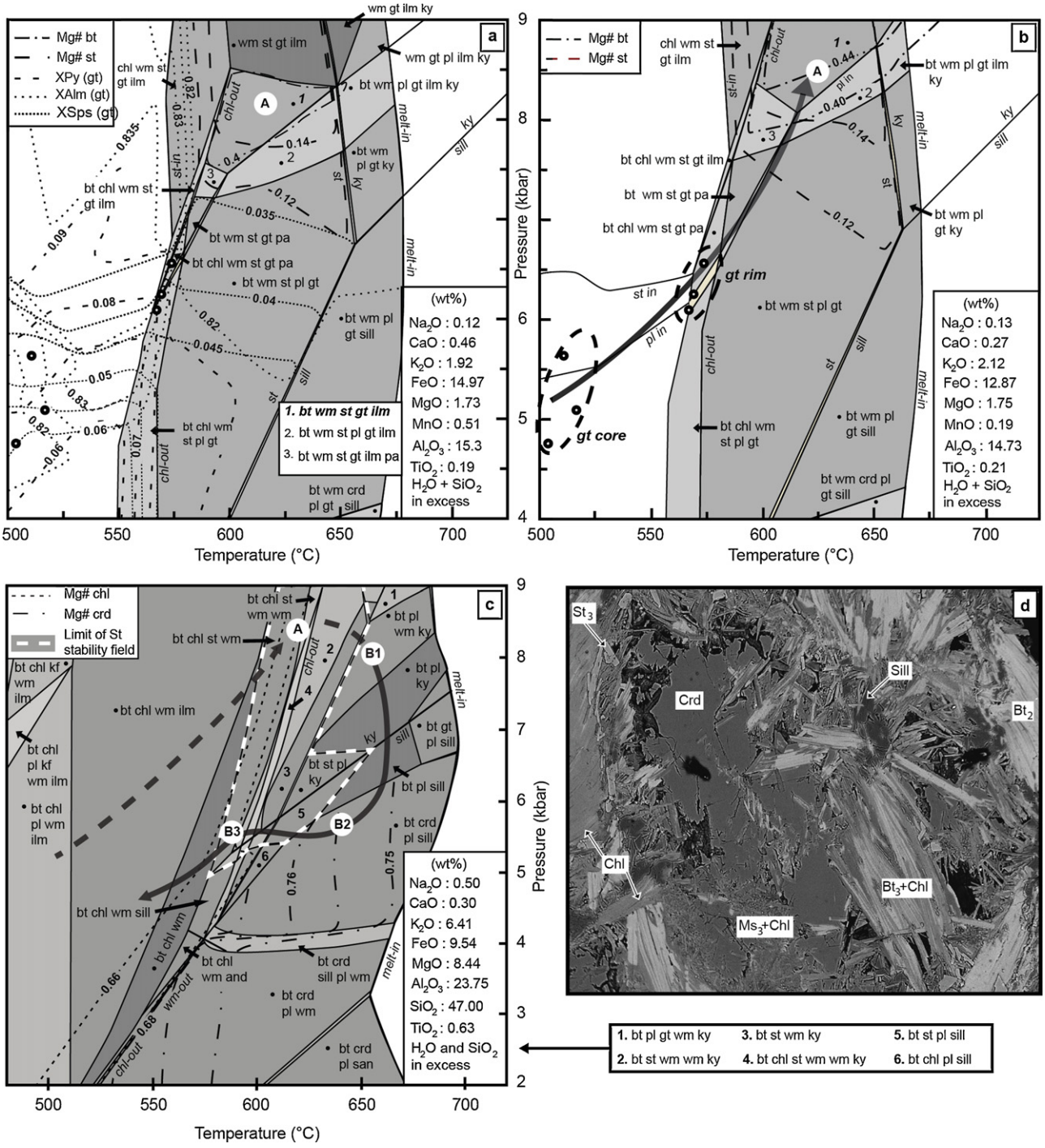

Fig. 5. *P–T* pseudosections for metapelitic rocks from the La France Formation, constructed in the model system (Mn)TiNCKFMASH (with H_2O and SiO_2 in excess). (a, b) *P–T* pseudosection for a garnet–staurolite micaschist (sample A) and (c) for a kyanite-bearing micaschist with retrograde cordierite and staurolite (sample B). The *P–T* pseudosection (a) is constructed by using the unfractionated bulk composition obtained by XRF analysis, and (b) is built by using the effective bulk composition after garnet growth ceased. Small open circles represent fit between calculated and measured garnet compositions, obtained from garnet cores and rims of zoned garnet in sample A. White circles labelled A, B1, B2, B3 mark the fields with the best agreement between observed and calculated mineral assemblages and mineral compositions. The arrows define the *P–T* path inferred from the petrological constraints. (d) SEM image of sample B showing tiny staurolite grains (St_3), which together with chlorite (Chl), biotite (Bt_3) and muscovite (Ms_3) surround a cordierite (Crd) porphyroblast, intergrown with sillimanite (Sill) and biotite (Bt_2). Wm = white mica.

Please cite this article in press as: Block, S., et al., The Murchison Greenstone Belt, South Africa: Accreted slivers with contrasting metamorphic conditions. Precambrian Res. (2012), doi:10.1016/j.precamres.2012.03.005

to either D_1 or D_2. None of our samples exhibit the D_3 crenulation cleavage, which was recognised by Vearncombe et al. (1988a, 1992) in rocks near to the Antimony Line. For *P–T* path estimates, we investigated a sample from a nearly undeformed metamafic rock from the centre of the Murchison Unit, south of the Antimony Line (sample M1); and a sample from a deformed quartzite with metapelitic layers from the southern edge of the Murchison Unit (sample M2), a few dozen metres north from the contact with the Makhutswi gneisses (Fig. 2). The metabasite sample M1 contains the following peak metamorphic mineral assemblage:

(M1) Act(actinolite) + Ab(albite) + Ep + Chl + Sph(sphene)

with Chl mostly in late shear bands. The actinolite needles display a garbenscheifer texture, which might represent pseudomorphs of primary magmatic textures, and have Mg# = 0.67–0.72. The feldspar is pure albite ($X_{An} \leq 0.01$). Chlorite has Mg# = 0.55–0.56 and Al^{vi} = 1.20 a.p.f.u.

The metapelitic–quartzitic sample M2 displays the following peak mineral assemblage:

(M2) Gt + Ms + Bt + Chl + Qtz,

and additionally contains retrograde chlorite along garnet cracks. Garnet porphyroblasts have diameters < 0.5 mm and do not display any chemical zoning. The garnets have a high almandine components of X_{Alm} = 0.8, low pyrope and spessartine components ($X_{Py} = X_{Sps} = \sim 0.1$), and Mg# = 0.08–0.10. Biotite is Ti-poor (Ti^{vi} = 0.07 a.p.f.u.) and has a Mg# = 0.39–0.44. Chlorite has Mg# = 0.36–0.39 and Al^{vi} = 1.55–1.70 a.p.f.u. Muscovite is Na-poor, with Na/(Na + K + Ca) = 0.13, and Si = 3.1 a.p.f.u.

4. Metamorphic *P–T* paths

P–T paths for the different units were inferred by comparison between the observed mineral assemblages, mineral compositions and zoning patterns, and those obtained by *P–T* pseudosection calculations for the respective samples. This methodology provides robust results, as has been shown by many examples in the past; for example see Zeh (2001), Zeh et al. (2004), Millonig et al. (2008, 2010). The methods used to estimate the effective bulk rock composition and to construct *P–T* pseudosections are described in Appendix A.2.

4.1. La France Formation

P–T pseudosections for the La France Formation were calculated for a Gt–St-bearing schist (sample A) and a Ky–St–Crd schist (sample B), which were collected about 300 m apart. In the absence of any tectonic break between the two outcrops we assume that both rocks underwent the same metamorphic history, and consequently, that the different mineral assemblages and compositions result from different bulk rock compositions. Thus a detailed *P–T* path can be constructed by superimposing the information obtained from the different rock samples (e.g. Zeh, 2001; Zeh et al., 2004; Reno et al., 2009).

Results of *P–T* pseudosections for sample A (Fig. 5a and b) indicate that the Gt–St-bearing shists of the La France Formation experienced a prograde *P–T* increase from about 5.5 kbar, 520 °C to 7.5–9.0 kbar, 590–650 °C. The prograde *P–T* evolution is constrained by the agreement between observed and calculated garnet zoning patterns, using the "garnet isopleths intercept method" (e.g., Evans, 2004; Zeh, 2006). The peak *P–T* conditions are determined from the correspondence between the calculated and observed peak mineral assemblage (A): Grt + St + Bt_1 + Ms_1 + Q, and related mineral compositions. It should be noted, however, that the fit between calculated and observed peak mineral compositions is not perfect, i.e. the calculated mineral compositions of garnet rims plot outside the phase field for the peak mineral assemblage (Fig. 5). This discrepancy may be explained by at least two reasons. Firstly, minerals in sample A underwent a retrograde equilibration (causing a change of the peak mineral composition of garnet rims and of biotites; e.g. Florence and Spear, 1991), and/or secondly, by internal fractionation, causing a change of the effective bulk composition during prograde garnet growth (e.g. Stüwe, 1997; Marmo et al., 2002; Zeh, 2006). The effects of chemical fractionation due to garnet growth are modelled in Fig. 5. Assemblage (A) is shifted from 7.5–8.5 kbar, 590–645 °C for the unfractionated rock (Fig. 5a) to higher *P–T* conditions of 8.0–9.0 kbar, 600–650 °C when fractionation is taken into account (Fig. 5b).

The peak metamorphic assemblage (B1) Ky_1 + Bt_1 + Pl + Ms_1 + Q ± St_1 observed in sample B requires peak *P–T* conditions of 6.8–9.0 kbar at 630–650 °C. Comparison of the peak metamorphic conditions for sample B and the prograde *P–T* vector inferred for sample A indicates that the formation underwent a limited heating after reaching peak pressure. Syn-D2 muscovite in sample B has a modal proportion < 1%, suggesting equilibration near the white mica-out reaction curve that limits the multivarient field at lower pressures. Sillimanite overgrowth around kyanite and the finding of cordierite in assemblage (B2): Sill + Bt_2 + Crd + Pl + Q, provide evidence for a nearly isothermal decompression to *P–T* conditions of <6 kbar at 600–660 °C during retrograde evolution (Fig. 5c). Cordierite is partly replaced by an assemblage including St, Bt, Ms and Chl (assemblage (B3): St_3 + Bt_3 + Chl + Ms_3 + Q, Fig. 5d), implying that the near isothermal decompression was followed by a near-isobaric cooling to <600 °C at ~5.5 kbar. The change in the *P–T* path from a near-isothermal decompression to a near-isobaric cooling may correspond to the onset of the D_3 deformation event.

4.2. Silwana Amphibolites

Results of *P–T* pseudosection calculations indicate that the observed peak metamorphic assemblage (S): Gt + Hbl + Pl + Bt + Ilm + Q is stable over a wide *P–T* range at temperatures between 540 and 690 °C and pressures between 4.6 and >11 kbar (Fig. 6). A prograde *P–T* path is inferred by comparing the observed and calculated mineral composition of garnet (cores and rims), amphibole inclusions in garnet and matrix amphibole, as well as of matrix plagioclase. Intersecting the isopleths for these minerals provides evidence for a *P–T* increase from ~4.5 kbar, 540 °C, to peak metamorphic conditions of 8.7–10 kbar at 630–670 °C.

4.3. Murchison Unit

The model multivariant field corresponding to the metamorphic assemblage of sample M1: Act + Chl + Ab + Ep + Sph + Q (Fig. 7a) constrains metamorphic *P–T* conditions of 340–370 °C at a wide pressure range from 1.3 to 5.8 kbar. The agreement between the measured and calculated actinolite composition restricts the metamorphic pressure conditions to 1.3–2.8 kbar at 340–370 °C (hatched field in Fig. 7a). However, it should be noted that clinozoisite (cz) instead of epidote has been calculated, due to the fact that the Fe^{3+} content was approximated to be 0 during the calculations (see Appendix A.2). The observed Mg# of chlorite falls in a *P–T* space characterised by even lower temperatures of 240–300 °C (not shown). The latter may be indicative of chlorite (which is present in late-stage shear bands) crystallisation and/or re-equilibration during retrograde cooling. In summary, the geobarometric constraints for sample M1 point to a lower greenschist-facies metamorphism.

The *P–T* pseudosection constructed for the metapelite sample M2, containing the peak metamorphic assemblage (M2) Gt + Ms + Bt + Chl + Qtz, indicates peak temperatures between 530

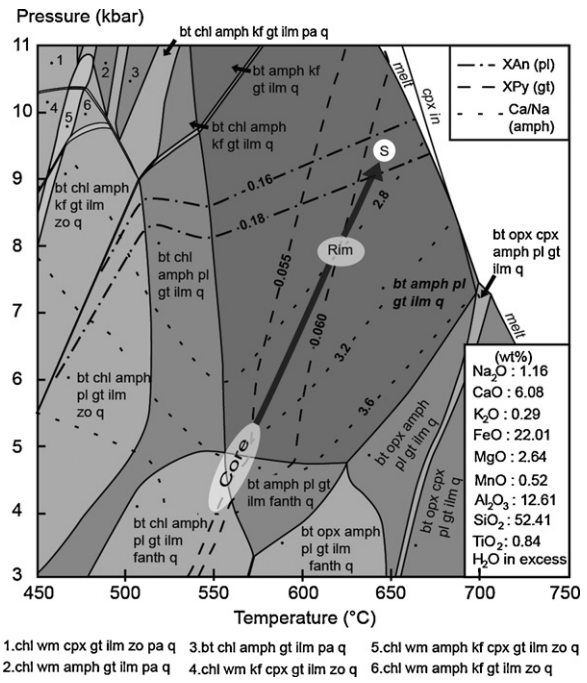

Fig. 6. *P–T* pseudosections for the Silwana Amphibolites. The pseudosection is constructed in the model system TiNCKFMASH system, with water in excess. White circles and ellipses mark the fields with the best agreement between observed and calculated assemblages and mineral compositions (core, rim, S). The multivariant field designated in bold–italics correspond to the observed peak assemblage. The arrows define the *P–T* vector inferred from petrological constraints. fanth = ferro-anthophyllite, pa = paragonite, zo = zoisite.

and 570 °C, at pressures between 5.0 and 6.2 kbar (hatched phase field in Fig. 7b). The peak metamorphic temperature conditions are constrained by two temperature-dependant field boundaries, the biotite-in and chlorite-out/staurolite-in phase boundaries, as well as by the the fit between modelled and measured Mg# of garnet (Fig. 7b). The finding of muscovite without other white micas in sample M2 furthermore requires peak pressure conditions between 5.0 and 6.2 kbar at 550–570 °C. The metamorphic grade of sample M2 is somewhat higher than that of sample M1, at the transition between high *T* greenschist and low *P* amphibolite facies, but is significantly lower than that of the rocks from the La France Formation and Silwana Amphibolites.

5. Geochronology

In order to constrain the timing of metamorphism and deformation in the MGB, LA-ICP-MS U-Pb dating was carried out on a syn-deformation granite intrusive in the Letaba Shear Zone (sample mur0982, see Fig. 2 for location). In addition, monazite and xenotime from the kyanite-bearing metapelite from the La France Formation (sample B) were dated.

The zircon grains were characterised by cathololuminescence imaging prior to analyses and were analysed on grain mounts, while monazite and xenotime U–Pb analyses were carried out on a thin section, after their characterisation by back-scattered electron imaging. The results are shown in Table 3 and in Fig. 8. Analytical techniques and data processing methods are detailed in Appendix A.3.

5.1. Zircons from magmatic rocks

Twenty zircons from the syn-deformation granite sample mur0982 intrusive into the LSZ to the North of the belt, displaying an oscillatory magmatic zoning, were analysed. Nineteen out of

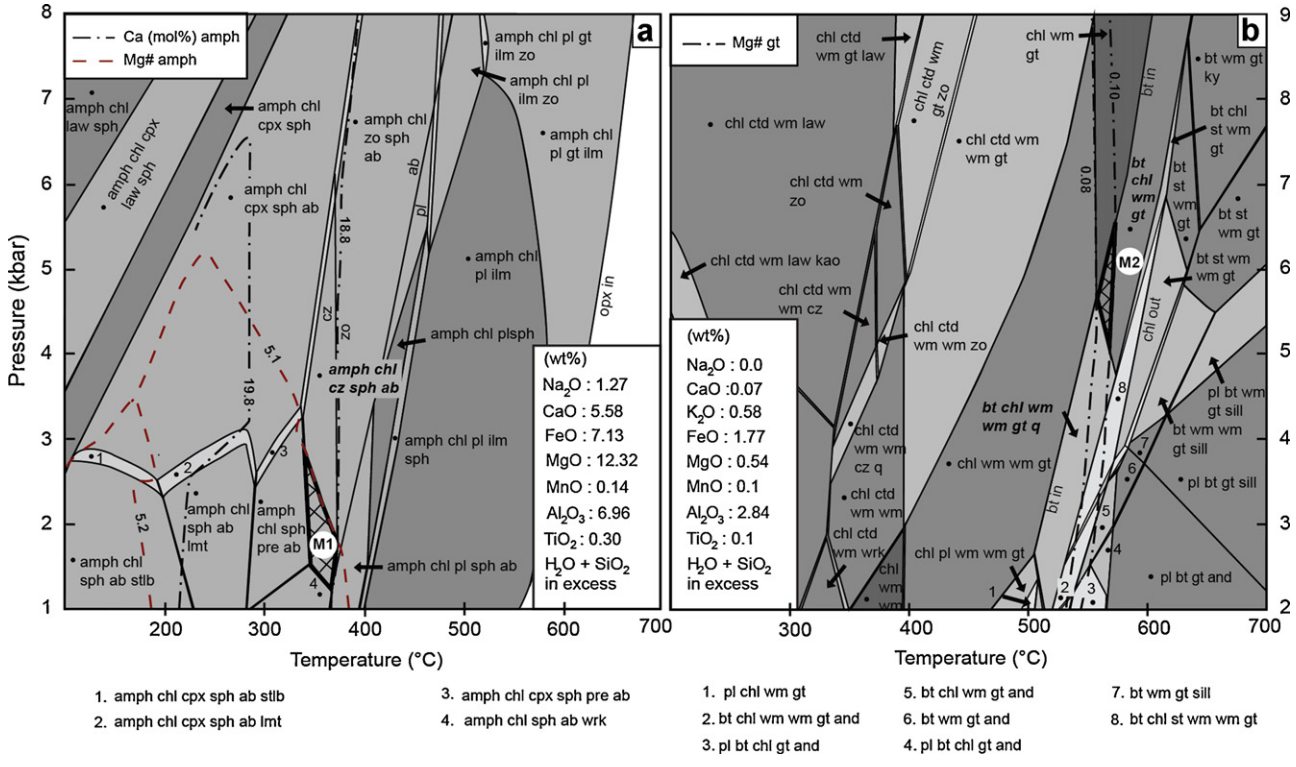

Fig. 7. *P–T* pseudosections for rocks from the Murchison Unit. (a) Metabasite from the center of the Murchison unit, sample M1. (b) Garnet-bearing aluminous quartzite from the southern edge of the Murchison Unit. Hatched areas labelled M1 and M2 mark the fields with the best agreement between observed and calculated assemblages and mineral compositions. Wm = white mica, and = andalusite, zo = zoisite, cz = clinozoisite, ab = albite, pre = prehnite, wrk = wairakite, lmt = laumontite, stlb = stilbite, kao = kaolinite.

Please cite this article in press as: Block, S., et al., The Murchison Greenstone Belt, South Africa: Accreted slivers with contrasting metamorphic conditions. Precambrian Res. (2012), doi:10.1016/j.precamres.2012.03.005

Table 3
(Top) U–Pb isotopic data obtained by LA–ICP–MS analyses carried out in GUF, and calculated ages from monazite and xenotime from sample B. (Bottom) U–Pb isotopic data obtained by LA–ICP–MS analyses carried out in Clermont–Ferrand and calculated ages from zircons from sample mur0982.

Sample		^{207}Pb[a] (cps)	U[b] (ppm)	Pb[b] (ppm)	Th/U[b]	^{206}Pb[c] (%)	$^{206}Pb/^{238}U$[d]	±2σ (%)	$^{207}Pb/^{235}U$[d]	±2σ (%)	$^{207}Pb/^{206}Pb$[d]	±2σ (%)	Rho[e]	$^{206}Pb/^{238}U$	±2σ (Ma)	$^{207}Pb/^{235}U$	±2σ (Ma)	$^{207}Pb/^{206}Pb$	±2σ (Ma)	Conc.[f] (%)
Results of U–Pb LA–ICP–MS analyses of monazite (mnz) and xenotime (xno) carried out at Goethe University Frankfurt																				
B																				
a04	mnz	253119	847	2900	21.1	0.57	0.4804	4.1	12.54	4.1	0.1894	0.5	0.99	2529	86	2646	39	2737	8	92
a05	mnz	536981	3062	6600	11.8	0.12	0.5312	2.0	14.00	2.1	0.1912	0.7	0.95	2747	45	2750	20	2752	11	100
a06	mnz	370826	2627	4100	7.7	1.07	0.4852	2.6	12.77	2.8	0.1909	1.0	0.93	2550	55	2663	27	2750	17	93
a07	mnz	519077	3342	5800	8.6	0.10	0.5504	2.4	14.53	2.5	0.1915	0.8	0.95	2827	54	2785	24	2755	12	103
a10core	xno	1149852	4946	3100	0.4	0.08	0.5562	8.1	16.11	8.2	0.2101	1.6	0.98	2851	189	2883	82	2906	26	98
a10	xno	1255656	4462	2700	0.4	0.09	0.5249	4.4	14.71	4.8	0.2033	1.9	0.92	2720	98	2797	46	2853	30	95
a12	mnz	630276	4092	8000	9.9	0.10	0.5122	2.1	13.43	2.2	0.1901	0.5	0.97	2666	46	2710	21	2743	9	97
a13	mnz	105973	403	1300	19.7	1.73	0.3219	13.4	8.25	13.5	0.1860	1.3	1.00	1799	214	2259	130	2707	21	66
a14	mnz	445663	4136	7900	8.9	0.08	0.5231	2.8	13.85	2.9	0.1921	0.7	0.97	2712	63	2740	28	2760	12	98
a15	mnz	404074	2226	5300	13.9	0.19	0.5245	2.1	13.71	2.2	0.1896	0.5	0.97	2718	47	2730	21	2739	9	99
a16	mnz	382514	2406	4800	10.6	0.43	0.5344	2.1	14.09	2.2	0.1912	0.7	0.95	2760	48	2756	21	2753	11	100
a19	mnz	448130	2403	6000	13.8	0.35	0.5410	2.4	14.24	2.7	0.1909	1.1	0.91	2788	55	2766	26	2750	18	101
a20	xno	1314118	6201	3500	0.2	0.05	0.5305	1.9	14.00	2.0	0.1915	0.5	0.96	2743	42	2750	19	2755	9	100
a21	mnz	118475	661	2200	24.6	0.92	0.4411	5.5	11.26	5.9	0.1851	2.1	0.94	2356	110	2545	57	2699	34	87
a22	mnz	268818	2076	5100	13.5	0.13	0.5268	3.7	13.91	3.7	0.1916	0.4	0.99	2728	82	2744	35	2756	7	99
a23	mnz	392774	2528	5200	11.1	0.11	0.5416	2.0	14.39	2.4	0.1928	1.2	0.86	2790	46	2776	23	2766	20	101
a25core	mnz	897089	3654	10000	17.4	0.10	0.5697	2.0	16.67	2.1	0.2122	0.7	0.95	2906	48	2916	21	2923	11	99
a25rim	mnz	509831	2393	6200	14.6	0.10	0.5254	1.8	13.86	2.0	0.1913	0.7	0.94	2722	41	2740	19	2754	11	99
a26	mnz	161910	845	1600	9.3	0.74	0.4560	6.2	12.09	6.4	0.1922	1.4	0.98	2422	127	2611	62	2761	23	88
a27	mnz	358562	2024	4900	14.3	0.10	0.5352	1.6	13.95	1.7	0.1890	0.4	0.97	2763	36	2746	16	2734	6	101
a28	mnz	381917	2499	5700	12.2	0.39	0.4678	3.0	12.18	3.1	0.1888	0.8	0.96	2474	62	2618	30	2732	14	91
a29	mnz	585399	3991	8300	10.5	0.24	0.5010	2.4	13.48	2.5	0.1952	0.8	0.94	2618	52	2714	24	2786	14	94
a30	xno	1764628	8893	5200	0.3	0.03	0.5292	1.8	14.04	1.8	0.1924	0.5	0.96	2738	39	2752	18	2763	9	99
a31	xno	1374114	8166	4700	0.2	0.03	0.5338	2.5	14.20	2.6	0.1929	0.7	0.96	2757	57	2763	25	2767	12	100
a32	mnz	52970	149	550	20.0	0.66	0.5146	6.3	13.27	6.3	0.1870	0.9	0.99	2676	139	2699	62	2716	15	99
a33	mnz	415719	2602	5100	10.7	1.14	0.5317	2.4	13.92	2.5	0.1899	0.8	0.95	2748	54	2744	24	2741	13	100
a34	mnz	519221	2744	6700	13.9	0.06	0.5319	2.4	14.02	2.5	0.1912	0.6	0.97	2749	54	2751	24	2753	10	100
a35	mnz	174257	741	2800	24.4	0.92	0.4369	3.7	11.37	3.9	0.1888	1.0	0.97	2337	73	2554	37	2732	16	86
a36	mnz	286783	1597	4100	15.4	0.13	0.5326	2.4	14.01	2.5	0.1907	0.6	0.97	2753	54	2750	24	2749	9	100
		^{207}Pb[a] (cps)	U[b] (ppm)	Pb[c] (ppm)	Th/U[b]	$^{206}Pb/^{238}U$[d]	±2σ (%)	$^{207}Pb/^{235}U$[d]	±2σ (%)	$^{207}Pb/^{206}Pb$[d]	±2σ (%)	Rho[e]	$^{206}Pb/^{238}U$	±2σ (Ma)	$^{207}Pb/^{235}U$	±2σ (Ma)	$^{207}Pb/^{206}Pb$	±2σ (Ma)	Conc.[f] (%)	
Results of U–Pb LA–ICP–MS analyses of sample mur0982 carried out in Clermont-Ferrand																				
mur0982																				
05110411d	zr	8180	39	23	0.20	0.5956	2.0	17.74	2.1	0.2161	2.2	0.94	3012	48	2976	21	2952	35	102	
06110411d	zr	42538	408	126	0.38	0.3051	2.0	8.85	2.0	0.2103	2.1	0.97	1717	30	2323	18	2908	33	59	
07110411d	zr	16914	98	47	0.24	0.4921	2.0	14.69	2.1	0.2165	2.1	0.96	2580	42	2796	20	2955	34	87	
08110411d	zr	13025	73	35	0.20	0.5011	2.0	15.17	2.2	0.2195	2.3	0.92	2619	44	2826	21	2977	36	88	
09110411d	zr	55162	669	157	0.47	0.2496	2.0	7.08	2.0	0.2058	2.1	0.97	1436	25	2122	18	2873	34	50	
10110411d	zr	11560	67	32	0.32	0.5004	2.0	14.98	2.1	0.2171	2.2	0.94	2615	43	2814	20	2959	35	88	
11110411d	zr	21853	318	70	0.53	0.2313	2.0	5.96	2.1	0.187	2.2	0.94	1341	24	1970	19	2716	36	49	
12110411d	zr	11361	54	32	0.20	0.6084	2.0	18.27	2.2	0.2177	2.3	0.92	3064	50	3004	21	2964	36	103	
15110411d	zr	15607	79	44	0.23	0.5785	2.0	17.42	2.1	0.2184	2.2	0.94	2943	48	2958	21	2969	35	99	
16110411d	zr	22058	142	63	0.35	0.4593	2.0	13.75	2.1	0.2171	2.1	0.95	2437	41	2733	20	2960	34	82	
17110411d	zr	20140	121	56	0.25	0.4916	2.0	14.82	2.1	0.2186	2.1	0.94	2578	43	2804	20	2971	34	87	
18110411d	zr	12592	91	36	0.29	0.4169	2.0	12.36	2.2	0.2151	2.2	0.93	2246	39	2633	21	2944	35	76	
19110411d	zr	14013	74	39	0.18	0.5605	2.0	16.91	2.2	0.2188	2.2	0.94	2869	47	2930	21	2972	35	97	
20110411d	zr	9774	85	28	0.73	0.3431	2.1	10.32	2.2	0.2182	2.3	0.92	1902	34	2464	21	2968	36	64	
21110411d	zr	9362	49	26	0.18	0.5792	2.1	17.40	2.2	0.2179	2.2	0.92	2945	49	2957	22	2966	36	99	
22110411d	zr	10061	87	29	0.22	0.3513	2.1	10.53	2.3	0.2175	2.2	0.92	1941	35	2483	21	2962	36	66	
25110411d	zr	12745	66	36	0.21	0.5848	2.1	17.65	2.3	0.2189	2.3	0.91	2968	49	2971	22	2972	36	100	
26110411d	zr	11260	59	32	0.22	0.5851	2.1	17.58	2.3	0.2179	2.3	0.91	2969	49	2967	22	2966	36	100	
27110411d	zr	8942	47	26	0.21	0.5872	2.1	17.52	2.4	0.2165	2.3	0.89	2978	50	2964	23	2955	37	101	
28110411d	zr	21485	105	55	0.35	0.5329	2.1	19.16	2.3	0.2607	2.3	0.91	2754	47	3050	22	3251	35	85	
29110411d	zr	25554	211	76	0.28	0.3868	2.1	11.33	2.3	0.2123	2.3	0.90	2108	38	2550	22	2924	37	72	

[a] Within run background-corrected mean ^{207}Pb signal in cps (counts per second).
[b] U and Pb content and Th/U ratio were calculated relative to GJ-1 reference zircon.
[c] Percentage of the common Pb on the ^{206}Pb. b.d. = below dectection limit.
[d] Corrected for background, within-run Pb/U fractionation (in case of $^{206}Pb/^{238}U$) and common Pb using Stacy and Kramers (1975) model Pb composition and subsequently normalised to GJ-1 (ID-TIMS value/measured value); $^{207}Pb/^{235}U$ calculated using $^{207}Pb/^{206}Pb/(^{238}U/^{206}Pb * 1/137.88)$.
[e] Rho is the $^{206}Pb/^{238}U/^{207}Pb/^{235}U$ error correlation coefficient.
[f] Degree of concordance = $^{206}Pb/^{238}U$ age/$^{207}Pb/^{206}Pb$ age × 100.

Please cite this article in press as: Block, S., et al., The Murchison Greenstone Belt, South Africa: Accreted slivers with contrasting metamorphic conditions. Precambrian Res. (2012), doi:10.1016/j.precamres.2012.03.005

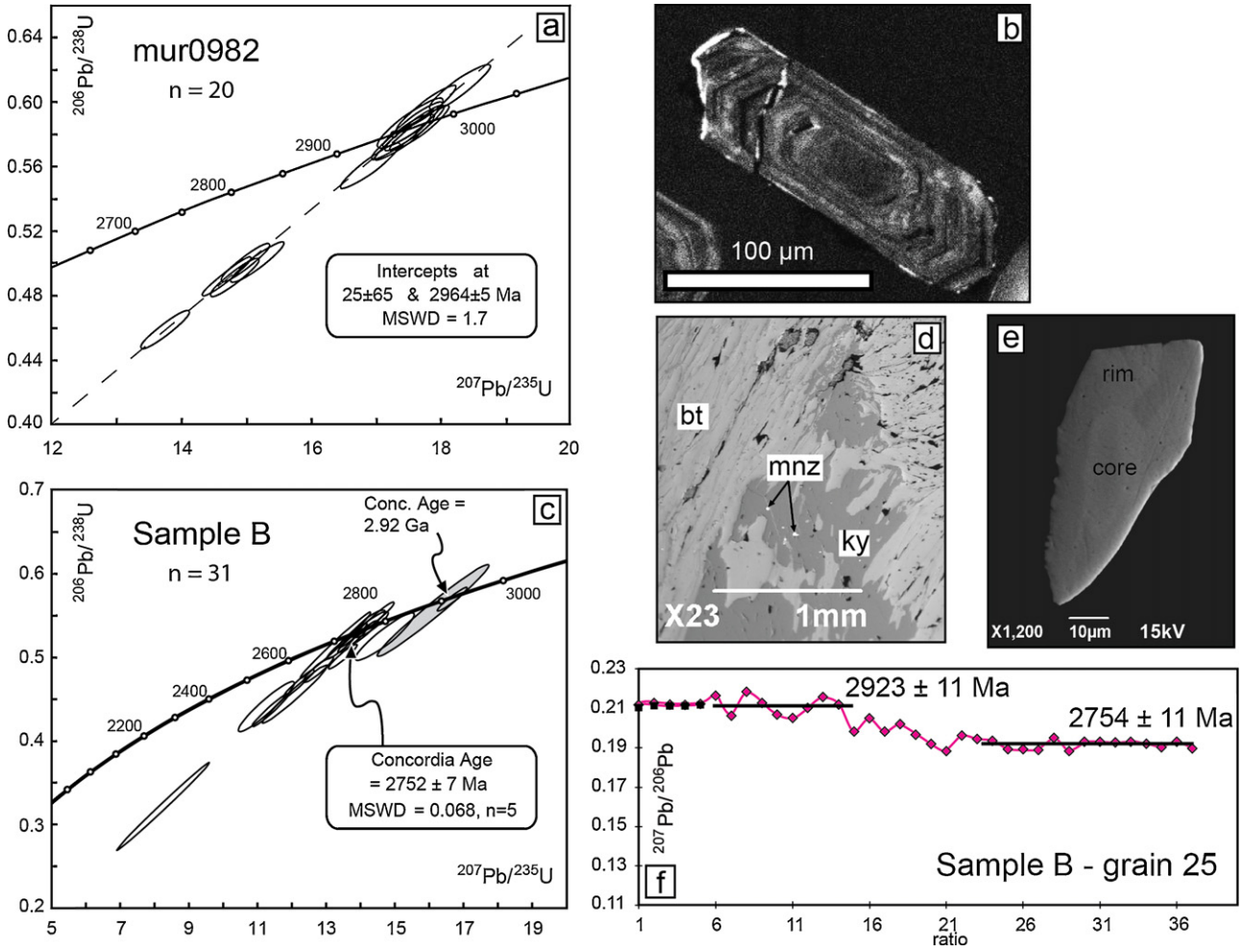

Fig. 8. Results of U–Pb LA–ICP–MS dating of zircon, monazite and xenotime from the La France Formation. (a) Concordia diagram with results of U–Pb zircon dating of the granitoid sample mur0982 from the Letaba Shear Zone. An upper intercept age of 2966.7 ± 7.1 Ma was obtained. (b) Cathodoluminescence image of a zircon of sample mur0982. (c) Concordia diagram showing results of monazite and xenotime analysis of sample B of the La France Formation, with concordant ages at 2752 ± 7. (d) BSE image of monazite inclusions in a kyanite porphyroblast in sample B. (e) BSE image of a monazite inclusion in kyanite (sample B) revealing a complex zonation. (g) Time resolved $^{207}Pb/^{206}Pb$ signal obtained from a monazite inclusion in kyanite (mnz grain 25 – Table 3). Note the stepwise decrease of the $^{207}Pb/^{206}Pb$ signal, corresponding to an age decrease from 2923 ± 11 Ma to 2754 ± 11 Ma (2 sigma).

twenty U–Pb analyses plot along a discordia with an upper intercept at 2964 ± 5 Ma (MSWD = 5.4), whereas a xenocryst zircon grain (28110411d) yields a much older $^{207}Pb/^{206}Pb$ age of 3251 ± 18 Ma (Table 3). The upper intercept age is within error identical to a Concordia age (as of Ludwig, 1998) of 2964 ± 8 Ma (MSWD = 0.24, probability of concordance = 0.63, $n = 6$) (Fig. 8a, b). It is interpreted to reflect the timing of the syn-tectonic granite emplacement. This interpretation is supported by the observation that the granite is intrusive in the Letaba Shear Zone and shows a mylonitic foliation that is coplanar with the mylonitic fabric of the greenschist-facies schists of the LSZ.

5.2. Monazite and xenotime dating

A total of 31 U–Th–Pb laser spot analyses were carried out on 18 monazite and 3 xenotime grains found in the La France micaschists, sample B. The grains yielded two sets of concordant ages (Fig. 8c). Most grains, which are intergrown with the matrix micas, yielded a concordant U–Pb age of 2752 ± 7 Ma. Xenotime and a monazite inclusions in kyanite porphyroblasts yielded much older concordant U–Pb ages of 2906 ± 26 and 2923 ± 11 Ma, respectively (grey ellipses in Fig. 8c). The stepwise decrease of the time resolved, common Pb corrected $^{207}Pb/^{206}Pb$ signal during the analysis of the monazite inclusion in kyanite indicated that this grain was zoned. The drop of $^{207}Pb/^{206}Pb$ signal corresponds to an age decrease from 2923 ± 11 Ma to 2754 ± 11 Ma (Fig. 8f). A possible explanation to this result is that kyanite and monazite formed at ca. 2923 Ma or prior to it, and that the monazite inclusion in kyanite subsequently underwent partial alteration and resetting at ca. 2754 Ma, simultaneous to the formation or complete re-crystallisation of matrix monazite and xenotime. We therefore suggest that the ca. 2923 Ma age represents a minimal age for the metamorphic peak in the La France Formation.

6. Discussion

6.1. Metamorphic conditions and geothermal gradients

The results of our *P–T* modelling reveal that the three investigated tectono-metamorphic units of the MGB underwent contrasted metamorphic evolutions. The volcano-sedimentary rocks of the Murchison Unit, that form the central part of the MGB, underwent metamorphism in the lower-greenschist to lower-amphibolite facies, at *P–T* conditions not exceeding

5–6.2 kbar and 530–570 °C; peak metamorphic conditions being highly variable within this unit. In contrast, the La France Formation, on the southern edge of the MGB, underwent high grade amphibolite-facies metamorphism at conditions of 8–9 kbar, and temperatures of 600–650 °C, corresponding to higher-amphibolite facies conditions. They subsequently underwent near-isothermal decompression to under 6.2 kbar, with temperature between 600 and 660 °C, followed by cooling to 570–610 °C, at pressures in excess of 5 kbar. The Silwana Amphibolites sliver, on the north-western edge of the MGB, experienced a metamorphic overprint in the upper amphibolite facies under *P–T* conditions of 8.7–10 kbar, 630–670 °C. Rocks of both units record a prograde pressure–temperature increase from about 4.5 to 5.5 kbar at 520–570 °C towards the metamorphic peak. Furthermore, rocks of the La France Formation additionally provide evidence for a complex retrograde *P–T* history, characterised by near-isothermal decompression from 9.0–6.8 to <6 kbar at 600–660 °C, followed by a nearly-isobaric cooling from 620–650 °C to 570–610 °C at about 5.5 kbar, accompanied by a secondary H_2O-rich fluid enrichment.

Peak *P–T* conditions for the La France supracrustals and the Silwana Amphibolites require a burial to mid-crustal levels, at depths of 27–30 km and 29–33 km respectively. Bearing in mind that the pressures determined from peak assemblages are in fact minimal pressures due to possible re-equilibration of the thermodynamic systems along the high-grade portions of the retrograde path, these values represent minimal burial depths. Therefore, the La France Formation and the Silwana Amphibolites underwent metamorphism along fairly similar minimal apparent geothermal gradients of 19–24 °C/km. Furthermore, a steep prograde *P–T* vector inferred for rocks from both formations, suggesting a fast burial. In contrast, much lower peak *P–T* conditions of 5–6.2 kbar and 550–570 °C for sample M2 indicate that rocks of the Murchison Unit were buried at shallower depths of 16–20 km, along an apparent geotherm of 27–34 °C/km. The peak *P–T* conditions of metabasite sample M1 are even lower and require even higher apparent geotherms (40–80 °C/km). The reasons for the different peak *P–T* conditions of the investigated rocks of Murchison Unit are not entirely clear. Apart from the fact that the peak pressures are not well constrained, in particular for sample M1, the enormous temperature differences could reflect either a metamorphic array (e.g. England and Thompson, 1984), whereby different slivers has reached different peak conditions at different times or, alternatively, a metamorphic gradient caused by magma intrusions within the MGB. A less likely option is that the enormous temperature difference represents an artefact of the used thermodynamic calculation method. If the latter holds true, the *P–T* results obtained from the metapelitic rocks are considered to be more appropriate than those from the metabasite, since thermodynamic activity models for metapelite phases are more robust and less sensitive to slight variations in Na, Ti and Fe^{3+} than those for metabasite phases, e.g. amphiboles (see Dale et al., 2005; Diener et al., 2007; Diener and Powell, 2010).

It is interesting to note that the maximum peak *P–T* conditions obtained for the Murchison Unit (5.0–6.2 kbar at 530–570 °C) overlap with those inferred from the retrograde *P–T* evolution of the La France Formations (assemblage (B3)). Despite this coincidence, it remains unclear, whether the identical *P–T* conditions in both units were reached at the same time, meaning that prograde heating in the Murchison Unit ceased while rocks of the La France Formation underwent isothermal decompression. In any case, our results show that the three tectono-metamorphic units of the MGB were buried along different apparent geotherms, at different crustal depths, and experienced contrasted metamorphic evolutions before being juxtaposed.

6.2. Timing of the evolution of the MGB

A maximum age for metamorphism in the Murchison Unit is provided by the youngest (meta)volcanic rocks of the Rubbervale Formation of the MGB, dated at ca. 2.97 Ga (Brandl et al., 1996; Poujol et al., 1997; Poujol, 2001). This age is identical within errors to the crystallisation age measured for the syn-deformation granitoid intrusive in the Letaba Shear Zone. It also is indistinguishable from the crystallisation ages of small granitoid bodies emplaced both along the Antimony Line (2970 ± 15 Ma Malati Pump granodiorite, Poujol et al., 1997), and to the south of the MGB (2969 ± 17 Ma Discovery granite, Poujol, 2001). However, it is significantly older that the U–Pb ages of 2752 ± 7 Ma, and rarely of 2910–2920 Ma, obtained from the monazites and xenotimes of the La France micaschists. The older ages of ca. 2.92 Ga which were only obtained from monazite or xenotime inclusions in kyanite, are interpreted to reflect a minimum age for peak metamorphism in the La France Formation. It is worth noting that these ages are within error identical to the emplacement age of the post-deformation Maranda Granite which intruded the southern part of the MGB at 2901 ± 20 Ma (Poujol et al., 1996), pointing to a possible synchronism of magmatism and metamorphism. The younger monazite and xenotime age of 2752 ± 7 Ma may results from re-activation of the MGB related to thermal processes in the Rooiwater Complex of the MGB (minimal intrusion ages of 2740 ± 4 Ma: Poujol et al., 1996), or in the Pietersburg Greenstone Belt (intrusion of the Turfloop granite at ca. 2780 Ma; Henderson et al., 2000).

6.3. Deformation localisation along major tectonic breaks

The break in metamorphic conditions between the Silwana Amphibolites and the Murchison Unit greenschists requires a 9–23 km vertical displacement across the Letaba Shear Zone. Strain increases sharply from moderately deformed greenschists of the Murchison Unit to intensely sheared mylonites, to the amphibolitic gneiss of the Silwana Amphibolites, Furthermore, there is a marked change in deformation patterns across the shear zone, with a high-grade metamorphic flattening fabric, that formed during prograde metamorphism, in the Silwana Amphibolites, and low grade greenschist-facies mylonitic fabric, consistent with a sinistral strike-slip deformation, dominating in the Murchison Unit schists. The fabrics of the Letaba Shear Zone provide evidence for a general transpressive tectonic setting with a top-to-the-south transport. The structures observed in the Letaba Shear Zones suggest that the Silwana Amphibolites, formed at a low crustal level, were juxtaposed to the greenschist- to lower amphibolite-facies rocks of the Murchison Unit along a transpressive shear zone, that was activated due to sustained crustal shortening in a general N–S direction, and that accommodated a large vertical displacement. As crustal shortening and thickening were ongoing, the tectonic regime may have shifted from transpression with a strong reverse component and a top-to-the-south directed transport, to strike-slip shearing. Locally, conjugated SE-trending shear zones were activated together with the predominant NE-trending structures. This late stage of tectonic activity was accompanied by the intrusion of syntectonic granitoids in the Letaba Shear Zone at 2967 ± 7 Ma. These granitoids intruded prior to or during the sinistral slip under greenschist-facies conditions, as is well reflected by the S–C fabrics they display.

The La France Fault displays a number of similarities with the Letaba Shear Zone. It localises an important amount of deformation that accounts for a large vertical displacement of 7–20 km. The fault zone also develops tectonic fabrics consistent with a general transpressive, sinistral regime and a top-to-the-south transport direction. Deformation in the La France Formation shows patterns that are not seen elsewhere in the MGB. Deformation in the fault zone can be correlated with the D_3 deformation within the

Please cite this article in press as: Block, S., et al., The Murchison Greenstone Belt, South Africa: Accreted slivers with contrasting metamorphic conditions. Precambrian Res. (2012), doi:10.1016/j.precamres.2012.03.005

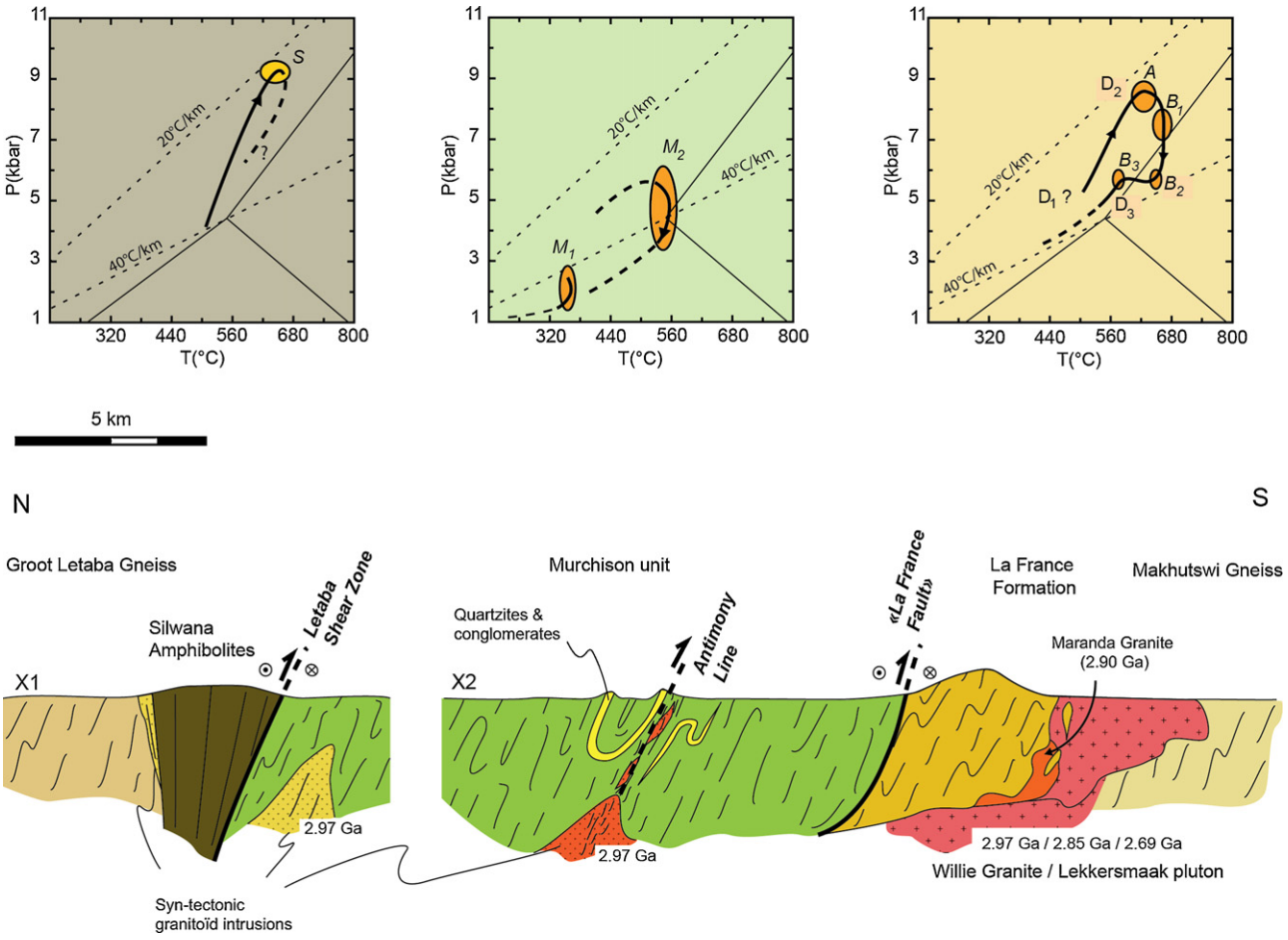

Fig. 9. Interpretative cross-section of the MGB. The MGB has an asymmetric structure, and structural units with distinct metamorphic *P–T* evolutions (see *P–T* diagrams) are juxtaposed along shear zones. The MGB is intruded by both syn-tectonic granitoids at 2.97 Ga and by late-stage granitoids as from 2.90 Ga. Profile lines labelled x_1 and x_2 are located in Fig. 2. Ellipses in the *P–T* diagrams indicate peak metamorphic and retrograde conditions obtained in this study. Dark solid curves represent *P–T* path segments inferred from our results of *P–T* modelling, while dashed curves show presumed portions of the paths. Deformation events (D_1, D_2, D_3) and studied assemblages (S, M_1, M_2, A, B_1, B_2, B_3) are shown along the *P–T* paths.

La France Formation, which is characterised by crenulations and small-wavelength open folds with shallow dipping axes. It post-dates the prograde *P–T* evolution of the La France Formation during the D_1 and D_2 deformation events. The structures of both shear zones illustrate a north-overriding-south relation.

6.4. Model of the tectono-metamorphic evolution of the MGB

The structutral–metamorphic data obtained during this study, along with previous works (e.g., Vearncombe, 1988b; Jaguin et al., 2012) indicate that the different units of the MGB underwent a similar style of penetrative, left-lateral deformation, as well as deformation localisation along the boundaries between units with contrasted metamorphic evolutions (Fig. 9). These features could be accounted for by a sequential evolution model as follows: During the early stage of the evolution of the MGB, shortening was accommodated by crustal thickening due to thrusts and/or transpressive shear zone activation, whereby the different units underwent prograde metamorphism upon burial at lower to mid-crustal level, along moderate apparent geothermal gradients. At some point during the thickening-shortening process, the reverse component of the shear zones attenuated, as they evolved into a strike-slip regime. Shortening was no longer accommodated solely along the primary shear zones that localised deformation, but rather by a penetrative deformation distributed in the rocks of the MGB and surrounding terrains, and homogeneous, moderate crustal thickening, coincident with a metamorphic overprint along a high-*T*, low-*P* apparent geothermal gradient. Our results allow to suggest that the tectonic juxtaposition of the Murchison Unit and La France Formation took place following crustal thickening, after peak metamorphism and partial exhumation of the La France Formation, at which point the latter and a portion of the Murchison Unit underwent a similar metamorphic evolution. The greenschist-facies metamorphism of the Murchison Unit may have been locally overprinted by a slightly higher-grade metamorphism as a consequence of tectonic accretion. Similarly, the final juxtaposition of the Silwana Amphibolites to the rest of the belt occurred after peak metamorphism and exhumation, along a late-stage strike–slip shear zone.

6.5. Implications for Archaean tectonic regimes

It is generally assumed that a higher average geothermal gradient prevailed in Archaean lithospheres relative to modern ones, thus maintaining weak lithospheres unable to withstand thickening (e.g. Rey and Houseman, 2006). Furthermore, a hot, more buoyant sub-continental lithospheric mantle in the Archaean (Griffin et al., 1998) would have inhibited lithosphere thickening by stacking in Archaean collisional belts, as it would have enhanced gravitational potential energy build-up as relief formed. Therefore, in an Archaean context, it is expected that convergence be accommodated by moderate thickening in its early stage, but quickly

Please cite this article in press as: Block, S., et al., The Murchison Greenstone Belt, South Africa: Accreted slivers with contrasting metamorphic conditions. Precambrian Res. (2012), doi:10.1016/j.precamres.2012.03.005

Table 4
Whole rock compositions of the studied samples. The pseudosections of samples from the Murchison Unit ((M1) and (M2)) were built using the whole rock compositions obtained by XRF analysis. Whole rock compositions were recalculated for the other samples to take into account the effect of large porphyroblasts on the composition of an equilibration volume (samples A, B and S) or to correct the effect of accessory phases (sample S, see Appendix A.2).

Whole rock XRF (wt%) – all Fe as Fe^{2+}						Recalculated (wt%)				
	A	B	M1	M2	S		A with Gt cores	A without Gt cores	B	S
SiO_2	75.62	56.51	62.55	92.99	55.68	SiO_2	61.67	64.24	47.00	52.41
Al_2O_3	11.76	17.39	6.96	2.84	12.09	Al_2O_3	15.30	14.73	23.75	12.61
FeO	6.68	8.08	7.13	1.77	16.21	FeO	14.97	12.87	9.54	22.01
MnO	0.04	0.07	0.14	0.10	0.18	MnO	0.51	0.19	0.00	0.52
MgO	1.52	8.45	12.32	0.54	2.77	MgO	1.73	1.75	8.44	2.64
CaO	<D.L.	0.52	5.58	0.07	7.19	CaO	0.46	0.27	0.30	6.08
Na_2O	0.17	0.61	1.27	0.00	2.89	Na_2O	0.12	0.13	0.50	1.16
K_2O	2.64	4.87	0.02	0.58	0.24	K_2O	1.92	2.12	6.41	0.29
TiO_2	0.20	0.58	0.30	0.10	2.04	TiO_2	0.19	0.21	0.63	0.84
P_2O_5	0.17	b.d.l.	0.02	0.00	0.81	H_2O	1.50	1.50	sat.	sat.
LOI	2.35	2.99	3.40	1.06	0.89	Fe_2O_3	0.00	0.00	0.00	0.00
Total	101.15	100.07	99.69	100.05	100.99	Total	98.37	98.01	96.57	98.56

volume forces would become dominant on boundary stresses as gravitational potential energy builds up with increased thickening. Further thickening would be limited, and shortening would be accommodated by lateral escape of material, leading to a steady state where lithospheric thickness remains constant as long as convergence goes on (Rey and Houseman, 2006). This shift between the dominance of boundary stress to volume forces would correspond to the transition from a tectonic regime dominated by oblique thrusting to one marked by strike-slip shearing. It has been recognised in the sequential evolution of a number of Archaean and Palaeoproterozoic orogens (e.g. Kusky and Polat, 1999, in the Superior province, Feybesse et al., 2006 in the Birimian of the West African Craton). On Archaean lithospheres, the threshold controlling this transition would be reached much earlier than in Phanerozoic orogens, thus aborting pronounced thickening.

The cold apparent geothermal gradients inferred for the La France Formation and Silwana Amphibolites of the Murchison Greenstone Belt are comparable to those encountered in collisional belts in Proterozoic and Phanerozoic orogens (Brown, 2009). Burial along low geothermal gradients to about 30 km implies that the lithosphere strength was sufficient to sustain substantial thickening and loading, at least for a period of time. Weakening of the crust could therefore not have occurred before burial of supracrustal sequences at mid-crustal depths. In fact, the *P–T* paths followed by the La France Formation and the Silwana Amphibolites (Fig. 9) inferred from our result are at odds with *P–T* paths expected from metamorphic terrains in hot orogens (Chardon et al., 2009; Gapais et al., 2009). Indeed, *P–T* paths followed by particles in hot orogens are reported to show cooling during decompression, a sign that exhumation is slow enough to enable thermal reequilibration (e.g., *P–T* paths from the Limpopo Belt: Zeh et al., 2004; Millonig et al., 2010). In contrast, the Silwana Amphibolites and La France Formation underwent a relatively fast burial, as is indicated by steep prograde *P–T* vectors, followed, for the latter, by a near-isothermal decompression. These features suggest that isotherms were not parallel to the surface at the time of metamorphism, and consequently exhumation must have been driven by tectonic processes rather than by homogeneous erosion. An intermediate model between typical Archaean and Phanerozoic orogens, where crustal shortening is accommodated by moderate crustal thickening, by deformation localisation along transpressive shear zones, as well as by strike-slip shearing and strain distribution at a regional scale, would better account for the tectono-metamorphic features of the MGB (e.g. Cagnard et al., 2011).

The results of this study echo the metamorphic conditions reported in the south of the older, 3.5–3.2 Ga, Barberton Greenstone Belt (Dziggel et al., 2002; Diener et al., 2005; Moyen et al., 2006). The tectono-metamorphic evolution of the BGB shows similar thermal and mechanical properties of the lithosphere of the Kaapvaal Craton before the formation of the MGB. It therefore seems likely that the Kaapvaal Craton was a rather cold craton compared to other Archaean provinces, thus illustrating certain variability in geodynamic processes within the Archaean.

7. Conclusion

The Murchison Greenstone Belt is a narrow volcano-sedimentary belt comprising various terrains that have been tectonically juxtaposed. The geological units that represent most of the belt underwent lower-greenschist to lower-amphibolite facies metamorphism along a relatively hot, ~30 °C/km apparent geothermal gradient. Two small slivers, at the north-eastern and southern edges of the MGB respectively, were metamorphosed in the higher amphibolite facies. They underwent burial at more than 30 km deep along a relatively cold, ~20 °C/km geotherm. The contact zones between the low-grade and high-grade formations are narrow and sharp. They represent high-strain shear zones that account for major breaks in metamorphic conditions across the belt. While deformation due to shortening is distributed at a regional scale, we show that shortening was also accommodated by localisation of deformation along transpressive, sinistral tectonic contacts accompanied by a top-to-the-south directed transport. This mode of shortening accounted for the final juxtaposition of terrains that were metamorphosed at different crustal levels in the MGB.

The evolution of orogenic belts during shortening, from a tectonic regime dominated by thrusting, thickening, and deformation localisation coincident with prograde metamorphism, to one dominated by strike-slip shearing, lateral flow and deformation distribution accompanied by retrograde metamorphic overprints, is not specific of or restricted to any time period in the geological record. As shown by our results and by studies of the Barberton Greenstone Belt, moderate thickening, high-*P*, moderate- to low-*T* metamorphism and high metamorphic gradients do occur in the Archaean. However, secular changes in the heat budget of the Earth must have affected the relative importance of the different modes of shortening, and probably account for the clearly contrasting tectonic features between the Archaean and Proterozoic eras. In any case, drawing geodynamic models illustrating the differential behaviour of Archaean and Proterozoic orogens should not be done without a consideration for the possible variations of the parameters determining the rheological profiles and, as a consequence, the behaviour of lithospheres at a given age.

Please cite this article in press as: Block, S., et al., The Murchison Greenstone Belt, South Africa: Accreted slivers with contrasting metamorphic conditions. Precambrian Res. (2012), doi:10.1016/j.precamres.2012.03.005

Acknowledgements

The authors thank Michael Brown for his detailed review of the manuscript which contributed to improve significantly the quality of the work. Timothy Kusky and an anonymous reviewer are also thanked for their constructive comments. The participation of Arnaud Villaros through discussions and advice was greatly appreciated. Preliminary results of this study were presented at the 5th International Archaean Symposium in Perth in 2010 thanks to a travel grant provided by Geoconferences (WA) Inc. Armin Zeh also thanks the Deutsche Forschungsgemeinschaft, grant ZE 424/11-1, for financial support.

Appendix A.

A.1. XRF and microprobe analysis

Whole rock chemistry analyses were obtained using an ACME at University of Stellenbosch, South Africa. Complementary analyses were obtained by XRF at the CRPG in Nancy and the at the Ecole des Mines in Saint-Etienne. Mineral chemical analyses were performed on a LEO 140VP scanning electron microscope coupled to a Link ISIS energy dispersive spectrometry system at the University of Stellenbosch. The microscope was operated at 20 kV with a beam current of 120 A and a probe current of 1.5 nA. Acquisition time was set at 50 s and spectra were processed by ZAF corrections and quantified using natural mineral standards. Details of the analytical procedure are provided in Diener et al. (2005). Complementary analyses were carried out at the Electron Microprobe Laboratory at Université Blaise Pascal in Clermont Ferrand, France, using a Cameca SX 100 electron microprobe analyser. Operating conditions were 20 kV, 20 nA, 5–10 μm beam size and counting time of 10 s per element. Natural silicates were used as standards. The analyses carried out in the different laboratories were identical within errors.

A.2. Pseudosection calculation

Pseudosections of rocks from the different terrains of the MGB were constructed using the Peple_X software (Connolly and Kerrick, 1987; Connolly, 2005, 2009) in the Na_2O–CaO–K_2O–FeO–(Fe_2O_3–)MgO–MnO–Al_2O_3–TiO_2–SiO_2–H_2O system, and using the thermodynamic database hp04 of Holland and Powell (1998, revised 2004). The solution models used for the pseudosections are as follows: Bio(TCC) for biotite (Tajcmanová et al., 2009), Chl(HP) for chlorite (Holland et al., 1998), St(HP) for staurolite (Powell et al., 1998), Ctd(HP) for chloritoïd (Holland and Powell), Amph(DPW) for amphibole (Dale et al., 2005), Gt(WPH) for garnet (White et al., 2000), Ilm(WPH) for ilmenite (White et al., 2000), hCrd for cordierite, Mica(CHA1) for titanium bearing white mica (Coggon and Holland, 2002; Auzanneau et al., 2010), Pheng(HP) for phengite (Holland and Powell, 1998), melt(HP) (Holland and Powell, 2001), Pl(h) for plagioclase feldspar (Newton et al., 1980), Kf for potassic feldspar (Waldbaum and Thompson, 1968), Opx(HP) for orthopyroxene (Holland and Powell, 1996), Cpx (HP) for clinopyroxene (Holland and Powell, 1996). Pseudosections were first built by using the bulk rock composition obtained by XRF analysis of each sample. However, this method failed to model accurately the observed assemblages and mineral compositions for samples bearing large, centimetric minerals. For such samples, the bulk rock composition was calculated from the mineral modes and average mineral compositions (e.g. samples A, B and S, Table 4). Modal proportions were estimated by image analysis, and average mineral compositions were obtained by averaging a large number of microprobe analyses acquired on minerals of a single thin section. In order to show the effect of garnet fractionation on the *P–T* pseudosection topology (e.g., sample A), we obtained the total bulk compositions by XRF, as well as the effective bulk composition after porphyroblast garnet growth, by subtracting the core composition of the zoned garnet grains (ca. 10 vol.%) from the total bulk composition, using a method similar to the procedure described by Marmo et al. (2002) and Zeh (2006).

Fe_2O_3 of the bulk rock was estimated by calculating the Fe^{3+} content of normalised structural formulae of analysed minerals (Droop, 1987) and from mineral modes. By applying this procedure we obtained Fe_2O_3 contents of less than 0.05 wt% for all samples. T–X pseudosections were constructed to test the implications of approximating all Fe as Fe^{2+}. In all cases, the consequences in terms of phase compositions and proportions were found to be negligible. Thus, Fe_2O_3 as a system component was ignored during this study, since it is little influential. Other corrections included correcting whole rock Ca content for apatite and calcite in the studied sample, using calcite modal proportions and bulk P_2O_5 composition. As a general rule, oxydes with a bulk rock content <0.05 wt% were ignored for pseudosection calculations.

The prograde history of fluid-bearing mineral assemblages involves the progressive dehydration and fluid loss with rising temperature. The water content of a rock decreases along the prograde path and reaches a minimum at peak metamorphic conditions. Unless a secondary water enrichment occurs (such as documented in sample B), the water content along the retrograde path is assumed to be close to the water content at peak T conditions. As the retrograde assemblages of the investigated samples require a post-peak metamorphism water influx, the *P–T* pseudosections for all samples were constructed under the assumption that water was in excess throughout the entire metamorphic history.

A.3. LA–ICP–MS U–Th–Pb dating

A classic mineral separation procedure has been applied to concentrate zircon grains using the facilities available at Géosciences Rennes. Rocks were crushed and only the powder fraction with a diameter < 250 μm was kept. Heavy minerals were successively concentrated by Wilfley table and heavy liquids. Magnetic minerals were then removed with an isodynamic Frantz separator. Zircon grains were handpicked under a binocular microscope and embedded in epoxy mounts. The grains were then hand-grounded and polished on a lap wheel with a 6 μm and 1 μm diamond suspension successively. Zircons were imaged by cathodoluminescence (CL) using a Reliotron CL system equipped with a digital color camera available in Géosciences Rennes.

U–Th–Pb geochronology of zircon from the sample mur0982 was conducted by in situ laser ablation inductively coupled plasma mass spectrometry (LA–ICPMS) at the Laboratoire Magmas et Volcans in Clermont-Ferrand, France, using a Resonetics M-50E 193 nm ArF excimer NewWave UP213 laser system, with a laser spot diameter of 26 μm and repetition rates of 3 Hz. Data were corrected for U–Pb fractionation and for the mass bias by standard bracketing with repeated measurements of the GJ-1 zircon (Jackson et al., 2004). Data reduction was carried out with the GLITTER® software package developed by the Macquarie Research Ltd. (Jackson et al., 2004). Further information on the instrumentation and the analytical technique is detailed in Hurai et al. (2010).

U–Pb dating of monazite and xenotime was carried out on polished thin sections at Goethe University Frankfurt, Germany. Prior to the U–Pb dating, the internal structures of the grains were investigated by back-scattered electron (BSE) imaging using a ThermoScientific Element 2 sector field ICP–MS coupled to a Resolution M-50 (Resonetics) 193 nm ArF excimer laser (ComPexPro 102F, Coherent) system. Data were acquired in time resolved–peak jumping–pulse counting/analogue mode over 356 mass scans, with a 20 s background measurement followed by 21 s sample

ablation. Laser spot-size for monazite and xenotime are 15 μm, and 23 μm for the standard zircons GJ1. Ablations were performed in a 0.6 L min^{-1} He stream, which was mixed directly after the ablation cell with 0.07 L min^{-1} N_2 and 0.68 L min^{-1} Ar prior to introduction into the Ar plasma of the SF–ICP–MS. All gases had a purity of >99.999% and no homogeniser was used while mixing the gases to prevent smoothing of the signal. Signal was tuned for maximum sensitivity for Pb and U while keeping oxide production, monitored as $^{254}UO/^{238}U$, below 0.5%. The sensitivity achieved was in the range of 9000–14,000 cps/μg g^{-1} for ^{238}U with a 23 μm spot size, at 5.5 Hz and 5–6 J cm^{-2} laser energy. The two-volume ablation cell (Laurin Technic, Australia) of the M50 enables detection and sequential sampling of heterogeneous grains (e.g., growth zones) during time resolved data acquisition, due to its quick response time of <1 s (time until maximum signal strength was achieved) and wash-out (<99.9% of previous signal) time of about 2 s. With a depth penetration of ~0.7 μm s^{-1} and a 0.46 s integration time (4 mass scans = 0.46 s = 1 integration) any significant variation of the Pb/Pb and U/Pb in the μm scale is detectable. Raw data were corrected offline for background signal, common Pb, laser induced elemental fractionation, instrumental mass discrimination, and time-dependent elemental fractionation of Pb/U using an in-house MS Excel© spreadsheet program (Gerdes and Zeh, 2006, 2009). A common-Pb correction based on the interference- and background-corrected ^{204}Pb signal and a model Pb composition (Stacey and Kramers, 1975) was carried out. The ^{204}Pb content for each ratio was estimated by subtracting the average mass 204 signal, obtained during the 20 s baseline acquisition, which mostly results from ^{204}Hg in the carrier gas (c. 180–420 cps), from the mass 204 signal of the respective ratio. For the analyzed sample the calculated common ^{206}Pb contents was mostly <1% of the total ^{206}Pb (see Table 3). For more details about data processing see (Gerdes and Zeh, 2006, 2009). The data were plotted using the software ISOPLOT (Ludwig, 2001).

References

Altermann, W., Nelson, D.R., 1998. Sedimentation rates, basin analysis and regional correlations of three Neoarchaean and Palaeoproterozoic sub-basins of the Kaapvaal Craton, Northern Cape Province, South Africa. J. Afr. Earth Sci. 13, 415–435.

Anhaeusser, C.R., 2006. A reevaluation of Archean intracratonic terrane boundaries on the Kaapvaal Craton, South Africa: Collisional suture zones. GSA Special Papers 40, 193–210.

Auzanneau, E., Schmidt, M.W., Vielzeuf, D., Connolly, J.A.D., 2010. Titanium in phengite: a geobarometer for high temperature eclogites. Contrib. Mineral. Petrol 159, 1–24.

Berthé, D., Choukroune, P., Jegouzo, P., 1979. Orthogneiss, mylonite and non-coaxial deformation of granites: the example of the South Armorican shear zone. J. Struct. Geol. 1, 31–43.

Binns, R.A., Gunthrope, R.J., Groves, D.I., 1976. Metamorphic patterns and development of greenstone belts in the eastern Yilgarn Block, Western Australia. In: Windley, B.F. (Ed.), The Early History of the Earth. Wiley, New York, NY, pp. 303–316.

Bouhallier, H., Choukroune, P., Ballevre, M., 1993. Diapirism, bulk homogenous shortening and transcurrent shearing in the Archaean Dharwar craton: the Holenarsipur area. Precambrian Res. 63, 43–58.

Bouhallier, H., Chardon, D., Choukroune, P., 1995. Strain patterns in Archaean dome-and-basin structures: the Dharwar craton (Karnataka, South India). Earth Planet. Sci. Lett. 135, 57–75.

Brandl, G., Kröner, A., 1993. Preliminary results of single zircon studies from various Archaean rocks of the Northeastern Transvaal. In: Ext. Abstr. 16th International Colloquium of African Geology, Mb, Swaziland, pp. 54–56.

Brandl, G., Jaeckel, P., Kröner, A., 1996. Single zircon age for the felsic Rubbervale Formation, Murchison greenstone belt, South Africa. S. Afr. J. Geol. 99 (3), 229–234.

Brandl, G., Cloete, M., Anhaeusser, C.R., 2006. In: Johnson, M.R., Anhaeusser, C.R., Thomas, R.J. (Eds.), Archaean Greenstone Belts. The Geology of South Africa.

Brown, M., 2007. Metamorphic conditions in orogenic belts: a record of secular change. Int. Geol. Rev. 49, 193–234.

Brown, M., 2009. Metamorphic patterns in orogenic systems and the geological record. In: Cawood, P.A., Kroner, A. (Eds.), Earth Accretionary Systems in Space and Time, vol. 318. Geol. Soc. Lond. Spec. Publ., pp. 37–74.

Brown, M., 2010. Paired metamorphic belts revisited. Gondwana Res. 18, 46–59.

Burger, A.J., Coertze, F.J., 1973. Radiometric age measurements on rocks from southern Africa to the end of 1971. Bull. Geol. Surv. S. Afr. 58, 46-46.

Caby, R., Delor, C., Agoh, O., 2000. Lithologie, structure et métamorphisme des formations birimiennes dans la région d'Odienné (Côte d'Ivoire): rôle majeur du diapirisme des plutons et des décrochements en bordure du craton de Man. J. Afr. Earth Sci. 30, 351–374.

Cagnard, F., Barbey, P., Gapais, D., 2011. Transition between Archaean-type and modern-type tectonics: insights from the Finnish Lapland Granulite Belt. Precambrian Res. 187, 127–142.

Cawood, P., Kröner, A., Collins, W.J., et al., 2009. Accretionary orogens through Earth histoiry. Geol. Soc. Lond. Spec. Publ. 318, 1–36.

Chardon, D., Choukroune, P., Jayananda, M., 1996. Strain patterns, décollement and incipient sagducted greenstone terrains in the Archaean Dharwar craton (South India). J. Struct. Geol. 18, 991–1004.

Chardon, D., Choukroune, P., Jayananda, M., 1998. Sinking of the Dharwar basin (South India): implications for Archaean tectonics. Precambrian Res. 91, 15–39.

Chardon, D., Andronicos, C.L., Hollister, L.S., 1999. Large-scale transpressive shear zone patterns and displacements within magmatic arcs: the Coast Plutonic Complex, British Columbia. Tectonics 18, 278–292.

Chardon, D., Jayananda, M., Chetty, T.R.K., Peucat, J.-J., 2008. Precambrian continental strain and shear zone patterns: South Indian case. J. Geophys. Res. 113, B08402, doi:10.1029/2007JB005299.

Chardon, D., Gapais, D., Cagnard, F., 2009. Flow of ultra-hot orogens: a view from Precambrian, clues for the Phanerozoic. Tectonophysics 477 (3–4), 105–118.

Chopin, C., 1984. Coesite and pure pyrope in high-grade blueschists of the western Alps: a first record and some consequences. Contrib. Mineral. Petrol 86, 107–118.

Choukroune, P., Bouhallier, H., Arndt, N.T., 1995. Soft lithosphere during periods of Archean crustal growth or crustal reworking. In: Coward, M.P., Ries, A.C. (Eds.), Early Precambrian Processes. Geol. Soc. Spec. Publ., 95, pp. 67–86.

Choukroune, P., Ludden, J.N., Chardon, D., Calvert, A.J., Bouhallier, H., 1997. Archaean crustal growth and tectonic processes: a comparison of the Superior Province, Canada and the Dharwar craton, India. In: Burg, J.-P., Ford, M. (Eds.), Orogeny through Time. Geol. Soc. Spec. Publ., 121, pp. 63–98.

Coggon, R., Holland, T.J.B., 2002. Mixing properties of phengitic micas and revised garnet-phengite thermobarometers. J. Metamorph. Geol. 20, 683–696.

Collins, W.J., Vernon, R.H., 1991. Orogeny associated with anticlockwise *P–T–t* paths: evidence from low-*P*, high-*T* metamorphic terranes in the Arunta inlier, central Australia. Geology 19, 835–838.

Compston, W., Kröner, A., 1988. Multiple zircon growth within early Archean tonalitic gneiss from the Ancient Gneiss Complex, Swaziland. Earth Planet. Sci. Lett. 87, 13–28.

Connolly, J.A.D., 2005. Computation of phase equilibria by linear programming. A tool for geodynamic modeling and its application to subduction zone decarbonation. Earth Planet. Sci. Lett. 236, 524–541.

Connolly, J.A.D., 2009. The geodynamic equation of state: what and how. Geochem. Geophys. Geosyst., 10.

Connolly, J.A.D., Kerrick, D.M., 1987. An algorithm and computer program for calculating composition phase diagrams. CALPHAD 11, 1.

Condie, K.C., Kröner, A., 2008. When did plate tectonics begin? Evidence from the geologic record. In Condie, K.C., Pease, V., (Eds.), When Did Plate Tectonics Begin on Planet Earth? Geological Society of America Special Paper 440, 281–294. doi:10.1130/2008.2440.(14).

Dale, J., Powell, R., White, R.W., Elmer, F.L., Holland, T.J.B., 2005. A thermodynamic model for Ca–Na clinoamphiboles in Na_2O–CaO–FeO–MgO–Al_2O_3–SiO_2–H_2O–O for petrological calculations. J. Metamorph. Geol. 23, 771–791.

Diener, J.F.A., Stevens, G., Kisters, A.F.M., Poujol, M., 2005. Metamorphism and exhumation of the basal parts of the Barberton greenstone belt, South Africa: constraining the rates of Mesoarchaean tectonism. Precambrian Res. 143, 87–112.

Diener, J.F.A., Powell, R., White, R.W., Holland, T.J.B., 2007. A new thermodynamic model for clino- and orthoamphiboles in the system Na_2O–CaO–FeO–MgO–Al_2O_3–SiO_2–H_2O–O. J. Metamorph. Geol. 25, 631–656.

Diener, J.F.A., Powell, R., 2010. Influence of ferric iron on the stability of mineral assemblages. J. Metamorph. Geol. 28, 599–613.

De Wit, M., 2004. Archean greenstone belts do contain fragments of ophiolites. In: Condie, K.C., Kusky, T.M. (Eds.), Precambrian Ophiolites and Related Rocks, Developments in Precambrian Geology, vol. 13, Elsevier Publishers.

Droop, G.T.R., 1987. A general equation for estimating Fe^{3+} concentrations in ferromagnesian silicates and oxides from microprobe analyses, using stoichiometric criteria. Mineralogical Magazine 51 (3), 361, 431–435.

Du Plessis, C.P., 1990. Tectonism along the Thabazimby-Murchison lineament. Ph.D. Thesis (unpubl.), Univ Witwatersrand, Johannesburg, 243 pp.

Dziggel, A., Stevens, G., Poujol, M., Anhaeusser, C.R., Armstrong, R.A., 2002. Metamorphism of the granite–greenstone terrane south of the Barberton greenstone belt, South Africa: an insight into the tectono-thermal evolution of the 'lower' portions of the Onverwacht Group. Precambrian Res. 114, 221–247.

England, P.C., Thompson, A.B., 1984. Pressure–temperature–time paths of regional metamorphism. Part I. Heat transfer during the evolution of regions of thickened continental crust. J. Petrol. 25, 894–928.

Ernst, W.G., 1973. Blueschist metamorphism and *P–T* regimes in active subduction zones. Tectonophysics 17, 255–272.

Ernst, W.G., 1975. Systematics of large-scale tectonics and age progressions in Alpine and circum – Pacific blueschist belts. Tectonophysics 26, 229–246.

Ernst, W.G., 1988. Tectonic history of subduction zones inferred from retrograde blueschist *P–T* paths. Geology 16, 1081–1084.

Evans, T.P., 2004. A method for calculating effective bulk composition modification due to crystal fractionation in garnet bearing schist: implications for isopleth thermobarometry. J. Metamorph. Geol. 22, 547–557.

Please cite this article in press as: Block, S., et al., The Murchison Greenstone Belt, South Africa: Accreted slivers with contrasting metamorphic conditions. Precambrian Res. (2012), doi:10.1016/j.precamres.2012.03.005

Feybesse, J.-L., Billa, M., Guerrit, C., Duguey, E., Lescuyer, J.-L., Milesi, J.P., Bouchot, V., 2006. The paleoproterozoic Ghanaian province. Geodynamic model and ore controls, including regional stress modeling. Precambrian Res. 149, 149–196.
Florence, F.P., Spear, F.S., 1991. Effects of diffusional modification of garnet growth zoning on *P–T* path calculations. Contrib. Mineral. Petrol. 107, 487–500.
Gapais, D., Cagnard, F., Gueydan, F., Barbey, P., Ballèvre, M., 2009. Mountain building and exhumation processes through time: inferences from nature and models. Terra Nova 21, 188–194.
Gerdes, A., Zeh, A., 2006. Combined U-Pb and Hf isotope LA-(MC)ICP-MS analyses of detrital zircons: Comparison with SHRIMP and new constraints for the provenance and age of an Armorican metasediment in Central Germany. Earth Planet Sci. Lett. 249, 47–61.
Gerdes, A., Zeh, A., 2009. Zircon formation versus zircon alteration: new insights from combined U–Pb and Lu–Hf in situ LA-ICP-MS analyses, and consequences for the interpretation of Archaean zircon from the Central Zone of the Limpopo Belt. Chem. Geol. 261, 230–243.
Good, N., De Wit, M.J., 1997. The Thabazimbi–Murchison Lineament of the Kaapvaal craton, South Africa: 2700 Ma of episodic deformation. J. Geol. Soc. 154 (1), 93–97.
Grambling, J.A., 1986. Crustal thickening during Proterozoic metamorphism and deformation in New Mexico. Geology 14, 149–152.
Griffin, W.L., O'Reilly, S.Y., Ryan, C.G., Gaul, O., Ionov, D., 1998. Secular variation in the composition of the subcontinental lithospheric mantle. In: Braun, J., et al. (Eds.), Structure and Evolution of the Australian Continent, Geodynamics Series, 26, American Geophysical Union, pp. 1–25.
Henderson, D.R., Long, L.E., Barton, J.M., 2000. Isotopic ages and chemical and isotopic compositions of the Archaean Turfloop Batholith, Pietersburg granite-greenstone terrane, Kaapvaal Craton, South Africa. S. Afr. J. Geol. 103 (1), 38–46.
Hurai, V., Paquette, J.-L., Huraiová, M., Konečný, P., 2010. U–Th–Pb geochronology of zircon and monazite from syenite and pincinite xenoliths in Pliocene alkali basalts of the intra-Carpathian back-arc basin. J. Volcanol. Geotherm. Res. 198, 275–287.
Holland, T., Powell, R., 1996. Thermodynamics of order-disorder in minerals. 2. Symmetric formalism applied to solid solutions. Am. Min. 81, 1425–1437.
Holland, T.J.B., Powell, R., 1998. An internally consistent thermodynamic data set for phases of petrological interest. J. Metamorph. Geol. 16, 309–343.
Holland, T., Baker, J., Powell, R., 1998. Mixing properties and activity–composition relationships of chlorites in the system $MgO–FeO–Al_2O_3–SiO_2–H_2O$. Eur. J. Mineral. 10, 395–406.
Holland, T., Powell, R., 2001. Calculation of phase relations involving haplogranitic melts using an internally consistent thermodynamic dataset. J. Petrol. 42, 673–683.
Jaguin, J., Gapais, D., Poujol, M., Boulvais, P., Moyen, J.F., 2012. The Murchison Greenstone Belt (South Africa): a general tectonic framework. S. Afr. J. Geol. 115 (1), 65–76.
Jackson, S.E., Pearson, N.J., Griffin, W.L., Belousova, E.A., 2004. The application of laser ablation-inductively coupled plasma-mass spectrometry to in situ U–Pb zircon geochronology. Chem. Geol. 211, 47–69.
Kamo, S.L., Davis, D.W., 1994. Reassessment of Archaean crustal development in the Barberton Moutain Land, South Africa, based on U–Pb dating. Tectonics 13 (1), 167–192.
Kisters, A.F.M., Stevens, G., Dziggel, A., Armstrong, R.A., 2003. Extensional detachment faulting and core-complex formation in the southern Barberton granite-greenstone terrain. South Africa: evidence for a 3.2 Ga orogenic collapse. Precambrian Res. 127, 355–378.
Komiya, T., Maruyama, S., Masuda, T., Nobda, S., Hayashi, M., Okamoto, K., 1999. Plate tectonics at 3.8–3.7 Ga: field evidence from the Isua Accretionary Complex, southern West Greenland. J. Geol. 107, 515–554.
Komiya, T., Hayashi, M., Maruyama, S., Yurimoto, H., 2002. Intermediate-P/T type Archaean metamorphism of the Isua supracrustal belt: implications for secular change of geothermal gradients at subduction zones and for Archaean plate tectonics. Am. J. Sci. 302, 806–826.
Kröner, A., Byerly, G.R., Lowe, D.R., 1991. Chronology of early Archean granite–greenstone evolution in the Barberton Moutain Land, South Africa, based on precise dating by single grain zircon evaporation. Earth Planet. Sci. Lett. 103, 41–54.
Kröner, A., Hegner, E., Byerly, G.R., Lowe, D.R., 1992. Possible terrane identification in the early Archaean Barberton greenstone belt, South Africa, using single zircon geochronology. EOS Trans. AGU, Fall Meeting Suppl. 73 (43), 616.
Kröner, A., Tegtmeyer, A., 1994. Gneiss–greenstone relationships in the Ancient Gneiss Complex of southwestern Swaziland, southern Africa, and implications for early crustal evolution. Precambrian Res. 67, 109–139.
Kröner, A., Hegner, E., Wendt, J.I., Byerly, G.R., 1996. The oldest part of the Barberton granitoid–greenstone terrain, South Africa: evidence for crust formation at 3.5 and 3.7 Ga. Precambrian Res. 78, 105–124.
Kröner, A., Jaeckel, P., Brandl, G., 2000. Single zircon ages for felsic to intermediate rocks from the Pietersburg and Giyani greenstone belts and bordering granitoid orthogneisses, northern Kaapvaal Craton, South Africa. J. Afr. Earth Sci. 30 (4), 773–793.
Kusky, T.M., 1991. Structural development of an Archean orogen, western Point Lake, Northwest Territories. Tectonics 10 (4), 820–841.
Kusky, T.M., Vearncombe, J.R., 1997. Structural aspects. In: de Wit, M., Ashwal, L.D. (Eds.), Greenstone Belts. Oxford Monogr. Geol. Geophys. 35, 91–124.
Kusky, T.M., Polat, A., 1999. Growth of granite–greenstone terranes at convergent margins, and stabilization of Archean cratons. Tectonophysics 305, 43–73.
Kusky, T.M., Jianghai, Li, Tucker, R.T., 2001. The Archean Dongwanzi ophiolite complex, North China Craton: 2.505 Billion Year Old Oceanic Crust and Mantle. Science 292, 1142–1145.
Ludwig, K.R., 1998. On the treatment of concordant uranium–lead ages. GeCA 62 (4), 665–676.
Ludwig, K.R., 2001. Isoplot/Ex, rev. 2.49: a geochronological toolkit for Microsoft Excel. Berkeley Geochronology Center, Spec. Publ. 1a, 55 p.
Marmo, B.A., Clarke, G.L., Powell, R., 2002. Fractionation of bulk rock composition due to porphyroblast growth: effects on eclogite facies mineral equilibria, Pam Peninsula, New Caledonia. J. Metamorph. Geol. 20, 151–165.
Millonig, L., Zeh, A., Gerdes, A., Klemd, R., 2008. Neoarchaean high-grade metamorphism in the Central Zone of the Limpopo Belt (South Africa): combined petrological and geochronological evidence from the Bulai pluton. Lithos 103, 333–351.
Millonig, L., Zeh, A., Gerdes, A., Klemd, R., Barton, J.M., 2010. Decompressional heating of the Mahalapye complex (Limpopo Belt, Botswana): a response to Palaeoproterozoic magmatic underplating? J. Petroleum 51 (3), 703–729.
Mints, M.V., Belousova, E.A., Konilov, A.N., Natapov, L.N., Shchipansky, A.A., Griffin, W.L., O'Reilly, S.Y., Dokukina, K.A., Kaulina, T.V., 2010. Mesoarchean subduction processes: 2.87 Ga eclogites from the Kola Peninsula, Russia. Geology 38, 739–742.
Miyashiro, A., 1961. Evolution of metamorphic belts. J. Petrol. 2, 277–311.
Moyen, J.F., Stevens, G., Kisters, A., 2006. Record of mid-Archean subduction from metamorphism in Barberton Terrain, South Africa. Nature 442, 559–562.
Newton, R.C., Charlu, T.V., Kleppa, O.J., 1980. Thermochemistry of the high structural state plagioclases. GeCA 44, 933–941.
Park, R.G., 1982. Archaean tectonics. Geol. Rundsch. 71, 22–37.
Percival, J.A., Fountain, D.M., Salisbury, M.H., 1992. Exposed crustal cross sections as windows on the lower crust. In: Fountain, D.M., Arculus, R.J., Kay, R.W. (Eds.), Continental Lower Crust. Elsevier, Amsterdam, pp. 317–362.
Percival, J., 1994. Archean high-grade metamorphism. In: Condie, K.C. (Ed.), Archean Crustal Evolution. Developments in Precambrian Geology, vol. 11. Elsevier, pp. 357–410.
Platt, J.P., Visser, R.L.M., 1980. Extensional structures in anisotropic rocks. J. Struct. Geol. 2, 397–410.
Poujol, M., Robb, L.J., Respaut, J.P., Anhaeusser, C.R., 1996. 3.07–2.97 Ga greenstone belt formation in the northeastern Kaapvaal Craton: implications for the origin of the Witwatersrand Basin. Econ. Geol. 91 (8), 1455–1461.
Poujol, M., Respaut, J.P., Robb, L.J., Anhaeusser, C.R., 1997. New U–Pb and Pb–Pb Data on the Murchison Greenstone Belt, South Africa and their Implications for the Origin of the Witwatersrand Basin, vol. 319, EGRU, Johannesburg.
Poujol, M., Robb, L.J., 1999. New U-Pb zircon ages on gneisses and pegmatite from South of the Murchison greenstone belt, South Africa. S. Afr. J. Geol. 102 (2), 93–97.
Poujol, M., 2001. U–Pb isotopic evidence for episodic granitoid emplacement in the Murchison greenstone belt, South Africa. J. Afr. Earth Sci. 33, 155–163.
Powell, R., Holland, T.J.B., Worley, B., 1998. Calculating phase diagrams involving solid solutions via non-linear equations, with examples using THERMOCALC. J. Metamorph. Geol. 16, 577–588.
Reno, B.L., Brown, M., Kobayashi, O.T., Nakamura, E., Piccoli, P.M., Trouw, R.A.J., 2009. Eclogite–high-pressure granulite metamorphism records early collision in West Gondwana: New data from the Southern Brasília Belt, Brazil. J. Geol. Soc. Lond. 166, 1013–1032.
Rey, P.F., Houseman, G., 2006. Lithospheric scale gravitational flow: the impact of body forces on orogenic processes from Archaean to Phanerozoic. In: Buiter, S.J.H., Schreurs, G. (Eds.), Analogue and Numerical Modelling of Crustal Scale Processes. Geol. Soc. Lond. Spec. Publ. 253, pp. 153–167.
Robb, L.J., Brandl, G., Anhaeusser, C.R., Poujol, M., 2006. In: Johnson, M.R., Anhaeusser, C.R., Thomas, R.J. (Eds.), Archaean Granitoid Intrusions. The Geology of South Africa, 2006.
Saha, L., Pant, N.C., Pati, J.K., Upadhyay, D., Berndt, J., Bhattacharya, A., Satynarayanan, M., 2011. Neoarchean high-pressure margarite–phengitic muscovite–chlorite corona mantled corundum in quartz-free high-Mg, Al phlogopite–chlorite schists from the Bundelkhand craton, north central India. Contrib. Mineral. Petrol. 161, 511–530.
Schwartz-Schampera, U., Terblanche, H., Oberthür, T., 2010. Volcanic-hosted massive sulfide deposits in the Murchison greenstone belt, South Africa. Mineral. Depos. 45 (2), 113–145.
Sizova, E., Gerya, T., Brown, M., Perchuk, L.L., 2010. Subduction styles in the Precambrian: insight from numerical experiments. Lithos 116, 209–222, 3-4.
Smith, D.C., 1984. Coesite in clinopyroxene in the Caledonides and its implications for geodynamics. Nature 310, 641–644.
South African Committee for Stratigraphy, 1980. The Murchison sequence. In: C.L.E. Hart (Ed.), Stratigraphy of South Africa. Part 1. Lithostratigraphy of the 560 Republic of South Africa, South West Africa/Namibia and the Republics of 561 Bophuthatswana, Transkei and Venda. South Africa Geological Survey Handbook, 45–562 (Chapter 2.3).
Stacey, J.S., Kramers, J.D., 1975. Approximation of terrestrial lead isotope evolution by a two-stage model. Earth Planet. Sci. Lett. 26 (2), 207–221.
Stüwe, K., 1997. Effective bulk composition change due to cooling: a model predicting complexities in retrograde reaction textures. Contrib. Mineral. Petrol. 129, 43–52.
Tajcmanová, L., Connolly, J.A.D., Cesare, B., 2009. A thermodynamic model for titanium and ferric iron solution in biotite. J. Metamorph. Geol. 27, 153–164.

Please cite this article in press as: Block, S., et al., The Murchison Greenstone Belt, South Africa: Accreted slivers with contrasting metamorphic conditions. Precambrian Res. (2012), doi:10.1016/j.precamres.2012.03.005

Van Kranendonk, M.J., Hickman, A.H., Smithies, R.H., Nelson, D.N., Pike, G., 2002. Geology and tectonic evolution of the Archaean North Pilbara terrain. Pilbara Craton, Western Australia. Econ. Geol. 97, 695–732.

Vearncombe, J.R., Barton, J.M., Walsh, K.L., 1987. The Rooiwater Complex and associated rocks, Murchison granitoid-greenstone terrane, Kaapvaal Craton. S. Afr. J. Geol. 90, 361–377.

Vearncombe, J.R., Cheshire, P.E., De Beer, J.H., Killick, A.M., Mallinson, W.S., McCourt, S., et al., 1988a. Structures related to the Antimony line, Murchison schist belt, Kaapvaal craton, South Africa. Tectonophysics 154 (3-4), 285–308.

Vearncombe, J.R., 1988b. Structure and metamorphism of the Archean Murchison Belt, Kaapvaal Craton, South Africa. Tectonics 7 (4), 761–774.

Vearncombe, J.R., Barton, J.M., Cheshire, P.E., De Beer, J.H., Stettler, E.H., Brandl, G., 1992. Geology, geophysics and mineralization of the Murchison Schist Belt. Rooiwater complex and surrounding granitoids. Mem. Geol. Surv. S. Afr. 81, 139.

Viljoen, M.J, Van Vuuren, C.J.J., Pearton, P.N., Minnitt, R.C.A., Muff, R., Cillier, P., 1978. The regional geological setting of mineralization in the Murchison Range with particular reference to antimony. In: Verwoerd, W.J. (Ed.), Mineralization in Metamorphic Terranes. Spec. Publ. Geol. Soc. S. Afr., 1, 661–668.

Volodichev, O., Slabunov, A., Bibikova, E., Konilov, A., Kuzenko, T., 2004. Archean eclogites in the Belomorian mobile belt, Baltic Shield. Petrology 12, 540–560.

Waldbaum, D.R., Thompson, J.B., 1968. Mixing properties of sanidine crystalline solutions. 2. Calculations based on volume data. Am. Min. 53, 2000.

Watts, A.B., Burov, E.B., 2003. Lithospheric strength and its relationship to the elastic and seismogenic layer thickness. Earth Planet. Sci. Lett. 213, 113–131.

White, R.W., Powell, R., Holland, T.J.B., Worley, B.A., 2000. The effect of TiO_2 and Fe_2O_3 on metapelitic assemblages at greenschist and amphibolite facies conditions: mineral equilibria calculations in the system K_2O–FeO–MgO–Al_2O_3–SiO_2–H_2O–TiO_2–Fe_2O_3. J. Metamorph. Geol. 18, 497–511.

Zeh, A., 2001. Inference of a detailed *P–T* path from *P–T* pseudosections using metapelitic rocks of variable composition from a single outcrop, Shackleton Range, Antarctica. J. Metamorph. Geol. 19, 329–350.

Zeh, A., Klemd, R., Buhlmann, S., Barton, J.M., 2004. Pro- and retrograde *P–T* evolution of granulites of the Beit Bridge Complex (Limpopo Belt, South Africa): constraints from quantitative phase diagrams and geotectonic implications. J. Metamorph. Geol. 22, 79–95.

Zeh, A., 2006. Calculation of garnet fractionation in natural metamorphic rocks, with application to a flat-top, Y-rich garnet population from the Ruhla Crystalline Complex, Central Germany. J. Petrol. 47, 2335–2356.

Zeh, A., Gerdes, A., Barton, J.M., 2009. Archean accretion and crustal evolution of the Kalahari Craton – the Zircon Age and Hf Isotope Record of Granitic Rocks from Barberton/Swaziland to the Francistown Arc. J. Petrol. 50, 933–966.

Please cite this article in press as: Block, S., et al., The Murchison Greenstone Belt, South Africa: Accreted slivers with contrasting metamorphic conditions. Precambrian Res. (2012), doi:10.1016/j.precamres.2012.03.005

Datation et caractérisation de processus minéralisateurs à l'Archéen : Application à l'Antimony Line, Ceinture de Roches Vertes de Murchison, Afrique du Sud

Les circulations de fluides dans la croûte sont les vecteurs de mobilités élémentaires dont une des conséquences est la concentration de métaux et la genèse de gisements. Ces fluides circulent dans les zones de déformation où ils modifient la composition des roches encaissantes. Dans la ceinture archéenne de roches vertes de Murchison (Afrique du Sud), l'Antimony Line est une zone déformée qui a été le siège de circulations de fluides minéralisateurs en Sb-Au.
Pour caractériser les processus minéralisateurs, des données pétro-géochimiques, en particulier en isotopes stables et inclusions fluides, ont été associées à la datation multi-méthode (U-Th-Pb, Pb-Pb et Ar-Ar) des corps minéralisés et de leur encaissant au cœur et autour de l'Antimony Line. L'étude structurale de la région souligne le caractère distribué de la déformation. La ceinture a ainsi subi une phase majeure de collision d'arc, associée à un magmatisme important vers 2.97 Ga, contemporain d'une minéralisation en Au (±Sb) qui pourrait être responsable d'une phase de pré-enrichissement en Sb. La minéralisation principale en Sb est la conséquence de la circulation d'un fluide métamorphique à H_2O-CO_2, à 2-3 kbar et 350-450°C. L'albitisation de granitoïdes intrusifs dans l'Antimony Line, datée à 2.8 Ga, est génétiquement liée à cette circulation, laquelle s'inscrit donc dans l'histoire tectono-métamorphique tardive de la ceinture et est contemporaine de la mise en place de leucogranites sur la bordure sud. Ces résultats illustrent la pertinence du couplage pétro-géochimie/géochronologie pour la compréhension globale d'un système métallogénique.

Terre, Écosystèmes et Sociétés

Observatoire des Sciences de l'Univers de Rennes

Dating and characterizing mineralization in Archean times: Example of the Antimony Line, Murchison Greenstone Belt, South Africa

Fluid flows through the crust result in the mobilization of elements that can, in turn, generate metal concentrations and the formation of ore bodies. The circulations of such fluids are mainly localized in zones affected by localized deformation, where they modify the chemical composition of the host lithologies. In the Archean Murchison Greenstone Belt (Kaapvaal Craton, South Africa), the Antimony Line is a brittle-ductile structure affected by the circulation of Sb-Au mineralizing fluids.
In order to characterize the ore-forming processes, we combined a petro-geochemical study, that focused on stable isotopes and fluid inclusions in particular, with a multi-method dating (U-Th-Pb, Pb-Pb and Ar-Ar) of the ore bodies and their host rocks in and around the Antimony Line. Furthermore, our structural study emphasizes the distributed character of the belt deformation. The Murchison Greenstone Belt experienced a major episode of arc collision and related magmatism at ca 2.97 Ga, contemporaneous with an Au(±Sb) mineralization that may be responsible for a pre-enrichment in Sb. The main Sb mineralization event must be related to the circulation of a metamorphic, H_2O-CO_2–dominated fluid at 2-3 kbar and 350-450°C. The albitization of the granitoids intrusive into the Antimony Line is dated at 2.8 Ga and is genetically linked to this fluid flow, which took place during the late tectono-metamorphic history of the belt contemporaneously with the emplacement of leucogranites along the southern border of the belt. Therefore, this study further demonstrates that coupling petro-geochemistry and geochronology is a powerful tool in order to study and characterize a given metallogenic system.

Illustration de couverture : vue vers le nord-nord-ouest de la colline de Witkop et de la veine géante de quartz, depuis le pluton de Baderoukwe.

GEOSCIENCES Rennes

UNIVERSITÉ DE RENNES 1